28TH European Young Geotechnical Engineers Conference

EYGEC 2024



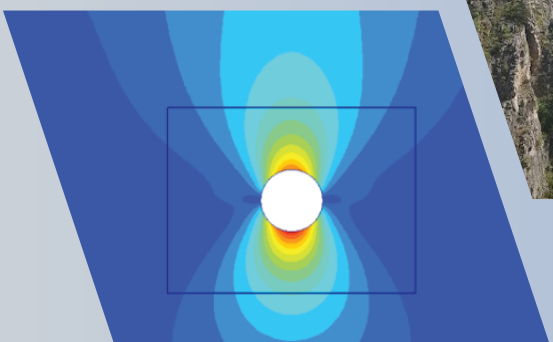


Demir Kapija, Macedonia









June 25 - June 29 2024

Proceedings of the 28th European Young Geotechnical Engineers Conference – EYGEC 2024
Demir Kapija, R. N. Macedonia

Editor

Igor Peševski
President of the Macedonian Association for Geotechnics

Proceedings of the 28th European Young Geotechincal Engineers Conference – EYGEC 2024

Издавач:
Друштво за геотехника на Македонија, седиште Партизански одреди бр.24, 1000 Скопје.

Илустратор: Тамара Јовановска

Компјутерска подготовка: Ангела Маринковска

Тираж: 100 примероци

The 28th European Young Geotechnical Engineers Conference – EYGEC 2024 is organized by the Macedonian Association for Geotechnics (MAG), with the support of the International Society for Soil Mechanics and Geotechnical Engineering (ISSMGE). The conference was held in Demir Kapija, R.N. Macedonia in period 25-29.06.2024

© 2024 Macedonian Association for Geotechnics, Skopje, R.N. Macedonia

All rights reserved. No part of this publication or the information contained herein may be reproduced, stored in a retrieval system, or transmitted in any form or by means, electronic, mechanical, by photocopying, recording otherwise, without written prior permission from the publishers.

Published by: Macedonian Association for Geotechnics
Copies 100
ISBN: 978-608-4510-61-1

TABLE OF CONTENTS

FOUNDATION SYSTEM OPTIMIZATION OF A HIGH-BAY WAREHOUSE USING FINITE ELEMENT MODELLING 1
Tamás Agárdi, Zsolt Szilvágyi

STATISTICAL ANALYSIS OF SITE INVESTIGATION DATA TO FIND IRREGULAR ZONES AND LAYERS 9
Maedeh Alinejad, Anders Beijer Lundberg

CLAY EXPERIMENTAL STUDY AND CRACKING MECHANISMS UNDER CONTROLLED DESICCATION PATHS USING DIGITAL IMAGE CORRELATION 17
Lamine Ighil Ameur, and Mahdia Hattab

LIQUEFACTION RESISTANCE OF SAND – FLY ASH MIXTURES 23
Elena Angelova , Vlatko Sheshov, Julijana Bojadjieva, Kemal Edip, Toni Kitanovski, Dejan Ivanovksi

ASSESSMENT OF THE IMPACT OF SOIL DEGRADATION DUE TO PILE DRIVING ON SLOPE STABILITY IN COHESIVE SOIL CONDITIONS 29
Yeganeh Attari, Gudmund Reidar Eiksund

SUSTAINABLE IMPROVEMENT OF A FINE SAND USING MICROBIALLY INDUCED CALCITE PRECIPITATION 34
Hanieh Babaeizad

THERMOGRAVIMETRIC ANALYSIS AS A USEFUL TOOL FOR ADSORBED WATER ASSESSMENT: CASE OF BENTONITE 42
S. Babiy, A. Tuttolomondo, L.Laloui

DETERMINATION OF FOUNDATION DAMPING COEFFICIENTS FOR MONOPILE SUPPORTED OFFSHORE WIND TURBINES 48
Mohammed Barzan, David Igoe

FIELD DATA BASED NUMERICAL ANALYSIS OF SAND BOIL REACTIVATION ALONG RIVER EMBANKMENTS 56
Ilaria Bertolini

CPTU AND MASW INVESTIGATION RESULTS FROM THE SISAK-MOSLAVINA COUNTY AREA AFTER THE PETRINJA EARTHQUAKE AND COMPARISON WITH THE GLOBAL EXPERIENCES 64
Marko Boričević, Pero Šiša, Igor Sokolić

INFLUENCE OF MSW LEACHATE CONTAMINATION DEGREE ON SOIL SHEAR BEHAVIOR 72
Feten Chihi, Gabriella Varga

COMPARISON DESIGN-MONITORING A DIAPHRAGM WALL FOR A DEEP EXCAVATION UP TO 11.60M 77
Ciumeică Daniel

1915 ÇANAKKALE BRIDGE EUROPEAN ANCHOR BLOCK EXCAVATION PROJECT: A CASE STUDY 85
Ahmet Dinc, Alp Gokalp, Senol Adatepe

IMPROVING AXIAL PILE DESIGN THROUGH FULL-SCALE FIELD TESTING AND FIBRE OPTIC SENSING 94
Kevin J. Duffy

CASE STUDY ON THE NUMERICAL MODELLING OF A CFA ENERGY PILE .. 100
Ugur Can Erginag, Semra Polat, Mert Guner, Melis Sutman, Ozer Cinicioglu

PARAMETER OPTIMIZATION FOR CONSTITUTIVE SOIL MODELS USING SUPERVISED MACHINE LEARNING 106
Haris Felić, Islam Marzouk, Franz Tschuchnigg

WATER RETENTION CHARACTERISTICS AND DRAINED SHEAR STRENGTH OF SOIL TREATED WITH NEWLY DEVELOPED SOIL CONDITIONERS 115
Barbara Fortuna, Alessandro Sorze, Francesco Valentini, Jasna Smolar

KINEMATIC EFFECTS ON INTERACTION DIAGRAMS FOR CAISSON FOUNDATIONS 123
Domenico Gaudio, Cristian Passeri, Sebastiano Rampello

AUTOMATED SIMPLE TELL-TALE DEVICE FOR DETECTING LOSS OF BACKFILL SOIL THROUGH JOINTS OF QUAYS 129
Carlos Laina-Gómez, Enrique Asanza-Izquierdo

DIRECT AND ALTERNATIVE METHODS FOR DETERMINING THE MAXIMUM SHEAR MODULUS (G_0) OF SOILS 135
Kristina Ilieva

GEOTECHNICAL MODELLING OF ROCK MASS - HYDROTECHNICAL STRUCTURES INTERACTION 143
Tamara Jovanovska

SHEAR MODULUS REDUCTION AND MATERIAL DAMPING CURVES MEASURED WITH RESONANT COLUMN DEVICE ON COHESIVE SOILS FROM THE LJUBLJANA MARSH 150
Timotej Jurček, Boštjan Pulko, Matej Maček

ADVANTAGES OF 3D FEM MODELLING AND BIM MODELLING FOR UNDERGROUND STRUCTURES 159
Kristóf Kelemen

A LIQUEFACTION SIMULATION FOR THE 1987 WILDLIFE CASE STUDY USING THE EXTENDED EQUIVALENT LINEAR MODEL (X-ELM) **167**
Samer Abou Kheir, Ziad Kteich, and Pierre Labbe

EVOLUTION OF THE MICROSTRUCTURAL AND CHEMICAL PROPERTIES OF THE CO_2-AGED BANCO VERDE SANDSTONE **175**
Cecilia B. Laskowski, Diego G. Manzanal, Mauro Muñiz-Menéndez, Sandra G. Orlandi, José O. Allard

OPTIMISATION OF TENSAR'S T-VALUE DESIGN METHOD FOR WORKING PLATFORMS **184**
Sandro A.R Lesar, Leo Kuljanski

EXPERIMENTAL INVESTIGATION ON THE HYDRO-MECHANICAL RESPONSE OF A SHALE SUBJECTED TO GAS INVASION **192**
Qazim Llabjani, Alessio Ferrari, Paul Marschall, Lyesse Laloui

MICROSTRUCTURE OF COMPACTED TRANSITIONAL SOIL **198**
Justyna Markowska

AUTOMATED GENERATION OF GROUND MODEL INCORPORATING SOIL SPATIAL VARIABILITY **206**
Ksenija Mićić, Zehao Ye, Miloš Marjanović, Jelena Ninić

SOIL LIQUEFACTION MITIGATION BY APPLYING THE DSM TECHNIQUE BELOW THE FOUNDATIONS OF A SILO BASE **214**
Nikolay Y. Milev

ANALYSES OF PILE DRIVING IMPACT USING VIBRATION MONITORING METHOD **223**
Diyar Mukhanov, Askar Zhussupbekov, Abdulla Omarov, Abzal Khamzin, Gulnaz Zhairbaeva

GEOTECHNICAL PERSPECTIVE ON SUSTAINABLE CONSTRUCTION IN SWEDEN **229**
David Nguyen

INVESTIGATIONS OF TESTING MICROPILES FOR STATIC LOADING **235**
M.Nurgozhina, A.Zhussupbekov, A. Omarov, A. Issakulov, D. Mukhanov

ADAPTABILITY OF FLOOD EMBANKMENTS TO CLIMATE CHANGE **240**
Milena Raković, Veljko Pujević, Sanja Jocković, Nikola Obradović

GEOTECHNICAL CHARACTERIZATION OF THE ROCKMASS SURROUNDING THE ALJUSTREL MINING COMPOUND **248**
Tiago Rodrigues

PHYSICAL AND MECHANICAL PROPERTIES OF COHESIVE SOIL GEOPOLYMERIZED WITH THE FLY ASH **256**
Luiza I. Rzepczyńska

NUMERICAL ANALYSIS OF UNDER-REAMED PILE IN LAYERED CLAY SUBJECTED TO PULLOUT FORCE 264
Husam M. Saleh, Maher Murad Jebur, Adnan Qahtan Mohammed, Mahdi. O. Karkush

DETERMINATION OF THE HETEROGENEITY OF A DENSE SAND SPECIMEN AND ITS EVOLUTION IN TRIAXIAL COMPRESSION 272
Selma Schmidt, Ivo Herle

INVESTIGATING THE IMPACT OF INHOMOGENEOUS SOIL PARAMETERS ON SHEAR STRENGTH IN BIAXIAL TESTS 280
Mona Siahkouhi, Gertraud Medicus, Franz Tschuchnigg, Barbara Schneider-Muntau

DYNAMIC SIMULATION AND OPTIMISATION OF PLATE COMPACTORS FOR SUBBALLAST COMPACTION DURING RAIL TRACK REHABILITATION 288
Julian Sigmund, Johannes Pistrol, Dietmar Adam

TRANSPENNINE ROUTE UPGRADE: GEOTECHNICAL ENGINEERING SOLUTIONS TO REPLACE FAILED STRUCTURES CAUSED BY PEAT AND DISSOLUTION HAZARDS 295
Jordan Sinnott

RELIABILITY VERIFICATION OF THE SEMI-PROBABILISTIC DESIGN OF CRANE MATS FOR THE GEOTECHNICAL STABILITY OF FOUNDATION MACHINES AT THE CONSTRUCTION SITE 304
Eleni Smyrniou, Mark van der Krogt

PREDICTIVE MODELING OF SANDY SUBGRADE SOIL'S RESILIENT MODULUS USING CYCLIC AND STATIC TRIAXIAL TEST VARIABLES AND RESULTS 312
Tadas Tamošiūnas, Šarūnas Skuodis

MODELING AND RESPONSE OF RETAINING WALL SUBJECTED TO STRONG GROUND MOTIONS 321
Maria K. Topalska

ASSESSMENT OF GEOTECHNICAL PARAMETERS FOR WIND TURBINE FOUNDATION DESIGN BASED ON CPT, DMT AND LABORATORY TESTS 329
Vișan I. Alexandra, Rebegea E. Angela, Cireșoiu A. Maria

ROCK-SCOUR PROTECTION SETTLEMENT DUE TO SEISMIC LIQUEFACTION FOR OFFSHORE WIND APPLICATIONS 337
Diarmid .M. Xu, Gopal S.P. Madabhushi, John M. Harris, Richard J.S. Whitehouse

GEOGRID REINFORCED SOIL MODEL CALIBRATION BASED ON LABORATORY TESTING 343
Mindaugas Zakarka, Šarūnas Skuodis, Johannes Kuhlmann

COMMITTEES

HONORARY COMMITTEE

Marc Ballouz–President of ISSMGE
Lyesse Laloui – Vice President of ISSMGE for Europe
Biljana Angelova–Rector of Ss. Cyril and Methodius University in Skopje, R.N. Macedonia
Goran Markovski–Dean of Faculty of Civil Engineering, Ss. Cyril and Methodius University in Skopje, R. N. Macedonia
Vlatko Šešov–Director of Institute of Earthquake Engineering and Engineering Seismology, Ss. Cyril and Methodius University in Skopje, R. N. Macedonia
Loretta Batali–President of Romanian Society for SMGE
Dietmar Adam – Secretary of Austrian Geotechnical Society
Milorad Jovanovski–Vice President at Large of ISRM
Hristina Spasevska–President of Engineering Institution of Macedonia
Kristinka Čulak, President of Chamber of certified architects and certified engineers of R.N.Macedonia

SCIENTIFIC COMMITTEE

Igor Peševski–Faculty of Civil Engineering (FCE), Ss. Cyril and Methodius University in Skopje (UKiM)
Dragan Dimitrievski–GEING Ltd Skopje
Nataša Nedelkovska–Geohydroconsulting Skopje (GHK)
Jovan Br. Papić–FCE, UKiM
Milorad Jovanovski–FCE, UKiM
Vlatko Šešov–Institute of Earthquake Engineering and Engineering Seismology (IZIIS),UKiM
Josif Josifovski–FCE, UKiM
Julijana Bojadžieva–IZIIS, UKiM
Kemal Edip–IZIIS, UKiM
Bojan Susinov–FCE, UKiM
Sead Abazi–FCE, UKiM

ORGANIZING COMMITTEE

Igor Peševski–FCE, UKiM
Elena Angelova–GHK
Tamara Jovanovska – MAG (Technical secretary of the conference)
Dejan Ivanovski –IZIIS, UKiM
Toni Kitanovski–IZIIS, UKiM
Bojan Janevski–Civil Engineering Institute “Macedonia” JSC, Skopje (GIM)
Done Nikolovski–International Balkan University
Mila Smiljanovska–GIM
Ana Bojadžieva–student at II cycle of Geotechnical engineering –IZIIS, UKiM
Teodor Dimitrievski–GEING Ltd Skopje
Marko Maraš–student at II cycle of Geotechnical engineering–FCE, UKiM
Lazar Božinovski–GIM
Aleksandar Andonov Sarev – MAG
Lence Nedeva – Popova Kula – Venue host

FOREWORD

Macedonian Association for Geotechnichs (MAG) is established in 1998 (before that it has been part of Yugoslav Society for Soil Mechanics and Foundation), while it is member of ISSMGE since 2001 and ISRM since 2017. Since 2002, each four years, MAG organises the national geotechnical symposiums, which have become a regional event at the least. With support of respective professionals from the geotechnical society throughout the world, MAG regularly organises lectures, seminars and courses for the Macedonian geotechnical students at all academic levels, as well as for geotechnical engineering practitioners. Meanwhile, MAG has organised several high profile events in wider regional terms. The 16th Danube-European Conference on Geotechnical Engineering was held in Skopje in 2018, where a rich variety of both experienced and young geotechnical audience attended. In 2022, the Fifth national geotechnical symposium was supported by the International Society for Rock Mechanics and Rock Engineering (ISRM) and was held in the form of ISRM Specialized Conference. This event also presented a 2nd Conference of the geotechnical societies from Macedonia, Serbia, Bosnia and Herzegovina, Croatia and Slovenia, thus being supported also by the ISSMGE. Thanks to the trust of ISSMGE board, MAG has been honored to organize the 28th European Young Geotechnical Engineers Conference (EYGEC 2024) in town Demir Kapija. 47 papers had been submitted by young geotechnical engineers from Europe and wider. MAG expresses gratitude to the invited lecturers, the participants, and the sponsors of this event.

With strong belief and wish that most of the participants of EYGEC 2024 will become leading force in the geotechnical family of the World,

Assoc. prof. Igor Peševski

President of MAG

28th European Young Geotechnical Engineers Conference – EYGEC 2024
© 2024 Macedonian Association for Geotechnics, ISBN 978-608-4510-61-1

Foundation system optimization of a high-bay warehouse using finite element modelling

Tamás Agárdi[a], Zsolt Szilvágyi PhD[a],

[a] *Geoplan ltd., Budapest, Hungary*

ABSTRACT

An automated high-bay warehouse with a floor area of approximately 37 m x 170 m and a total height of 36 m is being built as part of the extension of the LEGO plant near Nyíregyháza, Hungary. In this paper we present the design-optimization process of the building's foundations. In this type of system, the formerly separated structural and storage functions are cost-effectively combined in a single structure. The shelving system itself provides the support of the planned warehouse. In such structures, the focus is more on geotechnical and foundation issues. Taking into account both technical and economic aspects, 2D and 3D geotechnical finite element models were used to investigate the possibilities of slab foundations, rigid inclusion soil improvement and pile-supported slab foundations. The very strict deformation requirements can only be verified by such advanced modelling. In this study we emphasize the essential cooperation of the fields of structural and geotechnical engineering.

KEYWORDS

finite element modelling, deep foundation, automated warehouse

1. INTRODUCTION

Our design task was the foundation of the automatic high-bay warehouse that was built as part of the expansion of the LEGO plant in Nyíregyháza. Our company was involved in the construction of the LEGO factory as technical inspector, and in the current expansion project as a geotechnical designer. For this purpose, we used the previously completed soil investigation report and additional field tests carried out for the detailed design.

In the framework of the expansion, we prepared the execution plans of three building called MLB, Raw Material and PHB. The MLB and Raw Material buildings will be constructed using pile foundations widely used in the Hungarian practice. From a geotechnical point of view, the design of the foundation system of the PHB, i.e. the high bay warehouse building, was a challenge. The new building is an automated warehouse for palletised goods, 37 m wide, 170 m long and 36 m high (Figure 1).

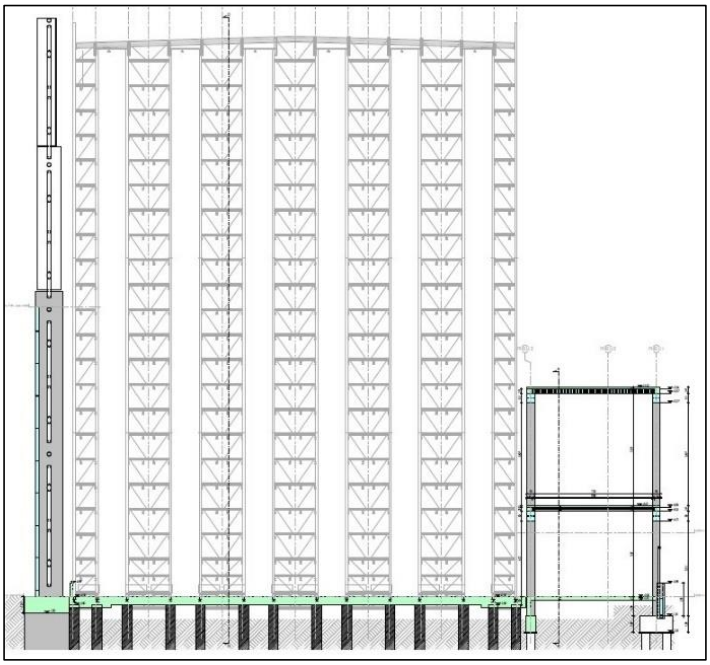


Figure 1. Typical section of the planned high-bay warehouse (firewall on the left, service building on the right)

2. ANTECEDENTS

The superstructure of the warehouse is made by a dutch manufacturer, Vanderlande Ltd. In the design of the shelving system, the structural calculation was carried out by using infinite rigid supports, taking into account the FEM specifications and standards [1]-[3]. In Hungary the general designer who was responsible for the structural design was provided with the loads on the shelf legs in each load case. Their task was to determine the combinations for the ULS and SLS limit states and then to proceed with the design of the floor slab. According to today's state-of-the-art design, the structural and geotechnical models of the floor slab had to be synchronised.

When designing the base plate, the most important task is to meet the rotation and displacement criteria given in the regulations. Without that the storage system might become unusable due to the automatic filling and emptying system's limit of tolerance. The displacement values were influenced by loads from several directions.

The new building will be connected to existing buildings. In these areas, it must be ensured that the construction does not place excessive additional loads on the pile foundations of the surrounding buildings. It was a challenge that the layout of the piles under the floor slab was also affected by the existing foundations on the boundaries of the adjacent buildings. A 36 m high firewall, with an independent foundation, was constructed from the adjacent buildings and match the height of the warehouse in accordance with fire regulations (Figure 1).

The firewall is built as a structurally independent fixed end structure. From the geotechnical point of view the pile cap (which was near the surface) was loaded with an unusual magnitude of moment, about ~4-6000 kNm, as the client's requirement was to assume that the firewall would be built before the warehouse. It is foreseen that the next high storage building will be built on the other side of the firewall. The impact of building this extension also needs to be assessed. On the other side of the warehouse, a two-storey utility building on pile foundations will be constructed. It should be noted that the rotations of the floor slab in SLS limit state are influenced by the loading of the warehouse. Therefore, the aim of the investigations is to optimise the foundation system and the calculations should take into account the directly connected existing and future structures.

3. GEOTECHNICAL CONDITIONS

The study area is located near Nyíregyháza, Hungary. The area is characterised by the presence of loamy, silty soils near the surface. The layers with bearing capacity for deep foundations are found at a depth of 10-12 m. The final geological model, based on field investigations and CPT testing, distinguishes 11 soil layers.

The soil investigation report [4] prepared in the previous design phase analysed the site conditions on the basis of 4 CPT tests. As the design progressed and before construction started, additional tests were carried out, so that a total of 11 CPT tests were used in the final calculations.

The planning area is characterised by heterogeneous stratification; sand, sandy silt, silty sand layers alternate. Between these with a varying thicknesses of fine grained layers occur frequently.

The CPT tests show that the cover of the area is composed of a clayey sand layer up to a depth of 1 - 1.5 m. Below this, sand and silty sand are deposited to an average depth of 10 m. The peak resistance of the cone vary from 4 - 8 MPa initially to 16 - 22 MPa below 5 m. The diagrams clearly show the silty regions where the cone resistance decrease. Overall, the sand layer is moderately dense, with occasional dense settlements.

Deeper, to the bottom of the tests, there is a layer of sand, silty sand, sandy silt with a lower bearing capacity than the previous one, the peak resistance of qc is about ~ 10 - 12 MPa. The layer is moderately dense, with fine grained layers characterized by stiff consistency. At these depths, sand layers also appear in variable thicknesses, with peak resitances of 20 - 24 MPa.

Based on the available test results and the previous geotechnical documentation the level of the groundwater table is near the surface.

4. APPLIED STANDARDS

The design had to consider the load combinations that could occur during the planned lifetime of the warehouse. It is not possible to combine meteorological loads and shelf loads in Plaxis software, this has to be done by the structural designer using their finite element software, AxisVM.

It is essential to analyse both total and partial loads to calculate the plate rotation and settlement. Total loading would not be expected to result in the largest settlement difference and rotation.

The partial load arrangements should be specified by the shelving system designer in agreement with the Client. This will depend on the further use, especially when using an automatic storage system. As no such information was provided in the data, loading schemes were defined by our company and applied in the calculations after the client has approved. In consultation with the structural designer of the superstructure, a total of 14 loading schemes were established (Figure 2). The settlement and rotation criteria were investigated in the SLS quasi-permanent limit state. The plate stresses were also calculated in the ULS limit state.



Figure 2. Schematic of load schemes

The schemes should be interpreted as the maximum SLS load from the legs of the actively loaded shelves (grey part of Figure 2) to the plate, and only the load from the shelf's self-weight and the meteorological load from the unloaded shelves (white part of Figure 2).
The first load scheme is total load, where the maximum load is applied to all shelves. This condition models the full load of the warehouse. In schemes 02-09, the shelving system is fully loaded longitudinally, while transversally some rows of shelves remain empty. Load conditions 10-13 show the change in the longitudinal fill level of the warehouse. In addition, the total loading in the ULS limit state was also investigated.

5. CONCIDERATIONS BEFORE NUMERICAL CALCULATION

The design of the foundations for the storage facility was started based on three CPT and one SCPT from the previous soil investigation report. The aim of the design was to define a foundation system that would satisfy both technical and economic criteria.
From a construction point of view, the simplest design would be a slab foundation. However, initial calculations made it clear that the structure would suffer from large, uneven settlements due to the compressible soil layers near the surface. A more rigid system could be created by bypassing the near-surface soils with stiffening piles. When rigid inclusion elements are used, the floor slab can be constructed on a compacted bedding. Detailed calculations have also been carried out for possible design options for piled raft foundations. Given the size of the warehouse, it is clear that a small change in the thickness of the large surface area floor slab and the large number of piles supporting it can have a significant impact on costs. Establishing these dimensions was a major part of the design task.
A structural analysis was carried out for the superstructure and the foundations of the shelving system. In Axis software, nodal forces were used in place of the shelf legs and the piles were modelled by nodal supports. The rails running between the shelves were included in the model as line loads. A separate structural calculation was performed for each of the loading schemes presented earlier. The node supports were set to infinite stiffness for the first run, and the stiffness and self-weight of the slab were not included in this model, knowing that it would be included in the geotechnical VEM model, and thus

its load-distributing effect would not be included twice in the scheme. Due to the size of the warehouse, the number of shelf supports exceeded 700, and the number of piles was also in this order of magnitude. Geotechnical finite element modelling was carried out using Plaxis software. The key to the foundation of the warehouse is to determine the final deformations as accurately as possible. With this in mind, the soil model was chosen for HardeningSoilSmall. The parameters of the soil model were taken from the CPT test obtained. By statistically evaluating the peak resistances of the layers identified in the CPTs, the average qc values of each layer were determined and their stiffness characteristics derived. The seismic CPT results were used to determine the parameters describing the small deformation range of the soil model.

6. CALCULATION OF THE CROSS SECTIONS

To investigate the types of foundation, calculations were performed on the cross-section of the warehouse as a starting point. The 2D calculations are approximations, but can be used to quickly analyse different variations. When building the model, we determined the soil stratification for 4 cross-sections based on the 4 CPTs available at the time, so we investigated the expected settlement differences due to stratification variations in 4 models. The result of the structural calculation included point loads, of which the values close to the cross-section were converted to line loads. These models were therefore not designed to provide accurate calculation results but to understand the overall behaviour of the structure. Their results give a reliable indication of the local behaviour of the plate in a given section. From a technical point of view, another major advantage of 2D models was that a smaller number of elements results a faster running time, so that it does not take days to analyse possible variations. It is worth mentioning that while the current latest version of the Plaxis2D software is capable of calculating plate rotations, in the 3D version the same values can be obtained by derivation the displacement function.

The results of the first calculations showed that neither the slab foundation nor the rigid inclusion soil improvement can meet the 1/2000 rad rotation criteria specified in the standard (Figure 3). Thus, these foundation methods cannot be used to prepare the foundations for the warehouse. Due to the height of the warehouse, it is exposed to significant wind loads. At the edge of the slab in the ULS limit state, large tensile forces are generated by the wind load, which cannot be absorbed by slab foundations.

With this in mind, we started to investigate deep foundation methods. Pile foundations were not an option due to the site layout and structural design. A possible good structural design is a piled raft foundation.

Two possible designs for piled raft foundations were investigated. One of them is the layout of piles in a uniform grid pattern. A warehouse similar to the present one is already in use on the site and it was built with this pile arrangement.

In the case of a grid layout, the structure can be optimised by varying the length of the piles and the distance between the rasters. In the case of the possible design mentioned above, i.e. piles under each shelf, the allocation is adapted to the support structure. The structure can then be made more economical by varying the length of the piles.

Additional 2D models were created to investigate the two versions in an approximate way. Their results showed that these foundation systems meet the rotation requirements of the standard (0.0005 rad). Based on the results of the models (Figure 3), it was decided to perform 3D testing of two designs, covering the entire warehouse floor area, its surroundings and the connected buildings. In this way, several of the impacts described in the previous chapter could be accurately quantified.

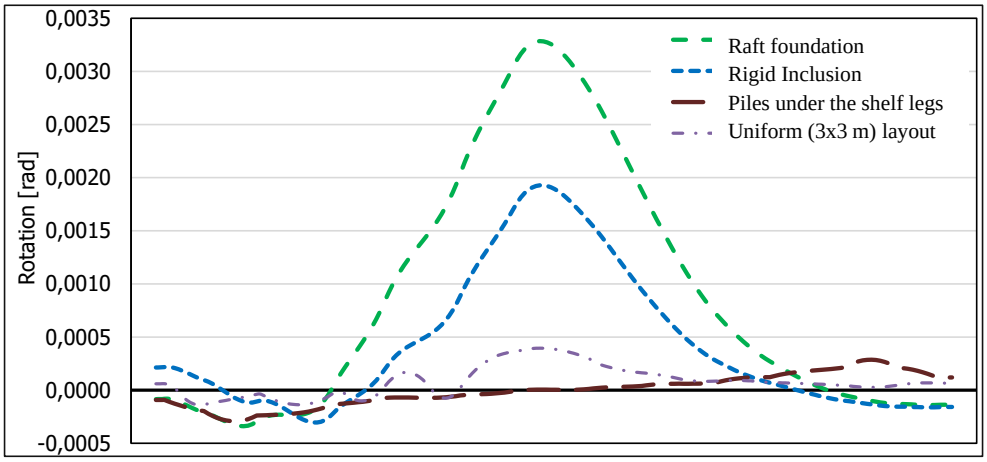


Figure 3. Analysis of the rotations of possible foundation types

7. SPATIAL CALCULATIONS

Using the 3D module of the Plaxis software, calculations were made with a more accurate view of the geometry. In our model, we considered both the floor slab currently being designed and the foundation of the warehouse in the future extension plan, considered as a negative effect. Over 1500 piles were placed under these slab foundations. Also included the foundations of the new firewall sections between the existing buildings and the new buildings, and the pile foundations for the utility building. The 3D model was thus 120 m wide and 230 m long and 40 m deep (Figure 4).

From more than 700 shelves, concentrated loads in the order of tens of thousands were applied to the floor slab in 14 different load patterns. When building the 3D model, the command line was used to define the point loads on the floor plate.

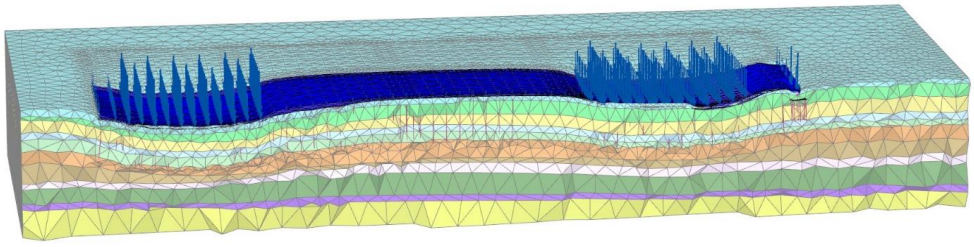


Figure 4. 3D finite element model of a high-bay warehouse

The 3D models of the two versions were modified several times and the calculations were carried out. The aim of the tests was to achieve a technically satisfactory, economical structure. During the data processing, the displacements of the cross-section calculated on the plate were read out from the software and the rotations were derived from them. The results were evaluated in cross sections and longitudinal sections taken at the same location.

For the pile layout under the shelf support, we first designed 14 m CFA piles, starting from the piles used in the previous building, (although the shelving system and load of these piles differed slightly from the current structure). Seeing that this solution met the deflection criteria (0.0005 rad) (Figure 5), we reduced the length of the piles and then ran the calculation again. The results for the shorter pile, 11 m, also met the specifications and we were closer to the criterion. The maximum value of the settlement is obtained by the total load in the middle of the pile. However, the maximum deflections are developed in the plate due to partial loading patterns.

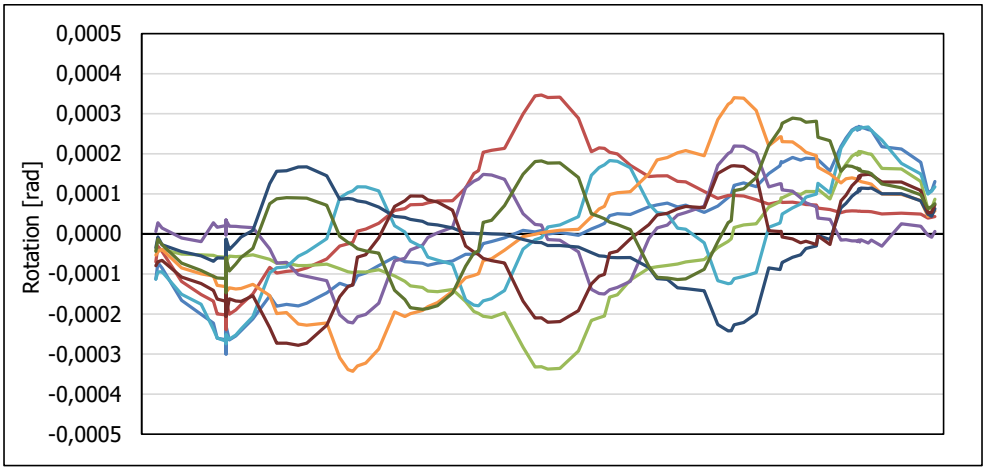


Figure 5. Rotation values in the cross-section of the plate calculated with the under-pole allocation

In the case of even pile distribution, we first examined a rarely distributed 11.0 m long pile in a 4.5x4.5 m grid. Then, as it did not meet the deformation criteria, a 3.0x3.0 m grid was considered. This allocation was at the limit of compliance. A more dense layout would have increased the number of piles significantly, so by increasing the length of the piles to 15.0 m, a technically compliant version was obtained (Figure 6).

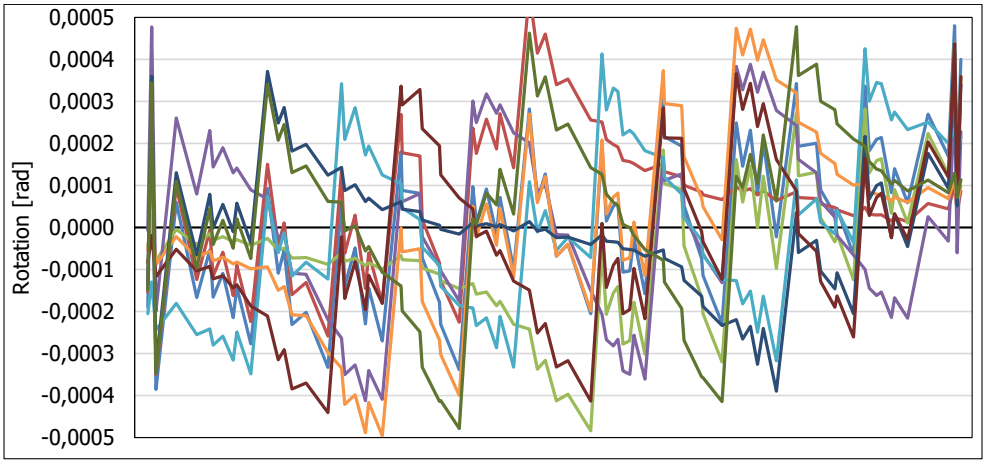


Figure 6. Rotation values calculated with uniform distribution in the cross section of the plate

For both designs, the impact of the foundations of the future building on the existing building was investigated. The results of these calculations showed that the increased load would cause the rise of the displacement towards the planned new building, but the increase in displacement would still be within the 1/2000 rad value.
During the spatial modelling, we also optimised the thickness of the slab, starting from 1 m thickness to 70 cm in the edge band and 50 cm in the middle, which resulted in significant cost reductions.

8. CONCLUSIONS

For this model size, with so many piles and loads, there is no other option but to use the embedded beam and plate element. The results obtained from the 2D model with approximations and the 3D model show

that the rotation curves calculated by the 2D program and the rotation curves calculated from the result of the section taken in the 3D model show good agreement (Figure 7).

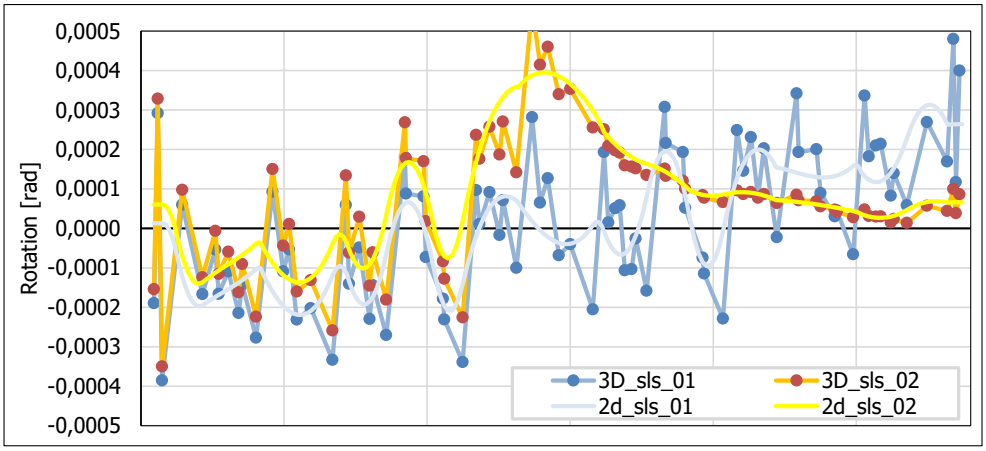


Figure 7. Comparison of 2D and 3D tests

There are fundamental differences in the nature of the rotation curves shown in Figures 5 and 6. By examining the graph of uniform distribution, we can conclude that the deformation of the base plate is fundamentally influenced by the relative positions of the load (shelf supports) and the support (piles). The dashed alternating rotation diagram highlights the approximation of the calculation that the loads and supports are point-defined on the plate. The value of the rotation changes abruptly depending on how close the attack point of the load to the support. From the point of view of piling, this modelling result therefore highlights a real problem. When using uniform distribution, the maximum rotation does not necessarily occur under the action of partial loadings, but can occur under any loading scheme. The amount of deformation depends on the geometric design. This effect can be handled by placing piles under the shelf supports. This eliminates the outward settlement and provides the plate with a stiffer support at the point of force application.

Due to the soft soil layers near the surface and the relatively stiff slab and the dense pile distribution, the calculated bedding under the slab was negligibly small. The plate is supported by the piles, acting as a slab.

REFERENCES

[1] Eferte Kft.: Talajvizsgálati jelentés, H-4400 Nyíregyháza, Lego utca 15. alatti LEGO Manufacturing Kft. területén tervezett MLB épület tervezéséhez (2020. december)

[2] FEM9.831 - FEDERATION EUROPEENNE DE LA MANUTENTION Section IX, STORAGE AND RETRIEVALMACHINES: Calculation principles of storage and retrieval machines Tolerances, deformations and clearances in the high-bay warehouse

[3] FEM9.832 - FEDERATION EUROPEENNE DE LA MANUTENTION Section IX, SERIES LIFTING EQUIPMENT: Basis of calculations for SIR machines, tolerances, deformations and clearances in automatic small parts warehouses (not silo design)

[4] FEM9.841/10.2.10 - FEDERATION EUROPEENNE DE LA MANUTENTION: Storage systems with rail dependent storage and retrieval equipment – Interfaces

[5] Magasraktár Alapozási Rendszerének Optimalizálása, Agárdi Tamás Szakdolgozat (2022 tavasz)

28th European Young Geotechnical Engineers Conference – EYGEC 2024
© 2024 Macedonian Association for Geotechnics, ISBN 978-608-4510-61-1

Statistical analysis of site investigation data to find irregular zones and layers

Maedeh Alinejad[a], Anders Beijer Lundberg[b]

[a] *GeoMind KB, Stockholm, Sweden*
[b] *ELU Konsult AB, Stockholm, Sweden*

ABSTRACT

The layers in a soil stratum are normally idealized to a uniform continuum. However, irregular inclusions of material in such layers can influence the geotechnical behavior of the soil layers significantly. This includes the presence of boulders in glacial till, which can be very detrimental to pile drivability in such layers, as well as silt inclusions in clay, which can drastically increase the horizontal hydraulic conductivity. The latter can also increase the risk of slope instability since silt layers constitute zones where the localized sliding can occur. Herein, a statistical approach is demonstrated to conduct a synthetic site investigation, in which the presence of irregular zones is simulated with Monte-Carlo simulation, which is subsequently compared to the real site investigation. This is demonstrated for boulders in a glacial clay, and the expansion of the method to an assessment of the presence of continuous drained layers of silts and sands in clay, and other irregular zones in soils, is elaborated. The suitable extent of a site investigations and the need for furthers tests can then be determined based on a comparison between the simulations and the actual site investigation.

KEYWORDS

Site investigation; Risk assessment; Probabilistic methods; Cone penetration testing

1. INTRODUCTION

The site investigation forms the basis of the geotechnical design process and should result in the necessary information to achieve the target reliability of the geotechnical structure subjected to the specified loads (Phoon et al., 2022). This includes (but is not limited to) the soil stratification, the material properties including the estimation of the stress-strain response of the soil in the specific deformation range, and the hydrogeological characterization of the soil strata (Wroth, 1984). Different in-situ and laboratory techniques for site investigations and the implementation in geotechnical design have been demonstrated extensively in the scientific literature, e.g. Wroth (1984) and Bilgin et al., (2019). In engineering practice, the layers of the strata are generally characterized by constant properties or by linear increasing, in order to facilitate the practical design and calculation model. In the research literature, the variability of the soil has been explored with the site investigations (Jaksa et al., 2005), but these advanced methods are rarely included in practice. However, in practice it is well understood that the idealization of the soil as a continuum is often associated with large simplification, which might not realistically represent the actual design situation (Phoon et al., 2002).

There are some soil properties which are not possible either to generalize to a continuum or present as a statistical distribution, but rather are discrete objects located in a continuum, e.g. boulders in a soil mass (Ditlevsen, 2006) or silt layers in a clay mass (Potkin et al., 2021). Another frequent item in site investigations are pollutants, such as lead which can be distributed in the ground water (Toyoda et al., 2022). Pollutants within the soil mass are not frequently well distributed within the soil but are rather closely associated with the permeability and drainage conditions of the soil mass (Arias-Estévez et al., 2008).

These deviations from the homogenous soil layers which are generally adapted in geotechnical practice present the need for a different methodology of site investigations and inference of the site investigation results. An adaptive approach to the site investigation is then needed, in which the amount and properties of the objects are estimated from the site investigation alongside conventional properties, as outlined in Wroth (1984). Furthermore, the site investigation should be adapted to be able to detect the presence of such objects. This article discusses some examples of irregular zones or objects, and how to assess the scope of such objects within a standard site investigation program. It expands the methodology discussed in L'Heureux, et al. (2012) and especially discusses the assumptions of the soil stratification and homogeneity during the interpretation of the in-situ tests and the consequences for practical geotechnical design.

The preferred method developed in this article is to conduct a synthetic site investigation, which can enable a simulation of the detection of the irregular zones. Different assumption about the properties of the irregular zones, whether these consists of layers or volumes, can then be analysed and compared to the real site investigation results.

2. BACKGROUND

Soil consists of grains, which from a mechanical perspective are assumed to be a continuum consisting of a large cluster of grains so that the behaviour of the individual soil grains can be disregarded (Klausner, 2012). Starting from this assumption, sophisticated models can be assembled describing the mechanical response of soils as evaluated in laboratory tests and subsequently used for numerical predictions, e.g. Schofield and Wroth (1968). The geological formation of the soil materials is significantly more complex, and in some cases central to the response of the soil during loading (L'Heureux, et al., 2012). As an example, Northern Europe was affected by the Weichsel ice age, which resulted in a redeposition of the material which had been collected in the ice, initially as moraine as the ice melted. This was followed by sedimentation of sand, silt and marine clay deposited on the moraine and the bedrock. Some features of the Scandinavian soil stratigraphy are consequently massive layers of clay deposited on and, silt and moraine. The typical stratigraphy is therefore straightforward to characterize both the cohesive soil (clay) and the non-cohesive soil layers (sand, silt and moraine) as homogenous layers. However, the geological deposition process has caused irregular zones in the soil, which can sometime be critical for the geotechnical design.

2.1. Irregular zones in a moraine layer

By definition, the moraine soil is not homogenous. It is a residual soil containing the ice glacial soil. Large boulders are frequently discovered in the moraine layer. This is shown in Figure 1 where a boulder has fallen out from the excavated surface. Obviously, such information is only available in the excavation itself, which is why as much as possible information should be obtained by the site investigations. A common site investigation in Scandinavia is the soil-rock probe, in which the soil strata can be detected by a drill bit which can penetrate the boulders and the bedrock. Figure 2 shows a site investigation record of the boulders in a soil-rock probe with the boulder and the bedrock displayed.



Figure 1. A boulder from an excavation

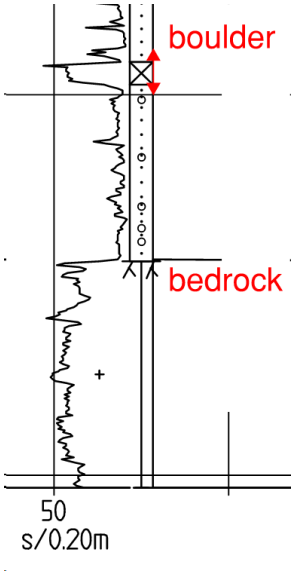


Figure 2. Detection of a boulder from a soil-rock probe, displaying the penetration resistance in seconds per 0,2 m of the probe as it advances through the soil profile. Notice the increase in the penetration resistance when the probe encounters the boulder and the bedrock.

Boulders such as those shown in figures above can influence the pile drivability, especially when very slender piles are driven into moraine sediments, which must be considered during pile design. The background to pile driving resistance is discussed in detail by Alinejad and Lundberg (2023). However, to estimate the consequences of the boulder in the soil strata on the pile drivability, the boulder content must be estimated from the site investigations.

2.2. Irregular zones in a clay layer

In Scandinavian soil conditions the clay layer is deposited on top of the moraine layer, or the intermediate silt and sand layer (L'Heureux, et al., 2012). If samples are obtained from the clay layers, there are frequently layers of silt deposited in the clay, due to periodic changes in the waterflow and climatic conditions during the deposition of the clay (Potvin et al., 2022). Figure 3 shows a piston sample

of clay, in which a layer of silt is located in the clay, just at the interface with the moraine. Such irregular layers can be detected during sampling but can also be shown in some in-situ tests. Figure 4 shows a CPT-record executed in soft clay, showing the total cone resistance q_t, the sleeve friction f_t, and the hydrostatic and pore pressure. Two irregular zones are shown in Figure 4, one located at the higher end of the clay layer, the other at the interface of the moraine and the clay layer.

The presence of more permeable silt layer can have significant influence on the soil response during loading. Settlements will occur much faster when the drainage length of the clay is smaller, as shown in Figure 4, in which the excess pore pressures during consolidation can dissipate through the silt layers. The stability of slopes in such soils during piling can also be reduced by the generation of excess pore pressures from the driving of the piles (Randolph and Wroth, 1979).

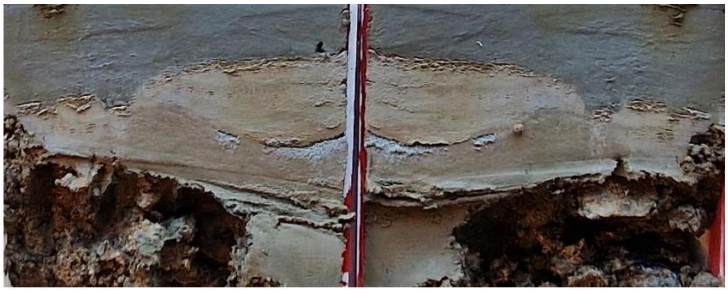


Figure 3. A cross-section of a piston sample of clay with silt inclusions

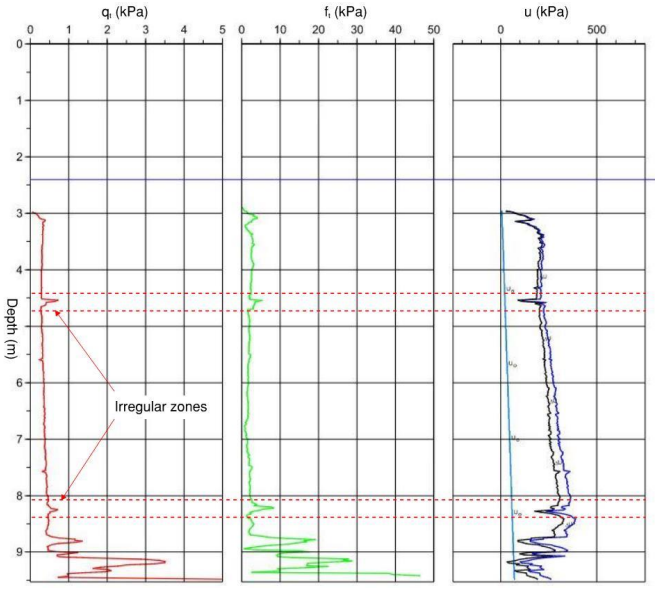


Figure 4. CPT-measurement showing the total cone resistance q_t, sleeve friction f_t and the hydrostatic and pore pressure measures (the hydrostatic pressure in light blue, the pore pressure in dark blue, and the excess pore pressure in black). Two irregular zones are displayed in the graph in which the cone resistance, the sleeve friction are significantly higher than in the surrounding clay, while the excess pore pressure is significantly lower.

2.3. Detection of the irregular zones

In this paper, a statistical approach is demonstrated to conduct a synthetic site investigation, in which the presence of irregular zones is simulated with Monte-Carlo simulation. This approach is demonstrated for boulders in a glacial clay, (Alinejad and Lundberg, 2023), but is further developed to include more geometries. The expansion of the method for assessment of the presence of continuous drained layers of silts and sands in clay is outlined, and the possible expansion to irregular zones with both a geometric shape and a scalar value is suggested.

3. ASSUMPTIONS DURING THE INTERPRETATION OF THE SITE INVESTIGATIONS

The interpretation of the site investigations tests is usually dependent on the initial assessment of the stratification and the behaviour of the soil layers (Wroth, 1984). Common assumption is the undrained response from CPT tests in sufficiently impermeable layers (Potvin et al., 2022). However, if irregular zones are detected during the site investigation campaign, the process to infer the magnitude of such irregular zones relies heavily on the assumptions about the geometrical range and the homogeneity of the zone. Here, the description is initially limited to planes, and subsequently expanded to homogeneous volumes, followed by volumes described by a scalar, which is suitable for pollutants in soil.

3.1. The irregular layers as a geometrical plane

An idealized description of the irregular zone in the soil strata is the Euclidian plane, which can be a unique continuous plane of several continuous or discontinuous planes in the soil. Notice that the true properties of the layer if it is continuous in the soil mass can only be determined by a full excavation of the soil and is therefore inferred from the site investigation. The plane is located somewhere in the soil volume, characterized by the geometry of the discrete points obtained from the site investigation records. Figure 5 shows different forms of the irregular layers in the soil. These are characterized by having a geometrical area, but a limited volume, which is quite similar to the silt layers shown in Figure 3. Figure 5a shows a continuous layer, while Figure 5b includes multiple continuous layers. In a real soil profile, there are obvious limitations to soil layers, and a more realistic description consists of the multiple discontinuous soil layers, as shown in Figure 5c.

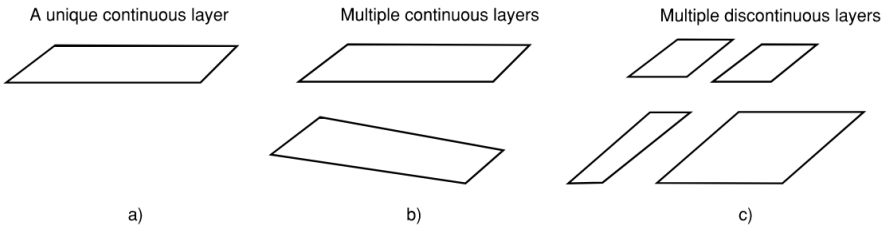


Figure 5. Different continuous and discontinuous layers in the soil.

3.2. The irregular zones described as a volume

A more realistic description of the boulders in the soil consists of volumes located in the soil mass as a result of the geological processes during deposition of the soil. Different levels of idealization are possible for volumes to get successively more realistic description of the reality, as shown in Figure 6a to 6c. The volumes can be considered as regular and uniform volumes, essentially spheres in the soil, as shown in Figure 6a. A more sophisticated assumption is to consider the items as spherical shapes but in different sizes in Figure 6b, following the empirical results of Ditlevsen (2006) for boulders. A furthermore realistic description is to consider the irregularity of the volumes, in which the shapes can be quite different depending on the geological processes, shown in Figure 6c.

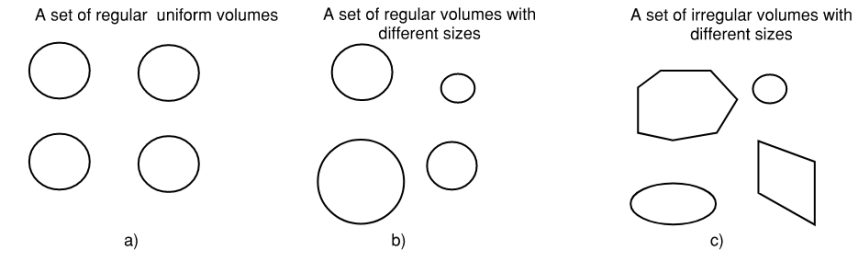


Figure 6. Different sets of regular and irregular volumes in the soil.

3.3. The irregular layers with a geometry and a scalar value

For some irregular zones, such as pollutants, a suitable description of the phenomenon consists both the geometric condition and the scalar value, e.g. displaying the lead content in the soil (Toyada et al., 2022). The geometries shown in Figure 5 and 6 can then be complemented by one or more scalar values of the pollutant of any other necessary condition as given in Equation (1) below.

$$C = f(x,y,z) \tag{1}$$

where *x*,*y*,*z* is part of the layer or the volume in Figure 5 and Figure 6. Sophisticated models can then be constructed from the site investigation information.

4. IRREGULAR ZONES DETERMINATION BY INVERSE ANALYSIS

Once the assumptions about the properties of the irregular zones are done, a synthetic simulation can be carried out. A more detailed description is discussed in Alinejad and Lundberg (2023). For this purpose, a probabilistic inverse analysis framework can be adopted to the description of irregular zones of the boulder content, or the drained soil layers in clay. For the clay layers, this stochastic framework includes a 3D domain of clay containing drained soil, and simulation of the suitable in-situ site investigation test, CPT. This model can be built to determine the presence and content of these irregular zones from the records of CPT. The content of drained soil can be defined by the geometrical location of the soil if it is assumed to be a layer. Alternatively, its volumetric content, VSC, can be assessed if the layer was a depth in the site investigation records. A methodology to address the statistical relation between the CPT results and the volumetric content of drained soil can be formulated in two steps, forward analysis and inverse analysis. The method permits generating a system with predetermined irregular zones, in which the site investigation methods can be simulated and the impact from the quantity of these tests can be studied in the synthetic model.

4.1. Simulation of the domain, irregular zones and CPT

A 3D domain representing the clay layer can be modelled. The depth of domain is based on the average thickness of clay in the area of interest. For glacial soil in Sweden 5 to 20 m is a reasonable choice. For the specific case, the depth of the soil is plugged into the model. The drained soil, silt layer, can be modelled with a plane, which can be finite/infinite. The inclination of the plane can be controlled by the angle it makes with the horizon. The amount of silt within the domain can be controlled with its volume.

As mentioned earlier, CPT is a suitable site investigation test to indicate an irregular zone. The test can be modelled with vertical lines where their length is equal to the depth of the domain. Here, irregular zone can be represented with the depth of CPT cone goes through them.

This is followed by a forward analysis and an inverse analysis described below.

4.2. Forward analysis

In this step, the synthetic records of CPT tests are generated from the simulation of this test for predetermined volumetric silt content, VSC. Here, Monte-Carlo simulation is incorporated to provide the random generations of the finite and infinite irregular zones. Figure 7 shows an example of the simulated penetration length (length of the probe in the boulder relative to the total drilling length of the probe) in a simulation of boulders by Alinejad and Lundberg (2023).

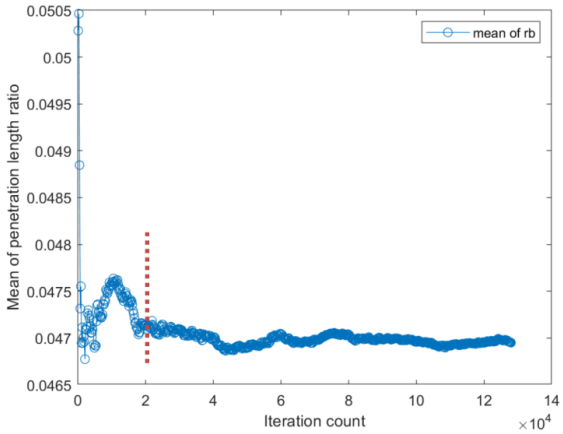


Figure 7. Example of simulated mean penetration length ratio of boulders and soil with Monte-Carlo simulation.

4.3. Inverse analysis

The forward simulation is followed by an inverse analysis, in which the real site investigation tests results are compared to the synthetic site investigation results. This can be carried out with a correlation of the results, flowing the methodology in Alinejad and Lundberg (2023), or with a direct comparison between the expected site investigation information and the results from the synthetic site investigation, shown in a flow chart in Figure 8.

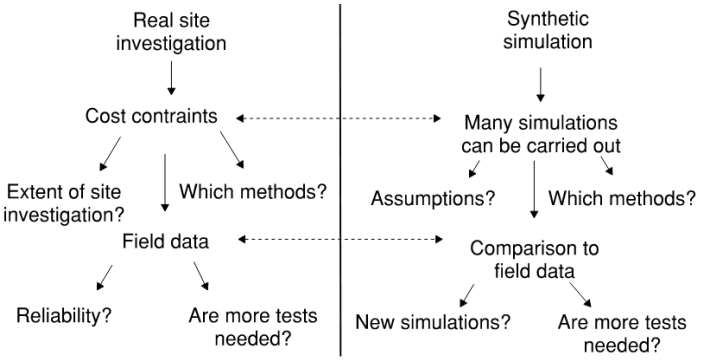


Figure 8. The role of the synthetic site investigation as a complement to the real site investigation.

5. CONCLUSIONS

The standard site investigation methods discussed in the literature are often not suitable for the detection of irregular zones in soil such as boulders or drained layers. An alternative methodology in which a

synthetic simulation of the site investigations is carried out and compared with the real site investigation results has been demonstrated. Especially in large project in which several site investigation campaigns are included, this methodology can help the designer to choose the necessary extent of the site investigations.

6. ACKNOWLEDGEMENTS

The authors both thank their colleagues for their help and their encouragement and the Swedish Geotechnical Association, SGF, for their support.

REFERENCES

Alinejad, M., Beijer Lundberg, A. 2023. Assessment of boulder content by stochastic modelling and inverse analysis. *Proceedings 10th NUMGE 2023.* London, UK.

Arias-Estévez, M., López-Periago, E., Martínez-Carballo, E., Simal-Gándara, J., Mejuto, J. C., and García-Río, L. 2008. The mobility and degradation of pesticides in soils and the pollution of groundwater resources. *Agriculture, ecosystems & environment*, 123(4), 247-260.

Bilgin, Ö., Arens, K., & Dettloff, A. 2019. Assessment of variability in soil properties from various field and laboratory tests. *Georisk: Assessment and Management of Risk for Engineered Systems and Geohazards*, 13(4), 247-254.

Chavan, D., and Babu, G. S. 2023. Site response analysis of liquefiable stratified ground comprising silt and sand: Numerical investigations. *Soil Dynamics and Earthquake Engineering*.

Ditlevsen, O. 2006. A story about distributions of dimensions and locations of boulders. *Probabilistic engineering mechanics*, 21(1), 9-17.

Hanna, T. H. 1967. The measurement of pore water pressures adjacent to a driven pile. *Canadian Geotechnical Journal*, 4(3), 313-325.

Hird, C. C., Johnson, P., & Sills, G. C. 2003. Performance of miniature piezocones in thinly layered soils. *Geotechnique*, 53(10), 885-900.

Jaksa, M. B., Goldsworthy, J. S., Fenton, G. A., Kaggwa, W. S., Griffiths, D. V., Kuo, Y. L., & Poulos, H. G. 2005. Towards reliable and effective site investigations. *Geotechnique*, 55(2), 109-121.

Klausner, Y. 2012. *Fundamentals of continuum mechanics of soils*. Springer Science & Business Media.

L'Heureux, J. S., Longva, O., Steiner, A., Hansen, L., Vardy, M. E., Vanneste, M., & Kopf, A. 2012. Identification of weak layers and their role for the stability of slopes at Finneidfjord, northern Norway. In Submarine mass movements and their consequences: *5th international symposium*. Springer Netherlands. pp. 321-330.

Phoon, K. K., Ching, J., and Shuku, T. 2022. Challenges in data-driven site characterization. *Georisk: Assessment and Management of Risk for Engineered Systems and Geohazards*, 16(1), 114-126.

Potvin, J. J., Woeller, D., Sharp, J., and Take, W. A. 2022. Stratigraphic profiling, slip surface detection, and assessment of remolding in sensitive clay landslides using the CPT. *Canadian Geotechnical Journal*, 59(7), 1146-1160.

Randolph, M. F., and Wroth, C. P. 1979. An analytical solution for the consolidation around a driven pile. *International Journal for Numerical and Analytical Methods in Geomechanics*, 3(3), 217-229.

Rowe, P. W. 1972. The relevance of soil fabric to site investigation practice. *Geotechnique*, 22(2), 195-300.

Schofield, A. N., and Wroth, P. 1968. *Critical state soil mechanics* (Vol. 310). McGraw-hill.

Stendahl, J., Lundin, L., & Nilsson, T. 2009. The stone and boulder content of Swedish forest soils. *Catena*, 77(3), 285-291.

Toyoda, K., Nakano, S., Tanaka, S., Banda, K., Nyambe, I. A., Ishikawa, T. & Ishizuka, M. 2022. Geochemical identification of particulate lead pollution in shallow groundwater in inhabited areas in Kabwe, Zambia. *Applied Geochemistry*, 139, 105215.

Wroth, C. P. 1984. The interpretation of in situ soil tests. *Geotechnique*, 34(4), 449-489.

28th European Young Geotechnical Engineers Conference – EYGEC 2024
© 2024 Macedonian Association for Geotechnics, ISBN 978-608-4510-61-1

Clay experimental study and cracking mechanisms under controlled desiccation paths using digital image correlation

Lamine Ighil Ameur[a], and Mahdia Hattab[b]

[a] *Cerema, GéoCoD: Géomatériaux et Géomécanique: couplages et dynamique pour les risques et les ouvrages géotechniques, Blois, France*
[b] *Laboratoire d'études des microstructures et de mécanique des matériaux (UMR7239), Université de Lorraine, Metz, France*

ABSTRACT

The aim of this research is to characterize the shrinkage phenomenon and the cracking mechanisms of a clayey soil subjected to the controlled desiccation in a laboratory experimental system. The approach consisted first to carry out a series of different controlled desiccation tests under three suction levels: high in 361MPa, middle in 110MPa and low in 38MPa. Using the digital image correlation (DIC) method, total local strains were measured. Drying and shrinkage kinetics analysis showed that strains are probably due to both a shrinkage part and another part that can be named "mechanical". Only the mode I of cracking mechanisms was observed basing only on calculations of the principal "mechanical" strains.

KEYWORDS

Clay; Desiccation; Cracking; Image Correlation; Shrinkage, Critical strains.

1. INTRODUCTION

The presence of cracks in a soil mass induces the creation of some zones of weak tension that drop down the mechanical resistance (Morris et al., 1992). Thus, this can have a significant impact on the hydraulic conductivity of clayey soils, which increases with the development of cracks. Relative humidity and temperature are the mainly influencing parameters during controlled desiccation tests. This can be characterized by a direct modification on drying variables such as: water content, saturation degree, shrinkage limit and local suction of the soil.

Desiccation cracking of clayey soils usually occurred when the developed tensile stress due to suction exceeds the tensile strength of the soil (Kodikara et al., 1999). Tensile stresses develop only in the case where the soil is restricted against shrinkage. This restriction can be external due to the interface of a rough layer for example or internal due to some parts of soil during non-uniform drying for example.

This research is mainly focused on the characterization of shrinkage phenomenon and understanding how controlled desiccation cracking initiate and propagate through a clayey material. A series of controlled desiccation tests where then performed under three levels of imposed suction. The experimental approach aims to estimate shrinkage using the digital image correlation (DIC) method and allows calculating a critical value of the mechanical local strain acting the cracking.

2. MATERIAL AND METHOD

2.1. Material properties and sample preparation

The tested clayey material employed in this study was *Kaolinite K13*, which is an industrial clay marketed by *Sibelco* (Paris, France). Some of its physical properties are: liquid limit, w_L = 40%; plastic limit, w_P = 20%; density of the solid grains, γ_s/γ_w = 2.65; and shrinkage limit, w_{SL} = 16%. This synthetic clay appears to be similar to the well-known *Kaolinite P300*. An elementary Kaolinite particle consists of a set of stacked sheets as described in Hattab et al. (2014). The mineralogical analysis of Kaolinite P300, carried out using X-ray diffraction technique performed by Hammad et al. (2013), reveals that in addition to Kaolinite, various secondary minerals such as Illite and Quartz have also been identified.

Soil samples were made by spreading mixed slurry with an initial water content w_0 = 1.2 w_L on a rectangular Teflon support. The dimensions of each specimen are 190 mm in length, 130 mm in width and 4 mm in thickness. The upper surface of soil sample was flecked with small and very dense spots of dark paint spraying. This was necessary for DIC calculations needing different grey levels.

2.2. Test equipment

The experimental device developed for this study is shown in Fig. 1 as a control chamber of glass used to create a confined volume for applying the Vapor Equilibrium Technique (VET) described in *section 2.4*. It is able to combine two techniques for performing controlled desiccation tests: (i) a balance with 0.1g accuracy to follow water content evolution, salt solution to impose the hygrometric parameters (relative humidity and temperature) that were measured with a hygrometer; (ii) DIC method which needs an HD camera to take images every fixed time interval, a computer to save the images and allows running calculations with Vic2D software which leads an accuracy about 3% for displacements.

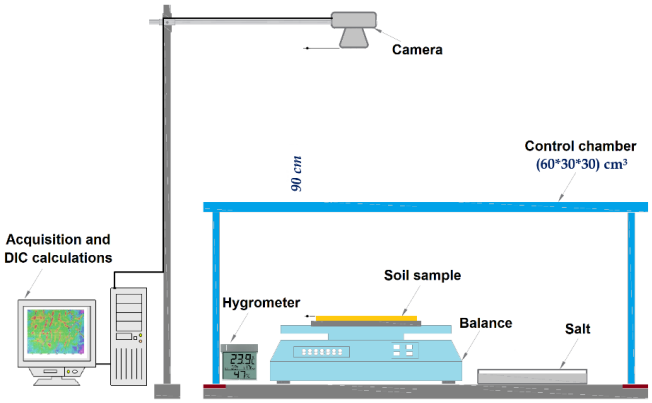


Figure 1. Experimental controlled desiccation test apparatus

To carry out the two-dimensional DIC method, Vic2D software was used similarly to that of Wei et al. (2016). It provides the displacement and strain fields to analyse precisely the local behaviour of the material during controlled desiccation paths.

2.3. DIC method parameters and Vic2D software

Before using Vic2D software, some parameters should be defined (Fig. 2): (i) scale calibration to convert pixels of saved images to milimiters of displacements, 1 pixel = 0.11 mm; (ii) subset = 17 and step = 5 of the selected area into the image, important parameters that allow to optimize DIC calculations in terms of the correlation quality and time needed to finish the run.

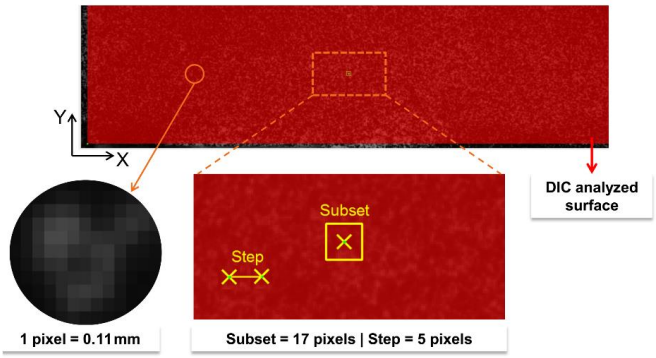


Figure 2. DIC parameters on Vic2D software

The outputs of running Vic2D software are: (i) displacements, u (mm) along the X-axis, and v (mm) along the Y-axis; (ii) strains generated in post-processing, ε_{xx} (%) normal component of strain in the X-direction, ε_{yy} (%) normal component of strain in the Y-direction, and ε_{xy} (%) shear strain.

2.4. Salt solutions technique characteristics

Controlled desiccation tests were performed using salt solutions technique based on Kelvin's law. Thus, the Equation (1), given by Fredlund and Rahardjo (1993), allows determining the imposed global suction s_{glob} (MPa) as a function of relative humidity *RH* and thermodynamic temperature *T* inside the control chamber.

$$s_{glob} = -\frac{\rho_w RT}{M_w} ln\left(\frac{RH\%}{100}\right) \quad (1)$$

where M_w *is the molar mass of water, R is the molar gas constant and* ρ_w *is volumetric mass of water*.

Three suction levels were fixed in this study corresponding to three salt solutions, selected according to the conditions cited in Delage et al. (1998):

(i) high in 361±11MPa using KOH;
(ii) middle in 110±5.7MPa using K_2CO_3;
(iii) low in 38±9.8MPa using NaCl.

Test names are given following this nomenclature: CD (controlled desiccation) _Test number (1 to 3) _Mean value of s_{glob} (MPa). Example: CD2-s361 (test number 2 for high suction level).

3. RESULTS AND DISCUSSION

3.1. Drying evolution under controlled desiccation path

Figure 3 shows the drying curves evolution under each suction level. The results highlight that drying velocity, defined by *dw/dt* (%/h), changes with suction level. Three characteristic intervals of time can be identified for each curve:

(i) first stage from t_1 to t_2, where the mean value of drying velocity noted $(dw/dt)_m$ is calculated;
(ii) second stage where t_2 is the beginning of drying velocity decrease and tends to zero at t_3;
(iii) final stage for $t > t_3$, *dw/dt* equals zero meaning there is no drying more.

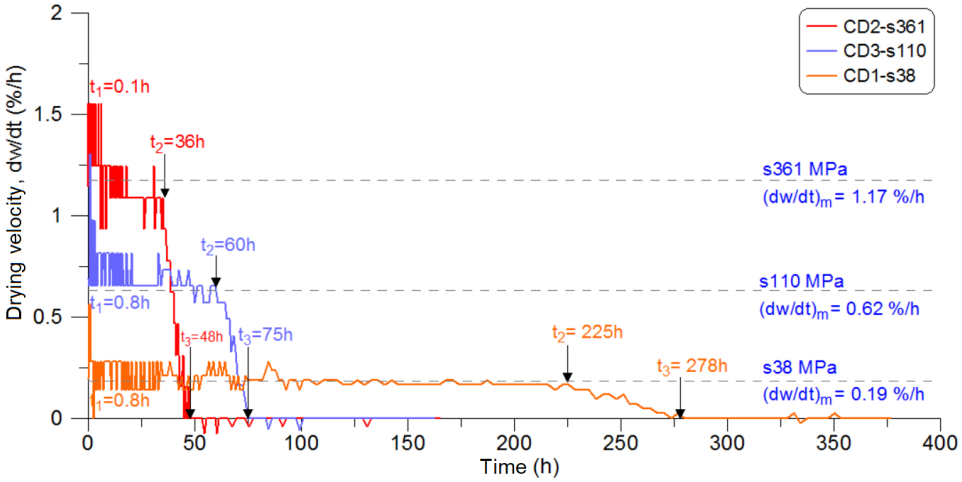


Figure 3. Drying velocity under different suction levels during controlled desiccation path (m = mean value)

3.2. Shrinkage phenomenon: analysis at the global scale

In order to analyse the shrinkage kinetic during drying, a shrinkage velocity was determined from an estimated volumetric strain defined by $d\varepsilon_v/dt$ (%/h) and plotted as a function of time on Figure 4. The results show a similar trend of curves compared to that of drying velocity (Figure 3) with an evolution in three stages. Here, time t_3 represents the shrinkage limit time t_{SL}. This comparison highlights that t_2 and t_{SL} on Figure 4 are less than t_2 and t_3 on Figure 3, respectively at each suction level. When shrinkage stops, drying of soil sample continues to happen and tends to zero later more.

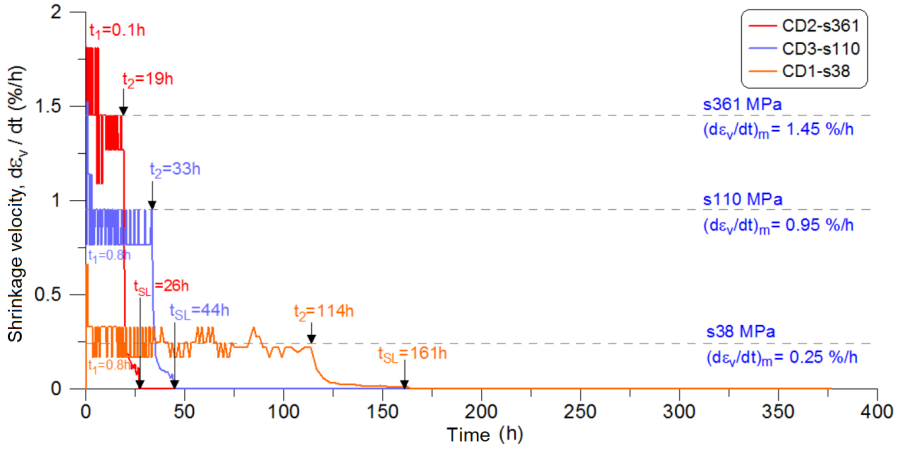


Figure 4. Shrinkage velocity under different suction levels during controlled desiccation path (m = mean value)

3.3. Discussion: controlled desiccation cracking

Only mode I (opening mode), developed in Ighil Ameur and Hattab (2022) through bending tests, was observed in all cracks of this study developed under high suction level. Generally, cracks initiate from edges and propagate to the center of soil sample. Two edge-cracking zones are localized on ε_{xx} and ε_{yy} maps shown in Figure 5 (a) and (b) and named *III-CD2-s361* and *II-CD2-s361*, respectively. To

highlight this cracking mechanism (mode I), principal "mechanical" strains analysis were carried out using a calculation program developed by Wei (2014). The results are shown in Figure 5 (a') and (b') for *III-CD2-s361* and *II-CD2-s361*, respectively. In these two zones, extension characterized by many long red vectors appears very dense and all perpendicular to the direction of the crack. This confirms the crack initiation by mode I.

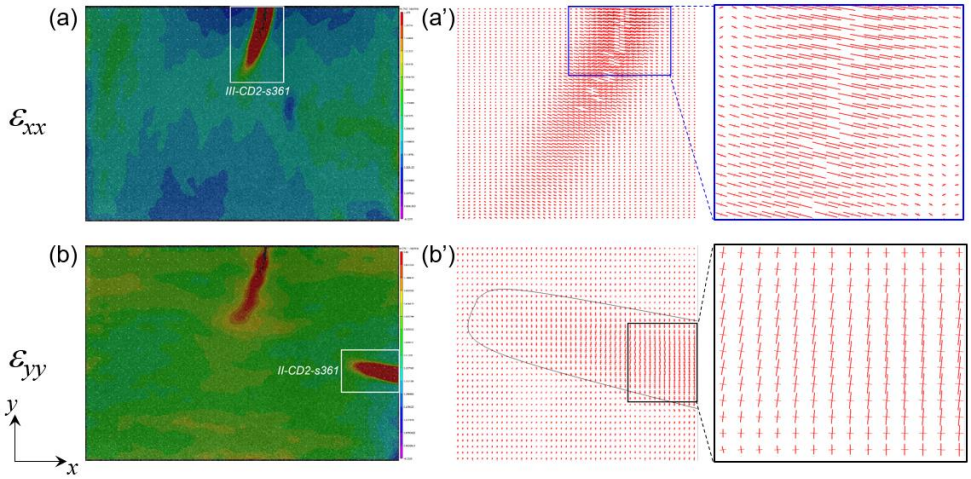


Figure 5. Identified cracks on ε_{xx} and ε_{yy} DIC maps and principal "mechanical" strains method (t = 161 h and w = 2.65%)

4. CONCLUSIONS

In this research, an experimental device based on both salt solutions technique and DIC method was developed in the laboratory. This allowed to perform controlled desiccation paths under different suction levels. Study is focused on characterizing shrinkage phenomenon and understanding cracks' initiation.

According to this analysis, there is an influence of suction level on drying and shrinkage kinetics evolution: more suction increases, more the kinetic is faster. Furthermore, a shrinkage part of strains can be distinguished and completed by an additional part assumed as "mechanical", acting cracks.

Cracking mechanism in mode I was observed under high suction level. Calculations of principal "mechanical" strains, without the shrinkage part, allowed confirming this mode of cracking. Thus, it can be assumed that cracks initiate when the "mechanical" strain part exceeds a critical value.

REFERENCES

Delage P., Howat M. D., Cui Y. J. 1998. The relationship between suction and swelling properties in a heavily compacted unsaturated clay. *Eng. Geology J*, 50, 31-48.

Fredlund D. G. and Rahardjo H. 1993. *Soil mechanics for unsaturated soils*. John Willey J.

Hammad T., Fleureau J. M. & Hattab M. 2013. Kaolin/montmorillonite mixtures behaviour on oedometric path and microstructural variations. *Eur. J. Env. Civ. Eng* 17, No. 9, 826–840.

Hattab M., Hammad T. & Fleureau J. M. 2014. Internal friction angle variation in a kaolin/montmorillonite clay mix and microstructural identification. *Géotechnique*, 65(1), 1–11.

Ighil Ameur L., Hattab M. 2022. Cracking of unsaturated clays using a newly developed small-beam bending apparatus and analysis by digital image correlation. *Geomechanics for Energy and the Environment*, 32, 100307. 10.1016/j.gete.2021.100307

Kodikara J. K., Barbour S. L., Fredlund D. G. 1999. Changes in clay structure and behavior due to wetting and drying. *Proc of the 8th Aust-NZ Conf on Geomech*, 179- 186.
Morris P. H., Graham J., Williams D. J. 1992. Cracking in drying soils. *Can. Geo. J*. 29, 263-277.
Wei X., Hattab M., Bompard P., Fleureau J. M. 2016. Highlighting some mechanisms of crack formation and propagation in clays on drying path. *Geotech. J*. 66(4), 287-300.
Wei X. 2014. Etude micro-macro de la fissuration des argiles soumises à la dessiccation. Doctoral dissertation, France.

28th European Young Geotechnical Engineers Conference – EYGEC 2024
© 2024 Macedonian Association for Geotechnics, ISBN 978-608-4510-61-1

Liquefaction resistance of sand – fly ash mixtures

Elena Angelova [a], Vlatko Sheshov[b], Julijana Bojadjieva[b], Kemal Edip[b], Toni Kitanovski[b], Dejan Ivanovksi[b]

[a,] *Geohydroconsulting, Skopje, Macedonia*
[b] *Institute of Earthquake Engineering & Engineering Seismology (IZIIS), Skopje, Macedonia*

ABSTRACT

Environmental studies have witnessed a surge in interest, as a result of the growing awareness of the substantial presence of waste materials on a global scale. Despite recycling and material reutilization, there is also trend for exploring novel ways for use of waste products. In geotechnical engineering one such materials is fly ash, a byproduct stemming from combustion of coal for electricity generation. While extensive research has been devoted to examining its efficacy in enhancing the properties of fine-grained soils, comparatively less attention has been directed towards investigating mixtures comprising granular materials and fly ash. Adding fly ash to granular materials for soil replacement purposes would significantly mitigate the use of natural materials, but also the volume of deposited fly ash. Combining fly ash with sand introduces an aspect of liquefaction potential, necessitating thorough evaluation of this phenomena. This paper presents a comparative analysis of findings derived from two distinct studies for liquefaction resistance of sand-fly ash mixtures from different origin. Both studies show similar reduction of the liquefaction resistance of the sandy materials upon introduction of fly ash.

KEYWORDS

Fly ash; sand; liquefaction resistance.

1. INTRODUCTION

Fly ash, a residual byproduct derived from coal combustion in electricity generation, is regularly deposited in landfills. To date, the primary and most prevalent application of fly ash has been within the concrete industry. Nevertheless, numerous investigations have been conducted to assess the viability of employing fly ash in the field of geotechnical engineering (Angelova and Sheshov, 2022). The aforementioned studies predominantly focus on the utilization of fly ash for soil enhancement and substitution, particularly in mixtures with fine-grained materials (Beeghly, 2003; Senol et al, 2006; McCarthy et al., 2009; Santos et al, 2011; Vukićević et al., 2019). Moreover, multiple case studies demonstrate the successful practical implementation of these methodologies. (Beeghly, 2003; Parsons and Kneebone, 2005; Edil and Benson, 2007; Jackson et al, 2007; Lin et al, 2009; Trast et al, 2011).

Considering the combination of sand and fly ash, there are less available studies, originating from diverse geographic locations, indicating the global interest in such research. The existing studies refer to testing of natural sand sourced from various origins combined with fly ash. Specifically, in the literature can be found mixtures of Skopje sand with 5, 10 and 20% fly ash (Angelova et al, 2021; Angelova et al, 2023; Angelova et al, 2024), and Ottawa sand with 10, 20, 25, 30, 40 and 50% fly ash (Kolay et al, 2019).

This paper compares the findings from cyclic triaxial tests conducted on mixtures with Skopje sand and Ottawa sand with fly ash, as investigated by Angelova et al (2024) and Kolay et al (2019). The comparability stems from the utilization of analogous ranges of fly ash percentages in the mixtures. Even though the sand and fly ash in the two compared studies have different origin, there are some

common trends which should be taken into consideration in further studies. Such findings hold particular significance if these composite materials are envisaged for application within seismically active regions.

2. EXISTING FINDINGS

2.1. Skopje sand-fly ash

Angelova et al (2024) performed cyclic triaxial tests on mixtures of Skopje sand and Class F fly ash with variable relative density. The mixtures contained 5, 10 and 20% fly ash. They were tested for 100 kPa effective stress and CSR from 0.1 to 0.5. These results were compared to existing study for clean Skopje sand by Bojadjieva (2015). Angelova et al (2024) observed reduction in the liquefaction resistance of the primary material when fly ash is added as in the studied range of 5-20%, without regular trend of this reduction with respect to the percentage of fly ash. Based on their results for the maximum and minimum unit weight of the sand-fly ash mixtures, they have concluded that the fly ash is attached to the sand particles, coating them and reducing the contact between sand particles. The results from the tests are presented in Table 1 and Table 2.

Table 1. Results from cyclic triaxial tests on clean Skopje sand by Bojadjieva (2015)

Sample	Relative density Dr [%]	CSR	No. of cycles
Clean Skopje sand	40	0.1	900
	40	0.15	63
	40	0.2	18
	40	0.25	9
	40	0.3	6
	40	0.5	2
	55	0.12	900
	55	0.2	83
	55	0.3	13
	55	0.5	5
	75	0.2	1351
	75	0.25	118
	75	0.3	54
	75	0.5	25

Table 2. Results from cyclic triaxial tests on sand-fly ash mixtures by Angelova et al (2024)

Sample	Relative density Dr [%]	CSR	No. of cycles
Skopje sand with 5% fly ash	61.19	0.1	500
	65.06	0.2	12
	53.32	0.3	5
	59.04	0.4	2
Skopje sand with 10% fly ash	74.33	0.1	500
	72.08	0.2	29
	65.39	0.3	7
	58.46	0.4	3
Skopje sand with 20% fly ash	59.58	0.1	152
	63.85	0.15	19
	65.40	0.2	9
	62.28	0.3	3

2.2. Ottawa sand-fly ash

Kolay et al. (2019) tested mixtures of Ottawa sand and Class F fly ash with relative density of 50% in order to study the liquefaction behaviour. The authors used high percentages of fly ash, namely 10, 20, 25, 30, 50 and 70% fly ash. The mixtures were tested for 103.42 kPa effective stress and CSR from 0.1 to 0.5. Based on their results the authors concluded that the liquefaction resistance initially decreases and then increases for mixtures with fly ash in the range 20-25%, whereas for more than 25% fly ash the liquefaction resistance decreases. Based on the results for the maximum and minimum void ratio which decreased with higher presence of fly ash, the authors concluded that the fly ash filled the voids of the sand. Also, they observed that with the increase of fly ash the samples deform abruptly, meaning that fly ash increases brittleness of the samples.

Table 3. Results from cyclic triaxial tests on clean sand and sand-fly ash mixtures at effective confining pressure 103.42 kPa by Kolay et al (2019)

Sample	Relative density Dr [%]	CSR	No. of cycles
Clean Ottawa sand	50	0.10	Not liquefied
	50	0.20	9
	50	0.30	4.5
	50	0.35	3.5
	50	0.40	3
Ottawa sand with 10% fly ash	50	0.10	234
	50	0.20	7.5
	50	0.30	2.5
	50	0.35	2.2
	50	0.40	2
Ottawa sand with 20% fly ash	50	0.10	290
	50	0.20	8
	50	0.30	3.5
	50	0.35	2.5
	50	0.45	2.1
Ottawa sand with 25% fly ash	50	0.10	Not liquefied
	50	0.20	520
	50	0.30	35
	50	0.40	5
Ottawa sand with 30% fly ash	50	0.10	68
	50	0.20	10
	50	0.30	3
	50	0.40	1
Ottawa sand with 50% fly ash	50	0.10	755
	50	0.20	30
	50	0.30	8
	50	0.40	2
Ottawa sand with 70% fly ash	50	0.10	Not liquefied
	50	0.20	Not liquefied
	50	0.30	14
	50	0.40	10
	50	0.50	3

3. COMPARISON OF THE STUDIES

In the study by Angelova et al (2023) the fly ash is classified as sandy silt, whereas the Skopje sand is poorly graded sand with silt. In the study by Kolay et al (2019) the used fly ash refers to silty clay with sand and the Ottawa sand is classified as poorly graded sand. The comparison of the sand and fly ash used in both studies can be seen in the common graph in Figure 1, showing the difference in the fractions of these materials.

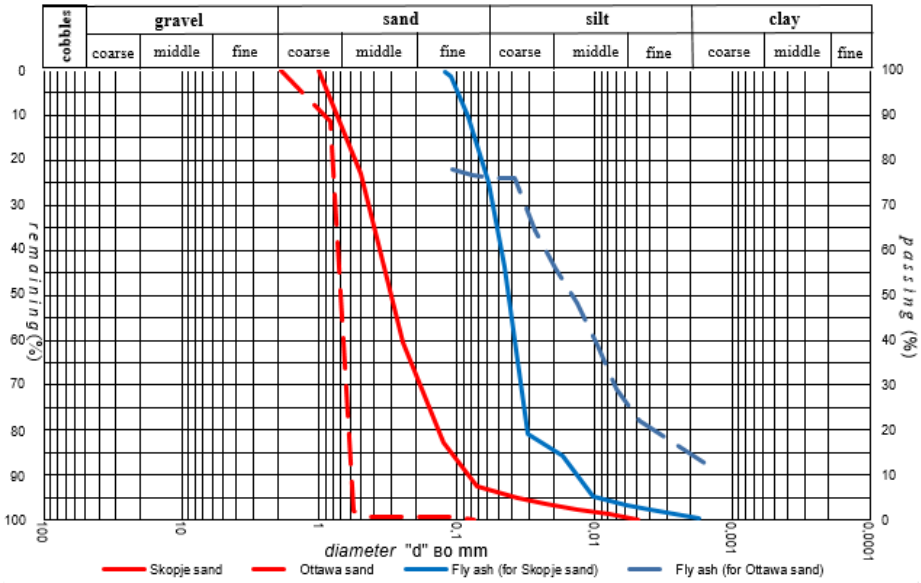


Figure 1. Comparison of grain size of clean Skopje sand and fly ash by Angelova et al (2023) and clean Ottawa sand and fly ash by Kolay et al (2019)

Figure 2 shows all results from the cyclic triaxial tests presented by Angelova et al. (2024), Bojadjieva (2015) and Kolay et al (2019). Angelova et al (2024) has recognized a consistent pattern across the compared studies, indicating a general decrease of the liquefaction resistance of sand upon addition of fly ash. Furthermore, their analysis reveals that in both studies there is an absence of particular trend in the liquefaction resistance reduction corresponding to incremental increases in fly ash percentage.

Furthermore, in line with the observations by Angelova et al. (2024), the shared graphical representation in Figure 2 illustrates that the majority of curves from both studies align within a distinct region before the curve representing clean Skopje sand with a relative density of 40%. Notably, an exception to this trend is observed in the case of the Ottawa sand mixture comprising 25% fly ash, which, according to the findings reported by Kolay et al. (2019), exhibits a marked enhancement in liquefaction resistance.

Numerous differences characterize the samples across the studies, spanning from variations in grain size of both sand and fly ash materials to variable relative density within the Skopje sand-fly ash mixtures, as well as a wider range of Ottawa sand-fly ash mixtures encompassing diverse percentages of fly ash. Despite these discrepancies, a noticable clustering of data points is evident, suggesting a common zone for the liquefaction resistance of sand-fly ash mixtures with variable properties. However, conclusive statements regarding the generalizability of this zone necessitate further testing.

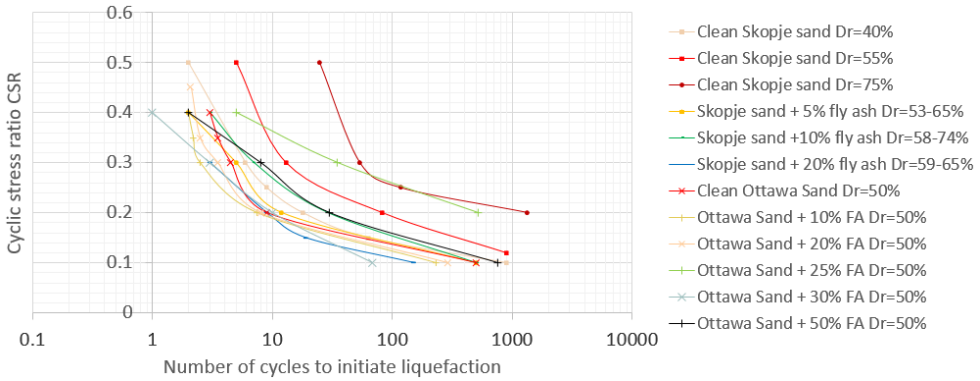


Figure 2. Comparison of liquefaction resistance of clean Skopje sand (after Bojadjieva, 2015), Skopje sand-fly ash mixtures (after Angelova et al, 2024), clean Ottawa sand and Ottawa sand-fly ash mixtures (after Kolay et al, 2019)

4. CONCLUSIONS

Environmental studies have gained significant interest due to increased awareness regarding the global abundance of waste materials. While recycling and reuse efforts are ongoing, there is a rapidly growing interest in exploring innovative possibilities for waste utilization. One such material of interest in geotechnical engineering is fly ash, a byproduct of coal combustion for electricity generation. While extensive research has focused on its effectiveness in enhancing fine-grained soils, less attention has been devoted to mixtures involving granular materials and fly ash. Incorporating fly ash into granular materials for soil replacement could reduce reliance on natural resources and decrease deposited fly ash volume. However, this introduces liquefaction potential, necessitating comprehensive evaluation. This study compares findings from two separate investigations on sand-fly ash mixtures' liquefaction resistance.

In conclusion, the comparative analysis of cyclic triaxial tests conducted on mixtures of Skopje sand and Ottawa sand with varying proportions of fly ash, as investigated by Angelova et al. (2024) and Kolay et al. (2019), shows several noteworthy insights. Despite inherent differences in sample properties such as grain size distribution, relative density, and fly ash content, a consistent reduction in liquefaction resistance of sand upon the addition of fly ash is observed across both studies. The clustering of data points behind the curve representing clean Skopje sand with a relative density of 40% suggests a common trend, which should be considered upon analysing the potential utility of fly ash in soil stabilization. However, the notable exception of the Ottawa sand mixture containing 25% fly ash, which exhibits an improved liquefaction resistance, highlights the different impact of varying mixture compositions. These findings highlight the importance of further research to comprehensively characterize the influence of material properties on the liquefaction behavior of sand-fly ash mixtures, particularly in contexts such as seismic-prone regions where soil liquefaction is a hazard.

5. ACKNOWLEDGEMENTS

I would like to thank the Macedonian company Geohydroconsulting, for supporting me to participate in renowned professional gatherings such as this conference.

REFERENCES

Angelova, E., Šešov, V., Dimitrijević, S. and Gardić, V. (2021): Chemical characterization of fly ash samples for further use in seismic geotechnical engineering, *Proceedings of the Fourth Macedonian Geological Congress*, Ohrid, North Macedonia, 11-17.

Angelova, E. and Sheshov, V. (2022): Utilization of fly ash from power plants in geotechnics and civil engineering, *Proceedings of the Fifth symposium of the Macedonian Association for Geotechnics, ISRM specialized conference ISBN 978-9989-2053-4-7,* Ohrid, North Macedonia, 784-791.

Angelova, E., Angelov, V., Sheshov, V., Bojadjieva, J., Edip, K., Kitanovski, T., Ivanovski, D. and Dimitrijević, S. (2023): Effects of fly ash on sand behaviour in monotonic triaxial tests, *Proceedings of the 17th Asian Regional Conference on Soil Mechanics and Geotechnical Engineering*, Astana, Kazakhstan, 691-695. DOI: 10.1201/9781003299127-90

Angelova, E., Sheshov, V., Bojadjieva, J., Edip, K., Kitanovski, T., Ivanovski, D. and Dimitrijević, S. (2024): Dynamic behaviour of sand-fly ash mixture by element testing, *Proceedings of the 8th International Conference on Earthquake Geotechnical Engineering*, Osaka, Japan

Beeghly, J. (2003): Recent Experiences with Lime- Fly Stabilization of Pavement Subgrade Soils, Bas, and Recycled Asphalt. *International Ash Utilization Symposium (Paper No. 46). Kentucky: University of Kentucky.*

Bojadjieva, J. (2015): *Dynamic behaviour of 15 saturated cohesionless soils based on element and 1-G experiments.* PhD Thesis. University "St. Cyril and Methodius", Institute of Earthquake Engineering and Engineering Seismology, Skopje.

Edil, T.B. and Benson, C.H. (2007): Sustainable Construction Case History: Fly ash Stabilization of Road-Surface Gravel. Paper presented at the World of Fly ash (WOCA), Lexington, KY, USA

Jackson, N.M., Mack, R., Schultz, S. and Malek, M. (2007): Pavement Subgrade Stabilization and Construction Using Bed and Fly Ash. Paper presented at the World of Fly ash (WOCA), Lexington, KY, USA

Kolay, P. K., Puri, V. K., Lama Tamang, R., Regmi, G. and Kumar, S. (2019): Effects of Fly Ash on Liquefaction Characteristics of Ottawa Sand. International Journal of Geosynthetics and Ground Engineering 5:6

Lin, L., Tuncer, E., Benson, C. (2009): Properties of Pavement Geomaterials Stabilized with Fly Ash. Paper presented at the World of Fly ash (WOCA), Lexington, KY, USA

McCarthy, M. J., Csetenyi, L. J., Sachdeva, A., and Jones, R. (2009): Role of Fly Ash in the Mitigation of Swelling in Lime Stabilised Sulfate Bearing Soils. Paper presented at the World of Fly ash (WOCA), Lexington, KY, USA

Parsons, R. L., and Kneebone, E. (2005): Field performance of fly ash stabilised subgrades. Proceedings of the Institution of Civil Engineers. Ground improvement, 9(1), 33-38.

Santos, F., Li, Lin., Li, Y. and Amini, F. (2011): Geotechnical Properties of Fly Ash and Soil Mixtures for Use in Highway Embankments. Paper presented at the World of Fly ash (WOCA), Denver, CO, USA

Senol, A., Edil. T.B., Acosta, Bin-Shafique, M.S. and Benson, C.H. (2006): Soil stabilization by using the sorts of fly ash at various sites in Wisconsin. Resources, conservation, and recycling, 46(4), 365.*87 Proc.INTERMAG Conf.*, pp. 2.2-1–2.2-6.

Trast, J.M., DeJardin D.M. and Skrzypchak, G.M. (2011): Beneficial Use of Fly Ash for an Airport Safety Way Extension over a Multiple Year Project. Paper presented at the World of Fly ash (WOCA), Denver, CO, USA

Vukićević, M., Marjanović, M., Pujević, V. and Jocković, S. (2019): The Alternatives to Traditional Materials for Subsoil, Stabilization and Embankments. Materials, 12, 3018; doi: 10.3390/ma12183018

28th European Young Geotechnical Engineers Conference – EYGEC 2024
© 2024 Macedonian Association for Geotechnics, ISBN 978-608-4510-61-1

Assessment of the impact of soil degradation due to pile driving on slope stability in cohesive soil conditions

Yeganeh Attari[a,b], Gudmund Reidar Eiksund[b]

[a] *Multiconsult AS, Oslo, Norway*
[b] *Norwegian University of Science & Technology, Trondheim, Norway*

ABSTRACT

Piles are a common foundation solution to support buildings, bridge abutments and embankments in soft soil deposits to transfer structural loads to deeper more stable soil layers or bedrock. During pile driving adjacent to slopes, stability of the slope can be negatively affected due to excess pore pressure generation, dissipation of the excess pore pressure into the slope, induced displacements, and cyclic degradation of the soil among other possible factors. However, there is a lack of understanding of the failure mechanisms involved in this phenomenon; as well as methods to account for the temporary reduction in slope stability during pile driving. This paper provides an overview of this problem. Furthermore, the paper introduces a method which couples pile driving analysis using wave theory with numerical finite element analysis to obtain the extent of cyclic soil degradation due to pile driving. This could be further used to assess stability of a slope during pile driving.

KEYWORDS

Pile driving, Installation effects, Cyclic degradation, Slope Stability.

1. INTRODUCTION

1.1. Piles and pile driving

Piles are foundation elements that transfer structural loads from weak soil layers to deeper more competent strata or the bedrock. Piles can be classified into replacement or displacement piles according to their method of installation. Piles that are driven into the soil by a piling hammer and displace the adjacent soil during lie in the displacement pile category. The magnitude of the displacement depends on the pile size and type (open vs close ended). In Scandinavia, onshore piles are generally precast concrete piles. For building foundations, pile diameter of 300mm or quadratic cross section piles of 230 or 270 are common choices. Bridge foundations are commonly built with concrete in close ended 0.8m wide steep pipes. Offshore structures which require larger foundations can have piles with diameter up to 3m and length in the order of 50 to 100m.

Driving piles into clay generates high shear strains in the soil as the pile tip goes through the ground. Hence, the soil close to the pile undergoes a high degree of remoulding. This process is usually considered to be undrained, except in high-permeability silty clays where certain degree of drainage may occur. The act of pile driving pushes the soil away and generates an increase in total horizontal stresses which depend on the undrained shear strength of the soil (typically in the order of 4 to 6 times the undrained shear strength), (Randolph and Gourvenec, 2011). Furthermore, changes in pore pressure occurs which arises from two different mechanisms: Firstly, an increase in pore pressure occurs in response to increase in total stress and secondly (and to a smaller degree of contribution), a change in excess pore pressure occurs due to undrained shearing of the soil (Randolph and Gourvenec, 2011). This change can be positive or negative with respect to the type of clay. Stiff clays show a dilative behavior during shearing and generate suction, whereas soft clays tend to contract and result in an increase in the pore pressure (Burns and Mayne, 1999).

1.2. Slope stability and pile driving in slopes

Addressing stability issues in natural or engineered slopes presents significant challenges in engineering design and construction. Various factors, such as changes in groundwater table due to heavy rainfall or rapid drawdown, seismic forces, and construction activities can lead to slope failure (Broms and Wong, 1991). Typically, slope failure occurs when the average shear stresses along the slip surface exceeds the shear strength of the soil or rock material (Broms and Wong, 1991). However, this isn't always the sole cause, particularly in the case of a progressive failure mechanisms -where a local failure can trigger a general slope failure. Preventing such incidents requires a comprehensive understanding of failure mechanisms, investigative and predictive tools, as well as stabilization measures (Abramson et al., 2001). The primary objective of slope stability analysis is to ensure safety for individuals, structures, and infrastructure, while also contributing to the economically and safely designed and constructed structures (Chowdhury, 1978).

Pile driving in clay induces rapid undrained soil behavior due to clay's low permeability (Randolph and Gourvenec, 2011). Early studies by Bjerrum et al. (1958) were among the first to address excess pore pressures around piles driven in clay. Subsequent research by Bjerrum and Johannessen (1960) highlighted that the increase in pore pressure during pile driving, followed by its dissipation, temporarily reduces the undrained shear strength and decreases the factor of safety of nearby slopes. The soil properties near the pile wall are influenced during the driving process, leading to the formation of plastic and elastic zones, as defined by Karlsrud and Nadim (1990). Zone I, characterized by high shear-induced and displacement-induced pore pressures, is confined to the immediate vicinity of the pile. Conversely, the elastic zone, representing excess pore pressure due solely to displacement, extends further and decays exponentially with distance. This elastic zone can be subdivided into zones II and III. In zone II, pore pressure decreases after pile driving ceases, while in zone III, dissipation of excess pore pressure leads to a delayed increase in pore pressure and subsequently a delayed reduction in effective stress (see Figure 1). The effects of the pore pressure migration into various zones in the slope is explained in detail in Attari et al. (2023). This paper aims to provide some insight into the cyclic effects of pile driving on slope stability.

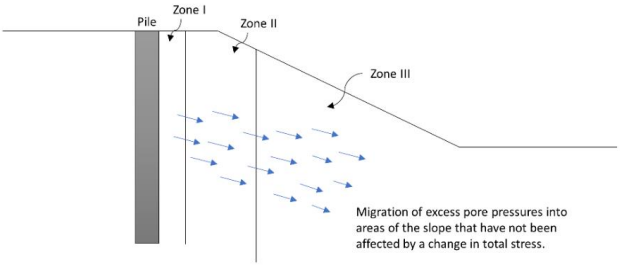


Figure 1. Affected zones around the pile wall due to pile driving, with regards to pore pressure generation and dissipation (Attari et al., 2023)

1.3. Cyclic loading and soil degradation due to cyclic loading

The response of soil to cyclic loading in clay differs from that in sandy materials due to the influence of time-dependent creep and preconsolidation periods (Yasuhara et al., 1992). Early investigations into clay behavior under cyclic loading were conducted by Sangrey et al. (1969), who performed triaxial tests on saturated clay samples. Their findings revealed the presence of a specific critical cyclic stress for each consolidation history, beyond which failure occurred. Subsequent studies by Andersen et al. (1976) extensively examined the behavior of Drammen clay under cyclic loading. Andresen et al. (1976) have developed calculation procedures to evaluate the impact of cyclic loading on various soil types,

based on extensive laboratory testing of clay samples and resulting contour diagrams. An example of these diagrams is presented in Figure 2.

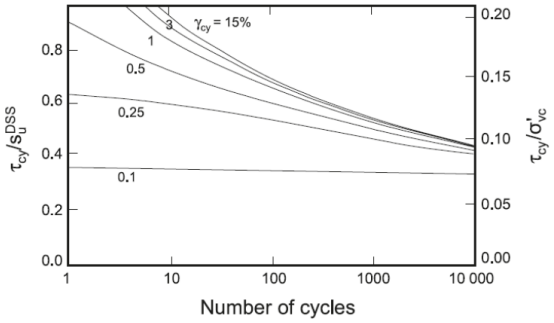


Figure 2. Extent of cyclic degradation of soil based on cyclic shear stress to undrained shear strength ratio, according to the number of cycles (Andresen et al., 1976).

2. SUGGESTED METHODOLOGY

2.1. Pile driving analysis

Pile driving transfers kinetic energy from the hammer to the top of the pile. Several hammer blows are required until the desired depth of the pile is reached (Woods, 1990). A compression body wave is generated in the pile by the hammer. As the wave travels down towards the pile toe, part of it is reflected in the pile and part of it transmits to the surrounding soil (Selby,1991). The energy transmitted to the soil from the pile depends on the pile and hammer characteristics. The elastic soil deformation due to this impact is propagated in the soil as elastic waves.
Pile driving analysis evaluates the ability of a hammer with a certain energy to safely drive a pile down to the required design depth into the soil (Stevens et al., 1982). A pile driveability analysis takes into account the pile geometry, type and energy of the hammer, as well as soil properties, which quantifies the soil's resistance to driving (Stevens et al., 1982). Pile driving analysis is typically performed using Wave Theory by means of software such as GRLWEAP.

For the purposes of the analysis, a pile driving analysis was conducted in GRLWEAP using a typical size onshore concrete pile, as delineated in the introduction. The pile driving analysis provides the number of blows among other results. The displacement versus time history related to one hammer blow in this case was accordingly used as input in the numerical model generated in the next step.

2.2. Finite element analysis and post-processing using cyclic degradation curves

A wished-in-place pile is modelled in Plaxis 2D, axisymmetric model (see overview of the model in Figure 3).

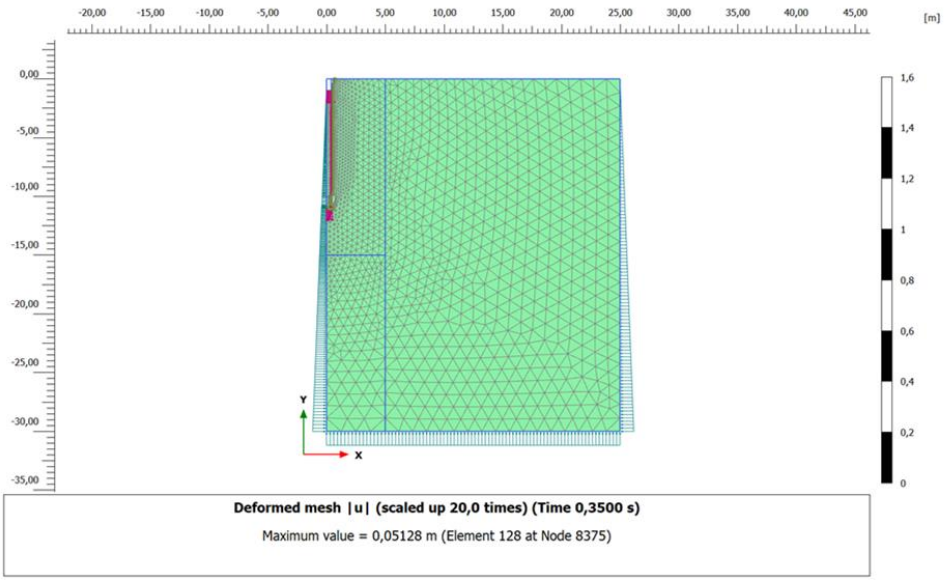


Figure 3. Overview of the Plaxis model.

The HSSs constitutive model is used for this analysis and a soil strength profile of Su=20+2z kPa, where undrained moel B is used. The displacement in dynamic time generated in the previous stage is used as a dynamic prescribed displacement in the Plaxis 2D model. Required boundary conditions and interface properties are considered accordingly. Among the results of this analysis, shear stresses generated in different points in the soil are looked at (See Figure 4, where X is the lateral distance between pile and considered output point, and Y denotes the vertical distance). The accumulation of the shear stress in the soil body is then calculated based on the piling layout. These results are used to assess the extent of the cyclic shear degradation (generation of cyclic shear strains and cyclic excess pore pressure).

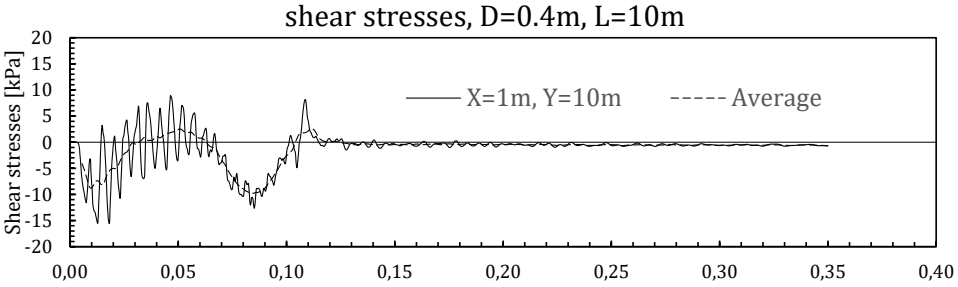


Figure 4. Shear stresses in the soil in dynamic time (related to one hammer blow)

3. DISCUSSION & CONCLUSION

Pile driving adjacent to slopes can pose challenges with regards to slope stability. The cyclic loading resulting from the hammer blows can in some cases depending on the soil properties, pile geometry and piling layout cause excessive soil degradation which can generate excess pore pressure and affect soil strength. A methodology in the early phases is suggested for this purpose, where pile driving analysis is conducted to provide time-displacement input to a simplified numerical model that aims to calculate the

shear stresses generated due to pile driving in each case. This can further on predict the magnitude of the generated excess pore pressure and evaluate the dynamic effects of pile driving on soil strength. This paper attempts to suggest a method to account for the cyclic degradation of soil due to pile driving in cohesive soil which could have the potential to be used with regards to slope stability problems. A challenge is to implement this into a slope where initially a degree of shear is being mobilized. This is being researched further and in more detail. It shall be noted that this is under development and final results will be presented in future publications.

4. ACKNOWLEDGEMENTS

This study was done within BegrensSkade (REMEDY) II research project financed by the Norwegian Research Council (grant 267674). The authors acknowledge the support of the research project leader, Dr. Jenny Langford at the Norwegian Geotechnical Institute. The authors also acknowledge the scientific support of Erik Sørlie at Multiconsult Oslo. The authors also appreciate the financial support provided by the Norwegian Geotechnical Society with regards to the conference attendance.

REFERENCES

Abramson, L. W., Lee, T. S., Sharma, S., and Boyce, G. M. (2001). Slope stability and stabilization methods. John Wiley & Sons.

Andersen, K. H., Brown, S. F., Foss, I., Pool, J. H., and Rosenbrand, W. F. (1976). Effect of Cyclic Loading on Clay Behaviour. In Nor Geotek Inst Publ, number 113, pages 1-6. Thomas Telford Publishing.

Attari, Y., Jostad, H. P., Grimstad, G., & Eiksund, G. R. (2023). Evaluation of Pile Driving Effe cts on Slope Stability in Clay. Geotechnical and Geological Engineering, 1-16.

Bjerrum L, Johannessen IJ (1960) Pore pressures resulting from driving piles in soft clay. Norwegian Geotechnical Institute. In: Pore pressure & suction in soils Conference, Londres.

Broms, B. B. and Wong, K. S. (1991). Landslides. In Foundation Engineering Handbook, pages 410-446. Springer.

Burns SE, Mayne PW (1999) Pore pressure dissipation behavior surrounding driven piles and cone penetrometers. Transp Res Rec 1675(1):17–23.

Chowdhury, R. N. (1978). Effective-Stress Parameters of Anisotropic Soil. Journal of the Geotechnical Engineering Division, 104(1):124-128.

Karlsrud K, Nadim F (1990) Axial capacity of offshore piles in clay. Offshore technology conference, OnePetro.

Matsui, T., Ohara, H., & Ito, T. (1980). Cyclic stress-strain history and shear characteristics of clay. Journal of the geotechnical Engineering Division, 106(10), 1101-1120.

Randolph M, Gourvenec S (2011) Offshore geotechnical engineering/Mark Randolph and Susan Gourvenec; with contributions from David White and Mark Cassidy. Abingdon, Spon Press, Oxon New York.

Sangrey, D. A., Henkel, D. J., & Esrig, M. I. (1969). The effective stress response of a saturated clay soil to repeated loading. Canadian Geotechnical Journal, 6(3), 241-252.

Stevens, Robert S., Wiltsie, Edward A., and Thomas H. Turton. (1982) Evaluating Drivability for Hard Clay, Very Dense Sand, and Rock. Paper presented at the Offshore Technology Conference, Houston, Texas, May 1982. doi: https://doi.org/10.4043/4205-MS.

Wood, D. M. (1990). Soil behaviour and critical state soil mechanics. Cambridge university press.

Yasuhara, K., Yamanouchi, T., & Hirao, K. (1982). Cyclic strength and deformation of normally consolidated clay. Soils and Foundations, 22(3), 77-91.

Yasuhara, K., Hirao, K., & Hyde, A. F. (1992). Effects of cyclic loading on undrained strength and compressibility of clay. Soils and Foundations, 32(1), 100-116.

28th European Young Geotechnical Engineers Conference – EYGEC 2024
© 2024 Macedonian Association for Geotechnics, ISBN 978-608-4510-61-1

Sustainable Improvement of a Fine Sand Using Microbially Induced Calcite Precipitation

Hanieh Babaeizad[a]

[a] *Department of Civil and Environmental Engineering, Ruhr University Bochum, Germany*

ABSTRACT

In recent years, the need for effective soil improvement methods to overcome challenges associated with problematic soils has grown significantly. However, many of the conventional methods come with considerable environmental impacts, energy consumption and financial costs. Microbially Induced Calcite Precipitation (MICP) has emerged as an alternative and promising soil improvement technology, utilizing the capabilities of urease-producing bacteria. This study investigates the feasibility of the MICP method for enhancing the engineering characteristics of a fine sand extracted from the Rhenish lignite mining area, Germany. The changes in the soil characteristics were evaluated by unconfined compressive strength (UCS) testing, acid washing, scanning electron microscopy (SEM) and energy-dispersive X-ray spectroscopy (EDX). Sand samples were prepared using the dry pluviation and moist tamping method. Subsequently, 1.5 pore volumes of Sporosarcina pasteurii bacteria solution was introduced into the samples, followed by the addition of a cementation solution comprising urea, calcium chloride, and ammonium chloride through 5 and 10 injection cycles. Furthermore, in an effort to decrease the costs associated with sterilizing bacteria nutrient media, the cultivation of bacteria in non-sterile media was investigated. The results showed a substantial increase in the engineering characteristics of MICP-treated soils, yielding UCS values of approximately 0.4 MPa and 1.2 MPa for samples treated with 5 and 10 injection cycles, respectively. However, a higher calcite precipitation uniformity was observed along the length of samples treated with 5 injection cycles.
For both treatment times, no discernible differences were observed in compressive strength or calcite precipitation uniformity between samples prepared initially using dry pluviation and moist tamping. Moreover, the results indicated that bacteria cultivated in non-sterile media can achieve comparable UCS values to those cultivated in sterile media, offering a cost-effective and time-efficient alternative.

KEYWORDS

Soil Improvement; Microbially Induced Calcite Precipitation; Sporosarcina pasteurii; Rhenish Lignite Mining Area

1. INTRODUCTION

The rapid rise in global population demands the provision of more construction and enhanced infrastructure. As not every soil type has the desired characteristics for construction, various methods have been developed to enhance the properties of problematic soils, including densification, stone columns, and cement/lime stabilization (DeJong et al., 2010, Shahin, 2017, Zamani, 2017). Despite the considerable efficiency, traditional soil improvement methods are often too costly and ecologically harmful. To overcome these issues, some biological soil improvement methods have been introduced in recent years. Among these, Microbially Induced Calcite Precipitation (MICP) has received considerable attention due to its sustainability and efficiency. The MICP method particularly relies on the urea hydrolysis pathway, accelerated by the presence of urease-producing microorganisms such as Sporosarcina pasteurii, leading to calcite production (DeJong et al., 2013). Calcite precipitation creates bridges between soil grains, effectively cementing them into a stiffer structure. The created cementation improves the compressive and shear strength of granular soils while preserving their permeability,

offering advantages over traditional soil improvement methods (Shahin, 2017). Various factors influence the pattern of calcite precipitation and its impact on the mechanical properties of soils. The key factors include the concentration of the injected bacteria and reactants, initial soil characteristics, number of treatment cycles, temperature, and pH (Lauchnor et al., 2015, Shahrokhi-Shahraki et al., 2015, Mahawish et al., 2018, Mahawish et al., 2019). Furthermore, besides the key factors, additional variables may also affect the efficiency of the MICP method in granular soils. For instance, most previous studies have relied on bacteria cultivated in sterilized nutrient media prepared in distilled water. Considering the substantial costs and extensive time required for sterilization and using large quantities of distilled water in large-scale projects, some samples in this study were treated with bacteria solutions prepared in non-sterile tap water. This approach aimed to examine the effects of sterilization and water purity more accurately on the resulting cementation pattern. Additionally, the effect of sample preparation method also remains unclear in the literature. To that aim, in some samples sand was poured into the molds using the dry pluviation, while in other sample series sand was filled into the mold using the moist tamping method. Furthermore, the effect of the number of injection cycles was examined on the final unconfined compressive strength (UCS) and uniformity obtained.

2. MATERIALS AND METHODS

2.1. Soils

The sand used for the experiments was collected from the dump site of the Inden opencast mine in the North-Rhine Westphalia state, Germany. The grain size distribution curve, determined through sieve analysis in accordance with the German standard code DIN 17892-4, is depicted in Figure 1. Additional soil properties, including fines content (FC), mean grain size (D_{50}), specific gravity (G_s), coefficient of uniformity (C_u), and minimum and maximum void ratios (e_{min} and e_{max}) are presented in Table 1. Based on the measured characteristics, the soil is classified as a poorly graded sand.

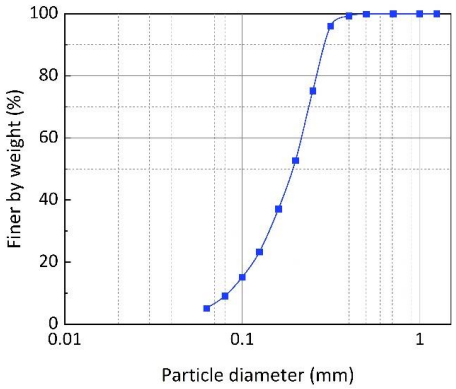


Figure 1. Grain size distribution curve of the used sand.

Table 1. Soil material properties.

Parameter	FC (%)	D50 (mm)	Gs	Cu	emin	emax
Value	5.08	0.194	2.64	2.6	0.622	1.079

2.2. Biological solutions

For this study, the bacteria strain Sporosarcina pasteurii (DSM-11), purchased from the German microorganisms collection (DSMZ) was used as the urease source. The bacteria were cultivated in a medium composed of constituents listed in Table 2. Except urea, all constituents were added to distilled water and subsequently sterilized using the autoclave device. Due to the high sensitivity of urea to heat,

it was added to the medium after cooling using 0.22 microliter syringe filters. Moreover, an alternate medium was prepared using tap water, mixing in all the ingredients without sterilization. The cementation solution utilized consisted of urea, calcium chloride, and ammonium chloride at the concentrations specified in Table 3. To investigate the effect of the cementation level on the final UCS and calcite content, the cementation solution was injected at 5 and 10 injection cycles across two experimental setups.

Table 2. Constituents of the medium culture.

Constituent	Concentration (g/L)
Peptone from Casein	15
Peptone from Soymeal	5
Sodium chloride	5
Urea	20

Table 3. Constituents of the cementation solution.

Constituent	Concentration (mol/L)
Urea	0.5
Calcium chloride	0.5
Ammonium chloride	0.374

2.3. Sample preparation

For both the dry pluviation and moist tamping methods, sand was initially dried at 100 °c for one day. In the dry pluviation method, sand was filled into the syringe mold to a height of 7 cm with a relative density of 30%. For the moist tamping method, the soil was mixed with deionized water to reach a water content of 5% and compacted into three distinct layers with an undercompaction ratio of 5%. All samples were saturated using deionized water before the injection of the bacteria solution. To ensure complete void space filling with the bacteria solution, 1.5 pore volumes of the solution was flushed through the samples from top to bottom at a flow rate of 10 mL/min. Following a 6-hour retention time, the cementation solution was introduced into the samples at the same volume and flow rate in 10 injection cycles every 12 hours. To determine the effect of injection frequency on the uniformity of calcite precipitation and UCS of the biocemented samples, a group of the samples, prepared through dry pluviation, was treated by 5 cycles of cementation solution injections at the same time intervals. In order to confirm the crucial role of Sporosarcina pasteurii in accelerating the reaction between urea and calcium chloride, control samples were prepared without the bacteria, where distilled water was injected at 1.5 pore volumes followed by 10 cycles of cementation solution. To remove the unreacted salts, all samples were rinsed with around 10 pore volumes of deionized water 24 hours after the last cementation cycle. Subsequently, samples were oven dried at 60 °c for approximately three days.

2.4. Unconfined compressive strength

After the drying phase, samples were removed from the molds and their top and bottom surfaces were smoothed using sandpaper. The UCS tests were then conducted on the biocemented samples with a height to diameter ratio of 2:1. These tests involved loading the samples at a strain rate of 1%/min until their complete failure.

2.5. Calcite content determination test

To evaluate the uniformity of calcite precipitation within the samples height, around 8 grams of material were cut from the top, middle, and bottom of the samples after the UCS tests. Following the German standard code DIN 18129, calcite content was determined by inducing a chemical reaction between calcite and hydrochloric acid.

This process generates carbon dioxide gas, causing an increase in pressure in the testing chamber, enabling the calculation of the calcite content. To achieve a representative measurement for each part of the sample, the calcite content was measured at least three times for each section.

2.6. Scanning electron microscopy and energy dispersive X-ray analysis

To investigate the pattern and composition of the calcite precipitation following mechanical testing, scanning electron microscopy (SEM) and energy dispersive X-ray (EDX) analysis were carried out on small biocemented samples. To that aim, small sections were cut from the cylindrical samples and gold coated prior to the microscopic examination.

3. RESULTS AND DISCUSSION

3.1. UCS and calcite distribution

Soils treated with both bacteria and cementation solution demonstrated a notable increase in UCS. As shown in Figure 2a, samples treated with sterile bacteria solution demonstrated an average UCS of 1.09 kPa, comparable to the 1.12 kPa observed in soils treated with bacteria from a non-sterile medium culture. Additionally, as demonstrated in Figure 2b, the average calcite content of samples from sterile and non-sterile bacteria solution are almost similar. However, higher calcite content was observed in the middle portion of the samples treated with non-sterile bacteria solution, possibly due to the presence of various bacteria strains with different sizes, limiting the movement of urease-producing bacteria to the bottom of the samples.
Nonetheless, all these observations could be a positive step towards the upscaling of the MICP method, as avoiding the sterilization process can considerably save in time and costs. Also, the strength results from using non-sterile medium for bacteria cultivation were within a suitable range for the prospective application of the biocementation technique on a larger scale.
Regardless of the sample preparation method used - moist tamping or dry pluviation - the influence on the UCS and calcite content was not significant. As illustrated in Figure 3a, samples prepared through dry pluviation and moist tamping exhibited average UCS values of 1.01 kPa and 1.11 kPa, respectively. Additionally, based on Figure 3b, the calcite content across the height of both sample types was observed to be between approximately 8.5% to 11%. These observations suggest that at a constant relative density, the different soil grains arrangements resulting from the two preparation methods will not cause any considerable changes in the uniformity and the compressive strength of a biocemented soil. Furthermore, as shown in Figure 4a, samples prepared using bacteria cultured in distilled and tap water produced similar UCS values. Yet, a more uniform calcite distribution was observed in samples from distilled water, possibly due to the chemical composition of tap water influencing the pattern of calcite deposition along samples height (Figure 4b).

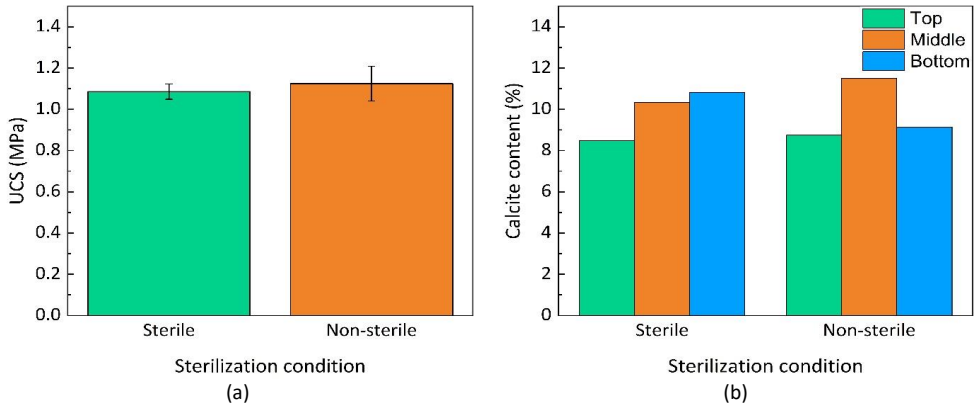


Figure 2. Effect of sterilization on the (a) UCS and (b) calcite content of the biocemented sand.

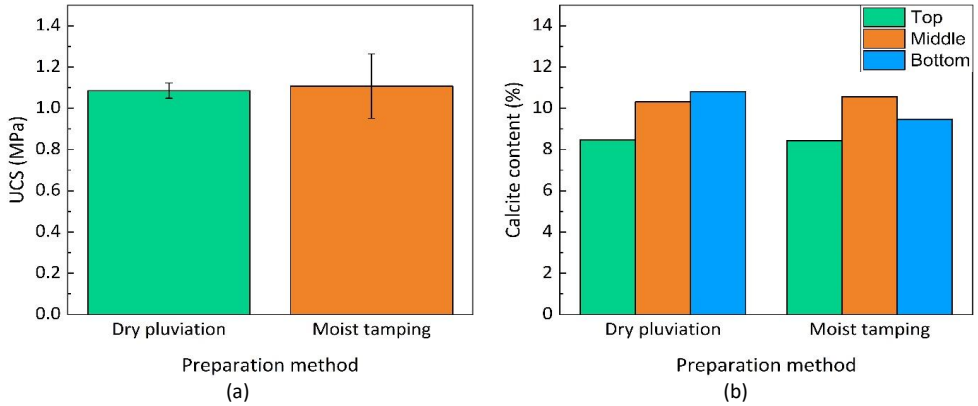


Figure 3. Effect of the sample preparation method on the (a) UCS and (b) calcite content of the biocemented sand.

Figure 5 shows that samples subjected to 5 injection cycles exhibited lower UCS and calcite content values compared to those treated by 10 cementation cycles, pointing to the significance of the treatment frequency on the cementation level. Moreover, samples receiving 10 cycles of cementation solution showed a higher average calcite content than those treated 5 times. Nonetheless, Figure 5b reveals that a higher calcite precipitation uniformity was achieved in samples subjected to 5 treatment cycles with a calcite content range of approximately 5.7%to 5.9% across the samples heights. Meanwhile, samples subjected to 10 injection cycles showed a wider calcite content range from approximately 8.5% to 10.8%. The reduced uniformity in samples receiving higher number of injection cycles may be attributed to a greater loss of bacteria from the samples bottom with each injection cycle, thereby negatively affecting the acceleration of the MICP process. Furthermore, bacteria are displaced towards the samples outlet, resulting in their accumulation and the consequent increase in calcite production in that area.

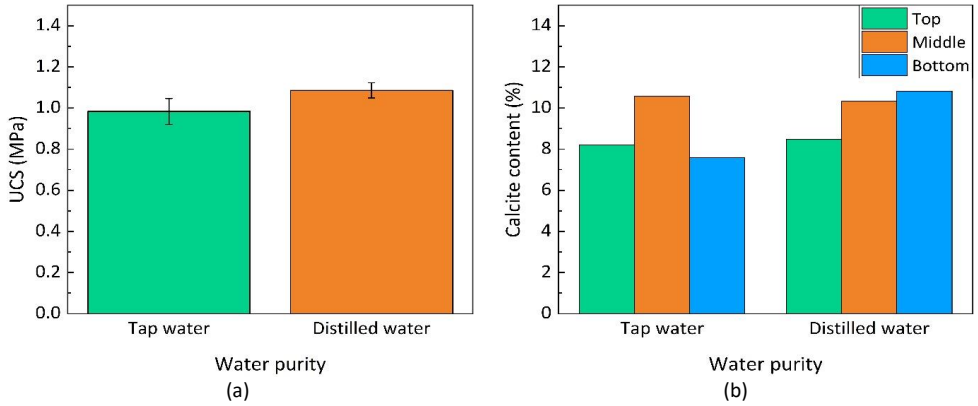


Figure 4. Effect of water purity on the (a) UCS and (b) calcite content of the biocemented sand.

Moreover, as shown in Figure 6, samples treated solely with water and the cementation solution preserved their loose structure without any improvement in their UCS. Also, similar to the uncemented sand, the calcite content in those control samples remained at zero. This phenomenon emphasizes the critical role the urease source plays in accelerating the MICP process, enabling the production of the desired calcite amounts in days rather than several years under natural conditions.

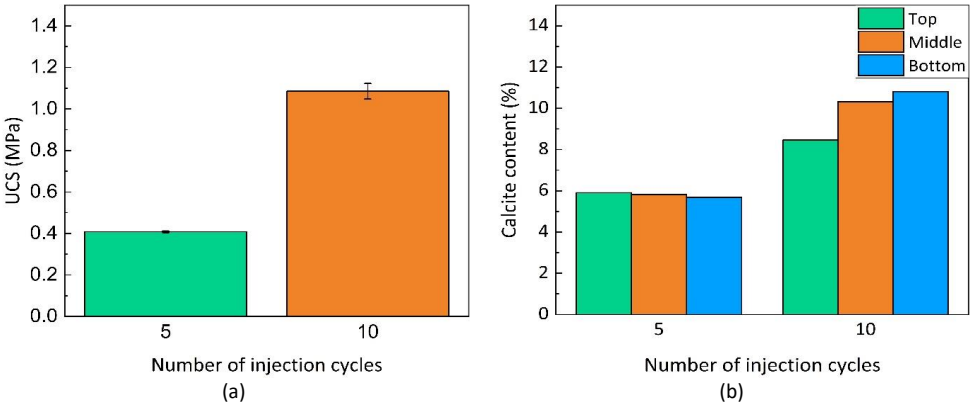


Figure 5. Effect of the number of injection cycles on the (a) UCS and (b) calcite content of the biocemented sand.



Figure 6. Control sample after the injection cycles.

The data presented in Figure 7, plotting the UCS versus the average calcite content, show a direct relationship between these two parameters similar to some previous studies (Ahenkorah et al., 2020, Hoang et al., 2020, Tian et al., 2020). The correlation highlights the significant impact of the calcite content on increasing the compressive strength of biocemented soils.

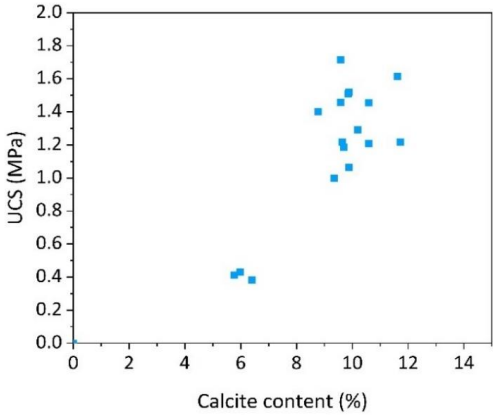


Figure 7. Relationship between the calcite content and UCS.

3.2. SEM-EDX analysis

As presented in Figure 8, calcite precipitation occurred both on the surface of sand particles and at particle-particle contact points. This mechanism suggests that the observed enhancement in the compressive strength can be attributed to both the roughening of particle surfaces and the bridge formation between particles through calcite deposits. Additionally, the chemical composition of the biocemented sand at the green point referenced in Figure 9a is shown in Figure 9b confirming the presence of calcite through the detection of of calcium (Ca), oxygen (O) and carbon (C) in the sand's composition.

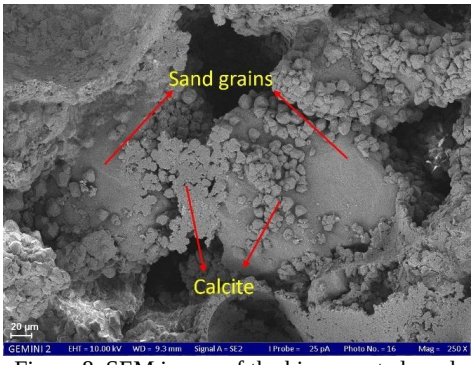
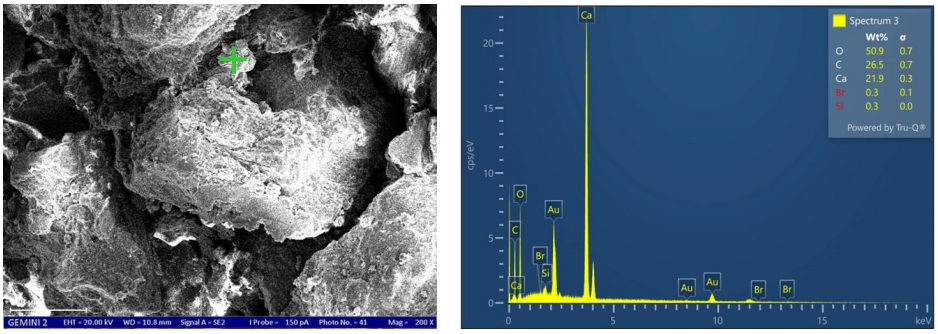


Figure 8. SEM image of the biocemented sand.



(a) (b)

Figure 9. SEM-EDX analysis of the biocemented sand: (a) SEM and (b) EDX.

4. CONCLUSIONS

In conclusion, biocementation via MICP has been demonstrated to be an effective approach for significantly enhancing the compressive strength of a sandy soil from an opencast lignite mine. Regarding the variables examined within this study, it was revealed that the initial sample preparation method has no specific influence on the UCS and calcite content of the biocemented sands. Additionally, the successful calcite precipitation under non-sterile conditions utilizing tap water also indicates a promising step towards reducing the costs of medium culture preparation for larger scale applications of this soil improvement method. The study also found that an increased frequency of injection cycles correlates with higher compressive strength, although this may lead to a non-uniform calcite precipitation pattern due to the bacterial detachment at the injection point. Furthermore, a direct relationship was found between the UCS and the average calcite content, proving the critical role of calcite in increasing the soil strength. Ultimately, for larger scale applications of the MICP method in some parts of the opencast mine, future research on soils with different initial characteristics under simulated field conditions is crucial.

5. ACKNOWLEDGEMENTS

The author would like to thank Professor Torsten Wichtmann and Dr. Wiebke Baille from the Ruhr University Bochum, Germany, for their scientific guidance throughout this research. The author is also thankful to the German Geotechnical Society (DGGT) for the support during the submission process of this paper. Moreover, the research was financially supported by the German Academic Exchange Service (DAAD).

REFERENCES

DIN 17892-4: Geotechnische Erkundung und Untersuchung - Laborversuche an Bodenproben - Teil 4: Bestimmung der Korngrößenverteilung, 2011.

DIN 18129: Baugrund, Untersuchung von Bodenproben - Kalkgehaltsbestimmung, 2011.

Ahenkorah, I., Rahman, M.M., Karim, M.R., and Tesdale, P.R. 2020. A comparison of mechanical responses for microbial and enzyme-induced cemented sand. *Geotechnique Letters*, 10(4), 1–26.

DeJong, J.T. et al. 2013. Biogeochemical processes and geotechnical applications: progress, opportunities and challenges. *Geotechnique*, 63, 287–301.

DeJong, J.T., Mortensen, B.M., Martinez, B.C. and Nelson, D.C. 2010. Bio-mediated soil improvement. *Ecological Engineering*, 36, 197–210.

Hoang, T., Alleman, J., Cetin, B. and Choi, S.G. 2020. Engineering properties of biocementation coarse- and fine-grained sand catalyzed by bacterial cells and bacterial enzyme. *Journal of Materials in Civil Engineering*, 32, 04020030.

Lauchnor, E.G., Topp, D.M., Parker, A.E. and Gerlach, R. 2015. Whole cell kinetics of ureolysis by sporosarcina pasteurii. *Journal of AppliedMicrobiology*, 118, 1321–1332.

Mahawish, A., Bouazza, A., and Gates, W.P. 2018. Effect of particle size distribution on the bio-cementation of coarse aggregates. *Acta Geotechnica*, 13, 1019–1025.

Mahawish, A., Bouazza, A., and Gates, W.P. 2019. Factors affecting the bio-cementing process of coarse sand. *Proceedings of the Institution of Civil Engineers: Ground Improvement*, 172, 25–36.

Shahin, M.A. 2017. Innovative solutions for construction on problematic soils in civil infrastructure developments. *Proceedings of the 2nd World Congress on Civil, Structural, and Environmental Engineering*, Barcelona, Spain.

Shahrokhi-Shahraki, R., Zomorodian, S.M.A., Niazi, A. and O'Kelly, B.C. Improving sand with microbial induced carbonate precipitation. 2015. *Proceedings of the Institution of Civil Engineers: Ground Improvement*, 168, 217–230.

Tian, K., Wang, X., Zheng, S., Zhang, H. and Yang, A. Effect of reactant injection rate on solidifying aeolian sand via microbially induced calcite precipitation. 2020. *Journal of Materials in Civil Engineering*, 32, 04020291.

Zamani, A. 2017. Liquefaction Mitigation of Silty Sands with Microbial Induced Calcium Carbonate Precipitation. *PhD thesis*, North Carolina State University, 2017.

28th European Young Geotechnical Engineers Conference – EYGEC 2024
© 2024 Macedonian Association for Geotechnics, ISBN 978-608-4510-61-1

Thermogravimetric analysis as a useful tool for adsorbed water assessment: case of bentonite

S. Babiy[1], A. Tuttolomondo[1], L.Laloui[1]

[1] *Laboratory of Soil Mechanics (LMS), Ecole Polytechnique Fédérale de Lausanne (EPFL), Lausanne, Switzerland*

ABSTRACT

The chemical structure of clays is a significant determinant of their behavior, particularly in the case of active clays renowned for their high-swelling and hydro-isolating characteristics. These properties make them valuable in diverse geotechnical applications, including nuclear waste repositories and landfills. High swelling capacity and low permeability originate from the water physically attracted to clay particles, often termed "adsorbed" or "physisorbed" water. This water exhibits distinct features such as an ordered structure, higher density, and unique dielectric constant compared to bulk liquid water. Its interaction is influenced by factors like pore water salinity, degree of saturation, and temperature of the waste at repository. Predicting the mechanical response, such as swelling upon hydration, necessitates advanced modelling considering the physical-chemical interplay between water and clay particles. Accurate multi-physical predictions rely on precise microstructural investigations, crucial for understanding active clay behavior. This study introduces a novel methodology utilizing Thermogravimetric Analysis (TGA) to quantitatively assess adsorbed water in active clays. Employing this approach provides fresh insights into the types and quantities of water retained at different saturation levels of MX-80 bentonite. These findings can be incorporated into mechanical prediction models to augment their precision.

KEYWORDS

Bentonite; Adsorption; Thermal analysis; Expansive clays

1. INTRODUCTION

Bentonite is extensively employed in waste disposal applications (Laine and Karttunen, 2010). Its advantageous characteristics in waste management include swelling and low hydraulic permeability upon moisture exposure, effectively preventing the migration of contaminants from waste disposal sites. Bentonite serves as a reliable "seal" for nuclear waste containment (Laine and Karttunen, 2010).
The uniqueness of bentonite is primarily dictated by its constituent mineral, montmorillonite. With a flat shape approximately 500x500nm in size and a thickness of 1nm, it has one of the highest surface-to-mass ratios (specific surface area up to 800 m2/g) among soil materials. Its natural chemical structure consists of an octahedral $AlO6$ sheet located between two tetrahedral sheets of $SiO4$. Isomorphic substitution can naturally occur in both types of sheets, resulting in a charge deficit (Rouquerol et al., 2014; Mitchell and Soga, 2005). The resulting negative charge at the surface is counterbalanced by exchangeable alkaline cations. This interaction between water and clay particles, facilitated by the exchangeable cations, induces water adsorption (here, physical adsorption is the process of enrichment of a material or increase in the density of the fluid in the vicinity of an interface without chemical bonding (Rouquerol et al., 2014)). This leads to the formation of water layers extending up to four times the thickness of the clay platelet itself. Consequently, the high specific surface area of bentonite becomes fully saturated with water upon hydration, resulting in swelling. While swelling upon hydration arises

from water-clay particle interaction, overlooking this interaction could yield inaccurate predictions of mechanical behavior.

Existing modeling approaches allow predicting hydration isotherms of bentonite by combining different mechanisms connected to types of water adsorbed (e.g., Wang et al., 2022; Qiao et al, 2021). Existing experimental assessments of adsorbed water are limited to platelets spacing assessment by X-Ray Powder Diffraction (XRPD) and it is assumed the space between platelets is filled with water. Moreover, XRPD requires fine powders and is unable to detect amorphous structure (such as water or randomly located surface cations) (Cockcroft and Fitch, 2008).

Montmorillonite, a key mineral in bentonite, attracts water in two forms: tightly bonded crystalline hydrates and weakly bonded osmotic hydrates. Mercury Intrusion Porosimetry (MIP) is unable to capture crystalline hydration (e.g. Norrish, 1962), occurring at humidities above 25% (Cases et al., 1992). Additionally, at low humidity levels, most of the surface area remains vacant from water layers.

Thermogravimetric Analysis (TGA) is a technique that allows to obtain the change of mass of a small specimen as a function of temperature (dynamic heating) or time (Tajeddine et al., 2015). Each temperature level corresponds to the energy needed for sublimation/evaporation of certain molecules in the sample (Vieillard, Tajeddine L, 2015). Thus, higher-level bonds removal would be visible at a higher temperature.

In case of clays, similar processes were distinguished to take place in kaolinite, montmorillonite, saponite and other clay minerals during heating from 30°C to 950°C: first step – evaporation of adsorbed water; second one – dehydroxylation – the release of structural OH in the form of water molecules, third – silica phase transformation. It is generally assumed that by the start of dehydroxylation no adsorbed water is left (Tajeddine et al., 2015; Saadatkhah et al., 2020; Zeng et al., 2022), however, that assumption remains not proved. Additionally, there is no consensus between authors on the temperature levels when all adsorbed water is removed.

Discrepancies between water retention mechanisms in literature require development of new experimental tools capable of detecting water-clay particle interactions at the nanoscale across different chemo-hydro-mechanical states. These tools are essential for later implementation into accurate modeling approaches.

In the present contribution, a new methodology for quantifying the different types of water retained by active clays is proposed. The proposed methodology involves using thermogravimetric analysis (TGA) on active clay specimens at different hydration stages, as well as using TGA on water samples having the chemical composition of the active clay specimens of interest.

2. MATERIALS AND METHODS

2.1. Tested material

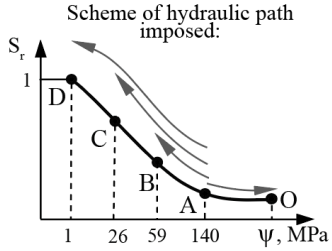
Bentonite MX-80 mixture was obtained by mixing the grains of fractions up to 4 mm with Fuller granulometry distribution. Smectite content of the material is 85%, Specific Surface Area (SSA) is 523m^2/g, specific gravity 2.74 (Seiphoori et al., 2014). Liquid and plastic limits are 544% and 110% respectively. Hygroscopic water content of the resulting mixture under laboratory conditions (imposed total suction 140 MPa, T=25°C) is 5.9%, dry density – 1.3 Mg/m^3.

2.2. Methodology

The proposed methodology involves, after an initial specimen preparation phase, performing TGA on clay and water samples (using unique heating programme for all samples). A comparison of the temperature-water content curves of the clay samples and of the water samples reveals the temperature ranges required to remove a certain type of retained water and allows the corresponding water content to be quantified.

2.3. Hydration procedure

Bentonite was placed into 3 “Microcells” (cells made of brass able to create constant volume conditions with small openings) for confined hydration in desiccators with the imposed total suction values of 1, 26, 59 MPa (D, C, B states on Figure 1). Total suction of bentonite was measured by WP4C dew point chilled-mirror potentiometer (Leong et al., 2003). Total suction value of 1 MPa was measured on fully saturated bentonite (saturation was performed in Microcell in a chamber with water pressure 2.5 MPa for 2 days until no change in water volume in the pump was observed).



State		Process	Dry density, Mg/m^3	Water content, %
initial	target			
A	A	-	1.3	5.9
	B	Vapour hydration		12
	C	Vapour hydration		17.5
	D	Liquid hydration, constant volume		50
	O	Oven-drying, 105°C		0

Figure 1. Hydro-mechanical states of tested samples represented in form of water retention curve.

2.4. Thermogravimetric analysis

Experimental part of TGA consists of 2 sub-parts: testing of bentonite samples and of distilled water (Figure 2).

Bentonite samples, taken immediately after opening microcells, are put in ceramic crucibles in the heating chamber of a Perkin Elmer TGA 4000 apparatus (Figure 2). The following heating (for all heating steps the rate is 10°C/min) is adopted: (i) isothermal step for 1 min at 30°C for equilibration; (ii) heating from 30 to 80°C; (iii) isothermal step for 15 min at 80°C; (iv) heating from 80 to 950°C; (v) isothermal step 1 min at 950°C. Bentonite samples included also those oven-dried (105°C) for more than 1 month to ensure the evaporation of all water in the sample. These long-dried samples are taken as reference state later in the analysis.

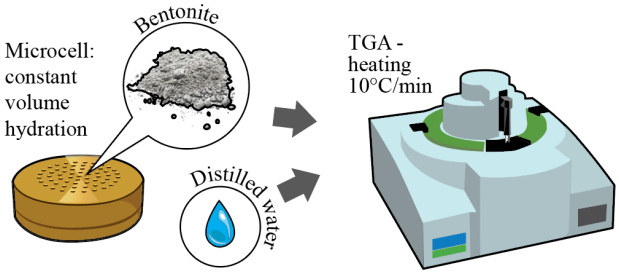


Figure 2. Samples for thermogravimetric analysis.

Water samples are put into crucibles in capillary form using syringe. The impact of capillarity on evaporation of water is presented on figure 3. Presence of capillars, that are created by ceramic grains and bentonite after heating, slows down the evaporation of water. However, the differences between various capillarities are negligible (Figure 3), which allows to use the curves of capillary water evaporation for later modelling. The initial mass of water varies from 2mg to 21mg (Figure 3). The following heating program is adopted: (a) isothermal step for 1 min at 30°C; (b) heating from 30 to 80°C; (c) isothermal step at 80°C; (d) heating from 80 to 150°C. The final curves of water used for the proposed methodology are shown on figure 4.

2.5. Accuracy of the measurements

The Perkin Elmer TGA 4000 apparatus makes measurements with accuracy of the balance 0.01% (for most of samples 0.005 mg), temperature accuracy 0.8°C.
Additionally, the influence of total mass of sample and granulometry on accuracy was measured. Mass of samples influences the first part of the normalized curves (30...450°C) with coefficient of variation 0.53% (standard deviation 0.57%). Granulometry of the sample influences predominantly the part between 600 and 800°C with coefficient of variation 0.42%, standard deviation 0.4%.

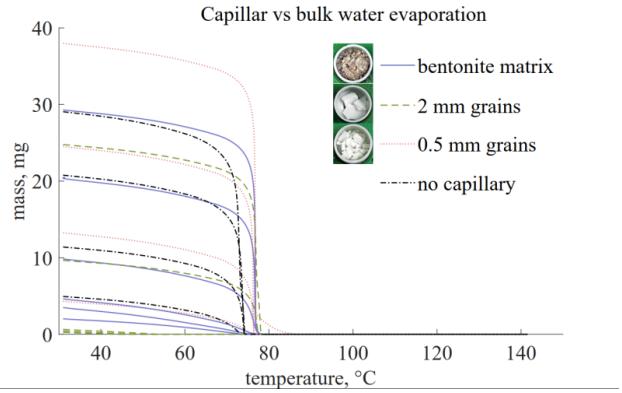


Figure 3. Analysis of water evaporation in capillary form and form of a drop. “Bentonite matrix” corresponds to bentonite after heating up to 950°C, which loses its activity due to dehydroxylation at high temperatures.

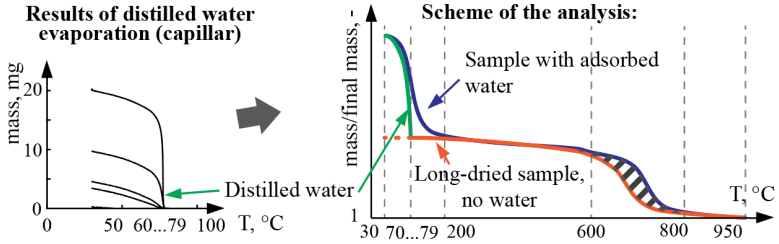


Figure 4. Output of TGA experiments and analysis after.

2.6. Results analysis

The experimental results are analyzed implementing the following procedure: (i) normalization of all bentonite TGA curves with respect to the final mass; (ii) combination of water evaporation curve with the long-dried sample TGA curve (Figure 4), representing the change of mass of bentonite without adsorption phenomena; (iii) difference between the actual sample with adsorbed water and the modelled curve. The combined curve is modelled in a way that it has the same water content as the samples in hydration path (Figure 1), in this way, the only difference between actual and modelled curve is the mass of water bonded to clay platelets. That mass is expressed as the mass of water per unit mass of dry clay on Figure 5 (the normalization changed to initial mass for interpretation of results).

3. RESULTS AND DISCUSSIONS

Figure 5 represents the results of presented methodology. Two main regions could be identified: (i) 30...200°C with sharp peaks at around 80°C and (ii) 600°C...800°C with peaks starting from 0 to 0.021. The first region of the difference represents the water bonded to clay, thus, this region corresponds to

adsorbed water (bulk water was removed by difference operation). According to the second region, the states of total suction 26, 59 and 140MPa show peaks of around zero, and the saturated sample has a higher value of 0,021. That fluctuation most probably corresponds to the change of fabric during saturation, as the accuracy evaluation due to granulometry was the highest at similar temperature zone. As samples from the mixture were picked randomly, most probably the variation in grain size and in the amount of water retained by big and small grains resulted in scatter data. Therefore, this methodology should be targeted on the grain size of interest.

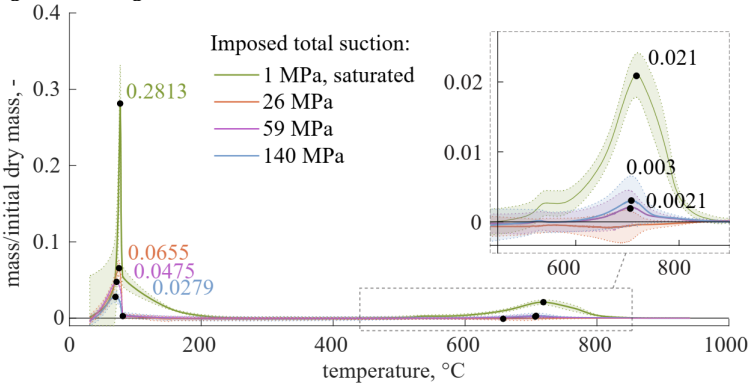


Figure 5. Final result of the difference between real and modelled TGA-curves at 4 hydraulic states.

Overall, the values of adsorbed water obtained in present analysis is similar to some of the other methodologies, reporting half of the water stored in adsorbed form (e.g., Warr and Berger, 2007). On Figure 6 the interpretation of results is presented in a form of soil water isotherm, representing the water types' amounts change upon hydration (capillary and adsorbed).

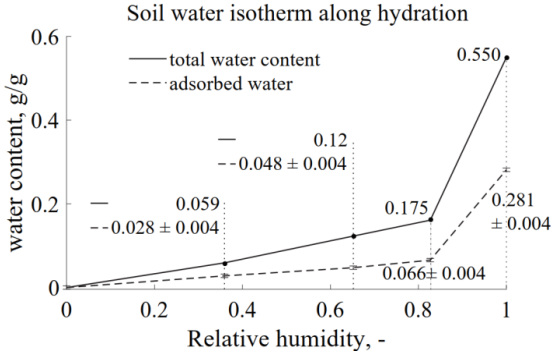


Figure 6. Outcome of the analysis.

4. CONCLUSIONS

In present work a novel thermogravimetric methodology for experimental quantification of adsorbed water has been developed for the first time. The advantage of this methodology lies in its reliance on energy-based measurements.

It was found that the adsorbed water and capillary water are present simultaneously and vary upon hydration. The abovementioned water types were quantified and a water isotherm was presented based on the findings.

Present methodology can be implemented for other materials with adsorption phenomena (clays, sulfate rocks and others).

5. ACKNOWLEDGEMENTS

The authors are grateful for the financial support provided by Swiss National Science Foundation (financial support No. 200021_204099, Division II).

REFERENCES

Cases, J.M., Berend, I., Besson, G., Francois, M., Uriot, J.P., Thomas, F., Poirier, J.E., 1992. Mechanism of adsorption and desorption of water vapor by homoionic montmorillonite. 1. The sodium-exchanged form. *Langmuir 8*, 2730–2739.

Cockcroft, J.K., Fitch, A.N., 2008. Chapter 2. Experimental Setups, in: Dinnebier, R.E., Billinge, S.J.L. (Eds.), Powder Diffraction. *Royal Society of Chemistry*, Cambridge, pp. 20–57.

Laine, H., Karttunen, P., 2010. Long-term stability of bentonite A literature review. Finland.

Leong, E.-C., Tripathy, S., Rahardjo, H., 2003. Total suction measurement of unsaturated soils with a device using the chilled-mirror dew-point technique. *Géotechnique* 53, 173–182.

Mitchell, J.K., Soga, K., 2005. Fundamentals of soil behavior, 3. ed. ed. Wiley, Hoboken, NJ.

Norrish, K., 1962. Effect of Freezing on the Swelling of Clay Minerals. *Clay Minerals* 5, 9–16.

Qiao, Y., Tuttolomondo, A., Lu, X., Laloui, L., Ding, W., 2021. A generalized water retention model with soil fabric evolution. *Geomechanics for Energy and the Environment* 25, 100205.

Rouquerol, F., Rouquerol, J., Sing, K.S.W., Llewellyn, P.L., Maurin, G., 2014. Adsorption by powders and porous solids: principles, methodology and applications, Second edition. *ed. Elsevier/AP*, Amsterdam.

Saadatkhah, N., Carillo Garcia, A., Ackermann, S., Leclerc, P., Latifi, M., Samih, S., Patience, G.S., Chaouki, J., 2020. Experimental methods in chemical engineering: Thermogravimetric analysis—TGA. *The Canadian Journal of Chemical Engineering* Eng 98, 34–43.

Seiphoori, A., 2014. Thermo-hydro-mechanical characterisation and modelling of MX-80 granular bentonite. Thesis №6159. Ecole Polytechnique Fédérale de Lausanne, Lausanne, Switzerland.

Seiphoori, A., Ferrari, A., Laloui, L., 2014. Water Retention Behaviour and Microstructural Evolution of MX-80 Bentonite during Wetting and Drying Cycles. *Géotechnique*, 64 (9), 721–734.

Tajeddine, L., Gailhanou, H., Blanc, P., Lassin, A., Gaboreau, S., Vieillard, P., 2015. Hydration–dehydration behavior and thermodynamics of MX-80 montmorillonite studied using thermal analysis. *Thermochimica Acta*, 604, 83–93.

Vieillard, P.H., Tajeddine, L., 2015. Thermo-Analytical Techniques on MX-80 Montmorillonite: A Way to Know the Behavior of Water and its Thermodynamic Properties during Hydration –Dehydration Processes. *Pharmaceutica Analytica Acta*, 07.

Wang, Y., Hu, L., Luo, S., Lu, N., 2022. Soil Water Isotherm Model for Particle Surface Sorption and Interlamellar Sorption. *Vadose Zone Journal*, 21 (5).

Warr, L., Berger, J., 2007. Hydration of bentonite in natural waters: Application of "confined volume" wet-cell X-ray diffractometry. *Physics and Chemistry of the Earth*, Parts A/B/C 32, 247–258.

Zeng, Z., Cui, Y.-J., Conil, N., Talandier, J., 2022. Effects of technological voids and hydration time on the hydro-mechanical behaviour of compacted bentonite/claystone mixture. *Géotechnique,,* 72, 34–47.

28th European Young Geotechnical Engineers Conference – EYGEC 2024
© 2024 Macedonian Association for Geotechnics, ISBN 978-608-4510-61-1

Determination of foundation damping coefficients for monopile supported offshore wind turbines

Mohammed Barzan, David Igoe

Trinity College Dublin, Dublin, Ireland

ABSTRACT

The interaction of the monopile foundation with the surrounding soil could have a substantial impact on the behaviour of the offshore wind turbine (OWT) structure in terms of the resonance frequency and the amplification of forces and bending moments. As a result, it is crucial to incorporate both the stiffness and the damping of the monopile into integrated numerical analyses in order to satisfy fatigue design requirements and to improve structural cost reductions. Foundation damping, which is mainly hysteretic, is formed as a result of the monopile moving against the soil volume in the vicinity, causing energy dissipation due to the development of plastic strains within the soil. This research project aims to derive foundation damping ratios to be used as viscous dashpot coefficients by calibrating the parameters of a nonlinear constitutive model to the results of cyclic triaxial tests and then building full 3D finite element (FE) models incorporating the soil volume with the monopile and the tower structure. The damping ratios are determined by applying cyclic loads at the rotor-nacelle-assembly (RNA) level, and then calculating the damping ratios from the hysteretic load-deformation loops at the mudline level. The small strain hardening soil model (HSsmall) is used due to its capability to exhibit nonlinearity upon load reversals. The coefficients determined with the approach yield valid results when comparing the critical damping ratios with those obtained from 3D FE analyses.

KEYWORDS

Monopile; Offshore wind turbine; Small strain hardening soil model; Foundation damping

1. INTRODUCTION

Offshore wind is now regarded as a promising renewable energy source to help in tackling climate change challenges, reducing the reliance on fossil fuels, and achieving net-zero carbon dioxide emissions. However, the greatest limitation that hinders the growth of offshore wind is the significant cost required for the installations. Furthermore, the support structure must be designed such that it can sustain the severe environmental loads of wind and waves that are applied throughout the design lifespan without compromising the fatigue limits of the different structural components. The internal forces of the OWT are greatly influenced by the interaction of the monopile with the soil which govern the stiffness and the damping. Research studies such as Carswell et al., (2015) highlighted the importance of foundation damping, by comparing the moments at the mudline for the case which incorporates foundation damping as a rotational viscous dashpot, against the simulation model without foundation damping. According to the analysis results, Carswell et al., (2015) estimated that foundation damping reduced the maximum and standard deviation of the mudline moment by 7-9% respectively during storm conditions. A more recent study by Carswell et al., (2022) showed that including foundation damping accounted for approximately 25-33% reduction in mudline bending moment under an emergency shutdown scenario when compared to the same undamped numerical model. There are two types of foundation damping: radiation and hysteretic damping. Radiation damping involves dissipating the energy by spreading the elastic waves away from the monopile. Since the effect of radiation damping is very small for vibration frequencies below 1 Hz, its effect is often neglected (Andersen, 2010). Hysteretic damping is the form of damping that is of concern in this research, which is mainly due to

the plastic shear strains within the soil. Unlike radiation damping, Hysteretic damping is relatively insensitive to the loading frequency (Damgaard et al., 2013). This research focuses on obtaining the foundation damping ratios that can be converted to viscous dashpot coefficients which could then be used in integrated wind turbine analysis. The damping ratios are obtained by carrying out FE analyses using the software package Plaxis 3D. To check if the damping ratios are adequate, free decay simulations are implemented with Plaxis 3D to obtain the critical damping ratios of the OWT structure, which are then compared with critical damping ratios determined by applying the viscous dashpots in a 1D FE model.

2. METHODOLOGY

Accurate determination of foundation damping requires obtaining the hysteretic damping of the soil at different mean effective stresses (i.e., variation of damping with depth). This section will discuss the procedure followed to carry out the triaxial laboratory tests along with the steps needed to calibrate the HSsmall parameters and building the 3D FE model. Bender element tests were also conducted to yield the small strain shear modulus G_o. Soil samples were taken from a quarry site in Ireland referred to as Blessington, and then reconstituted in the laboratory to 60% relative density using the moist tamping under-compaction approach. Cyclic and monotonic tests were carried out to obtain damping and effective shear strength parameters according to ASTM (D3999) and ASTM (D7181) standards respectively. The difference between the cyclic and the monotonic tests is only during the loading stage, while the preceding steps of sample preparation, saturation, and consolidation are identical. All samples were consolidated isotropically to the desired mean effective stresses. Cyclic loading was performed in undrained conditions as recommended by ASTM (D3999) standard. The initial dimensions of the samples were 70 mm in diameter and 140 in height. Each soil sample was divided into 10 layers with approximately 14 mm thickness. To achieve the desired compaction with relative ease, each layer is dampened to around 15% moisture content. The under-compaction method was proposed by Ladd (1978) to achieve uniform void ratio samples by increasing the density successively for each layer to account for the compaction that occurs in the underlying soil layers. The amount of under-compaction is controlled by the percent under-compaction according to the following equation:

$$Un = Uni - \left(\frac{Uni - Unt}{nt - 1}(n - 1)\right) \quad (1)$$

where *Uni* is the under-compaction percent for the initial layer, and Unt is the under-compaction for the topmost layer. The total number of layers is represented by nt, while n is the current layer. The value for Uni is 2% as suggested Escribano (2015) for relative densities higher than 40%, and the value for Unt is set as zero. On sample local transducers were used to overcome the issues related to compliance of the apparatus and bedding errors. Two diametrically opposite axial LVDTs (Linear Variable Displacement Transducer) were used to measure the average axial strain. The distance between the pads, that hold the axial LVDTs against the soil, is adjusted such that the gauge length is around one-third of the soil height. The radial strain is measured with a calliper which has the LVDT at one end, and a hinge that permits the calliper to open and close at the other end. All the pads are fixed with pins that pierce through the latex membrane. To prevent water from leaking into and out of the sample, Silicon sealant is applied onto to the pads prior to inserting the pins. The triaxial tests were conducted in fully saturated conditions. To facilitate saturation, the sample was initially flushed with CO2 which replaces the air in the soil voids and is more soluble in water. Afterward, water is allowed to flow upwards from the bottom of the sample and to escape from the drainage valve at the top cap. This is followed by back pressure saturation whereby the back pressure and cell pressure are increased simultaneously so that the pore pressure increase allows the remaining air pockets to dissolve in the water. The cell pressure is kept higher than the back pressure by a small offset of 20 kPa to allow the sample to remain stable. To check if full saturation is accomplished, the B value is checked by raising the cell pressure and closing the drainage valve. The sample is regarded to be fully saturated when the output B value is larger than 0.95. During the consolidation stage, the pore water is permitted to dissipate from the top cap drainage valve

to the back pressure controller which can be used to calculate the volume of the dissipated water, and hence, the volume change of the sample.
The cyclic tests were two-way stress controlled in which the deviatoric stress was oscillating around a mean deviator of 0 kPa. The amplitude of the cyclic deviatoric stress increased gradually from one stage to another, and the number of load cycles was 40 for each stage. Consolidation stages were added after each dynamic stage to restore the initial mean effective stress before the succeeding dynamic stage began. The stresses were applied at 0.1 Hz which is within the range of frequencies encountered for OWTs in the field.

The small strain shear modulus Go is determined by bender element tests. The bender elements consist of two piezoelectric ceramic plates that can convert electrical signals into mechanical waves when operating as a transmitter, and as a receiver, when the vibrations are transformed into electrical signals. The bender elements were procured from GDS. The input and the output signals from the bender elements are recorded by PicoScope 5242D oscilloscope. The input signals to the transmitter are supplied by TTI TGA1241 arbitrary function generator which can produce pulse sine signals of up to 10 Volts amplitude. Frequencies in the range of 1-20 kHz were applied by the function generator. Figure 1 shows the schematics of the main triaxial and bender element testing systems.

The results of the triaxial and bender element tests are then used for calibrating the HSsmall constitutive model. The soil test facility in Plaxis 3D allows to recreate of the tests in the laboratory to check whether the values used as inputs yield satisfactory simulations when compared to the laboratory results. Only the monotonic tests were evaluated in the soil test facility. The reliability of the input values for damping is examined by comparing the damping ratio curves displayed by Plaxis 3D when the parameters of HSsmall are inserted, against the damping ratio graphs from the cyclic triaxial tests.

The overall model of the monopile, tower structure and soil domain is created by Plaxis 3D software. This research aims to study foundation damping for the reference 15 MW wind turbine (Gaertner et al., 2020). To create the hysteretic load-deformation loops at the foundation, cyclic loads are applied at the RNA level. The loads are applied statically without taking inertia into account. The damping ratio determined from the horizontal load-displacement response is denoted as the translational damping ratio, whereas the damping ratio calculation from the moment-rotation loops is referred to as the rotational damping ratio. The translational and rotational damping ratios can consequently be converted to viscous dashpots to be employed in integrated dynamic structural analysis. Furthermore, free vibration simulations are also performed to obtain the variation of the critical damping ratio with the mudline displacement. A 1D FE model with the same structural properties as the 3D FE model is used to assess whether the damping coefficients lumped at the foundation level yield critical damping ratio values matching those of Plaxis 3D FE.

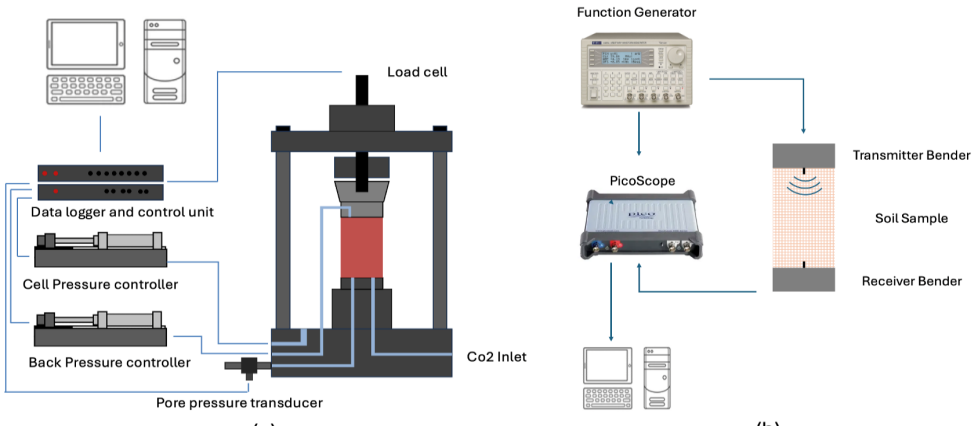


Figure 1. (a) Triaxial apparatus testing system; (b) Bender element testing system

3. SOIL CALIBRATION

This research is concerned with calibrating Blessington sand at a relative density of 60%. Cyclic tests were carried out at mean effective stresses of 25, 50, 150, 300 kPa and the results were used in curve fitting to obtain the coefficients of the hyperbolic function proposed by Hardin and Drnevich (1972). The hyperbolic function with the determined coefficients is used to obtain damping (D) versus shear strain (γ) at different mean effective stresses. The hyperbolic function is as follows:

$$\frac{D}{D_{max}} = \frac{\frac{\gamma}{\gamma_r}\left[1 + a\ exp(-b\frac{\gamma}{\gamma_r})\right]}{1 + \frac{\gamma}{\gamma_r}\left[1 + a\ exp(-b\frac{\gamma}{\gamma_r})\right]} \quad (2)$$

where a and b are varied to obtain a good fit for the laboratory results. *Dmax* is the maximum damping ratio and γr is the reference strain taken as $\sqrt{P'/100}$. $P`$ is the mean effective stress and 100 kPa is the reference atmospheric pressure. This form of γr is different than the one used by Hardin and Drnevich (1972), which is the ratio of the maximum shear strength to the shear modulus.

HSsmall parameters are adjusted such that the damping ratios displayed by Plaxis 3D are similar to the damping ratios obtained by the hyperbolic function for the required mean effective stresses. The main parameter that is manipulated is the $\gamma_{0.7}$ which reduces the damping ratio as it is increased. The monotonic tests are performed for mean effective stresses of 50, 150, 300, and 500 kPa. The parameters that are adjusted are φ, ψ, $E50_{ref}$, $Eoed_{ref}$, Eur_{ref}, Go_{ref}, and ν_{ur}. The stiffness parameters are maintained constant, while the shear strength parameters (φ and ψ) are varied based on the mean effective stress. The value of Go_{ref} is obtained by the bender element tests. As mentioned previously, the soil test facility is utilised to inspect the validity of the input parameters by comparing the monotonic triaxial results with Plaxis 3D simulations as shown in Figure 2.

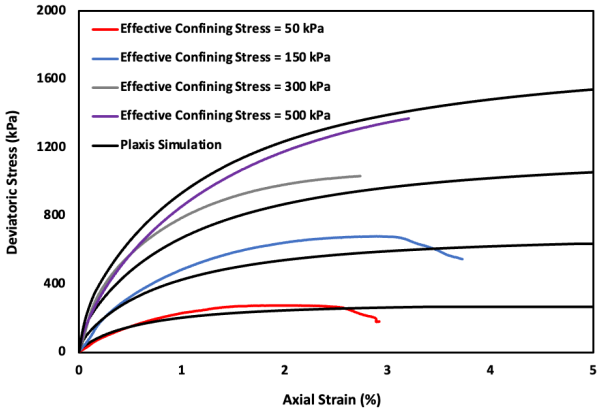


Figure 2. Monotonic triaxial test results and simulations

Figure 2 shows that the simulations match the triaxial results and thus can be used for the numerical 3D FE analyses. The maximum axial strain measured by the LVDTs before reaching their limit is roughly around 3%. However, the tests are further continued to determine the critical angle of shearing resistance which is approximately 35 degrees for the sand used in this research. The parameters and the stratigraphy for the model are summarised in Table 1. The overall stratigraphy is divided into 7 layers and the parameters are determined for mean effective stresses of 25, 75, 125, 175, 225, 275, and 300 kPa. Figure 3 shows the damping ratio from Plaxis versus the damping ratio obtained from the hyperbolic function. The maximum damping ratio remains constant for all the layers since the same ratio of Go_{ref}/Eur_{ref} is used. The Poisson's ratio is 0.20 and the interface R_{inter} is kept as 0.7. Parameters that are not mentioned are maintained as the standard values in Plaxis 3D.

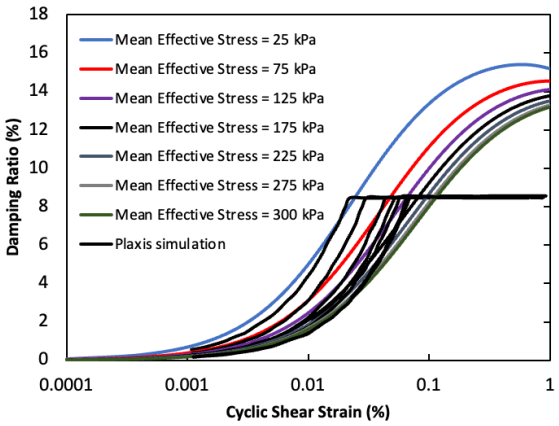


Figure 3. Calibrated damping curves

Table 1. Soil stratigraphy and input parameters

Soil layer	Depth (m)	γ'(kN/m^3)	φ'	ψ	E_{50ref} (kN/m^2)	E_{oedref} (kN/m^2)	E_{urref} (kN/m^2)	G_{oref} (kN/m^2)	$\gamma_{0.7}$
1	0-5	9.74	49.29	17.86	45000	30000	90000	83690	0.00016
2	5-10	9.74	45.17	12.71	45000	30000	90000	83690	0.00024
3	10-15	9.74	43.25	10.31	45000	30000	90000	83690	0.00034
4	15-20	9.74	41.99	8.74	45000	30000	90000	83690	0.00041
5	20-25	9.74	41.05	7.56	45000	30000	90000	83690	0.00045
6	25-30	9.74	40.29	6.62	45000	30000	90000	83690	0.00052
7	30-80	9.74	39.97	6.21	45000	30000	90000	83690	0.00055

4. NUMERICAL MODEL

The 3D FE model is comprised of beam and plate elements. The monopile beneath the mudline is represented using plate elements, while the tower is modelled with beam elements. A weightless plate with a very large Young's modulus is created 1m above mudline (so no soil is in contact with the plate) and is connected to the beam elements to allow the transfer of shear and bending moment between the tower and the foundation. The mass at the RNA level is represented by modelling a small beam element with equivalent unit weight. The dimensions of the tower (diameter and thickness) and the mass of the RNA were taken from IEA Wind TCP 37 technical report (Gaertner et al., 2020). Since the loading and the structure are symmetrical, only half of the model is created. The length of the entire soil domain is taken as 16 times the diameter of the monopile, while the width is taken as 8 times the diameter. The effective unit weight of the soil is used and hence the water table is placed at the bottom of the model. For the free decay analyses, viscous boundaries are activated to prevent wave reflections. The diameter of the monopile is 10 m and the embedment depth is assigned as 30 m which makes the slenderness ratio (embedment depth/diameter) appropriate for current monopile geometries. The thickness of the monopile is taken as 0.1 m. The number of the beam elements for the tower is 90 and the length for each element is 2 m. The number of cyclic loads at the RNA was 5 and the hysteretic loop created by the last cycle was used for the damping ratio determination. The damping ratio is determined using the following equation:

$$Damping\ Ratio = \frac{1}{4\pi}\frac{\Delta W}{W} \tag{3}$$

where ΔW is dissipated energy (area of the hysteretic loop), and W is the elastic strain energy stored during the cycle. The overall model of the wind turbine structure and the soil domain is shown in figure 4.

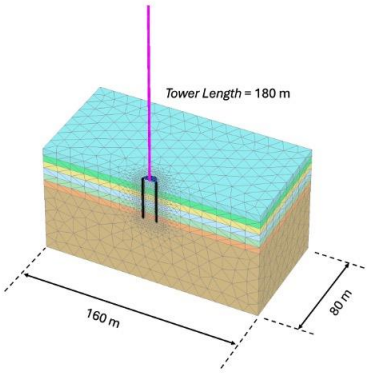


Figure 4. 3D FE model

5. RESULTS

The translational damping ratio is depicted in Figure 5, whereas the rotational damping ratio is shown in Figure 6. This research aimed for obtaining the damping ratios for small level deformations which are of concern when designing for fatigue limit states.

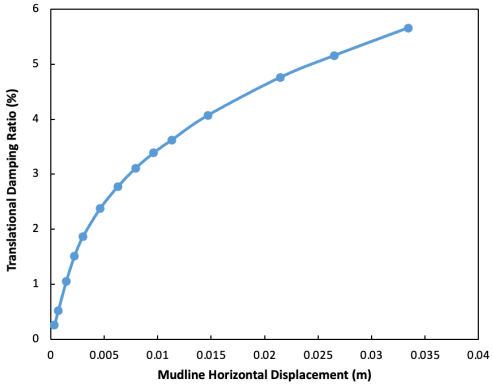


Figure 5. Translational damping ratio at the mudline

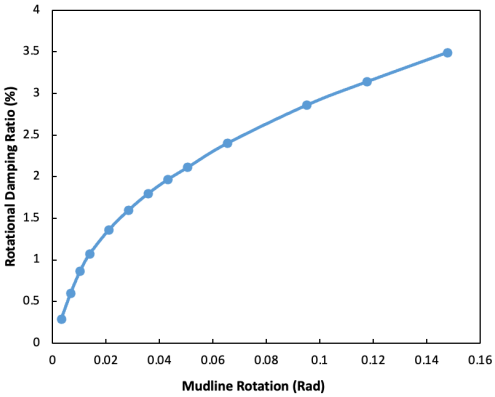


Figure 6. Rotational damping ratio at the mudline

These damping ratios are subsequently converted to translational and rotational damping coefficients according to the following equation:

$$Damping\ Coefficient = \frac{2DK}{\omega} \tag{4}$$

where D is the damping ratio, K is the secant stiffness of the foundation (Not shown in this paper) and ω is the angular frequency of the load applied. Since the loads applied on OWTs are within a wide range, the natural frequency of the simulated OWT structure (0.16 Hz), is used in this study as was done by Carswell et al., (2022). It is important to note that the choice of ω may underestimate or overestimate the effect of hysteretic damping and hence Fourier spectrum analysis must be carried out initially to determine the primary vibration frequency. The damping coefficients are lumped at the foundation level for a 1D FE model to check whether the critical damping ratio values are approximately similar to those of 3D FE. Free vibration in Plaxis is conducted by applying a load at the RNA level and then removing the load to allow the structure to freely vibrate. The 1D FE analysis is carried out by a Python script which assembles the global stiffness, mass, and damping matrices. The constant acceleration time integration approach is used to solve the equations of motion. A sufficiently small time step increment of 0.005 seconds is used to ensure the stability and accuracy of the solution. The free vibration is performed by increasing the load linearly at the RNA and then dropping the load to zero. The following equations are used for calculating the logarithmic decrement ratio (δ) and the damping ratio (ξ):

$$\delta = \frac{1}{n} ln\left(\frac{Ao}{A1}\right) \tag{5}$$

$$\xi = \frac{1}{\sqrt{1+(\frac{2\pi}{\delta})^2}} \tag{6}$$

where Ao and A1 are two successive amplitudes at the RNA level and n is number of cycles apart. Figure 7 compares the critical damping ratio from 3D FE and 1D FE with the viscous dashpot attached at the mudline. According to the results in Figure 7, the critical damping ratios determined from the 1D FE yields very close values to those obtained from 3D FE. As a results, the viscous dashpots calculated from the damping ratios can readily be used in integrated structural analysis for OWTs.

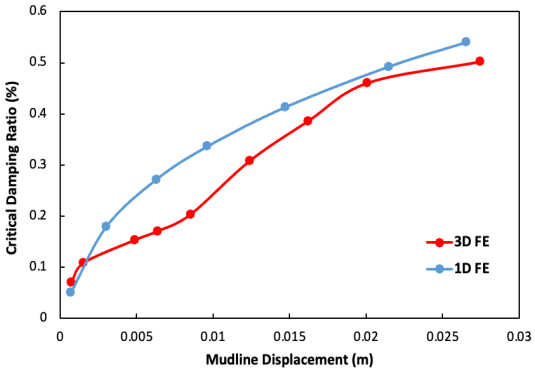


Figure 7. Comparison between 3D FE and 1D FE

6. CONCLUSIONS

This paper aimed to obtain the damping ratios at the foundation level to incorporate them into full wind turbine numerical analyses. The main objective was to calibrate the non-linear HSsmall constitutive model based on results obtained from dynamic triaxial tests to allow for a realistic representation of hysteretic soil damping for monopile foundations. This combined approach of conducting laboratory

tests along with implementing numerical analyses can lead to optimised structural support design. Furthermore, the overall critical damping ratios determined from free decay simulation can give a perspective on the damping that can expected for large-size OWT's.

7. ACKNOWLEDGEMENTS

The authors are grateful for the financial support provided by the funding agency Sustainable Energy Authority of Ireland (SEAI).

REFERENCES

Andersen, L. 2010. Assessment of lumped-parameter models for rigid footings. *Computers and Structures*, *88*(23), 1333-1347. https://doi.org/https://doi.org/10.1016/j.compstruc.2008.10.007.

ASTM D3999. 2013. Standard test methods for the determination of the modulus and damping properties of soils using the cyclic triaxial apparatus. ASTM International, West Conshohocken.

ASTM D7181-20. 2020. Standard Test Method for Consolidated Drained Triaxial Compression Test for Soils. ASTM International, West Conshohocken.

Carswell, W., Arwade, S. R., Johansson, J., and DeGroot, D. J. 2022. Influence of foundation damping on offshore wind turbine monopile design loads. *Marine Structures*, *83*. https://doi.org/10.1016/j.marstruc.2021.103154.

Carswell, W., Johansson, J., Løvholt, F., Arwade, S. R., Madshus, C., DeGroot, D. J., and Myers, A. T. 2015. Foundation damping and the dynamics of offshore wind turbine monopiles. *Renewable Energy*, *80*, 724-736. https://doi.org/10.1016/j.renene.2015.02.058.

Damgaard, M., Ibsen, L. B., Andersen, L. V., and Andersen, J. K. F. 201). Cross-wind modal properties of offshore wind turbines identified by full scale testing. *Journal of Wind Engineering and Industrial Aerodynamics*, *116*, 94-108. https://doi.org/https://doi.org/10.1016/j.jweia.2013.03.003.

Escribano, D. 2014. Evolution of stiffness and deformation of Hostun sand under drained cyclic loading, PhD thesis, University of Oxford.

Gaertner, Evan, Jennifer Rinker, Latha Sethuraman, Frederik Zahle, Benjamin Anderson, Garrett Barter, Nikhar Abbas, Fanzhong Meng, Pietro Bortolotti, Witold Skrzypinski, George Scott, Roland Feil, Henrik Bredmose, Katherine Dykes, Matt Shields, Christopher Allen, and Anthony Viselli. 2020. *Definition of the IEA 15-Megawatt Offshore Reference Wind*. Golden, CO: National Renewable Energy Laboratory. NREL/TP-5000-75698.

Hardin, B., and Drnevich, V. 1972. Shear Modulus and Damping in Soils: Design Equations and Curves. *J. Soil Mech. Found. Div.*, *98*. https://doi.org/10.1061/JSFEAQ.0001760.

Ladd, R. 1978. Preparing Test Specimens Using Undercompaction. *Geotechnical Testing Journal*, *1*(1), 16-23. https://doi.org/10.1520/gtj10364j.

28th European Young Geotechnical Engineers Conference – EYGEC 2024
© 2024 Macedonian Association for Geotechnics, ISBN 978-608-4510-61-1

Field data based numerical analysis of sand boil reactivation along river embankments

Ilaria Bertolini[a]

[a] *DICAM Department, Alma Mater Studiorum, Università di Bologna, viale del Risorgimento 2, Bologna, 40136, Italy*

ABSTRACT

The Po River, the longest watercourse in Italy (652 km), flows eastward from the western Alps to the Adriatic Sea confined for half of its course within major river embankments. Over the centuries, many urban centres, industrial and agricultural settlements developed near these structures and today 16 million people reside here. Among the possible failure mechanisms affecting these structures, backward erosion piping (BEP) results one of the most threatening. BEP refers to the process in which, in presence of high-water events, seepage forces gradually erode the coarse material of the embankment foundation, creating a shallow pipe at the interface with the cohesive top layer.
The paper addresses the safety assessment of river sections to sand boils reactivations. The focus is on the modelling of water dynamics in proximity of the sand ejection pipe able to reliably simulate the phenomenon at the verge of activation. The study refers to a section in Mazzorno Sinistro (RO) along Po River affected by recurrent phenomenon reactivations. A 2D FE model of the section is developed to reproduce accurately the hydraulic behaviour upon transient seepage. The distribution of the hydraulic parameters of the different soil units has been estimated initially from in-situ and laboratory tests then validated in back analysis on piezometric data. Finally, the variations in the hydraulic gradients and in the flow rate in proximity of the pipe are traced upon increasing stationary hydrometric levels and the obtained results compared to literature critical gradients.

KEYWORDS

Erosion; Piping, Numerical modelling; sand boil, Po River embankments

1. INTRODUCTION

The Po River (Figure 1C) meanders eastward toward the Adriatic Sea through the landscapes of Northern Italy, proudly claiming its title as the longest waterway in the nation. Its wide drainage basin gave birth to a vast and fertile floodplain, on which approximately 16 million people, a quarter of Italy's population, are settled. The Po Basin also plays a central role in the country's economy, hosting uncountable agricultural and industrial activities. Given its significance, the Po River necessitated to be bordered for over half of its course within major embankments in order to protect the territory against periodic surges. These man-made structures, constructed over centuries, were erected upon a relatively impermeable top layer (blanket) atop a sandy foundation (aquifer), as illustrated in Figure 2.

The management of the Po River and the surrounding territories falls under the supervision of various Italian public bodies, with AiPo (Interregional Agency for the Po River) having central role. AiPo, with the support of universities, is at the forefront of pioneering investigations and studies, particularly focusing on a critical threat to Po River embankments: backward erosion piping (acronym BEP). BEP is a specific form of internal erosion process occurring during water events in which soil particles are eroded by seepage forces from beneath river embankment structures. The erosive phenomenon starts at an unfiltered seepage exit and progresses backward along the boundary between an erodible, granular layer (such as sand) and a cohesive top layer (such as clay). Once initiated, the erosion process develops if the hydraulic load is maintained, gradually forming a "pipe" beneath the structure, potentially leading

to the structural failure of the section. The progression of the phenomenon is well evident at the exit point because the fluidized sand particles settle in a ring outside the boiling zone, forming a “volcano”. Volcanoes, commonly referred to as "*fontanazzi*" in Italian dialect, often develop in the middle to lower sections of the Po watercourse, where the riverbed results pensile and thus higher hydraulic forcings may establish between the river and the exit point of the flux. Ringing the sand boil, is a typical temporary solution for reducing hydraulic gradients in proximity of the seepage exit after BEP activation/reactivation (Figure 1B). In fact, an appropriate height of the sack ring reduces the hydraulic head between river and exit point preventing sand transport and the upstream progression of the erosion pipe. Generally, after the equilibrium is reached, a further increase in water level is required in order to reactivate the phenomenon and for the pipe to extend beneath the embankment base and reach upstream levels. The reactivation of the process can eventually lead to the widening of the pipe and finally to the structure collapse.

The paper presents the case study of a river embankment section along the Po River, 35 km from its deltaic area, and close to the city of Mazzorno Sinistro (RO) (Figure 1C). This section is characterized by the periodical reactivation of historical sand boils in conjunction with medium-high water events. An in depth geotechnical-geological campaign has been carried out in the area in order to investigate the local stratigraphy and estimate the relevant parameters for the problem (Figure 1A). A two-dimensional (2D) numerical model of the section has been elaborated and the trend of the average exit hydraulic gradient in the vertical pipe is traced with changes in the model parameters upon increasing hydraulic load. Finally, the obtained results are compared to literature critical gradients.

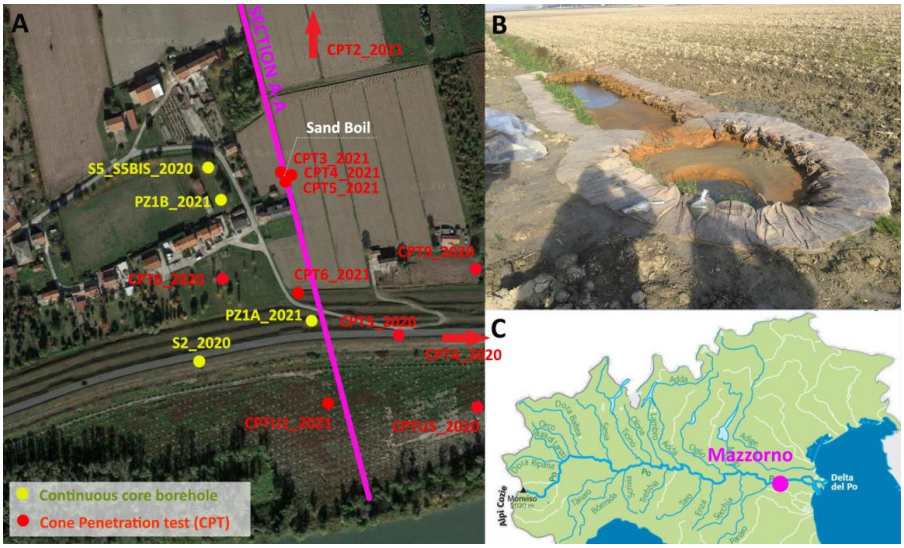


Figure 1. In image C, schematization of the Po river with its tributaries and, indicated with a pink point, the location of the investigated section in Mazzorno Sinistro (RO). In image A, map of section reporting the location of the performed in situ tests (continuous core boreholes and cone penetration tests). Image B shows the sack ring positioned around the sand boil during the reactivation occurred in November 2019.

2. THE CASE STUDY

The chosen embankment segment has been interested by two geotechnical campaigns, the first one carried out in 2020 and the second one in 2021 for a total of 9 continuous core boreholes performed and 14 cone penetration tests with pore water pressure measurement. The length of the embankment covered by the investigations is approximatively 1 km, in order to acquire sufficient data to characterize the deposit in proximity of all the historical sand boils scattered in the area. The paper focuses on the sand boil located within a ditch (exact position in Figure 1A) which reactivated during the floods registered

in 2019, 2018 and 2016 and probably even before, when no records were kept. The cross-section A-A (Figure 2) passing in proximity of the investigated sand boil (trace of the section in Figure 1A) shows the soil stratigraphy obtained by CPTs standard interpretation according to Robertson (2009). Profiles with depth of corrected cone penetration resistance q_t and pore water pressure u_2 of CPT tests, performed at different distances from the river, have been superimposed on the cross-section. The erosion process triggered by BEP reactivation affects the aquifer (unit A), constituted by an alternation of sands and silty sands, and the cohesive top cover (unit B), confining superiorly the aquifer and constituted by an alternation of silty mixtures. In proximity of the exit pipe, a cohesive layer ~2.5m thick is interposed within the aquifer, reducing considerably the flow section.

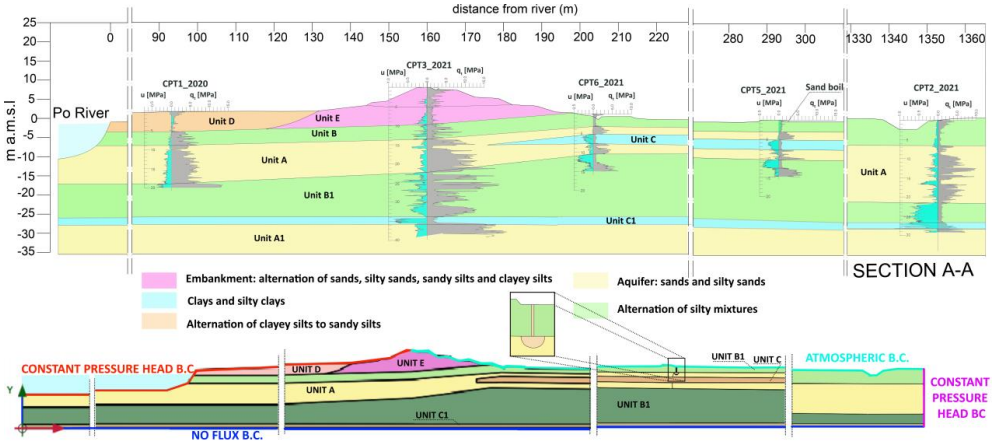


Figure 2: Top) Soil stratigraphy along section A-A (trace of the section in Figure 1A) with superimposition of the CPT profiles of corrected cone penetration resistance q_t and pore water pressure u_2. Bottom) The numerical 2D FE model of the section elaborated in Plaxis 2D with indication of the stratigraphy and of the applied boundary conditions (B.C.). An enlargement of the geometry in proximity of the exit vertical pipe is also provided.

3. SOIL PARAMETERS

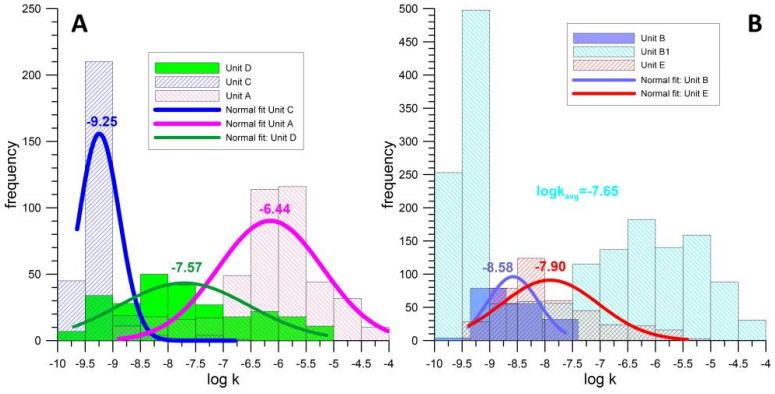


Figure 3: Frequency distributions of permeability data in terms of *logk* obtained from CPTs interpretation and, superimposed, the gaussian probability distributions.

The hydraulic properties of the sediments composing the river embankment section were primarily estimated through cone penetration tests interpretation, leveraging insights gained from the use of in-situ tests for the geotechnical characterization of a similar river segment located 40 m upstream, in Guarda Ferrarese (FE) (Bertolini et al., 2022a; Bertolini et al., 2022b; Martinez et al., 2020a). In

particular, the coefficients of saturated permeability (*k*) of the different soil units were estimated from the *log(k)* profiles with depth obtained applying the well-known CPT-based empirical correlations by Robertson and Cabal (2010) (eq.s 1 and 2), formulated in function of the Soil Behaviour Type Index (I_c).

$$1.0 < I_c < 3.27: \quad \log(k) = 0.952 - 3.04\, I_c \tag{1}$$

$$3.27 < I_c < 4.0: \quad \log(k) = -4.52 - 1.37\, I_c \tag{2}$$

The *log(k)* profiles were compared to the punctual estimations of the permeability coefficient from Lefranc tests and dissipation tests (carried out during CPTs) performed in the sandy units and in the cohesive ones, respectively. Direct laboratory estimations of *k* were obtained through permeability tests in triaxial equipment on undisturbed soil samples. The successful outcome of the data match has entitled the use of CPT tests for a reliable estimation of *k* for each soil unit located below the phreatic water level. It is worth noting that the application of CPT to unsaturated soils can be misleading both in soil profiling and in parameter estimation, while it can provide valuable insight on the parameter spatial variability (Miller et al., 2018; Marchi et al., 2022). Hence, CPT data from the unsaturated zones of units E (embankment), D (berm) and B (blanket) have been excluded from the analyses.

Figure 3 displays the frequency distributions of *log(k)* derived from CPT data. Most of the soil units exhibit a bell-shaped distribution, which is typical of a normal distribution. Conversely, the heterogeneous unit B1, located underneath Unit A and characterized by alternating silty clays and sandy silts, displays a bimodal distribution. In this case, the smaller peak is observed at *log(k)* = -6.25, typical of sandy silts, while the higher peak corresponds to *log(k)* = -9.25, consistent with silty clays. Since the BEP phenomenon affects mainly the aquifer (unit A) and the blanket (Unit B), it was deemed unnecessary to further subdivide B1 in subunits to reduce the parameter dispersion. The mean value of the normal distribution approximating B1 data and equal to $\log(k_{avg})$=-7.65 has been considered as representative of the average behaviour of the whole unit and thus, it has been adopted for the following analyses. The mean values of the Gaussian distributions, indicated in Figure 3 in correspondence of the curve peaks and in the first three rows of Table 1, have been selected as representative log(*k*) parameters for each soil unit.

Table 1. Average value (μ) and standard deviation (б) of the parameters adopted in the numerical FE model. σ_k/μ_k (i.e., ratio between the average value and the standard deviation) represents the percentage of variation of each parameter.

	$\log(k_A)$	$\log(k_B)$	$\log(k_C)$	$\log(k_D)$	$\log(k_{B1})$	$\log(k_E)$	
μ_{logk}	-6.44	-8.58	-9.25	-7.57	-7.65	-7.90	
σ_{logk}	1.30	0.46	0.35	1.36	1.77	0.90	
	k_A	k_B	k_C	k_D	k_{B1}	k_E	k_{exit}
μ_k	3.19e-05	4.69e-09	7.86e-10	3.74e-06	1.75e-07	1.06e-07	6.38e-05
σ_k	3.66e-07	3.21e-09	8.11e-10	2.72e-08	2.24e-08	1.27e-08	3.19e-05
σ_k/μ_k (%)	1.1	68.5	103.2	0.7	12.8	11.9	50
	Pipe diameter (m)		Semisphere diameter (m)		Blanket thickness (m)		
μ	0.2		2		3.15		
σ	0.1		2		0.06		
σ_k/μ_k (%)	50		100		1.8		

The coefficient of permeability *k* is a soil property that exhibits a significant natural variability. Several authors have suggested that this property can be described satisfactorily with the two-parameters lognormal distribution, irrespective of the soil class considered (Freeze, 1975; Sudicky, 1986; Benson, 1993 among others). It was thus assumed a lognormal distribution of *k* and, as stated before, a normal distribution of *log(k)*, for all the soil units. In order to estimate the two governing parameters of the *k* distribution (average, μ_k, and the standard deviation, σ_k) to be used in the numerical modelling, initially, the *log(k)* parameters ($\mu_{logk;}$ σ_{logk}) have been converted to the natural logarithm base (i.e., multiplying for

log(e)), then the properties of the lognormal distribution have been applied (i.e., μ_k and σ_k estimated in function of μ_{lnk} and σ_{lnk}).

4. NUMERICAL MODELLING OF THE BEP PHENOMENON

A 2D finite element (FE) model of the groundwater flow beneath the examined river embankment section has been developed to investigate the hydraulic gradient and the discharge within the exit hole of the sand boil (Figure 2 bottom). The analysis is conducted by incrementally increasing the water head (H) regulated by the river hydrometric level and applied to the model boundary. The numerical model, which measures 36 meters in height and 1556 meters in length, is designed to prevent any potential boundary effects on the simulated groundwater flow. The discretized model consists of 22524 triangular elements and 183541 nodes, generated using the Plaxis2D commercial code by Bentley Systems. The average dimension size of the mesh element in the model domain is equal to 1.9m, refined up to 0.5m in Units A, B and C1, affected by BEP phenomenon, and up to 0.02m in proximity of the vertical pipe of the sand boil. Following the approach of García Martínez et al. (2020a) and Bertolini et al (2022b), the sand boil exit volume is represented as a cylindrical vertical pipe with a hemispheric cluster at its base (as depicted in the enlarged detail in Figure 2 top). The hemisphere is included to simulate the presence of a previously eroded soil volume formed during the past reactivations and characterized by a permeability higher than that of the aquifer. Data collected by a system of piezometers installed in proximity of the sand boil allowed a calibration of the coefficient of permeability of the hemisphere and of the pipe that turned out equal to twice the one of the aquifer (Bertolini et al., 2024) and its variation range between [k(A), 3k(A)] (see k_{exit} in Table 1).

Figure 2 bottom reports the geometry and the stratigraphy of the elaborated numerical model and the applied boundary conditions. The bottom of the model is located within a clayey layer (deep Unit C1) unaffected by the underseepage responsible for the BEP erosion process. Therefore, a no-flux boundary condition (BC) is assigned to it. Similarly, the left vertical boundary of the model is also designated as a no-flux boundary, corresponding to the centerline of the river. Underseepage phenomenon is influenced by the river water level, thus a constant head is applied to the interface between the river and the aquifer, the berm and the inner slope of the river embankment. Specifically, a sequence of 19 steady-state stages of constant hydraulic head has been set in succession in the analyses to simulate a variation in water level from 0 meters, the riverbed, to 18.7 meters corresponding to the crest of the embankment. The hydraulic BC applied to the right side of the model replicate the piezometric far field observations obtained from a recently installed piezometer in the aquifer and consequently, a constant head condition is imposed to each stage.

Table 1 reports the average values and the standard deviations of each parameter or geometric dimensions which can possibly have an influence on the underseepage and BEP phenomena. In particular, the average diameter of the exit hole is assumed equal to 0.2 meters, based on field observations obtained in another investigated section along the Po River and located close to Guarda Ferrarese (Marchi et al., 2021 and Garcia Martinez et al., 2020b). A diameter of the exit vertical pipe equal to 0.1 meters is assumed as initial activation diameter and therefore sets the lower boundary for the range of this random variable, which spans from 0.1 to 0.3 meters. A hypothesis on the average dimension of the hemisphere has been made (d = 2m) and its possible range of variation is set between 0 and 4 meters. The average value and the standard deviation of the blanket thickness has been obtained from the soil profile interpretation of the CPT tests performed in proximity of the sand boil (CPT 3, 4 and 5 in Figure 1A) and of the embankment toe (CPT 6).

4.1. Results of seepage analyses

N° 21 seepage analyses have been performed: one adopting the average values of the properties and element dimensions (diameter of the pipe and hemisphere and blanket thickness) indicated in Table 1 and the remaining simulations adopting, one at a time, their average values (μ) +/- the standard deviation (б). In particular, the focus is on the pore pressure distribution around the exit hole of the sand boil and

on the average hydraulic gradient reached at each stage in the vertical pipe, as a function of the incremental changes in river water head. A further simulation (n° 22) has been carried out in order to investigate the response of the model in proximity of the exit hole in a hypothetical configuration of the aquifer (Unit A) without the interposed clayey layer (Unit C). The average hydraulic gradient (i_{avg}) in the exit pipe has been calculated, for each analysis, from the ratio between the pressure head loss between top and bottom of the pipe and the pipe length (~2.7m). A constant 0.2-meter water level has been assumed in the ditch. Comparing the average hydraulic gradients of the 22 simulations, differences are observed for hydraulic loads greater than ~9 meters (i.e., water level above the berm height) and they increase more than linearly with the hydrometric level (Figure 4 A). To ease a comparison between simulations, an enlarged detail of the results of the model for the highest water levels (H from 17 to 19m) is reported in Figure 4 B.

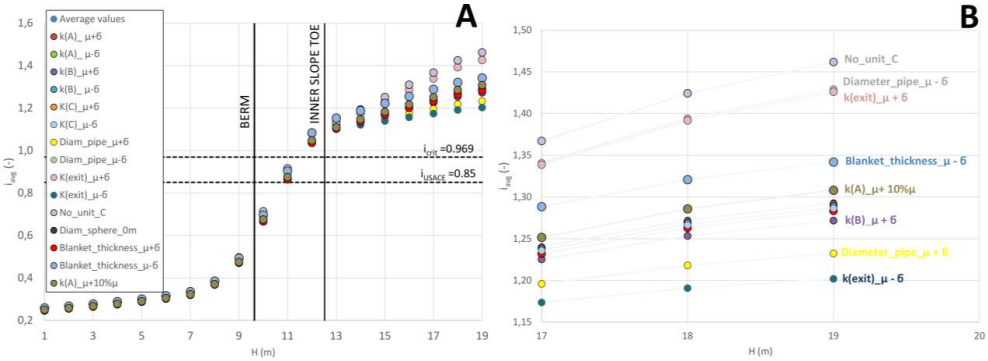


Figure 4: In graph A, trend of the average hydraulic gradient (i_{avg}) in the vertical pipe with increasing hydraulic loads applied to the river hydrometric boundary and obtained from the 2D seepage analysis. Different parameter configurations have been analysed. The reference simulation is Sim_1 which adopted the average values of each parameter, the remaining ones have varied, one at a time, the parameters within the variation range obtained by in situ tests elaboration or initial assumptions. In graph B, an enlargement of the i_{avg} trend for hydraulic loads between 17 and 19m is shown. "μ" stands for "average" while "б" for "standard deviation".

As expected, the lowest seepage velocity and hydraulic gradient (i_{avg}) are observed for the lowest coefficient of permeability of the vertical pipe (k(exit)_μ-б = 3.19E-05 m/s), with an i_{avg} reduction equal to ~6.8% for H=19m, with respect to Sim_1 (Figure 4 B). Sim_1 is the "base simulation" that is the simulation that adopts the average values of the parameters. Similarly, to an increment in the vertical pipe diameter (Diameter_pipe_μ+б = 0.3m) corresponds a reduction of the flow velocity and, according to the Darcy's law, of i_{avg} (the latter of ~4.4% with respect to Sim_1). A much smaller incidence on model results (~1.4%) is obtained adopting the upper boundary of the blanket permeability variation range (i.e., k(B)_μ+б = 7.9E-09 m/s). Variations in the permeability coefficients of Units D, E and B1 (see stratigraphy in Figure 2 bottom) do not produce any changes in i_{avg} with respect to Sim_1, being these units not affected by the BEP phenomenon. More interesting (and somewhat less predictable) is the observation that changes in the hemisphere diameter (from 0 to 4m) have negligible effects on the i_{avg} in the pipe. Conversely, a reduction in the diameter of the vertical pipe, an increment in the permeability of the vertical pipe and hemisphere or a reduction of the blanket thickness (i.e., of the pipe length) have relevant incidence on the simulated i_{avg}, showing an increase, with respect to Sim_1, equal to ~10.8%, ~10.6% and 4%, respectively. The absence of a clayey layer (Unit C), within the aquifer (Unit A), causes a marked increment in the simulated hydraulic gradients (of ~13.3%) with respect to Sim_1, which seems against the Darcy's idea that an increment in the flow area is always accompanied by a decrement in flow velocities and hydraulic gradients, for a constant seepage discharge. An explanation could be found analysing, from a numerical point of view, the water dynamics in the pervious layer (Unit A) in proximity of the exit pipe. The flux mainly one-dimensional and preponderant in the horizontal direction turns into bi-dimensional in proximity of the exit pipe, with an increase of the vertical discharge within the pipe (q_y) caused by the greater afflux of water from the wider aquifer section (q_y increments of ~88% with respect to the configuration without the interposed layer). A

separate consideration is reserved to the incidence in the seepage modelling of the permeability coefficient of the aquifer. The range of variation of k(A) deduced from CPT tests is quite reduced (σ_k is ~1.1% of μ_k, see Table 1) and thus the adoption in the numerical modelling of the upper or lower bounds of this parameter (i.e., μ +/- σ) affect only slightly the outcome of the simulation in proximity of the exit pipe. Considering a wider k(A) variation range (e.g., σ_k is 10% of μ_k), i_{avg} increases of ~1.4% with respect to the outcome of Sim_1 (see k(A)=μ+10%μ =3.51E-05 m/s in Fig. 4 B) resulting more in line with the expected results.

The critical hydraulic gradient of Terzaghi (1960) (i_{crit} = 0.969), estimated in function of the void ratio and the specific weight of the solid particles of the aquifer, and the one suggested by USACE (1999) (i_{USACE} = 0.85) express the limit hydraulic gradient in the pipe causing a BEP activation/reactivation. Reached these values, a lifting and, to a further increase, also a transport, of soil particles occurs from the vertical pipe. From the superimposition of these values on the trend of i_{avg} in Figure 4 A, it can be observed that the critical gradients are overcome when the river water level floods the berm but not the inner slope of the embankment. Moreover, in this range of hydraulic loads (11-13m), the dispersion of the hydraulic gradients estimated by the FE model, adopting different sets of initial parameters, is quite narrow (range of variation [0.864; 0.916] for H=11m) with the blanket thickness individuated as the most sensitive parameter. The remaining model parameters that show a low or null sensitivity over this range of hydraulic loads, do not require a calibration, easing the subsequent process of parameter tuning. It is important to recall that the discussed results have been obtained from a 2D modelling of the section which could be somewhat inaccurate in the simulation of the pore water pressure distribution in proximity of the vertical exit pipe and of the hemisphere, being their geometry axisymmetric and not correctly approximated by bi-dimensional elements. This is especially true when it comes to the evaluation of the incidence on the i_{avg} of the hemisphere diameter, whose tri-dimensional configuration guarantees most likely an increased convergence of the flow into the pipe with respect to the 2D configuration and thus a consequent increment in the simulated exit hydraulic gradient. Consequently, a possible confirmation or adjustment of the obtained results should be sought in a three-dimensional modelling of the problem.

5. CONCLUSIONS

The paper presents the results of a series of numerical two-dimensional FE seepage analyses of Backward Erosion Piping (BEP) affecting a river embankment section located in Mazzorno Sinistro (RO) along Po River. Several field tests have been conducted in the site in order to estimate the parameters possibly affecting the phenomenon, among which the coefficients of saturated permeability of the soil units and the thickness of the cohesive top layer (blanket). These simulations consider the variability of the parameters as emerged from the elaboration of cone penetration tests by varying, one at a time, each parameter within the range [average+/- standard deviation] and investigating the outcome of the model in proximity of the vertical exit pipe of the sand boil under increasing hydraulic load applied to the river boundary. Other analyses investigate the incidence on the seepage simulation of a variation in the diameter of the exit vertical pipe and of the hemisphere, located at its base and used as a stratagem to take into consideration the presence of a previously eroded soil volume. Comparing the obtained hydraulic gradients within the pipe, it turned out that the permeability of the aquifer, in which the erosion pipe may develop, together with the permeability of the exit vertical pipe, of the hemisphere and of the blanket, have relevant incidence on the simulated seepage outcomes. On the contrary, the permeability of the embankment and berm units and of the cohesive units underneath the aquifer have a null incidence on them. The identification of the sensitivity of each parameter in its range of variation eases the future calibration process of the model by allowing an exclusion from the parameter tuning process of the non-sensitive ones. Surprisingly, the presence of an interbedded cohesive soil layer within the aquifer causes a decrease of the vertical discharge in the pipe accompanied by a reduction of the hydraulic gradient, with respect to the configuration without this layer. As future development of the present work, a 3D analysis of the problem may allow the quantification of the error committed in the simulation of the 2D pore water pressure distributions in proximity and within tri-dimensional geometries, as the vertical pipe and the hemisphere, whose conditions, in some cases, may result badly approximated to bi-dimensional.

Likely, these approximations account for the minimal impact on the 2D model outcome of the variations in the hemisphere diameter. However, this hypothesis requires further investigation for confirmation.

6. ACKNOWLEDGEMENTS

Part of the activities presented in this paper were carried out within the RETURN Extended Partnership and received funding from the EuropeanUnion Next-GenerationEU (National Recovery and Resilience Plan – NRRP, Mission 4, Component 2, Investment 1.3 – D.D. 1243 2/8/2022, PE0000005 - Spoke TS 2). Other activities were conducted formerly thanks to a research grant of AIPO (Interregional agency for the Po River).

REFERENCES

Benson, C.H. 1993. Probability distributions for hydraulic conductivity of compacted soil liners. *Journal of Geotechnical Engineering*, 119(3).

Bertolini, I., Gottardi, G., Marchi, M., Tonni, L., Bassi, A., Rosso, A. 2022a. Application of CPT to the evaluation of permeability in a Po River embankment prone to backward erosion piping. *Proceedings of the 5th international Symposium on Cone Penetration Testing*, CPT'22, Bologna, Italy, 8-10 June, pp. 300-305. eBook ISBN 9781003308829

Bertolini, I., Gottardi, G., Marchi, M., Tonni, L. 2022b. Probability of reactivation of a sand boil near a river embankment of the Po River (Italy). In: *Proceedings of the 8th International Symposium for Geotechnical Safety & Risk*, Newcastle, Australia, 14-16 December. http://dx.doi.org/10.3850/978-981-18-5182-7_00-16-004.xml

Bertolini, I., Marchi, M., Tonni, L. Gottardi, G. 2024. Reliability analysis of a Po River embankment affected by underseepage. *Proceedings XVIII European Conference on soil mechanics and geotechnical engineering*, Lisbon, Portugal, 26-30 August.

Freeze, R.A. 1975. A stochastic-conceptual analysis of one-dimensional groundwater flow in non-uniform homogeneous media. *Water Resources Research*, 11 (5), 725-741. https://doi.org/10.1029/WR011i005p00725

García Martínez, M.F., Tonni, L., Marchi, M., Tozzi, S. and Gottardi, G. 2020a. Numerical tool for prediction of sand boil reactivations near river embankments. *Journal of Geotechnical and Geoenvironmental Engineering*, 146(12). https://doi.org/10.1061/(ASCE)GT.1943-5606.0002380

García Martínez, M.F., Gottardi, G., Marchi, M., Tonni, L. 2020b. On the Reactivation of Sand Boils Near the Po River Major Embankments. *Lecture Notes in Civil Engineering*, 40, 328- 337. ISSN 2366-2565. https://dx.doi.org/10.1061/(ASCE)GT.1943-5606.0002380

Marchi, M., Bertolini, I., Marchi, G., Lancellotta, R. 2023. Intrinsic and induced vulnerability of the Osservanza Church in Bologna (Italy). *Rivista Italiana di Geotecnica*, 4/2023, 34-54. http://dx.doi.org/10.19199/2023.4.0557-1405.034

Marchi, M., García Martínez, M.F., Gottardi, G. and Tonni, L. 2021. Field measurements on a large natural sand boil along the river Po (Italy). *Quarterly Journal of Engineering Geology and Hydrogeology*, 54(4). https://doi.org/10.1144/qjegh2020-097

Miller, G.A., Tan, N.K., Collins, R.W., Muraleetharan, K.K. 2018. Cone penetration testing in unsaturated soils, *Transportation Geotechnics*, 17 (B), 85-99. https://doi.org/10.1016/j.trgeo.2018.09.008.

Robertson, P.K. 2009. Interpretation of cone penetration test-a unified approach. *Canadian Geotechnical Journal*,46(11),1337-1355. http://dx.doi.org/10.1139/T09-065.

Sudicky, E.A. 1986. A natural gradient experiment on solute transport in a sand aquifer: spatial variability of hydraulic conductivity and its role in the dispersion process. *Water Resources Research*, 22(13), 2069-2083. https://doi.org/10.1029/WR022i013p02069

Terzaghi, K. 1960. *From theory to practice in soil mechanics*. Wiley, New York, 114-118. https://doi.org/10.2136/sssaj1961.03615995002500010002x

USACE. 1999. *Risk-Based Analysis in Geotechnical Engineering for Support of Planning Studies*. Report No ETL 1110-2-556, Washington, DC.

28th European Young Geotechnical Engineers Conference – EYGEC 2024
© 2024 Macedonian Association for Geotechnics, ISBN 978-608-4510-61-1

CPTU and MASW investigation results from the Sisak-Moslavina County area after the Petrinja earthquake and comparison with the global experiences

Marko Boričević[a], Pero Šiša[b], Igor Sokolić[c]

[a,] *Geotehnički studio d.o.o., 10000 Zagreb, Croatia*

ABSTRACT

On 29th of December 2020, an earthquake of M_w 6.4 (M_L 6.2) with epicenter around 4km SW of Petrinja hit the wider area of Sisak-Moslavina County (Croatia). Following disastrous earthquake, company Geotehnički studio d.o.o. carried out geotechnical investigation works for the purpose of reconstruction of the earthquake-damaged buildings. Applied methods were geomechanical CPTU and geophysical MASW. The investigations were carried out for determining the liquefaction potential of the underlying soil at a particular location and for determining the type of soil according to the Eurocode-8. The obtained results served as guidelines for the design of new or renovation of existing buildings. In this paper, an overview of the obtained investigation results is presented, where a total of 103 locations were investigated. The results were processed statistically, and an insight is given into the conducted CPTU depths, obtained liquefability classes, defined soil types according to Eurocode-8 and S-wave velocities in the first 30 m of the subsoil.With further data analysis those locations that contain the largest number of potentially liquefiable layers at depths greater than 5m were identified. At such locations, the values of normalized tip resistance (Q_{tn}), estimated values of S-wave velocities ($V_{s,CPTU}$), CSR variable values and CRR variable values for individual liquefiable interlayers were extracted. Ultimately, overburden-stress corrected shear wave velocity $V_{s1,\,CPTU}$ was calculated for every interlayer. Finally, all parameters in the potentially liquefiable zones are correlated and compared with global experiences.

KEYWORDS

CPTU; Liquefaction; Earthquake; Sisak-Moslavina

1. INTRODUCTION

The area of Sisak-Moslavina County (Croatia) belongs to the so called Pokupsko-Petrinja epicentral area. Until the most recent and devastating earthquake on December 29th 2020, that area was characterized by a smaller number of stronger earthquakes and larger number of weaker ones in the past. The earliest recorded stronger earthquake (by Croatian Earthquake Catalog) in the mentioned epicentral area occurred on August 17th 1903. with the estimated magnitude of M_L=4.6 its effects were described as VI° by MCS. Next, the strongest earthquake, until the recent one, and at the same time the most famous one, not only in Croatia, but also globally, occurred on 8th of October 1909., with the epicenter 3.5km SW of Kravarsko and 9km N from Pokupsko and is known as *"Pokupsko earthquake"*. The magnitude was M_L=5.8, with the focal depth of 14km. Effects that it caused were assessed as VIII° by MCS.

In the last 25 years the strongest earthquake, within mentioned epicentral area, occurred on 10th of September 1996, it had magnitude M_L= 4.5 with its epicenter 3km S of the Petrinja. Effects that it caused were assessed as VI° MCS. Finally, the most recent earthquakes in mentioned epicentral area occurred on 28th and 29th of December 2020. First one with magnitude of M_L=5.0 on the 28th of December which preceded a devastating earthquake with epicentre about 5km SW of Petrinja with the magnitude of M_w=6.4 (M_L=6.2) on 29th of December. Effects of that latter were assessed as VIII-IX° by MCS. That earthquake was followed by many aftershocks, and it has not calmed down even today.

During and shortly after the earthquake many people noticed specific phenomena on their lands or near them, as they called it *"sand molehills"* which are result of process called liquefaction. Liquefaction is defined as transformation of granular material from solid to liquefied state as a consequence of increased pore-water pressure and reduced effective stress (Marcuson, 1978.). Increased pore-water pressure is induced by tendency of granular material to compact when subjected to cyclic shear deformations. The change of state occurs most readily in loose to moderately dense granular soils with poor drainage, such as silty sands or sands and gravels capped by or containing seams of impermeable sediment. Loose soils also compact during liquefaction and reconsolidation, leading to ground settlement (Youd, Idriss, 2001) which widely happened at the area of Sisak-Moslavina County and damaged residential and public buildings. But, as the time showed, ground settlements were not the only threat to the habitants and their homes. Because of specific geological conditions the area was characterized by extreme secondary post seismic near-surface effects, namely suffusion and opening of almost a hundred sinkholes during the first months after the first foreshock (Terzić et al., 2021.).

Precisely because of the mentioned specific geological characteristics of the Sisak-Moslavina County area and the poor quality of the post-war reconstruction of the buildings, specialized geotechnical companies, such as Geotehnički studio d.o.o., with specific professional staff and equipment were engaged in order to carry out investigative works for the purpose of obtaining data on the quality of the underlying soil and gathering information to ensure quality reconstruction of the earthquake damaged buildings or construction of the new ones.

2. INVESTIGATION APPROACH AND OVERVIEW OF THE RESULTS

2.1. Investigation approach

During investigation works on location sites, two methods for data acquisition were used: piezocone penetration test (CPTU) and multichannel analysis of surface waves (MASW). Both methods were used because of their minimum time consumption and their low cost regarding to regular geomehanical investigative drilling. Furthermore, advantage of CPTU method is continuous profile of penetration resistance and results which are more consistent and repeatable. Continuous profile also allows a more detailed definition of soil layers than the other methods, so CPTU has advantage for developing liquefaction-resistance profiles.

On the other hand, MASW has advantage of being non-invasive, covers surface continuously and provides more complete coverage with improved resolution, which complements CPTU results very well. Also, measured V_s values are possible to obtain in soils that are difficult to penetrate with CPTU and at the sites where soundings may not be permitted. Furthermore, V_s is a basic mechanical property of soil materials, directly related to small-strain shear modulus, and small-strain shear modulus is a parameter required in analytical procedures for estimating dynamic soil response and soil structure interaction analyses. But, according to Youd and Idriss, (2001), there are three notable concerns about using V_s results for liquefaction-resistance evaluations, they are as follows:

- those measurements are made at small strains, whereas pore-water pressure buildup and the onset of liquefaction are medium to high-strain phenomena,
- seismic testing does not provide samples for classification of soils and identification of nonliquefabile soft clay-rich soils,
- thin strata may not be detected if the measurement interval is too large.

Because of these concerns, and delicacy of the assignment, values of V_s obtained by MASW method were used only to define ground types according to Eurocode-8 (EC8) and to get insight into S-wave velocities in the first 30 m of the subsoil. However, within this paper, calculated V_s values based on CPTU data from liquefiable layers were used for correlation analysis and comparison with the world experiences data.

2.2. Investigation scope

Until the release of this paper there were in total 103 investigated locations that were considered. Within those both CPTU and MASW methods were done on 101, and on extra 2 locations only MASW method was conducted (there was no ability to perform CPTU with the rig). On the following figure, georeferenced positions of all locations can be seen on a map within area of Sisak-Moslavina County.

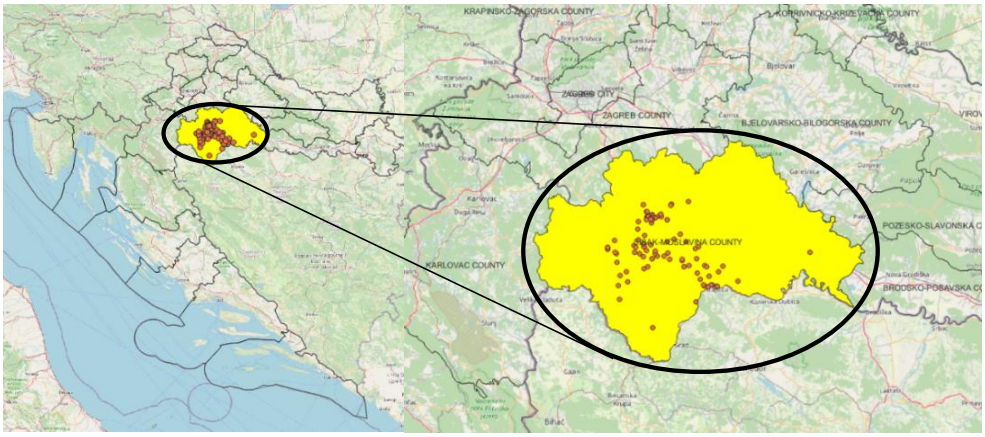


Figure 1. Georeferenced positions of 103 investigated locations at the area of Sisak-Moslavina County (Croatia)

2.3. Results of CPTU investigations

Regarding a CPTU method, the investigation depths reached ranged from 1.0 to 14.66 m, with the average depth of 7.33 m. All acquired CPTU data was analyzed and interpreted using CPeT-IT and CLiq software. Input parameters for the liquefaction analysis were as follows:

- earthquake magnitude M_w=6.50
- peak ground acceleration a_{gR}= 0.12
- depth to water table (insitu) GWT=1.00m

Evaluation method used for calculating resistance of soils to liquefaction at the investigated locations was based on NCEER (1998). Results were displayed in the form of $Q_{tn,cs}$ and CSR plot. Furthermore, to classify potential of liquefaction at the particular location sites, approach by Chen and Juang (2000) was used which is based on relationship between probability of liquefaction and factor of safety. Implementing the same approach, resulting data on liquefaction probability obtained by CPTU is given in the following table.

Table 1. Overview of the resulting liquefability classes on the Sisak-Moslavina County area

		Liquefaction classes				
	Total	Class 1	Class 2	Class 3	Class 4	Class 5
Nr. of locations	101	53	27	15	5	1
Percentage (%)	100	52.48	26.73	14.85	4.95	0.99

By reviewing the table 1, it can be noted that for 53 locations is almost certain that liquefaction will not happen, for 27 of them liquefaction is unlikely, furthermore, there is a rather small number, 15, of those locations that are uncertain, while 5 locations show a rather high certainty for liquefaction. Finally, only 1 location, out of total 101 locations, shows very high certainty for liquefaction. Roughly speaking, it can be said that about 80% of all investigated locations is rather safe from liquefaction processes, about 15% of them are uncertain and about 6% of locations are at higher risk of liquefaction.

2.4. Results of MASW investigations

Regarding the MASW method, all field acquired data was processed using ZondST2D software. Data processing included the preparation of field recordings, transformation from the time domain to the frequency domain (spectral analysis), extraction of dispersion curves and finally the inversion, which, through an iterative process, obtains a 1D V_s profile from dispersion curves. That profile shows the change in the velocity of propagation of the shear wave V_s with depth, and by accordance to the EC8 that velocity is observed in the first 30 m of depth. Results of the MASW detected ground types according EC8 for the investigated area of Sisak-Moslavina County are given in the following table.

Table 2. Overview of the resulting ground types according to EC8 on the Sisak-Moslavina County area

		Ground types in accordance with EC-8						
	Total	A	B	C	D	E	S1	S2
Nr. of locations	103	0	45	35	0	22	0	1
Percentage (%)	100	0.00	44.55	34.65	0.00	21.78	0.00	0.99

It can be noted that the most common ground type that occurs on the area of the Sisak-Moslavina County is type B, with 45 location occurrences. Type C is second one with 35 location occurrences, then comes type E with 22 location occurrences and finally special ground type S2 with occurrence at only 1 location. Furthermore, results showed that statistically lowest measured shear wave velocity in the first 30 m of the depth was $V_{s,30low}$=197 m/s, whereas highest measured shear wave velocity in the first 30 m of the depth was $V_{s,30high}$=702 m/s with average shear wave velocity of $V_{s,30aver}$=407 m/s.

3. COMPARISON OF RESULTS WITH GLOBAL EXPERIENCES

3.1. Filtering and adjusting of the data used

For the purpose of comparison of the data results obtained from Sisak-Moslavina County area with world experiences, filtering of locations was done. Out of 103 total locations only 24 of them was used in analysis. Only CPTU data was used for this purpose because of limitations of MASW measured velocities as mentioned in chapter 2.1. Location filtering was based on:

- reached depth of CPTU that is at least 5m or greater,
- higher number of detected liquefiable layers per location with FS<1.

Depths of CPTU at those filtered locations ranged from 5.32 to 14.66m and there were 111 liquefiable interlayers detected in total with the FS range from 0.46 to 0.99.

Since the fact that world experience plots used data such as normalized tip resistance (Q_{tn}), estimated and/or measured values of S-wave velocities ($V_{s,\,CPTU}$), CSR variable values and CRR variable values those data were extracted for every individual liquefiable interlayer within our 24 filtered locations. Furthermore, it is important to emphasize, that the analysis of the liquefability of an individual location at the Sisak-Moslavina County area was based on an earthquake magnitude of M_w=6.4, but for comparison purposes with global results, it was necessary to adjust, reduce, our results to an earthquake magnitude equivalent to M_w=7.5 since global experiences are shown in that form. Therefore, the values of normalized tip resistance $Q_{tn7.5}$ and values of the variables $CSR_{7.5}$ and $CRR_{7.5}$ were used. Those reduced parameters were calculated in the CLiq software during the interpretation of the CPTU data.

When it comes to $V_{s,\,CPT}$ parameter, those data were not used directly for liquefaction analysis at the investigated locations since they are not measured by MASW rather calculated using specific relations, so their usage within the scope of this paper was only for comparison purposes and to see how well those data fits to world experience V_{s1} plot. For successful comparison, values of $V_{s,\,CPT}$ for every extracted interlayer needed to be corrected to a reference overburden stress using the following equation (Sykora 1987., Kayen et al. 1992., Robertson et al. 1992.):

$$V_{s1} = V_s \left(\frac{P_a}{\sigma'_{v0}}\right)^{0.25} \quad (1)$$

where V_{s1} is overburden-stress corrected shear wave velocity, P_a is atmospheric pressure approximated by 100 kPa and σ'_{v0} is initial effective vertical stress in the same units as P_a.

Finally, the following table presents a summary of the mentioned and considered parameters for comparison and their median value obtained from the 111 liquefiable layers.

Table 3. Median values of parameters considered for comparison with global experiences

$Q_{tn7.5, med}$	$V_{s1(CPTmed)}$	$CSR_{7.5, med}$	$CRR_{7.5, med}$
28.80	161.94	0.133	0.112

3.2. Correlation of the data

All considered parameters for liquefaction analysis, reduced to magnitude M_w =7.5, were paired and correlated so that the best extent of relationship between pairs would be found. Values of $V_{s1, CPT}$ were also correlated for the purpose of comparison with global experiences. Two types of correlation methods were used, Pearsons's correlation which measures the strength of the linear relationship between two variables, and Spearman's rank correlation which evaluates the monotonic relationship between the ranked values. The usage of Spearman's correlation is decided because of outlier data that is often occurring in our measures and Spearman's correlation is not sensitive to outliers because it performs calculations on the ranks, so the difference between actual values does not have meaning. Following table presents magnitudes of both Pearson's and Spearman's correlation coefficient calculated for the specific pair of parameters:

Table 4. Calculated correlations between studied pairs of parameters

Nr. of pair	Studied parameters	Correlation values		
		Pearson's linear corr.	Spearman's ranked corr.	Abs. difference
1	$V_{s1, CPT}$ and $Q_{tn, 7.5}$	0.857	0.881	2.72 %
2	$V_{s1, CPT}$ and $CSR_{7.5}$	0.409	0.201	103.25 %
3	$V_{s1, CPT}$ and $CRR_{7.5}$	0.780	0.709	10.04 %
4	$Q_{tn, 7.5}$ and $CSR_{7.5}$	0.368	0.485	24.02 %
5	$Q_{tn, 7.5}$ and $CRR_{7.5}$	0.559	0.485	15.29 %

Reviewing above table and comparing the magnitudes of both Pearson's and Spearman's coefficients, pairs that can be highlighted are pair 1 and pair 3. Those studied parameters have the highest magnitudes of correlation coefficient by both methods so they can be considered as highly correlated.

Furthermore, if we compare values of the magnitudes for pair 1 it is visible that Spearman's coefficient is slightly higher, 2.72% higher in magnitude. That indicates that data in that pair is in favor of not being normally distributed, or it is in somewhat greater non-linear relationship and that there are outliers which affect a value of Pearson's correlation. But, when it comes to the pair 3, then the situation is reversed. Magnitude of Pearson's coefficient is greater for 10.04% than the Spearman's, which indicates that data in that pair is in favor of being in linear relationship rather than non-linear.

Overall, it is also evident that in addition to the mentioned pair 3, pairs 2 and 5 have greater values of Pearson's coefficient compared to Spearman's. So, in summary 3 out of 5 studied parameters (pairs 2, 3 and 5) are in favor of Pearson's correlation method which can be interpreted in the way that most of the studied data pairs tend to have linear relationship. Nevertheless, the magnitudes of most of these higher valued coefficients are not high enough from the point of correlation view since they can be considered as mostly moderately correlated variables (pair 2 and 5), excluding pair 3 which shows already mentioned high correlation.

From the Spearman's correlation point of view, except of mentioned pair 1 which represents highly correlated data, there is also pair 4 that has higher correlation magnitude compared to Pearson's, but that magnitude value is not high enough from the point of correlation view since that data pair is considered as low corelated. In the following figures, a plotted view of Pearson's and Spearman's correlations are given for both pair 1 and pair 3 data which are highlighted as highly correlated pairs by both methods used.

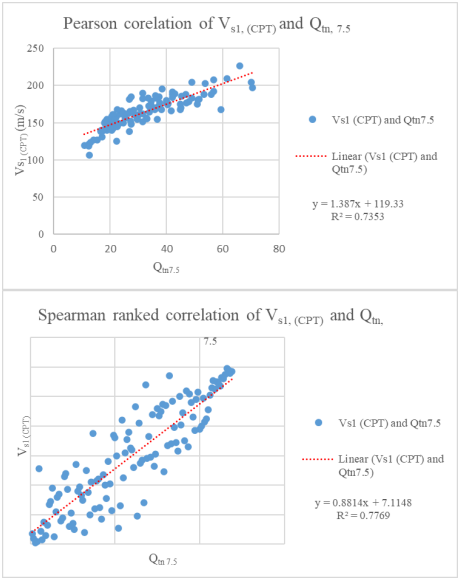


Figure 2. Relationship overview of data pair 1 ($V_{s1,\ CPT}$ and $Q_{tn,\ 7.5}$)

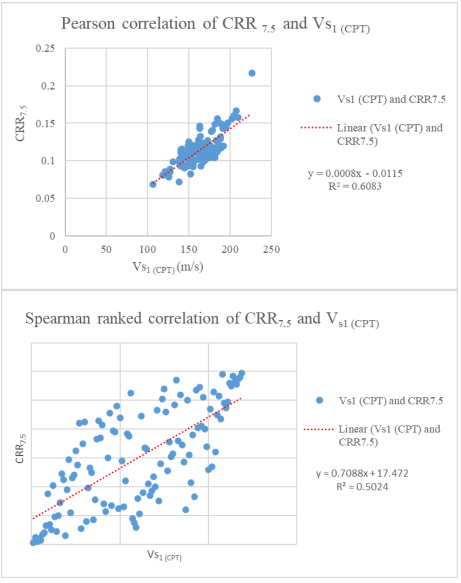


Figure 3. Relationship overview of data pair 3 ($CRR_{7.5}$ and $V_{s1,\ CPT}$)

3.3. Global experiences plots

Comparison of our data with the global experiences was based on the plots given in Youd and Idriss (2001). First, and most important plot used, is based on CPTU data. It is valid for magnitude 7.5 earthquakes only and shows calculated cyclic resistance ratio plotted as a function of dimensionless, corrected and normalized CPTU resistance q_{c1N} (Q_{tn}) from sites where surface effects of liquefaction were or were not observed following past earthquakes (figure 4). Plot also provides curves prepared by Robertson and Wride (1998) for direct determination of CRR for clean sands from CPTU data. That clean sand curve conservatively separates regions of the plot with data indicative of liquefaction from regions indicative for nonliquefaction. Following relationship gives us normalization calculation of cone penetration resistance:

$$q_{c1N}(Q_{tn}) = C_Q \left(\frac{q_c}{P_a}\right) \tag{2}$$

where

$$C_Q = \left(\frac{P_a}{\sigma'_{v0}}\right)^n \tag{3}$$

and where C_Q is normalizing factor for cone penetration resistance, P_a =1 atm of pressure in the same units as σ'_{v0}, n is exponent that varies with soil type and q_c is measured filed cone penetration resistance at the tip.

Second plot used for comparison is based on CRR versus V_{s1} curves recommended for engineering practice by Andrus and Stokoe (2000) for magnitude 7.5 earthquakes and uncemented Holocen age soils

with various fines content (figure 5). It should be once more noted that V_s data plotted in figure 5 is not MASW measured data, rather than $V_{s1,\,CPT}$ data. That $V_{s1,\,CPT}$ data are overburden stress corrected V_s velocities calculated in CPT interpretation and analysis software by using following relationship:

$$V_s = \left(\frac{G_0}{\rho}\right)^{0.50} \tag{4}$$

Where V_s is shear wave velocity, G_0 is small strain shear modulus and ρ is density of material. Overburden stress correction of calculated V_s is done by applying relationship (1).

Also, plot contains points (black and white) calculated from liquefaction case history for magnitude 5.9 to 8.3 earthquakes. Three curves shown on the plot were determined by iterative process following relationship between CRR and V_{s1}:

$$CRR = a\left(\frac{V_{s1}}{100}\right)^2 + b\left(\frac{1}{V_{s1}^* - V_{s1}} - \frac{1}{V_{s1}^*}\right) \tag{5}$$

Where V_{s1}^* is limiting upper value of V_{s1} for liquefaction occurrence and a and b are curve fitting parameters.

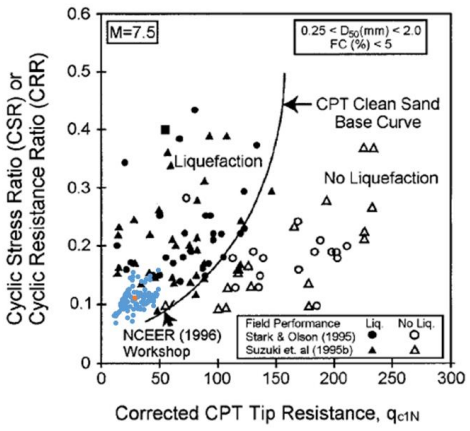


Figure 4. Overview of the $Q_{tn7.5}$ (q_{c1N}) and $CRR_{7.5}$ data from the area of Sisak-Moslavina County in comparison with the global experiences

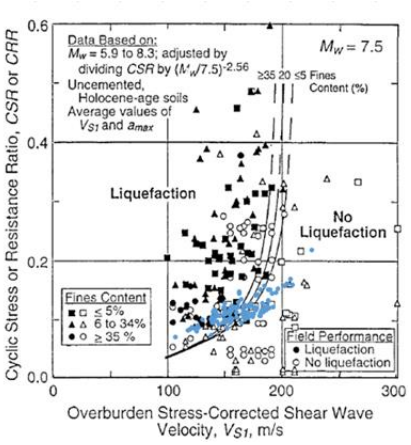


Figure 5. Overview of the overburden stress corrected shear wave velocity V_{s1} and CRR data from the area of Sisak-Moslavina County in comparison with the global experiences

Reviewing figure 4 and the plotted data one can see that the results from investigated locations of area of Sisak-Moslavina County (blue point cloud and orange median point) sit roughly within 0 – 50 Q_{tn} region, and 0,1 – 0,2 CRR region. Overall, plotted data falls in expected, liquefiable, region of the global experience chart since only liquefiable interlayers were used in analysis and there are no illogicality.

Reviewing the above figure 5 it can be said that overburden stress corrected shear wave velocity $V_{s1,\,CPT}$ based on CPTU correlations and calculations shows roughly good match with the world experience data plot. But there are some points that illogically fall in "no liquefaction" part of the plot, that indicates that there could possibly be some more appropriate relationship for calculation of V_s data based on CPTU than the one mentioned above (4) which could give us potentially better results, or fine tuning of the proposed curve could be done by using appropriate a and b fitting parameters for our conditions.

4. CONCLUSIONS

Two field tests, CPTU and MASW, were used on the epicenter area of Sisak-Moslavina County for the purpose of obtaining data on the quality of the underlying soil and gathering information to ensure quality reconstruction of the earthquake damaged buildings or construction of the new ones. In total, until the release of this paper, 103 locations were investigated. CPTU data was given priority for determining liquefaction potential of the investigated locations and for further analysis of results because of data which is more consistent, while MASW results were primarily used for determining ground type with accordance to EC8 because of specific concerns about using measured V_s results for liquefaction-resistance evaluations as mentioned in chapter 2.1.

Because of mentioned MASW concerns, scope of this paper was mainly focused on presentation of the work done and on comparison of our results with existing global experiences. Parameters used were extracted from isolated locations and 111 detected liquefiable layers, those parameters were normalized CPTU tip resistance Q_{tn}, CRR variables and CSR variables since they were used in liquefaction probability calculations. Furthermore, since MASW obtained V_s values were not used in liquefaction analysis in any way, decision on using $V_{s,\ CPT}$ data for solely comparison purposes with global experiences was made. Finally, it is noted that Q_{tn} studied data from the area of Sisak-Moslavina County fits as expected with world experiences plot and falls into "liquefable region" of the plot. Furthermore, CPTU based calculated, and corrected V_s values from the same locations fit rather well, but there are some data points that fall into "no liquefaction region" of the plot even though only V_s values from the already liquefied layers were used in analysis. That indicates that relationship used for calculation of the V_s values based on CPTU could be revised or that there is a need for fine tuning of the plot curve parameters that will give us a curve that better fits our specific case. Unfortunately, these processes are beyond the scope of this paper.

REFERENCES

Chen C.J. and Juang C.H. 2000. Calibration of SPT- and CPT-Based Liquefaction Evaluation Methods

Markušić, S., Stanko, D., Penava, D., Ivančić, I., Bjelotomić Oršulić, O., Korbar, T., Sarhosis, V. 2021. Destructive M6.2 Petrinja Earthquake (Croatia) in 2020—Preliminary Multidisciplinary Research. Remote Sens.

Terzić J., Frangen T., Kosović I., 2021. Urušavanje tla u Mečenčanima i okolici izazvano potresom magnitude 6.2 kod Petrinje, te prethodnim i naknadnim potresima, izvješće s podacima do kraja siječnja 2021.

Youd T.L. and Idriss M.I. 2001. Liquefaction resistance of soils: *Summary report from the 1996 NCEER and 1998 NCEER/NSF workshops on evaluation of liquefaction resistance of soils*

28th European Young Geotechnical Engineers Conference – EYGEC 2024
© 2024 Macedonian Association for Geotechnics, ISBN 978-608-4510-61-1

Influence of MSW leachate contamination degree on soil shear behavior

Feten Chihi[a], Gabriella Varga[a],

[a,] *Department of Engineering Geology and Geotechnics, Faculty of Civil Engineering, Budapest, University of Technology and Economics, Muegyetem rkp. 3. Budapest 1111 Hungary*

ABSTRACT

This investigation assesses the influence of leachate contamination on the shear strength of soil and its microstructural implications over a six-month period. Employing a combination of macroscopic shear tests and microscopic SEM analyses, the study interprets the dynamic interactions between soil stability and varying leachate concentrations. Shear strength parameters, including peak and residual friction angles, alongside cohesion, were measured at leachate concentrations of 5%, 10%, 15%, 20%, and 25% relative to the soil's dry weight. The results indicate a decrement in both friction angles with increased contamination, while cohesion initially rises at lower contamination levels, peaking at 15%, before deteriorating. SEM imaging reveals significant microstructural transformations, highlighting the chemical and physical alterations in the soil matrix. These microstructural changes correspond to the observed macroscopic mechanical behavior, with increased contamination compromising the mechanical interlocking critical for soil shear strength.

KEYWORDS

Leachate; Soil Contamination; Shear Parameters; SEM

1. INTRODUCTION

In the contemporary era marked by exponential urban growth and industrial proliferation, society faces serious environmental challenges when it comes to waste management. The most common waste management strategy adopted worldwide is landfilling. Consequently, environmental regulations have evolved to require landfill designs to incorporate inclusive isolation barriers aimed at reducing leachate penetration to the subsurface and reducing the contamination risk. Despite these measures, the threat of environmental accidents that can develop is still reported in the literature.

Understanding the interaction between soil mechanics and environmental contaminants in leachate is essential for the safety and stability of structures in contaminated areas, especially with the reintegration of former landfills for community use as parks and green places. The infiltration of leachate into the subsurface can significantly affect the shear strength of soils, a fundamental parameter that dictates the soil's ability to resist shear stress and, consequently, its structural integrity (Mosavat and Nalbantoglu, 2013; Moody and Townsend, 2017). This modification also raises significant environmental concerns due to the potential for hazardous substances to migrate and impact the surrounding environment. Therefore, a comprehensive investigation into the shear strength parameters of leachate-contaminated soil is essential for assessing the risks associated with land development and formulating effective soil remediation strategies (Shariatmadari et al., 2018; Khodary et al., 2021).

This paper is part of extensive research on the influence of municipal solid waste (MSW) leachate contamination on soil behavior. It focuses on the leachate influence on soil shear parameters. This investigation offers a cautionary framework for both environmental and geotechnical engineering methodologies in addressing the complexities of waste management and soil contamination.

2. METHOD

2.1. Leachate characteristics:

This study focuses on soil shear strength alterations due to leachate contamination, and for that, the leachate used for the testing was directly taken from the leachate collecting system of the Pusztazámor landfill in Hungary in order to preserve its initial characteristics. The chemical properties of the used leachate are given in Table 1.

Table 1. Leachate characteristics (CODcr= Dichromate oxygen consumption; BOI5= Biological Oxygen Demand; TIN =Total inorganic N; ASS= All suspended solids; P= Total phosphorus; TDS= Total dissolved salts; Fe= Iron; F = Fluoride; S =Sulfides)

Tested parameter	pH	Conductivity	CODcr	BOI5	TIN	ASS	P	TDS	Fe	F	S
Unit	-	µS/cm	O_2 mg/L	mg/L	N mg/L	mg/L	mg P/L	mg/L	mg/L	mg/L	mg/L
	8,9	25900	7110	1280	2070	753	8,9	12300	5,6	<5	47.8

2.2. Soil characteristics

The soil used in this experiment was collected from the same landfill, typical of that region and very abundant, used as levelling soil and daily cover. The samples were subject to rigorous geotechnical testing to determine their properties, essential for the study of leachate impact on shear strength. Table 2 summarizes their characteristics.

Table 2: Soil characteristics

Property	Sand	Silt	Clay	K	C	Fi
Value	30.14%	55.59%	10.73%	6.428×10^{-7}	10.3 (kPa)	36.5°

2.3. Test program

This study presents a comprehensive evaluation of how various leachate concentrations affect the shear strength of soil in a 6-month time frame. This experimental setup offers a thorough analysis of leachate's impact on soil, combining both macroscopic mechanical tests and microscopic structural examinations. Soil samples were mixed with leachate in concentrations of 5%, 10%, 15%, 20%, and 25% relative to the soil's dry weight. This range was chosen to cover an extensive array of contamination scenarios. Rigorous mixing ensured an even distribution of leachate within the soil.

Post-preparation, the samples were stored at a steady laboratory temperature of 25°C in airtight containers. This was crucial to isolate them from external variables such as atmospheric composition, oxygen, and light, which could potentially modify their characteristics. The samples were conditioned over six months to maintain a consistent interaction between the soil and leachate.

After the conditioning period, the soil samples were subjected to shear strength tests using a 60 mm x 60 mm direct shear apparatus, in line with the ISO 17892-10:2018 standards. The samples underwent a series of loads under normal stresses of 50, 100, 200, 300, 400, and 500 kPa to assess the impact of leachate concentration on the soil's shear resistance.

To further understand the changes in shear strength, Scanning Electron Microscopy (SEM) was employed on selected samples. This analysis aimed to reveal the microstructural changes due to leachate interaction, linking these changes to the overall mechanical behavior of the soil. This multi-scale analysis approach provides a more in-depth understanding of the soil's response to contamination.

3. RESULTS

3.1. Shear parameters

The influence of leachate concentration on the shear strength parameters of the soil was examined over a six-month conditioning period. Incremental additions of leachate to soil samples showed a discernible impact on both the friction angle and cohesion of the soil, as illustrated in Figure 1.

For clean soil, the friction angle (Fi) was observed at its maximum. However, with the introduction of leachate at concentrations ranging from 5% to 25%, a marginal decrement in the friction angle was noted. The trend was not strictly linear but indicated a general inclination towards reduced friction angles as the concentration of leachate increased, suggesting a diminution in the soil's intrinsic resistance to shear deformation.

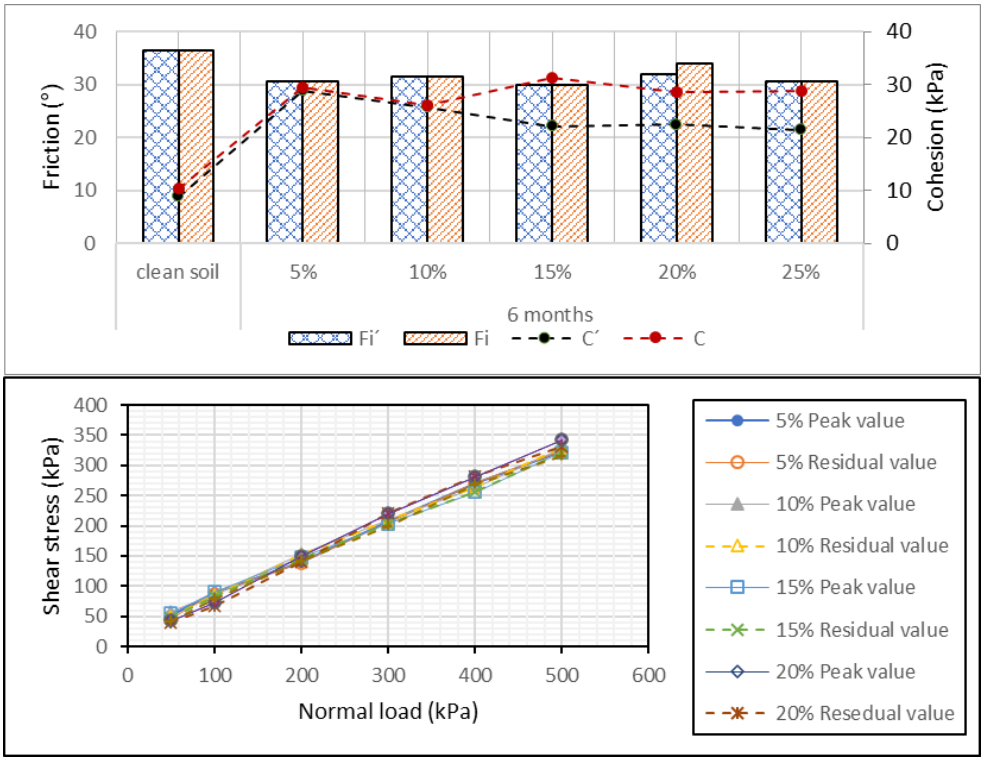


Figure 1. Shear parameters of contaminated soil [above: Cohesion (peak, C, and residual, C', values) and friction angle (peak, Fi, and residual, Fi', values) of clean and contaminated soil; below: Shear envelope]

Conversely, peak cohesion (C) values exhibited an initial increase, peaking noticeably at a 15% leachate concentration, which suggests a threshold level at which the leachate-induced interparticle forces contribute positively to the soil's cohesive strength. Nonetheless, a subsequent decline in cohesion was recorded at concentrations beyond 15%, alluding to a potential oversaturation effect that undermines the aggregative forces within the soil matrix. On the other hand, residual cohesion (C') values, despite the increase compared to the initial clean soil cohesion, displayed a different liner trend of reduction after a remarkable peak at 5% of the contamination rate. The disparity observed between the peak and residual cohesion values is attributable to the interaction between the soil and the leachate, which facilitated the formation of new soil bonds. However, these newly established bonds were insufficiently robust to

withstand the applied shearing forces. These findings are in accordance with several results reported in the literature (Shrihari and Nayak, 2009; George and Beena, 2011; Sujatha et al., 2013).

3.2. SEM

The Scanning Electron Microscopy (SEM) analysis provided a stark portrayal of the microstructural evolution in soil samples subjected to varying degrees of leachate contamination. The SEM images, presented in Figure 2, effectively illustrate the progression from pristine to contaminated soil conditions and the ensuing microstructural transformations.

Panel A captures the baseline condition of the clean soil, characterized by a relatively uniform and undisturbed matrix of soil particles. The granular integrity and lack of agglomeration serve as a control against which the effects of contamination are measured.

Panels B and C reveal the onset of particle agglomeration in soils with increasing leachate contamination. This agglutination is a direct reflection of the cohesive forces at play, induced by the leachate, which is also suggested by the enhanced cohesion values observed in the shear strength tests. The extent of this agglomeration is more pronounced as we progress from Panel B to C, indicating a higher degree of contamination and suggesting a correlation with the observed increase in cohesive strength noted in our mechanical tests.

Panels D and E depict a noticeable shift in the soil structure with clear signs of surface alteration and corrosion. The integrity of individual soil particles appears compromised, with the particle surfaces exhibiting signs of disintegration. This degradation is symptomatic of the chemical interactions between the leachate and the soil constituents, potentially contributing to the observed decrease in the soil's friction angle.

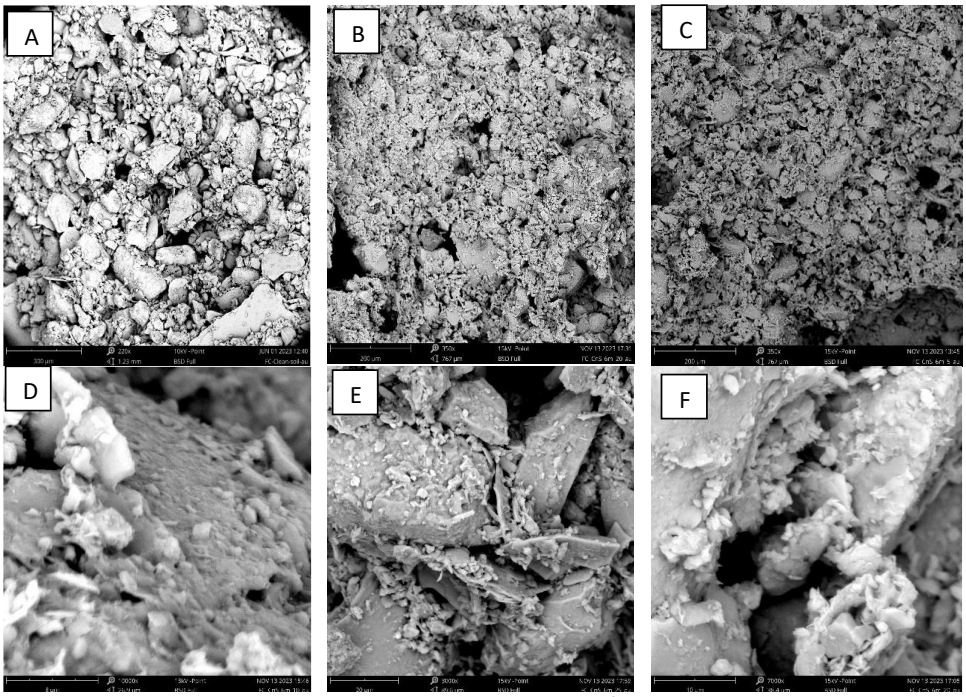


Figure 2. SEM results (A: Clean soil, B and C: agglomeration of contaminated soil; D and E: Soil particles alteration and corrosion; F: new mineral crystals formation)

Panel F illustrated an advancing formation of new mineral crystals throughout the specimens. The emergence of these crystals was significantly more evident in samples subjected to higher levels of contamination. Specifically, at a contamination intensity of 25%, these crystalline structures seemed to enhance the soil matrix's robustness. Similar results were reported by Sitaram et al., and Oztoprak and Pisirici (Shrihari and Nayak, 2009; Oztoprak and Pisirici, 2011).

4. CONCLUSIONS

The experimental investigation has yielded pivotal insights into the interaction between leachate contamination and soil stability, with direct implications for environmental safety and landfill management. The study presents a multifaceted picture of how varying degrees of contamination modulate soil behavior.

A complex pattern of cohesion is observed. Regardless of the degree of contamination, the cohesion registered was much higher than the clean soil. Nevertheless, an initial increase at lower contamination levels suggests enhanced particle bonding, followed by a decrease at higher levels of contamination. An optimal contamination threshold, identified at a 15% leachate concentration, enhances soil cohesion, likely due to chemical interactions among soil particles. Beyond this concentration, the beneficial effects are surpassed by detrimental impacts on new soil integrity.

SEM analyses have uncovered alterations within the soil, including the formation of novel mineral crystals at elevated levels of contamination. Leachate-induced microstructural changes in soil, particularly at higher contamination levels, including the formation of novel mineral crystals at elevated levels of contamination. These changes manifest as a reduction in interparticle friction, undermining the soil's inherent shear strength and an increase of cohesion. The findings indicate a critical contamination threshold (15%), exceeding which may lead to a deterioration of the soil's structural and mechanical characteristics.

REFERENCES

George, M. and Beena, K. 2011. Geotechnical characteristics of leachate- contaminated lateritic soil. *Proceedings of Indian Geotechnical Conference*. Koch, pp.769–772.

Khodary, S.M., Fath, H., Negm, A. and Tawfik, A. 2021. Measuring the engineering properties of landfill leachate-contaminated soil in Egypt. *Euro-Mediterranean Journal for Environmental Integration*, 6(1), pp. 1–12. Available at: https://doi.org/10.1007/s41207-020-00232-5.

Moody, C.M. and Townsend, T.G. 2017. A comparison of landfill leachates based on waste composition. *Waste Management*, 63, pp. 267–274. Available at: https://doi.org/10.1016/j.wasman.2016.09.020.

Mosavat, N. and Nalbantoglu, Z. 2013. The impact of hazardous waste leachate on performance of clay liners. *Waste Management and Research*, 31(2), pp. 194–202. Available at: https://doi.org/10.1177/0734242X12467395.

Oztoprak, S. and Pisirici, B. 2011. Effects of micro structure changes on the macro behaviour of Istanbul (Turkey) clays exposed to landfill leachate. *Engineering Geology*, 121(3–4), pp. 110–122. Available at: https://doi.org/10.1016/j.enggeo.2011.05.005.

Shariatmadari, N., Lasaki, B.A., Eshghinezhad, H. and Alidoust, P. 2018. Effects of Landfill Leachate on Mechanical Behaviour of Adjacent Soil: a Case Study of Saravan Landfill, Rasht, Iran. *International Journal of Civil Engineering*, 16(10), pp. 1503–1513. Available at: https://doi.org/10.1007/s40999-018-0311-2.

Shrihari, S. and Nayak, S. 2009. Shear strength characteristics and chemical characteristics of leachate-contaminated lateritic soil. *Engineering Geology*, 106(1–2), pp. 20–25. Available at: https://doi.org/10.1016/j.enggeo.2008.12.011.

Sujatha, E.R., Gurucharan, R., Chandrasekaran, R. and Sornakumar, V. 2013. Impact of municipal solid waste dumping on the geotechnical properties of soil and ground water in Ariyamangalam, Trichy, India. *Electronic Journal of Geotechnical Engineering*, 18 K(August 2021), pp. 2119–2132.

28th European Young Geotechnical Engineers Conference – EYGEC 2024
© 2024 Macedonian Association for Geotechnics, ISBN 978-608-4510-61-1

Comparison design-monitoring a diaphragm wall for a deep excavation up to 11.60m

Ciumeică Daniel[a]

[a,] *SBR Soletanche Bachy Fundații, Bucharest, Romania*

ABSTRACT

This article presents a comparison design-monitoring a diaphragm wall for a deep excavation up to 11.60 meters in Sibiu. Works were done between May and August 2021. Scope of the works were design and execution of a pit enclosure to accommodate an infrastructure for an administration building with two underground levels 3.00 meters below groundwater level. A retaining system supported with modular struts on one level at -2.80 m was the adopted solution, which has been modelled by means of finite element method (FEM), using Plaxis 2D, which offer conservative values compared to the behaviour on the overall behaviour of the excavation due to the reduced plan dimensions of the enclosure which lead to a stiffening of the field areas of the enclosure from its corner areas

KEYWORDS

Diaphragm wall; Monitoring; Deep excavation; Groundwater

1. INTRODUCTION

1.1. Scope of the works

The project scope was the design, execution and monitoring of a pit enclosure in order accommodate an infrastructure for an administration building with two underground levels 3.00 meters below groundwater level, to the depth of 11.60 meters, from original ground level.

1.2. General description

The project required a deep excavation support solution for the construction of the infrastructure of an administration building (Figure 1 and 2).

By adopting the presented solution, it was aimed at obtaining an efficient structural system in terms of execution, productivity, and technologies for carrying out the works, optimally adapted to the particularities of the project which are mainly the obtaining of an enclosure pit that has relatively small dimensions in plan and that is in the vicinity of existing buildings.

The location of the construction, with an area of 2010 sqm, is in Sibiu. The ±0.00 m architectural level of the building is +434.30 msl.

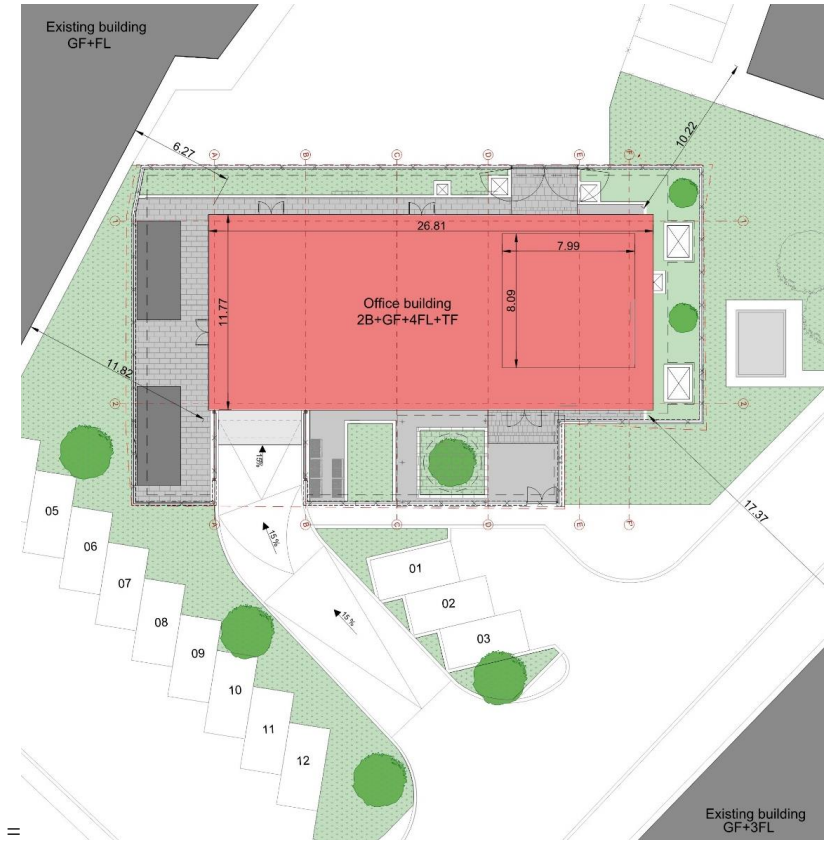


Figure 1. Project layout

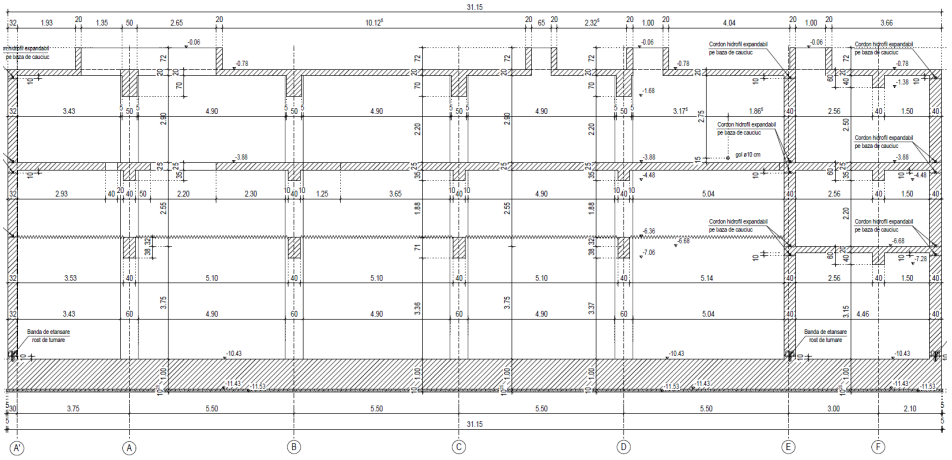


Figure 2. Cross section

The outline of the designed pit is in the vicinity of some existing buildings, according to the Urban Planning Certificate, constructions and buildings with different height and functionality, whose foundation depth is located at variable elevations below the elevation of the original ground.

1.3. Ground conditions

The Geotechnical survey was made in 2021 period and was based on profiles of four boreholes, with a maximum length of 20 m, carried out together with in-situ geophysical tests and laboratory investigations.

According to the geotechnical study, the sequence of the layers intercepted by the boreholes are described in table 1.

Table 1. Average lithology for design

Layer	Level relative to natural terrain level	Description of intercepted lithology
1	0.00 m … -0.40/-0.70 m	Top soil – uncohesive fill, loose, with leavings construction materials
1a	-0.40/-0.70 m … -1.00/-1.70 m	Vegetal soil – firm blackish clay
2	-1.00/-1.70 m … -4.50/-5.50 m	Clay / silty clay / silty-sandy clay, brown, firm to stiff
3	-4.50/-5.50 m … -9.40/-12.00m	Gravel with sand / sand with gravel / brown-grey sand, dense
3a	-9.40/-12.00 m … -15.00/-18.00 m	Sand / brown-grey silty sand, medium dense / dense, with rare gravel
3b	-15.00 m … -17.00 m	Brown - ferruginous sandy-clayey silt, medium dense / dense
4	-17.00/-18.00 m … -20.00 m	Sandy-clayey silt / sandy silt, marl, gray, very stiff

Ground water table was intercepted in geotechnical boreholes between -8.60 m and -8.80 m below ground level, stabilizing at elevations between -8.40 m and -8.50 m (Figure 3).

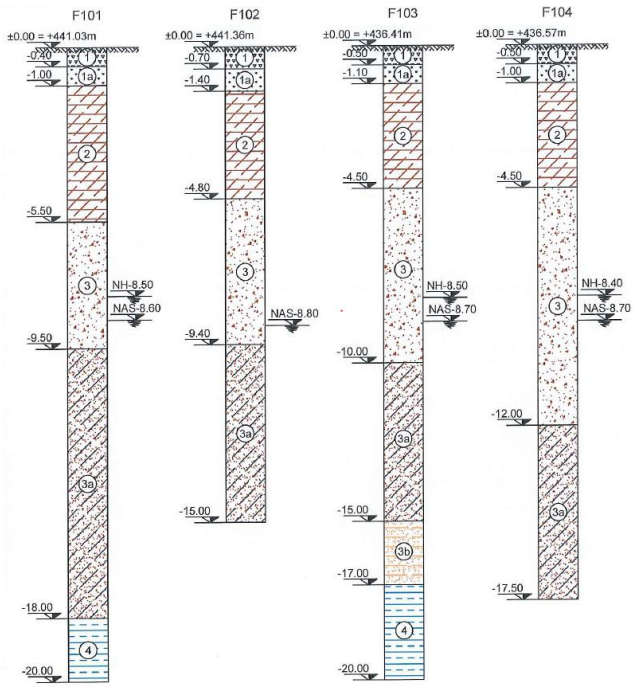


Figure 3. Lithology boreholes

The design values of the physical-mechanical parameters of the soil considered in the design process of the premises are based on the data provided by the geotechnical investigations (Table 2).

Table 2. Design value used in modelling (Hardening soil model)

Layer	γunsat [kN/m3]	γsat [kN/m3]	E_{50}^{ref} [kN/m2]	E_{oed}^{ref} [kN/m2]	E_{ur}^{ref} [kN/m2]	m [-]	c'ref /su,ref* [kN/m2]	φ' [º]	Ψ [º]	K_0^{nc} [-]
1	18.50	19.00	6500	6500	19500	0.5	0	20	-	0.658
1a	18.20	19.00	5000	5000	15000	0.5	10.00	10	-	0.826
2	20.20	21.00	5000	5000	12300	0.66	24.5	16.25	-	0.720
3	18.75	20.00	84940	70000	250000	0.5	0	46.85	16.85	0.270
3a	19.00	20.00	50000	50000	150000	0.5	0	42	12	0.331
3b	20.00	21.00	16260	16260	48780	0.5	20	28	-	0.531
4	19.90	21.00	25000	25000	75000	0.55	150*	-	-	-

2. SOLUTION

2.1. General structural considerations

The infrastructure of the construction is conformed in a rigid box type system with floors, beams, columns, and inner walls made of reinforced concrete.

The foundation of the interior structure is designed as a general reinforced concrete raft, with a thickness of 100 cm.

2.2. Excavation support system

Because of the depth of excavation (about 11.60 m compared to ±0.00 m level) and the penetration beneath hydrostatic level, as well as because of the execution of the structure below ground level, it was necessary to build a diaphragm wall retaining structure (figure 5).

Diaphragm wall execution works continued from a stable working platform 0.75 meters below ±0.00 level.

Reinforced concrete panels of the diaphragm wall were made with the use of bentonite slurry support.

The technological characteristics of the project and the structural configuration of the newly designed construction imposed the necessity of choosing a retaining system supported with modular struts on one level at -2.80 m, the strut-diaphragm wall connection was made by steel plates embedded in reinforced cage panel through the rebars anchors which can provide excavation protection as well as an increased productivity of execution (Figure 4).

The entire perimeter of the pit was solidarized by capping beam measuring 60 x 80 cm.

Calculations were performed with design approaches according to current regulations such as Eurocode 7 with corresponding national annexes, or local Romanian regulations, NP 120 (2014) and NP 124 (2010).

To obtain the design stress, the support system was modelled using two-dimensional numerical calculation, in plane state of stress and deformations. The calculation is based on the finite element method, through the numerical geotechnical calculation application Plaxis 2D.

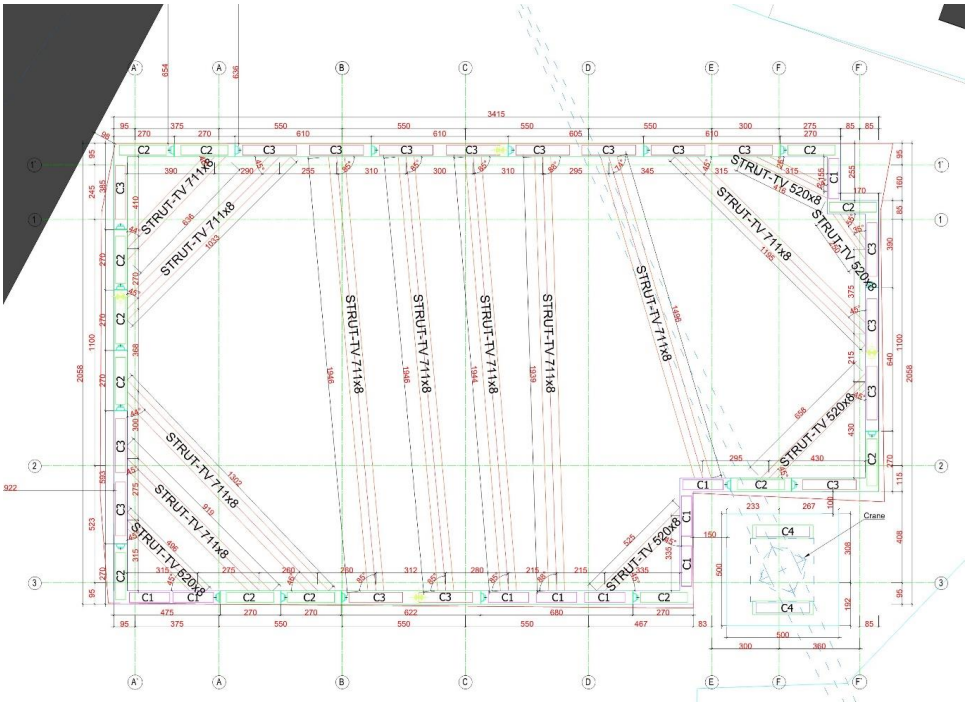


Figure 4. Diaphragm wall geometry and support system

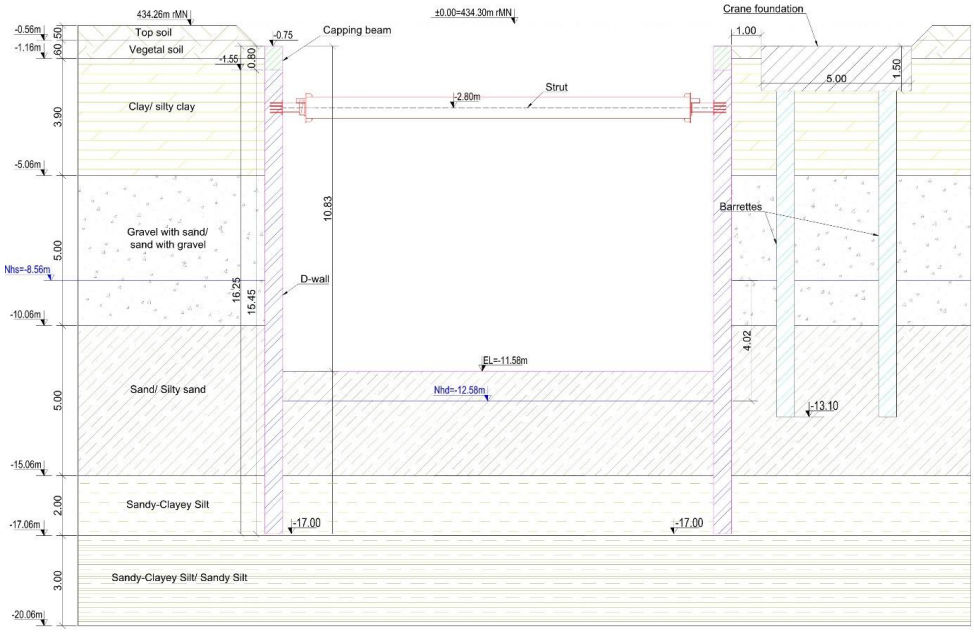


Figure 5. Pit general cross section

3. COMPARISON DESIGN-MONITORING

3.1. Inclinometer monitoring

For the inclinometer monitoring, the design - monitoring comparison will be presented for the two characteristic sections 1-1 and 2-2, which have two characteristic stages of execution for which monitoring was done (Figure 6).

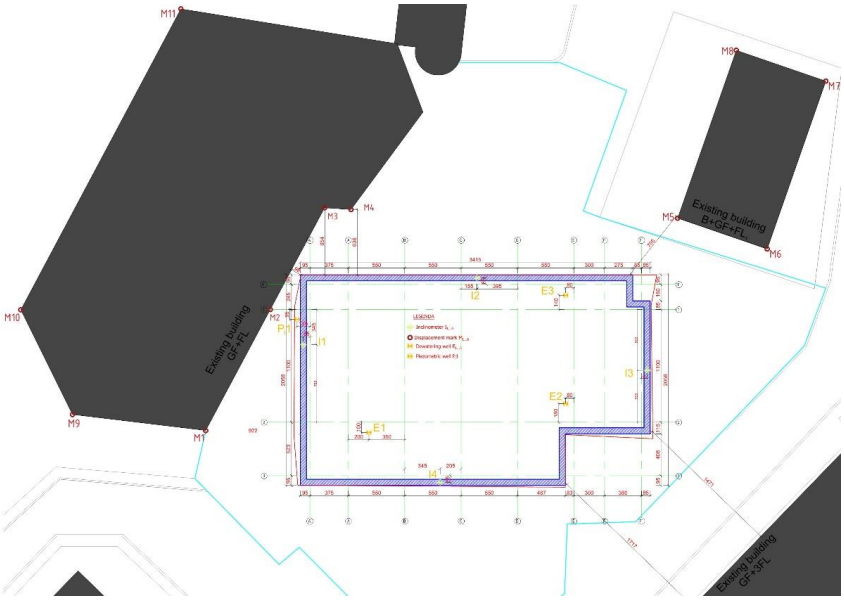


Figure 6. Position of the monitoring

The characteristic section 1-1, the current section that has no vicinities, presents the following values of the displacement of the diaphragm wall (Table 3).

Table 3. Comparison diaphragm wall displacements cross section 1-1

Stage	Elevation at which the maximum displacement was recorded	Design displacement	Elevation at which the maximum displacement was recorded	Measured displacement
Excavation -3.80 m	0.00m	6.13 mm	0.00 m	0.90 mm
Final excavation (-11.55 m)	-8.50 m	17.90 mm	-5.50 m	7.70 mm

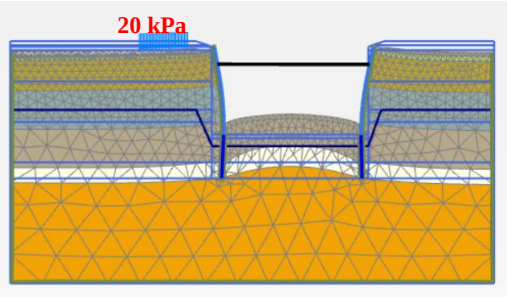


Figure 7. Design cross section 1-1

The characteristic section 2-2, the section through the building that is abutting the pit, presents the following values of the displacement of the diaphragm wall (Table 4).

Table 4. Comparison diaphragm wall displacements cross section 2-2

Stage	Elevation at which the maximum displacement was recorded	Design displacement	Elevation at which the maximum displacement was recorded	Measured displacement
Excavation -3.80 m	0.00m	5.14 mm	0.00 m	2.00 mm
Final excavation (-11.55 m)	-8.20 m	18.26 mm	-5.50 m	6.80 mm

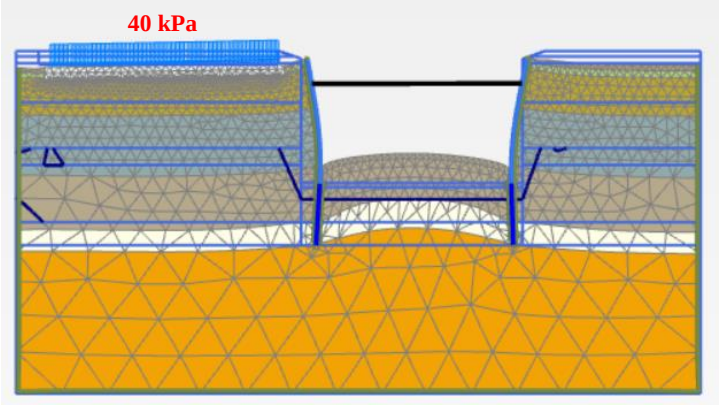


Figure 8. Design cross section 2-2

It can be observed that the measured displacement values are about 57%-85% lower than the calculated ones, which shows us that the numerical modelling offers a conservative behaviour on the overall behaviour of the excavation.

3.2. Settlement marks

For the comparison of the settlements of vicinity building P+E, the values of the maximum differential settlements measured are found between the settlement marks M2 and M3 in the final excavation stage according to the table 5.

Table 5. Comparison differential settlements

Design settlement	Measured settlement
2.45 mm	2.90 mm

3.3. Strain gauge

Table 5. Comparison compression force in struts

Section	Design compression force	Average measured compression force
1-1 / Strut 7	1100 kN	706.5 kN
2-2 / Strut 2	1300 kN	614. 7 kN

It can also be observed that the values measured in the struts are about 36%-53% lower than the calculated ones, as in the displacement situation, which shows us that there is a correlation in the way of transmission of stress from the d-wall to the struts.

4. CONCLUSIONS

Through presented retaining system the main objective was to build an effective structural system. But also, easiness of carrying out structural works inside the shaft and site efficiency were important factors, adapted and optimised based on this project features.

We can observe conservative values of the calculated displacements compared to the measured ones due to the way in which the calculation sections were considered. The reduced plan dimensions of the enclosure lead to a stiffening of the field areas of the enclosure from its corner areas, a fact that cannot be quantified with certainty in a 2D calculation model.

Also, the same thing happens for the strain in the struts, which according to the measurements resulted in comparatively lower values by 35-50% compared to the designed ones.

This retaining system was conceived and designed based on the experience gained from similar projects and modern numerical methods, based on geotechnical applications software.



Figure 9. Pit top view

REFERENCES

Eurocode 7: Geotechnical design - Part 1: General rules, SR EN 1997-1:2004.

Eurocode 7: Geotechnical design - Part 1: General rules. National Annex, SR EN 1997-1:2004 / NB: 2007.

Execution of special work – Diaphragm walls. SR EN 1538:2010 + A1:2015.

National norm regarding the geotechnical design of retaining works, NP 124-2010

28th European Young Geotechnical Engineers Conference – EYGEC 2024
© 2024 Macedonian Association for Geotechnics, ISBN 978-608-4510-61-1

1915 Çanakkale Bridge European anchor block excavation project: a case study

Ahmet Dinc, Alp Gokalp, Senol Adatepe

Kasktas A.S., Istanbul, Turkey

ABSTRACT

This paper presents a deep excavation of the reinforced concrete anchor block structure with a volume of 68,000 m³, located on the European side of the 1915 Çanakkale Bridge. Slope stability, excavation, and dewatering works within the scope of the European Anchor Block Project with a maximum excavation depth of 46,0 m were completed within the tight schedule in a very heterogeneous soil profile consisting of Miocene-based sandstone-mudstone layers and Holocene deposits containing gravelly sand-clay units, especially on the seaside. Within the scope of the project, 170,000 m³ of excavation work, 10,000 m of rock bolts, 12,000 m² of shotcrete applied with ±1cm construction tolerance, besides 431 no's of secant piles and 28 no's of dewatering wells were executed. In order to verify the in-situ design capacity of the rock bolts, a total of 26 no's of preliminary pull-out tests were performed, on each side of the excavation pit and each excavation stage prior to the commencement of the production rock bolts. In this study, the design of the slope stabilization project, details of the construction works, and the results of the rock bolt tests are presented. Detailed information about the quality control tests followed within the scope of the project and the performance of the slope protection system has also been presented.

KEYWORDS

Slope stability, Deep Excavation, Rock bolt, Pull-out test, Quality control tests.

1. INTRODUCTION

The 1915 Çanakkale Bridge, with a main span of 2,023 meters, commemorating the centenary of the founding of the Republic of Turkey, has become the largest mid-span suspension bridge in the world, surpassing the Akashi Kaikyo Bridge in Japan. The 1915 Çanakkale Bridge has a total length of 4,608 meters, with a central span of 2,023 meters, side spans of 770 meters, and approach viaducts of 365 and 680 meters. The approach viaduct on the Asian side (Lapseki) of the 1915 Çanakkale Bridge is 680 meters long, and the approach viaduct on the European side (Gallipoli) is 365 meters long. The anchor block is to comprise two front pads and a rear concrete massif. The rear concrete massif is to be 16.0m deep (below natural ground level), 50.2m wide, and 74.4m long, and the front anchor pads are to be 18.0m by 17.5m in plan and 5.0m deep (below ground level). Each front pad is to be connected to the rear massif with a connecting beam. The project map photo of the study area is given in Figure 1. The excavation geometry for the anchor block is mainly defined by the distance between the pier PE1 and the abutment, which is defined as 51 meters horizontally. The maximum excavation depth is approximately 46 meters. Within the scope of the study, detailed information about anchor block excavation, the design of the shoring system, monitoring of shoring performance, quality control test results, and production details are presented.



Figure 1. Map photo of the study area.

2. SITE CHARACTERIZATION

Detailed soil investigation was carried out at the project site by Fugro. 4 boreholes with depths ranging from 30-70 m and 6 CPT tests with depths ranging from 10.6 m to 35.70 m were performed. Soil classification was made using the Robertson 1990 classification chart by taking into account results obtained from CPT experiments. The idealized soil profile is given in Figure 2.

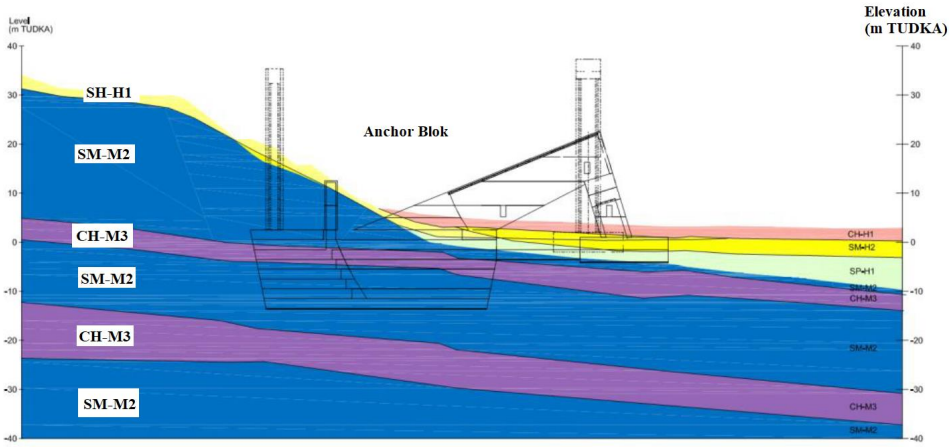


Figure 2. Idealized soil profile.

Generally, thickness of the Holocene deposits; described as mixed layers of lean, sandy to fat clay (CL-H1 to CH-H1) to fine, silty sand (SM-H1/-H2) to well-graded, gravelly sand (SP-H1) is significantly

larger on the European side, than on the Asian side, while the Miocene basement mainly comprises Sandstone, SM-M2, embedded with layers of extremely weak to weak mudstone, CH-M3. Geotechnical design parameters of soil layers are given in Table 1.

Table 1. Geotechnical design parameters of soil layers.

Soil layer	γ [KN/m³]	w [%]	ϕ' [°]	c' [kPa]	c_u [kPa]	E [MPa]	v_u	C_c [-]	C_r [-]	k [m/s]
CL-H1	19	28.5	29	0	40	-	0.5	0.15	0.02	$5 \cdot 10^{-9}$
CH-H1	19	24	29	0	40	-	0.5	0.15	0.02	$5 \cdot 10^{-9}$
SM-H1	18	30	30 1)	0	-	6	0.5	-	-	$5 \cdot 10^{-5}$
SM-H2	19	25	33 1)	0	-	24	0.5	-	-	$5 \cdot 10^{-5}$
SP-P1	19	18.5	35	0	-	37	0.5	-	-	>0.001
SM-M2	21	17	37	300	-	-	0.5	-	-	-
CH-M3	22	10	40	40	600	-	0.5	-	0.008	-

3. ANCHOR BLOCK EXCAVATION

The general layout plan of the project site is given in Figure 3. The excavation geometry for the anchor block is mainly defined by the distance between the pier PE1 and the abutment, which is horizontally, 51 m as shown in Figure 4. The maximum excavation depth is 46 m approximately.

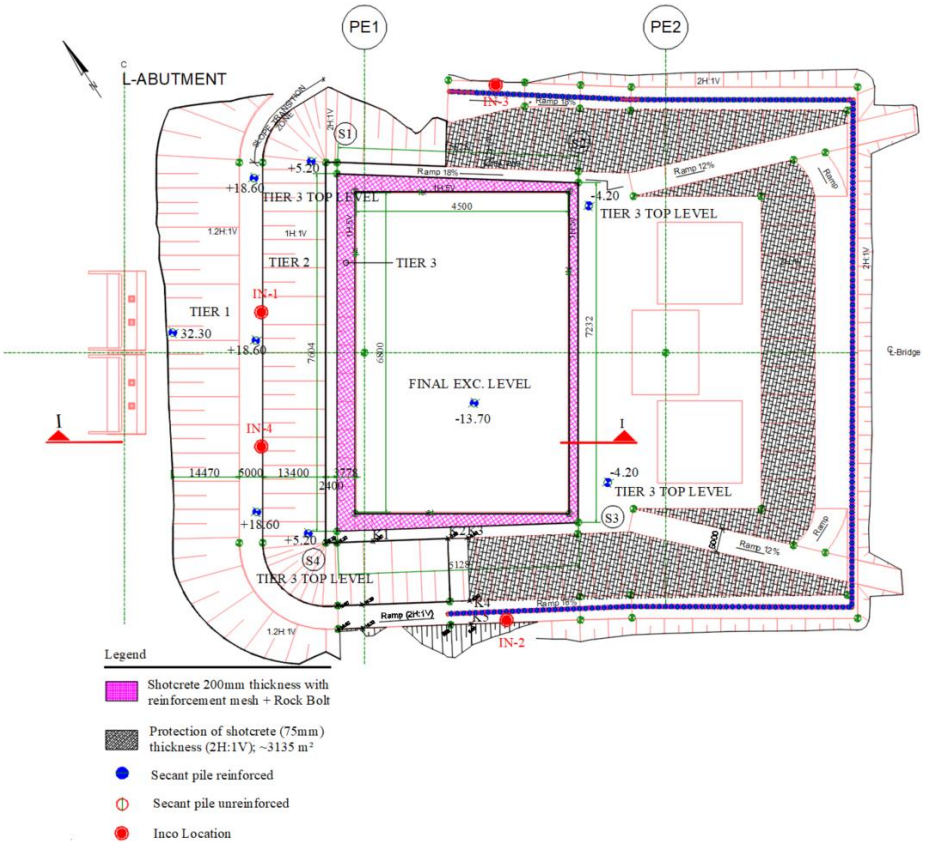


Figure 3. General layout plan.

The slope of the upper section is 1.2H:1V with a height of 13.7 m; the slope of middle section is 1H:1V with a height of 13.4 m and and the slope of bottom section is 1H/5V with a height of 18.9 m. A U-shaped secant pile wall on the sea side of the excavation is designed in order to cut-off water inflow from the Holocene deposits and Sandstone layers into the excavation area. The toe level of the secant pile wall is -8.00 m, in such a way that the piled wall reached the mudstone level.

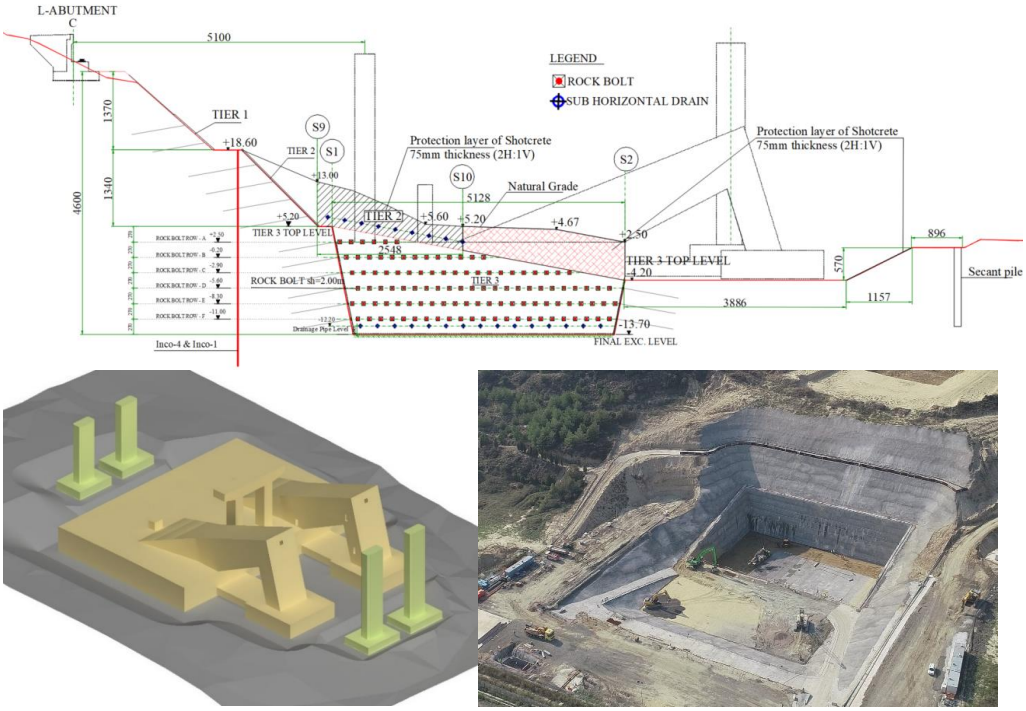


Figure 4. Excavation section and 3D view of anchor block.

3.1. Safety factors for global stability

Conservatively, the global stability calculations have been performed considering the unit SM-M2 with a reduced effective cohesion (see Figure 5) due to possible weakened zones in the soil mass and a 6 m thick layer close to the excavation face with the residual strength properties of the sandstone to consider the weakening of the sandstone due to the unconfinement and weathering effects during the excavation. The analysis of the slope stability for the excavation works at the anchor block has been carried out using PLAXIS 2D. For verification of the global stability, the specified minimum safety factors are given in Table 2, according to the KGM Technical Specification (both for temporary and permanent structures).

Table 2. Safety factors for global stability analysis

Soil Parameter/Condition	With undrained strength parameters	With Effective strength parameters
Long term analysis (Static)	-----	1.5
Short term analysis (Static)	1.5	-----

The values defined in KGM specifications are total factor of safety for analyses performed with characteristic soil parameters ($\gamma c'=\gamma\varphi'=\gamma cu=1.0$). Effective strength properties have been considered only for the evaluation of the stability of the excavation due to the nature of the prevailing soil

conditions. The finite element analysis model, maximum displacement at the final excavation stage, and critical shear envelopes are summarized in Figure 5.

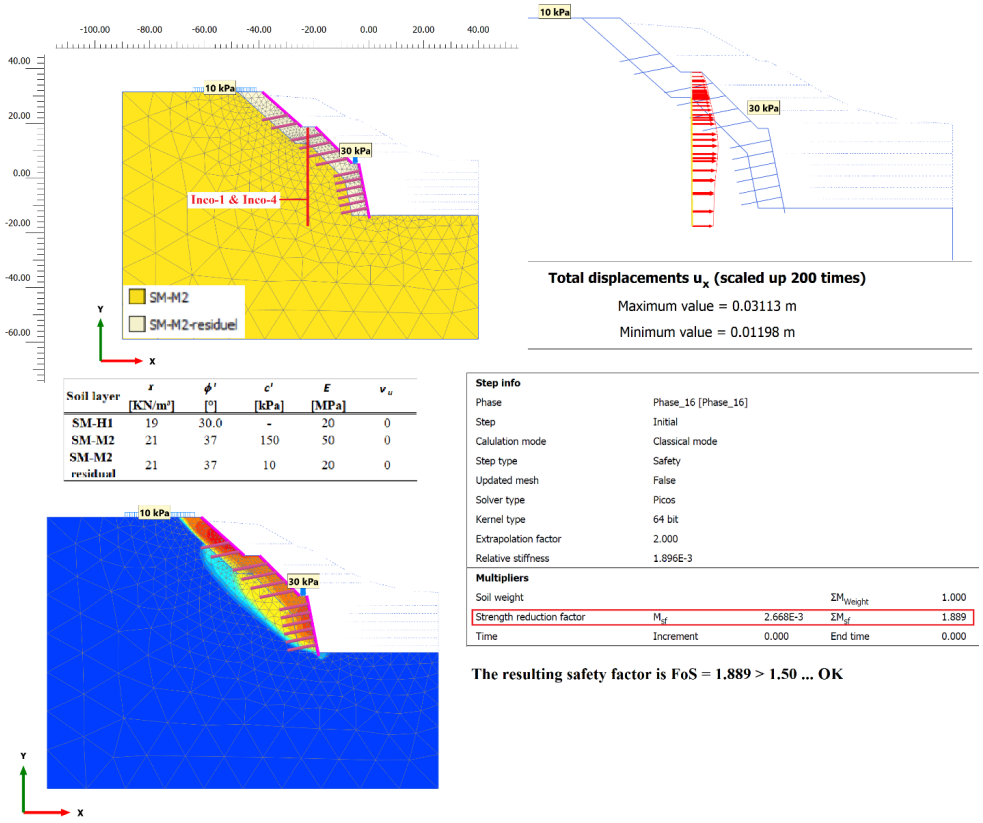


Figure 5. Plaxis 2D analysis summary.

As a result of the finite element analysis, the safety factor against total collapse was estimated to be 1.89.

In the final excavation stage, the variation of the displacement amount obtained with the Plaxis finite element software with depth and the displacement values obtained from the inclinometer boreholes No:1 and No:4 are given in Figure 6. As can be seen from the graph below, the calculated (estimated) displacement values and the actual displacement values were very close to each other.

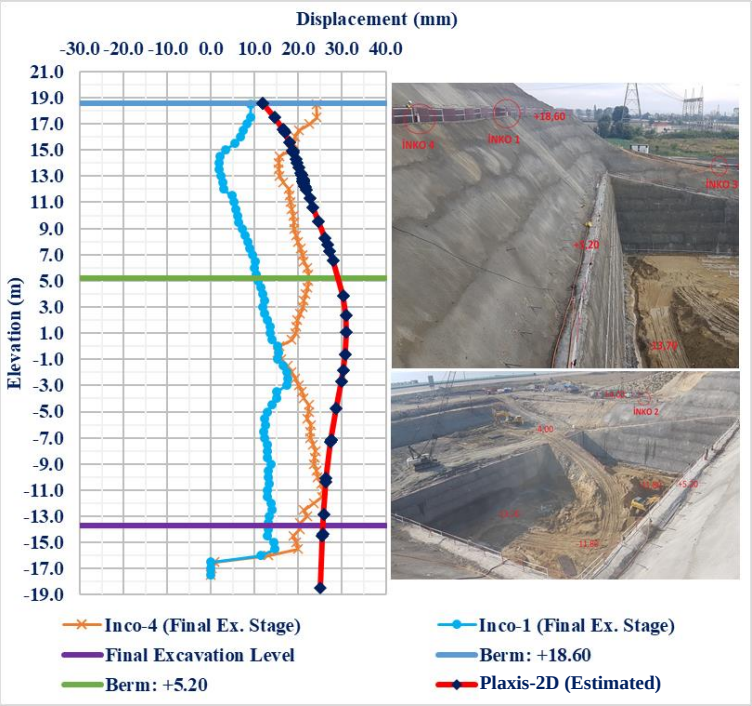


Figure 6. Estimated and actual displacement

4. ROCK BOLT PULL-OUT TESTS

The slope stability of the excavation is designed by shotcrete and grouted rock bolts drilled into the rock (sandstone), as shown in Figure 4. In order to calculate the maximum pull-out resistance per grouted bar, lateral skin resistance has been estimated as follows:

$$T_{skin,max} = \pi x \emptyset_{drill} x \tau \quad (1)$$

where, $\emptyset_{drill}$, is the diameter of the drilling, which is defined as $\emptyset_{drill} = 76.2mm$. τ, represents the characteristic soil/grout bond strength. The estimated value for the bond strength τ in the Sandstone can be obtained from Table 3, assuming conservatively an upper value of the bond strength for weathered sandstone proposed in the table. This bond strength is considered to be a conservative/lower bound value for the inner "intact" sandstone. For the verification of the pull-out force, a bond strength of τ=300kPa has been assumed.

Table 3. Bond strength estimation for rock bolts in rock (Lazarte 1 et al., 2003).

Material	Construction Method	Soil/Rock Type	Ultimate Bond Strength, qu (kPa)
Rock	Rotary Drilled	Marl/limestone	300 - 400
		Soft dolomite	400 - 600
		Fissured dolomite	600 - 1000
		Weathered sandstone	**200 - 300**
		Weathered shale	100 - 150
		Basalt	500 - 600
		Slate/Hard shale	300 - 400

The ultimate characteristic pull-out force per meter of rock bolt is, then:

$$T_{skin,max} = \pi x \emptyset_{drill} x \tau = \pi \text{x} 0.0762 \text{x} 300 = 71.82 \text{ kN/m}$$

Since the EN1997-1 does not consider the design of the soil nails or rock bolts a reasonable partial factor on pull out resistance of γ=1.50 has been adopted following the BS 8006-2.

$$T_{skin,max,d} = \frac{T_{skin,max,d}}{\gamma} = \frac{71.82}{1.5} = 47.88\ kN/m \quad (2)$$

Nevertheless, the maximum bond strength was verified during the pull-out tests to be carried out on-site before the excavations. The maximum force in the rock bolt will be limited by the maximum tensile capacity of the steel bar, as follows:

$$F_{y,d} = \frac{F_{y,k\,y}}{\gamma} = \frac{500x10^3}{1.15} x \frac{\pi x 0.032^2}{4} \quad (3)$$

Sacrificial Tests

26 pull-out tests were performed within the scope of the Sacrificial testing program. The location of these tests in the project site is given in Figure-7.

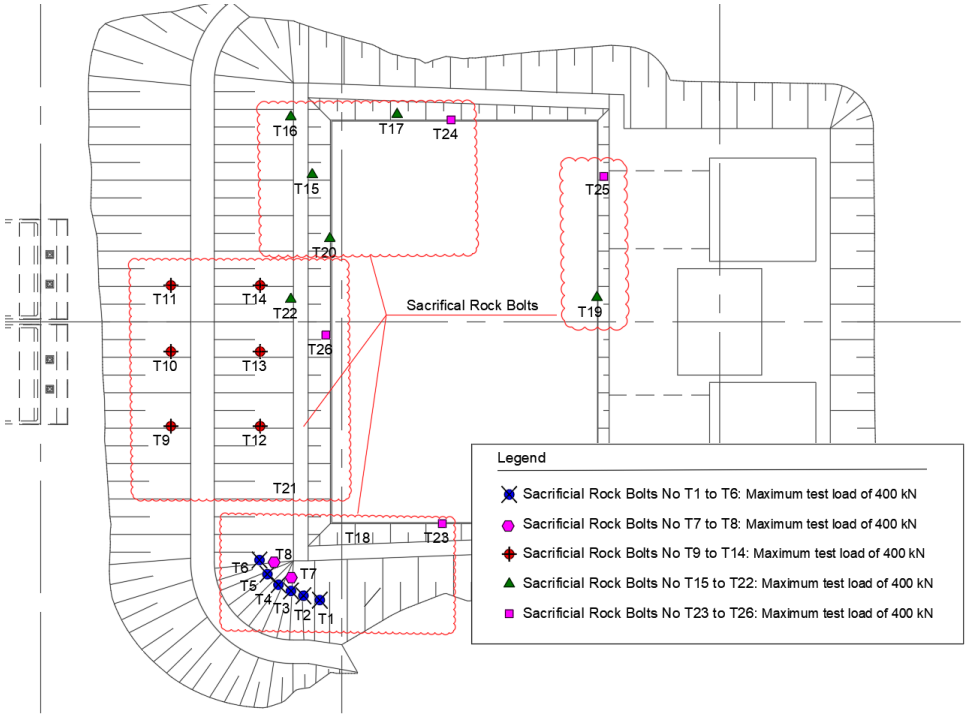


Figure 7. Rock bolt pull-out tests layout plan.

For the all-sacrificial tests, maximum test load of 400 kN was achieved successfully without pull out failure of bond. By considering third cycle of sacrificial rock bolt test for T8, no bond failure was observed until 450-460 kN load of which was near yielding limit of reinforcement. The mobilized bond stress (without failure) of sacrificial rock bolts is given in Table 4.

Table 4. Mobilized Bond Stress (without failure) of Sacrificial Rock Bolts.

Rock Bolt No	Dia. (mm)	Datum Load (kN)	Max. Load (kN)	Elongation Difference (mm)	Permanent Displacement (mm)	Theoretical Displacement (mm)	Apparent Free Length (m)	Rock Bolt Length (m)	Actual Bond Length (m)	Mobilized Bond Stress (kPa)
T1	76.2	40	400	19.2	3.8	15.4	6.5	12.0	5.5	303.8
T2	76.2	40	400	20.2	2.0	18.2	7.3	12.0	4.7	355.5
T3	76.2	40	400	19.1	0.7	18.4	7.4	12.0	4.6	363.2
T4	76.2	40	400	21.7	1.0	20.6	8.3	12.0	3.7	451.6
T5	76.2	40	400	19.4	0.7	18.7	7.5	12.0	4.5	371.3
T6	76.2	40	400	21.1	1.2	19.9	8.0	12.0	4.0	417.7
T7	76.2	40	400	19.8	-1.3	21.1	8.3	12.0	3.1	539.0
T8	76.2	40	460	-	-	25.0	-	12.0	3.3	591.2
T9	76.2	40	400	-	-	20.3	-	12.0	3.9	434.0
T10	76.2	40	400	-	-	20.3	-	12.0	3.9	434.0
T11	76.2	40	400	-	-	20.3	-	12.0	3.9	434.0
T12	76.2	40	400	-	-	20.3	-	12.0	3.9	434.0
T13	76.2	40	400	-	-	20.3	-	12.0	3.9	434.0
T14	76.2	40	400	-	-	20.3	-	12.0	3.9	434.0
T15	76.2	40	400	14.5	3.3	7.5	5.0	10.0	7.0	238.7
T16	76.2	40	400	23.4	-0.6	26.6	10.7	12.0	1.3	1285.3
T17	76.2	40	400	19.8	1.2	15.7	8.3	10.0	3.7	451.6
T18	76.2	40	400	-	-	16.8	-	10.0	3.3	514.1
T19	76.2	40	400	-	-	16.8	-	10.0	3.3	514.1
T20	76.2	40	400	-	-	16.8	-	10.0	3.3	514.1
T21	76.2	40	400	-	-	20.3	-	12.0	3.9	434.0
T22	76.2	40	400	-	-	20.3	-	12.0	3.9	434.0
T23	76.2	40	400	20.6	8.2	8.7	5.5	10.0	6.5	257.1
T24	76.2	40	400	19.6	3.1	13.4	7.4	10.0	4.6	363.2
T25	76.2	40	400	22.5	4.1	15.4	8.2	10.0	3.8	439.7
T26	76.2	40	400	18.4	1.1	14.2	7.7	10.0	4.3	388.6
Average Mobilized Bond Stress (kPa)										**455.1**

During testing of rock bolt; T7, it was observed that elongations based according to measured displacement in both cycles were near to theoretical values. However, displacements and related elongations at both cycles were far away from the theoretical values for rock bolt no T8. This issue can be explained with the fact that datum load of 160 kN, applied for steel plate to set on shotcrete face, was higher than the datum load specified in the test procedure. For this reason, the calculations in Table-4 for determination of actual bond length do not consider rock bolt no T8. Related with this issue, creep performance under maximum test load was evaluated for only rock bolt no T7 and it is concluded that creep rate below the limit defined in relative standard (EN 14490:2010). Having reviewed mobilized bond stress without bond failure and observation of no bond failure at nearly yielding point of reinforcements for T8, T18 to T22, it is clearly seen that installation of production rock bolts with diameter of 76.2 mm will be adequate for assumed maximum bond stress (300 kPa) and maximum design loads for static condition (270 kN per rock bolt). The variation of mobilized bond stress for weathered sandstone according to actual rock bolt lengths is given in Figure 8.

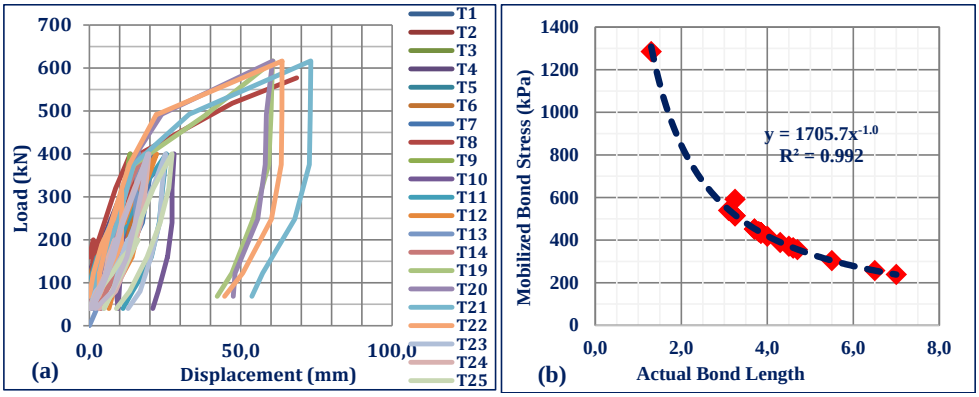


Figure 8. Load-displacement curve (a) and variation of mobilized bond stress with actual bond length (b) for weathered sandstone.

$$\sigma_{mob} = {}^{1705.7}/_{L_{bond}} \quad (4)$$

5. CONCLUSIONS

This article delves into the extensive excavation of the reinforced concrete anchor block structure, boasting a volume of 68,000 m³, situated on the European side of the 1915 Çanakkale Bridge. In the scope of the project, 170,000 m³ of excavation work, 10,000 m of rock bolts, 12,000 m² of shotcrete application, 431 no's of secant piles, and 28 no's of dewatering wells were executed successfully. The amount of displacement obtained in the finite element analysis performed with residual soil parameters was very closely related to the inclinometer readings (Inco-4 and Inco-1) made in the final excavation stage. To verify the in-situ design capacity of the rock bolts, a total of 26 no's of preliminary pull-out tests side of the excavation pit, and results are summarized. Design of temporary excavation works was performed by assuming rock bolts having pull-out resistance of 300 kPa with borehole diameter of 76.2mm. All the sacrificial rock bolts were produced with a borehole diameter of 76.2 mm. All rock bolt tests successfully met the test load without creep.

6. ACKNOWLEDGEMENTS

We would like to thank all DLSY Joint Venture employees, with whom we are very happy to work within the scope of the project. Moreover, we also would like to thank our project manager Ahmet Metin Akkaya and entire Kasktaş site team for successfull site works.

REFERENCES

British Standard Code of Practice for strengthened/reinforced soils and other fills Standard, BS 8006, Part 1 and Part 2, 22 June 2010-2011.

BS EN 14490:2010-Execution of Special Geotechnical Works. Soil Nailing (British Standard).

COWI 1915 ÇANAKKALE Bridge - Excavation Works Anchor Block, European, Doc. no. DLSY03-CS-DR-ANE-STD-2004-DD.

COWI 1915 Çanakkale Bridge, Detailed design - Anchor block European - General arrangement Drawing, Doc. No. DLSY03-CS-DW-ANE-STD-2101-DD, 2018.

Lazarte, C. A., Victor Elias, R. David Espinoza and Paul J. Sabatini Geotechnical Engineering Circular N0. 7 – Soil Nail Walls Washington D.C.: Publication FHWA0-IF-03-017, 2003.

28th European Young Geotechnical Engineers Conference – EYGEC 2024
© 2024 Macedonian Association for Geotechnics, ISBN 978-608-4510-61-1

Improving axial pile design through full-scale field testing and fibre optic sensing

Kevin J. Duffy[a]

[a] *Delft University of Technology, Delft, The Netherlands*

ABSTRACT

Recent advancements in fibre optic sensing have increased the range of monitoring techniques available for measuring the axial response of full-scale piles. For instance, distributed fibre optic sensing gives a continuous measurement of normal force with depth in a pile, meaning the shaft resistance of a pile can be accurately quantified in each soil layer. Other fibre optic sensing methods, such as Fibre Bragg Gratings, have been shown to provide accurate and robust high-frequency measurements of pile installation. With these improved measurement techniques, detailed insights can be obtained into not just the geotechnical response of the pile, but also the structural response. Presented in this paper is some first-hand fibre optic data collected from axial load tests on piles founded in dense to very dense sand, ranging from driven piles to screw displacement piles. Using fibre optic sensing, key insights could be gained into both the structural and geotechnical response of these piles at large base and shaft resistances, facilitating changes to CPT-based pile design methods at a site-specific and nationwide level.

KEYWORDS

Fibre optic sensing; Cone Penetration Test; Axial pile design; Pile design;

1. INTRODUCTION

Recent changes to the Dutch design code (NEN, 2017; Gavin, Kovacevic and Igoe, 2021) has prompted a large amount of research (Duffy et al., 2022) in recent years into the axial capacity of piles in sand, through field testing, numerical modelling (both finite and discrete element modelling) and laboratory testing (calibration chamber and centrifuge). In terms of field testing, static load tests were performed on full-scale piles representative of typical piles installed in practice. Four of the most common pile types in the Dutch piling industry were tested:

- Driven closed-ended piles
- Driven open-ended piles
- Driven cast-in-situ piles
- Screw displacement piles

The research focused on specific aspects of axial pile behaviour and how these aspects are integrated into design method which use the Cone Penetration Test (CPT) to predict the pile base and shaft capacity. One aspect included an investigation into pile-specific design factors and how depth-dependent effects, such as friction fatigue, should be incorporated into design, particularly for driven cast-in-situ piles (Flynn and McCabe, 2016). Another aspect focussed on the necessity of limiting resistances for piles in dense to very dense sands.

In total, twenty full-scale piles were tested, spread across three different test sites. Uniquely, all piles were instrumented with state-of-the-art fibre optic sensors, giving detail insights into the pile base and shaft response under axial compressive loading. A short summary of these results are provided in this paper and for further information, readers should refer to Duffy et al. (2022; 2024a; 2024b).

2. FIBRE OPTIC SENSING

Fibre optic sensing techniques look at small changes in the frequency of scattered lightwaves within an optical fibre. Many different types of fibre optic sensing techniques are available, although two types of fibre optic sensors tend to be the most prevalent in geotechnical monitoring: Fibre Bragg Gratings (FBG) and distributed fibre optic sensing (DFOS, Brillouin-based sensing). Both sensing techniques were used during the research programme to monitor the change in strain or deformation of each test pile under axial compressive loading.

FBG and DFOS technologies provide complimentary benefits in the context of pile testing. FBGs are similar to traditional strain gauges in that they are short-gauge sensors, comprising a small grating that is laser-etched into an optical fibre. FBGs also allow for high frequency measurements (>5 kHz) and have been successfully used in monitoring stress wave propagation along a pile during installation (Doherty et al., 2015; Buckley et al., 2020). In contrast, DFOS uses the entire length of the fibre optic cable as a sensing element, measuring the strain acting on every single portion of the cable. However, while DFOS gives spatially rich data, the measurements come at a much lower frequency compared to FBG sensors—two minutes per measurement in the case of the pile load tests.

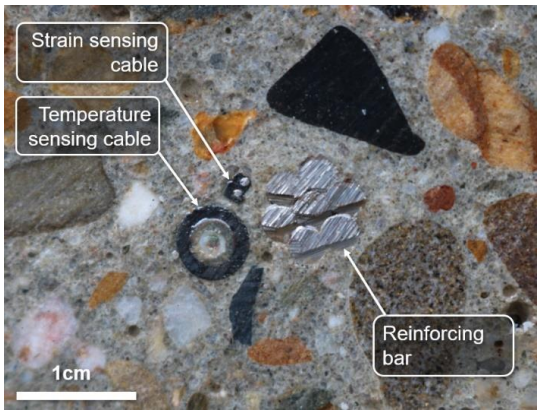


Figure 1. Fibre optic sensors embedded in a concrete pile

The fibre optic cables used for both DFOS and FBG are not much different to standard telecommunication cables. However, pile hammering or concrete pouring can be particularly harsh environments for fibre optic cables. Steel-reinforced fibre optic cables were used to provide more robustness, whilst sacrificing very little in terms of their sensing capabilities. The small size of the fibre optic cables (Figure 1) reduces the space required for instrumentation within a pile. As a result, fibre optic instrumentation provides little impedance to concrete flow and maximises the structural stiffness and integrity of the pile.

Strain is the primary measurement quantity in pile load tests and gets subsequently converted to a normal force based on the assumed cross-sectional stiffness of the pile. Temperature-induced changes on the strain measurements are generally considered to be negligible during a load test. However, the installation of a driven pile also results in locked-in stresses along the pile shaft and underneath the pile base, known as residual stresses. To accurately measure these stresses, a reference measurement should be made before installation with the pile above ground and with a known load acting on the pile, if any load at all. The temperature change between the measurement periods can be substantial, and so thermistors or “loose-buffered” fibre optic cables (Figure 1) were used to correct for the temperature change in the pile between the reference measurement and any measurement after pile installation, described in Duffy et al. (2022).

3. LOAD TEST PROGRAMME

Two different types of test frames were used across the different test sites, one with grout reaction anchors (Figure 2a) and another with heavy concrete blocks, also known as kentledge (Figure 2b). The choice of test frame was dependent on the local site conditions and mobilisation cost. Both test frames used hydraulic jacks to generate the load on the pile, with each pile loaded incrementally to a pile base displacement of 10% of the pile diameter, referred to as pile failure.

During each load-holding increment, the fibre optic sensors measured the pile response in each soil layer. The test results of a cast-in-situ pile (Figure 3) gives a comparison between the DFOS and FBG sensors. Both sensors compare well, showing a gradual reduction in normal force across the looser upper layers. A sharp reduction in force is seen at a depth of 28 m, corresponding to the top of a very dense sand layer. The DFOS readings also shows deviations between FBG measurement points. For instance, the small, localised reduction in load between 15 m and 20 m depth could suggest local deviations in pile diameter or stiffness. These deviations would otherwise not be picked up by FBG sensors and can be crucial in identifying outliers or discrepancies in the measured data.

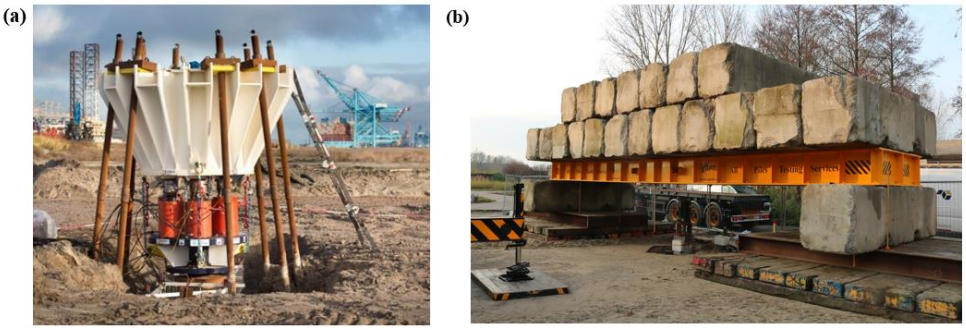


Figure 2. Load test frame (a) with grout reaction anchors (b) with kentledge

4. RESULTS

At one of the test sites (Duffy et al., 2024a), three driven closed-ended piles were installed in very dense sand, where the average CPT cone resistance was 45 MPa at the base of each pile. Crucially, the measurements in the pile prior to load testing showed that at least 10 MPa of residual base stresses were already present (Figure 4) in the piles. To sustain an equilibrium with this 10 MPa base load, negative shear stresses were mobilised all along the upper part of the pile.

From a starting point of 10 MPa, all three piles reached peak of loads of around 30 MPa (Figure 4), mobilising this load within a displacement of 15 mm or 3% of the pile equivalent diameter. Notably, these base stresses were well in excess of limiting resistances prescribed in design standards, such as the Dutch design standard (NEN, 2017) or the API RP 2A standard (API, 2011). Similar findings were also shown for the measured shaft resistance, suggesting pile design methods could be refined to account for this overconservatism.

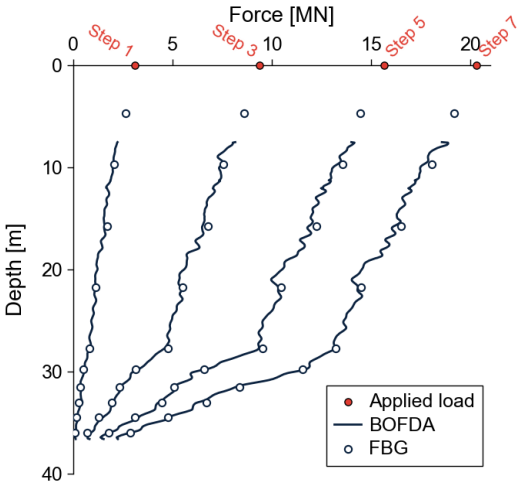


Figure 3. Fibre optic measurements during a load test on a cast-in-situ pile (850 mm diameter)

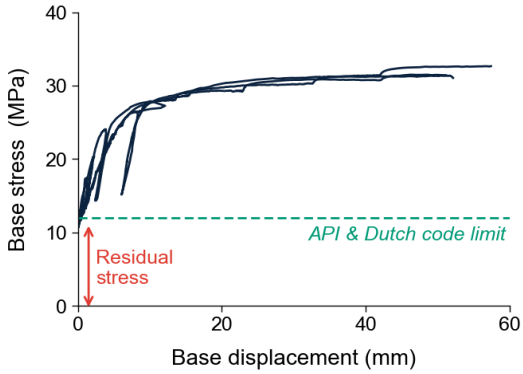


Figure 4. Mobilised base resistances of three driven closed-ended piles (400 mm square) in very dense sand

5. IMPLICATIONS FOR DESIGN

Some of the load tests were performed as part of the construction of 1.8 km long deep-sea quay wall in the port of Rotterdam (Figure 5), to be used as a berth for some of the largest container ships in the world. Around 2,600 foundation piles have recently been installed on the site, all being used to support the target retaining height of 29 m. The results of the driven pre-cast piles, along with tests on other pile types, showed areas in which the design method could be improved. This included a change in the pile base and shaft limiting resistances, along with pile-specific design factors. Specifically for the quay wall project, optimisation of the pile design led to financial savings of roughly €11 million and an 8 kton reduction in carbon emissions associated with pile manufacturing. Clearly, well-instrumented pile testing can be hugely beneficial, both from a research and industry context, and work is ongoing at TU Delft in improving the understanding of pile behaviour and pile design.

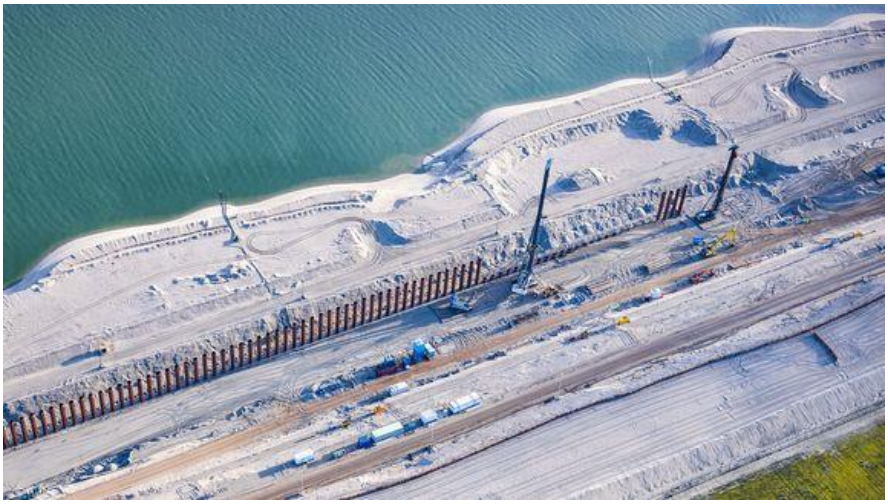


Figure 5. Tubular pile installation at Amaliahaven in the port of Rotterdam

6. ACKNOWLEDGEMENTS

The author would like to express their sincere thanks for the support of the Geotechnical Society of Ireland and for the guidance of Prof. Mike Long during the Bachelors and Masters programmes at University College Dublin.

The research presented in this paper is part of the first author's PhD project, supervised by Prof. Ken Gavin at Delft University of Technology. The project is funded by TKI Deltatechnologie and seven industry partners: Delft University of Technology, Deltares, Dutch Association of Piling Contractors (NVAF), Dutch Ministry of Infrastructure and Water Management, Fugro, Port of Rotterdam Authority and the Municipality of Rotterdam. The author is very grateful for the support of the project partners and the research group at Delft.

REFERENCES

API 2011. *Recommended practice for planning, designing, and constructing fixed offshore plat-forms—Working stress design*. API RP 2GEO. Washington DC, USA: American Petroleum Institute.

Buckley, R.M., McAdam, R.A., Byrne, B.W., Doherty, J.P., Jardine, R.J., Kontoe, S., and Randolph, M.F. 2020. Optimization of impact pile driving using optical Fiber Bragg Grating measurements. *Journal of Geotechnical and Geoenvironmental Engineering*, 146(9). https://doi.org/10.1061/(ASCE)GT.1943-5606.0002293.

Doherty, P., Igoe, D., Murphy, G., Gavin, K.G., Preston, J., McAvoy, C., Byrne, B.W., McAdam R.A., Burd, H.J., Houlsby, G.T., Martin, C.M., Zdravković L., Taborda, D.M.G., Potts, D.M., Jardine, R.J., Sideri, M., Schroeder, F.C., Muir Wood, A., Kallehave, D. and Skov Gretlund, J., 2015. Field validation of Fibre Bragg Grating sensors for measuring strain on driven steel piles. *Géotechnique Letters*, 5(2), 74–79. https://doi.org/10.1680/geolett.14.00120.

Duffy, K.J., Gavin, K.G., Askarinejad, A., Korff, M., de Lange, D.A. and Roubos, A.A. 2022. Field testing of axially loaded piles in dense sand. *20th International Conference on Soil Mechanics and Geotechnical Engineering*, Sydney, Australia.

Duffy, K.J., Gavin, K.G., de Lange, D.A. and Korff, M., 2022. Residual stress measurement of driven precast piles using distributed fibre optic sensors. *11th International Stress Wave Conference*, Rotterdam, The Netherlands. https://doi.org/10.5281/zenodo.7146663.

Duffy, K.J., Gavin, K.G., Korff, M., de Lange, D.A. and Roubos, A.A. 2024a. Influence of the installation method on the axial capacity of piles in very dense sand. *Journal of Geotechnical and Geoenvironmental Engineering*, 150(6). https://doi.org/10.1061/JGGEFK/GTENG-12026.

Duffy, K.J., Gavin, K.G., Korff, M., de Lange, D.A., 2024b. Base resistance of screw displacement piles in sand. *Journal of Geotechnical and Geoenvironmental Engineering*. https://doi.org/10.1061/JGGEFK/GTENG-12340. [Forthcoming].

Flynn, K.N. and McCabe, B.A. 2016. Shaft resistance of driven cast-in-situ piles in sand. *Canadian Geotechnical Journal*, 53(1), 49–59. https://doi.org/10.1139/cgj-2015-0032.

Gavin, K.G., Kovacevic, M.S. and Igoe, D. 2021. A review of CPT based axial pile design in the Netherlands. *Underground Space*, 6(1), 85–99. https://doi.org/10.1016/j.undsp.2019.09.004.

NEN 2017. *Geotechnisch ontwerp van constructies - Deel 1: Algemene regels [Geotechnical design of structures – Part 1: General rules]*. [In Dutch.] NEN 9997-1+C2. Delft, The Netherlands: Dutch Standardisation Institute.

28th European Young Geotechnical Engineers Conference – EYGEC 2024
© 2024 Macedonian Association for Geotechnics, ISBN 978-608-4510-61-1

Case study on the numerical modelling of a CFA energy pile

Ugur Can Erginag[a], Semra Polat[a], Mert Guner[a], Melis Sutman[b], Ozer Cinicioglu[a]

[a] *Bogazici University, Istanbul, Turkiye*
[b] *The University of Edinburgh, Edinburg, United Kingdom*

ABSTRACT

Rapid growth of the world population necessitates the exploration of alternative and clean energy sources to meet growing demand. As a renewable energy source, geothermal energy ranks only second to solar energy. Energy geostructures makes it possible to extract and utilize ground heat. Therefore, utilization of energy piles as shallow geothermal heat exchangers between soil and structure is gaining momentum in the last decade to provide hot water and climate needs of the buildings. Within an energy pile, heat exchanger pipes are embedded, facilitating the transfer of temperature-affected fluid from the ground heat to a heat pump and subsequently to the building. Consequently, this process involves a complex heat interaction among the ground, pipes, and pile, necessitating thermo-hydro-mechanically coupled analyses. In this study, a field scale energy pile test conducted in Houston, Texas was numerically modelled, and it was validated in terms of computed thermally induced stress and temperature evolved along the pile as compared to the measured values at the site.

KEYWORDS

Provide Thermal Pile, Field Test Case, Numerical Modelling, Thermal Behavior separated by semicolons. Capitalize first letter of each word.

1. INTRODUCTION

The world population has been continuously increasing over last century. The current population of approximately 8 billion and it is expected to reach 9.8 billion by 2050 (United Nations, 2019). Therefore, this situation boosts the world's need for energy. Today, about 60% of energy needs are derived from fossil fuels (International Energy Agency, 2016). The use of fossil fuels in energy production has two major disadvantages. The first drawback is the damage caused to nature by increasing greenhouse gases, and the other is the exhaustible nature of these energy resources. As an alternative to fossil fuels, geothermal energy is the heat energy accumulated in the earth's crust. Geothermal energy is the most abundant renewable energy source in the world after solar energy. This renewable energy type is continuously available all over the world, regardless of weather conditions (Lee et al. 2007). The use of geothermal energy, which is a clean energy source, is attracting increasing interest due to its advantages in terms of accessibility and sustainability. Thermoactive piles, which are shallow geothermal systems and called energy piles, are frequently used to utilize geothermal energy (Brandl 2006; Hamada et al. 2007). Unlike conventional piles, energy piles allow heat transfer between the ground and the pile. Energy piles contain pipes in addition to reinforcing rebars. The temperature of the liquid in the pipes can be adjusted by the heat pump and the liquid that has reached the desired temperature circulates throughout the structure and meets the air conditioning and hot water needs of the structure. In essence, thermal heat transfer occurs in soil-pile and pile-pipe.

Many studies have been conducted on the behavior of energy piles under thermal loads. The thermal behavior of energy piles can be determined by field experiments (Bourne-Webb et al., 2009, Laloui et al., 2006, Sutman et al., 2019, Laloui and Sutman, 2021) and verified by numerical models (Gao et al. 2008a., Moradshahi et al., 2021). In this study, a numerical model of a field-scale energy pile experiment

conducted in Houston, Texas was created and validated with a numerical model using stress and temperature measurements obtained in the experiment.

2. FIELD TEST INFORMATION

2.1. Thermal pile properties

An energy pile test was conducted in Houston, Texas (Sutman, 2016). The diameter of the pile was 45.7 cm and the length of the pile was 15.24 m. The pile was manufactured using the "Continues Flight Auger" (CFA) technique. As pile instrumentation, strain gauges with vibration wires were placed in the reinforcement cage at 5 different depths along the pile (see Figure 1). The heat transfer pipes inside the pile are HDPE with a diameter of 25.4 mm and a wall thickness of 3.2 mm. The pipe shape is a single U pipe located in the center of the pile. The liquid used in the pipe consists of 80% water and 20% antifreeze. The liquid flow rate in the pipe is 0.88 m/s throughout the experiment. The thermal conductivity coefficient of the pipe is 0.42 W/m/°C. The modulus of elasticity of the energy pile is 36 GPa and the coefficient of linear thermal expansion is 1.29 × 10-5 με/°C. The instrumentation depths are -2.7 m, -5.7 m, -8.7 m, -11.6 m and -14.5 m, respectively.

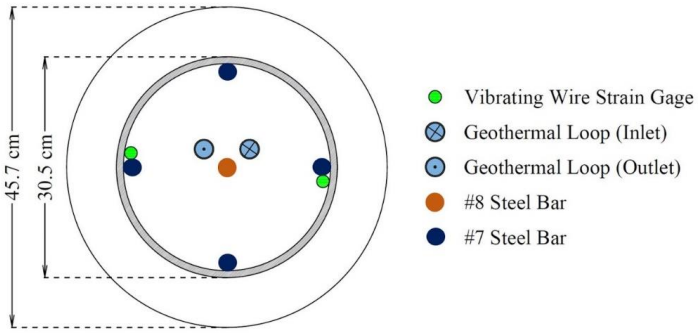


Figure 1. Energy pile instrumentation

2.2. Soil properties

According to the soil investigations, the site is clay for the first 9.8m and then sandy. The groundwater level is 3.7m below the surface. The soil geotechnical parameters used in the numerical analysis are given in Table 1.

Table 1. Soil properties

Soil type	Elastic modulus (MPa)	Poisson's ratio	Cohesion (kPa)	φ' (°)
Clay	45	0.495	114	0
Sand	75	0.3	5	43

2.3. Test schedule

The energy pile investigated in this study was statically loaded in the field and the vertical load capacity of the pile was determined as 2558 kN. The static load was then removed and cyclic thermal loading was applied. Cyclic thermal loading consisted of 5 thermal cycles lasting 6 weeks. The temperature of the fluid circulated in the pipes inside the pile is given in Figure 2.

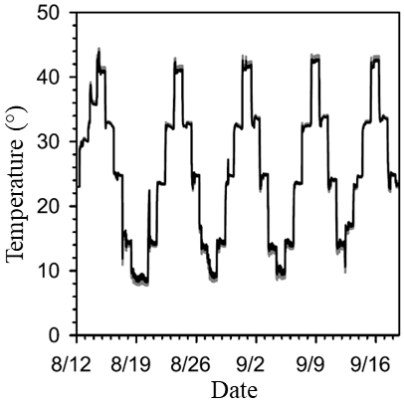


Figure 2. Cyclic thermal load

3. NUMERICAL MODELLING

A 3D numerical model of the energy pile was created using COMSOL Multiphysics software (see Figure 3). The dimensions of the numerical model are 50mx50mx40m. The model boundary conditions are rollers for the vertical direction at the model edges and fixed at the model base. The model boundaries are thermally isolated except for the top surface to create thermal boundary conditions. The initial temperature of the pile and soil was modelled as 21.6°C in accordance with field measurements. The Mohr-Coulomb constitutive model was used for clay and sandy soils, while the linear elastic constitutive model was used for the thermal pile. In the numerical model, the first of the 5 cycles shown in Figure 2 was applied for thermal loading. The initial stresses represent the geostatic case.

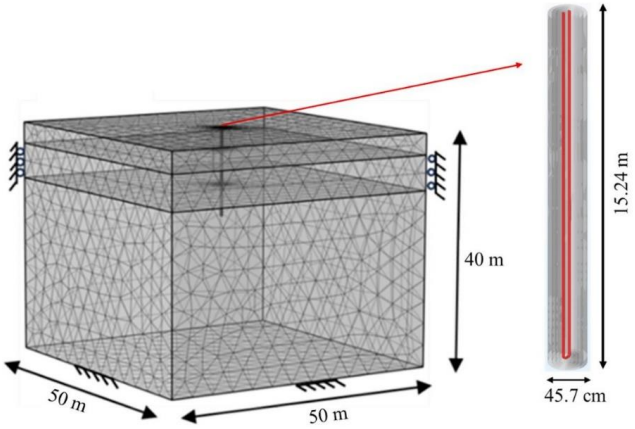


Figure 3. Numerical model and boundary conditions

4. COMPARISON OF FIELD EXPERIMENT AND NUMERICAL MODEL RESULTS

The temperatures measured along the pile in the field experiment and the values calculated with the numerical model are presented in Figure 4 for the first three days. Temperature and strain measurements along the pile were made with the vibrating wire strain gauge sensors shown in Figure 1. All values presented in the graphs are the average of the values obtained from these two sensors. There exist positional differences in pipe and sensor placement along pile cross section in the field during piling

implementation. The distance of the sensors from the pile center varies between 11.7 cm-12.9 cm. Therefore, the numerical model results are given for this range. The corresponding values in Figure 4 represent the analysis results at a distance of 11.7 cm and 12.9 cm from the pile center to the pile wall, respectively. The field measurements and the temperature values calculated by the finite element numerical model are consistent with each other.

Stresses due to thermal loading are presented in Figure 5. The stress values obtained from the sensor located at a depth of approximately 8.7 m are higher than the value obtained from the numerical model. Except for the mentioned case, the stresses measured in the field and the values calculated from the numerical model are compatible with each other.

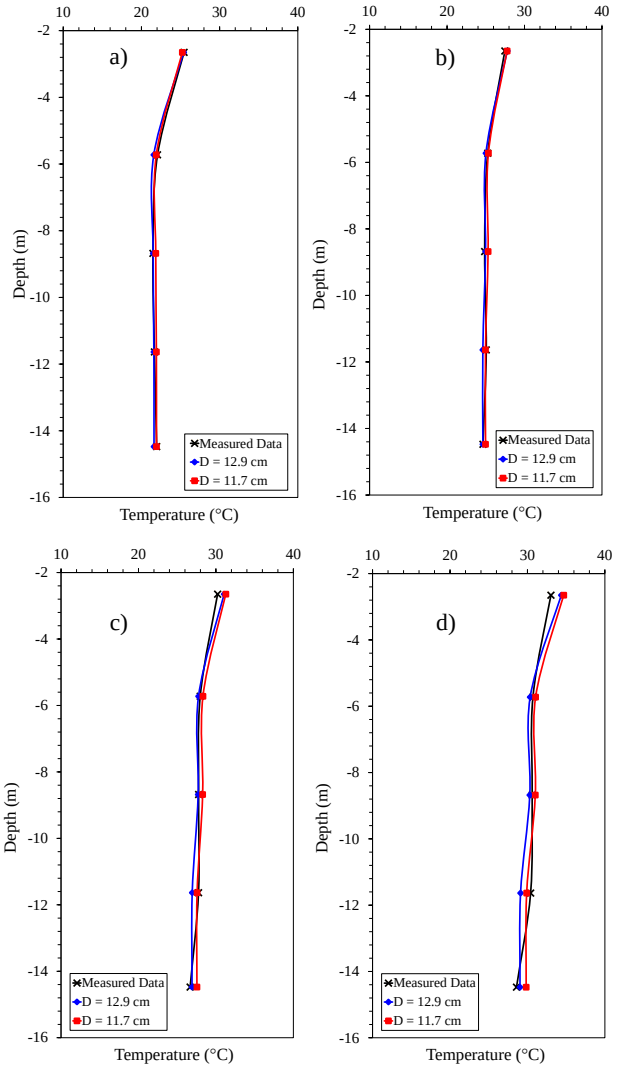


Figure 4. Comparison of temperatures along the pile between the field test and numerical analysis for a) Initial field conditions b) Day-1 c) Day-2 d) Day-3

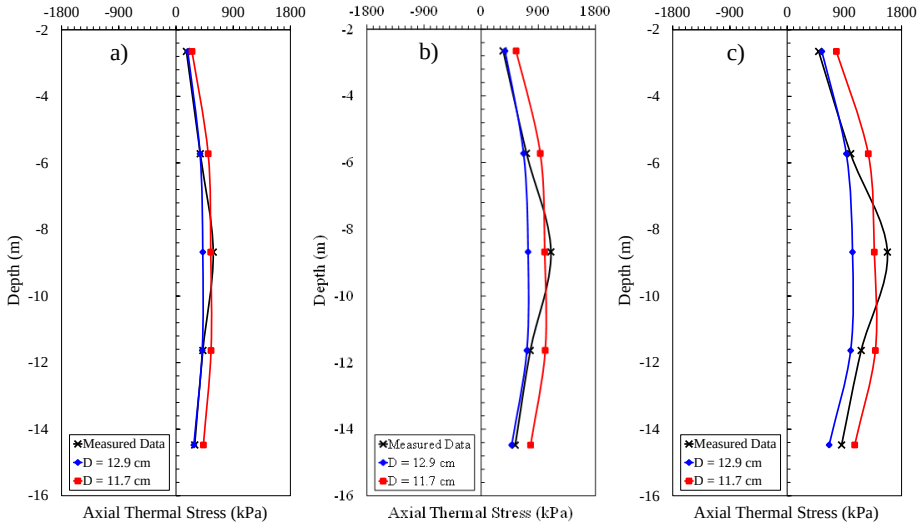


Figure 5. Comparison of thermally induced stresses along the pile between the field test and numerical analysis for a) Day-1 b) Day-2 c) Day-3

5. CONCLUSIONS

As a result of the numerical analysis, the thermomechanical behavior of the pile under thermal effects was investigated. Temperatures and stresses measured along the pile in the field were compared with the numerical model. The thermal fluid passed through the pipes inside the pile caused a temperature increase in the pile. The measured temperature increase in the pile during testing and the values computed in the finite element numerical model are compatible with each other. The temperature increase in the pile causes thermal elongation in the pile. This elongation causes additional axial stresses along the pile depending on the pile boundary conditions. The stress increases due to thermal strain measured in the field and obtained from the numerical model are consistent with each other except for the sensor at 8.7 m depth. The difference of the stress value at this depth from the value obtained from the numerical model can be explained by the change in the sensor position during pilling implementation in the field.

There are number of issues to be considered in the numerical modelling of energy piles. The first of these considerations is that the thermal boundary conditions and consequently the pile and soil surface temperatures should be compatible with the data obtained in the field test. The second issue is the placement and positioning of sensors in the field. The position of the sensors should be placed in the reinforcement so that they are not affected by external influences and the implementation process. The third point to be considered is that the thermal properties of water should also be taken into account, especially in water-saturated soils.

6. ACKNOWLEDGEMENTS

The authors would like to thank the Scientific and Research Council of Boğaziçi University (BAP) for supporting this study with project number 19881. Financial support for the field test from the National Science Foundation Grant CMMI-1100752 is greatly appreciated.

REFERENCES

Bourne-Webb, P.J., Amatya, B., Soga, K., Amis, T., Davidson, C., Payne, P. 2009. Energy pile test at Lambeth College, London: geotechnical and thermodynamic aspects of pile response to heat cycles. *Géotechnique*, 59(3),237–248.

Brandl, H. 2006. Energy foundations and other thermo-active ground structures. *Geotechnique*, 56(2),81-122.

Gao, J., Zhang, X., Liu, J., Li, K., Yang, J. 2008a. Numerical and experimental assessment of thermal performance of vertical energy piles: An application. *Appl. Energy*, 85, 901–910.

Hamada, Y., Saitoh, H., Nakamura, M., Kubota, H., Ochifuji, K. 2007. Field performance of an energy pile system for space heating. *Energy Build.*, 39,517–524.

International Energy Agency, I. E. A. 2016. *Key World Energy Statistics*. International Energy Agency, Paris.

Laloui, L., Nuth, M., Vulliet, L. 2006. *Experimental and numerical investigations of the behaviour of a heat exchanger pile*. *Int. J. Numer. Anal. Methods Geomech.*, 30(8),763–781.

Lee, S., Speight, J.G., Loyalka, S.K., 2007. *Handbook of Alternative Fuel Technologies*. CRC Press.

Moradshahi, A., Faizal, M., Bouazza, A., McCartney, J.S. 2021. Cross-sectional thermo-mechanical responses of energy piles. *Computers and Geotechnics*, 138(4),104320.

Sutman, M. 2016. *Thermo-mechanical behavior of energy piles: Full-scale field testing and numerical modeling*. Doctoral thesis, Virginia Tech.

Sutman, M., Brettman, T., Olgun, C.G. 2019. Full-scale in-situ tests on energy piles: Head and base-restraining effects on the structural behaviour of three energy piles. *Geomechanics for Energy and the Environment*, 2352-3808, 56-68.

Sutman, M., Olgun, C.G., Laloui, L. 2019a. Cyclic load–transfer approach for the analysis of energy piles. *J. Geotech. Geoenviron. Eng.*, 145(1),04018101.

United Nations, U. N. 2019. *World Population Prospects: The 2019 Revision*. Department of Economic and Social Affairs, P. D., United Nations, New York

28th European Young Geotechnical Engineers Conference – EYGEC 2024
© 2024 Macedonian Association for Geotechnics, ISBN 978-608-4510-61-1

Parameter Optimization for Constitutive Soil Models using Supervised Machine Learning

Haris Felić[a], Islam Marzouk[a], Franz Tschuchnigg[a]

[a] *Graz University of Technology, Institute of Soil Mechanics, Foundation Engineering and Computational Geotechnics, Graz, Austria*

ABSTRACT

Soil constitutive models have evolved significantly over the years, with more advanced constitutive models being able to capture soil behaviour better. This advancement often results in an increasing number of constitutive material parameters. It is essential to determine these parameters accurately for the success of numerical analysis. Material parameters can be obtained through either in-situ tests (such as cone penetration tests) or laboratory tests (such as triaxial and oedometer tests). This study exclusively focuses on laboratory tests. The calibration of parameters becomes time-consuming, especially when dealing with multiple parameters, which demands expertise in managing the model to be calibrated. With sufficient data and appropriate optimization approaches, the determination and optimization of soil parameters can be conducted more efficiently. Consequently, the integration of Machine Learning applications has the potential to enhance the reliability of parameter determination and improve the fidelity of objective parameter calibration. To mitigate uncertainty in the parameter calibration process, the working group Computational Geotechnics (TU Graz) aims to determine soil parameters for constitutive models using Machine Learning algorithms applied to standard soil tests. In this paper, supervised Machine Learning algorithms are employed, using synthetic laboratory data (drained triaxial and oedometer test) as input to predict constitutive model parameters. The results demonstrate good agreement with the parameter optimization tool in PLAXIS. These findings underscore the efficacy of ML models in predicting parameters for constitutive models thereby significantly reducing the complexity of the calibration process and facilitating access to more complex constitutive soil models.

KEYWORDS

Constitutive Soil Model; Parameter Determination; Parameter Optimization; Machine Learning.

1. INTRODUCTION

The soil behaviour complexity presents significant challenges in geotechnical analysis, influencing the selection of constitutive soil models and their corresponding parameters for simulating soil behaviour. Despite the variety of available constitutive models, none can fully model all soil types (Yin and Jin, 2019). Potts (2003) highlighted that some commonly used constitutive models may yield unrealistic results in numerical analyses. Mohr–Coulomb (MC) model is known to predict unrealistic ground heaves in excavation problems (Schweiger, 1998), contributing to uncertainty in model selection and parameter determination. In addressing uncertainties in any system, the development of an uncertainty model (UM) is necessary. A UM comprises parameter uncertainty, model uncertainty, and the evaluation technique of the system response (Nasekhian, 2011). Parameter uncertainty plays a critical role in numerical analysis, particularly in constitutive soil parameter determination. The model prediction accuracy significantly depends on the calibration of these parameters, which also helps mitigate model uncertainty. However, parameter calibration is often time-consuming and needs expertise in handling the model calibration. Besides the knowledge of the constitutive model, many

parameters cannot be directly identified through standard soil tests or empirical equations (Machaček et al., 2022).

Machine learning (ML) has already been applied for determination of soil parameter (e.g. Su et al., 2023), offering possibility to enhance the reliability of parameter determination and improve model fidelity. To reduce the uncertainty in the ML-based parameter calibration process, the Computational Geotechnics Group at Graz University of Technology is employing ML algorithms on standard soil tests and in-situ data to determine soil parameters for constitutive models (e.g. Erharter et al., 2023). In this paper, supervised ML algorithms are applied using laboratory test data to predict constitutive soil model parameters. The paper begins with a background on the selection of the constitutive soil model and the discussion of parameter optimization in general. To confirm the ML applicability to parameter determination, various parameter optimization techniques are assessed using the parameter optimization tool in PLAXIS. The ML model performance is evaluated with respect to the parameter optimization tool on a synthetic sand example.

2. BACKGROUND

The quality of numerical predictions in geotechnical problems generally depends on various factors: site characterization, soil characteristics, appropriateness of (idealized) boundary value problem, selection of constitutive model, calibration of the constitutive model, and the relevance and accuracy of the numerical tool (Boulanger 2022). With the development of numerical methods such as the finite element method, it is possible to investigate complex structures and soil-structure interaction problems (Granitzer et al., 2024; Felic et al., 2023). These analyses of course depend on the realistic representation of soil behaviour (stress-strain behaviour) (Tschuchnigg and Schweiger, 2013; Tschuchnigg et al., 2014). In computational geotechnics, the relationship between stresses and strains is represented by constitutive soil models which reflect the model behaviour at single stress points (Lade, 2005). Different constitutive models result in various numerical simulation results that may lead to different design considerations for geotechnical projects. In numerical analysis, the influence of constitutive models on the decision-making process and its associated consequences should be considered in more detail. While current research primarily focuses on proposing more accurate (advanced) soil constitutive models, there is limited research regarding the evaluation, selection, and application of existing models in general. In practical applications, the selection of constitutive models often relies on user preferences and previous experience (Yin and Jin, 2019). It is crucial for users engaged in numerical analysis to understand how to select the appropriate models and their parameters for specific applications. Consequently, understanding a model's possibilities and limitations is necessary to generate realistic numerical results (Brinkgreve, 2005). After selecting the appropriate constitutive model, accurately calibrating input parameters is crucial for realistic numerical predictions. Parameter determination techniques typically rely on inverse methods, involving trial and error to fit desired target values (Meier, 2008). However, this calibration process is time-consuming and demands a high level of expertise (Machaček et al., 2022). To enhance efficiency, optimization algorithms can be employed. These algorithms incrementally refine the design values until specified optimization targets, such as minimum error or maximum iteration number, are achieved by evaluating an objective function. However, misspecifications in the optimization problem or the use of unsuitable optimization algorithms can lead to suboptimal solutions. If properly conducted, optimization algorithms can mitigate human error in the final design stage (Kochenderfer and Wheeler, 2019), as demonstrated by Leo et al. (2023).

3. SIMULATING SOIL TESTS

Numerical simulations of laboratory tests, based on a single stress-point algorithm, are a powerful tool that provides insights into the behaviour of constitutive model parameters. It can be utilised to examine the impact of the parameters on the behaviour and to compare the simulated tests with (real and/or synthetic) laboratory test data. This step is crucial for validating the constitutive model or calibrating the material set (input parameters). The SoilTest tool provided by the finite element software PLAXIS

(PLAXIS 3D, 2021) is used in this study. This tool enables the modelling of various tests, including triaxial, cyclic triaxial, oedometer, constant rate of strain compression, direct simple shear, cyclic direct simple shear, and general tests, where arbitrary stress and strain conditions can be defined.

3.1. Parameter Optimization Tool

In addition to the simulation of laboratory tests, the SoilTest tool can be employed to optimise constitutive model parameters to reach the “best” fit between the results of the simulated tests and target tests. The optimization process takes place over several steps as follows:

- **Step 1: Selecting parameters**

The first step is to select the parameters to be optimized, along with their upper and lower bounds. It is not necessary to optimize all parameters simultaneously.

- **Step 2: Selecting test results**

In this step, the 'target' tests are uploaded. These tests can be either real or synthetically created (as in this study). The optimization tool can handle tests that consist of multiple phases (cycles); however, it is necessary to consider only one phase at a time.

- **Step 3: Configuring optimization settings**

The optimization process is performed using a particle swarm algorithm, which can overcome local minima (PLAXIS 3D, 2021). The accuracy of this process is directly influenced by the optimization settings. Users can select from three levels of search intensity, with the most precise option likely to produce more accurate results at the cost of increased calculation time. Additionally, the calculation time is influenced by the number of parameters being optimized (see Step 1). In this study, the thorough search intensity is used along with a relative tolerance of 10^{-3}.

The optimization process is highly dependent on several factors, including the number of optimized parameters, their upper and lower bounds, the number of tests used, and whether the optimization process is carried out iteratively or not (see Section 3.3). These aspects were carefully considered in preliminary studies focusing on a synthetic case to formulate a reliable optimization procedure.

3.2. Synthetic case

The synthetic case focused on optimizing the Hardening Soil model (Schanz et al., 1999) parameters for a sand sample. The "target" material set represents “typical” values for a medium-dense sand sample and is presented in Table 2. Using this material set, one triaxial test (corresponding to cell pressures of 100 kPa) and an oedometer test (loading to 400 kPa then unloading to 50 kPa) were generated using the SoilTest tool. These two tests will serve as the optimization targets for the optimization process.

3.3. Recommended optimization procedure (for sands)

The procedure is based on optimizing E_{50}^{ref} and φ' from the triaxial test(s), while E_{oed}^{ref} and m from the oedometer test(s) and E_{ur}^{ref} from the unloading curve of the oedometer test(s). K_0^{nc} is determined by Jaky’s empirical formula $(1 - \sin\varphi')$. This (iterative) procedure was formulated based on preliminary studies that investigated several methods to achieve the “best” agreement for the material set in various synthetic cases. The recommended optimization procedure for sands comprises two iterations. The first iteration involves two optimization steps. Firstly, the triaxial tests are used to optimize E_{50}^{ref}, E_{oed}^{ref}, E_{ur}^{ref}, φ', m and K_0^{nc} (step a). Initial values, lower and upper bounds for these parameters, are provided in Table 1, selected based on experience with similar soil types. The wide range between the bound’s accounts for the high uncertainty in this step. Secondly, E_{50}^{ref}, E_{oed}^{ref}, E_{ur}^{ref} and m (initial values obtained from step a) are further optimized using the oedometer test(s) (step b). Subsequently, the material set is updated by selecting E_{50}^{ref} and φ' from step a) and E_{oed}^{ref} and m from step b). At this stage, E_{ur}^{ref} can be selected using the rule of thumb ($E_{ur}^{ref} \approx 3E_{50}^{ref}$) or it can be selected from step b). The final value for E_{ur}^{ref} is optimized in the second iteration. K_0^{nc} is set to $1 - \sin\varphi'$. The second iteration includes three optimization steps. Firstly, the triaxial tests are employed to optimize E_{50}^{ref} The range between the

lower and upper bounds can be reduced in this step due to lower uncertainty compared to the first iteration (e.g., lower bound $\approx E_{50}^{ref}$ (from step a)$/2$ and upper bound $\approx 2E_{50}^{ref}$ (from step a). However, in this study, the lower and upper bounds remained constant (see Table 1). The second step includes optimizing E_{oed}^{ref} and m from the oedometer test(s). Finally, E_{ur}^{ref} is optimized from the unloading curve of the oedometer test(s). This optimization procedure has been applied to several synthetic cases representing different types of sands (loose, medium dense, and dense), showing very good agreement with the synthetically created target material sets. It is important to note that all the synthetically created sets excluded the dilatancy angle or cohesion. The inclusion of these parameters, as well as extending the procedure to fine-grained material sets, is part of ongoing research.

Table 1. Lower, initial, and upper values used in the optimization procedure

Parameter	Lower bound	Initial value	Upper bound
E_{50}^{ref}(kPa)	1000	30 000	100 000
E_{oed}^{ref} (kPa)	1000	30 000	100 000
E_{ur}^{ref} (kPa)	1000	90 000	500 000
φ' (°)	0	30	50
m (-)	0	0.50	1
K_0^{nc} (-)	0	0.50	1

3.4. Performance of the optimization procedure

To assess the performance of the recommended optimization procedure described above, it is compared to two alternative approaches. These approaches differ in the required level of expertise. Optimization Approach (OA) 1 assumes low expertise in both the constitutive model and the optimization process. OA 2 assumes low expertise in optimization process but high expertise in the constitutive model. OA 3 (see Section 3.3) assumes high expertise in both the constitutive model and the optimization process. It should be noted that OA 1 requires the least time to conduct the optimization procedure, whereas OA 3 requires significantly more time and knowledge of a suitable iterative procedure.

- **OA 1 – Beginner level**

All parameters (E_{50}^{ref}, E_{oed}^{ref}, E_{ur}^{ref}, φ', m and K_0^{nc}) are optimized simultaneously over three steps. In the first step, the parameters are optimized using the triaxial test(s), followed by optimization using the oedometer test(s) in the second step. Finally, the parameters are further optimized using the unloading branch of the oedometer test(s).

- **OA 2 – Intermediate level**

In this approach, the optimization is conducted in three steps. Firstly, E_{50}^{ref}, φ' and K_0^{nc} are optimized from the triaxial test(s). Secondly, E_{oed}^{ref}, E_{ur}^{ref} and m are optimized from the loading branch of the oedometer test(s). Finally, E_{ur}^{ref} is optimized from the unloading branch of the oedometer test(s).

- **OA 3 – Expert level**

Approach 3 refers to the recommended optimization procedure described in Section 3.3.

Figure 5 illustrates, anti-clockwise from a triaxial test, the volumetric strains ε_{vol} with axial strain ε_1 (top right corner), deviatoric stress q versus axial strain ε_1 (top left corner), stress path with q and effective isotropic stress p' (bottom left corner), and effective axial stress σ'_1 with axial strain ε_1 (bottom right corner) from an oedometer test for all three OAs. Since all optimization approaches utilize stress-strain curves (q-ε_1) from a triaxial tests without considering dilatancy, the volumetric behaviour shows a good fit for all three OAs. In the q-ε_1 subfigure, OA 1 overestimates the maximum stress compared to the target values. Similar behaviour is also observed in the stress path. In the oedometer test, OA 1 shows a stiffer behaviour compared to the target values. OA 2 and OA 3, at first sight, demonstrate a good match compared to the target values for both the triaxial and oedometer tests.

The material sets obtained from all three approaches, alongside the target values, are presented in Table 2. Bold-marked entries in the table represent parameters that were chosen for optimization, while non-bold values remained constant throughout the OA. Results for OA 1 indicate a significant overestimation

of stiffness parameters (E_{50}^{ref}, E_{oed}^{ref}, and E_{ur}^{ref}) by an average of 10%, along with an effective friction angle φ' overestimation of 33% compared to the target values. The stress-dependent stiffness power parameter m is underestimated by 6%. Although OA 2 initially appears to provide a good match, closer investigation reveals a 6% underestimation in stiffness when observing E_{50}^{ref}. Other parameters exhibit minor deviations around 1%. Only OA 3 demonstrates a strong alignment compared to the target values, exhibiting a divergence of less than 1%.

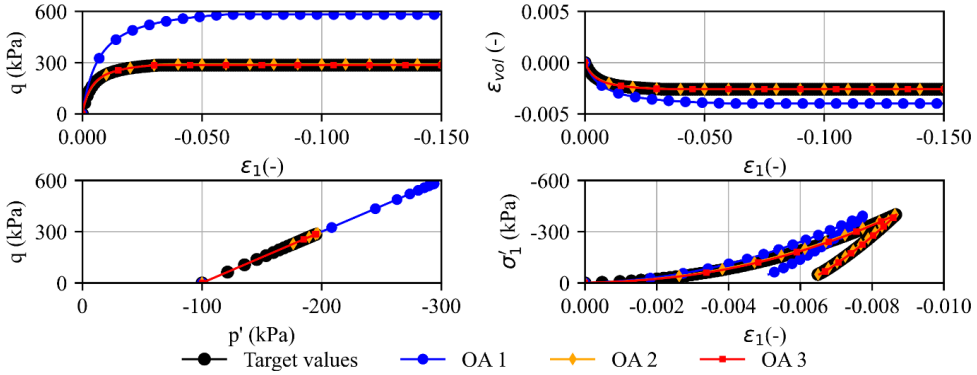


Figure 5. Comparison of optimization approaches with triaxial and oedometer tests

Table 2. Material sets of a synthetic target example and all Optimization Approaches (OAs)

Parameter	Unit	Target value	OA 1	OA 2	OA 3
E_{50}^{ref}	kPa	45 000	**51 220**	**42 130**	**44 950**
E_{oed}^{ref}	kPa	45 000	**48 550**	**44 800**	**44 970**
E_{ur}^{ref}	kPa	135 000	**144 000**	**137 400**	**136 000**
ν_{ur}	-	0.20	0.20	0.20	0.20
c′	kPa	0.00	0.00	0.00	0.00
ϕ'	°	36.00	**48.08**	**36.29**	**36.02**
ψ	°	0.00	0.00	0.00	0.00
m	-	0.55	**0.5187**	**0.5400**	**0.5558**
K_0^{NC}	-	0.4122	**0.2890**	**0.4081**	**0.4119**
R_f	-	0.90	0.90	0.90	0.90

The optimization results underline the critical need for both a profound understanding of the constitutive model and a high level of expertise in the optimization process to achieve effective parameter calibration.

4. MACHINE LEARNING APPROACH

This section presents the machine learning (ML) approach, covering sampling and feature selection, as well as the overall ML training workflow. Additionally, the performance of the trained ML model is evaluated by comparing its predictions with the results obtained using OA 3, using the same synthetic target example as in Section 3.4). The ML algorithm used in this paper exclusively focuses on the utilization of *XGBoost*. Figure 6 illustrates the proposed ML approach, which integrates stress-strain curve data obtained with the SoilTest tool and an ML algorithm to predict constitutive model parameters.

4.1. Sampling and feature selection

Before model training the ML model, data generation is necessary. In this study, a sample representing sand (effective cohesion c' = 0 kPa) is established. The sampling method assumes randomly normally distributed values for various parameters: E_{50}^{ref} ranging from 13,000 to 75,000 kPa, E_{oed}^{ref} ranging from

0.80 to 1.20 times E_{50}^{ref}, E_{ur}^{ref} ranging from 2.00 to 4.00 times E_{50}^{ref}, ν_{ur} ranging from 0.10 to 0.30, φ' ranging from 28 to 40, ψ ranging from φ' - 30 ± 3 (randomly selected), m ranging from 0.30 to 0.70, and R_f ranging from 0.70 to 0.97. This sampling is utilized to generate curve data using the SoilTest tool. The total number of simulations based on the sampling involved 15,300 simulations, including both triaxial and oedometer tests. For ML model training, a feature matrix (input matrix) comprises vectors of data quantities from one triaxial and one oedometer test, which are then used to predict HS parameters (target matrix).

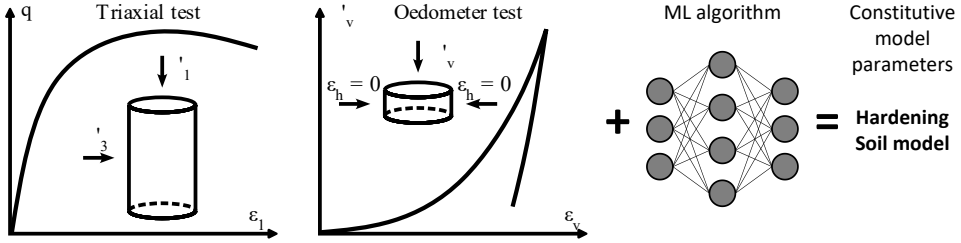


Figure 6. Machine learning approach

4.2. Model training workflow

The ML workflow typically includes training and validating the model, testing the model, and training the final model, as outlined by Deisenroth et al. (2021). Initially, the database is divided into training and test sets, often at an 80% to 20% ratio, similar to Rauter and Tschuchnigg (2021). In the first step, the model is trained using the training data and initial hyperparameters, with loss computed at each step by comparing ML predictions to the actual dataset. Subsequently, the model generalization is evaluated through a validation step. During this step, the model performance is analysed by computing the validation loss on a separate validation set, derived from the 80% training data. To prevent overfitting, early stopping with a criterion of five iterations is applied (Deisenroth et al., 2021). To optimize hyperparameters, Optuna, an automatic hyperparameter optimization framework, is used (Akiba et al., 2019). Optuna evaluates various hyperparameter settings based on training and validation losses to maximize (or minimize) an objective function The termination criterion for the optimization process in this study is based on the maximum iteration number. Finally, the model is trained using the combined training and validation sets with the best hyperparameters and evaluated using the test set to assess generalization. If the derived test loss is acceptable, a final training can be conducted using all data points and optimized hyperparameters.

4.3. Application of machine learning model

Figure 7 displays (similar to the parameter optimization section), anti-clockwise from a triaxial test, the volumetric strains ε_{vol} with axial strain ε_1 (top right corner), deviatoric stress q versus axial strain ε_1 (top left corner), stress path with q and effective isotropic stress p' (bottom left corner), and effective axial stress σ'_1 with axial strain ε_1 (bottom right corner) from an oedometer test for OA 3 and the ML model prediction. The ML results for the triaxial test demonstrate good agreement with the target values and OA 3. In the oedometer test, the ML prediction exhibits good agreement; however, it indicates a slightly stiffer behaviour compared to the target values and OA 3.

Table 3 displays the material sets of target values, OA 3 (also referenced in Table 2), and the ML prediction. Entries in bold within OA 3 denote parameters selected for the optimization process, while non-bold values remained constant throughout optimization. The results of the ML prediction exhibit a good match compared to the target values. Specifically, the ML prediction of the stiffness parameters E_{50}^{ref}, E_{ur}^{ref}, m, and ν_{ur} deviate by less than 5%, except for E_{oed}^{ref} which deviates by approximately 5.1%. Additionally, the strength parameters (φ' and ψ), as well as R_f, demonstrate an even better alignment with the target values (approximately 1% divergence).

The results indicate that the ML model accurately predicts the HS model parameters, requiring significantly less expertise in the parameter optimization process. Nevertheless, validating the ML model predictions still demands a high level of expertise in the constitutive model. It is important to highlight that after the ML model training, the ML model application only requires a few seconds, eliminating the need for complex optimization approaches (see Section 3.4). Consequently, parameter determination should be considered as a powerful alternative compared to standard optimization techniques.

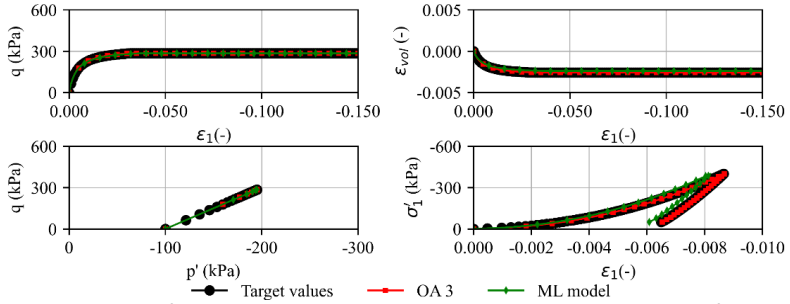


Figure 7. Comparison of optimization approach (OA) 3 and the ML model prediction of synthetic test

Table 3. Material sets comparison obtained with OA 3, and ML prediction (* denotes not predicted parameters)

Parameter	Unit	Target value (TV)	OA 3	ML prediction	ML / target value (%)
E_{50}^{ref}	kPa	45 000	**44 950**	43 736	+2.81
E_{oed}^{ref}	kPa	45 000	**44 970**	47 310	-5.13
E_{ur}^{ref}	kPa	135 000	**136 000**	138 457	-2.56
ν_{ur}	-	0.20	0.20	0.19	+5.00
c'	kPa	0.00	0.00	0.00*	-
ϕ'	°	36.00	**36.02**	35.98	+0.06
ψ	°	0.00	0.00	0.19	-
m	-	0.55	**0.5558**	0.54	+1.82
K_0^{NC}	-	0.4122	**0.4119**	0.4125*	-0.07
R_f	-	0.90	0.90	0.91	-1.11

5. CONCLUSIONS

The primary aim of this contribution is to develop a predictive model for acquiring constitutive soil model parameters. The presented findings underscore the effectiveness of ML models in predicting these parameters, significantly reducing the efforts, and required knowledge in the calibration process. However, validating the ML model predictions still requires a deep understanding of the constitutive model. It is noteworthy that evaluating the ML model takes only a few seconds; thus, the parameter determination can be less time-consuming. The optimization results emphasize the importance of not only having a profound understanding of the constitutive model but also possessing a very high level of expertise in the optimization process for effective calibration. Moreover, specific knowledge of which parameter exactly influences certain aspects of the constitutive model (e.g., the slight influence of E_{50}^{ref} in the oedometer test) is not necessary. Therefore, the proposed approach can facilitate easier access to more complex constitutive soil models. Further studies (not included in this paper) have revealed the limited extrapolation ability of ML models beyond the sampled data, emphasizing the need for additional training data. Preliminary studies suggest promising results in obtaining reliable parameters for real lab tests; however, more research with real lab test data is required. Future investigations will also concentrate on addressing the limitations of ML predictions for soil parameters.

REFERENCES

Akiba, T., Sano, S., Yanase, T., Ohta, T., and Koyama, M. 2019. Optuna: A Next-generation Hyperparameter Optimization Framework, *KDD '19: The 25th ACM SIGKDD Conference on Knowledge Discovery and Data Mining*, New York, USA, 2623–2631. DOI: 10.1145/3292500.3330701.

Boulanger, R. W. 2022. Nonlinear dynamic analyses involving soil liquefaction or cyclic softening. *Proceedings, 20th ICSMGE State of the Art and Invited Lectures*, Sydney, Australia, Australian Geomechanics Society, 351–379.

Brinkgreve, R. B. J. 2005. Selection of Soil Models and Parameters for Geotechnical Engineering Application. *Geo-Frontiers Congress 2005*, Austin, United States, 69–98. DOI: 10.1061/40771(169)4.

Deisenroth, M. P., Ong, C. S., and Faisal, A. A. 2021. *Mathematics for machine learning*, Cambridge University Press, Cambridge.

Erharter, G. H., Nøst, H. A., Marzouk, I., Oberhollenzer, Simon, Holmen, Wilhelm, Jostad, H. P., and Tschuchnigg, F. 2023. MLpFEM - towards Machine Learning based parameter calibration. *4th International Symposium on Machine Learning and Big Data in Geoscience*, Cork, Ireland.

Felic, H., Schlicke, D., Granitzer, A.-N., and Tschuchnigg, F. 2023. Enhanced Interoperability between Geotechnical and Structural Engineering for 3D Building Models. *International RILEM Conference on Synergising Expertise towards Sustainability and Robustness of Cement-based Materials and Concrete Structures, SynerCrete 2023*, Cham, 217–228. DOI: 10.1007/978-3-031-33211-1_20.

Granitzer, A.-N., Stastny, A., Felic, H., Leo, J., Buss, C., and Tschuchnigg, F. 2024. Einfluss der Pfahlmodellierung bei FE-Analysen am Beispiel von zwei komplexen Großprojekten. *14. Österreichische Geotechniktagung*, Vienna, Austria, 313–324.

Kochenderfer, M. J., and Wheeler, T. A. 2019. *Algorithms for optimization*, The MIT Press, Cambridge Massachusetts.

Lade, P. V. 2005. Overview of Constitutive Models for Soils, *Geo-Frontiers Congress 2005*, Austin, Texas, United States, 1–34. DOI: 10.1061/40771(169)1.

Leo, J., Granitzer, A.-N., and Tschuchnigg, F. 2023. Interface Constitutive Model Calibration of Embedded Beam with Interaction Surface using Particle Swarm Optimisation. *4th International Symposium on Machine Learning & Big Data in Geoscience*, Kork, Ireland, 102–104.

Machaček, J., Staubach, P., Tavera, C. E. G., Wichtmann, T., and Zachert, H. 2022. On the automatic parameter calibration of a hypoplastic soil model. *Acta Geotechnica*, 17(11), 5253–5273. DOI: 10.1007/s11440-022-01669-4.

Meier, J. 2008. *Parameterbestimmung mittels inverser Verfahren für geotechnische Problemstellungen*. PhD Thesis, Fakultät Bauingenieurwesen der Bauhaus-Universität Weimar.

Nasekhian, A. 2011. *Application of non-probabilistic and probabilistic concepts in finite element analysis of tunnelling*, PhD thesis, Graz, University of Technology Graz.

PLAXIS 3D. 2021. Material Models Manual. CONNECT Edition V21.01.

Potts, D. M. 2003. Numerical analysis: a virtual dream or practical reality?, *Géotechnique*, 53(6), 535-573. DOI: 10.1680/geot.2003.53.6.535.

Rauter, S., and Tschuchnigg, F. 2021. CPT Data Interpretation Employing Different Machine Learning Techniques. *Geosciences*, 11(7). DOI: 10.3390/geosciences11070265.

Schanz, T., Vermeer, P. A., and Bonnier, P. G. 1999. The hardening soil model: Formulation and verification. *Beyond 2000 in Computational Geotechnics*, Boca Raton, FL.

Schweiger, H. F. 1998. Results from Two Geotechnical Benchmark Problems. *Application of Numerical Methods to Geotechnical Problems*, Vienna, Austria. 645–654. DOI: 10.1007/978-3-7091-2512-0_62.

Su, M., Guo, N., and Yang, Z. 2023. A multifidelity neural network (MFNN) for constitutive modeling of complex soil behaviors. *Numerical and Analytical Methods in Geomechanics*, 47(18), 3269–3289.
DOI: 10.1002/nag.3620.

Tschuchnigg, F., and Schweiger, H. F. 2013. Comparison of Deep Foundation Systems using 3D Finite Element Analysis Employing Different Modeling Techniques. *Geotechnical Engineering Journal of the SEAGS & AGSSEA*, 40–46.

Tschuchnigg, F., Schweiger, H. F., and Pausz, S. 2014. 3D finite element analysis of a RCC dam. *Numerical methods in geotechnical engineering*. London, European Conference on Numerical Methods in Geotechnical Engineering, NUMGE 2014, 627–632.

Yin, Z.-Y., and Jin, Y.-F. 2019. *Practice of Optimisation Theory in Geotechnical Engineering*. Springer Singapore, Singapore. DOI: 10.1007/978-981-13-3408-5.

28th European Young Geotechnical Engineers Conference – EYGEC 2024
© 2024 Macedonian Association for Geotechnics, ISBN 978-608-4510-61-1

Water retention characteristics and drained shear strength of soil treated with newly developed soil conditioners

Barbara Fortuna[a], Alessandro Sorze[b], Francesco Valentini[c], Jasna Smolar[d]

[a, d] *University of Ljubljana, Faculty of Civil and Geodetic Engineering, Jamova 2, 1000 Ljubljana, Slovenia*
[b, c] *University of Trento, Department of Industrial Engineering and INSTM Research Unit Via Sommarive 9 38123 Trento, Italy*

ABSTRACT

The impact of climate change has become increasingly severe also in forests, where droughts and strong winds on one, and extreme rainfall events on the other hand can damage forest ecosystems. To mitigate the effects of drought and to increase the soil water retention capacity, various soil conditioners (SCs) are being developed. The laboratory investigation focused on the influence of Xanthan-gum (XG) based SCs with different cellulose fillers on forest soil properties. The primary emphasis was placed on assessing the impact of SCs on water retention ability and hydraulic conductivity. Additionally, a part of the research was directed towards evaluating the drained shear strength of SCs treated forest soil, which is crucial for assessing slope stability, particularly when SCs are used in thick layers on larger, steeper slopes.

This paper deals with the results of laboratory investigations carried out on untreated and treated forest soil, sampled on the ONEforest project case study site in the Alpine part of Slovenia, Ljubelj. The results show significant increase in water absorption of treated soil and favourable impact of SCs on the soil water retention curve (SWRC) in the suction range of plant available water. The increase depends on the amount and type of the SC. A less favourable impact of SCs on drained shear strength was found. The drained shear strength of treated and saturated forest soil was lower than drained shear strength of untreated soil. The decrease in drained shear strength also depends on the amount and type of used SC.

KEYWORDS

Forest Soil; Soil Conditioner; Drained shear strength; Soil hydraulic properties

1. INTRODUCTION

Reports on extreme climatic events over the world, such as droughts and floods, are becoming more and more frequent. Changing environmental conditions require novel solutions to mitigate the negative effects of such extreme events also in the forest ecosystems. Soil conditioners are one of the attempts to elevate soil properties, e.g., enhancing soil's physical, mechanical, chemical and biological attributes. An important aspect is also the retention of water in time of its abundance and regulating its release when plants and trees are in need (Thakur et al., 2023).

Development of commercial SCs is based on implementing highly absorbent hydrogels from organic or inorganic sources (El-Saied et al., 2004; Thakur et al., 2023). The application of synthetic, inorganic soil conditioners is limited by high cost and can represent negative effect on environment (El-Saied et al., 2004; Cabalar et al., 2018; Kwon et al., 2019; Lee et al., 2023b; Sorze et al., 2023b). Organic polymers, on the other hand, offer a sustainable alternative for soil treatment and can foster soil microorganisms and enhance soil structure (Thakur et al., 2023). Cellulosic material, for example, is known for its high absorption properties (El-Saied et al., 2004; Pan and Ragauskas, 2012; Sorze et al., 2023b) and is easily accessible. Hydrogels made of organic material are reported to retain up to 100 % more water than untreated soil even after 5th day of irrigation (Yangyuoru et al., 2009). A significant

increase in water retention properties of soil treated by hydrogel made from lignocellulosic waste was reported by (El-Saied et al., 2004).
Another example of organic polymer is Xanthan Gum (XG), which is a natural polysaccharide produced by fermentation process that increases material's viscosity and shear stability even at low concentrations (Tran et al., 2018; Cabalar et al., 2018; Kwon et al., 2019). Addition of XG into the soil has been extensively reported in the literature in recent years exhibiting promising results. Due to a significant reduction in its market price has become one of the most investigated biopolymers in geotechnical engineering (Mendonça et al., 2020; Oliveira and Reis, 2023). Compared to other biopolymers, XG demonstrates superior improvements of soil in terms of strength properties, erosion resistance and reduction of hydraulic conductivity along with increased vegetation (Tran et al., 2018; Cabalar et al., 2018; Kwon et al., 2019; Soldo and Miletić, 2019; Lee et al., 2023b).
However, promising results of XG treated soils in partially saturated state are accompanied by the fact that XG is extremely sensitive to presence of water, which transforms high strength polymeric network to a weak gel-like material (Chen et al., 2020; Lee et al., 2023a), inherently affecting the soil strength and stability.
Within European project ONEforest, new types of SCs were developed Cellulose fillers were added to the XG to enhance and optimize the performance of XG in terms of hydraulic properties and structural stability (Sorze et al., 2023a, 2023b). The main objective of our research was the assessment of the influence of newly developed SCs on the soil properties with the focus on the length of cellulose fillers in the SCs. Investigations were performed on mixtures of Slovenian forest soil and three types of SCs. The influence of the SCs type and the dosage of SCs on drained shear strength of treated soil was assessed. Using falling head permeameter, saturated hydraulic conductivity was measured. Comparison between water absorption capacity of untreated soil and mixtures was made. Water retention characteristics were determined for untreated soil and mixtures over a wide suction range.

2. MATERIALS AND METHODS

For the research, the forest soil from Ljubelj area in the Alpine region of Slovenia was used, which was one of the case study sites within ONEforest project (CESEFOR, 2021). A soil sample was taken from a layer beneath the fresh organic layer, approximately 10 cm below the surface. Despite the depth of sampling, the soil sample contained a minimal amount of partially decomposed organic matter. All visible undegraded organic material, such as leaves and needles, was removed before laboratory investigations. Sample of Ljubelj soil at natural water content is shown in Figure 8 (left picture).
Three types of SCs were used for the investigation, i.e., Arbocell R (SC_R), Cellugrün (SC_CG) and ZZC500 (SC_ZZC). All are based on XG with different types and amounts of fillers with diverse fibre lengths. SC_R has the highest cellulose content (>99 %) and shortest fibres (200-300 μm), while SC_CG and SC_ZZC has the same cellulose content (80 %) and fibres with length of 1400 μm and 400 μm, respectively. The appearance of the SCs is shown in Figure 8 in dry (left half of the picture) and wet state (right half of the picture). It is evident that the addition of water extremely alters the texture of SCs resulting in hydrogel-like paste with significantly increased volume due to swelling.
More information about the SCs and their development can be found in (Sorze et al., 2023a, 2023b).
Laboratory tests were performed on untreated soil and mixtures of soil and SCs according to the test program as shown in Table 4, where list of executed investigations and corresponding standards and methods are reported. In mixtures, the soil conditioner SC_R was used in low (L) and high (H) dosage with 0.4 % and 1.7 % of SC per dry soil weight, respectively, while soil conditioners SC_CG and SC_ZZC were used only in high (H) dosage of 1.7 %.

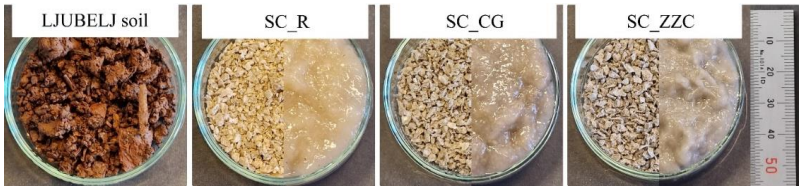


Figure 8. Sample of Ljubelj soil (picture on the left) and three types of soil conditioners in dry and wet state (three pictures on the right)

Table 4. Laboratory investigations, associated standard and investigation plan

Parameter	Standard/Method	Soil	Mixtures
(gravimetric) water content	EN ISO 17892-1 / T_{drying} = 45°C	✓	✓
sieving analysis	EN ISO 17892-4	✓	×
particle density	EN ISO 17892-3	✓	×
water absorption	DIN 18132 / Enslin-Neff – 1.0 g	✓	✓
shear strength – direct shear test	EN ISO 17892-10 / 60-60-20 mm	✓	✓
liquid limit, plastic limit	EN ISO 17892-12	✓	×
soil suction (SWRC)	ASTM D6836, manufacturer's instructions	✓	✓
hydraulic conductivity	EN ISO 17892-11 / falling head	✓	✓

Prior to measurements of water absorption, the soil was dried until constant mass. Dry soil and SCs were separately grinded and sieved through 0.355 mm sieve and then mixed together. 1.0 g of specimen were used for Enslin-Neff absorption test. For other tests, the mixtures were prepared by mixing the soil at natural water content and dry soil conditioners.
For the direct shear (DS) test, the specimens of soil and mixtures were compacted into the mold at dry density of approx. 1.5 g/cm^3. To achieve full saturation of the specimen, the assembly was submerged under water before consolidation stage. For the mixtures, the swelling took place for at least 24 hours. Afterwards, the specimens were consolidated gradually until final effective vertical stresses (50 kPa, 100 kPa and 150 kPa) were achieved. The specimens remained submerged also during shearing stage. Shearing rate was set at 0.002 mm/min. To prove the repeatability of the DS test, two repetitions were carried out for mixtures with the addition of SC_R H and SC_ZZC H.

Specimens for measurements of saturated hydraulic conductivity in oedometer cell, were prepared in a similar manner, with swelling stage at the beginning of the test with 4.5 kPa of vertical load. Hydraulic conductivity *k* was measured at the end of consolidation process at two vertical loading stages, i.e., 25 kPa and 50 kPa.
Water retention curves for soil and mixtures (SWRC) were determined using two devices:

- Hyprop was used for measurements of matric suction below approx. 100 kPa with evaporation method (Peters and Durner, 2008). The specimens of soil and mixtures were assembled into the sampling ring with diameter and height of 8 cm and 5 cm, respectively, at density of approx. 1.5 g/cm^3. Specimens were immersed in water to their 4/5 height until saturation higher than 90 % was achieved. Due to considerable swelling, vertical deformations were reduced by porous discs on upper and lower surface of the specimen and with the 10 kPa weight on top of the specimen during saturation process. After saturation, two Hyprop tensiometers were installed in pre-drilled boreholes within the specimen. Prepared specimen was placed on a balance and measurements were started. To ensure quasi constant hydraulic conditions within the sample, water evaporation rate was slowed down by covering specimens with perforated plastic bag. It was assumed that decrease in mass of the specimen corresponds to the amount of evaporated water thus potential degradation during the investigation, which lasted at least 1 month, wasn't considered.
- Dew point potentiometer WP4-T was used for suctions higher than 100 kPa. (WP4 Operator's manual, 2003; Maček et al., 2013). For the sample preparation, the water was gradually added to the mixtures, so the sample was wetted near full saturation state. Approximately 5 g of the

mixture was placed into dedicated plastic container for suction measurements of the specimen in saturated state. Remaining mixture was gradually air dried until required water content was reached. Before each measurement, the containers were airtight sealed for at least 24 h in order to provide uniform water content distribution throughout the specimens.

The dry mass of all specimens was determined after suction measurements by drying in an oven at 45 °C.

3. RESULTS

3.1. Index properties of soil

Natural water content w_0, liquid limit w_L and plasticity index I_P of the Ljubelj soil was 43 %, 67 % and 26 %, respectively and particle density was 2.52 g/cm^3. Investigated soil was fine grained and contains 83 % fines (< 0.063 mm), while the maximum particle diameter was 8 mm. According to the USCS classification the Ljubelj soil was classified as elastic silt with sand.

3.2. Water absorption

While the water absorption tests on untreated soil were finished within 1 h, the addition of the SCs into the soil resulted in prolongation of the tests. The tests on mixtures were carried out for at least 48 h to ensure that full capacity of the SCs was exploited. For each specimen 2 to 4 test repetitions were performed and average values were considered. In Figure 9, the water absorption capacities after 24 h ($w_{A,24\ h}$) and maximal water absorption capacities ($w_{A,max}$) are shown. The addition of high dosage of SCs notably increased water absorption capacity of Ljubelj soil. After 24 h, the highest impact had the SC_R H, while the overall highest increase in water absorption was achieved by mixture with SC_CG. The dosage of the SCs played an important role in increasing water absorption capacity of the soil, as can be seen from Figure 9, while the impact of the SC type was not as considerable.

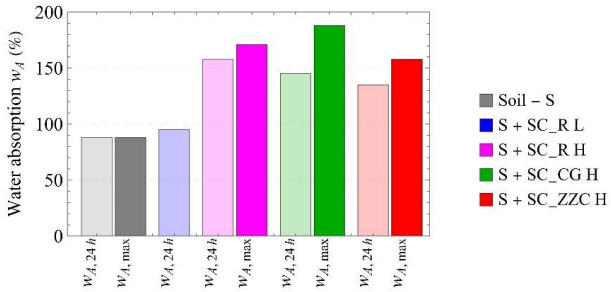


Figure 9. Water absorption capacity for Ljubelj soil and mixtures

3.3. Drained shear strength

The results of direct shear tests carried out on saturated untreated soil and mixtures are shown in Table 5. In order to exclude the influence of inhomogeneities in the prepared mixtures, the tests of S+SC_R H and S+SC_ZZC H were performed with two independent replicates, labelled 1 and 2 in Table 5. The obtained results demonstrate satisfactory repeatability in the direct shear tests.

The addition of SCs generally reduced the drained shear strength of saturated specimens. The friction angle φ' was lower for all mixtures compared to the untreated soil. With a low dosage of SC_R, the decrease in the friction angle was slightly lower than with a high dosage of SC_R. Among the mixtures with a high dosage of SC, the highest friction angle was achieved by SC with the longest fibre length,

i.e., SC_CG, which also had the lowest effective cohesion c'. Interestingly, the low dosage of SC_R resulted in a considerably higher cohesion compared to untreated soil and mixtures with high dosage of SC.

Table 5. The results of direct shear tests: effective cohesion c' and effective friction angle φ' of the untreated soil and of the mixtures in saturated state

Specimen	c' (kPa)	ϕ' (°)
Untreated soil – S	4.4	33.5
S + SC_R L	11.0	27.0
S + SC_R H – 1	4.0	26.0
S + SC_R H – 2	7.7	25.0
S + SC_CG H	1.6	26.5
S+SC_ZZC H – 1	4.7	24.0
S+SC_ZZC H – 2	5.9	24.0

3.4. Saturated hydraulic conductivity

For each specimen, at least 2 replicates were performed at each loading stage. As the results of the first and subsequent measurements were similar, the average values of the hydraulic conductivity, $k_{10°C}$, are shown in Figure 10 together with the corresponding void ratio. It is evident that SCs reduce the hydraulic conductivity and that the influence of a low dosage of SC_R was considerably lower compared to a high dosage of SC_R.

Among the mixtures with high dosage, the specimens with SC_CG show the highest values of $k_{10°C}$ at comparable void ratios. This could be an indication of the influence of the filler properties. The results also show that the hydraulic conductivity of soil and mixtures depends on the void ratio as expected.

In the literature, similar findings were reported, indicating that the addition of 1 % of XG reduced hydraulic conductivity from $1.42*10^{-7}$ m/s for untreated soil to $4.46*10^{-10}$ m/s for treated silty clay (Anandha Kumar and Sujatha, 2022). The decrease in hydraulic conductivity can be attributed to the inherent rheology modification tendency of XG hydrogels. They elevate the viscosity of the soil pore water and obstruct capillary spaces due to their high viscosity. Consequently, this impedes the free movement of water within the soil pore space (Singh and Das, 2020).

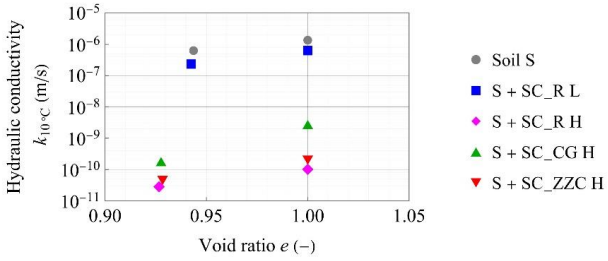


Figure 10. Hydraulic conductivity of untreated soil and mixtures

3.5. Soil water retention curve (SWRC)

Figure 11 shows SWRCs of the untreated soil and mixtures measured by Hyprop (solid line) and WP4-T (scatter plots). The highest (initial) water content of the mixtures was higher than of untreated soil and in the case of SC_R rises with increasing dosage. The lowest measured suctions were between 0.6 kPa (soil) and 9 kPa (S + SC_R H) and reflect initial saturation of specimens. The presence of SCs leads to pore clogging in soils treated with XG-based SCs. This resulted in a prolonged equilibrium time required for the saturation of specimens prior to the tests. Due to difficulties in the saturation process of specimens from mixtures, tests were started when at least 90 % (in most cases 95 %) of initial saturation was

achieved. In comparison to untreated soil, specimens from mixtures with a high dosage of SC (1.7 %) exhibit an initial water content that is 16 % to 34 % higher. These findings align with those reported by (Wang et al., 2023; Zhang et al., 2023). (Wang et al., 2023) observed a 1.3-fold increase in initial water content for silty soil treated with 1% XG, while (Zhang et al., 2023) noted a 1.2-fold increase for sandy soil treated with 2% XG.

SWRCs indicate that, at high suction (> 2000 kPa), there was no notable difference in the water retention capacity between mixtures and untreated soil. In the low suction range (< 100 kPa), the water retention capacity of mixtures was higher than that of the untreated soil. In the medium suction range (100 kPa – 2000 kPa), the scatter of the results was similar for mixtures and soil. The observed scatter could be a consequence of WP4-T device accuracy, which is declared to be ± 10 kPa for the suctions below 1000 kPa and/or reflect the influence of SCs. Higher efficacy of XG in low suction ranges has been confirmed also by previous studies. (Wang et al., 2023) found out that the improvement in water retention of silty soil was the highest in the suctions up to 100 kPa, while at suctions higher than 10000 kPa, the effect of XG was negligible.

The observed differences in the position of SWRCs of mixtures in the range of suction up to 100 kPa indicate the influence of the SC type. The SWRCs of the mixtures with high dosage of SC_R and SC_ZZC are the highest, while the mixture with high dosage of SC_CG is close to the SWRC of the mixture with low dosage of SC_R. As shown in Figure 11, two independent investigations were performed to determine the SWRC for the mixture with SC_R H, which is depicted in detail within the black rectangle in Figure 11. Although the mixtures were prepared in two replicates and tests were performed with different tensiometers and Hyprop devices, the results are in good agreement.

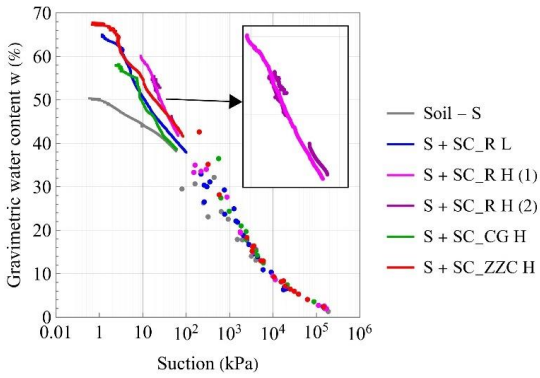


Figure 11. SWRC for untreated soil and mixtures

4. CONCLUSIONS

The study investigated the influence of newly developed XG based SCs on the drained shear strength and hydraulic properties of forest soil from the Alpine region of Slovenia. The SCs differ from each other in the properties of the fillers within the XG matrix.

The study acknowledged the importance of the type of SC, especially in relation to the length of the cellulose fibers. The main conclusions can be summarized as follows:

- In saturated conditions, the effective cohesion and friction angle of mixtures decreased compared to untreated soil, except for the low dosage of SC_R, whose mixture had higher effective cohesion than untreated soil. Among the high dosage mixtures, SC_CG with the longest fibers showed the highest effective friction angle. It has been shown that dosage of the SCs is more important than type of the SC.

- The addition of a high dosage of SCs strongly increased the water absorption capacity compared to untreated soil. The low dosage mixture had a comparable water absorption capacity to untreated soil.
- Due to the gel-like texture of the SCs in wet state, their addition to the soil resulted in a decrease in saturated hydraulic conductivity. The decrease was greater in mixtures with high dosage of SC_R than with low dosage. The mixture with SC_CG exhibited in the highest hydraulic conductivity among the high dosage mixtures.
- The water retention ability was notably increased by the addition of all types of SCs in the range of low suctions (< 100 kPa). The increase depends on the amount of SC added. In the case of a high dosage of SCs, the SWRC of the mixture with SC_CG H was lower than the SWRC of the other high dosage mixtures.

The results confirmed the influence of SC dosage on the drained shear strength and the hydraulic properties of the soils. The impact of SC_CG slightly differed from SC_R and SC_ZZC at the same dosages, indicating the importance of cellulose fiber length.
The authenticity of the results was confirmed by a repeatability check for all investigations. However, it should be noted, that the type of soil treated may also be a crucial factor in validating the influence of SC on drained shear strength and hydraulic properties.

5. ACKNOWLEDGEMENTS

The authors acknowledge the funding provided by the European Union's Horizon 2020 Research and Innovation Program within the project ONEForest: A Multi-Criteria Decision Support System for A Common Forest Management to Strengthen Forest Resilience, Harmonise Stakeholder Interests and Ensure Sustainable Wood Flows (Grant Agreement No 101000406).

REFERENCES

Anandha Kumar, S. and Sujatha, E. R. 2022. Assessing the potential of xanthan gum to modify in-situ soil as baseliners for landfills. *International Journal of Environmental Science and Technology*, **19**(11), 10613–10624. https://doi.org/10.1007/s13762-021-03721-4

Cabalar, A. F., Awraheem, M. H. and Khalaf, M. M. 2018. Geotechnical Properties of a Low-Plasticity Clay with Biopolymer. *Journal of Materials in Civil Engineering*, **30**(8), 04018170. https://doi.org/10.1061/(ASCE)MT.1943-5533.0002380

CESEFOR. 2021. ONEforest project web page. https://www.oneforest.eu/content/project (accessed 2024-10-03)

Chen, C., Wu, L. and Harbottle, M. 2020. Exploring the effect of biopolymers in near-surface soils using xanthan gum–modified sand under shear. *Canadian Geotechnical Journal*, **57**(8), 1109–1118. https://doi.org/10.1139/cgj-2019-0284

El-Saied, H., Waley, A. I., Basta, A. H. and El-Hadi, O. 2004. High Water Absorbents from Lignocelluloses. II. Novel Soil Conditioners for Sandy Soil from Lignocellulosic Wastes. *Polymer-Plastics Technology and Engineering*, **43**(3), 779–795. https://doi.org/10.1081/PPT-120038064

Kwon, Y.-M., Chang, I., Lee, M. and Cho, G.-C. 2019. Geotechnical engineering behavior of biopolymer-treated soft marine soil. *Geomechanics and Engineering*, **17**(5), 453–464. https://doi.org/10.12989/GAE.2019.17.5.453

Lee, M., Chang, I. and Cho, G.-C. 2023a. Advanced Biopolymer–Based Soil Strengthening Binder with Trivalent Chromium–Xanthan Gum Crosslinking for Wet Strength and Durability Enhancement. *Journal of Materials in Civil Engineering*, **35**(10), 04023360. https://doi.org/10.1061/JMCEE7.MTENG-16123

Lee, M., Chang, I., Park, D.-Y. and Cho, G.-C. 2023b. Strengthening and permeability control in sand using Cr3+-crosslinked xanthan gum biopolymer treatment. *Transportation Geotechnics*, **43**, 101122. https://doi.org/10.1016/j.trgeo.2023.101122

Maček, M., Smolar, J. and Petkovšek, A. 2013. Extension of measurement range of dew-point potentiometer and evaporation method. https://www.cfms-sols.org/sites/default/files/Actes/1137-1142.pdf

Mendonça, A., Morais, P. V., Pires, A. C., Chung, A. P. and Oliveira, P. V. 2020. A Review on the Importance of Microbial Biopolymers Such as Xanthan Gum to Improve Soil Properties. *Applied Sciences*, **11**(1), 170. https://doi.org/10.3390/app11010170

Oliveira, P. J. V. and Reis, M. J. F. C. C. 2023. Effect of the Organic Matter Content on the Mechanical Properties of Soils Stabilized with Xanthan Gum. *Applied Sciences*, **13**(8), 4787. https://doi.org/10.3390/app13084787

Pan, S. and Ragauskas, A. J. 2012. Preparation of superabsorbent cellulosic hydrogels. *Carbohydrate Polymers*, **87**(2), 1410–1418. https://doi.org/10.1016/j.carbpol.2011.09.031

Peters, A. and Durner, W. 2008. Simplified evaporation method for determining soil hydraulic properties. *Journal of Hydrology*, **356**(1–2), 147–162. https://doi.org/10.1016/j.jhydrol.2008.04.016

Singh, S. P. and Das, R. 2020. Geo-engineering properties of expansive soil treated with xanthan gum biopolymer. *Geomechanics and Geoengineering*, **15**(2), 107–122. https://doi.org/10.1080/17486025.2019.1632495

Soldo, A. and Miletić, M. 2019. Study on Shear Strength of Xanthan Gum-Amended Soil. *Sustainability*, **11**(21), 6142. https://doi.org/10.3390/su11216142

Sorze, A., Valentini, F., Dorigato, A. and Pegoretti, A. 2023a. Development of a Xanthan Gum Based Superabsorbent and Water Retaining Composites for Agricultural and Forestry Applications. *Molecules*, **28**(4), 1952. https://doi.org/10.3390/molecules28041952

Sorze, A., Valentini, F., Smolar, J., Logar, J., Pegoretti, A. and Dorigato, A. 2023b. Effect of Different Cellulose Fillers on the Properties of Xanthan-Based Composites for Soil Conditioning Applications. *Materials*, **16**(23), 7285. https://doi.org/10.3390/ma16237285

Thakur, P., Shubham, H. W. and Kaushal, S. 2023. Soil Conditioners: Refinement of Soil Health for Better Tomorrow. *Current Journal of Applied Science and Technology*, **42**(42), 1–9. https://doi.org/10.9734/cjast/2023/v42i424268

Tran, T. P. A., Cho, G. C., Lee, S. J. and Chang, I. 2018. Effect of xanthan gum biopolymer on the water retention characteristics of unsaturated sand.

Wang, S., Zhao, X., Zhang, J., Jiang, T., Wang, S., Zhao, J., et al. 2023. Water retention characteristics and vegetation growth of biopolymer-treated silt soils. *Soil and Tillage Research*, **225**, 105544. https://doi.org/10.1016/j.still.2022.105544

WP4 Operator's manual. 2003. WP4 Operator's manual. file:///C:/Users/bfortuna/Downloads/wp4t.pdf

Yangyuoru, M., Boateng, E., Adiku, S., Acquah, D., Adjadeh, T. and Mawunya, F. 2009. Effects of natural and synthetic soil conditioners on soil moisture retention and maize yield. *West African Journal of Applied Ecology*, **9**(1). https://doi.org/10.4314/wajae.v9i1.45676

Zhang, J., Liu, J., Cheng, Y., Jiang, T., Sun, D. and Saberian, M. 2023. Water-retention behaviour and microscopic analysis of two biopolymer-improved sandy soils. *Construction and Building Materials*, **403**, 133202. https://doi.org/10.1016/j.conbuildmat.2023.133202

28th European Young Geotechnical Engineers Conference – EYGEC 2024
© 2024 Macedonian Association for Geotechnics, ISBN 978-608-4510-61-1

Kinematic effects on Interaction Diagrams for Caisson Foundations

Domenico Gaudio[a], Cristian Passeri[b], Sebastiano Rampello[c]

[a] *Sapienza University of Rome, Department of Structural and Geotechnical Engineering, via Eudossiana 18, 00184, Rome, Italy*

ABSTRACT

Caisson foundations are typically designed against combined loading since they are usually adopted for long-span bridges and viaducts. Their capacity can be usefully expressed in terms of Interaction Diagrams (IDs), which represent the *locus* of the generalised forces (*N*-*Q*-*M*) bringing the soil-caisson system to limit conditions. Caisson IDs have been recently proposed for static conditions only, meaning that the limit generalised forces were computed assuming no inertial forces acting within the foundation soils. However, it is worth investigating whether these inertial forces may bring to a reduction of the system resistance, what is usually referred to as *kinematic effect*.

In this paper, the *kinematic effects* on the IDs for caisson foundations are assessed from the results of a parametric study, where 3D Finite Element pushover analyses were performed. A pseudo-static approach was followed, which implies that the inertial forces within the soil deposit were proportional to the self-weight of the soil via the seismic coefficient, k_h, which was assumed as constant and uniform over the calculation. The parametric study involved different caisson slenderness ratios, H/D, and initial loading factors, χ, the latter representing the degree of mobilisation of the soil-caisson strength against vertical loading before the earthquake: nonetheless, here only the results obtained with the values $H/D = 1$ and $\chi = 0.21$ are discussed, for the sake of space.

An analytical formulation of the IDs taking *kinematic effects* into account is finally provided, which may be adopted in the seismic design of caisson foundations.

KEYWORDS

Caisson foundation; Interaction Diagram; Kinematic effects; Pseudo-Static approach.

1. INTRODUCTION

Massive and rigid onshore caisson foundations are becoming increasingly popular over the years, due to the increasing span length of bridges and viaducts. Under these circumstances, loading conditions are becoming increasingly challenging indeed, due to the increase of inclination and eccentricity of loads acting atop the foundation. At the same time, safety requirements are getting stricter, particularly in the seismic design of Critical Infrastructures (CIs), which may be attributed to the higher level of performance needed to ensure their operation during and after the occurrence of destructive earthquakes.

From the foregoing it follows that the bearing capacity of soil-caisson systems is to be estimated carefully. Therefore, their resistance has increasingly been evaluated via Interaction Diagrams (IDs), which represent the *locus* of the generalised forces (*N*-*Q*-*M*) bringing the soil-caisson system to limit conditions. In seismic-prone areas, the detrimental effect of the inertial forces acting within the soil deposit, usually referred to as *kinematic effects*, should be considered in the design of caisson foundations. However, caisson IDs have only been proposed for static conditions so far (Gerolymos *et al*., 2015; Zafeirakos and Gerolymos, 2016; Rosati *et al*., 2023).

In this paper, the *kinematic effects* on caisson IDs are first evaluated from the results of 3D pushover analyses performed with the Finite Element (FE) method. In the analyses, a pseudo-static approach was followed to simulate the inertial forces acting within the soil deposit. The results obtained for a slenderness ratio $H/D = 1$ and an initial loading factor $\chi = 0.21$ are only discussed in this paper, for the sake of space, despite additional values were also considered in the parametric study, such as $H/D = 0.5$ and 2 and $\chi = 0, 0.42$. An analytical formulation of the IDs taking *kinematic effects* into account is finally given.

2. PROBLEM LAYOUT

The problem layout is given in Fig. 1: a caisson with a diameter D equal to its height H (= 12 m, $H/D = 1$), is embedded in a 5-m-thick gravelly sand layer over a 55-m-thick, slightly overconsolidated, silty clay stratum. The water table is located at the sand-clay contact and the pore pressure regime is hydrostatic. The Load Reference Point (LRP) was assumed at the caisson centroid, whereto the generalised forces *N*-*Q*-*M*, and displacements *w*, *u* and θ, are referred hereafter.

Fig. 1 also shows the profiles adopted in the Finite Element (FE) analyses both for the OverConsolidation Ratio, *OCR*, and the small-strain shear modulus, G_0, the latter calibrated against the theoretical profile proposed by Hardin and Richart (1963) for the gravelly sand layer (relative density $D_R = 60\%$) and Rampello *et al*. (1995) for the silty clay (plasticity index $PI = 25\%$). The mechanical parameters adopted in the analyses are given in Tab. 1, where γ is the unit weight, ν is the Poisson ratio, c' and φ' are the effective cohesion and internal friction angle, and ψ is the dilatancy angle.

Table 1. Soil mechanical parameters

soil	γ (kN/m^3)	ν (-)	c' (kPa)	φ′ (°)	ψ
sand	20	0.2	0	30	0
clay	20	0.2	20	23	0

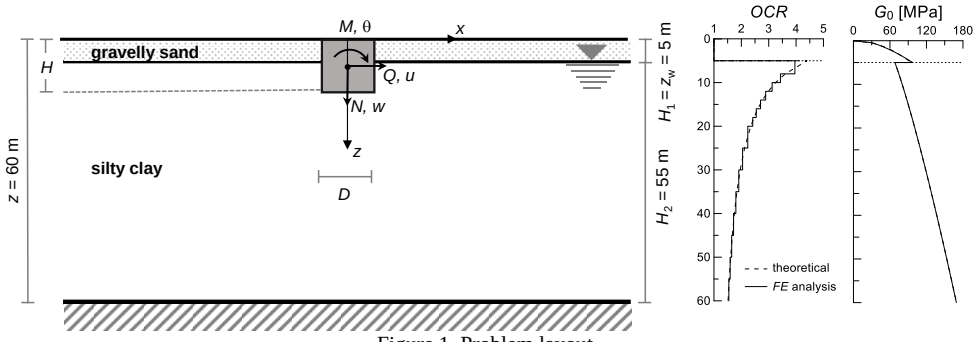


Figure 1. Problem layout

3. 3D FINITE ELEMENT MODELLING

The 3D FE mesh in Fig. 2 consists of 95500 10-node tetrahedral elements with 4 Gauss points (Bentley, 2021): this numerical domain was adopted to perform the pushover (*i.e*., static nonlinear) analyses bringing the soil-caisson systems to limit conditions, as detailed below. Since the generalised forces applied to the caisson belong to the *x*-*z* plane, only half of the domain was considered. The bottom of the numerical model was fixed both against horizontal and vertical displacements ($u_x = u_y = u_z = 0$), whereas the horizontal displacements only were fixed along the vertical boundaries (either $u_x = 0$ or $u_y = 0$); the ground surface was left free to move. Preliminary analyses ensured that the presence of the outer boundaries did not alter the response of the soil-caisson systems (Gaudio *et al*., 2024).

The clay stratum was subdivided into fifteen sublayers to reproduce the analytical profiles of *OCR*, which provided the stepwise profile plotted in Fig. 1. The mechanical soil behaviour was described with the *Hardening Soil with Small-Strain stiffness* model (*HSsmall*; Benz *et al*., 2009) and a Mohr-Coulomb failure criterion (Tab. 2).

Table 2. *HSsmall* parameters

soil	G_0^{ref} (MPa)	m (-)	$\gamma_{0.7}$ (%)	$E'_{ur}{}^{ref}$ (MPa)	ν_{ur} (-)	$E'_{50}{}^{ref}$(MPa)	$E'_{oed}{}^{ref}$ (MPa)
sand	145.7	0.61	0.024	174.9	0.2	58.3	58.3
clay	65.7	0.75	0.045	58.2	0.2	19.4	19.4

The mechanical behaviour of the caisson foundation was simulated with a non-porous elastic material, characterised by the concrete Young modulus, E_c = 30 GPa, and a Poisson ratio ν_c = 0.15, while its weight was reproduced via a vertical force applied atop the caisson rather than with imposing the unit weight, in order not to induce any pseudo-static force into the caisson. Purely attritive interface elements were assigned to the soil-caisson contact to simulate any relative sliding, with a reduced friction angle, $\delta = \tan^{-1}[2/3 \cdot \tan\varphi']$.

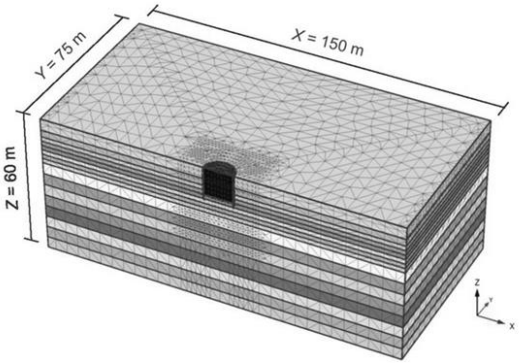


Figure 2. 3D FE model adopted in the parametric study

In the parametric study, the wished-in-place caisson was first subjected, in drained conditions, to a vertical load *N*. The value of *N* was determined to provide specific values of the initial loading factor, here defined as the inverse of the static safety factor under vertical loading only, $\chi = 1/F_{Sv}$. Then, the entire numerical domain which had been previously assigned a unit weight (*i.e.*, the soil deposit) was subjected to a field of uniform horizontal body forces, proportional to the pseudo-static coefficient k_h: in this phase, undrained conditions were adopted, to mimic what typically observed during seismic shaking for soil deposits such as the one at hand. Finally, a horizontal force *Q* and a moment *M* were applied to the caisson until limit conditions were reached, by keeping the pseudo-static coefficient k_h on. The generalised loads were applied with a ratio $\alpha_G = M_G/Q_G$, where the subscript G indicates that the generalised forces were referred to the caisson centroid (LRP).

The ID obtained for the specific case H/D = 1, χ = 0.21, and k_h = -0.2, is plotted in Fig. 3a (sign convention for k_h is also provided in the Figure). The ID was computed considering two distinct criteria to detect the ultimate conditions of the soil-caisson system, such as the proper triggering of bearing capacity under inclined and eccentric loading conditions (*plateau* in the legend) and the attainment of a global stiffness *K* equal to 1% of the unstressed, initial stiffness, K_0, as first proposed by Zafeirakos and Gerolymos (2016). Both criteria are defined based on the non-dimensional pushover curve $\bar{F}$-$\bar{u}$, where $\bar{F}$ and $\bar{u}$ are:

$$\bar{F} = \sqrt{\xi^2 + \mu^2};\ \bar{u} = \sqrt{\left(\frac{u_G}{D}\right)^2 + \theta^2} \tag{1}$$

where ξ and μ are the non-dimensional horizontal force and moment, respectively, defined as

$$\xi = \frac{Q}{N_{lim,net}};\ \mu = \frac{M}{D \cdot N_{lim,net}} \tag{2}$$

with $N_{lim,\,net}$ being the limit vertical load computed in drained conditions, while u_G and θ are the caisson horizontal displacement and rotation at the caisson centroid, respectively.

The pushover curve obtained for the specific value α_G = -6 m is plotted in Fig. 3b, whose *plateau* is reached for excessive caisson displacements. Hence, the ultimate conditions along this pushover curve were detected imposing the criterion $K/K_0 = 1$ %, where $K = \Delta\bar{F}/\Delta\bar{u}$. The remarkable outcome stemming from the comparison of the IDs computed with the two criteria is that they are homothetic, which implies that the tangent criterion can be adopted as a displacement-based criterion for detecting ultimate conditions for caisson foundations.

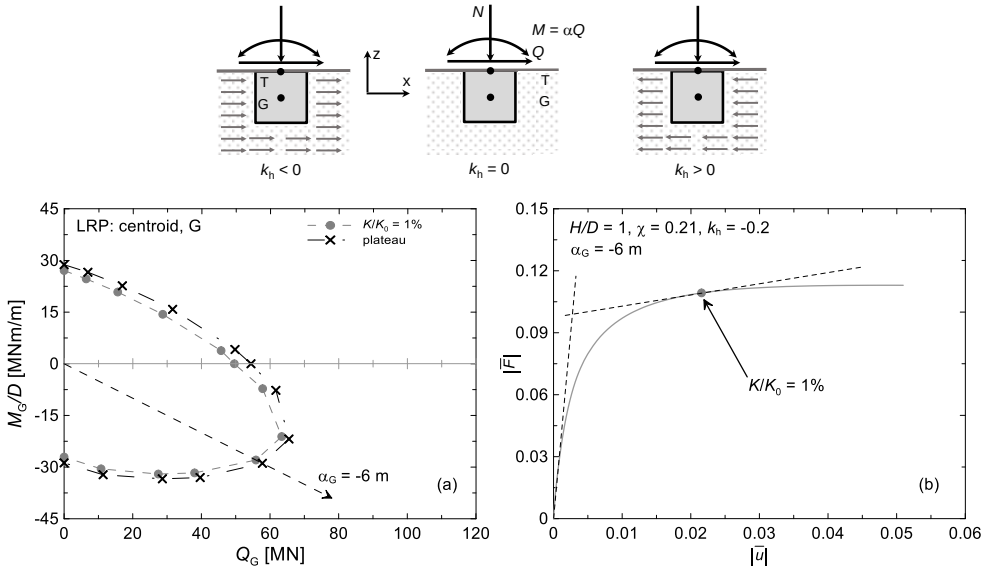


Figure 3. (a) ID from different criteria; (b) dimensionless pushover curve obtained for α_G = -6 m

4. KINEMATIC EFFECTS

The kinematic effects obtained for the specific case of a caisson with H/D = 1 subjected to an initial loading factor χ = 0.21 are represented in Fig. 4, for all values of the horizontal seismic coefficient k_h considered in the parametric study (0, ± 0.10, ± 0.15, and ± 0.20), representative of a small-to-medium intensity seismic events. The IDs are plotted through dimensional (Fig. 4a) and non-dimensional (Fig. 4b) representations, where the former exhibits the influence of k_h on the ID size, whereas the latter reveals the role of kinematic effects on the ID shape (Q_u and M_u represent the limit values of Q and M when the other component is null: $Q_u = Q_{(M=0)}$ and $M_u = M_{(Q=0)}$).

It is apparent that the ID size (Fig. 4a) is influenced by the seismic coefficient k_h, with an ID shrinkage for $k_h < 0$, which can be ascribed to the soil inertial forces acting along the same direction as Q. Indeed, these forces add to the load already coming from the superstructure, whereas the opposite is observed for $k_h > 0$, where the inertial forces counteract Q. This holds true particularly in the fourth quadrant, where the overstrength of the soil-caisson system is exhibited, whereas the limit overturning moment is almost insensitive to k_h. Similarly, the ID shape turned out not to be affected by the kinematic effects

(Fig. 4b), which would strongly simplify the analytical derivation of caisson IDs for seismic conditions, as shown in the following.

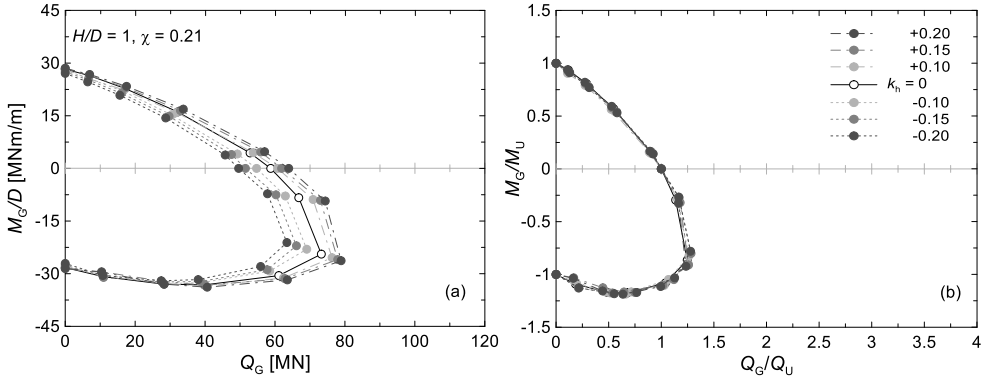


Figure 4. Kinematic effects on the ID: (a) size; (b) shape (H/D = 1, χ = 0.21)

5. ANALYTICAL RELATIONSHIPS FOR IDS ACCOUNTING FOR THE KINEMATIC EFFECTS

The numerical results were fitted in the non-dimensional space χ-ξ-μ by adopting the following implicit functional form to describe the 3D surface, after Butterfield and Gottardi (1994):

$$\left(\frac{\cos^2\omega}{a_\xi^2}+\frac{\sin^2\omega}{a_\mu^2}\right)\xi^2+\left(\frac{\sin^2\omega}{a_\xi^2}+\frac{\cos^2\omega}{a_\mu^2}\right)\mu^2+\sin 2\omega\left(\frac{1}{a_\xi^2}-\frac{1}{a_\mu^2}\right)\xi\mu=1 \quad (3)$$

where a_ξ and a_μ are the semi-axes of the ellipse in the ξ-μ plane and ω is its counterclockwise angle of inclination measured starting from the ξ axis. These geometrical parameters express the 3D surface enclosing the dependency of both the ID size and shape on the slenderness ratio, H/D, the initial loading factor, χ, and the horizontal seismic coefficient, k_h. For the sake of brevity, the relevant functional forms are not reported here, but the values attained for the specific cases under consideration are reported instead (H/D = 1, χ = 0.21), namely a_ξ = 0.142, a_μ = 0.047 and ω = -15.082° for k_h = + 0.2 and a_ξ = 0.110, a_μ = 0.045, and ω = -19.518° for k_h = -0.2. The comparison between the FE and the analytical ID is given in Fig. 5, where the static ID (k_h = 0) is also plotted: the ID expansion and shrinkage with respect to the static conditions is well reproduced. More details on this are discussed in Gaudio *et al*. (2024).

6. CONCLUDING REMARKS

In this paper, IDs for caisson foundations were computed from an extensive parametric study where 3D FE pushover analyses were conducted in undrained conditions, until limit conditions were attained for the soil-caisson system. In the analyses, the inertia forces developing into the soil deposit during seismic shakings were simulated following a pseudo-static approach, thus being proportional to the unit weight of the soil through the seismic coefficient k_h. A general, displacement-based criterion to detect the limit load was adopted, which consisted in a reduction of the global soil-caisson stiffness up to 1% of the unstressed one. The results of the parametric study clearly showed that kinematic effects may significantly alter the ID size with respect to the reference static conditions (k_h = 0), making the ID expand or shrink, while almost keeping the static ID shape. Analytical equations were finally proposed for a preliminary design of caisson foundations under seismic shaking, enclosing kinematic effects.

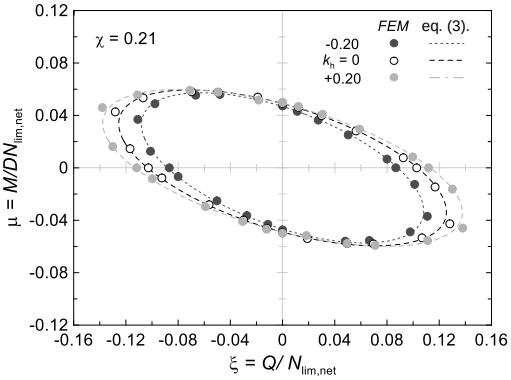


Figure 5. FE and analytical IDs computed for H/D =1, χ = 0.21, and k_h = 0, ± 0.2

7. ACKNOWLEDGEMENTS

The Authors would like to express their sincere gratitude to Prof. Claudio di Prisco for his useful comments and suggestions. The help provided by Dr. Alessandra Rosati is also acknowledged.

REFERENCES

Bentley. 2021. *Plaxis 3D CE Reference Manuals*.

Benz, T., Vermeer, P. A. and Schwab, R. 2009. A small-strain overlay model. *Int. J. Numer. Anal. Meth. Geomech.*, 33(1), 25–44.

Butterfield, R. and Gottardi, G. 1994. A complete three-dimensional failure envelope for shallow footings on sand. *Géotechnique*, 44(1), 181-184.

Gaudio, D., Passeri, C. and Rampello, S. 2024. Interaction domains for caisson foundations under seismic loading. *Computers & Geotechnics (submitted for evaluation)*

Gerolymos, N., Zafeirakos, A, and Karapiperis, K. 2015 Generalized failure envelope for caisson foundations in cohesive soil: Static and dynamic loading. *Soil Dyn. Earthq. Eng.*, 78, 154-174.

Hardin, B. O., Richart, F. E. 1963. Elastic wave velocities in granular soils. *J. Soil. Mech. Found. Div*., 89, 33-65.

Rampello, S., Viggiani, G. M. B. and Silvestri, F. 1995. The dependence of G0 on stress state and history in cohesive soils. In: *Shibuya S et al. (ed) Pre-Failure Deformation Characteristics of Geomaterials – Measurements and application*. Balkema A.A., Rotterdam, Brookfield, Sapporo, vol 2, pp 1155-1160.

Rosati, A., Gaudio, D., di Prisco, C. G., Rampello, S. 2023. Use of interaction domains for a displacement-based design of caisson foundations. *Acta Geotechnica*, 18(1), 445-468. DOI: 10.1007/s11440-022-01547-z

Zafeirakos, A. and Gerolymos, N. 2016. Bearing strength surface for bridge caisson foundations in frictional soil under combined loading. *Acta Geotechnica*, 11(5), 1189-1208.

28th European Young Geotechnical Engineers Conference – EYGEC 2024
© 2024 Macedonian Association for Geotechnics, ISBN 978-608-4510-61-1

Automated simple tell-tale device for detecting loss of backfill soil through joints of quays

Carlos Laina-Gómez[a] & Enrique Asanza-Izquierdo[a]

[a] *Laboratorio de Geotecnia, Centro de Estudios y Experimentación de Obras Públicas (CEDEX), Madrid, Spain*

ABSTRACT

Unlike most hydraulic structures, quays withstand high, bidirectional, and highly changing gradients. Thus, since discontinuities (joints in the former and gaps in the latter) are unavoidable when quays are engineered as concrete diaphragm walls or alignments of caissons, the backfilling soil in their vicinity is likely to be flushed out due to poor conditions of the joints at the wall face or of the sealing grout at the gaps. Soil loss may progress backward, causing eventually sinkholes on the yard pavement near the capping beam. The presence of unmapped growing cavities or "chimneys" beneath the pavement is even more hazardous for operating vehicles. The Laboratory for Geotechnics (Laboratoria de Geotecnia) (LG) at CEDEX devised the so-called "sand tell-tales": they consist of vertical short pipes (~ 1m long) refillable with clean medium-size sand, located halfway in potential erosion pathways, which initiate start near discontinuities. This new device allows for measurement of the loss of soil produced by previous inspection, in view of detecting incipient cavities. The combined analysis of all of them along the quay alignment leads to an overall assessment of the infrastructure. The purpose of this publication is to review the most important points of this elementary and innovative monitoring system.

KEYWORDS

Backfill Soil Loss; Sand Tell-Tale Device; Automated *Ad Hoc* Device; Quay Maintenance.

1. INTRODUCTION

As a part of the commission launched by Puertos del Estado for technical assistance, applied research and technological development in the scope of the state-owned port system, the Laboratory for Geotechnics (Laboratoria de Geotecnia) (LG) at CEDEX is involved, among other issues, in the detection of incipient cavities in a quay with a 750 m berthing line, which came into service in 2005.

For more than a decade, the corresponding Port Authority has periodically recorded the sudden episodes of metric sinkholes on the pavement near the cantilever beam, even though repair work has been carried out in the past. However, as a result of increased activity on the quayside in recent years, the occurrence of sinkholes has worsened.

The presence of unmapped growing cavities or "chimneys" occur suddenly because of a gradual process of upward washing of soil due to, firstly, poor conditions of the joints at the wall face or of the sealing grout at the gaps; and, secondly, to the high, bidirectional, and highly changing gradients withstand by the quays.

Since discontinuities (joints in the former and gaps in the latter) are unavoidable when quays are engineered as concrete diaphragm walls or alignments of caissons, it is important to have a simple tell-tale device for early detecting loss of backfill soil. In this way, it would be possible to warn the

occurrence of such unmapped growth cavities under the pavement and mitigate the operational hazard of working near the cantilever beam.

2. DESCRIPTION OF STUDIED QUAY

The structure of the studied quay is a 32 m long buttressed diaphragm wall of reinforced concrete, embedded in the seabed, leaving a berthing depth at -13 m. The diaphragm wall, built inland on an auxiliary approach embankment, consists of a series of "T-shaped" modules. The "T's" are 3 m wide and long and 0.6 m thick. These elements are anchored to a conventional passive concrete diaphragm wall (0.8 m thick) by means of two steel tie bars every module. The passive diaphragm wall also serves as a foundation for the rear crane rail for containers. The general cross section is depicted in the figure presented below. The edge beam has a service gallery and two front crane rails.

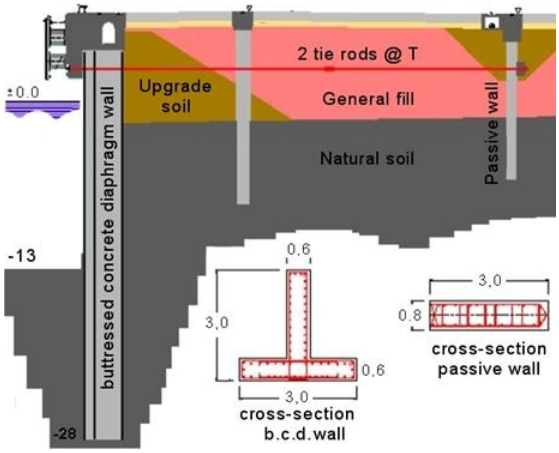


Figure 1. Cross-section of studied quay.

3. WORKS PERFORMED BY THE LABORATORIO DE GEOTECNIA AT CEDEX

To date, the LG at CEDEX has been in charge of completing a series of different tasks when collaborating with the corresponding Port Authority. Among them, gathering and analysing profuse historical documentation, during construction and subsequent reparation works, could be mentioned. Aditionally, the inspection of quays, using the Multichannel Analysis of Surface Waves (MASW) technique, geo-radar and the Panda penetration equipment (with its own staff) has also been a task performed.

Seeking for the prevention of the occurrence of backfill soil loss, the LG at CEDEX considered an essential task to detect incipient cavities. The main reason for this is that if cavities are not detected in time, water erosion can gradually conduct to backfill soil loss, producing the collapse of the corresponding zone of the quay (Figure 2), which could involve accidents with circulating vehicles. In this context, the LG at CEDEX was in charge of overseeing the "sand tell-tales" (refillable vertical pipes with medium-size sand where the loss of soil is measured), providing global assessment, together with previous inspection carried out by private companies, and, finally, a proposal for a specific inspection programme, both from surface and underwater. The following figure shows the erosion mechanism next to the edge beam.

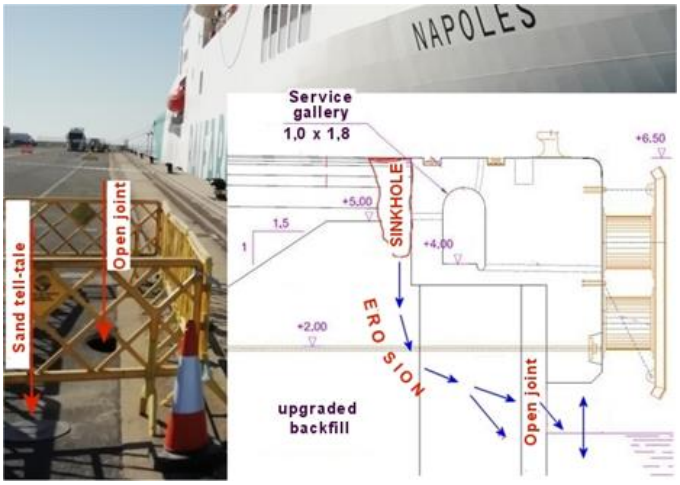


Figure 2. Erosion mechanism next to the edge beam.

4. SAND TELL-TALES DEVICES

4.1. Description

To deal with the sudden appearance of these sinkholes, in order to anticipate repair work and focus human and material resources on the most hazardous points along the 750 m berthing line of the quay, the LG at CEDEX designed the so-called “sand tell-tales” devices.

As it is shown in Figure 3, the sand tell-tale devices developed consist of short vertical tubes ~1 m long and 4" in diameter, refillable with clean medium-size sand, located halfway in potential erosion pathways, which are triggered in zones near discontinuities. Specifically, they are placed every 6 m on the pavement of the backside, at a distance of around 50 cm from capping beam (coinciding with a joint of the wall face in cross-section).

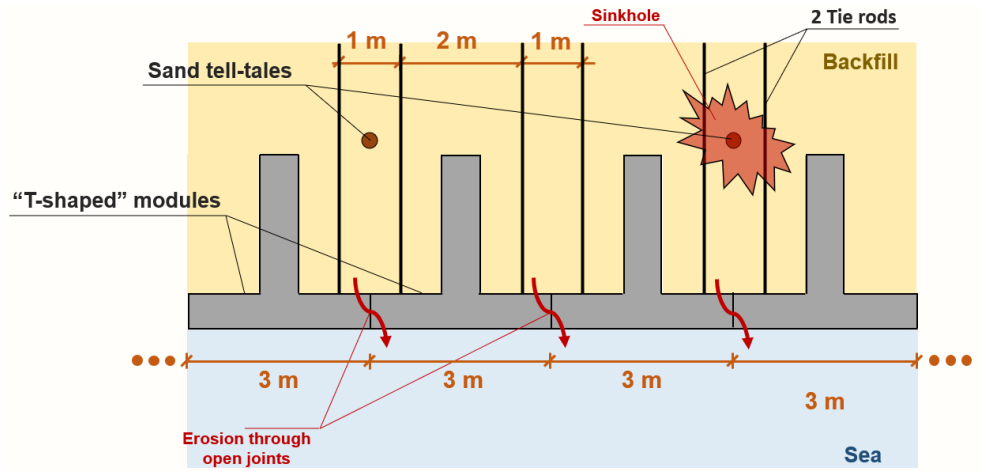


Figure 3. Detail of "T-shaped" modules of buttressed diaphragm wall and sand tell-tales devices in view of detecting incipient cavities.

The newly developed device allows the measurement of the loss of soil produced by consecutive inspections (two or three times a month), with the aim of detecting incipient cavities. The combined analysis of them all along the quay alignment leads to an overall assessment of the infrastructure. Details of a sand tell-tales device are shown in Figure 4.

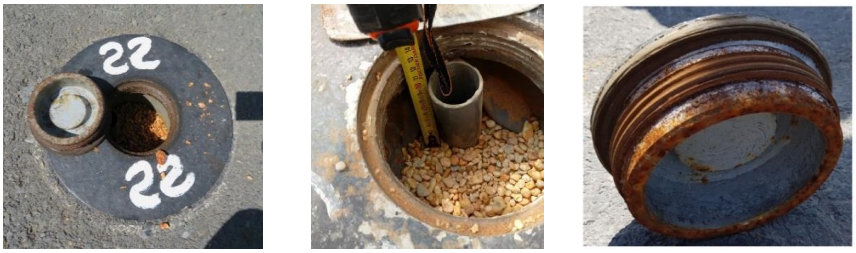


Figure 4. Details of a sand tell-tales device.

4.2. Weaknesses and strengths of this *ad hoc* site investigation

Although the system is highly regarded for its utility, it falls upon conscientious workers to report soil erosion several times a month, the physical phenomenon of washing soil through the open joints occurs suddenly, and sometimes even faster than the time it takes to collect, store, process the data obtained into sand tell-tales devices and to make decisions. Consequently, it is very difficult to anticipate the repair works before the sinkhole occurs.

Motivated by the weaknesses observed in the *ad hoc* site investigation system designed, two improvements were implemented. On the one hand, a web form was designed and implemented associated with each sand tell-tales device and accessible via a QR code, thus facilitating the task of reading and automatically storing the data in real time, as well as its subsequent processing, analysis and graph export of the results and trends, minimising the time interval between data acquisition and decision-making (Figure 5).



Figure 5. App web accessible via-QR code.

On the other hand, due to the impossibility of carrying out very frequent data acquisition due to the existing human resources and the high activity level in the quay, this system will be complemented with the introduction of microprocessors with low-cost sensors in the most critical sand tell-tales devices (Figure 6). In this way, it will be possible to provide continuous records of the soil loss by Time of Flight (ToF) technology.

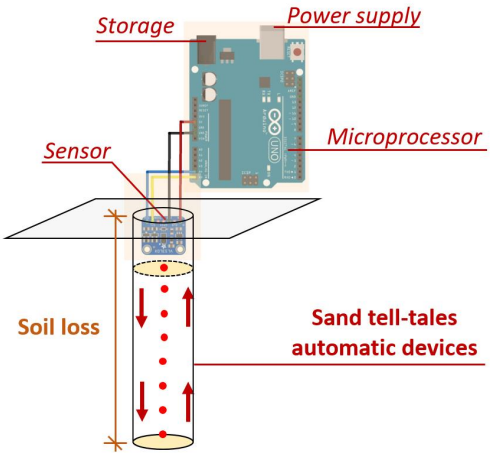


Figure 6. Sand tell-tales automatic devices.

The final product will allow the implementation of an early warning system on any mobile device of the Port Authority (Figure 7).

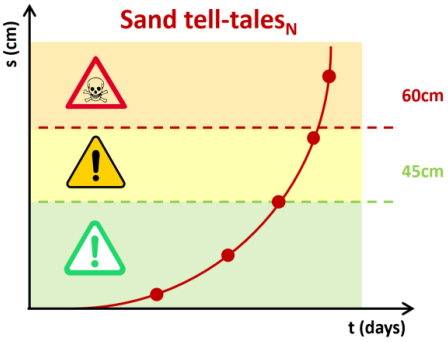


Figure 7. Real-time decision-taking tool.

5. CONCLUSIONS

Puertos del Estado is constantly recording the occurrence of sinkholes in quays belonging to different Ports along Spain, being this a common produced abnormality. Despite this fact, during the past few years, these type of irregularities have become more and more frequent, due to the increase produced in the activity developed in the quays. Considering that the occurrence of sinkholes could be prevented, it is of great importance their early detection, and further automatic treatment. In this context, the main objective of the presented research is to minimize the time between data collection in the field, its analysis and processing by a third party, and the decision-making by the infrastructure manager.

Bearing in mind which the main problematic was, an automated *ad hoc* device was proposed. The mentioned equipment consisted of two main parts. The first one, a sand tell-tale gadget, representing this the element in charge of indicating the occurrence of the backfill soil loss, provided of low-cost microprocessors, constantly recording lectures. The second part, consisted of a web form, which could be accessed through a QR code characterizing each sand tell-tale, in charge of showing the real-time data stored by the mentioned microprocessor.

The automated developed equipment has shown to be an all-in-all low-cost solution for preventing unmapped growing cavities in the port quays pavement, avoiding in this way, possible accidents. This fact is supported by the idea that the data acquisition is made in real time, being possible not only to get direct access to it with just having a mobile device, but also to make an instantaneous analysis of the results and consequent decision-making on how to proceed if needed.

6. ACKNOWLEDGEMENTS

The principal author would like to acknowledge the LG at CEDEX, for providing the opportunity of being part of the project titled “Desarrollo de técnicas de auscultación geotécnica de estructuras costero-portuarias y de técnicas de tratamiento del terreno y su control” (“Development of new geotechnical site investigation and ground improvement techniques for coastal areas and port structures.”). The results presented in this paper were obtained in the framework of a Research and Development employment contract.

REFERENCES

Asanza-Izquierdo, E. 2019. Revisión histórica de estudios y actuaciones geotécnicas realizados en el Muelle Sur del Puerto de Huelva (2004-2018). *Informe Técnico N° 5 para Puertos del Estado del Laboratorio de Geotecnia*, Madrid, España.

Laina-Gómez, C. 2022. Desarrollo y control de técnicas de auscultación geotécnicas, económicas y sostenibles, para estructuras costero-portuarias. *Jornadas I+D+i CEDEX 2022*, Madrid, España.

Laina-Gómez, C. 2024. Desarrollo y control de técnicas de auscultación geotécnicas, económicas y sostenibles, para estructuras costero-portuarias. *Memoria I+D+i CEDEX 2024*, Madrid, España.

28th European Young Geotechnical Engineers Conference – EYGEC 2024
© 2024 Macedonian Association for Geotechnics, ISBN 978-608-4510-61-1

Direct and alternative methods for determining the maximum shear modulus (G_0) of soils

Kristina Ilievaa

[a] *PhD student at University of Architecture, Civil Engineering and Geodesy, Sofia, Bulgaria*

ABSTRACT

In the recent years a complex soil modelling has been already established in the engineering practice. New constitutive models represent non-linear soil behaviour but require many soil parameters. Some of these soil parameters can be determined with classically laboratory method. Nevertheless there are also specific ones such as maximum shear modulus (G_0), shear wave velocity (v_s), reference shear strain parameter ($\gamma_{0.7}$) which needs specific methods for determination. Cross hole seismic, down hole seismic and geophysical methods are in-situ tests that are dependent on the availability of personnel, equipment and atmospheric conditions. They are very expensive and are not appropriate for soil investigation of residential buildings. In laboratory these specific parameters can be obtained by triaxial bender test and resonant column, but they are not widespread, and require technological time. In most cases the price is also the driving force. The increasing use of complicated computer methods, impose the search for methods that can easily, directly and cheaply obtain the specific parameters, listed above. This article summarizes most used and known laboratory and in-situ methods. They are compared by price, duration, equipment, atmospheric conditions. The article also focuses on describing of alternative methods that offer easier determination of the specific parameters or obtain sufficient information for their indirect determination in laboratory conditions with the use of standard soil testing equipment.

KEYWORDS

Initial Shear Modulus; Maximal Shear Modulus; Small Strain Stiffness; Laboratory Tests

1. INTRODUCTION

With the development of computer technologies in engineering practice (Tsvetkova and Kerenchev, 2020), more complex constitutive model, such as Hardening soil model, Hardening soil model with small strain stiffness (Obrzud and Truty, 2018; Mihova and Tanev, 2015) and etc., become usable. These models determine the nonlinear soil behaviour and take into account the soil stiffness at small and very small strains (Benz, 2007; Schanz and Vermeer, 1999). The result obtained from them, in the form of deformations, stresses or interaction between structure and soil (Ilieva, 2023), are significantly closer to the actual ones (Kerenchev and Markov, 2016). For comparison, the results from classical geotechnical models differ a lot (Ilieva, 2019) (Figure 1 and Figure 2). This difference arises from the use of limit equilibrium approach or linear-elastic, perfectly plastic soil behaviour models, such as Mohr-Coulomb.

These more sophisticated models lead to improved design quality, performance of the structures and also more relevant shear forces in the structure itself. These models are still not preferred in Bulgaria because of the relative high use of the old design codes and practices. In recent years the world codes began to change and the uses of these models and the small strain stiffness will be imposed. This, along with other reasons, discussed below, lead to development of alternative methods for determining the initial shear modulus and other sophisticated parameters.

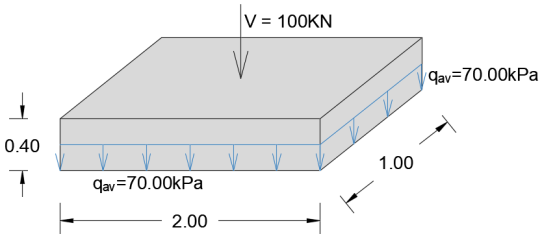


Figure 1. Geometry of investigated strip foundation

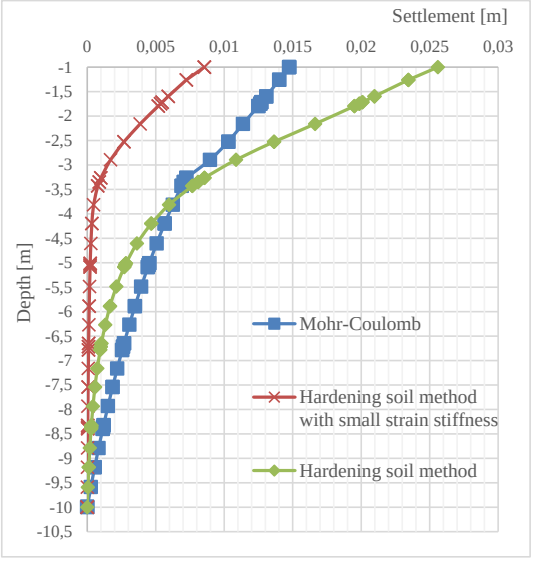


Figure 2. Comparison of deformations under a strip foundation using different constitutive models

Non-linear models require specific soil parameters, for example modulus of unloading and reloading (E_{ur}), modulus at 50% of shear strength (E_{50}), initial shear modulus (G_0) etc. See table 1 below (Mihova and Tanev, 2014). Worldwide there is a large set of non-classical laboratory methods and in-situ experiments to determine specific parameters. Most of them are expensive and require highly qualified specialists. The prices are the main reason why geotechnical engineers in Bulgaria use only correlations to find these specific parameters, (Kerenchev, 2022). Lack of expensive equipment also impose a search for new, alternative and cheaper methods for determining the specific parameters especially the initial shear modulus.

Table 1. Comparison of the soil parameters used in different constitutive models

Constitutive models	γ_n, kN/m^3	γ`, kN/m^3	ϕ, °	c, kPa	E, MPa	E_{oed}, MPa	E_{50}, MPa	G, MPa	$\gamma_{0,7}$ -
Mohr – Coulomb model	+	+	+	+	+	-	-	-	-
Hardening soil model	+	+	+	+	-	+	+	-	-
Hardening soil model with small strain stiffness	+	+	+	+	-	+	+	+	+

2. CLASSICAL TESTS TO DETERMINE THE INITIAL SHEAR MODULUS

In most cases the methods use the shear wave velocity to determine the initial shear modulus related to the soil density:

$$G_0 = E_0 = \rho_n v_s, \quad (1)$$

where ρ_n $[kN/m^3]$ is soil density and v_s $[m/s]$ is shear wave velocity.

2.1. Laboratory methods

Laboratory methods for determining the initial shear modulus are widely distributed. Resonant column test (Kerenchev, 2014) use torsion to generate waves and when the specimen resonates accelerations are measured. Local deformation transducer test (Xu and Borana, 2014) uses triaxial chamber where the specimen is placed. Additional elements are attached to the specimen to measure axial and radial small deformations. The problem with this method is that in some case local deformation transducer (LDT) can be destroyed because of very large deformations that are not in the range of the transducers. Triaxial apparatus with bender elements attached to the specimen use voltage signal to measure shear wave velocity. This method is still the most distributed among all laboratory tests.

The laboratory tests are performed in controlled environment and are not influenced by atmospheric conditions. The test duration is long, especially if specimen should be fully or partially water-saturated. The results are near to the actual ones. These tests have relative high price and in some cases specifically for Balkan region financially unaffordable. The main problem with all laboratory tests is the need of special equipment, special apparatus and also a high qualified specialist (see table 2).

Table 2. Comparison between different laboratory methods

Laboratory tests	Price	Equipment	Staff qualification	Distribution
Triaxial apparatus with bender elements	high	special non-standard additional elements	well qualified	relative widespread
Resonant column	very high	non-standard apparatus	well qualified	not widespread
Local deformation transducer	very high	non-standard apparatus	well qualified	rare

2.2. In-Situ methods

There are two categories of in-situ methods. First one includes test that determine large deformations, for example CPT, SPT, DSPT and etc. It is important to note that obtaining an initial shear modulus from them is inappropriate methodology. The second category include methods that determine small strain based on shear wave velocity propagation. There are several ways to measure it.

The well-known cross hole and down-hole seismic tests require drilling – one borehole for down-hole seismic and at least two for cross-hole test. They use the same principal - impact to generate waves and geophones for example to receive them. That`s why special equipment and high qualified specialists are needed. Terrain surface and access to the survey site is a major factor due to use of heavy mechanization and drilling techniques. It is expensive and time consuming. As a variation of the down-hole test, SCPT is adopted. It eliminates the problem with drilling. Only one transport vehicle is used but the problem of more difficult terrain remains, large particle diameters and higher depths are also an obstacle. The test is relatively cheap and gives relative correct results.

Other in-situ methods are seismic reflection and seismic refraction tests (Wuttke and Schanz, 2008). They are based on reception of refraction or reflection generated waves. Geophone or another equipment is placed on the terrain surface which receive transmitted waves that receive passed waves. To carry out these experiments, an initial study of the geological basis is necessary, especially the individual layers

thicknesses. Too thin layers may lead to test invalidity. These two methods do not require drilling works, they are not directly dependent of the terrain surface at the study site. The problem is that they are dependent on the atmospheric conditions and only rare specialists can work with the equipment.

The in-situ test that eliminates the shortcomings of the ones explained so far is the ground-based spectral analysis, also known as Spectral analysis of surface waves. In this experiment, no drilling is performed, no geological survey is necessary. It can determine the strata in depth, and this does not affect the obtained results. It is not affected by terrain. The indirect data collection and the need for additional processing to obtain the shear wave velocity can be defined as a disadvantage. This method is expensive and, like the others, depends on atmospheric conditions.

As a summary of the in-situ methods, it can be said that in some situations, they would be useful. For a complete geological survey, soil samples from boreholes must be taken and fully studied, so that`s why the cross-hole or down-hole seismic tests are more appropriate. Soil samples study allows determine of the initial shear modulus also with laboratory methods. Considering this and also the high price, most of the in-situ tests becomes meaningless for low to average level of geotechnical investment (table 3). An alternative method for down-hole seismic, but not so expensive is SCPT. This method can be used also to compare the results obtained from the laboratory analysis. In most cases it is relevant to use it for high category structures.

Table 3. Comparison between different in-situ methods

In-Situ tests	Price	Need for drilling equipment	Need for wave velocity propagation equipment	Staff qualification	Distribution
Cross-hole seismic	Very high	yes	yes	well qualified	widespread
Down-hole seismic	High	yes	yes	well qualified	widespread
SCPT	Medium high	no	yes	well qualified	widespread
Seismic reflection and seismic refraction test	High	no	yes	well qualified	not widespread
Spectral analysis	High	yes	yes	require high qualified specialists	not widespread

3. ALTERNATIVE METHODS

3.1. Correlation method

Correlations are the easiest method to determine the initial shear modulus based on soil parameters obtained from classical laboratory test. They are time proven and the results are near to actuals, but only for already well-studied soil types. Base parameter which is used for calculations of initial shear modulus in the past was the void ratio *e*. Nowadays the main parameters are water content (w_n) and Plasticity index (I_p,). The problem with such a correlation is that difference between actual water content and that obtained from the laboratory is often presented (Kerenchev, 2022). It could be caused by improper soil sampling, storage and transport. See equation 2 and equation 3 below:

$$G_0 = E_0 = AF(e)(\sigma_0^{`})^n, \tag{2}$$

where A and n are coefficients, $F(e)$ is pore coefficient function and $\sigma_0^{`}$ $[kN/m^2]$ is effective normal stress.

$$G_0 = E_0 = \frac{5150}{(0.3+5.1w^2)}(OCR)^2(\sigma_v^{`})^n \tag{3}$$

where w $[-]$ is water content, OCR $[-]$ is overconsolidation ratio and $\sigma_v^{`}$ $[kN/m^2]$ is effective stress vertical pressure.

3.2. Cameras in triaxial test

The use of cameras to determine the deformations in a soil sample placed under load in a triaxial apparatus is a new and innovative method. It requires a number of high-speed cameras with high resolution, which track the deformations in the soil sample over a short period of time. Through additional processing of the obtained images and after calibration, the very small and small deformations can be deduced with relatively high accuracy. The lack of placement of any transducers or flexures reduces the problem of their anchorage and potential failure of the soil specimen. No modification to the three-axis rig is required and the equipment can always be removed when not needed. Calibration is fast and can be done for several cameras at the same time. More about this method can be read in (Wang, Du and Lehane, 2024).

3.3. Ultrasonic sounding method

This method is based on wave velocity propagation. The compression and shear waves are generated by transducer. Another transducer receives the passes waves. This method is laboratory test to measure stabilized soils but it can also be implemented in-situ. It is very important to conserve the soil water content because this parameter is essential for determining the initial shear modulus. Worldwide this test is used to determine the dynamic soil parameters (Yesiller, Inci and Miller, 2000; Sephenson, 1978).

3.4. Determine the initial shear modulus from unloading-reloading curve

The idea of deriving the initial shear modulus from the unloading and reloading curve obtained by a standard triaxial experiment is an alternative way that allows some deviations in the results, but is significantly cheaper than those already established. This method is less time consuming to perform and other additional parameters can be extracted as well. No modification of the device is required. The test can be performed by a less qualified specialist. It is possible to experiment with both fully water-saturated and partially water-saturated soil samples (Tanev, 2015).

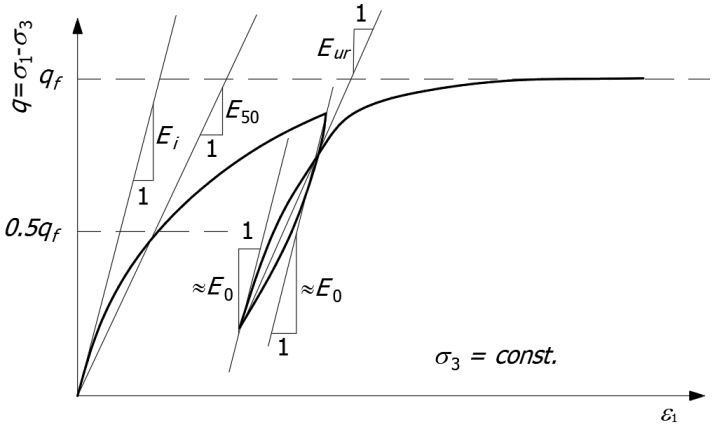


Figure 3. Unloading – reloading curve from standard triaxial test

4. DETERMINE THE INITIAL SHEAR MODULUS FROM OEDOMETER TEST

An alternative method based on scientific developments that are in the field of oedometric testing could also be proposed. The vertical deformation of the soil sample in oedometer apparatus could be determined with the help of a linear variable differential transformer. The high accuracy deformation values could be sequenced over a short period of time. The unloading curve could provide small and very small deformations as well. Precise measurement of those values can also lead to initial shear modulus assessment. See figure 4 below.

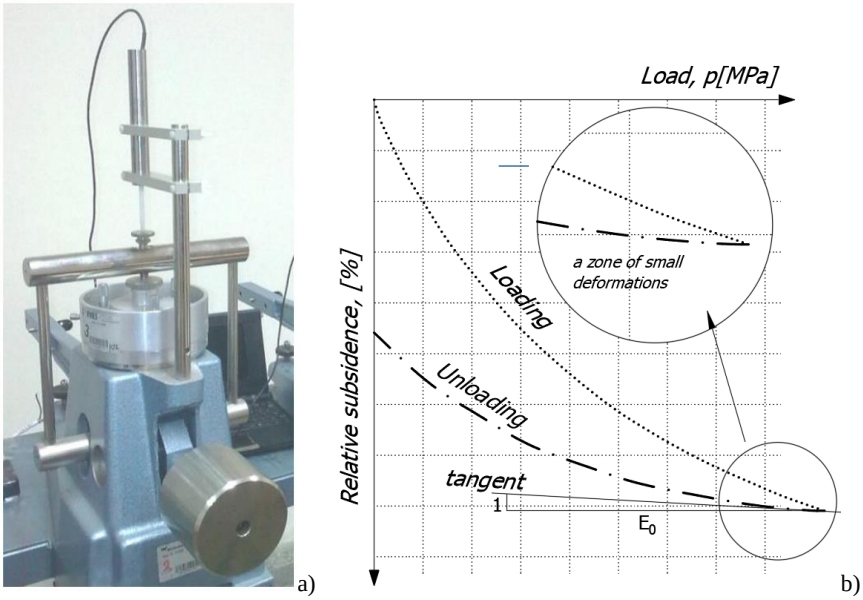


Figure 4. a) Experimental production,
b) Determine initial shear modulus from loading – unloading oedometric curve

In such an experimental procedure, an accelerometer could also be used to isolate background noise. Temperature sensor could also be placed to reduce the influence of ambient temperature fluctuations for the deformation measurement (Kerenchev, 2014).

5. CONCLUSIONS

The development of computer technology and the use of more complicated constitutive models requires a specific soil parameters to be assessed. Most of the methods are expensive, dependent of atmospheric conditions, need special equipment and highly qualified specialists. See Table 4 below:

Table 4. Comparison between different methods

Methods	Base	Price	Accuracy	Equipment	Specialists
In-Situ	Shear wave velocity	Very High	Very high	special	Highly qualified
Laboratory	Shear wave velocity or direct measurements	High	High	special	Qualified
Alternative	Other soil parameters (Oedometric test)	Medium/Low (Oedometric test)	Satisfactory	Normal (Oedometric test)	Qualified/ Normally Qualified (Oedometric test)

The higher end methods are almost not used in the Bulgarian geotechnical practice, because of high price and specific equipment. This leads to search for new alternative options to determine the initial shear modulus. The new options could help to develop modern geotechnical engineering. The most applicable methods should be cheap, easy to implement and generally available. One of these methods is modified oedometric test with high strain reading accuracy. The apparatus modifications are accessible for most of the laboratories.

The alternative oedometric test is in conceptual phase. A lot of research, analysis and comparisons of the result are needed to prove the method validity. Once proven, this method is a basis for new researches in the field of geotechnical constructions, seismic engineering etc. It will help also in understanding and using the more complex constitutive models in engineering practice.

REFERENCES

Zewen, W., Wenhan, D., Lehane, B. M. 2024. A 3D image-based method to measure soil stiffness in triaxial test. *Acta Geotechnica*, pp651-668.

Kerenchev, N., Milev, N. 2019 Assessment of the dynamic soil properties for the FEM model of the Liuliakovitsa tailings dam, *Proceeding of the 8th conference Geotechnics in civil engineering*, Vrnjačka Banja, Serbia, manuscript, 13-15 November.

Ilieva, K. 2023. Comparison of the deformation under a strip foundation with applying different constitutive models. *Annual of the University of architecture, Civil Engineering and Geodesy,* Sofia, Bulgaria, ISSN 2534-9759, S1277-S1288.

Kerenchev N. 2014. Deformation properties of Sofia valley clays, determined with resonant column. *XIV International scientific conference VSU'2014*', Sofia, Bulgaria.

Kerenchev, N., Markov, I. 2016. Determining the axial bearing capacity of pile based on common methods and comparison with pile load. *Proceedings of the 3rd International conference Vietgeo*.

Kerenchev, N. 2013. Determining the dynamic modulus and dynamic settlement for the "New Lead processing" foundation – KCM Plovdiv. *Annual of the University of Architecture, Civil Engineering and Geodesy,* Sofia, Bulgaria, ISSN: 1310-814X.

Kerenchev, N. 2014. Developing an experimental laboratory setting for determining soil parameters related to deformation. *Annual of the University of architecture, Civil Engineering and Geodesy,* Sofia, Bulgaria, Vol. XLVI, ISSN: 1310-814X

Kerenchev, N., Mihova, L. 2019. Dynamic analysis of the Liuliakovitsa tailings dam. *Proceeding of the 8th conference Geotechnics in civil engineering*, Vrnjačka Banja, Serbia, manuscript.

Mihova, L., Tanev, T. 2015. Elastic and elasto-plastic constitutive models in soil mechanics. *Annual of the University of Architecture, Civil Engineering and Geodesy*. Fascicule IV, Vol. XLVII, Sofia.

Wuttke, F., Schanz, T., Schmidt**, H. 2008.** Factors Influencing Small-Strain Stiffness of soils and its Determination. *Bauhaus University Weimar.*

Schanz, T., Vermeer P. A. 1999. Formulation and verification of the Hardening-Soil model, *Beyond in Computatuinal geotechnics*, Amsterdam

Ilieva, K. 2023. Interaction between ground foundation/structure and determination of spring constants at pile foundation of an integral bridge. *XXIII International scientific conference VSU'2023*, Sofia, Bulgaria. ISSN: 1314-071X. pp117-329, 2023.

Xu, D., Borana, L., Yin, J. 2014. Measurement of small strain behavior of a local soil by fiber Bragg grating-based local displacement transducers. *Acta Geotechnica* 9:935–943, DOI 10.1007/s11440-013-0267-y

Kerenchev, N. 2019. On the 50 modulus of tailings dam materials. *19th International Multidisciplinary Scientific GeoConference SGEM 2019. Manuscript.*, ISSN: 1314-2704.

Mihova, L., Tanev T. .2014. Parameters of critical state constitutive models for clays from Sofia field. *Annual of the University of Architecture, Civil Engineering and Geodesy,* Sofia. Fascicule IV, Vol. XLVI, pp: 97 – 108.

Kerenchev N. 2022. Parameters in geotechnical modeling. Geotechnical soil properties. ISBN 978-619-191-886-7.

Tsvetkova T., Kerenchev N. 2020. Review of open source software for modelling and analysis of structures. *IOP Conference Series: Materials Science and Engineering, manuscript.* DOI: 10.1088/1757-899X/951/1/012003.

PhD. eng. Tanev. T. 2015. Soil modeling with consideration of isotropic strain hardening. PhD Thesis. *University of Architecture, Civil Engineering and Geodesy*.

Benz, T. 2007. Small strain stiffness of soils and its numerical consequences. *PhdThesis. University Sttitgart*.

Rafat, F., Obrzud, A., Truty. 2018. The hardening soil model – A practical guidebook. *Z_Soil.PC 100701 report*, revised 21.10.2018.

Yesiller, N., Inci, G., Miller, C. J. 2000. Ultrasonic Testing for Compacted Clayey Soils", *Geotechnical Special Publication.* DOI: 10.1061/40510(287)5.

Sephenson, R.W. 1978. Ultrasonic Testing for Determining Dynamic Soil Moduli. *ASTM Special Technical Publication*. ASTM International. pp 179-195.

28th European Young Geotechnical Engineers Conference – EYGEC 2024
© 2024 Macedonian Association for Geotechnics, ISBN 978-608-4510-61-1

Geotechnical Modelling Of Rock Mass - Hydrotechnical Structures Interaction

Tamara Jovanovska[a]

[a] *Macedonian Association for Geotechnics, Skopje, Macedonia*

ABSTRACT

This article proposes a methodology of geotechnical modelling as a basis for successful analyses of the interaction between rock mass and complex structures such as dams, hydrotechnical tunnels, etc. Several types of analytical and numerical models were formed based on analyses and synthesis of laboratory and field investigations of rock masses on the location of the dam "Sveta Petka" in the Republic of Macedonia. In the frame of the article, several examples of numerical models, formed by using the programs Examine 2D and Plaxis are presented. An example of determination of potentially unstable blocks using discontinuum methods is given.

KEYWORDS

Geotechnical Model, Rock Masses, Method Of Boundary Elements, Method Of Finite Elements

1. INTRODUCTION

Even at the current level of technological development, it is considered that the construction of underground structures, such as tunnels, is a difficult task. Before deciding about the methods and the design of future tunnel construction, it is necessary to perform detailed analyses, which include a huge number of different parameters.

The first stage is the description of the physico-mechanical behavior of rock masses, which are known to have a complex nature. Hence numerical methods as the method of boundary elements and the method of finite elements are a good auxiliary tool for conducting many different analyses related to this issue.

Geotechnical modelling in a wider sense includes statistical analysis for finding the distribution functions of all input geotechnical parameters, the definition of the safety factor, determination of the possible failure mechanisms and the probability of failure, risks analysis, the definition of the acceptable level of risk, etc. The whole procedure is described in (Jovanovska, 2019), while in the frames of this article only a part of the process, using the method of boundary and finite elements and their comparison, is explained. Also, a short example of using the program UnWedge for determination of potentially unstable blocks along the tunnel is given,

2. DESCRIPTION OF THE ANALYSED TUNNEL

The analyzed tunnel is a part of the Kozjak-Matka hydroelectric complex, at the Sveta Petka dam, in Skopje, the Republic of Macedonia.

Dam "St. Petka" is a thin concrete arched dam with double curvature in the horizontal and vertical directions (Slavevski M. et al, 2013). The top elevation is at +364.00 m.a.s.l., the bottom elevation is +300.00 m.a.s.l., the construction height is 64.0 m, not counting the fence. The body of the dam has a variable thickness. At an altitude of +364.00 m.a.s.l. it is 2.0 m thick and in the lower part at an altitude

of +300 m.a.s.l. - 10.0 m. The length of the arched part at the top of the dam is 115.00 m, and in the lower part, the length is 25.0 m. Figure 1 shows the layout of the "St. Petka" dam.

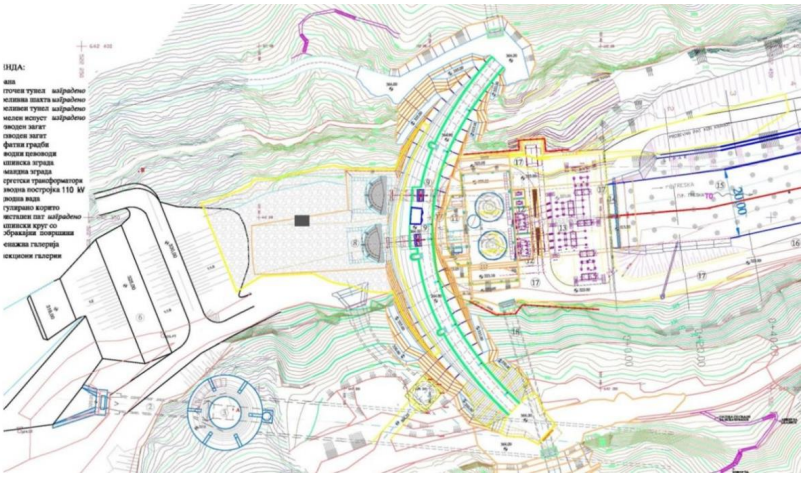
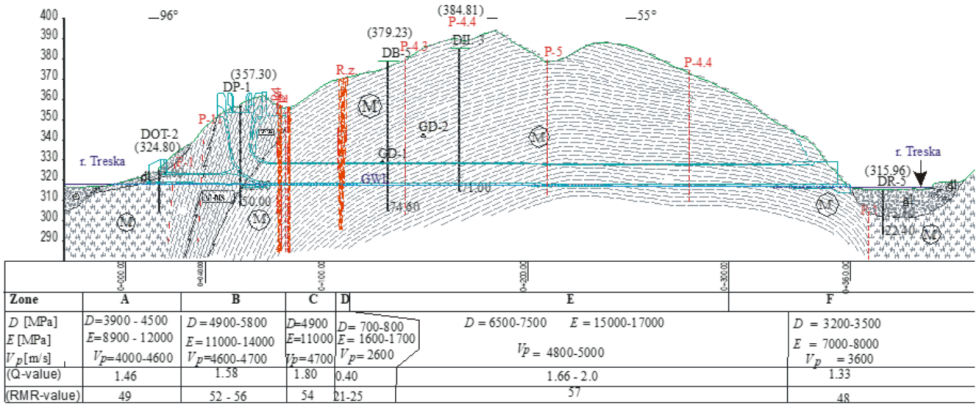


Figure 1. Layout of “St.Petka” dam

The length of the analyzed free-flow tunnel is 360 m, the diameter is 10 m, and the cross-section is circular. It is built in gray-white marbles, which have an average compressive strength of 44 MPa.

The geological data used in the calculation is presented in Figure 2. Based on these data, the tunnel is divided into 6 quasi-homogeneous zones. The GSI value in further analysis is calculated by the following equation: GSI=RMR-5.



Zone	A	B	C	D	E	F
D [MPa]	D=3900 - 4500	D = 4900-5800	D=4900	D= 700-800	D = 6500-7500 E = 15000-17000	D = 3200-3500
E [MPa]	E=8900 - 12000	E = 11000-14000	E=11000	E = 1600-1700		E = 7000-8000
V_p[m/s]	V_p=4000-4600	V_p=4600-4700	V_p=4700	V_p= 2600	V_p = 4800-5000	V_p = 3600
(Q-value)	1.46	1.58	1.80	0.40	1.66 - 2.0	1.33
(RMR-value)	49	52 - 56	54	21-25	57	48

Figure 2. Longitudinal profile of the “Sveta Petka” tunnel

3. METHOD OF BOUNDARY ELEMENTS

Using the Examine2D software package, the stress around a hydrotechnical tunnel constructed in a rock mass environment was simulated. Using the numerical model, a representation of the behavior of the rock mass is obtained, which is especially useful at the initial stages of design, while avoiding extensive and costly field investigations.

Figure 3. shows a diagram of the maximum stress around a hydotechnical tunnel excavation, with a diameter of 10 meters, at a depth of 60 m, with a deformation module of the rock mass (D) of 7000 MPa. Stresses were checked at 4 test points. All calculations are based on the Hoek-Brown criterion (Ulusay 2019).

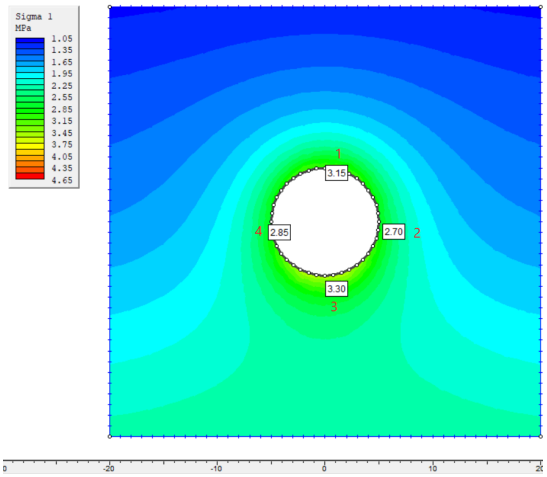


Figure 3. Diagram of the main stresses of the tunnel at a depth of 60 m

The same calculations were made at depths of 30, 40, and 10 m. In the calculations, the value of the deformation module (D) was varied. The input parameters and the results of the analysis are shown in Table 1.

Table 1. Results of the analysis of changes in the main stresses for different depths and deformation modules

Depth (m)	D (MPa)	σ_1 point 1 (MPa)	σ_1 point 2 (MPa)	σ_1 point 3 (MPa)	σ_1 point 4 (MPa)
60	6500	3.15	2.7	3.3	2.85
60	6800	3.15	2.7	3.3	2.85
60	6900	3.15	2.7	3.3	2.85
60	7250	3.15	2.7	3.3	2.85
60	7500	3.15	2.7	3.3	2.85
40	700	2.04	1.84	2.24	1.94
40	800	2.04	1.84	2.24	1.94
10	3200	0.35	0.45	0.7	0.5
10	3500	0.35	0.45	0.7	0.5
30	4900	1.5	1.35	1.72	1.42

The table shows that the change in the maximum stresses depends in direct proportion to the depth of the excavation of the tunnel, and the change in the value of the deformation module did not affect the stress value.

4. METHOD OF FINITE ELEMENTS

In this calculation, a two-dimensional analysis of the planar state of deformations is performed, in which the rock as a continuous medium is approximated by the Mohr-Coulomb model. The type of finite elements used in this model is 15 node triangular. Also, in these analyses, it is considered that the tunnel is in its operation phase when it is filled with water to a certain level. Since the Republic of Macedonia is a seismically active region, the seismic fore must be considered.

The seismic force is taken through the coefficients of seismic acceleration in the horizontal direction a_x = 0.15g and in the vertical direction a_y = 0.075g.

Using the model, static values at the intersection are determined: bending moments, axial and transverse shear forces. Also, the resulting displacements, i.e. deformations, are calculated, which determines the overall picture of the behavior of the structure.
The obtained value of the bending moment is 112.04 kN·m/m, axial force -3890 kN/m, transverse force -43.02 kN/m. The total deformation is 8 mm. The results for the total displacements are shown in figure 4.

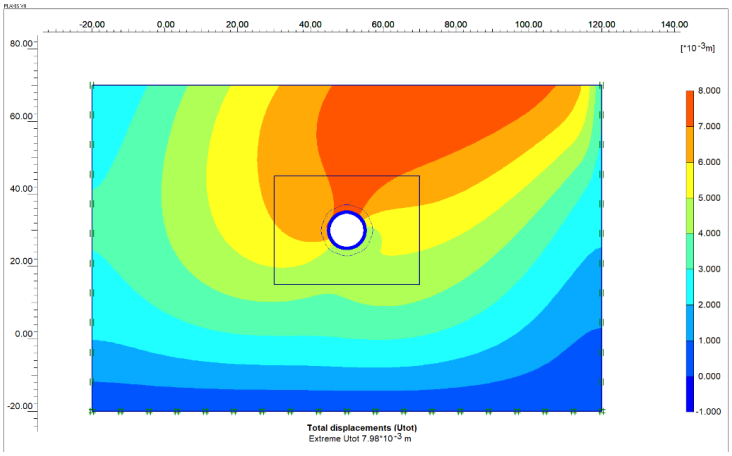


Figure 4. Total displacements in seismic analysis

5. COMPARISON OF THE METHOD OF BOUNDARY AND THE METHOD OF FINITE ELEMENTS

To prove the reliability of the data obtained by the numerical analysis, the deformation values obtained by the program Examine 2D and Plaxis were compared. To obtain several points, the deformation module was varied in the range from 1600 MPa to 15000 MPa. The results are presented in Table 2.

Table 2. Total deformations in the rock mass obtained in Examine 2D and Plaxis

Plaxis u (m)	Examine u (m)	E (MPa)
0.00558	0.0051	1600
0.00298	0.0027	3000
0.00149	0.00133	6000
0.00112	0.00099	8000
0.000744	0.000665	12000
0.000595	0.00054	15000

Based on these data, a graph of the dependence of the deformations on the deformation module was constructed (Figure 5).

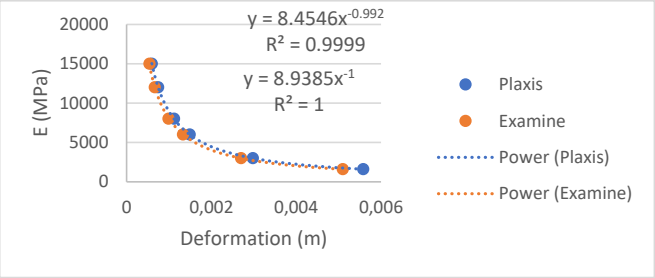


Figure 5. Dependence of the deformation value on the deformation module

It can be concluded that despite the different principles of calculation, both programs give almost the same results and the difference, which is 10.03% is negligible on the initial phases of design.

6. DETERMINATION OF POTENTIALLY UNSTABLE BLOCKS USING DISCONTINUUM METHODS

When designing long objects such as tunnels, it is necessary to analyse the orientation of the excavation in relation to the spatial orientation of the discontinuities to determine whether certain unstable large blocks of rock are likely to occur.

Such analyses were made for the tunnel “St.Petka”. using the programme UnWedge. In table 3. The orientation of the four main joint systems and the tunnel are given.

Table 3. Orientation of the main joint systems and the tunnel “St.Petka”

Joint system	Orientation
1	81/165
2	78/289
3	32/75
4	83/336
Tunnel	10/2

To analyse the stability of the potentially unstable blocks, it is necessary to enter the data on the angle of internal friction and cohesion. The internal friction angle varied in the range from 35 to 39 degrees. For all these values, analyses were made with cohesion equal to zero, 0.0001 MPa, and 0.0002 MPa.

As an output of the analysis, the program provides information about the weights and safety factors (SF) of the blocks. An example of the output data is given in Figure 5, and the results for all other cases are shown in Table 4.

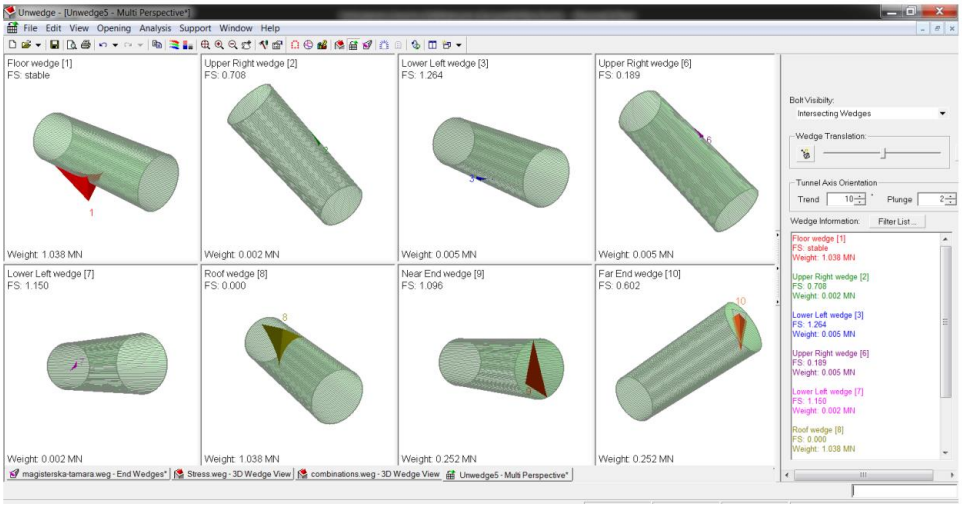


Figure 5. Output from analysis, block weight and safety factor

Table 4. Results from the analysis of potentially unstable blocks in UnWedge

c (MPa)	φ (◦)	FS 1	FS 2	FS 3	FS 6	FS 7	FS 8	FS 9	FS 10
0	35	/	0.503	0.989	0.135	0.943	0	0.943	0.503
0	36	/	0.522	1.026	0.14	0.978	0	0.978	0.522
0	37	/	0.542	1.064	0.145	1.014	0	1.014	0.542
0	38	/	0.562	1.103	0.151	1.052	0	1.052	0.562
0	39	/	0.582	1.143	0.156	1.09	0	1.09	0.582
0.0001	35	/	0.566	1.049	0.151	0.973	0	0.945	0.513
0.0001	36	/	0.585	1.086	0.156	1.008	0	0.981	0.532
0.0001	37	/	0.605	1.125	0.162	1.044	0	1.017	0.552
0.0001	38	/	0.625	1.164	0.167	1.082	0	1.055	0.572
0.0001	39	/	0.645	1.204	0.173	1.12	0	1.093	0.592
0.0002	35	/	0.629	1.11	0.168	1.003	0	0.948	0.523
0.0002	36	/	0.648	1.147	0.173	1.038	0	0.984	0.542
0.0002	37	/	0.668	1.185	0.178	1.074	0	1.02	0.562
0.0002	38	/	0.687	1.224	0.183	1.112	0	1.057	0.582
0.0002	39	/	0.708	1.264	0.189	1.15	0	1.096	0.602

From the above results, the following conclusions can be drawn:
-Block No. 1 is stable in any case, since it is located at the bottom of the tunnel.
-All other blocks have a safety factor less than the required 1.5, which indicates the need to take measures, such as installing tunnel protection, to increase it.

7. CONCLUSIONS

From the results presented above, it can be concluded that numerical methods are a practical auxiliary tool in various analyzes in construction and geotechnics. It should be emphasized that the results of such analysis should not be the only ones that engineers will rely on when making decisions. To verify the proposed methods, over time they should undergo a critical review regarding the possibility of its use for rock mass in other places, at other objects, and certain stages of design.

REFERENCES

Jovanovski, M., Peshevski, I., and Papich, J. 2018. Empirical-Statical-Dynamic (ESD) methodology for extrapolation in rock mechanics. *Eurock Congress*, Saint-Petersburg, Russia.

Ulusay, R. (ed.) 2015. The ISRM suggested methods for rock characterization, testing and monitoring.

Йовановска, Т. 2019. Численное моделирование взаимодействия гидротехнических туннелей и масс горных пород.

Јовановски, М., Гапковски, Н., Пешевски, И., and Аболмасов, Б. 2012. Инженерска Геологија.

Славевски, М., Николовски, З., Михајловски, Р., Јанков, П., Алексовски, Г., and Миловановиќ, С. 2013. Изградба на браната "Света Петка". *Трет конгрес за брани*, Струга, Република Македонија.

28th European Young Geotechnical Engineers Conference – EYGEC 2024
© 2024 Macedonian Association for Geotechnics, ISBN 978-608-4510-61-1

Shear modulus reduction and material damping curves measured with resonant column device on cohesive soils from the Ljubljana Marsh

Timotej Jurček, Boštjan Pulko, Matej Maček

University of Ljubljana, Faculty of Civil and Geodetic Engineering, Chair of Geotechnical Engineering, Ljubljana, Slovenia

ABSTRACT

In recent decades, the expansion of the Slovenian capital of Ljubljana has focused primarily on the Ljubljana Marsh. The uppermost layers of the Ljubljana Marsh consist of soft lacustrine sediments, which pose considerable geotechnical challenges. In order to better predict the soil behaviour under dynamic and static loading, it is important to determine the dynamic soil properties, which are usually represented by the shear modulus reduction curve normalised to the initial shear modulus and the material damping as a function of shear strain. In the absence of specific measurements on local soils, the dynamic soil properties are often taken from the literature, assuming that soils with similar intrinsic properties exhibit similar behaviour. It should be noted that the different empirical models are not always directly comparable. In addition, the authors give a wide range of measurements for soils with similar intrinsic properties in the literature.

In this study, we evaluate the applicability and reliability of the empirical correlations of dynamic soil properties by comparing them with laboratory measurements of soft soils in the Ljubljana Marsh. The dynamic soil properties were measured using a resonant column with integrated bender elements, which increased the reliability of the measurements. Given the significant differences between empirical models, it is critical to account for these differences in soil behaviour, which necessitates sensitivity analyses in engineering practise. The study also emphasises the importance of direct measurements of dynamic soil properties, especially at sites where the empirical relationships have not yet been confirmed.

KEYWORDS

Shear Modulus; Material Damping; Resonant Column; Laboratory Testing

1. INTRODUCTION

The Slovenian capital lies partly on the Ljubljana Marsh. The upper soil layer of the Ljubljana Marsh consists mainly of soft lacustrine sediments such as silt and clay (Gaberc, 2000). The thick soft lacustrine sediments pose a high earthquake risk and are geotechnically challenging. Despite the challenging site conditions, there is a lack of data on soil behaviour under small to large strains, which is a major shortcoming in the area of comprehensive and reliable analyses. To overcome the lack of data, experts rely on empirical correlations from existing literature that are not validated for the specific site. Recently, Jurček et al. (2024) presented laboratory measurements of the shear modulus in the resonance column device for a site at the periphery on the Ljubljana Marsh and found some discrepancies between the measurements and empirical correlations.

This paper presents the measurements of dynamic soil properties of 36 soil samples collected from three different sites in the area of the Ljubljana Marsh and its periphery. The dynamic soil properties were determined using bender elements (BE) and resonant column (RC) tests on soils with a plasticity index

in the range of 13 to 63%. Furthermore, these measurements were compared with established empirical models for dynamic soil properties to check the results of Jurček et al. (2024).

2. DYNAMIC SOIL PROPERTIES

The stress-strain behaviour of soils is highly nonlinear. The shear modulus G decreases rapidly with increasing engineering shear strain amplitude γ and forms S-shaped curve on a semi-logarithmic scale. Typically, this behaviour is represented by the maximum shear modulus G_0 at infinitesimal shear strain ($\gamma \approx 10^{-6}$) and the normalised shear modulus degradation curve G/G_0 as a function of γ (G/G_0 curve). In contrast, the energy dissipation increases with increasing γ, which leads to an increase in material damping ξ. The ξ is usually represented as a function of γ (ξ curve).

In soil dynamics G is often defined as the secant modulus, represented by the slope between two extreme points of the hysteresis loop (Figure 1) at a given γ under cyclic loading (Equation 1):

$$G = \frac{\Delta\tau}{\Delta\gamma} \tag{1}$$

where τ represents the shear stress.

In engineering, there are different types of damping, which are described in detail by Yoshida (2015). From a geotechnical point of view, the most important types are hysteresis and viscous damping (Soból et al., 2019), which are grouped in material damping. Viscous damping includes internal and external components. Internal damping is the result of energy dissipation within the soil due to differences in internal velocities. External damping accounts for energy dissipation outside the system (Yoshida, 2015) and is often referred to as parasitic damping. Hysteretic damping is the result of the G/G_0 curve forming a loop when the soil is cyclically loaded (Figure 1). The material damping ξ is defined as the ratio of dissipated energy (area of the hysteresis loop, W_D) to supplied energy (area of the triangle, W_S) during the loading/unloading cycle (Equation 2).

$$\xi = \frac{1}{4\pi}\frac{W_D}{W_S} \tag{2}$$

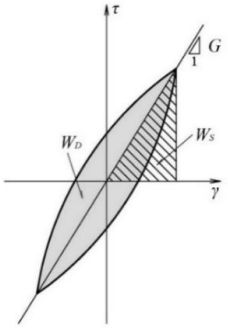


Figure 1. Definition of G and ξ for cyclic test (modified after Hayashi et al., 2018)

2.1. Empirical models for description of dynamic soil properties

All soil types follow a common principle: with increasing γ, G decreases nonlinearly, which leads to an S-shaped decrease in stiffness on a semi-logarithmic scale. For cohesive soils, it can be shown that the curve G/G_0 gradually shifts to the right as the plasticity index I_P increases (Díaz-Rodríguez and López-Molina, 2008). Hardin and Drnevich (1972) proposed a basic hyperbolic model for the G/G_0 curve.

Later this basic model was further modified to obtain a better fitting model of the G/G_0 curve to the laboratory test results for different soil types. One of these modifications is the introduction of the power factor n into the Hardin-Drnevich model (Equation 3).

$$\frac{G}{G_0} = \frac{1}{1+\left(\frac{\gamma}{\gamma_{ref}}\right)^n} \tag{3}$$

where γ_{ref} is the reference shear strain.

Over the decades, numerous researchers have proposed empirical models to describe the dynamic soil properties based on the most important influencing factors. Some of these models and the corresponding influencing factors are listed in Table 1.

In general, these empirical equations for estimating G_0 are often expressed in the form proposed by Hardin and Black (1968), which is based on the void ratio e, the overconsolidation ratio OCR and the effective stress mean σ'. Thanks to advances in measurement technology and cost-effective methods, direct field, or laboratory measurements of G_0 are increasingly preferred in everyday engineering practice (Mayne and Rix, 1995).

The opposite applies to G/G_0 and ξ curves, which can only be determined by laboratory measurements. For cohesive soils, it has been shown that the shape of the G/G_0 curve mainly depends on I_P, σ' and OCR (e.g., Darendeli, 2001; Ishibashi and Zhang, 1993; Lanzo et al., 1997). However, some studies neglected the influence of OCR on the G/G_0 curve (e.g., Kokusho et al., 1982; Vardanega and Bolton, 2013; Vucetic and Dobry, 1991).

The influence of various factors on the ξ curve is not as uniform in the literature as in the case of G/G_0 curve. According to Zhang et al. (2005), the most important factors influencing the ξ curve include σ', I_P, the loading frequency f and the number of cycles N. With an increase in σ', ξ tends to decrease for all γ (e.g., Darendeli, 2001; Hardin and Drnevich, 1972; Ishibashi and Zhang, 1993). The influence of I_P is complex (Zhang et al., 2005). Some authors (e.g., EPRI, 1993; Stokoe et al., 1994) found that ξ_{min} increase with increasing I_P, while ξ decreases for larger γ with increasing I_P. However, some previous studies (Seed et al., 1986; Vucetic and Dobry, 1991) have not shown this complex effect of I_P on ξ. The N is another quantity on which the authors differ. Vucetic and Dobry (1991) have shown that there is no influence of N on ξ, while others such as Hardin and Drnevich (1972) and Darendeli (2001) find that N is a crucial factor. In general, a higher f leads to a higher ξ for all γ (Ciancimino et al., 2020; Darendeli, 2001; Zhang et al., 2005). The influence of N and f on the measured ξ can be explained by the differences between the various devices used to determine the dynamic soil properties (Zhang et al., 2005), the performance of the experiment under drained or undrained conditions and the method used to calculate the energy lost (Stokoe et al., 1995). In addition, it has been suggested that ξ should be measured at f and N according to the expected dynamic loading.

Table 1 list models for the description of dynamic soil properties from various authors. These equations are usually formulated based on a series of laboratory test results for different soils and typically represent average soil behaviour. Darendeli (2001) also gave the standard deviation of his proposed models, which can be used to estimate the range of possible G/G_0 and ξ curves. Yoshida (2015) has shown that the exclusive use of average values can lead to inaccuracies and that the range of possible dynamic soil properties should be considered.

Table 1. Empirical models for G/G_0 and ξ for cohesive soils.

Reference	Presentation	G/G_0	ξ
		Input parameter	
Vucetic and Dobry (1991)	graphically	I_P	I_P
EPRI (1993)	graphically	I_P	I_P

Darendeli (2001)	equation	I_P, OCR, σ'	I_P, OCR, σ', N, f
Zhang et al. (2005)	equation	I_P, σ'	I_P, σ'
Ciancimino et al. (2020)	equation	I_P, σ'	I_P, σ', f

3. EQUIPMENT AND METHODS

The fix-free torsional RC device from Wille Geotechnic was used in this study. With this device, both RC and BE tests can be performed simultaneously under isotropic stress conditions.

In the preparation stages, the soil samples were trimmed to produce cylindrical specimens with a diameter of 70 mm and a height of between 100 and 140 mm. To determine the water content and density, the specimens were measured and weighed before and after the test. Each specimen was isotopically reconsolidated to the effective vertical stress under in-situ conditions. The final dimensions and density were used to calculate the dynamic properties (i.e., the dimensions after the consolidation stage).

After the consolidation stage, both BE and RC tests were performed. The BE test was performed three times with different frequencies of the transmitter. The travel time t was determined using the first-arrival method. The G_0 was then calculated from the mean value of the shear wave velocities v_s determined from the measured t. Following the BE test, an RC test was carried out with different γ under undrained conditions. The excess pore water pressure Δu was measured throughout the RC testing. However, the influence of Δu on the soil of the Ljubljana Marsh can be neglected (Jurček et al., 2024). A more detailed description of the measurements can also be found herein.

From the RC measurements, ξ can be calculated using two methods: the Bandwidth method and the Lissajous method. Only the Lissajous method is used in this study, as it has proven to be less prone to errors. Further details on this method can be found in Wichtmann et al. (Wichtmann et al., 2001).

4. MATERIALS

In this study, 36 soil samples were taken from three sites in the Ljubljana Marsh, referred to as Location 1, 2, and 3. The soft lacustrine sediments at these sites consist of normally consolidated ($OCR \approx 1$) clays and silts of low to very high plasticity with up to 30% fine sand and I_P between 13 and 63% (Table 2). The classification in Table 2 was carried out in accordance with EN ISO 14688-2:2017. The void ratio in the RC test is represented as e_{RC}.

Table 2. Properties of soil and testing conditions and test results.

Sample	Soil type	e_{RC}	I_P	fines	σ'	G_0(BE)	Model (Equation 3)		
							G_0	γ_{ref}	n
		[/]	[%]	[%]	[kPa]	[MPa]	[MPa]	[/]	[/]
Location 1-1	ClM	0.885	23	97	100	52	54	$2.8 \cdot 10^{-4}$	0.96
Location 1-2	SiH	0.720	28	98	120	67	71	$3.2 \cdot 10^{-4}$	0.90
Location 1-3	ClM	0.710	27	99	130	84	88	$2.4 \cdot 10^{-4}$	0.89
Location 1-4	ClH	0.728	33	97	140	49	45	$4.4 \cdot 10^{-4}$	0.93
Location 1-5	ClL	0.582	13	80	150	85	89	$2.2 \cdot 10^{-4}$	0.83
Location 1-6	ClH	0.800	35	97	160	55	50	$5.0 \cdot 10^{-4}$	1.10
Location 1-7	ClM	0.583	23	98	180	108	104	$2.6 \cdot 10^{-4}$	0.92
Location 1-8	ClH	0.802	30	92	180	66	65	$4.7 \cdot 10^{-4}$	1.11
Location 1-9	ClM	0.527	33	98	240	100	98	$3.3 \cdot 10^{-4}$	1.05
Location 1-10	ClM	0.527	20	74	260	140	135	$2.8 \cdot 10^{-4}$	0.95

Location 1-11	ClM	0.632	21	91	280	120	118	$3.0 \cdot 10^{-4}$	1.01
Location 2-1	ClL	0.610	14	85	80*	76	79	$1.2 \cdot 10^{-4}$	0.88
Location 2-2	ClM	0.559	14	93	80*	71	74	$1.4 \cdot 10^{-4}$	0.91
Location 2-3	ClL	0.628	15	98	80	83	82	$1.3 \cdot 10^{-4}$	0.90
Location 2-4	ClM	0.526	18	100	90	81	89	$1.4 \cdot 10^{-4}$	0.94

Continued on next page.

Table 2. Continued from previous page.

Location 2-5	ClM	0.601	15	99	100	67	76	$1.9 \cdot 10^{-4}$	0.92
Location 2-6	ClL	0.506	16	97	110	113	107	$1.5 \cdot 10^{-4}$	0.98
Location 2-7	ClL	0.601	14	96	120	113	110	$1.8 \cdot 10^{-4}$	0.90
Location 2-8	ClL	0.536	14	96	140	114	121	$1.9 \cdot 10^{-4}$	0.95
Location 2-9	ClM	0.542	18	100	170	98	101	$2.1 \cdot 10^{-4}$	0.98
Location 3-1	ClH	1.012	41	98	100*	49	45	$6.5 \cdot 10^{-4}$	0.88
Location 3-2	SiVO	1.758	61	70	100*	24	26	$5.5 \cdot 10^{-4}$	0.71
Location 3-3	SiVO	2.327	62	74	100*	27	25	$6.4 \cdot 10^{-4}$	0.74
Location 3-4	SiV	1.787	61	99	100*	29	30	$6.2 \cdot 10^{-4}$	0.90
Location 3-5	SiV	1.992	49	99	100*	37	37	$4.2 \cdot 10^{-4}$	0.84
Location 3-6	SiV	1.423	52	99	100*	39	42	$4.5 \cdot 10^{-4}$	0.90
Location 3-7	SiV	1.627	44	99	100*	48	51	$3.2 \cdot 10^{-4}$	0.89
Location 3-8	SiV	1.631	41	100	100	53	52	$3.2 \cdot 10^{-4}$	0.93
Location 3-9	SiV	1.603	40	100	110	52	57	$3.0 \cdot 10^{-4}$	0.88
Location 3-10	SiV	1.483	38	100	110	59	64	$2.9 \cdot 10^{-4}$	0.84
Location 3-11	SiV	1.469	43	100	120	58	60	$3.4 \cdot 10^{-4}$	0.90
Location 3-12	SiV	1.750	63	99	140	43	43	$5.4 \cdot 10^{-4}$	0.90
Location 3-13	SiV	1.569	53	100	150	55	57	$4.6 \cdot 10^{-4}$	0.92
Location 3-14	ClV	1.315	48	99	150	49	53	$5.5 \cdot 10^{-4}$	1.02
Location 3-15	ClV	0.979	44	99	170	64	61	$4.3 \cdot 10^{-4}$	0.98
Location 3-16	ClL	0.650	13	89	190	136	134	$1.5 \cdot 10^{-4}$	0.81

* Are the lowest σ' at which an RC test could be performed due to equipment limitations.

5. TEST RESULTS AND DISCUSSION

The parameters of the modified Hardin-Drnevich model (G_0, γ_{ref} and n) were fitted to the measurements performed with the RC device. The results of the adjustment are shown in Table 2.

The G_0 measured with the BE ($G_0(\mathrm{BE})$) were within ±10 % of the G_0 determined by fitting the modified Hardin-Drnevich model to the measurements ($G_0(\mathrm{model})$), indicating good agreement between BE and RC tests.

To determine the G/G_0 curve, G was normalised by $G_0(\mathrm{model})$. Figure 2 shows the G/G_0 curves for all 36 samples, which are colour-coded for different locations. A slightly different position in the graph can be seen for the different locations. It can also be observed that due to the soft nature of the soil specimens, the RC device had problems measuring G in the range of γ smaller than $5 \cdot 10^{-5}$, especially for the samples from Location 2 and 3. The upper and lower bounds for the G/G_0 and ξ curves were calculated (Equation 3) for the lowest (13%) and highest (63%) I_P with γ_{ref} ranging from $1.2 \cdot 10^{-4}$ to $6.5 \cdot 10^{-4}$, respectively, and based on the average n value of 0.92 for all soil samples. Since the ξ curve is correlated with the G/G_0 curve via the hysteresis loop (i.e., the Masing curve), the G/G_0 curve was used to calculate the material damping. Figure 2 shows that the Masing behaviour at higher γ leads to higher ξ than the experimental observations in this study. Similar results were also reported by Darendeli (2001), who

pointed out that the direct application of Masing behaviour to nonlinear soil behaviour is limited and often leads to poor results. Therefore, modifications were proposed to achieve a better fit to laboratory data (Darendeli, 2001). A similar approach was also used by Ciancimino et al. (2020), while Zhang et al. (2005) only fitted the model ξ curve to the torsional shear device measurements. The ξ curves given by EPRI (1993) do not correspond to the G/G_0 curves as they were specifically modified for direct application in earthquake engineering. It is therefore difficult to compare the ξ curves determined in this study with empirical models. This is due to the modification of the ξ curves in the models and the limitations of the RC device, which generally provides higher ξ curves due to the effect of N and f. The two measurements with the lowest ξ were carried out on organic silts.

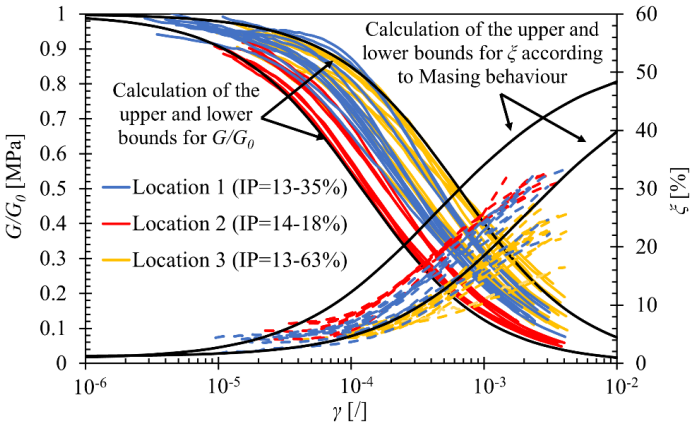


Figure 2. G/G_0 and ξ for soil samples from three locations.

A comparison was made between the γ_{ref} fitted to the measurements and the empirical models listed in Table 1. Darendeli (2001), Zhang et al. (2005) and Ciancimino et al. (2020) give the parameters of the modified Hardin-Drnevich model based on the input parameters listed in Table 1. These proposed models are dependent on σ', therefore σ' was set to 120 kPa, which corresponds to the average σ' at which the RC tests were performed. For the graphical models of Vucetic and Dobry (1991) and EPRI (1993), the parameters of the modified Hardin-Drnevich model were determined by a best-fit analysis. Both the empirical G/G_0 curves and the parameters fitted to the RC measurements show that γ_{ref} increases with increasing I_P. However, the γ_{ref} from RC measurements are lower than those of other authors, with the exception of Zhang et al. (2005) for Tertiary and Residual/Saprolite soils. The width of the interval in which 90% of the fitted γ_{ref} fall is about 50% away from the trend line. Similar results were reported by Vardanega and Bolton (2013). It can also be observed that different locations within the Ljubljana Marsh have a slightly different γ_{ref} trend, as indicated by their position to the global trend. It should be emphasized that the empirical models reflect an "average" soil behaviour, considering soils with identical intrinsic properties. As Darendeli (2001) notes, the measurements used in the development of these models show considerable variability in soil behaviour.

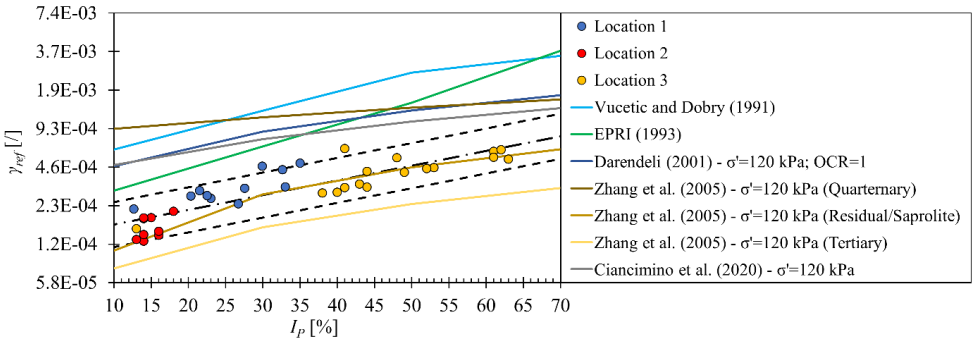


Figure 3. The comparison between the empirical models and the fitted γ_{ref} to the measurements. Dotted black lines deviating ±50% from the trend.

Empirical models, with the exception of Zhang et al. (2005), as well as parameters derived from the RC measurements show that n is not dependent on I_P. The average n for the measurements was 0.92, with a 90% confidence interval of ±0.14 for the fitted n. Again, this shows that the different sites in the Ljubljana Marsh have slightly different n. The two lowest n, which deviate from the general trend, were observed in organic silts.

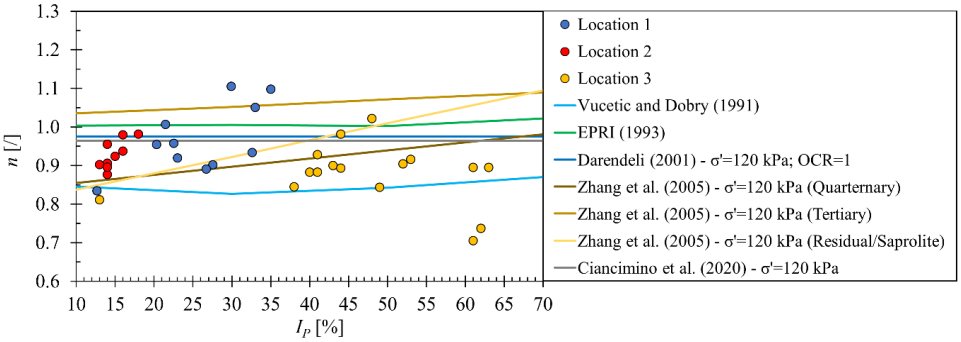


Figure 4. The comparison between the empirical models and n fitted to the measurements.

6. CONCLUSION

Based on the BE in the RC test carried out on soft sediments from the Ljubljana Marsh, we can draw the following conclusions:

1. Both G_0 (BE) and G_0 (model) were within 10% of each other, indicating good agreement between BE and RC tests. The integration of the BE into the RC device is useful for quality control of the RC measurements and is therefore strongly recommended.
2. The soil properties reported by Jurček at al. (2024) were confirmed by measurements on samples from two other locations.
3. It was confirmed that γ_{ref} depends on I_P and that n is independent of it. Similar trends to the empirical models were observed, with the exception that γ_{ref} was lower compared to the values reported by most other authors. Significant differences were also found between the empirical models.
4. Not all soils are “average” soils. The differences in soil behaviour should be considered when using empirical models and in engineering practice, where sensitivity analyses are highly recommended.
5. It is advisable to perform direct measurements to obtain dynamic soil properties. This is especially true in cases where the empirical relationships have not yet been confirmed.

7. ACKNOWLEDGEMENTS

This research was funded by the Slovenian Research Agency (research core funding No. P2-0180) within Young Researcher program.

REFERENCES

Ciancimino, A., Lanzo, G., Alleanza, G.A., Amoroso, S., Bardotti, R., Biondi, G., Cascone, E., Castelli, F., Di Giulio, A., d'Onofrio, A., Foti, S., Lentini, V., Madiai, C., Vessia, G., 2020. Dynamic characterization of fine-grained soils in Central Italy by laboratory testing. *Bulletin of Earthquake Engineering*, 18, 5503–5531. https://doi.org/10.1007/s10518-019-00611-6

Darendeli, M. 2001. Development of a New Family of Normalized Modulus Reduction and Material Damping Curves. Ph.D. Thesis, University of Texas, Austin, TX, USA.

Díaz-Rodríguez, J.A., López-Molina, J.A., 2008. Strain thresholds in soil dynamics. *Proceedings of the 14th World Conference on Earthquake Engineering*, Beijing.

Electric Power Research Institute—EPRI. 1993. Guidelines for Determining Design Basis Ground Motions; Report EPRI TR-102293; Palo Alto, CA, USA, 1993.

Gaberc, A. 2000. Napovedano in opazovano posedanje Južne obvoznice. *Proceedings of the 1st Šuklje Symposium*, Slovenia, 12 October 2000; Gaberc, A.M., Majes, B., Eds.; Slovenian Geotechnical Society: Ljubljana, Slovenia, pp. 121–128.

Hardin, B.O., Black, W.L., 1968. Vibration Modulus of Normally Consolidated Clay. *Journal of the Soil Mechanics and Foundations Division*, 94, 353–369. https://doi.org/10.1061/JSFEAQ.0001100

Hardin, B.O., Drnevich, V.P., 1972. Shear Modulus and Damping in Soils: Design Equations and Curves. *Journal of the Soil Mechanics and Foundations Division*, 98, 667–692. https://doi.org/10.1061/JSFEAQ.0001760

Hayashi, H., Yamanashi, T., Hashimoto, H., Yamaki, M., 2018. Shear Modulus and Damping Ratio for Normally Consolidated Peat and Organic Clay in Hokkaido Area. *Geotechnical and Geological Engineer*ing, 36, 3159–3171. https://doi.org/10.1007/s10706-018-0527-6

Ishibashi, I., Zhang, X., 1993. Unified Dynamic Shear Moduli and Damping Ratios of Sand and Clay. *Soils and Foundations* 33, 182–191. https://doi.org/10.3208/sandf1972.33.182

ISO 114688-2:2017. 2017. Geotechnical Investigation and Testing—Identification and Classification of Soil-Part 2: Principles for a Classification. ISO copyright office: Geneva, Switzerland.

Jurček, T., Pulko, B., Maček, M., 2024. Small Strain Shear Modulus of the Ljubljana Marsh Soil Measured with Resonant Column and Bender Elements under Isotropic and Anisotropic Stress Conditions. *Applied Sciences*, 14, 1984. https://doi.org/10.3390/app14051984

Kokusho, T., Yoshida, Y., Esashi, Y., 1982. Dynamic Properties of Soft Clay for Wide Strain Range. *Soils and Foundations*, 22, 1–18. https://doi.org/10.3208/sandf1972.22.4_1

Lanzo, G., Vucetic, M., Doroudian, M., 1997. Reduction of Shear Modulus at Small Strains in Simple Shear. *Journal of Geotechnical and Geoenvironmental Engineering*, 123, 1035–1042.

Mayne, P.W., Rix, G.J., 1995. Correlations Between Shear Wave Velocity and Cone Tip Resistance in Natural Clays. *Soils and Foundations*, 35, 107–110. https://doi.org/10.3208/sandf1972.35.2_107

Seed, H.B., Wong, R.T., Idriss, I.M., Tokimatsu, K., 1986. Moduli and Damping Factors for Dynamic Analyses of Cohesionless Soils. *Journal of Geotechnical and Geoenvironmental Engineering*, 112, 1016–1032. https://doi.org/10.1061/(ASCE)0733-9410(1986)112:11(1016)

Soból, Głuchowski, Szymański, Sas, 2019. The New Empirical Equation Describing Damping Phenomenon in Dynamically Loaded Subgrade Cohesive Soils. *Applied Sciences*, 9, 4518. https://doi.org/10.3390/app9214518

Stokoe, K.H., Hwang, S.K., Darendeli, M.B., Lee, N.J., 1995. Correlation study of nonlinear dynamic soils properties. Aiken, SC, Westinghouse Savannah River Company.

Stokoe KH II, Hwang SK, Lee JNK, Andrus RD. 1994. Effects of various parameters on the stiffness and damping of soils at small to medium strains. In: prefailure deformation of geomaterials: proc., int. symp. on pre-failure deformation characteristics of geomaterials. Balkema, Rotterdam; 1995, p. 785–816.

Vardanega, P.J., Bolton, M.D., 2013. Stiffness of Clays and Silts: Normalizing Shear Modulus and Shear Strain. J. *Journal of Geotechnical and Geoenvironmental Engineering*, 139, 1575–1589. https://doi.org/10.1061/(ASCE)GT.1943-5606.0000887

Vucetic, M., Dobry, R., 1991. Effect of Soil Plasticity on Cyclic Response. *Journal of Geotechnical Engineering*, 117, 89–107.

Wichtmann, T., Sonntag, Th., Triantafyllidis, Th., 2001. Über das Erinnerungsvermögen von Sand unter zyklischer Belastung. *Bautechnik*, 78, 852–865. https://doi.org/10.1002/bate.200105950

Yoshida, N., 2015. Seismic Ground Response Analysis, Geotechnical, Geological and Earthquake Engineering. Springer Netherlands, Dordrecht. https://doi.org/10.1007/978-94-017-9460-2

Zhang, J., Andrus, R.D., Juang, C.H., 2005. Normalized Shear Modulus and Material Damping Ratio Relationships. *Journal of Geotechnical and Geoenvironmental Engineering*, 131, 453–464. https://doi.org/10.1061/(ASCE)1090-0241(2005)131:4(453)

28th European Young Geotechnical Engineers Conference – EYGEC 2024
© 2024 Macedonian Association for Geotechnics, ISBN 978-608-4510-61-1

Advantages of 3D FEM modelling and BIM modelling for underground structures

Kristóf Kelemen

HBM Soletanche Bachy, Budapest, Hungary

ABSTRACT

How do the results of 2 and 3 dimensional finite element calculations compare? What are the effects of 3-dimensional modelling? These topics will be discussed using the example of a deep excavation in Debrecen. I intend to present a comparison of the results of 2D and 3D calculations of a deep excavation pit measured with an inclinometer. I will compare the measured and calculated results and search for the best possible fit by varying the calculation parameters. Based on some field experience, measurement results and numerical analysis, the soil environment of an area can be better understood.

How can 3D BIM modelling help the design? The example is a deep excavation in the urban environment, where an old factory is being converted into a modern office. How does BIM help manage the construction and planning? What are the advantages and disadvantages?

KEYWORDS

Deep excavation, PLAXIS, Monitoring, BIM

1. INTRODUCTION

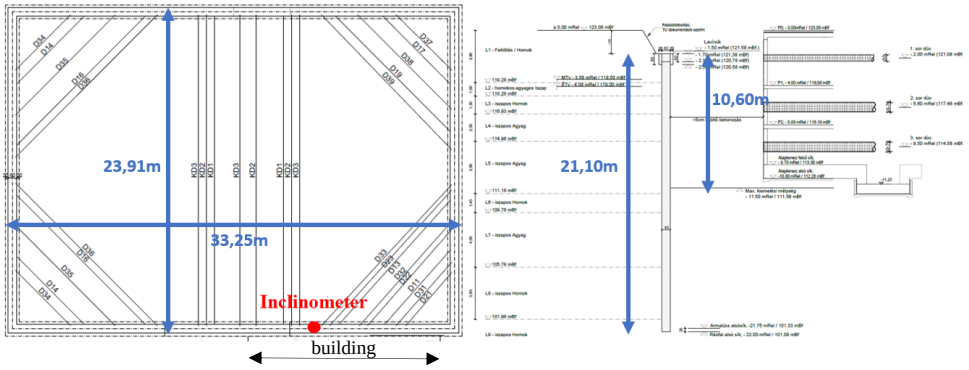
The analysed deep excavation is located in Deberecen, Hungary and was designed, constructed and monitored by HBM Soletanche Bachy in 2020-2021. For the monitoring of the diaphragm wall, 1 inclinometer was installed on the section of the workings adjacent to the building. This provided the possibility to back analyse the movements of the wall. By modifying the soil parameters within realistic range, I was looking for the best possible match between the measured and calculated results.

2. PROJECT INTRODUCTION

2.1. Geometry

The working pit functions as a 3-storey underground garage for a future residential building. In temporary state, the 60 cm thick diaphragm wall is supported on 3 levels by steel struts. In its final state, the diaphragm wall is supported by the internal reinforcement structure.

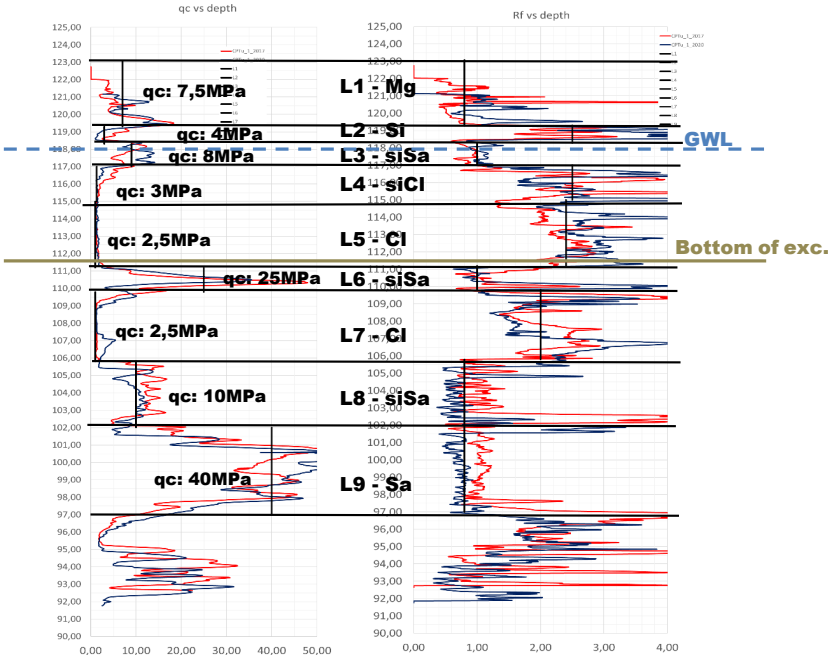
The layout of the diaphragm is shown in the following figure wall. The height of the structure is 21,10 metres, the excavation is 10,60 metres from the upper of the diaphragm. The following diagrams show the geometry of the structure.



1. Figure Layout and cross section of the wall

2.2. Geotechnical conditions

Excavations and soil mechanics tests indicate that the surface is covered by a heterogeneous sandy fill of 2.3-2.8 m thickness, typically of building-derived loose condition. Under this layer, a single-fraction, medium-fine grained, medium compacted, settled sand was present to a depth of approximately 5.1-7.2 m. This was followed by a thin layer of soft state silt 1.7-2.5 m thick, the cone resistance shows a decreasing trend. Below this, a lean to medium clay was identified at depths of 6.9-11.2 m. Below this layer was found silt and silty fine sand. The thickness of this layer is ~2.3-4.5 m. The temporary layer is followed by a dark-coloured organic lean-medium clay. The consistency of this layer is rigid, which extends between depths of 13.5 and 16.8 m. Below this are largely temporary and granular layers. From depths 15.8-16.8 m to depths 21.5-22.4 m, a fine sandy soft silt layer is present, followed by a silty fine sand layer to a depth of ~25.3 m. Below this, a sandy silt/sand layer extends to a depth of 30.0 m based. Groundwater was reported at -4.93m.



2. Figure CPT chart

2.3. Inclinometer

The inclinometer was placed on the south side of the diaphragm wall, where the adjacent building is located, near by the KD1-2-3 struts (Figure 1) and used to measure the displacements of the diaphragm wall. Measurements were taken before and after each major construction phase (e.g. excavation, strut installation, strut remove, slabs/base slab construction). In the modelling, I measured the displacements up to the full excavation of the working pit.

3. BACK ANALYSIS

The 3D and 2D modelling of the deep excavation simulated the different phases of construction, the construction of the diaphragm wall, excavation, and the installation of the struts. During the calculations, I investigated the displacements of the diaphragm wall the moment and the shear force.

I created 5 different soil models, where I increased the soil strength parameters to find the best fit with the measured values. The varied parameters between 100-150% range are ϕ, cohesion, compressive modulus, and shear parameter values.

In the section under study, I compared the results of the 2D and 3D models. The aim of the study was to determine the relationship between the 2-dimensional and 3-dimensional models, which can be used to determine the approximate stresses and displacements of the wall near the corners where 3D effects are applied, without the need for 3D modelling.

3.1. Soil model

A number of advanced material models are available in Plaxis3D software. These can be used to model the behaviour of soils and structures more accurately. In this study I used the HS Small (Hardening Soil with small strain stiffness) material model to model the soil environment.

The soils under low stress produce very little deformation. If the soil is loaded and unloaded cyclically, the deformations at the beginning of the re-loading are smaller, or in other words the initial modulus of elasticity (E0) is larger than the modulus of elasticity (Eur) for the whole cycle. Eur=3*Eoed was applied for all layers. The G0 and $\gamma 0.7$ values were estimated using formulas listed by Benz and from the shear velocity.

The small strain parameters were determined from empirical formulas and diagrams and from the results of CPT soundings.

The latter was derived from Ákos Wolf's 2017 thesis entitled Estimation of Shear Wave Propagation Velocity from CPT Data for Domestic Soil Conditions, using the following formula:

$$v_s = 11{,}97 * q_t^{0{,}262} * I_c^{0{,}709} * D^{0{,}107} \quad (1)$$

where qt: corrected cone resistance with pore water pressure [kPa], Ic: soil behaviour factor [-], D: depth [m]

Based on the shear wave propagation velocities and the wet density of the layers, the value of G0 can be calculated with the following formula:

$$G_0 = v_{s.average}^2 * \gamma_{unsat} \quad (2)$$

And for clays and silts, I used the empirical relationship shown in the following figure, with the formula (Zs. Rémai, 2012):

$$G_0 = 49{,}4 * q_t^{0{,}695} * e^{-1{,}130} \quad (3)$$

To do this, we need the average corrected cone resistance with pore water pressure, and the characteristic void factor of the soil layer.

The following parameters used for modelling:

1. Table Basic model parameters

Soil model		Layers								
		L1 - Fill	L2 - Si	L3 - siSa	L4 - siCl	L5 - Cl	L6 - siSa	L7 - Cl	L8 - siSa	L9 - Sa
γ_{unsat}	kN/m³	17	18	18	18	18	19	18	19	19
γ_{sat}	kN/m³	18	19	19	19	19	20	19	20	21
e	-	0,8	0,65	0,75	0,65	0,7	0,6	0,7	0,7	0,5
E_{50}	MN/m²	14	9	18	5	4	35	4	20	60
E_{oed}	MN/m²	14	9	18	5	4	35	4	20	60
E_{ur}	MN/m²	42	27	54	15	12	105	12	60	180
m	-	0,7	0,75	0,7	0,85	0,9	0,7	0,9	0,7	0,65
ν_{UR}	-	0,2	0,22	0,2	0,23	0,23	0,2	0,23	0,2	0,2
φ	◦	30	20	30	18	18	33	18	30	36
c	kN/m²	0,1	20	5	25	20	0,1	20	5	0,1
$G_{0,ref}$	MN/m²	52	172	102	96	84	187	89	200	289
$\gamma_{0,7}$	-	4,28E-05	7,21E-05	8,61E-05	1,50E-04	1,78E-04	1,16E-04	2,20E-04	1,48E-04	1,29E-04
k	m/day	8,64E+04	8,64E+00	8,64E+00	8,64E-03	8,64E-03	8,64E+01	8,64E-04	8,64E+01	8,64E+02

3.2. Plaxis models

I modelled the diaphragm wall with plate elements and the struts with a beam element. The struts are hinged to the diaphragm wall. All soil layers were modelled with drained behaviour. The modelled construction phases are:

1. Initial phase
2. Working platform, and wall construct
3. 1st row strut working platform
4. 1st row strut application
5. 2nd row strut working platform
6. 2nd row strut application
7. 3rd row strut working platform
8. 3rd strut application
9. Complete excavation of the working pit

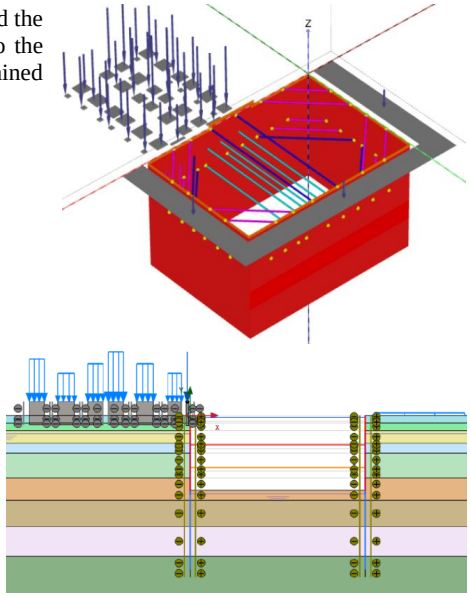


Figure 3. Plaxis 2D and 3D model

4. RESULTS

4.1. Back analysis

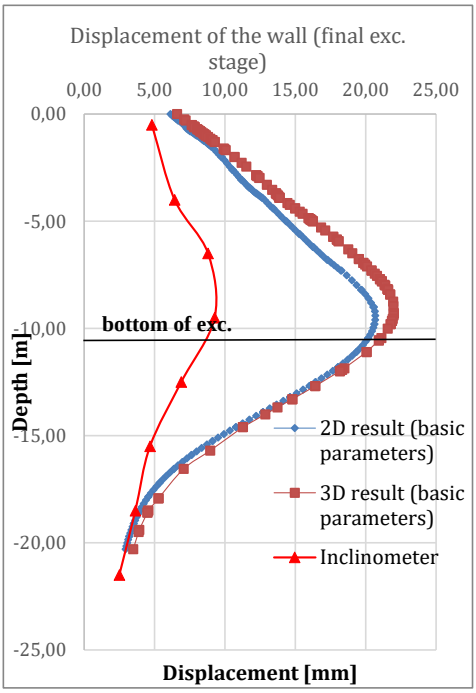


Figure 4. Measured and calculated displacement

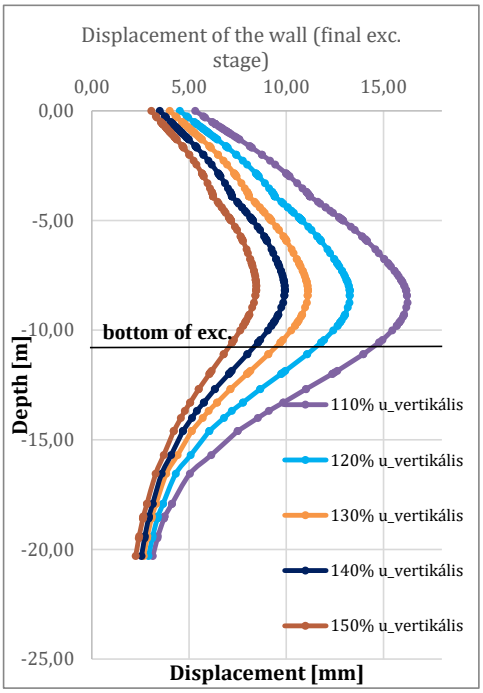


Figure 5. Calculated displacement with increased soil parameters

Examining the computed results, it can be concluded that the calculated displacements are twice the measured values when using the basic soil parameters. The largest deviation occurs at maximum excavation (255%) (fig. 5).

With a gradual increase of the soil parameters, the displacement values became closer and closer to the measured values, in several cases the calculated values were smaller than their measured counterparts. Not only the values in mind, the shape and slope of the curves also matched the curves determined by the inclinometer measurements. To find the best-fitting curve, I determined the average deviation between the measured and calculated curves. The soil behaves more and more rigidly as the construction phases progress, as models with increasingly higher strength parameters approximate the measured results. After the final excavation, the soil behaviour is even stiffer, as the best fit is obtained for soil parameters of 140%. The average deviation was found to be 0.50 mm, with the curves fitting almost perfectly.

4.2. Corner effect

The results show that the maximum value of PSR (Ratio of 3D to 2D results in the analysed cross-section) for displacements and moments gradually decreases with increasing soil parameters. For displacements, the PSRU (displacement) value decreases from 1.23 to 1.04 and the PSRM (moment) value decreases from 1.02 to 0.75. The changes in these values are shown in the figures below. They show that 3D effects are more pronounced in stiffer soils, in narrow excavations.

Ou et al. (1996) and A. Szepesházi (2023) found the PSR to be around 0.7-0.8 for pits with the present lateral length, which is approximated for stiffer soils, especially for moments, but it is worth noting that the pit was made in a different soil environment, with different geometry and support than in the above mentioned tests.

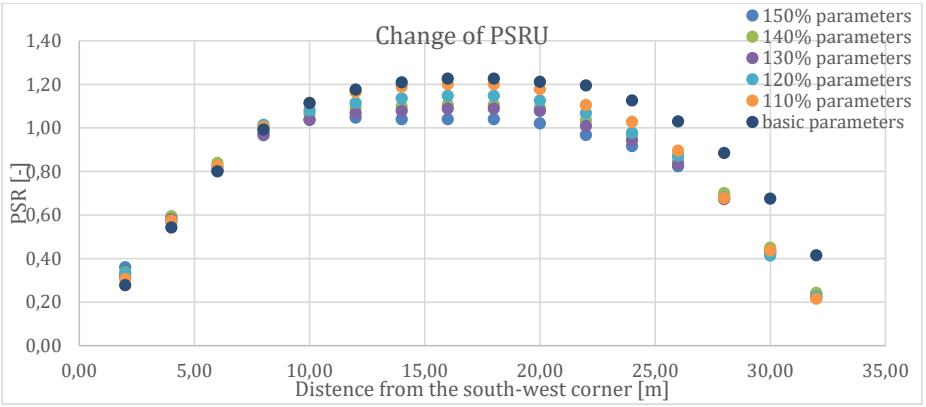


Figure 6. Value of PSRU along the wall

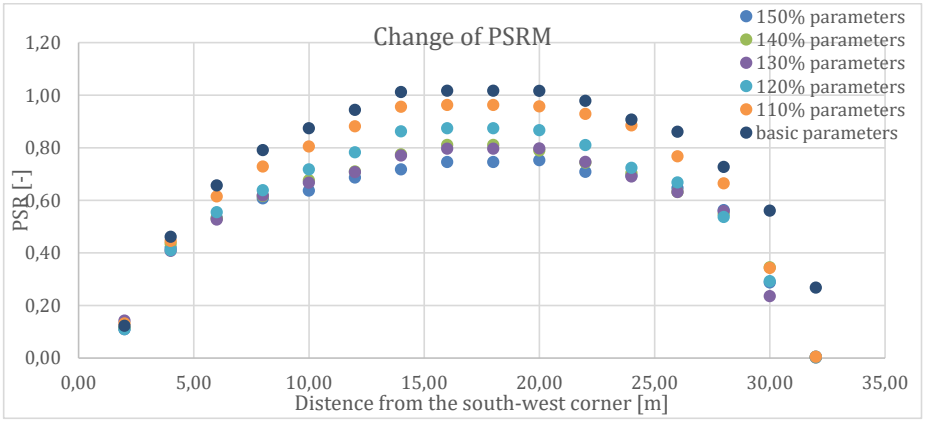


Figure 7. Value of PSRM along the wall

5. BIM

BIM as a methodology allows the various participants in the design, construction, and operation of buildings to work together in the virtual space. It is not only about classical 3D modelling, but also about the data that can be assigned to model elements, allowing them to be managed, identified, and listed individually.

Methodology has several advantages that help those involved in the process to work efficiently and quickly. In addition to the rapid production of design documentation, the 3D environment facilitates communication between disciplines, such as the detection and correction of errors and conflicts, which helps to minimise forced solutions on the construction site, so reducing its resource requirements. However, this means additional resource requirements on the planning side.

With a properly created BIM model, you can create automatic consignments, listings, statements and perform inspections.

BIM can be used not only in the building construction sector, but also in any other field of construction, from landscape to geotechnical engineering.

We can also automatically create the reinforcement (pile or diaphragm wall), which speeds up the design process and reduces the risk of error.

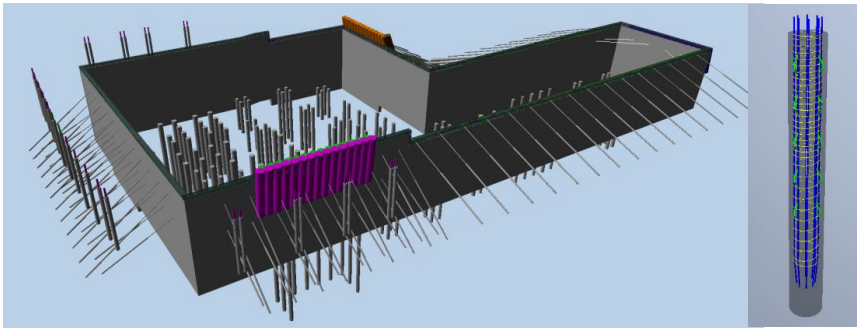


Figure 8. 3D modell of a diaphragm wall and pile reinforcement

6. CONCLUSIONS

From the calculation results, it can be concluded that the soil behaves more and more rigidly as the construction phases progress, as models with increasingly higher strength parameters approximate the measured results. This may be due to the consolidation of the soil, which increases the strength of the soil and the passive resistance, resulting in smaller deformations and lower stresses.

In the corner effect study, the PSR indices calculated from 2D and 3D results (displacement and moment) gradually decreased with soil stiffening. They conclude that 3D effects are more pronounced for stiffer soils than for narrow working pits.

The increasing use of BIM in various sectors of the construction sector allows for the detection of defects before construction and helps in the digitalisation process.

7. ACKNOWLEDGEMENTS

I would like to thank Attila Szepesházi and Benedek Nagy from HBM Soletanche Bachy and János Szendefy from the University of Technology for their professional and modelling assistance.

REFERENCES

Chang-Yu Ou, Dar-Chang Chiou, Tzong-Shiann Wu. 1996. Three-Dimensional Finite Element Analysis of Deep Excavations. *Journal of Geotechnical Engineering*

Szepesházi A. 2023. Comparative evaluation of planar and spatial finite element computational results for diaphragm wall. *PhD thesis. Budapest University of Technology and Economics.*

Wolf Á. 2017. Estimation of Shear Wave Propagation Velocity from CPT Data for Domestic Soil Conditions. *Geotechnice Conference 2017, Velence*

Rémai Zs. 2012. Testing of water-saturated clays under fillings. *PhD thesis. Budapest University of Technology and Economics.*

Benz T. 2007. Small-Strain Stiffness of Soils and its Numerical Consequences. *Mitteilung 55 des Instituts für Geotechnik der Universität Stuttgart*.

28th European Young Geotechnical Engineers Conference – EYGEC 2024
© 2024 Macedonian Association for Geotechnics, ISBN 978-608-4510-61-1

A liquefaction simulation for the 1987 Wildlife case study using the extended equivalent linear model (X-ELM)

Samer Abou Kheir[1] , Ziad Kteich[1,2], and Pierre Labbe[2]
[1]*Pole GEOS, TRACTEBEL, Gennevilliers, France*
[2]*ESTP, Cachan, France*

ABSTRACT

Liquefaction-induced ground failure poses significant challenges to engineering practices, particularly in seismic regions. Earthquake events commonly result in liquefaction failures, including settlements, building tilting, sand boils, and slope instabilities. Consequently, assessing liquefaction risk becomes imperative for critical infrastructure. This study introduces a liquefaction simulation approach, specifically tailored for the Wildlife site, utilizing the simplified extended equivalent linear model (X-ELM) method. This method facilitates the simulation of liquefaction within a 1D horizontally layered soil profile. The X-ELM method, being a linear equivalent model, incorporates the effects of pore water pressure buildup through experimental and semi-empirical relationships. It also integrates non-linear soil response due to shear strain and pore water pressure. The practicality of the X-ELM method for engineering applications is emphasized. It is applied to the Wildlife site, which experienced the 1987 Superstition Hills earthquake. The study compares liquefaction triggering response and pore water pressure buildup simulated by the X-ELM method with actual observations from the Wildlife profile array. Through this comparison, the efficacy of the X-ELM method is evaluated, providing insights into its performance and suitability for practical engineering assessments.

KEYWORDS

X-ELM, EERA, Liquefaction, Pore water pressure, Sand, Wildlife site.

1. INTRODUCTION

Probabilistic and statistical analyses of seismic-induced shear stress and experimental soil shear strength have led to the development of empirical methods for assessing liquefaction risk. While simplified methods offer ease of use, they are limited in accuracy and often require significant design margins. In response, complex methods have been proposed to simulate the intricate physics of liquefaction. These methods involve transient nonlinear calculations coupled with excess pore water pressure generation, requiring advanced engineering skills, extensive laboratory tests for soil model calibration, and considerable time investment. As an intermediate solution, the Extended Equivalent Linear Model (X-ELM) offers a simpler approach to studying liquefaction triggers by earthquakes. This method integrates semi-empirical and experimental relationships to combine excess pore water pressure with the linear equivalent response of soil profiles. By doing so, X-ELM provides a more precise and cost-effective means of evaluating liquefaction risk for engineering projects.
In a study by (Kteich, et al., 2019), the X-ELM was applied to twelve soil profiles in the city of Urayasu, where real liquefaction observations were recorded following the 2011 Tohoku earthquake. The X-ELM qualitatively predicted liquefaction occurrences, demonstrating its efficacy. Subsequently, the authors introduced the X-ELM into the VBA/Excel environment for enhanced ease of use in engineering practice. They utilized the model to simulate real observations from the Wildlife profile, comparing the results to in-situ data and acceleration records to assess its reliability. Furthermore, this paper highlights the advantages of utilizing in-situ Cone Penetration Test (CPT) data over Standard Penetration Test

(SPT) data for liquefaction assessment, emphasizing the importance of accurate and comprehensive data inputs in liquefaction risk evaluation.

2. X-ELM/EERA MODEL PRESENTATION

2.1. Theory and background

The extended equivalent linear method X-ELM integrates the excess pore water pressure influence into the conventional equivalent linear method. This method follows the near surface assumption and neglects the effect of volumetric wave propagation. It analyses the response of a 1D soil profile using only the preponderant component of the shear wave with a vertical propagation. To calculate the pore water pressure, this method integrates the generation of the volumetric deformation in function of the shear distortion and the cumulated volumetric deformation using Byrne model (Byrne, 1991). Moreover, it uses the (Martin, et al., 1975) approach and the updated (Wu, 2001) elastic rebound modulus to predict the excess pore water generation into the profile. The previous models combined with an equivalent linear method forms the X-ELM approach, it is used to simulate the response of an undrained soil profile under cyclic loading.

A brief summary of the X-ELM main integrated models will be presented in the following sections, (Kteich, et al., 2019) explain the detailed operation of the X-ELM in his article.

2.2. Modelling of the soil behaviour

The soil response under seismic motion is governed by the shear modulus degradation of the soil profile and is regulated by the intrinsic and geometric energy dissipation of the soil. Based on laboratory tests, it is observed that the soil material under shear loading presents hysteretic response, this behaviour is due to the instantaneous degradation of the shear modulus G in function of the distortion level and the pore water pressure buildup. Equation (1) presents the shear modulus of (Seed & Idriss, 1970) that accounts for the previous observations.

$$G = AF(e)\frac{G}{G_{max}}[\gamma](p')^n \quad (1)$$

AF(e) is considered constant for undrained conditions and can be calculated from the initial maximum shear modulus at very low distortion levels; $\frac{G}{G_{max}}[\gamma]$ is derived from experimental tests on each material, it governs the degradation of the shear modulus in function of the distortion level; $(p')^n$ integrates the influence of the excess pore water pressure on the shear modulus degradation of the soil. (Oztoprak & Bolton, 2013) showed that the experimental shear modulus degradation curves with a maximum of 10 distortion cycles do not incorporate the influence of the pore water pressure. For this reason, the X-ELM incorporate the pore water pressure generation model into the degradation of the soil shear modulus.

2.3. Determination of the volumetric plastic deformation

To determine the pore water pressure generation under undrained cyclic loading, the excess pore water pressure is related to the cumulated volumetric plastic deformation. (Byrne, 1991) proposed equation (2) to quantify the generation of permanent volumetric plastic deformation via cyclic loading. The incremental volumetric deformation is calculated in function of the cumulated deformation, the shear distortion amplitude, and two tuning parameters C1-C2.

Byrne demonstrated that for a single sand with the same relative density a single incremental volumetric

$$\Delta\varepsilon_v^p = C_1 exp\,(-C_2\frac{\varepsilon_v^p}{\gamma}) \quad (2)$$

deformation curve can be plotted for different distortion level, while a sand with different relative density the fitting curve can be adjusted by updating the volume control C_1 parameter and the shape C_2 parameter. Byrne demonstrated that for different densities the curves preserve identical shapes and proposed relating parameter C_2 to parameter C_1 by the following equation: $C_2 = \frac{0.4}{C_1}$.

The success of the Byrne model derives from the ability to relate : the parameter C_1 with the relative density D_r using equation (3) of (Silver & Seed, 1971) or the normalized SPT blow count $(N_1)_{60}$ using the equation (4) of (Tokimatsu & Seed, 1987) or the corrected equivalent clean sand cone tip resistance q_{c1Ncs} using equation (5) of (Boulanger & Idriss, 2014).

$$C_1 = 7600\ (D_r)^{-2.5} \tag{3}$$

$$C_1 = 8.7\ (N_1)_{60}^{-1.25} \tag{4}$$

$$D_r = \{0.478(q_{C1Ncs})^{0.264} - 1.063\}.100 \tag{5}$$

2.4. Pore water pressure calculation

To determine the excess pore water pressure that is generated from the cumulated plastic volumetric deformation of (Byrne, 1991), the (Martin, et al., 1975) model with the updated (Wu, 2001) rebound modulus is proposed.

The pore water pressure generation is related linearly to the volumetric deformation via the drained bulk modulus. (Seed, et al., 1975) studied the reversibility of the volumetric deformation and noted that it is 20% more reversible in a cyclic loading compared to a monotonic loading. Therefore (Wu, 1996) performed a study to determine the cyclic rebound modulus E_r of the soil and noted that it exists a unique relationship between the soil relative density and the required volumetric deformation to cause liquefaction. Wu proposed the equation (6) to represent the rebound modulus E_r in function of the vertical effective stress and a constant M that is expressed in equation (7) as a function of the SPT $(N_1)_{60}$ and a constant α. The maximum value of M is limited to 480 and the value of α ranges between 150 and 180.

$$E_r = M\sigma'_v \tag{6}$$

$$M = 10(N_1)_{60} + \alpha \tag{7}$$

(Kteich, et al., 2019) proposed equation (8) to calculate the excess pore water pressure considering the corrected rebound modulus of (Wu, 1996) and (Wu, 2001).

$$r_u = \frac{\Delta u}{\sigma'_{v0}} = 1 - exp\ (-M\varepsilon_v^p) \tag{8}$$

To model the response of the soil profile, (Kteich, et al., 2019) integrated the effect of the excess pore pressure into the (Seed, et al., 1975) shear modulus equation as follows:

$$G' = G^0_{max}\frac{G}{G_{max}}[\gamma_{eff}](1 - r_{ueff})^n \tag{9}$$

Integrating the pore water pressure generation model into an equivalent-linear analysis does not consider the instantaneous time effect of the pressure generation and the distortion levels. Therefore, equivalent to the idea proposed by (Seed, et al., 1975) to use an effective distortion level when calculating the shear modulus degradation curve, a weighting coefficient χ is introduced to the pore water pressure ratio $r_{ueff} = \chi r_{umax}$ and integrated into equation (9).

3. CASE STUDY - LIQUEFACTION ANALYSIS OF THE WILDLIFE SITE

3.1. Overview of the Wildlife site

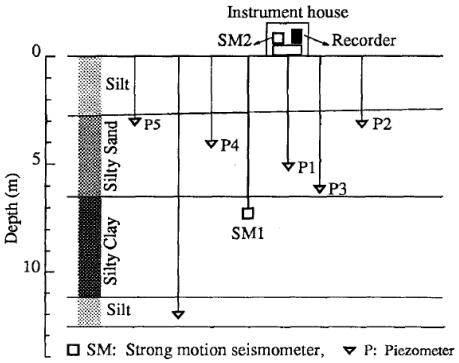


Figure 1. Wildlife profile section and instrumentation. (Bennett, et al., 1984).

The Wildlife site, situated on the western bank of the Alamo River in Imperial County, Southern California, was flagged for liquefaction susceptibility following observed evidence. To comprehensively understand the interplay between ground motion, pore water pressure buildup, and site degradation, instrumentation was installed to record seismic responses. These data, collected post-liquefaction suspicions, have been pivotal in analyzing the dynamics of ground behavior strength (Bennett, et al., 1984).

The site's profile, illustrated in Figure 1, delineates critical instrumentation placements: the SM2 accelerometer atop the ground surface and the SM1 accelerometer positioned 7.5 meters beneath the silty sand stratum. Identified as liquefiable, the silty sand layer warranted further monitoring, prompting the installation of five piezometers (P1 to P5) to track pore water pressure variations during seismic events. Notably, the water table lies 1.3 meters beneath the ground level, rendering soil layers above this threshold immune to liquefaction.

On November 23, 1987, the Wildlife site experienced the Superstition Hills earthquake, registering a magnitude of Mw=6.6. This seismic event induced a sharp escalation in pore water pressure, as evidenced by field observations revealing the emergence of sand boils—an unmistakable sign of liquefaction occurrence. In response to these findings, the X-ELM approach is proposed to simulate liquefaction dynamics within the Wildlife profile, aiming to enhance understanding and predictive capabilities regarding ground behavior under seismic stressors.

3.2. The X-ELM liquefaction model

The creation of the X-ELM model for the Wildlife site involves utilizing various geotechnical parameters obtained from field investigations and laboratory tests. Figure 2 depicts the SPT N values, shear wave velocity, and Cone Penetration Test (CPT) data, crucial inputs for model development. Additionally, the soil granulometry test conducted by (Bennett, et al., 1984) discerns susceptible zones for liquefaction, utilizing the PS92 criterion for sandy and silty soils and the (Seed et al. 2003) criterion for clayey soils. Regions highlighted in Figures 2 and 3 denote susceptibility to liquefaction.

To refine input parameters for the X-ELM model, the soil fines content is employed to adjust the SPT N values and CPT q_{cN} values, yielding clean sand equivalents $(N_1)_{60CS}$ and $(q_{cN})_{cs}$, respectively. These adjusted values are then incorporated into the (Byrne, 1991) model. Notably, the NS record captured by the SM1 accelerometer, positioned 7.5 meters below the ground surface, is integrated into the X-ELM model with a borehole configuration, accurately simulating motion at this depth layer. This meticulous approach ensures the fidelity of the model in capturing the site-specific dynamics and behavior of the Wildlife site during seismic events.

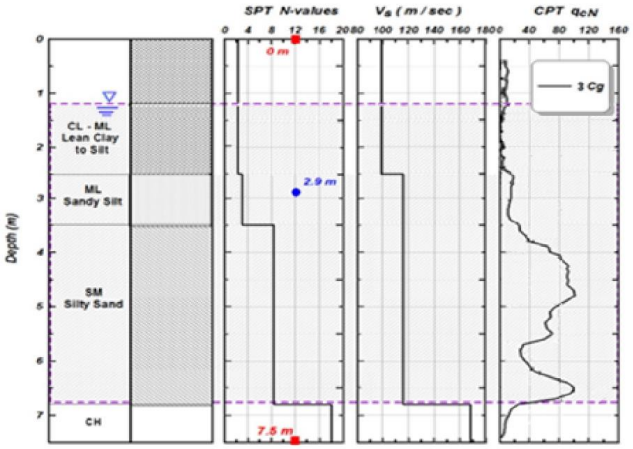


Figure 2. Wildlife liquefaction array profile showing: SPT N values, shear wave velocities, CPT tip resistances, depths of recordings (accelerometers at 0 and 7.5 m; pore-pressure transducer at 2.9 m) and highlighting the liquefiable strata [(Bennett, et al., 1984), (Ziotopoulou, et al., 2012)]

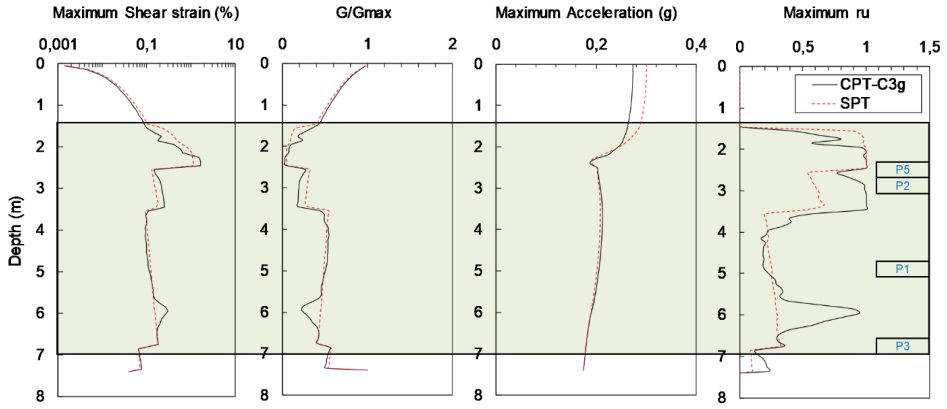


Figure 3. The results of the Wildlife profile showing the maximum shear strain profile, the shear modulus ratio profile, the maximum acceleration profile, the pore water pressure ratio and the highlighted critical layer for the X-ELM model with CPT and SPT input

For comparison, two X-ELM models were developed for the Wildlife profile using in situ data from (Bennett, et al., 1984). These models incorporate adjustments to pore water pressure buildup parameters, namely Byrne C1 and C2, related to the first model with SPT clean sand $(N_1)_{60CS}$ and to the second model with C3g CPT clean sand $(q_{cN})_{cs}$ using using equation (3) and (5). Results from the Wildlife simulation in Figure 3 reveal critical parameters including maximum shear strain, shear modulus ratio, maximum acceleration, and maximum pore water pressure ratio for both X-ELM models. Remarkably, both models exhibit comparable outcomes, with a maximum shear strain of 1.6% and a G/Gmax nearing 0 at a depth of 2.4 meters, indicating a pronounced nonlinear response of the Wildlife profile during the Superstition Hills earthquake.

Applying liquefaction susceptibility criteria, highlighted zones in the Wildlife profile denote regions prone to excess pore water pressure buildup. A notable observation emerges: the model utilizing CPT input presents higher excess pore water pressure ratios, covering a larger area compared to the SPT input model. Furthermore, the SPT input model fails to identify a liquefied zone at a depth of 6 meters. Consequently, the efficacy of liquefaction response assessment hinges on the quality of input profile characteristics, notably observed discrepancies between CPT and SPT inputs. It is evident that the CPT in situ test yields more accurate results, proved more suitable for liquefaction risk assessments.

3.3. Liquefaction results - pore water pressure buildup

Figure 4 presents the pore water pressure buildup visualization, combining in-situ data from piezometers P1, P2, P3, and P5 with the results obtained from the X-ELM model utilizing Cone Penetration Test (CPT) input data. Analysis of the in-situ data reveals a consistent trend in pore water pressure buildup across all four piezometers. This consistency suggests interconnected pores within the susceptible layer, indicating susceptibility to liquefaction across all layers concurrently, typically observed approximately 40 seconds after the onset of shaking. Comparing the pore water pressure buildup between the X-ELM model and real observations, a similar order is noted. Specifically, the pore water pressure buildup (Ru) at P1 and P3 is lower than that at P2 and P5, aligning with the lower soil characteristics observed at P2 and P5 as illustrated in Figure 2. However, while the X-ELM model effectively predicts liquefaction in localized zones, it fails to do so comprehensively. In piezometers P2 and P5, the calculated Ru exceeds the liquefaction triggering threshold of 0.8, indicating liquefaction occurrence. However, despite observed liquefaction, calculated Ru values in piezometers P1 and P3 remain below the triggering limit. Furthermore, the X-ELM model predicts liquefaction occurring after 14 seconds from the onset of the earthquake, contrasting with the 40-second timeframe observed in reality. This discrepancy in timing is attributed to the model's lack of consideration for flow interaction between different layers within the profile. Typically, sand permeability is high, facilitating pressure migration from zones with higher pore water pressure buildup (such as P2 and P5) towards zones with lower buildup (such as P1 and P3), thereby delaying liquefaction occurrence in the former.

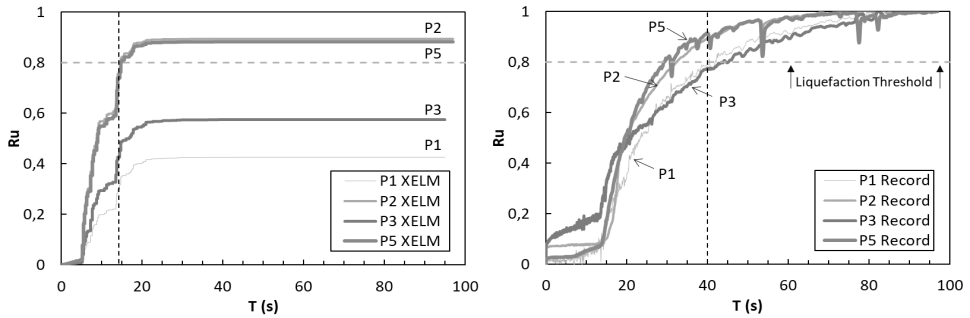


Figure 4. The pore water pressure generation of the X-ELM model for the Wildlife profile and the pore water pressure observations of the P1, P2, P3, and P5 Wildlife

3.4. Liquefaction results - acceleration records

Figure 5 displays the ground surface acceleration records for both the Wildlife real observation and the simulated X-ELM, segmented into four distinct stages for analysis:

- Stage 1 (0.0-13.7 s): During this initial stage, the ground acceleration exhibits a low amplitude (0.13g), accompanied by minimal pore water pressure buildup. The response from the X-ELM simulation closely mirrors the real observation but with smoother amplitude characteristics.
- Stage 2 (13.7-20.6 s): This stage corresponds to the peak of the shaking event, characterized by the strongest ground acceleration reaching a peak of 0.21g. Pore water pressure rapidly increases during this period. While the real observation shows slight smoothing, the X-ELM simulation demonstrates higher peak amplitudes compared to the real observations.
- Stage 3 (20.6-40.0 s): Acceleration amplitudes in the real observation decrease to 0.06g during this stage, accompanied by longer periods compared to previous stages. Pore pressure buildup continues, and the X-ELM simulation exhibits more peaks (higher frequencies) than the recorded data.
- Stage 4 (40.0-96 s): At this stage, excess pore water pressure reaches its maximum value. The registered surface acceleration displays low amplitudes and very high periods, while the X-ELM simulation consistently shows more peaks than the real observations. The smoothing of acceleration amplitudes is attributed to excessive soil softening, where the soil layer undergoes significant deformation and becomes overly plasticized, hindering upward signal transfer.

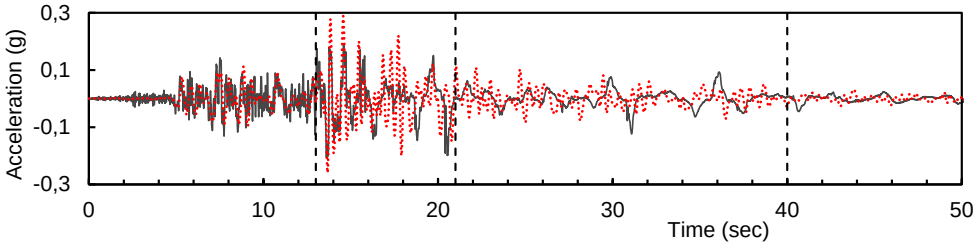


Figure 5. The different stages of the acceleration record at the ground surface level of the Wildlife real observation (solid line) and the simulated X-ELM model (dotted line).

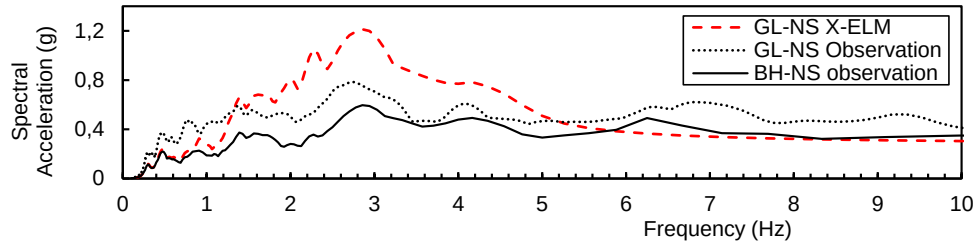


Figure 6. The pseudo spectral acceleration of the Borehole signal for the Wildlife real observation (solid line), the ground surface signal for the Wildlife real observation (soft dotted line), and the ground surface signal for the linear equivalent X-ELM (rough dotted line), with a 5% critical damping ratio.

Figure 6 illustrates the pseudo spectral acceleration of both the real observation and the X-ELM simulation. Notably, all three spectral accelerations exhibit a maximum pseudo spectral acceleration at the same frequency value of 2.9 Hz, indicating that the X-ELM possesses natural frequencies similar to those of the actual profile. However, there are discrepancies in pseudo acceleration amplitudes between the X-ELM model and the real observation. Specifically, the X-ELM model overestimates pseudo acceleration amplitudes within a central frequency range of 1.3 Hz to 5.2 Hz and underestimates them outside this range. The observed decay in high frequencies of the real acceleration record in Figure 5 is attributed to the liquefaction effect. During liquefaction, there is an instantaneous sharp shift in shear modulus and damping values, resulting in a decay of high frequencies in the signal.

The X-ELM model, however, employs a constant and averaged modulus and damping throughout the calculation, incapable of simulating the instantaneous changes in these parameters over time. This averaging effect results in smoothed frequencies in the X-ELM signal, particularly evident in Stage 1. Consequently, the X-ELM model produces lower acceleration amplitudes at high frequency levels.

Conversely, in the low frequency range of the spectrum, the real observation exhibits higher frequencies than the X-ELM simulation in Stages 2, 3, and 4, leading to lower acceleration amplitudes for the X-ELM. Furthermore, the constant shear modulus over time utilized by the X-ELM model results in amplification at the natural frequencies of the profile, explaining the higher acceleration amplitudes observed at central spectral frequencies.

4. CONCLUSION

The X-ELM method aims to create a liquefaction risk analysis tool that surpasses simple empirical methods in accuracy while maintaining ease of use compared to transient effective stress models. In practice, the X-ELM model successfully identifies soil profile liquefaction triggers during seismic events. However, it diverges from reality in terms of excess pore water pressure generation. Notably, due to the absence of flow calculations, the X-ELM model produces faster pore water pressure changes for highly susceptible layers and slower changes for resistant layers. When assessing liquefaction risk using the X-ELM method, it's crucial to qualitatively consider layer interactions that influence the liquefaction response. In summary, the X-ELM model detects liquefaction but falls short in simulating

post-liquefaction effects due to limitations in shear modulus averaging within the linear equivalent method at high distortion and pore water pressure levels.

5. ACKNOWLEDGEMENT

Sincere gratitude are expressed to TRACTEBEL Engie for funding this work and École des Ponts ParisTech for their academic support during the (GCGOE) master program.

REFERENCES

Bennett, M. J., McLaughlin, P. V., Sarmiento, J. S. & and Youd, T. L., 1984. Geotechnical investigation of liquefaction sites, Imperial Valley, California. *Open-file Rep. 84-252, U.S. Geological Survey, Washington, D.C.*.

Boulanger, R. & Idriss, I., 2014. *CPT and SPT Based Liquefaction Triggering Procedures,* s.l.: Report No. UCD/CGM-14/01, Center for Geotechnical Modeling, University of California, Davis, April 2014.

Byrne, P. M., 1991. *A cyclic shear volume coupling and pore pressure model for sand.* St. Louis, Missouri, USA, s.n.

Kteich, Z. et al., 2019. Extended equivalent linear model (X-ELM) to assess liquefaction triggering: Application to the City of Urayasu during the 2011 Tohuko earthquake. *Soils and Foundations* , Volume 59(3), 750-763..

Martin, G., Finn, W. & Seed, H., 1975. Fundamentals of liquefaction under cyclic loading. *J. Geotech. Eng. Division, ASCE 101 (GT5),* pp. 423-438.

Oztoprak, S. & Bolton, M., 2013. Stiffness of sands through a laboratory test database. *Geotechnique, 63(1) :54.*

Seed, H. & Idriss, I., 1970. Soil moduli and damping factors for dynamic response analysis. *EERC.*

Seed, H., Idriss, I., Makdisi, F. & Banerjee, N., 1975. Representation of irregular stress times histories by equivalent uniform stress series in liquefaction analyses. *Report No. EERC 75-29.*

Silver, M. & Seed, H., 1971. Deformation characteristics of sands under cyclic loading. *Journal of soil mechanics & foundations Div, 97,* pp. 1081-1098.

Tokimatsu, K. & Seed, H., 1987. Evaluation of settlements in sands due to earthquake shaking. *Journal of geotechnical engineering, 113(8),* pp. 861-878.

Wu, G., 1996. *Volume change and residual pore water pressure of saturated granular soils to blast loads.*, Burnaby: The natural sciences and engineering research council of canada AGRA earth & Environmental Ltd.,.

Wu, G., 2001. earthquake-induced deformation analyses of the upper san fernando dam under the 1971 san fernando earthquake. *Canadian geotechnical journal, 38(1) : 1-15.*

Ziotopoulou, k., Boulanger, R. W. & Kramer, S. L., 2012. *Site Response Analysis of Liquefying Sites.* , s.n.

28th European Young Geotechnical Engineers Conference – EYGEC 2024
© 2024 Macedonian Association for Geotechnics, ISBN 978-608-4510-61-1

Evolution of the microstructural and chemical properties of the CO_2-aged Banco Verde sandstone

Cecilia B. Laskowski[a, b], Diego G. Manzanal[a,b], Mauro Muñiz-Menéndez[c], Sandra G. Orlandi[b], José O. Allard[b]

[a] *Escuela Técnica Superior de Ingenieros de Caminos, Canales y Puertos de la Universidad Politécnica de Madrid, Madrid, Spain*
[b] *Universidad Nacional de la Patagonia San Juan Bosco, Comodoro Rivadavia, Argentina*
[c] *Laboratorio de Geotecnia, CEDEX, Madrid, Spain*

ABSTRACT

With the exponential increase in the World's mean temperature, produced due to the worrying rise in CO_2 emissions, more and more international entities are looking for options to mitigate this natural phenomenon. In this context, researchers have proposed storing this gas in the subsoil. Among the different types of CO_2 underground storage, a commonly mentioned alternative is the use of depleted oil and gas reservoirs. These formations are characterized by being composed of sedimentary porous reservoir rocks, covered by a caprock layer that stands out due to its low permeability. In Argentina, three main basins are considered as possible CO_2 storages, being the Salamanca Formation from the Golfo San Jorge Basin the case study of this article. This formation is composed of three seal layers (Lignitífero, Fragmentosa, and Banco Negro) alternated with two reservoir rocks (Glauconítico and Banco Verde). It is of particular interest the study of the Banco Verde layer, as it is a depleted oil and gas reservoir that seems to gather the necessary properties to be used as a permanent underground CO_2 storage. In previous research, laboratory mechanical tests were performed on pristine and CO_2-aged sandstone samples, showing a notable variation in their properties after CO_2 exposure. Aiming for a better understanding of this property evolution, microstructural and chemical analysis such as X-ray diffraction, and Mercury Intrusion Porosimetry, were performed. The observed modifications in the behaviour of the reservoir rock seem to be consequent with the microstructural and chemical evolution produced.

KEYWORDS

Sandstone CO_2-aged; Carbon capture and storage; Depleted oil and gas reservoir; Micro structural and chemical property evolution.

1. INTRODUCTION

According to the Intergovernmental Panel on Climate Change, in the last 100 years, the average global temperature has increased by about 1.1ºC (Working Groups I, II and III of the Intergovernmental Panel on Climate Change (2023)). This notable increase in temperature leads to substantial changes in the daily activities of the species that inhabit the earth's surface. This is why the issue of climate change is constantly being addressed. Considering the fact that this phenomenon is mainly produced due to the exponential increase in the emission of greenhouse gases (Siddiqui et al. (2022)), 75% of which are carbon dioxide (CO_2) (Working Group III of the Intergovernmental Panel on Climate Change (2014)), researchers are currently looking for ways to adequately dispose these fluids.

Carbon dioxide capture and storage is a practice that is being increasingly mentioned, as it represents a viable alternative in the process of mitigating global warming. It is intended to reduce the concentration

of CO_2 in the atmosphere through the geological storage of the gas in a suitable rock stratum. There are different types of geological formations whose geomechanical properties classify them as suitable to be considered as CO_2 reservoirs. These include coal beds, salt beds, depleted oil and gas reservoirs, and saline aquifers (Bachu et al. (2000)).

In 2015, in the context of the United Nations Framework Convention on Climate Change, the Secretariat of Environment and Sustainable Development of Argentina met with the aim of proposing measures to mitigate global warming. Thus, among the options mentioned, the geological storage of CO_2 was highlighted, proposing different depleted gas and oil formations as possible reservoirs of this greenhouse gas. Among them, particular interest was shown in the oil formations distributed in the Golfo San Jorge Basin. At that time, it was considered that the country did not have the resources or the necessary experience to start applying these practices, so the corresponding investigations were not carried out. Despite this, in recent years, several Argentinian researchers have shown interest in focusing on this research area (Manzanal et al. (2013), Barría et al. (2018), Martín et al. (2022), and Grasetti et al. (2022)). Except for particular cases (Grasetti et al. (2022)), the studies developed focus on the study of the interaction between the cement of the injection well and the injected CO_2 and on the modelling of the CO_2 interaction with the cement and not on the evolution of the properties of the rock in charge of storing the gas in question.

When considering the feasibility of using a certain rock as a CO_2 reservoir, it is essential to study the modifications produced in its properties due to the action of supercritical carbon dioxide ($scCO_2$). The geomechanical properties of interest depend mainly on two factors, on the one hand, to ensure that the gas is fixed (Bradshaw et al. (2007)), and on the other hand, to ensure the long-term integrity of the reservoir (Hawkes et al. (2004)). Thus, the main geomechanical properties analysed are usually porosity and permeability, composition and strength.

Considering the national interest in developing geological storage of carbon dioxide, and the scarce research developed on this subject, this article proposes the Banco Verde stratum of the Salamanca Formation, belonging to the Golfo San Jorge Basin, as a possible CO_2 store. The proposed stratum is formed by a glauconitic sandstone of marine origin, which is characterized by being a reservoir of depleted gas and oil (Foix (2009)). Thus, a detailed analysis of the compositional and micro structural properties of the chosen sandstone, before and after subjecting it to the action of $scCO_2$ for a period of 30 days, is presented below.

2. MATERIALS AND METHODS

2.1. Salamanca Formation description

According to Feruglio (1949), the Salamanca Formation is composed of five different layers. The lower layer, known as Lignitífero, composed of grey clays with thin sandy banks containing abundant carbonaceous remains, with a thickness varying between 15 and 20m (TERMAP S.A. (2011)). Directly in contact with this last is Glauconítico (10-30m), which, as its name indicates, is a glauconitic sandstone stratum with low clay content, being this the first oil and gas reservoir found and exploited from the Golfo San Jorge Basin. The Fragmentosa layer, is characterized for being the thickest of the stratum composing the Salamanca Formation (140m), representing the cap rock of the Glauconítico, being composed of a fractured grey claystone filled with sandy sediments from the above layer. The two strata left, Banco Verde and Banco Negro, from bottom to up, represent the shallower oil and gas reservoir of the Golfo San Jorge Basin and its corresponding cap rock. The special interest shown in them as possible geological storage of CO_2 resides in the fact that the Banco Verde reservoir rock is depleted. Additionally, this layer is composed of coarse to very fine-grained greenish-gray sandstone, material discontinuities such as gypsum veins, glauconite and vulcanite clasts and clay lenses that come from the Banco Negro stratum (Foix (2009)). According to Rodríguez et al. (2014), Banco Verde is characterized for having high values of porosity and permeability, which make it a suitable reservoir rock for CO_2 injection. The Banco Negro layer, represents the cap rock of the Banco Verde reservoir rock, adding

safety to the possible underground CO_2 storage. This claystone is composed of dark gray clays, with black speckles, characterized for presenting low permeability values, which make it a potentially effective sealing rock for potential gas leaks.

The presented study aimed to analyze the variation produced in the properties of the Banco Verde reservoir rock layer due to its aging with $scCO_2$ during a 30-day period. To achieve this, it was first necessary to obtain samples from which to extract specimens to be further tested in both its pristine and carbonated state. Bearing in mind that it was economically unfeasible to obtain underground samples, the alternative chosen was to extract samples from outcrop. Even when Salamanca Formation can be reached superficially in several geological locations, such as "Estancia las Violetas", "Puerto Visser", "Meseta del Curioso", among others (Foix et al. (2009)), just in some of them, the Banco Verde layer is reachable, being this the reason why the "Punta Peligro Norte" outcrop was selected. In this location, Fragmentosa, Banco Verde and Banco Negro layers of the Salamanca Formation can be reached. With the help of a pickaxe, samples were extracted from the lower part of the Banco Verde sandstone and taken to the "Laboratorio de Investigación de Suelos, Hormigones y Asfaltos" of the Universidad Nacional de la Patagonia San Juan Bosco (UNPSJB) for further treatment.

2.2. Specimen obtention

Once the samples were obtained from outcrop, the next step was to extract and prepare the specimens to be tested. Bearing in mind that the specimens to be subjected to mineralogic and micro structural analysis had to be pieces of rock of around 50g, depending on the test, and with no particular shape, it was considered adequate to take advantage of the pieces that resulted from performing the mechanical tests.

The cores to be used for mechanical property determination were obtained according to the ASTM D 4543 – 01 normative, using a coring machine and a saw. Once these were measured and weighed, the specimens were paired according to their property similarity, considering them "twin" specimens. Half of the twin specimens were stored in a constant humidity and temperature chamber, while the other half were subjected to a $scCO_2$-aging process. The CO_2 was injected into the chosen sandstone specimens during a 30-day period, completed using a carbonation cell available in the UNPSJB's laboratory. The gas was characterized for having a pressure of approximately 10MPa and a temperature of 60ºC, conditions selected with the aim of injecting the CO_2 in a supercritical state of matter (according to Ranjith et al. (2013), CO_2 is supercritical at 7.38MPa and 31.48ºC) and reaching the real underground temperature of the reservoir. Both groups of specimens, pristine and carbonated, were subjected to the desired mechanical tests.

As it was previously mentioned, after performing the mechanical tests on the twin cores, the resting pieces of rock were used to obtain the necessary specimens to perform the mineralogic and micro structural analysis. Considering that the objective of the research was to study the variation of the chemical properties of the glauconitic sandstone due to its exposure to CO_2, pieces of rock were extracted from the already tested cores from two zones: centre and edge. In this way it would also be possible to view the degree of penetration of CO_2 in the carbonation process, bearing in mind that the edge of the cores would be exposed to the gas from the first moment, while the centre wouldn't.

2.3. Laboratory tests

Previously, it was pointed out that when studying the feasibility of using a certain geological stratum as a storage for CO_2, it was necessary to consider, on the one hand, the available volume and, on the other hand, the type of trapping that occurs (Bradshaw et al. 2007). Thus, the need arose to study the evolution of the microstructural properties of the sandstone that forms the Banco Verde after CO_2 injection. This analysis also allows a better understanding of the modifications presented in terms of the mechanical properties of the rock. In this context, it was proposed to study the evolution of the rock composition, as well as its porosity and pore distribution.

In order to analyse the variation of the aforementioned microstructural properties, two different tests were carried out, X-ray diffraction (XRD) using the Panalytical X'Pert PRO X-ray diffractometer equipment and Mercury Intrusion Porosimetry (MIP) using the Micromeritics 9500 AutoPore IV equipment, both available at the Laboratorio de Geotecnia - CEDEX. These were carried out using pieces extracted from both groups of specimens, exposed and unexposed to the action of $scCO_2$, previously subjected to mechanical tests. Additionally, to complement the compositional tests, thin sections were obtained from the pristine sandstone.

3. RESULTS AND DISCUSSION

3.1. Porosity and pore size distribution

When performing the MIP tests, two general aspects of the specimens studied can be analysed. On the one hand, the porosity variation in terms of the pore diameter can be determined. From here, not only the porosity to mercury intrusion of the specimen can be determined, but also, a certain idea of the pore size distribution can be reached. Both analyses can be developed based on a porosity vs. pore diameter plot. On the other hand, by representing the differential intrusion in terms of the pore diameter, a more detailed analysis of the pore size distribution present in the specimen tested can be obtained.

In Figure 1.a, the porosity of the tested specimens is plotted in terms of the pore diameter. The curves represent a mean curve obtained from averaging the results derived from performing several tests for each type of specimen tested (5 pristine sandstone specimens, 3 30-day carbonated sandstone specimens from the centre and 3 from the edge). Three main observations can be made from these curves. Firstly, it can be observed that there is a reduction in the porosity of the sample, varying from 10.65% for the pristine sandstone to 10.34% for the 30-day carbonated sandstone from the centre of the core and 10.08%. Secondly, the amount of mercury that remains inside the specimen once the extrusion process is completed, reduces in a higher rate than the porosity of the sample, starting at a value of 5.93% for the pristine sandstone and decreasing to 4.53% y 3.49% for the CO_2-aged specimens from the centre and edge respectively. According to Cebeci et al. (1978), this remaining or entrapped mercury, is related to the ink-bottle pores (pores connected to a narrower-neck capillary) present in the specimen. Bearing this in mind, it seems reasonable to think that the CO_2 injection produces a reduction in the specimen's ink-bottle pore content. Finally, from comparing the shape of the curves, it might be noted that there is an important change produced in the pores with a diameter varying between 100nm and 10000nm. For a better understanding of this last, Figure 1.b should be analysed in detail.

When studying the pore size distribution that characterizes the pristine glauconitic sandstone specimens, it might be mentioned that it seems to have pores of two main sizes: 40nm-90nm and 800nm-4000nm. These pore size distribution might be observed in Figure 1.b, noting that for the 30-day carbonated specimen from the centre, the two groups of pore sizes continue to predominate, while in the case of the altered sandstone specimens obtained from the edges of the core, the pores corresponding to the 800nm-4000nm group, seem to have suffered an important reduction, while the pores with a size between 40nm and 90 nm, seem to have increased in amount. Similar changes in pore distribution were reported by Zheng et al. (2015), presenting a reduction in porosity as well. As it was previously mentioned, from observing this figure together with Figure 1.a, to understand why the change in the plotted in porosity vs. pore diameter have a different shape for each specimen type.

The variations produced in terms of the porosity and pore distribution of the Banco Verde sandstone after exposing it to a CO_2-rich environment can be summarized as follows. In the first place, as Laskowski et al. (2023) had shown for different samples obtained from outcrop, the glauconitic sandstone studied seems to always present a reduction in its porosity. Additionally, there could be a reduction in the amount of ink-bottle type of pores, noted from comparing the entrapped mercury at the end of each of the tests performed for each type of specimen, which could also be related to the reduction in bigger pores and the increment in smaller pores. Finally, it has been made evident from comparing

the three types of specimens, that the centre of the carbonated core is less affected by CO_2 than the edge. This is reasonable to think as the exposure time of the outer part of the core is longer, given the fact that this zone is in contact with CO_2 from the first moment while the inner part becomes exposed when the diffusion process is completed and reaches the centre.

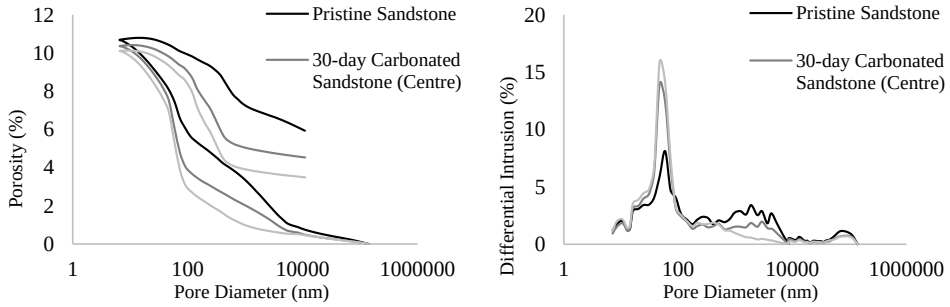


Figure 1.a) Porosity vs. Pore Diameter plot. b) Differential Intrusion vs. Pore Diameter. Plots obtained from performing MIP tests on pristine and carbonated specimens, from both edge and centre zones.

3.2. Element composition and mineralogy

With the aim of analysing the variation produced in the composition of the sandstone due to its exposure to a CO_2-rich environment, X-ray diffraction (XRD) tests were performed in pristine, and 30-day carbonated specimens previously subjected to mechanical testing. In particular, when testing the altered rock, pieces were extracted from the edge and centre of the core, in order to analyse the penetration degree of the CO_2 in the core during the carbonation process. To complement the XRD, the petrography of thin sections of pristine sandstone was studied.

In general terms, sandstones are characterized for being composed of quartz, feldspar, mica, and rock fragments, among other components (Davies et al. (1975)). When analysing the petrography of the Banco Verde sandstone (Figure 2), the prevailing mineral was the quartz, representing around a 30% of the total composition. Additionally, feldspar (~10%), glauconite (~10%), carbonates (~5%) and volcanic rock fragments (~5%) were detected. From this analysis, it was also noted that the rock matrix was composed of calcite cement, presenting in some grain contacts, dolomite crystals and clay (Figure 2.b). From observing various thin sections of the pristine sandstone in the microscope, it could be concluded that the sandstone layer studied had also plagioclase grains (type of feldspar) throughout its volume.

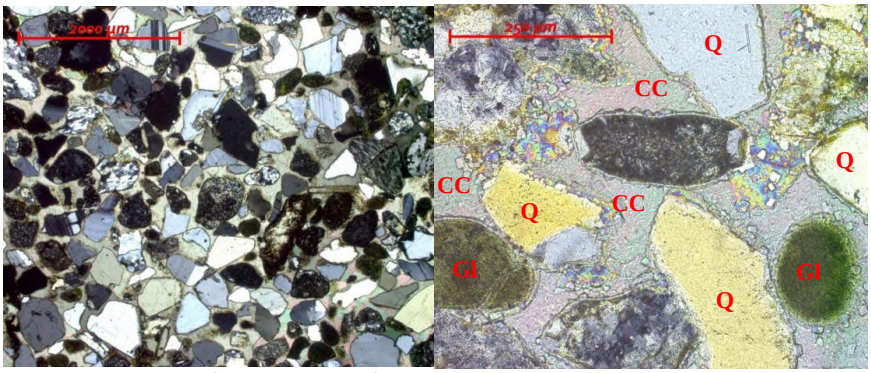


Figure 2.a) General aspect of the thin section of pristine sandstone under analyzed or cross polarized light. b) Zoom into the thin section of the pristine sandstone under analyzed or cross polarized light. Q: quartz, Gl: glauconite, CC: calcite cement.

All the aforementioned minerals composing the Banco Verde sandstone, were also present in the XRD tests. As it can be observed in Figure 3, the quartz content is approximately 30%, as indicated by the petrographic analysis of the thin sections, and there is presence of plagioclase, indicated by the appearance of albite and anorthite. When studying the variations produced in the sandstone due to its exposure to a CO_2-rich environment, four main changes seem to occur in compositional terms. One of the most notable changes is that quartz content seems to be increasing. It can also be observed that there are changes in percentage of albite and anorthite present in the sandstone after its exposure, indicating that plagioclase is being altered by CO_2. Finally, there is a reduction in calcite content, mineral principally composing the cement matrix of the Banco Verde sandstone.

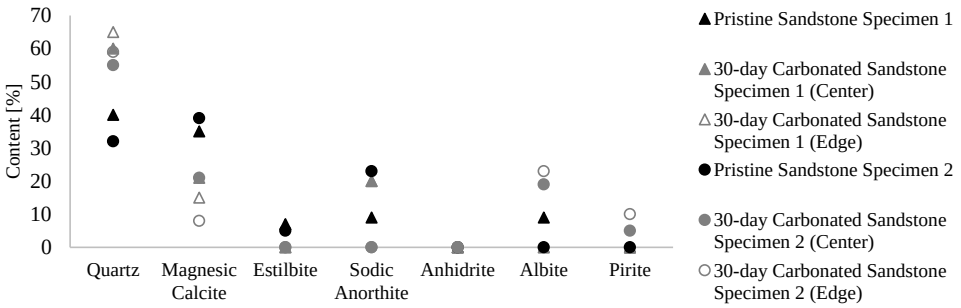


Figure 3. Mineralogic content determined through XRD tests over two groups of twin specimens.

Before analysing the mentioned changes in quartz and plagioclase, two aspects should be considered. On the one hand, a reduction in the core's weight after being exposed to CO_2, has been noted. This might indicate that dissolution mechanisms are occurring at a higher rate than precipitation (Peng et al. (2022)). On the other hand, quartz is not a mineral of quick reaction (Wigand et al. (2008), and Othman et al. (2018)), which indicates that in a 30-day period, no changes should be noted. In this context, the increment produced in quartz content could be related to the reduction in content of other minerals, which would proportionally increase its content in the big picture.

When referring to the variation produced in the plagioclase, the same changes were observed by Cui et al. (2017) and Peng et al. (2022), the first researcher indicating a reduction in the anorthite and an increment in the albite, while the second author presented a general decrease in plagioclase content. As it might be observed from Figure 3, the plagioclase present in the Banco Verde sandstone is characterized for being composed of anorthite in greater proportions. This is the case presented by Hangx et al. (2009), in which it is demonstrated that anorthite reacts with water saturated CO_2, producing calcite and clay minerals consequently. Even when the XRD do not show an increment in calcite content, the Bernard Calcimetry test was performed in pristine and carbonated specimens, and an increase in the carbonate content was observed.

3.3. Discussion

To begin with, it is important to note that, as it was expected, the degree of variation of the properties of the sandstone were more notable in the pieces of sandstone obtained from the edge of the core, rather than the ones obtained from the centre. This is mainly due to the difference in the exposure time to CO_2. It should be highlighted that even when the centre was less altered than edge, CO_2 reached this zone during the aging period, as the sandstone's properties in this area were also altered.

To continue, according to Laskowski et al. (2023), from the analysis of X-ray fluorescence, it was concluded that clay mineral dissolution occurred when injecting CO_2. It was considered that the clays dissolved came from the glauconite, but having observed the thin sections, it would also be reasonable to affirm, that the clay grains present in the calcite cement in some grain contacts. This would contribute

to explaining the reduction in the mechanical strength of the rock (Laskowski et al. (2023)), considering there is a modification not only in the grain-to-grain interaction but also in the rock matrix.

Finally, in terms of porosity and pore size distribution, some observations should be made. On the one hand, a reduction in the porosity was observed, being this previously related to fines migration and further precipitation in bigger pores, produced due to clay dissolution (Laskowski et al. 2023). This precipitation would produce a reduction in the bigger pores' diameter, increasing the number of smaller pores, and reducing the amount of ink-bottle pores, which could be observed in the micro structural analysis of the MIP tests. The reduction in porosity had also been related to the increment produced in carbonate content, which was shown to be produced due to the interaction between the plagioclase, more specifically the anorthite, and the water saturated CO_2.

4. CONCLUSION

CO_2 underground storage has proven to be a feasible alternative to mitigate climate change. In Argentina, the interest in this particular solution has increased over the past few years. In this context, the Banco Verde layer from the Salamanca Formation has been proposed as a possible storage for CO_2. With the aim of contributing to a better understanding of the interactions produced between CO_2 and the reservoir sandstone chosen, a series of micro structural and compositional analysis were conducted. Among the main conclusions reached, a reduction in porosity should be mentioned, as well as deposition of fines and carbonates, due to the reaction of CO_2 with clay minerals, glauconite and the anorthite in the plagioclase. This research would be enriched if it was complemented with a petrographic analysis of thin sections of 30-day carbonated sandstone and scanning electron microscopy (SEM) imaging, which would allow a more graphical understanding of the chemical and micro structural phenomena involved in the injection of CO_2 into the glauconitic sandstone studied.

5. ACKNOWLEDGEMENTS

The principal author thanks the Fundación José Entrecanales Ibarra for funding the development of the investigations related to her Ph.D. Thesis, which permitted the obtention of the results presented in this article. Special thanks are extended to Alberto Velasco from the Laboratorio Central de Estructuras y Materiales - CEDEX, for the petrography analysis provided of the sandstone thin sections, shown in this article. The authors acknowledge the financial support provided by the European Commission (H2020 MSCA-RISE 2020 Project DISCO2-STORE, Grant Agreement No 101007851), the UNPSJB (Project PI1614 80020190200006 IP), and FONTAR from the Argentinian Republic (PICT 2020–0288).

REFERENCES

ASTM D 4543 – 01. 2001. Standard Practices for Preparing Rock Core Specimens and Determining Dimensional and Shape Tolerances. *American Society for Testing and Materials: West Conshohocken.*

Bachu, S. 2000. Sequestration of CO_2 in geological media: criteria and approach for site selection in response to climate change. *Energy Conversion & Management 41: pp. 953-970.*

Barría, J., Martín, C., Piqué, T., Pereira, J. M. and Manzanal, D. 2018. Analysis of modified cement paste in the context of CO_2 geological storage. *International Symposium on Energy Geotechnics: pp. 402-409.* https://doi.org/10.1007/978-3-319-99670-7

Bradshaw, J., Bachu, S., Bonijoly, D., Burruss, R., Holloway, S., Christensen, N. P. and Mathiassen, O. M. 2007. CO_2 storage capacity estimation: Issues and development of standards. *International Journal of Greenhouse Gas Control I: pp. 62-68.*

Cebeci, Z., Demirel, T., and Lohnes, R. A. 1978. Evaluation of Hysteresis in Mercury Intrusion Porosimetry by Second-Intrusion Method. *Research Record, (675), 15-20.*

Cui, G., Zhang, L., Tan, C., Ren, S., Zhuang, Y., and Enechukwu, C. 2017. Injection of supercritical CO_2 for geothermal exploitation from sandstone and carbonate reservoirs: CO_2–water–rock interactions and their effects. *Journal of CO_2 Utilization (20): pp. 113-128.*

Davies, D. K. and Ethridge, F. G. 1975. Sandstone Composition and Depositional Environment. *AAPG Bulletin 1975, 59 (2): 239–264.*

Feruglio, E. 1949. Descripción Geológica de la Patagonia. *Dirección General de Yacimientos Petrolíferos Fisca les, 2: 1-349. Buenos Aires.*

Foix, N. 2009. Doctoral thesis. Tectónica de sedimentación del registro paleógeno (Formaciones Salamanca y Río Chico), Cuenca del Golfo San Jorge, Argentina. *Universidad Nacional de la Patagonia San Juan Bosco, Comodoro Rivadavia, Argentina.*

Grasetti, C., Piqué, T., Noya, M., Vila, G., Manoni, R., Brisson, I., De Leo, D., Dzelalija, F., Canale, N., Zalazar, M., Cabana, C., Tunik, M., Fortunatti, N., Lebinson, F., Bahía, M. and Grill, S. 2022. Atlas AR-CO_2. An Argentinian atlas for underground CO_2 storage potential. *16th International Conference on Greenhouse Gas Control Technologies.*

Hangx, S. J. T., and Spiers, C. J. 2009. Reaction of plagioclase feldspars with CO_2 under hydrothermal conditions. *Chemical Geology (265): pp. 88-98.*

Hawkes, C., Mclellan, P. and Bachu, S. 2004. Geomechanical factors affecting geological storage of CO_2 in depleted oil and gas reservoirs. *Journal of Canadian Petroleum Technology 44 (10).*

Laskowski, C.; Manzanal, D.; Muñiz-Menéndez, M.; Orlandi, S. & Allard, J. 2023. Evolución de las propiedades micro y macroestructurales de la arenisca de Banco Verde (Formación Salamanca) bajo la acción de dióxido de carbono. *Proceedings XXVI Congreso Argentino de Mecánica de Suelos e Ingeniería Geotécnica, 30/31 august and 1 september 2023, Comodoro Rivadavia, Argentina.*

Manzanal D., Vallin V., Pereira, JM. 2013. A chemo-poromechanical model for well/caprock interface in presence of CO_2. *Poromechanics V - Proc 5th Biot Conf Poromechanics.* https://doi.org/10.1061/9780784412992.175

Martín, C., Piqué, T., Pereira, J. M. and Manzanal, D. 2022. Performance of lightweight cement pastes under CO_2 storage conditions. *16th International Conference on Greenhouse Gas Control Technologies.*

Othman, F., Yu, M., Kamali, F. and Hussain, F. 2018. Fines migration during supercritical CO_2 injection in sandstone. *Journal of Natural Gas Science and Engineering 56: pp. 344-357.*

Peng, H., Yang, J., Peng, J., Pu, J., Liu, Q., Su, J., and Liu, J. 2022 Experimental investigation of the mechanism of supercritical CO_2 interaction with tight sandstone. *Frontiers in Energy Research (10).*

Ranjith, P., Perera, M. and Khan, E. 2013. A study of safe CO_2 storage capacity in saline aquifers: a numerical study. *International Journal of Energy Research 37: pp. 189-199.*

Rodríguez, J. J., Bardelli, J., Tichno, M. A. and Limarino, C. O. 2014. Integración petrofísica-geológica en la caracterización de la porosidad de un reservorio de gas en el yacimiento Diadema (Formación Salamanca, Paleoceno). *Proceedings XIV Reunión Argentina de Sedimentología: pp. 239-240. ISBN: 978-987-96296-5-9.*

Siddiqui, A. H., Hasnain, M. D., Alam, M. M. and Fatima, S. 2022. Climate Change: Causes, Impacts and Solutions. *International Research Journal of Engineering and Technology 9: pp. 928-934. e-ISSN: 2395-0056.*

TERMAP S.A. 2011. Etudio de impacto ambiental previo a la constucción de un nuevo tanque de 50.000 m3. *Terminal de Caleta Córdova. Comodoro Rivadavia – Provincia de Chubut.*

Wigand, M., Carey, J. W., Schutt, H., Spangenberg, E. and Erzinger, J. 2008. Geochemical effects of CO_2 sequestration in sandstones under simulated in situ conditions of deep saline aquifers. *Applied Geochemistry 23: pp. 2735-2745.*

Working Groups I, II and III of the Intergovernmental Panel on Climate Change [Core Writing Team, H. Lee and J. Romero (eds.)]. 2023. *AR6 Synthesis Report: Climate Change 2023.* http://doi.org/10.59327/IPCC/AR6-9789291691647

Working Group III of the Intergovernmental Panel on Climate Change [Edenhofer, O., Pichs-Madruga, R., Sokona, Y., Farahani, E., Kadner, S., Seyboth, K., Adler, A., Baum, I., Brunner, S., Eickemeier, P., Kriemann, B., Savolainen, J., Schlömer, S., von Stechow, C., Zwickel, T. and Minx, J.C. (eds.)].

2014. *AR5 Climate Change 2014: Mitigation of Climate Change. Cambridge University Press, Cambridge, United Kingdom and New York, NY, USA.*

Zheng, H., Feng, X., and Pan, P. 2015. Experimental investigation of sandstone properties under CO_2–NaCl solution-rock interactions. *International Journal of Greenhouse Gas Control (37): pp. 451-470.*

28th European Young Geotechnical Engineers Conference – EYGEC 2024
© 2024 Macedonian Association for Geotechnics, ISBN 978-608-4510-61-1

Optimisation of Tensar's T-value design method for working platforms

Sandro A.R Lesar[a], Leo Kuljanski[b]

[a, b] *Tensar International B.V., 's-Hertogenbosch, Netherlands*
[a] *HZ University of Applied Sciences, Middelburg, Netherlands*

ABSTRACT

This paper aims to introduce the T-value bearing capacity method as a concept, as well as explaining the improvement of one of its key limitations. The T-value is a rigorously tested design method, which calculates the maximum allowed pressure that can be applied to a working platform, with either a drained or undrained subsoil. However, the deriving of this analytical equation is based on the assumption of a fully homogeneous subsoil. Therefore, when dealing with stratified soil, which is often the case, this analytical equation allows room for optimisation. The stratified soils can broadly be grouped into undrained, drained or mixed stratified cases. In this paper, a potential mixed stratification improvement will be analysed and discussed. Said improvement has been derived with a combination of insights gained from finite element modelling, as well as a literature review. Furthermore, this improvement consists of two parts; an influence depth calculation and a summarisation procedure. The bearing capacity outcomes of this improvement were tested against 36 randomised stratified PLAXIS 2D soil models, based on a monitored trial test. The results obtained show a strong correlation between the data sets, indicating the potential for this improvement to accurately estimate the bearing capacity of stratified soils. Along with a brief statistical analysis aimed at further validating this approach, a demonstration of this improvement's added benefit is also highlighted in this paper. Therefore, this new addition to the T-value method will be thoroughly explained, with its improvements in stratified cases demonstrated.

KEYWORDS

T-value method; Mechanically stabilised aggregate layers; Stratified soil models; PLAXIS 2D

1. INTRODUCTION

The T-value method, is an easy to use, rigorously tested bearing capacity design method. Within its application of calculating working platforms it can be applied to many situations, such as crane hard stands. The heavy loads applied in these situations, as well as the often weak subsoil, make this an ideal case for the use of mechanically stabilised aggregate layers (MSL). An MSL is made up of a well-graded aggregate and often multiple layers of stabilising geogrids. The stabilising effect of the geogrids greatly increase the bearing capacity, reduce the thickness of the MSL or allow for the use of lower quality aggregate. Therefore, the T-value method was developed as an analytical method to accurately incorporate the effect of stabilising geogrids. The equations used calculate the load transfer efficiency T and use this within other bearing capacity equations. Both of these require the soil parameters of a single homogeneous subsoil. Furthermore, these equations are also differentiated between undrained and drained cases. The soil parameter required in an undrained situation is the undrained shear strength, while the drained situation requires the internal friction angle and unit weight of the subsoil. This presents a problem when working with a stratified subsoil, as the influence of lower soil layers is not taken into account in the final calculation. Therefore, an improvement to eliminate this limitation is presented in this paper in order to further improve the value gained in using an MSL. There are three ways to approach this limitation based on possible stratification situations. A subsoil could consist of stratified undrained layers, stratified drained layers or a combination of both drained and undrained

layers. Deriving improvements for the first two situations is easier as they each have dedicated bearing capacity equations, while a combination can present further challenges. For the scope of this paper a provisionally validated mixed stratification improvement is presented. The data used as a basis to test this was derived from a monitored trial case. Using finite element modelling, a total of 36 unique cases were created with different loading areas, soil parameters and layer thicknesses. Separately, the improvement was derived as a combination of insights gained from this finite element modelling and by analysing the current NEN approach of weighted average soil parameters within an influence depth. A modification of these existing approaches has resulted in predictions that can more accurately predict the bearing capacity of an MSL compared to the current T-value method. In essence the modifications apply a greater weight to weaker subsoils and a smaller weight to stronger subsoils. The results have been validated with a statistical approach and their added benefit demonstrated. Improving the T-value will lead to MSLs that are more safe, environmentally friendly and cost effective.

2. CURRENT ANALYTICAL T-VALUE METHOD

2.1. Bearing capacity equations

Previous research analysed 60 centrifugal tests to determine a linear relationship between *qu/qs* and *H/B* for a plane strain case (Lees, 2021). However, for the case of an axisymmetric loaded area, the square root of *qu/qs* was applied. For cases between these extremes a simple linear interpolation is performed. The gradient of these lines created the load transfer efficiency value *T*. This research led to the creation of the T-value bearing capacity equations for plane strain and axisymmetric situations as is seen in Equation (1) and Equation (2), respectively.

$$\frac{qu}{qs} = 1 + T\frac{H}{B} \quad \leq \frac{qg}{qs} \tag{1}$$

$$\frac{qu}{qs} = (1 + T\frac{H}{B})^2 \quad \leq \frac{qg}{qs} \tag{2}$$

where: *qu* is the total bearing capacity on the top of the loaded area, *qs* is the bearing capacity of the subsoil, *H* is the thickness of the granular layer, *B* is the width of the loaded area, *T* is the load transfer efficiency and *qg* is the ultimate bearing capacity of a granular layer that has an infinite depth.

The inequality ensures that within a given case the subsoil also contributes to the bearing capacity. The *qs* mentioned in Equation (1) and Equation (2) is one of the centre points in the improved T-value method. In order to calculate the *qs*, usually parameters of a single subsoil are used, both in the undrained and drained situation. Therefore, it is important to summarise the total effects of all subsoil layers within a given influence depth into a single working *qs* value. The regularly applied equations for the *qs* of a homogeneous undrained or drained subsoil, are shown below in Equation (3) and Equation (4), respectively.

$$qs = Cu * Nc * Sc \tag{3}$$

$$qs = 0.5 * \gamma'_2 * N\gamma'_2 * W * S\gamma'_2 \tag{4}$$

where: *Cu* is the undrained shear strength, *W* is the width of the loaded area, γ'_2 is the unit weight of the subsoil and all other parameters are common, load and shape factors.

2.2. Deriving of the T-value for undrained and drained situations

As the T-value is based on the subsoil strength and as there is a substantial difference between sand and clay, two separate methods were derived for each case. Both were based on replotted outputs from

different parametric studies, which were validated with centrifugal testing (Lees, 2021). A best fit line of this data determined good results for plane strain situations and conservative results for axisymmetric cases. Using the undrained shear strength for undrained cases and the internal friction angle and unit weight for drained cases, two separate equations were created as is shown in Equation (5) and Equation (6), respectfully.

$$T = C\left(\frac{Cu}{p'0}\right)^{A} + B \tag{5}$$

$$T = St\left(\frac{5.6}{\Phi'_2} - 5\right)\left(\frac{y'_1}{y'_2}\right)^{St} \tag{6}$$

where: *C*, *A*, *B* are constants filled in for geogrid and aggregate specific circumstance, *Cu* is the undrained shear strength of the subsoil, *p'0* is the effective vertical stress at the bottom of the granular layer, *St* is a shape factor for axisymmetric cases, Φ'_2 is the internal friction angle of the subsoil, γ'_1 is the unit weight of the MSL and γ'_2 is the unit weight of the subsoil. A further correction is applied to Equation (5) as it falls below 1.25 due to uncertainty within this region (Lees, 2021).

These T-value equations were derived for MSLs with the use of finite element modelling in PLAXIS 2D. The T-values were determined for the most common geometries and subsoil cases in order to be applicable for typical working platform situations (Lees, 2021). As can be seen, only soil parameters of a single homogeneous subsoil can be used for these equations, which is also altered within the T-value method improvement. Lastly, full scale testing on an undrained situation (A. Lees, 2022) and a drained situation (Lees, 2021) further validated the effectiveness of this design method.

3. STRATIFICATION DATA SET

In order to test a possible improvement a monitored trial case was examined. This test was chosen as it had many different layers and thicknesses within the influence depth, making it ideal for this purpose. A total of 5 soil layers consisting of 4 undrained layers and 1 drained layer, allowed for many different soil situations to be tested. Furthermore, the 0.8m thick MSL consisted of an aggregate with 3 stabilising geogrids equally spaced apart starting with the first on the bottom. This case was recreated in PLAXIS 2D and validated with a multi-faceted approach. By comparing the load-to-displacement curve of the surveyed data to the PLAXIS 2D output, a strong correlation could be determined. Surrounding survey points were also compared with their PLAXIS 2D counterparts. The final comparison between the trial and PLAXIS 2D output can be seen in Figure 1.

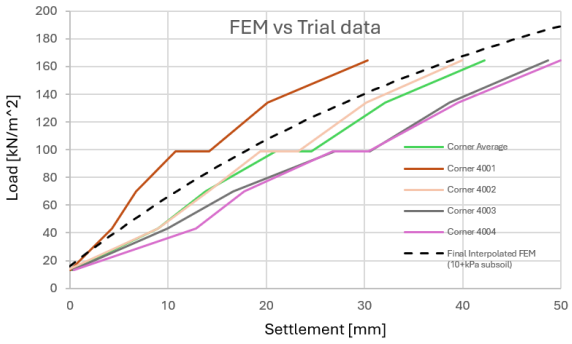


Figure 1. Trial data versus PLAXIS 2D output.

With this validated PLAXIS 2D model, the bearing capacity of this numerical method was noted. Thereafter, a further 11 stratified soils were created with a subset of 3 cases based on an axisymmetric, plane strain and interpolated case. The 33 (36 including the original trial) total versions were derived from the original trial and each had unique stratifications and layer thicknesses. Thereafter, using PLAXIS 2D the best estimate of the bearing capacity was determined for all cases, with homogenous layers also tested as a control.

With this information, the percentage differences between a homogeneous (as would be optimal for the current T-value method) and stratified subsoil were noted. The corresponding homogeneous subsoil depended on the first layer in the stratification, as is the current status quo when approaching these equations. The data resulted in great percentage differences between the versions, which ranged from an almost -100% under prediction to an almost 20% over prediction. This range of data ensures appropriate testing for the improvement.

4. CREATION AND IMPLEMENTATION OF THE T-VALUE IMPROVEMENT

As was mentioned previously, in order to solve this limitation, a distinction must be made between which type of stratification is intended to be solved. With this, accurate undrained stratification improvements were developed, which were adjusted to also take into account a mixed situation. Furthermore, as the drained layers in the original case were limited, the estimations mentioned in this paper could only be validated for undrained and mixed stratification situations. Ideally, this would also include a drained situation, however that is beyond the scope of this paper.

The key improvement consisted of two equally important parts; determining the influence depth and being able to summarise the shear strengths within that depth into one usable value. The Dutch Eurocode annex, the NEN, already has a way of calculating the influence depth of a soil. This process is iterative and starts with the assumption of an influence depth. Thereafter, the weighted average internal friction angle within this influence depth is used to calculate the new influence depth. This process is repeated until a sufficient similarity between the last iterated influence depths is achieved. The working platform's aggregate is assumed as a layer in the ground and therefore also contributes to the final depth. The relationship used to find the influence depth is thoroughly explained in the NEN (NEN, 2017), with different considerations depending on the applied loads. The weighted average method described here became the inspiration for how to summarise multiple subsoil layers into a single usable value. Furthermore, when analysing the created PLAXIS 2D models it became clear that not every layer in the subsoil influences the bearing capacity equally. When looking at two subsoil layers, the effect of the bottom layer was dependent on the strength of the top layer. If the second layer was weaker, it had a much greater effect on the overall bearing capacity than if the second layer was stronger than the first. This observation followed for every created model, which showed that using a simple weighted average based on layer thickness and depth would not suffice. Therefore, a further scale weight was applied to every soil layer beneath the first based on the ratio of the two layers. The following approach of non-linear weighing assigns a different weight to second layers as they become more extreme in either direction compared to the first layer. This means that the higher the undrained shear strength of a lower layer in comparison to the first, the less of a weight it will have. Similarly, as weaker layers resulted in bigger reductions in bearing capacity, this new approach assigns an even weaker undrained shear strength to the weak lower layers. This approach is summarised for both of the cases with Equation (7) and Equation (8) showing the weighing of a weaker and stronger bottom layer, respectively.

$$Cu;_{weighted} = Cu_b * \sqrt{\frac{Cu_b}{Cu_1}} \tag{7}$$

$$Cu;_{weighted} = Cu_b * \sqrt{\frac{Cu_1}{Cu_b}} \tag{8}$$

where: $Cu;_{weighted}$ is the new scale weighted undrained shear strength of the bottom layer, Cu_b is the original undrained shear strength of the bottom layer and Cu_1 is the undrained shear strength of the first reference layer.

This new shear strength has only been tested as an application for undrained layers, with potential scale weighted drained layers still having to be optimised. Thereafter, the effects of layer thicknesses were also analysed, with a similar pattern emerging. Overall, as the first layer reduced in thickness, the effects of the bottom layers became more pronounced, with weaker layers once again having a larger effect than stronger layers. Therefore, the same general idea was applied to the thicknesses of the layers below the first, effectively giving a larger weight to weaker layers and a smaller weight to stronger ones. The application of this approach can be more easily visualised in Table 1 below.

Table 1. Example of the new scale weighted thickness applied to lower layers

Example	Change in new scale weighted bottom thickness	Equation
Weaker undrained shear strength and smaller thickness below	Larger	$New\ Th. = Th._b * \sqrt{\frac{Th._1}{Th._b}}$
Weaker undrained shear strength and larger thickness below	Larger	$New\ Th. = Th._b * \sqrt{\frac{Th._b}{Th._1}}$
Stronger undrained shear strength and smaller thickness below	Smaller	$New\ Th. = Th._b * \sqrt{\frac{Th._b}{Th._1}}$
Stronger undrained shear strength and larger thickness below	Smaller	$New\ Th. = Th._b * \sqrt{\frac{Th._1}{Th._b}}$

where: *New Th.* is the new scale weighted thickness of the bottom layer, $Th._b$ is the original thickness of the bottom layer and $Th._1$ is the thickness of the reference layer.

With the addition of drained layers no direct comparison can be made in choosing the appropriate scaling method. Therefore, a general assumption was applied that all drained layers are stronger than undrained layers and are applied as such in the equations. All the discussed scale weights will be applied to the general weighted average NEN equation (NEN, 2017). Therefore, they will simply apply a heavier or smaller weight dependent on the properties of the first layer. The new scale weighted undrained shear strength of every layer is used to calculate the *qs* of that layer as in Equation (3). In case of a drained layer the regular Equation (4) is used. Thereafter, a slight modification of the original NEN weighted average equation is used with *qs* being the summarised value as can be seen in Equation (9) below.

$$qs;avg = \frac{\sum_{j=1}^{j=n} New\ Th.j * qsj * Xj}{\sum_{j=1}^{j=n} hj * Xj} \tag{7}$$

where: *qs;avg* is the weighted average subsoil bearing capacity, *qsj* is the subsoil bearing capacity for layer *j*, *New Th.j* is the scale weighted thickness of layer *j*, *n* is the number of horizontal soil layers within the influence depth and *Xj* is the distance from the centre of layer *j* to the bottom of the influence depth.

With this scale weighted *qs* the undrained shear strength can be simply back-calculated by substituting *qs;avg* into Equation (3) to find the *Cu*. This process is done for undrained and mixed stratification

situations, with fully drained layers being beyond the scope of this paper. Finally, having calculated the new Cu, Equation (5) can be used to calculate the T-value. Thereafter, depending on the shape of the loading area, Equation (1) or Equation (2) calculate the bearing capacity at the top of the platform.

5. RESULTS

The percentage increase or decrease for the optimised T-value method was calculated for the same stratified versions as were created in numerical modelling. Therefore, a direct comparison could be made between the PLAXIS 2D outputs and the improved analytical T-value method. Here the percentage difference between the two should ideally be 0 and therefore the closer each version came to 0 the better it was able to predict the bearing capacity. This process was done for all 36 soil models mentioned earlier, with a full summarisation displayed in Table 2.

Table 2. The summarisation of differences between the PLAXIS 2D models and the improved T-value method.

	Over or underprediction of differences between numerical and analytical modelling	Absolute differences between numerical and analytical modelling
Average of all points	-2	7.3
Average of Interpolated points	-1.8	6
Average of Plane Strain points	-2.8	10
Average of Axisymmetric points	-1.3	6
Average of weaker clay over stronger clay	-0.4	3
Average of stronger clay over weaker clay	0	11.1
Average of Mixed Stratification Layers	-6.6	9.9
Average of all points based on validity	-0.2	6.3
Average of all over predictions in bearing capacity	6.9	/
Average of all under predictions in bearing capacity	-7.6	/
Highest value of all over predictions in bearing capacity	19.6	/
Highest value of all under predictions in bearing capacity	-19.5	/

As can be seen the variant performed well among all tested categories and had on average only a percentage difference of around 7 between the numerical and analytical method. When looking at the highest over and under predictions of this improvement the most extremes have a difference of almost 20 between the numerical and analytical method. This might seem quite high, especially as an over prediction, but when looking at the raw data these become more reasonable. Firstly, these extremes are the result of the most extreme tested versions. Meaning that versions with big shear strength ranges and proportionally thin first layers, resulted in higher over and under predictions. For the same versions the percentage decreases were even higher in the numerical method. In this context the improvement did well to predict the bearing capacity, but could have been even more extreme. This means that there is further optimisation to be achieved, by further scaling the discussed parameters. It is important to note that the improvement still out performed the current analytical method in almost every version. Where this was not the case the differences were small, which can not be said for the versions where the improvement out performed the current analytical method. With these results it was shown that the improvement of the current T-value method was successful, with further optimisations also being possible.

6. STATISTICAL VALIDATION

As was demonstrated in earlier chapters the validity of this method was tested by comparing it to a set of numerical data. A simple linear regression was also performed in order to determine the degree to which the analytical equation was able to predict the numerical results. Firstly, using the Pearson Product Moment Correlation a value of 0.95 was found. A positive value so close to 1 means that one increasing

variable is able to explain the other increasing variable very well. Thereafter, the R^2 of the data was plotted by finding the fitted regression line as is seen in Figure 2.

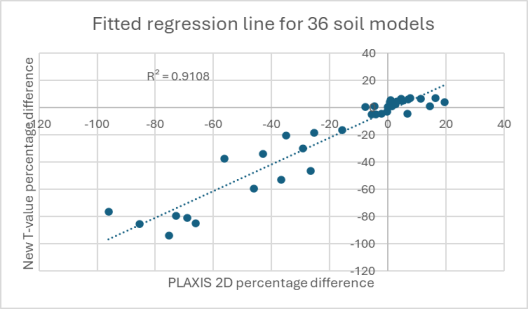


Figure 2. R^2 and fitted regression line examined data.

As can be seen the R^2 is once again close to 1, meaning that the analytical equation does a good job of predicting the numerical outcomes. Furthermore, to ensure that there is no bias in the data, a residual plot is also analysed as is seen in Figure 3, to determine if there are any patterns.

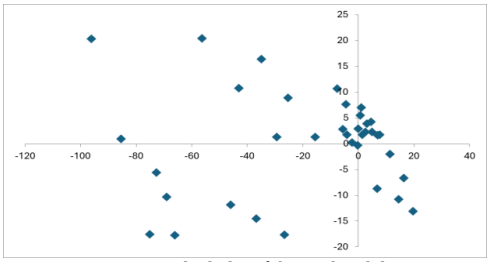


Figure 3. Residual plot of the analysed data.

As can be seen the pattern is in general random, meaning that the bias in this equation is low. However, there is some grouping close to the right side of Figure 3, which suggests that further analysing is required in order to ensure the validity of the model. Finally, a simple plot of every analysed data point is shown in Figure 4.

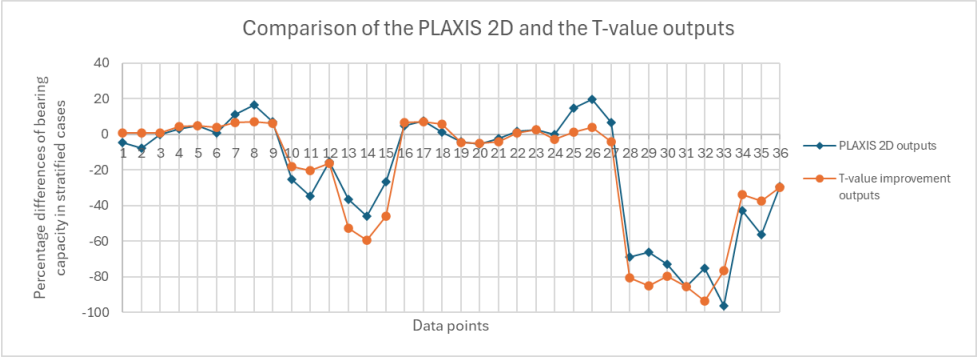


Figure 4. A display of the differences between PLAXIS 2D and the T-value improvement for the same soil models.

This graph simply gives a visual representation of how each soil model was predicted by the T-value improvement.

7. ADDED BENEFIT

Using the optimised T-value a simple demonstration of the quantifiable benefit is demonstrated for data points 9 and 14. Here data point 9 resulted in a moderate increase in bearing capacity gained as a result of applying the improvement. With this, 5cm of aggregate in the MSL was able to be saved in the example. With a loading area of 2.5m * 8m this resulted in overall minimal savings for a standard project as is shown in Table 3.

Table 1. Example of the quantifiable added benefit.

	Original	Reduction	Difference
Thickness [m]	0.8	0.75	**0.05**
Construction Cost [€/m^2]	66	62.5	**3.5**
Environmental Cost [kgCO_2e]	120	110	**10**
Dump truck visits	2	2	**0**
Fuel required [litres]	40	40	**0**
Water required [litres]	609	571	**38**

As can be seen while minimal savings would be achieved for a single project, it is easy to see how larger and more extreme cases could result in beneficial gains. Lastly, looking at data point 14, there is a total decrease of -46% in bearing capacity compared to a homogeneous first layer. The improvement on the other hand predicted a decrease of -59%. When comparing this to the status quo of 0%, the important gains in safety are shown when using the optimised T-value method.

8. CONCLUSION

In conclusion, the current T-value method is a rigorously tested design method that has been fully validated. However, one of its key limitations is that it cannot reliably be used on stratified subsoils. This is because the equations have been derived separately for either a homogeneous drained or undrained layer. Therefore, when approaching this limitation a weighted average of all subsoil values within an influence depth was analysed. It was also determined that the effects of a stronger or weaker layer beneath the first are not equal. Therefore, additional scale weighting was applied to both the shear strengths and thicknesses of each layer beneath the first. Now using a modification of the existing NEN method, more accurate summarised soil parameters could be determined. Thereafter, a statistically significant relationship between the numerical and improved analytical methods, showed the first step of validating this approach. Furthermore, isolating two data points showed the added benefit of the optimised T-value method. Further validation of this method is required, with a separate drained analysis. In addition, further optimisation of the scale weights could also lead to better result. Finally, expanding the tested soil models, with larger ranges in both shear strength and thicknesses is required in order to apply this improvement to all soil cases. Taking these limitations into account, will result in a more optimised and validated T-value method, which is not only more safe, but is a more cost saving and environmentally friendly alternative to the current approach.

REFERENCES

A. Lees, J. (2022). The design of mechanically stabilized working platforms. *Eurogeo 7* (pp. 380-390). Warsaw: Eurogeo 7.

Lees, A. (2021). RIGOROUS DESIGN OF THINNER WORKING PLATFORMS. *ice publishing*, 335-341.

NEN. (2017). *NEN 9997-1+C2*. Delft: NEN.

28th European Young Geotechnical Engineers Conference – EYGEC 2024
© 2024 Macedonian Association for Geotechnics, ISBN 978-608-4510-61-1

Experimental investigation on the hydro-mechanical response of a shale subjected to gas invasion

Qazim Llabjani[a], Alessio Ferrari[a] , Paul Marschall[b], Lyesse Laloui[a]

[a] *Swiss Federal Institute of Technology Lausanne (EPFL), Laboratory of Soil Mechanics, Lausanne, Switzerland*
[b] *Nationale Genossenschaft für die Lagerung radioaktiver Abfälle (NAGRA), Wettingen, Switzerland*

ABSTRACT

In the context of deep geological radioactive waste disposal, significant amount of generated gas is expected to migrate from the repositories into the surrounding host rock, affecting its hydro-mechanical state. In Switzerland, Opalinus Clay is the selected host geological formation and requires a comprehensive understanding of the relevant phenomena that characterize its behaviour associated with gas transport regarding the long-term safety assessment of the repository. In this context, water and gas injection tests were performed using a high pressure oedometer cell. The results suggest that gas-induced porewater displacement is a key feature during gas invasion processes in clay-rich host rock. Furthermore, water intrinsic permeability was not impacted by gas transport and consistently found in the order of 10^{-21} (m^2) before and after the gas invasion tests. The experimental outcome of the study provided unique observations of the hydro mechanical behaviour of Opalinus Clay when subjected to gas transport in the short-term and long-term.

KEYWORDS

Nuclear Waste Repository; Opalinus Clay; Hydro-Mechanical Behaviour; Gas Invasion

1. INTRODUCTION

Regardless of the national strategies concerning nuclear energy production, there is an urgent need to address the problem of disposing high-level nuclear waste produced by power plants. Switzerland foresees a deep geological repository which relies on a multi barrier system to isolate the waste from the biosphere for dozens of thousands of years. However, uncertainties still exist about the late stage of the repository when a significant amount of gas will be produced due to various processes. This gas production may cause gas pressure build-up with a potential propagation of the gas front into the host rock. Those circumstances can result in the loss of the mechanical integrity of the multi-barrier system and may impact the long-term safety of the repository (Levasseur et al., 2021).

In Switzerland, Opalinus Clay has been selected as the host geomaterial for the underground disposal of radioactive waste. More experimental evidence for a comprehensive understanding of the relevant phenomena that characterize the hydro mechanical (H-M) behaviour of Opalinus Clay (OPA) when subjected to gas invasion is thus required.

In this paper we are showing the results of an experimental campaign on OPA conducted with a high pressure oedometer apparatus allowing the performance of water and gas injection tests while assessing the vertical deformation of the tested material with the aim to better observe and understand the involved phenomena.

2. MATERIAL AND METHODS

2.1. Material

Opalinus Clay is a fine-grained sedimentary geomaterial with a mineral composition consisting mainly of silicates, carbonates and quartz. The tested material was retrieved from the deep borehole in Trüllikon in the Zürich Northeast siting region in Switzerland (Ammen and Palten, 2021) and was sourced at a depth of about 848 m. Complete geotechnical characterization has been performed and included: bulk density ρ = 2.50 g/cm^3, density of solid particles ρ_s = 2.78 g/cm^3, water content w = 0.05, void ratio e = 0.15, degree of saturation Sr = 0.63, initial total suction ψ = 66 MPa.

The pore structure of Opalinus Clay was studied by Mercury Intrusion Porosimetry (MIP), using the freeze-drying technique for sample preparation. To overcome the conformance effect and the compressibility of the sample below the entry pressure of mercury, a correction was applied to the MIP data according to (Comisky et al., 2011). As depicted in Figure 1, a unimodal pore size distribution was obtained in the range of 8 to 16 nm with a peak value at about 12 nm. The size of the detected porosity was from 4 to 60 nm; 4 nm being the smallest pore size detectable with the apparatus. The results are in good agreement with values from the literature on the same material (e.g., Crisci et al., 2019; Minardi et al., 2021). From the larger detected pores, air is expected to enter the pore space of the initially saturated porous medium at a capillary pressure of about 5 MPa according to Young-Laplace equation:

$$p_c = \frac{2\gamma \cos\theta}{r} \tag{1}$$

where p_c is the capillary pressure and is related to the differential pressure between gas and water phase, γ is the water-air surface tension, θ the water-solid contact angle, and r the pore-throat radius.

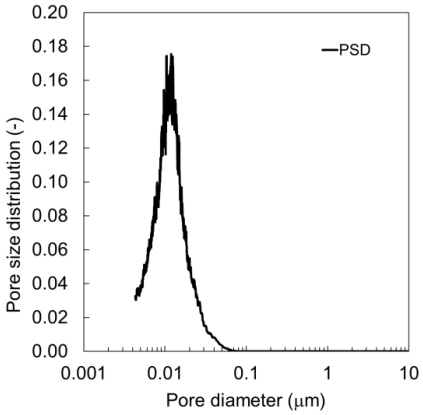


Figure 1. MIP test results of the OPA specimen

2.2. Experimental set-up and procedure

The experimental work used a high-pressure oedometer cell, as depicted in Figure 2 (left), that allowed to apply a vertical total stress up to 100 MPa with the possibility to perform water and gas injection from the bottom and top side of the specimen with a fluid pressure up to 16 MPa and 20 MPa, respectively (Minardi et al., 2021). The vertical deformation was assessed using three LVDTs with 0.2 μm resolution. The height and diameter of the specimen were 12 and 35 mm, respectively. The specimen was tested with the vertical load and fluid injection perpendicular to the bedding planes (S-sample).

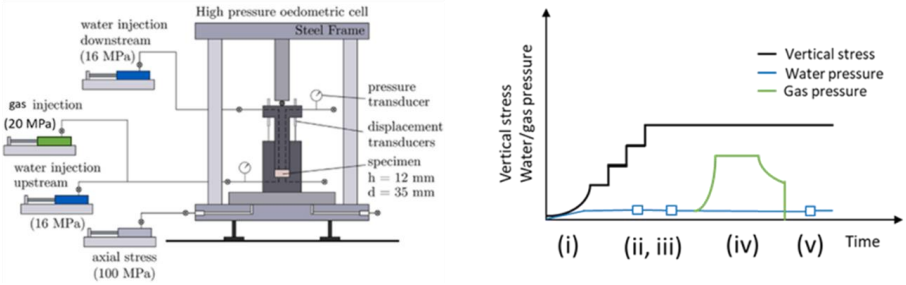


Figure 2. High-pressure oedometer test set-up (left); sequence of the water and gas injection tests (right)

The experimental procedure was composed of five test sequences (phases i to v) which are illustrated in Figure 2 (right) and described hereafter. As the preparation of the specimen from the core led to drying of the material, the experimental procedure started with (i) a water resaturation in isochoric conditions with synthetic water mimicking the in-situ porewater (Aschwanden et al., 2021). (ii) Mechanical loading up to the target vertical effective stress was performed to simulate in situ conditions. To do so, constant water pressure at the bottom ($u_{w,bot}$) and top ($u_{w,top}$) of the specimen was applied ($u_{w,bot} = u_{w,top} = 1$ MPa) and the vertical total stress was increased in steps up to $\sigma_v = 15$ MPa. (iii) Constant head water permeability tests were performed at different vertical effective stresses by applying a differential pressure of 1 MPa between the top and bottom side of the specimen ($u_{w,bot} = 1.5$ MPa and $u_{w,top} = 0.5$ MPa). (iv) Then, in order to perform the first gas injection test, the water pump connected at the bottom side of the specimen was replaced by the gas pump, and gas pressure (nitrogen, N_2) was increased at a fast constant flow (0.2 ml/min for an initial gas volume of 500 ml in the reservoir) until the target gas pressure ($u_{g,bot} = 10$ MPa) was reached; gas pressure was then kept constant until steady state conditions were observed for both gas flow and volumetric response of the tested specimen. Finally, the gas pump was stopped, ensuring constant gas volume at the inlet, and gas pressure decay was monitored (so called shut in). Water back-pressure at the top side of the specimen was kept constant during the entire phase at $u_{w,top} = 1$ MPa. (v) After the gas injection phase, water resaturation was performed under constant vertical total stress, followed by a second water permeability test in order to assess the evolution of the intrinsic permeability due to gas transport.

3. RESULTS AND DISCUSSION

3.1. Hydro-mechanical results (phases I to iii)

During resaturation, the tested specimen was put in contact with water at low pressure, and as water was sucked in, contributing to induce swelling of the material, vertical total stress was progressively increased to ensure isochoric conditions and minimize damage due to swelling. To further enhance saturation, the water pressure was increased up to 1 MPa and a differential water pressure was applied between the bottom and the top of the specimen so that water could flow across the specimen and flush the trapped gas within the pore space. The swelling pressure developed during this phase was $S_p = 3$ MPa and is shown in Figure 3.

The mechanical compression up to the target vertical effective stress allowed an assessment of the relationship between void ratio and the applied stress. The deformation of the oedometer system was accounted for every loading step (Ferrari et al., 2016). Figure 3 shows the compression of the specimen with increasing vertical effective stress. The water intrinsic permeability was computed from the constant head tests performed at different vertical effective stresses. The water intrinsic permeability was obtained in the range of 2 $3 \cdot 10^{-21}$ m^2 and is in good agreement with values reported in the literature for the same material (Crisci et al., 2019; Minardi et al., 2021).

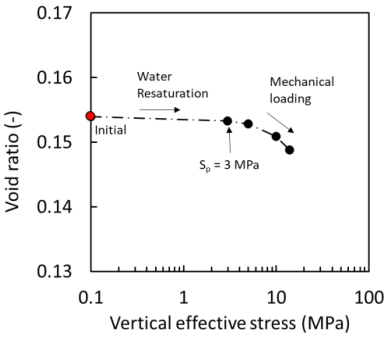


Figure 3. Oedometer curve for the tested specimen

3.2. Gas injection (phase iv)

The gas injection test was performed at fast gas pressure build-up rate with the intention to favour an undrained response of the material. The applied boundary conditions, such as vertical stress and fluids pressures are shown in Figure 4 (top).

The global axial strain of the specimen computed from the measurement of the vertical deformation, shown in Figure 4 (middle), indicates that almost no deformation was observed at the early phase as gas pressure was likely below the entry pressure and had not yet invaded the pore space. Once gas reached a pressure of about 5 MPa at t = 17 h, expansion of the specimen was observed, indicating the start of gas invasion, which was associated with porewater displacement and development of capillary pressure. The air entry value was consistent with the estimation from the MIP test. Expansion continued as gas pressure increased further. Once gas pressure was kept constant at 10 MPa from t = 30.5 h, expansion continued to slightly increase and reached a strain of 0.14% and was followed by a slow reduction and stabilization at about -0.07% until t = 193 h. As gas pressure decreased during the shut-in phase, t > 193 h, the specimen experienced compression. Gas pressure after shut-in was measured at 5.7 MPa.

The observed mechanical response was consistent with the measured outflow from the specimen. Gas breakthrough was observed only after the maximum gas pressure was reached (t = 50 h). This suggests that gas movement was impaired by the low permeability of the specimen. With time, as gas further invaded the pore space, the measured outflow increased until steady state conditions were observed at about t = 193 h. The gas outflow at standard temperature and pressure (STP) conditions was about 2 mm^3/s. During the shut-in, gas outflow decreased until almost no flow was observed anymore.

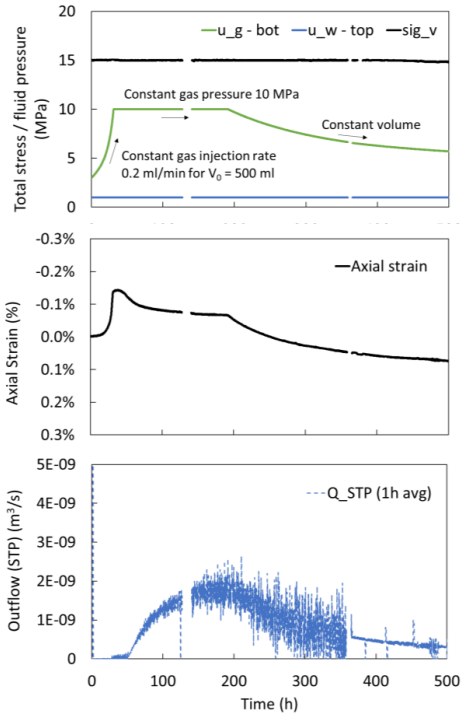


Figure 4. Gas injection test results

3.3. Hydro-mechanical results (phase v)

No significant strain (less than 0.01%) due to water uptake was observed during resaturation at constant vertical stress. The water intrinsic permeability after resaturation was found very similar to prior to the gas injection, $2\text{-}3 \cdot 10^{-21}$ m^2, suggesting that gas transport did not impair the intrinsic permeability of the tested material.

4. CONCLUDING REMARKS

In this study, the hydro-mechanical response of Opalinus Clay associated with gas transport was investigated. Water and gas injection tests have been performed using a high pressure oedometer cell to replicate the in-situ stress conditions. In particular, the short- and long-term responses to gas invasion were assessed during fast gas pressure build-up.

The interpretation of the results in terms of drained/undrained behaviour is consistent with the general deformation behaviour of clayey geomaterials. If the tested material is subjected to fast gas pressure build-up, it is more likely that gas transfer is initially associated with larger deformation due to generation of excess porewater pressure during the transient phase. The results suggested that gas-induced porewater displacement is a key feature during gas invasion processes in clay-rich host rock. Furthermore, the consistent water permeability values obtained before and after the gas injection test suggest that the involved gas transport processes are unlikely to impact the long-term barrier function of the host rock.

The experimental outcome of the study provided additional observations of the hydro-mechanical behaviour of Opalinus Clay associated with gas transport in the short-term and the long-term. Further

experimental investigation, as well as numerical analysis, are required to better understand the involved processes, such as the development of non-uniform and localized strains associated with gas invasion.

5. ACKNOWLEDGEMENTS

The authors are grateful to the Swiss agency for radioactive waste management (Nationale Genossenschaft für die Lagerung radioaktiver Abfälle - Nagra) for the financial support (Nagra order 18'713). Furthermore, the acknowledgements are extended to the European Joint Programme on Radioactive Waste Management (EURAD WP-GAS) within the European Union's Horizon 2020 research and innovation programme under grant agreement No 847593.

REFERENCES

Ammen, M., and Palten, P.J. 2021. TBO Trüllikon-1-1: Drilling. NAB 20-09, Nagra, Wettingen, Switzerland.

Aschwanden, L., Camesi, L., Gimmi, T., Jenni, A., Kiczka, M., Mäder, U., Mazurek, M., Rufer, D., Waber, H.N., Wersin, P., Zwahlen, C., and Traber, D. 2021. TBO Trüllikon-1-1: Rock Properties, Porewater Characterisation and Natural Tracer Profiles. NAB 20-09, Nagra, Wettingen, Switzerland.

Comisky, J.T., Santiago, M., McCollom, B., Buddhala, A., & Newsham, K.E. 2011. Sample Size Effects on the Application of Mercury Injection Capillary Pressure for Determining the Storage Capacity of Tight Gas and Oil Shales. *Unconventional Resources Conference, SPE*.

Crisci, E., Ferrari, A., Giger, S.B., & Laloui, L. 2019. Hydro-mechanical behaviour of shallow Opalinus Clay shale. *Engineering Geology*, 251, 214–227.

Ferrari, A., Favero, V., & Laloui, L. 2016. One-dimensional compression and consolidation of shales. *International Journal of Rock Mechanics and Mining Sciences*, 88, 286–300.

Levasseur, S., Collin, F., Daniels, K., Dymitrowska, M., Harrington, J., Jacops, E., Kolditz, O., Marschall, P., Norris, S., Sillen, X., Talandier, J., Truche, L., & Wendling, J. 2021. Deliverable D6.1 of the project EURAD, Work Package Gas.

Minardi, A., Stavropoulou, E., Kim, T., Ferrari, A., & Laloui, L. 2021. Experimental assessment of the hydro-mechanical behaviour of a shale caprock during CO_2 injection. *International Journal of Greenhouse Gas Control*, 106, 103225.

28th European Young Geotechnical Engineers Conference – EYGEC 2024
© 2024 Macedonian Association for Geotechnics, ISBN 978-608-4510-61-1

Microstructure of compacted transitional soil

Justyna Markowska

Doctoral School of Bialystok University of Technology, Bialystok, Poland

ABSTRACT

Fly ash and non-plastic silt are transitional soils that macroscopically resemble non-cohesive soils. However, their characteristics after compaction strictly depend on water content at compaction, as in the case of cohesive soils. Therefore, water content at compaction should always be considered in geotechnical analyses of these soils. The study aimed to investigate the microstructure of fly ash samples compacted by the Standard Proctor method at optimum water content ± 5%. The fly ash samples were qualitatively evaluated by an environmental scanning electron microscope (ESEM). Afterward, ESEM images and their computer analysis were used to define the pore structure and pore size distribution of the compacted fly ash.

KEYWORDS

Soil Microstructure; Compacted Fly Ash; ESEM Image Analysis; Pore Size Distribution

1. INTRODUCTION

Microstructural studies of compacted soils are significant for a deeper understanding of their macroscopic behaviour. They can provide essential information about the arrangement and distribution of particles, aggregates and pores, and their contacts. An important objective of these studies is to determine the relationship between microstructural characteristics and physical properties of soils (Romero, 2008; 2013). Mercury Intrusion Porosimetry (MIP), Scanning Electron Microscopy (SEM), especially in Environmental mode (ESEM), and Micro Computed Tomography (micro-CT) are commonly used methods for microstructural studies to understand various macroscopic soil behaviour (Romero and Simms, 2008; Zabielska-Adamska et al., 2019; Safari et al., 2022; Zhang et al., 2022). The MIP technique is used to estimate soil porosity, pore volume and size by applying controlled pressure to samples that are surrounded by liquid mercury (Hg). Dehydration of soil samples is necessary before using the MIP method. This is particularly important for samples compacted above the optimum water content. Drying of soils, that are sensitive to changes in water content, modifies their structure, which would affect the accuracy and reliability of the MIP test results. Therefore, it is recommended to apply freeze drying, which involves removing water at reduced temperature and pressure to eliminate surface tension forces and soil shrinkage. Sasanian and Newson (2013) observed that the reduction in water content, caused by natural drying under ambient conditions, resulted in a change from a bimodal pore distribution to a unimodal one. Microstructural studies of non-cohesive soils are more complex because they do not contain clay particles (Zabielska-Adamska et al., 2019). This method is not preferred for them due to the injection of mercury under pressure into the pores of the material (Romero and Simms, 2008). In this case, ESEM image analysis and the micro-CT method can be used to assess the pore size distribution. ESEM analysis is a qualitative and, where possible, quantitative method for defining soil microstructures. A scanning electron microscope in environmental mode, compared to conventional SEM, works under controlled environmental conditions and enables the study of soil samples without drying. The advantage is that their natural characteristics are preserved (Romero and Simms, 2008). Delage (1996), Otálvaro et al. (2015) and Zabielska-Adamska et al. (2019) used SEM images to define and describe the microstructure of the analysed soils, where aggregates and pore spaces were well visible. Micro Computed Tomography (micro-CT), also known as high-resolution X-ray Tomography,

is a 3D imaging technique that uses X-rays. It is a non-invasive and non-destructive method. Micro-CT provides qualitative and quantitative data on soil microstructure in a spatial manner (Taina et al., 2008). Safari et al. (2022) and Zhang et al. (2022) presented image processing analysis for extracting microstructure characteristics from micro-CT and SEM images.

Cohesive soils are characterised by a diverse microstructure – a flocculated arrangement when they are compacted at $w < w_{opt}$ and dispersed when compacted at $w > w_{opt}$. Cohesive soils compacted by the Proctor method at $w < w_{opt}$ show a distinct bimodal pore size distribution. They consist of aggregates with small pores separated by macropore spaces. However, compaction at $w > w_{opt}$ results in a unimodal pore size distribution. Macropore spaces decrease with increasing water content or compaction energy, while smaller pores remain unchanged during compaction (Delage et al., 1996; Otálvaro et al., 2015). In addition to cohesive and non-cohesive soils, which are characterised by a series of typical characteristics, there is a group of soils known as transitional or mixed soils. Macroscopically, they resemble non-cohesive soils, whereas their mechanical properties and hydraulic conductivity strictly depend on water content during compaction, as with cohesive soils. A representative example of transitional soil is fly ash (Zabielska-Adamska, 2020). It is an industrial by-product of coal combustion for energy production, considered an environmental pollutant. Its spherical grains range in size from around 1 to 100 μm. Fly ash is a non-plastic material. Nevertheless, it should be analysed considering the initial water content at compaction (Zabielska-Adamska et al., 2019; Zabielska-Adamska, 2020).

The work aimed to investigate the microstructure of the fly ash samples. They were compacted at three different water contents and next analysed. Scanning Electron Microscopy, combined with computer image analysis, was used to define the pore structure and pore size distribution of the soil.

2. MICROSTRUCTURAL STUDIES

2.1. Material

The tested fly ash was a by-product of hard coal combustion at the Bialystok Thermal-Electric Power Station in Poland, collected and deposited in a dry storage area. The physical and mineralogical properties of the tested fly ash are given after Zabielska-Adamska et al. (2019). The quantitative mineralogical composition of the soil samples was determined by X-ray diffraction (XRD) analysis. The soil consisted mainly of quartz (SiO_2), mullite ($3Al_2O_3 \cdot 2SiO_2$) and calcite ($CaCO_3$). The specific surface area of the fly ash, estimated by the methylene blue test, was 21.01 m^2/g. The particle density (ρ_s) was 2.12 g/cm^3. The grain size distribution curve, based on sieve and hydrometer analysis, is presented in Figure 1. The anthropogenic soil was comparable in grain size to sandy silt with the median grain diameter, D_{50}, equalled 0.060 mm. Following EN ISO 14688-2:2018, based on coefficients of uniformity, C_u, and curvature, C_c, the fly ash was poorly graded.

Before soil compaction, the fly ash was dried to constant weight in a laboratory drying oven at a temperature of 105°C to 110°C and cooled in a desiccator. Then the assumed amount of water was added to the dry soil. Samples with different water contents were moisturised for 24 hours, each separately in tight containers. The compaction curve, as well as optimum water content, w_{opt}, and maximum dry density, $\rho_{d\,max}$, of the fly ash, were obtained by the Standard Proctor compaction test according to EN 13286-2:2010. Each of the samples, prepared with different water contents, was compacted only once. This is particularly important for fly ash. Its spherical grains are partially crushed during a compaction process and filled with smaller fly ash particles. Reusing the same sample for testing would increase its dry density and compactability without adding water to the fly ash. Recompacted samples of fly ash are not representative of correctly determining compaction parameters (Zabielska-Adamska, 2008; Gupta and Sachan, 2018). The compaction curve of the fly ash is presented in Figure 2 and its physical parameters are given in Table 1.

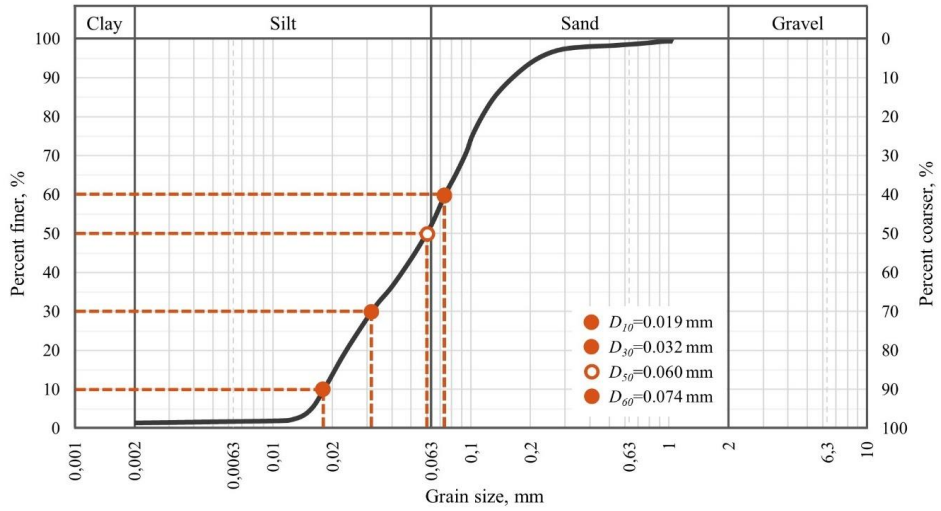


Figure 1. Grain size distribution curve of the fly ash after Zabielska-Adamska et al. (2019)

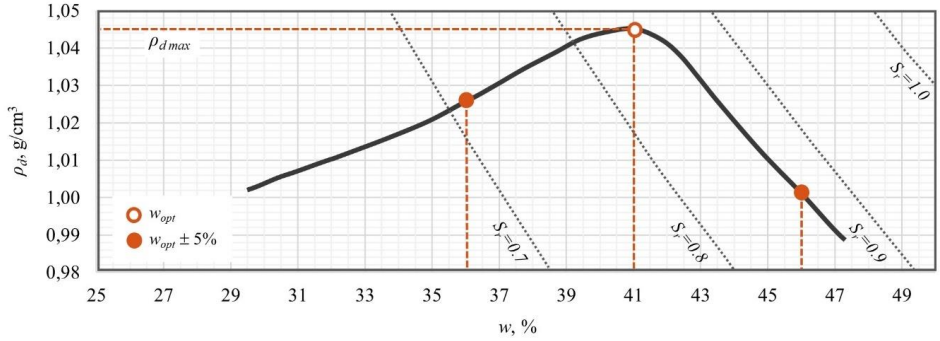


Figure 2. Compaction curve of the fly ash after Zabielska-Adamska et al. (2019)

Table 1. Physical parameters of the fly ash samples (Zabielska-Adamska et al., 2019)

Sample ID	Water content w (%)	Dry density ρ_d (g/cm³)	Porosity n	Void ratio e	Degree of saturation S_r
w_{opt} – 5%	36	1.026	0.516	1.066	0.715
w_{opt}	41	1.045	0.507	1.029	0.844
w_{opt} + 5%	46	1.001	0.528	1.118	0.872

2.2. Microstructural tests, results and discussions

Microstructural studies were performed on the samples compacted by the Standard Proctor method at three different water contents: optimum, w_{opt}, and within the range of w_{opt} ± 5% – on the dry and wet side of the curve. The samples for microstructural analysis were tested immediately after compaction.

The fly ash microstructure was qualitatively observed at natural fractures of the samples using a FEI Quanta 250 FEG Scanning Electron Microscope in Environmental mode (ESEM). Thus, the soil samples did not require drying or coating and were tested at the assumed water contents. The ESEM images were taken at a magnification of 350X (Figure 3).

The ESEM images were subjected to quantitative image analysis using ImageJ and MATLAB. ImageJ is free and open-source software. It was developed at the National Institutes of Health. It enables the processing and analysis of scientific images (Figure 4).

The microstructure of the sample with a water content of 36% (w_{opt} – 5%) was characterized by the presence of aggregates with small pores inside, separated by macropores (Figures 3a and 4a). The smallest number of pores occurred for the sample compacted at the optimum water content of 41% (w_{opt}). The compact structure of the sample is shown in Figures 3b and 4b. Compaction at a water content of 46% (w_{opt} + 5%) resulted in the loosest structure of the fly ash (Figures 3c and 4c).

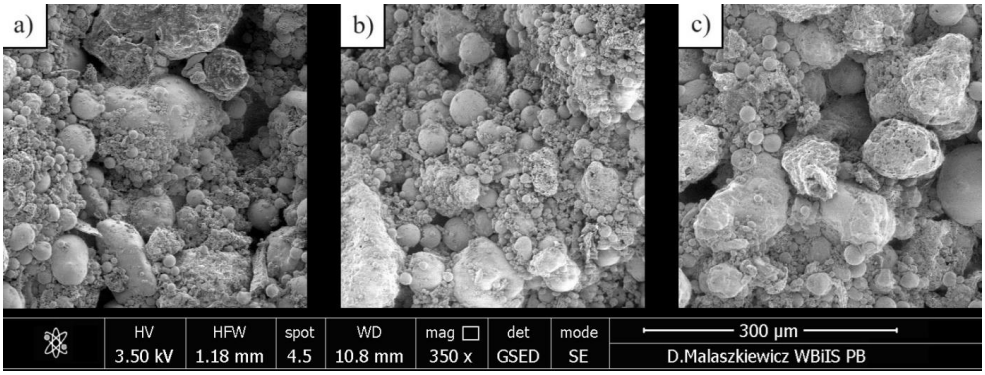


Figure 3. ESEM images of the fly ash (Zabielska-Adamska et al., 2019) compacted at: a) w_{opt} – 5% = 36%; b) w_{opt} = 41%; c) w_{opt} + 5% = 46%

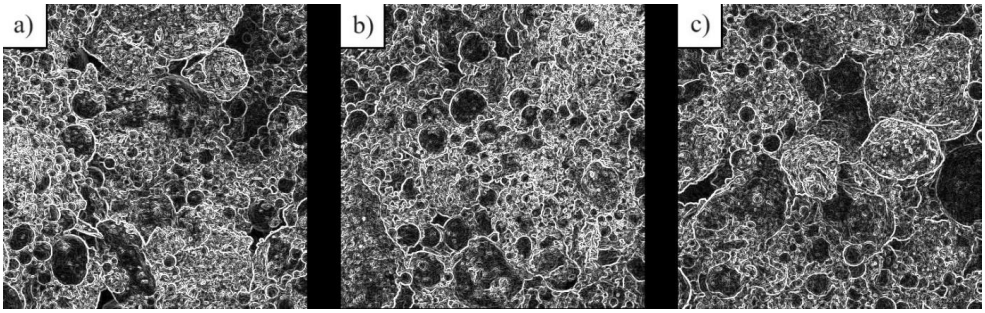


Figure 4. ESEM images (Fig. 3) after using the 'Find egdes' function in ImageJ for the fly ash samples compacted at: a) w_{opt} – 5% = 36%; b) w_{opt} = 41%; c) w_{opt} + 5% = 46%

ImageJ was used to determine the threshold values corresponding to the porosities of the fly ash samples, calculated from physical tests, and generate histograms of grey value distributions based on the ESEM images. The highest histogram peak corresponded to the grey value that occurred most frequently in the image. The possible grey values were within the range from 0 (black) to 255 (white) and were shown on the X axis, and the number of pixels for each grey value was presented on the Y axis. The results obtained from using ImageJ are shown in Table 2 and Figure 5.

Table 2. Threshold values obtained with ImageJ corresponding to the porosities of the fly ash samples

Sample ID	Water content w (%)	Porosity n (%)	Threshold value
w_{opt} – 5%	36	51.6	115
w_{opt}	41	50.7	142
w_{opt} + 5%	46	52.8	140

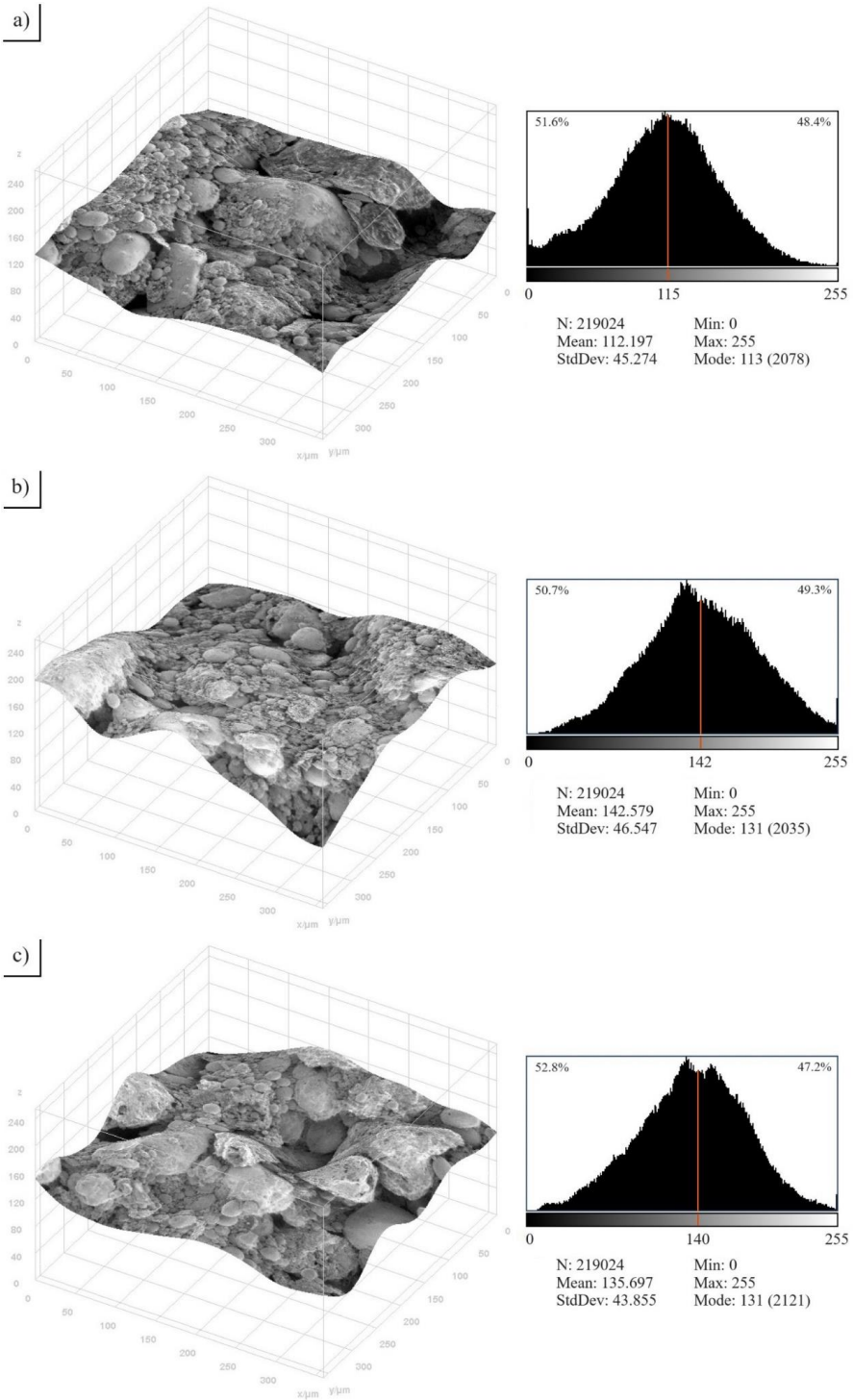


Figure 5. Histograms of grey value distributions based on the SEM images of the fly ash compacted at: a) w_{opt} – 5% = 36%; b) w_{opt} = 41%; c) w_{opt} + 5% = 46%

MATLAB is a platform for programming and numeric computing to analyse and visualise data, develop algorithms, and create applications and models. The 'SEM Image Porosity and Pore Size' code, developed by Arash Rabbani, was adapted and used in MATLAB. It provided the ability to identify pore spaces and estimate pore radius from the normalised ESEM images and presented the data as histograms of pore size distributions. The input ESEM images were greyscale. It was assumed that the darker parts of the images corresponded to pore spaces. The input parameters were the spatial resolution, defined in micrometres per pixel, and the threshold values, defined in ImageJ. Figure 6 presents the image processing flowchart during the ESEM image analysis, developed by Rabbani and Salehi (2017). The results obtained from using MATLAB are shown in Figures 7–9 and Table 3.

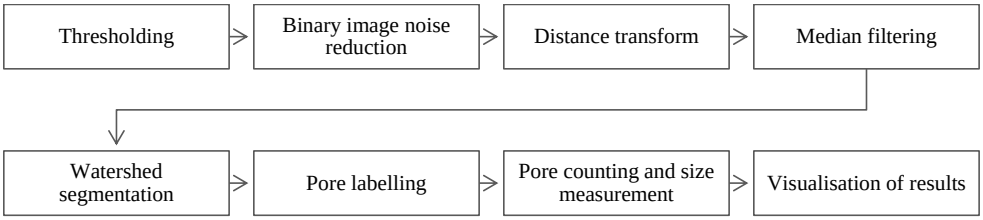


Figure 6. Image processing flowchart for identifying and estimating pore sizes of soil from ESEM images by Rabbani and Salehi (2017)

Table 3. Results obtained from MATLAB

Sample ID	Water content w (%)	Porosity n (%)	Threshold value	Porosity from MATLAB (%)	Average pore radius (μm)	Standard deviation of pore radius (μm)
w_{opt} – 5%	36	51.6	115	51.8	4.5	3.7
w_{opt}	41	50.7	142	50.7	4.7	3.3
w_{opt} + 5%	46	52.8	140	52.9	5.2	4.4

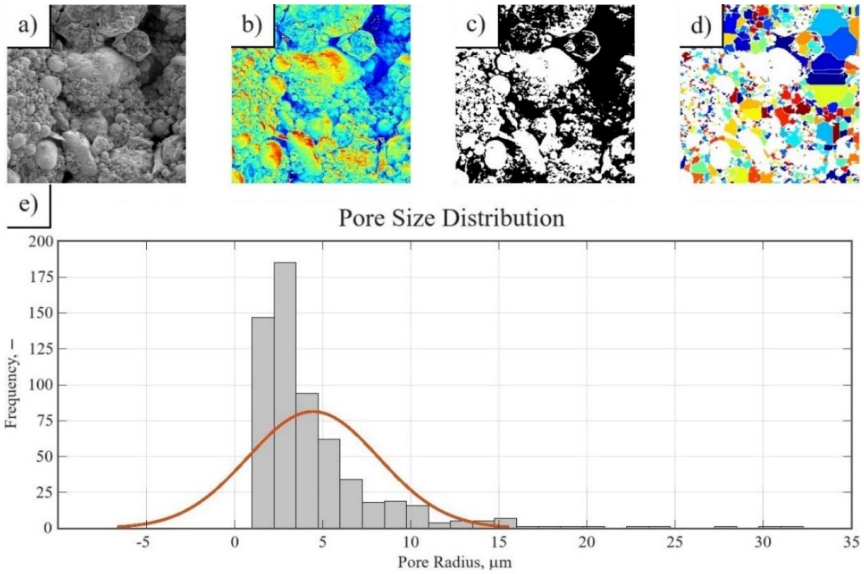


Figure 7. Results obtained from MATLAB for the fly ash sample compacted at 36% (w_{opt} – 5%): a) original ESEM image; b) depth map; c) binary segmentation; d) pore space segmentation; e) pore size distribution

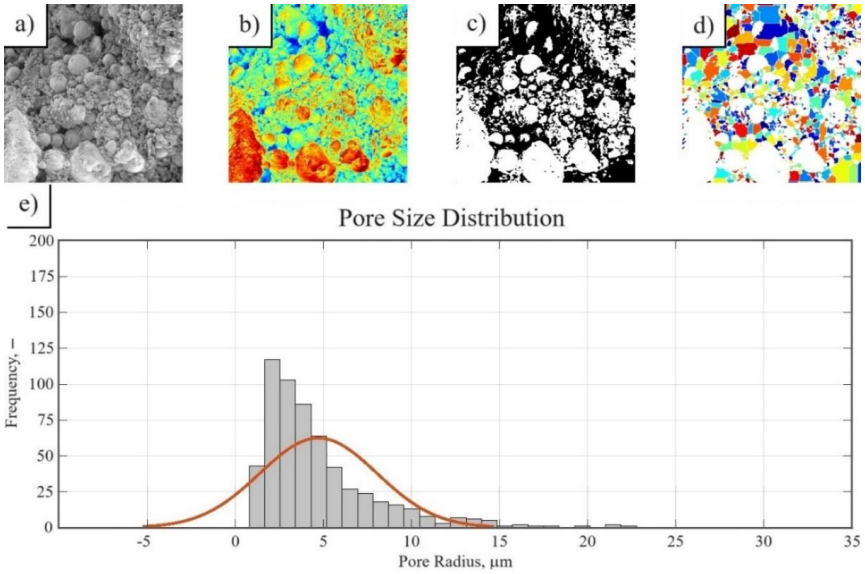


Figure 8. Results obtained from MATLAB for the fly ash sample compacted at 41% (w_{opt}): a) original ESEM image; b) depth map; c) binary segmentation; d) pore space segmentation; e) pore size distribution

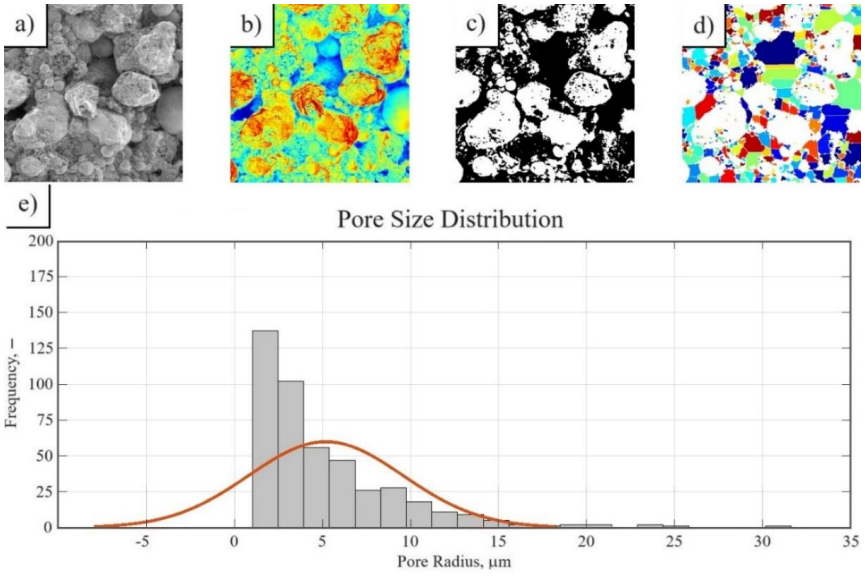


Figure 9. Results obtained from MATLAB for the fly ash sample compacted at 46% (w_{opt} + 5%): a) original ESEM image; b) depth map; c) binary segmentation; d) pore space segmentation; e) pore size distribution

3. CONCLUSIONS

The paper aimed to investigate the microstructure of the compacted fly ash samples. Scanning Electron Microscopy, combined with computer image analysis, was used to define the pore structure and pore size distribution of the tested soil. The following conclusions are drawn based on the results:

1. Fly ash is transitional soil that macroscopically resembles non-cohesive soils. However, its characteristics after compaction strictly depend on water content at compaction, as with cohesive soils. Therefore, water content at compaction should always be considered in geotechnical analyses of this soil.
2. Qualitative observation of the ESEM images showed that the microstructure of the sample with a water content of 36% (w_{opt} – 5%) consisted of aggregates with small pores inside, separated by macropores. The smallest number of pores occurred for the sample compacted at the optimum water content of 41% (w_{opt}). Compaction at a water content of 46% (w_{opt} + 5%) resulted in the loosest structure of the fly ash.
3. The application of image processing methods enables the semi-automatic development of fundamental characteristics that describe soil microstructure.

4. ACKNOWLEDGEMENTS

The research was carried out at the Bialystok University of Technology in Poland. It was supported by Polish financial resources for science. The author is grateful to PhD supervisor Prof. Katarzyna Zabielska-Adamska for her invaluable help and substantive support.

REFERENCES

Delage, P. 2010. A microstructure approach to the sensitivity and compressibility of some Eastern Canada sensitive clays. *Geotechnique*, 60, 353-368.

Delage, P., Audiguier, M., Cui, Y.J., Howat, M. 1996. Microstructure of a compacted silt. *Canadian Geotechnical Journal*, 33(1), 150-158.

Gupta, K., Sachan, A. 2018. Effect of crushing and strain rate on mechanical behaviour of type-F fly ash. *Transportation Infrastructure Geotechnology*, 5(1), 4-23.

Otálvaro, I.F., Neto, M.P.C., Caicedo, B. 2015. Compressibility and microstructure of compacted laterites. *Transportation Geotechnics*, 5, 20-34.

Rabbani, A., Salehi, S. 2017. Dynamic modeling of the formation damage and mud cake deposition using filtration theories coupled with SEM image processing. *Journal of Natural Gas Science and Engineering*, 42, 157-168.

Romero, E. 2013. A microstructural insight into compacted clayey soils and their hydraulic properties. *Engineering Geology*, 165, 3-19.

Romero, E., Simms, P.H. 2008. Microstructure investigation in unsaturated soils: a review with special attention to contribution of Mercury Intrusion Porosimetry and Environmental Scanning Electron Microscopy. *Geotechnical and Geological Engineering*, 26(6), 705-727.

Safari, H., Balcom, B.J., Afrough, A. 2022. Characterization of pore and grain size distributions in porous geological samples: An image processing workflow. *Computers and Geosciences*, 156, 104895, 1-14.

Sasanian, S., Newson, T.A. 2013. Use of mercury intrusion porosimetry for microstructural investigation of reconstituted clays at high water contents. *Engineering Geology*, 158, 15-22.

Taina, I.A., Heck, R.J., Elliot, T.R. 2008. Application of X-ray computed tomography to soil science: A literature review. *Canadian Journal of Soil Science*, 88, 1-20.

Zabielska-Adamska, K. 2008. Laboratory compaction of fly ash and fly ash with cement additions. *Journal of Hazardous Materials*, 151(2-3), 481-489.

Zabielska-Adamska, K. 2020. Characteristics of compacted fly ash as a transitional soil. *Materials*, 13(6), 1387, 1-10.

Zabielska-Adamska, K., Małaszkiewicz, D., Konopko, M. 2019. Microstructure of compacted fly ash. *17th European Conference on Soil Mechanics and Geotechnical Engineering*, Reykjavik, Iceland. 1-8.

Zhang, Y., Yang, G., Chen, W., Sun, L. 2022. Relation between Microstructures and Macroscopic Mechanical Properties of Earthen-Site Soils. *Materials*, 15(17), 6124, 1-23.

28th European Young Geotechnical Engineers Conference – EYGEC 2024
© 2024 Macedonian Association for Geotechnics, ISBN 978-608-4510-61-1

Automated Generation of Ground Model Incorporating Soil Spatial Variability

Ksenija Micić[a], Zehao Ye[b], Miloš Marjanović[c], Jelena Ninić[d]

[a, c] *University of Belgrade, Faculty of Civil Engineering, Department of Geotechnical Engineering, Belgrade, Serbia*
[b, d] *University of Birmingham, Department of Civil Engineering, Birmingham, United Kingdom*

ABSTRACT

The field of geotechnics undergoes a significant transformation in solving complex engineering problems by adopting digital technologies and automation processes. Among many other improvements, digital ground modelling has become state of the art when it comes to infrastructure projects as one of the most comprehensive ways to represent geological and geotechnical conditions of soil and rocks. It also allows for integration of digital ground models with other subsystems, including underground infrastructure, utilities, above ground infrastructure, and construction processes. While the domain of 2D and 3D geological modelling has advanced significantly in the past decades, incorporating soil spatial variability, and thus assessing the underground heterogeneity and parameter uncertainty, remains a challenge. In this regard, this paper proposes an automated framework for generating a digital ground model based on site-specific borehole data within a Building Information Modelling (BIM) framework. Furthermore, the digital ground model incorporates geotechnical parameters' spatial variability using Conditional Random Fields (CRFs). The soil parameter variability is simulated through CRF randomization of soil strength parameters to determine their values at the non-sampled points. Borehole-based ground modelling is conducted using GSTools and a BIM software environment for the case study of the New Belgrade area in Serbia. Integrating the above-mentioned data into one holistic digital ground model offers numerous advantages and leads to more reliable probabilistic-based predictive numerical models of structures embedded in variable strata.

KEYWORDS

Digital ground model; Conditional random fields; BIM; Automation

1. INTRODUCTION

Current digitization-dominated engineering practice increasingly demands the collaborative application of expert-knowledge, digital technologies, and automated approaches for solving real-life geotechnical problems. Always being the foundation of the geotechnical pyramid, ground modelling is a complex and challenging task to complete.

Building Information Modelling (BIM) offers a comprehensive digital platform and establishes a spatial structure for the storage and management of data with geometric and semantic data integration seamlessly achieved. BIM also serves as a foundational source of information for numerical analysis (Ninić et al., 2019). The practical application of BIM in structural engineering has become exceptionally widespread, while its application in BIM Ground Models (BIMGM) is rapidly evolving, seeking practical use cases (Erharter et al., 2023). This provides a better description of the surrounding environment for projects and enhances the interaction between structural information and geological conditions (Huang et al., 2021). The main challenge is that geological data is heterogeneous and varies in three dimensions. The collection, management, modelling, and visualization of complete geological data differ significantly from structures such as buildings, bridges, and tunnels, because the spatial structure and semantics of geological elements are unique (Khan et al., 2023).

Owing to their composite tectonic and depositional processes, soil physical and mechanical properties can considerably vary in 3D space. Spatial variability, if not considered during structural analysis, can be the cause of incomplete and unsafe design. As for the existing probabilistic methods, site-specific ground conditions and soil properties variability can be simulated within the powerful frameworks of the Random Field Theory. Underground heterogeneity and parameter uncertainty can be captured through the process of generating random fields by using the measurement data obtained from boreholes (or other investigation works). Conditioning random fields with measurement data at sampling points ensures reflecting "known" parameters during the randomization process. Research conducted in the domain of conditional random field site-characterization has mostly been focused on introducing novel approaches for assessing geo-properties uncertainty (Li et al., 2016a; Ching et al., 2020; Gong et al., 2021; Yang and Ching, 2021; Zhao et al., 2023), for slope reliability evaluation (Li et al., 2016b; Huang et al., 2019; Huang et al., 2020) and underground construction design and performance (Gong et al., 2018; Hu and Wang, 2019; Xie et al., 2023; Shi et al., 2023).

This paper presents a fully automated approach for generating a digital ground model based on site-specific borehole data by coupling BIM geological modelling and simulating soil spatial variability through a conditional random field generation process. The capacity of the proposed automated framework and digital tools has been confirmed through a case study for the New Belgrade area in Serbia.

2. GROUND MODEL

2.1. Borehole database structure

Borehole data is usually obtained from geotechnical reports, in the form of Excel tables. While the scope and level of details of such reports is often relatively correct, the data structure can vary significantly. Therefore, we developed an automatic Excel data parser in Python in order to extract the borehole data into a more convenient and structured format.

First, the database structure is designed to account for all the available borehole data. The general borehole database structure is designed as follows: Borehole > SoilZone > SoilSample (Figure 1). Borehole data contains XYZ coordinates, designated names, groundwater level (GWL) and basic information such as drilling diameter/company/date etc. Each borehole consists of soil segments called SoilZones, which have their corresponding geological name and description (e.g. silty clay), depth (limits) and penetration test data (SPT, CPT). SoilZones contain SoilSamples at certain depths, which carry basic information on laboratory testing data and USCS classification. Inside the database, parent-child links (one-to-many relationships) are established between boreholes, soil zones, and soil samples.

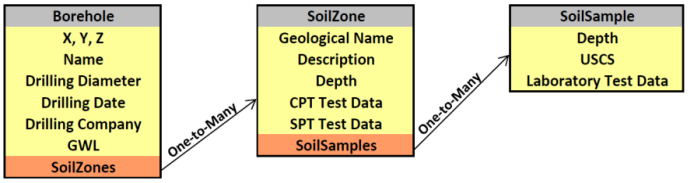


Figure 1. Borehole database structure

2.2. BIM Ground Model (BIMGM)

Several methods for BIMGM modelling have been proposed, and mainly include mesh modelling, like triangulated irregular networks (TIN), tetrahedron network (TEN) and voxelization. The former is typically used for the rough-level geological model construction, with limited refinement capability, making it difficult to support varying scales or lower-level heterogeneous geological information. Voxel models, on the other hand, offer greater flexibility in representing heterogeneous geological information

and integrating semantic data (Khan et al., 2023). Regardless of the method chosen, the main objective of BIMGM is to ensure reliable documentation, and its content aligns with traditional planning standards and existing BIM standards, facilitating communication among stakeholders through a centralized repository of geological data (Erharter et al., 2023).

In this paper, we employ the voxelization method for the detailed description of BIMGM. As shown in Figure 2, there are four main steps: (1) using the Delaunay triangulation method to create a 2D mesh onto a plane based on the coordinates of borehole data points. The borehole data for the four rectangle boundary corner points (⊗) are supplemented by inheriting the nearest borehole point; (2) generation of voxel centre point matrices based on user-defined voxel dimensions; (3) searching for the plane triangles to which the voxel centre points belong and selecting the nearest neighbouring vertices (borehole points); (4) inheriting vertex attributes and calculating soil types based on Z-coordinates. During the search process, points within a certain range will inherit the attributes of the same triangle vertex. We refer to this range as the influence zone, where the boundary lines dividing the influence zones within a triangle intersect at the circumcentre (O) of that triangle. For any point in the voxel centre point matrix, its attributes include its 3D coordinates, voxel dimensions in the x, y, and z directions, soil type name, and soil strength parameter value, totalling eight attributes. With these attributes, the automatic visualization process can be executed in Revit using Dynamo, generating voxel model following these points.

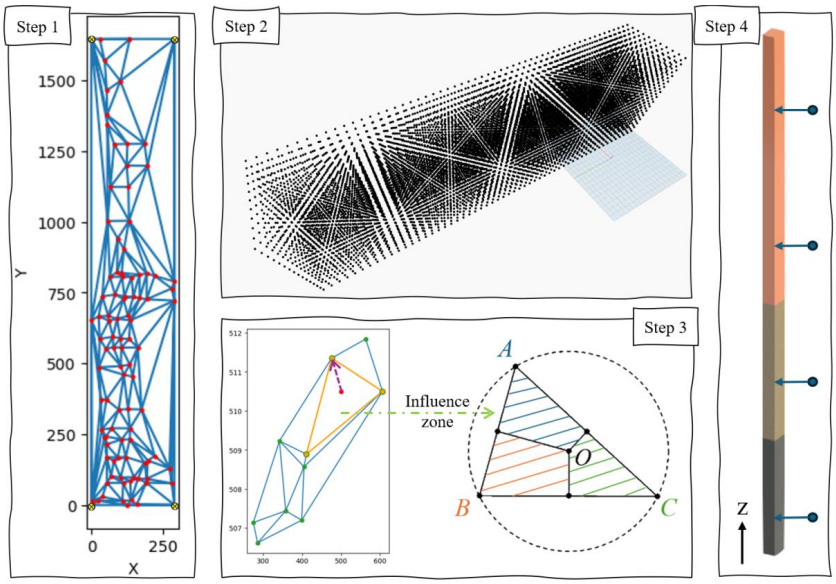


Figure 2. Flowchart of obtaining voxel model attributes

3. SOIL SPATIAL VARIABILITY

3.1. Random Field Theory and Kriging

For structures embedded in variable strata, it is of the utmost importance to perform a comprehensive full-scale soil parameter characterization, to be able to proceed to the probabilistic structural analysis. Given that these parameters are only obtainable at sampling points, and as the scope of site investigations is often budget-limited, introducing different parameter interpolation methods becomes essential. While various spatial interpolation techniques have been commonly utilized in the current practice, they exhibit

limited capabilities in capturing soil spatial variability, compared to the Random Field Theory (Micić and Marjanović, 2023).

Unconditional random fields simulate the soil properties distribution based on general trends and patterns in relation to the statistical properties (such as mean, coefficient of variation, spatial correlation structure), but without incorporating any site-specific measured data as constraints. Conditioning random fields with local measurement data at sampling points tackles the issue of more accurate and site-specific predictions of spatial variables.

The Kriging algorithm is one of the common ways to interpolate spatial data when generating conditional random fields. It is an interpolation technique based on predefined covariance models that estimates the value of a field, denoted as z, at a non-sampled point x_0, with respect to the fixed conditioning values $z(x_1) \dots z(x_n)$ at specified points $x_1 \dots x_n$. The best linear unbiased prediction of the value z_0 at a point x_0 is computed as a weighted average, represented by the Equation (1):

$$z_0 = \sum_{i=1}^{n} \omega_i \cdot z_i \tag{1}$$

in which n is the number of conditioning points and ω_i is the weighting factor determined by the specific kriging method. Various kriging methods, such as simple, ordinary, and universal kriging, can be employed to address the needs of diverse datasets (Müller et al., 2022).

3.2. Automated Conditional Random Field Generator

In this paper, for automation in generating the spatial variability, we adopted GSTools and PyVista. GSTools (Müller et al., 2022) is an open-source Python-based software package designed for solving geostatistical problems. It provides a comprehensive set of tools and algorithms for automated spatial data analyses, focusing on unconditional and conditional random field generation, kriging interpolation methods, variogram modelling and uncertainty analysis. PyVista (Sullivan and Kaszynski, 2019), an open-source Python library and a helper module for the powerful Visualization Toolkit (VTK), can be used to visually represent the output CRFs. It provides mesh data structures and filtering methods for spatial datasets, as well as tools for 2D and 3D visualization for complex data geometries.

The process of automatically generating conditional random fields includes two main steps: generating an Unconditional Random Field (UCRF) of soil parameters and generating its Conditional realization (CRF). There are different approaches to generating UCRFs, such as covariance matrix decomposition methods, spectral methods, sequential simulations, and turning bands methods. GSTools produces spatial random fields with a given covariance function or a semi-variogram through a randomization method within the spectral Fourier domain (Heße et al., 2014; Müller et al., 2022). A Gaussian random field *u(x)* can be represented by the Equation (2):

$$u(x) = \sqrt{\frac{\sigma^2}{N}} \cdot \sum_{i=1}^{N} \left(Z_{1,i} \cdot cos(k_i \cdot x) + Z_{2,i} \cdot sin(k_i \cdot x) \right) \tag{2}$$

where N is the number of Fourier modes of the approximation, $Z_{1,i}$ and $Z_{2,i}$ are the standard normal random variables that are mutually independent, and k_i are mutually independent random samples for every mode *i*.

Conditional random fields that coincide with the given observations, but maintain randomness based on predetermined covariance model beyond the observation's proximity, are generated combining kriging routines and UCRF. Ordinary kriging, as one of the most widely used kriging routines, assumes an unknown mean of the random field across the study area, and calibrates it as a part of the interpolation process (Müller et al., 2022).

4. CASE STUDY

4.1. Scope of Study

In the following section, we present a case study to illustrate the application of the proposed methods to a realistic site-specific dataset. Existing borehole data for New Belgrade's blocks 61, 62, 63 and 64 is used to generate a 3D Revit geological model, including spatial variability modelled employing a 3D conditional random field. The study site represents an urban, mainly residential area, covering an area of approximately 0.5 km^2. It mostly consists of alluvial deposits represented with the interchange of silt, clay, sand, and gravel. Based on the chosen area and quality of the raw sampling data, 94 boreholes are included in the digital ground modelling process. Among various available laboratory tests data, effective cohesion (c') has been recognized as a representative example to conduct the proposed conditional random field generation process with GSTools. All the included boreholes contain at least one soil sample with known effective cohesion c'.

The borehole data extraction was not straightforward, because the raw data contained some anomalies. In general, the raw data rows consisted of soil sample, soil zone and borehole data mixed together. Therefore, we created a mapping file, containing class type, data type and property of each data column for all the raw data files. Some boreholes and samples were duplicated, sometimes samples in the same borehole were overlapping, and some files included mixed borehole and CPT test data. All these problems were handled using Python scripts. Duplicated boreholes and soil samples were grouped together, and available data was merged. Geological names were in Serbian, so a dictionary was applied for translation. Strings were automatically converted to numerical values (e.g. sample depths) when needed. At the end, some boreholes contained empty (unknown) soil zones, and in that case, adjacent known zones were expanded.

4.2. Results

For BIMGM modelling, each borehole carries information on spatial coordinates (X, Y and Z) and soil layer types with their corresponding depths. The visualization can be seen in Figure 3.

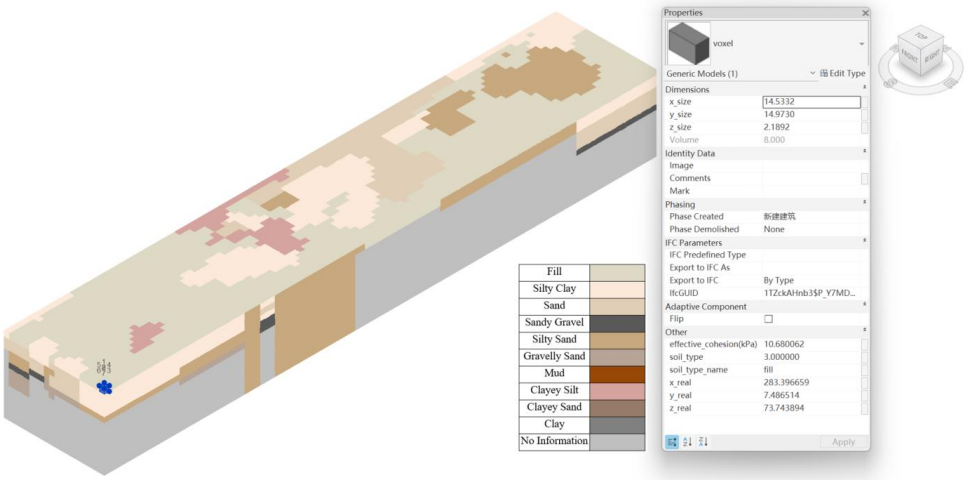


Figure 3. Visualization of the BIMGM voxel model based on soil type name

The attributes of each voxel were obtained according to the steps outlined in Section 2.2. The true dimensions of each voxel in the x, y, and z directions are 14.53 m, 14.97 m, and 2.19 m, respectively. A total of 33000 voxels were generated (20x110x15 in x, y, z directions, respectively).

The borehole information needed to perform parameter randomization in 3D are the spatial coordinates of the boreholes, and the spatial coordinates and effective cohesion values at sampling points. The soil sample mean depth was chosen as the sampling point Z-coordinate. We performed the conditional randomization process in three main steps: 1) UCRF generation; 2) CRF generation and 3) 2D and 3D visualization of the obtained results. The UCRF was estimated as a Gaussian spatial random field by using the spectral density randomization method in the Fourier domain. The conditional random field realization of the effective cohesion was generated by applying ordinary kriging to interpolate the spatial data, after which the field's estimated effective cohesion values were constrained for 152 local conditioning point values (borehole samples). The randomization process was carried out within the structured XYZ field grid, matching the grid of the voxel model. The obtained 3D conditional realization of effective cohesion for the study area is shown in Figure 4a. The longitudinal 2D section plot is shown in Figure 4b.

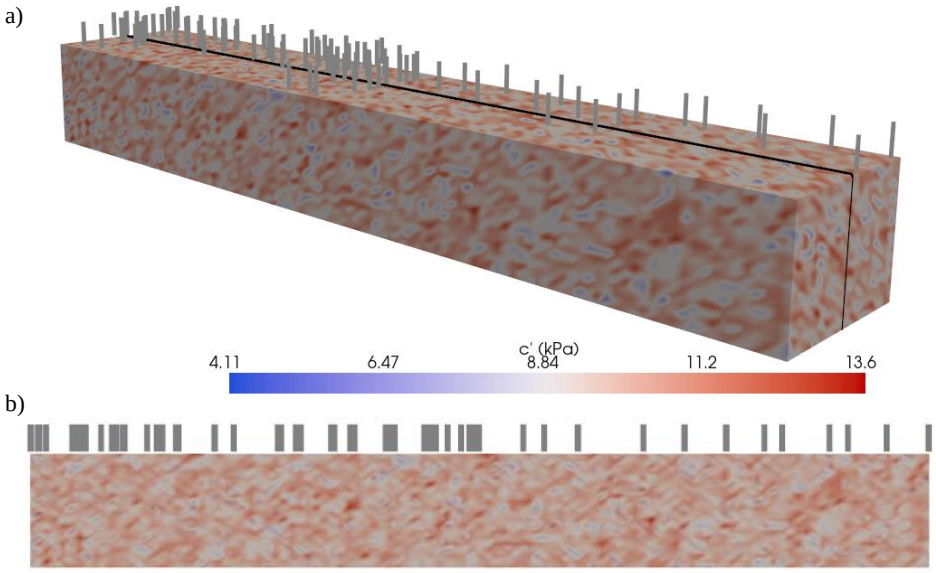


Figure 4. a) 3D CRF realization of effective cohesion and b) longitudinal cross-section of effective cohesion over the study area. Grey lines represent borehole locations. Black line represents longitudinal cross section position

Estimated values range from 4.11 to 13.6 kPa, realistically representing the site's spatial variability in terms of heterogenous material cohesion expectations. However, the generated CRF could not adequately meet the conditioning values of effective cohesion in sandy-gravelly material ($c' = 0$). This might be the consequence of the CRF being generated only in regard to the positions of sampling data, without explicitly considering different lithological layers' spatial distribution.

Finally, BIMGM and CRF model were united by extracting the effective cohesion values of the centre point of each generated voxel and inscribing it to the voxel attributes, thus incorporating soil spatial variability into the framework of the BIM model, as visually represented in Figure 5.

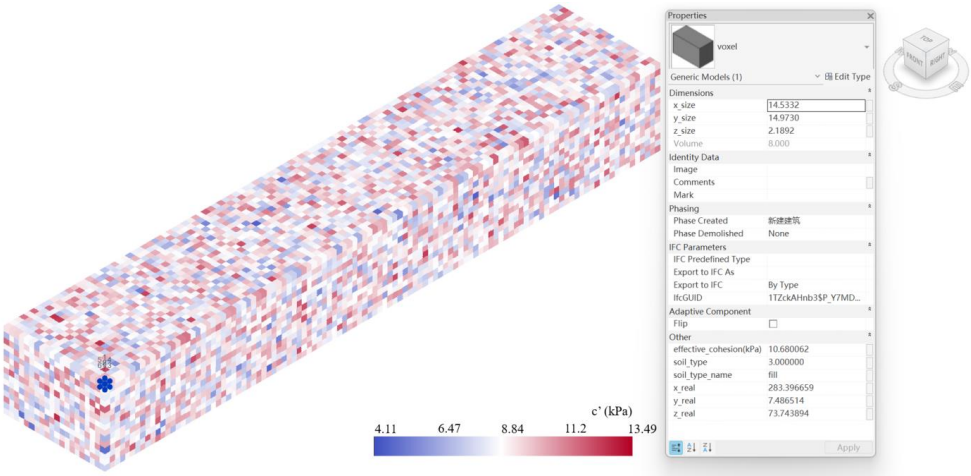


Figure 5. Visualization results of effective cohesion in the BIMGM voxel model

5. CONCLUSIONS

In this paper, we presented an automated framework for the development of a 3D holistic digital ground model in BIM software, incorporating soil spatial variability via CRF soil parameter randomization. For BIM ground modelling, voxelization method in combination with influence zones concept was recognized as efficient when it comes to heterogeneous soil representation. Soil parameter variability was assessed through the process of conditional random field generation coupled with kriging interpolation method. Proposed methodology was applied on a real case site characterization based on site-specific borehole data. Results showed reasonable soil layer distribution achieved in Revit and efficient soil cohesion conditional randomization in GSTools.

Further research should be focused on developing more robust CRF methodology to constrain the lithological data with the expected soil parameter values. Proposed ground modelling concept, combined with FEM numerical models, should be validated on real infrastructure projects and different borehole databases. Also, additional work is to be done in the integration of all developed tools with numerical modelling software to obtain fully automated and more accurate predictive probabilistic modelling of underground infrastructure and development of digital twins.

6. ACKNOWLEDGEMENTS

This work is supported by Serbian Ministry of Science, Technological Development and Innovation via Project 200092. Borehole Excel data provided by Prof. dr Zoran Radić (Radić, 2007) is acknowledged.

REFERENCES

Ching, J., Huang, W. H., Phoon, K. K. 2020. Three-dimensional probabilistic site characterization by sparse Bayesian learning. *Journal of Engineering Mechanics*, 146 (12) 04020134.

Erharter, G. H., Weil, J., Bacher, L., Heil, F., Kompolschek, P. 2023. Building information modelling based ground modelling for tunnel projects–Tunnel Angath/Austria. *Tunnelling and Underground Space Technology*, 135, 105039.

Gong, W., Juang. C. H., Martin, J. R., Tang, H., Wang, Q., Huang, H. 2018. Probabilistic analysis of tunnel longitudinal performance based upon conditional random field simulation of soil properties. *Tunnelling and Underground Space Technology*, 73, 1–14.

Gong, W., Zhao, C., Juang, C., Zhang, Y., Tang, H., Lu, Y. 2021. Coupled characterization of stratigraphic and geo-properties uncertainties – A conditional random field approach. *Engineering Geology*, 294, 106348.

Heße, F., Prykhodko, V., Schlüter, S., Attinger, S. 2014. Generating random fields with a truncated power-law variogram: A comparison of several numerical methods. *Environmental Modelling & Software*, 55, 32-48.

Hu, B., Wang, C. 2019. Ground surface settlement analysis of shield tunneling under spatial variability of multiple geotechnical parameters. *Heliyon*, 5 (9) e02495.

Huang, L., Cheng, Y., Leung, Y., Li, L. 2019. Influence of rotated anisotropy on slope reliability evaluation using conditional random field. *Computers and Geotechnics*, 115, 103133.

Huang, L., Zhang, Y., Lo, M., Cheng, Y. 2020. Comparative study of conditional methods in slope reliability evaluation. *Computers and Geotechnics*, 127, 103762.

Huang, M. Q., Ninić, J., Zhang, Q. B. 2021. BIM, machine learning and computer vision techniques in underground construction: Current status and future perspectives. *Tunnelling and Underground Space Technology*, 108, 103677.

Khan, M. S., Kim, I. S., Seo, J. 2023. A boundary and voxel-based 3D geological data management system leveraging BIM and GIS. *International Journal of Applied Earth Observation and Geoinformation*, 118, 103277.

Li, X. Y., Zhang, L. M., Li, J. H. 2016a. Using conditioned random field to characterize the variability of geologic profiles. *J. Geotech. Geoenvironmental Eng*. 142 (4), 04015096.

Li, Y., Hicks, M., Vardon, P. 2016b. Uncertainty reduction and sampling efficiency in slope designs using 3D conditional random fields. *Computers and Geotechnics*, 79, 159-172.

Micić, K., Marjanović, M. 2023. Conditional random fields for simulating spatial variability of geotechnical parameters in tunnelling. *Proceedings of International Scientific Forum: Geotechnical Aspects of Civil Engineering and Earthquake Engineering*, Vrnjacka Banja, Serbia, 510-519.

Müller, S., Schüler, L., Zech, A., Heße, F. 2022. GSTools v1.3: a toolbox for geostatistical modelling in Python. *Geosci. Model Dev*., 15, 3161–3182.

Ninić, J., Bui, H. G., Koch, C., Meschke, G. 2019. Computationally efficient simulation in urban mechanized tunneling based on multilevel BIM models. *Journal of Computing in Civil Engineering*, 33(3), 04019007.

Radić, Z. 2007. Geotehnički modeli aluvijalnih sedimenata Novog Beograda (In Serbian). University of Belgrade, Faculty of Mining and Geology.

Shi, J., Wang, F., Huang, H., Zhang, D. 2023. Horizontal convergence reconstruction in the longitudinal direction for shield tunnels based on conditional random field. *Underground Space*, 10, 118-136.

Sullivan, B., Kaszynski, A. 2019. PyVista: 3D plotting and mesh analysis through a streamlined interface for the Visualization Toolkit (VTK). *Journal of Open Source Software*, 4(37), 1450.

Xie, P., Chen, K., Skibniewski, M., Wang, J., Luo, H. 2023. Parametric geological model update and probabilistic analysis of shield tunnel excavation: A borehole-based conditional random fields approach. *Computer and Geotechnics*, 157, 105349.

Yang, Z., Ching, J. 2021. Simulation of three-dimensional random field conditioning on incomplete site data. *Engineering Geology*, 281, 105987.

Zhao, C., Gong, W., Juang, C., Tang, H., Hu, X., Wang, L. 2023. Optimization of site exploration program based on coupled characterization of stratigraphic and geo-properties uncertainties. *Engineering Geology*, 317, 107081.

28th European Young Geotechnical Engineers Conference – EYGEC 2024
© 2024 Macedonian Association for Geotechnics, ISBN 978-608-4510-61-1

Soil Liquefaction Mitigation by Applying the DSM Technique Below the Foundations of a Silo Base

Nikolay Y. Milev [a]

[a] *University of Architecture Civil Engineering and Geodesy (UACEG), Sofia, Bulgaria*

ABSTRACT

This paper presents a conceptual approach for mitigating soil liquefaction by applying the deep soil mixing (DSM) technique beneath the shallow foundations of a silo base slated for future construction in Varna, Bulgaria. Preliminary analyses of the site's seismic, geological, and hydrogeological conditions indicate that the water table is near the ground level and some zones are prone to liquefaction, with an anticipated surface settlement of 20 to 30 cm during a major seismic event. Additionally, a saturated layer of backfill, which requires removal during construction, exists on the site. To address both issues simultaneously, a 6 by 6 m grid of DSM containment cells (with a chosen diameter for overlapping DSM columns of 900 mm) has been proposed. For economic reasons, the suggested improvement depth does not extend to a non-liquefiable layer but is still expected to ensure acceptable performance by reducing settlement. The paper aims to offer a new perspective on a relatively well-known soil liquefaction mitigation measure, taking additional advantage by eliminating the need for a dewatering system, thereby achieving a technological and economic balance in the project.

KEYWORDS

Soil liquefaction, mitigation measures, deep soil mixing, shallow foundation

1. INTRODUCTION

The project site is located at the port of Varna, Bulgaria, characterized by a predominantly sandy soil profile with a groundwater level close to the surface (Figure 1). An initial geotechnical challenge is the presence of approximately two meters of submerged fill with poor engineering properties, necessitating removal. This layer, if left unaddressed, presents a risk due to its unsuitable bearing capacity for the planned infrastructure.



Figure 1. Key elements of soil liquefaction engineering

Additionally, an initial evaluation of the liquefaction potential has identified certain zones, extending up to 20 meters in depth, that are susceptible to liquefaction, which could lead to excessive settlement as indicated by preliminary assessments. To circumvent the need for dewatering during the removal of the problematic fill and to enhance subsoil stability, a deep soil mixing technique has been selected. This approach incorporates the use of soil-mix cells designed to provide both reinforcement and a reduction in settlement potential.

The targeted construction comprises 12 steel silos, each with a unit volume of 8,300 cubic meters, a height of 29.40 meters, and a diameter of 22.30 meters. These structures are engineered to endure a Peak Ground Acceleration (PGA) of 0.15*g*, associated with a 475-year return period according to Eurocode 8. The project is designed with an allowable average settlement of 15 centimeters to maintain structural integrity over the lifetime of the silos, taking into account the identified geotechnical risks. This paper will explore the intricate balance between addressing the engineering challenges posed by the site conditions and achieving the operational requirements of the steel silos in the sandy soils of Varna Port in Bulgaria.

2. GEOTECHNICAL INVESTIGATIONS

A network of five boreholes, each extending to a depth of 25 meters, was methodically laid out and drilled to procure samples for evaluating the physical and mechanical properties of the subsurface materials. From these boreholes, a total of 16 soil samples were extracted and subjected to laboratory testing. Supplementing the borehole data, "*in-situ*" Dynamic Penetration Tests (Super Heavy) (DPSHs) were also conducted, with seven penetrations reaching a depth of 35 meters each. The spatial arrangement of both boreholes and DPSHs is illustrated in Figure 2.

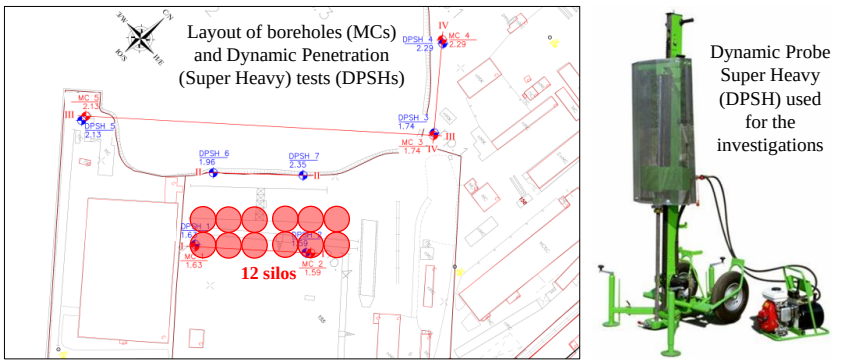


Figure 2. Geotechnical investigations for the project

Results from these investigations have identified three main soil types shown in Figure 3. The first is a fill layer, approximately 1.5 to 2 meters thick. Beneath this lies a significant loose sand stratum, reaching a thickness of around 20 meters. The deepest layer encountered comprises plastic silty clay and dense sand, which the investigations have not probed further. The water table lies between 1.0 and 1.5 meters below ground level, rendering the loose sand layer saturated.

Key conclusions drawn from the soil analysis, specifically pertaining to the loose sand layer, are presented in Figure 3. This layer's susceptibility to liquefaction is a point of focus due to its granular, fully saturated nature, and geological youth. The findings denote a low relative density indicating a loose state, along with a low uniformity coefficient pointing to poor grading. This evidence strongly suggests that the loose sand layer is prone to liquefaction.

Given this assessment, the paper emphasizes the need for additional investigations to thoroughly evaluate the seismic hazard and incorporate these factors into the site's risk mitigation strategy.

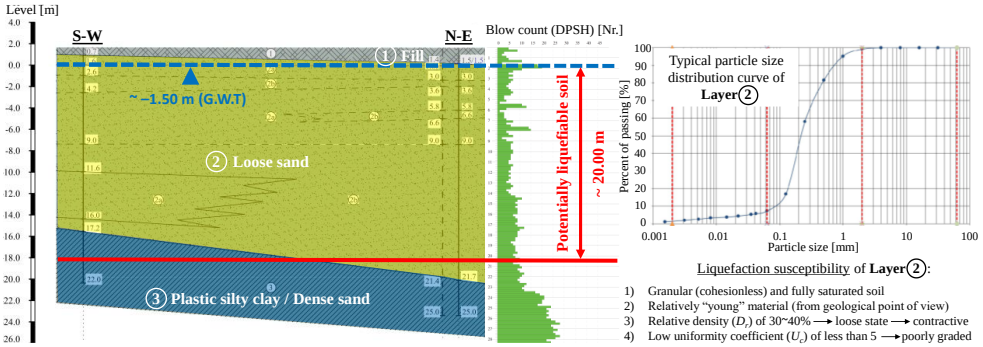


Figure 3. Typical geological profile of the site and key conclusions drawn from the geotechnical investigations

3. SEQUENCE OF ACTIONS IN LIQUEFACTION ENGINEERING

Soil liquefaction engineering has evolved into a distinct and increasingly mature field of practice, characterized by several specific subtopics and issues. As outlined in a schematic representation in Figure 4, the foundational step in most soil liquefaction engineering approaches remains the assessment of liquefaction potential, or the likelihood of its initiation. Recent years have witnessed significant advancements in this area, which are worth exploring.

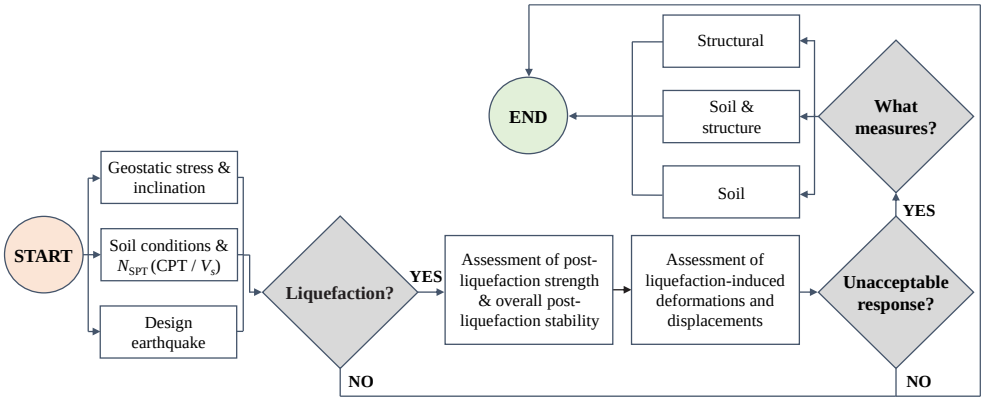


Figure 4. Key elements of soil liquefaction engineering

Upon recognizing the potential risk of liquefaction at a site, the focus shifts to evaluating the possible consequences. This evaluation often involves determining the post-liquefaction strength and the subsequent overall stability of the site, structure, or other built facilities. If this evaluation indicates a deficiency in post-liquefaction stability, indicating a high potential for deformation or displacement, engineered remediation becomes necessary. Conversely, if the post-liquefaction stability is deemed acceptable, the next step is to account for the anticipated settlement and lateral spreading in design. This area of practice remains somewhat underdeveloped, with significant work needed in the development, calibration, and verification of relevant engineering tools and methods. Furthermore, there is a lack of comprehensive engineering guidelines on the impact of liquefaction-induced deformations and displacements on structures and engineered facilities, and the standards for acceptable performance are yet to be firmly established.

In situations where satisfactory performance is deemed unlikely, engineered mitigation of liquefaction risk is generally the next step. This aspect of soil liquefaction engineering is rapidly evolving, often

marked by debate and controversy. The continuous development of new mitigation methods offers a growing array of engineering solutions. However, the effectiveness and reliability of some of these methods are still subjects of debate, and the accurate and reliable analysis of performance improvements post-mitigation remains challenging.

Given the scope of this study, it is not feasible to comprehensively address all these aspects. However, key recent and ongoing advancements, controversial areas, and domains, either in practical application or understanding, will be highlighted.

4. SIMPLIFIED STRESS-BASED APPROACH

In situ "index" testing stands as the predominant method in geotechnical engineering for evaluating the potential for "triggering" or the onset of liquefaction. This approach encompasses several widely-used techniques, including the standard penetration test (SPT), the cone penetration test (CPT), and the measurement of shear wave velocity (V_s). The assessment of liquefaction risk involves comparing the seismic loading, quantified as the Cyclic Stress Ratio (*CSR*), against the soil's resistance to liquefaction, denoted as the Cyclic Resistance Ratio (*CRR*). This comparison is typically expressed in the form of a factor of safety (*FS*) against liquefaction, as detailed in the following equation:

$$FS = [(CRR_{7.5}\text{MSF})/CSR]K_\sigma K_\alpha \quad (1)$$

where:
FS – factor of safety
$CRR_{7.5}$ – cyclic resistance ratio for an earthquake with magnitude 7.5
CSR – cyclic stress ratio
MSF – magnitude scaling factor according to (NCEER, 1997)
K_σ – overburden correction factor according to (NCEER, 1997)
K_α – correction factor for the effects of an initial static shear stress ratio according to (NCEER, 1997)

4.1. Demand – Cyclic Stress Ratio (*CSR*)

The Cyclic Stress Ratio (*CSR*) quantifies the cyclic shear stress at a specific depth resulting from seismic activity. In locations where the ground slope is under 6%, the shear stresses induced by earthquakes are assumed to arise solely from the vertical propagation of shear waves. These stresses can be calculated using a one-dimensional dynamic response analysis of the soil layer, as suggested by (Seed & Idriss, 1971). However, considering the complexity and time-intensive nature of dynamic response analyses at that time, and the challenges in acquiring accurate site characterization and suitable input ground motions, (Seed & Idriss, 1971) have proposed a simplified formula which is grounded in Newton's second law:

$$CSR = \tau_d/\sigma'_v = 0.65(a_{max}/g)(\sigma_v/\sigma'_v)r_d \quad (2)$$

where:
CSR – cyclic stress ratio
τ_d – average cyclic shear stress
σ'_v – effective overburden stress at depth *z*
σ_v – total overburden stress at depth *z*
a_{max} – maximum horizontal ground surface acceleration
g – gravitational acceleration
r_d – shear stress reduction coefficient which starts at 1.0 at the surface and diminishes with increasing depth, reflecting the non-rigid behavior of the soil column under the influence of the vertically propagating shear wave. Practical procedures for evaluating r_d are given in (NCEER, 1997; Cetin et al., 2004).

The factor of 0.65 in Equation 2 adjusts the *CSR* from the peak value of earthquake-induced shear stress, which occurs only momentarily during the quake, to a more typical value experienced multiple times during intense shaking.

4.2. Demand – Cyclic Stress Ratio (*CSR*)

The concept of Cyclic Resistance Ratio (*CRR*) is pivotal in understanding soil's resistance to liquefaction, essentially representing the Cyclic Stress Ratio (*CSR*) necessary to initiate liquefaction. The simplified method relies on field observations to establish correlations between in situ parameters and *CRR*, as derived from a plethora of case histories involving both liquefaction and non-liquefaction events. Common corrected *in situ* parameters used for this evaluation include the standard penetration test (SPT) blow count, [$(N_1)_{60\text{-}cs}$ – equivalent clean-sand normalized N_{SPT}-value], Cetin et al., 2004; Idriss & Boulanger, 2008, the cone penetration test (CPT) tip resistance, ($q_{c1\text{-}Ncs}$ – normalized tip resistance) Robertson & Wride, 1998; Moss et al., 2006; Idriss & Boulanger, 2008, and small strain shear wave velocity, (V_{s1} – shear wave velocity corrected to an effective overburden stress of 1 atm), Andrus & Stokoe, 2000. The use of SPT and CPT profiles is more frequent than V_s profiles for liquefaction triggering assessment.

5. LIQUEFACTION-INDUCED RECONSOLIDATION SETTLEMENT

Evaluating the potential deformations and displacements that may arise from liquefaction or ground softening due to increased pore pressure presents a complex and demanding challenge in many engineering projects. Accurately predicting post-liquefaction deformations, particularly in the "small to moderate" range (displacements less than about 0.75 m), remains a significant challenge in the field of geotechnical engineering. This range is crucial for most standard buildings and engineered facilities, yet current tools fall short in providing reliable estimates.

In general, geotechnical earthquake engineering practice, the determination of post-liquefaction reconsolidation settlement can typically be based on the results of the standard penetration test (SPT) – (Ishihara & Yoshimine, 1992; Shamato, 1998; Wu et al., 2003), cone penetration test (CPT) or through seismic testing for the evaluation of shear wave velocity (V_s). Such post-liquefaction settlement is calculated by integrating the values of post-cyclic volumetric strain (ϵ_v) across the depth of the soil layer:

$$S = \int_0^{z_{max}} \epsilon_v \, . \, dz \tag{3}$$

where:
S – post-liquefaction reconsolidation settlement
ϵ_v – post-cyclic volumetric strain
z_{max} – maximum depth
dz – liquefiable layer height

(Ishihara & Yoshimine, 1992) have proposed a specific equation for the evaluation of post-cyclic volumetric strain (ϵ_v):

$$\epsilon_v = 1.5 \cdot \exp(-2.5 D_r) \cdot \min(0.08, \gamma_{max}) \tag{4}$$

where:
D_r – relative density
γ_{max} – maximum cyclic shear strain

Studies (Wu et al., 2003) suggest graphical approaches for evaluation of on the post-cyclic volumetric strain (ϵ_v) on the basis of corrected SPT blow count data. Another method (Ishihara & Yoshimine, 1992) involves the adoption of the calculated factor of safety (*FS*) and relative density of the soil (D_r). In order to determine post-liquefaction reconsolidation settlement, at first, the *in-situ* shear stress ratio (e.g., *in situ* cyclic stress ratio – *CSR*) might be calculated using a simplified method (e.g., Seed & Idriss, 1971)

and corrected results from standard penetration tests (SPT) shall be adopted. Secondly, post-cyclic volumetric strain (ϵ_v) is graphically determined. Lastly, ϵ_v is multiplied by the thickness of the related liquefiable layer. The same approach is repeated for all liquefiable layers and all calculated settlement values are summed up.

6. EVALUATION OF LIQUEFACTION POTENTIAL AND EARTHQUAKE-INDUCED SETTLEMENTS FOR THE SPECIFIC SOILS AT VARNA PORT

The evaluation of liquefaction potential at the site was conducted using a simplified stress-based approach, as outlined in this paper. The cyclic stress ratio (*CSR*) was calculated based on a Peak Ground Acceleration (PGA) of 0.15*g* for a seismic event with an assumed moment magnitude (M_w) of 6.5. The cyclic resistance ratio (*CRR*) was determined from Dynamic Penetration Test (Super Heavy) (DPSHs) data, which was then correlated to standard penetration test (SPT) blow count. The Factor of Safety (*FS*) against liquefaction was subsequently established by the ratio of *CRR* to *CSR*. In alignment with Eurocode 8 provisions, a safety factor of 1.35 was applied to account for resistance reduction.

For areas where the *FS* fell below 1.0, liquefaction-induced settlements were calculated using methodologies proposed by (Ishihara & Yoshimine, 1992; Shimamoto, 1998; Wu, 2003). Example outcomes for tests DPSH-6 and DPSH-7 are depicted in Figure 5, indicating potential settlements ranging from 20 to 30 cm – a magnitude deemed unacceptable for the structural integrity of the silos.

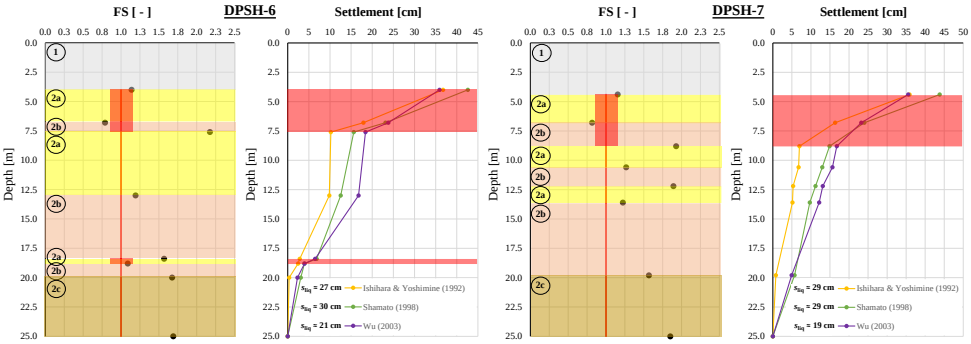


Figure 5. Liquefaction assessment and evaluation of earthquake-induced settlements

The findings necessitate the implementation of countermeasures to mitigate the risk of significant damage to these crucial industrial facilities, ensuring their stability and operational continuity in the event of seismic activity.

7. MITIGATION OF LIQUEFACTION-INDUCED DAMAGE

Ground improvement methods are essential for enhancing soil resistance to liquefaction and improving seismic performance. These methods can be broadly categorized into five principal types: replacement, densification, solidification, reinforcement, and drainage. The reinforcement method has been adopted in the current study.

Reinforcement generally involves the construction of intersecting subterranean walls, creating a network of containment cells, or establishing a series of tightly packed, robust vertical pillars. These structures, particularly the interlocking wall lattices (grids), are known for their superior ability to impede the flow of excess porewater and confine liquefied soil masses, thereby offering a more fail-safe solution compared to standalone column grids. While open grid systems lack this level of confinement and pressure control, the redundancy and robustness of lattice structures make them a significantly more

dependable option for soil reinforcement. This reinforcement method can be applied to soil strata extending down to 20 meters, with the possibility of reaching even deeper with specialized construction techniques and machinery. Its merits include applicability to various ground conditions, including sites with silty or inconsistent soil profiles, minimal construction-induced vibration, and the capability to reinforce ground beneath existing structures in space-constrained environments, enhancing their seismic resilience. Notably, in the case of lattice reinforcement, it is often feasible to position the surrounding containment wall below the building's footprint, which is particularly advantageous for developments situated close to property boundaries. A noted drawback of reinforcement methods is the challenge in conclusively verifying their efficacy in controlling shear strain in the soil segments between reinforcement elements. When juxtaposed with densification and drainage strategies, reinforcement approaches generally incur higher costs.

The initial step in the design procedure is to conduct an equilibrium analysis to ensure that the system remains stable under anticipated loads (Figure 6, top-left). This is followed by assessment of global stability, where the balancing act between stabilizing and destabilizing moments shall be evaluated (Figure 6, bottom-left). Subsequently, an internal check is crucial to confirm that the soil-mix body has the requisite strength to withstand shear stresses and to prevent the occurrence of both vertical and horizontal fissures (Figure 6, right). This sequential approach ensures a robust and reliable design, safeguarding against potential failures.

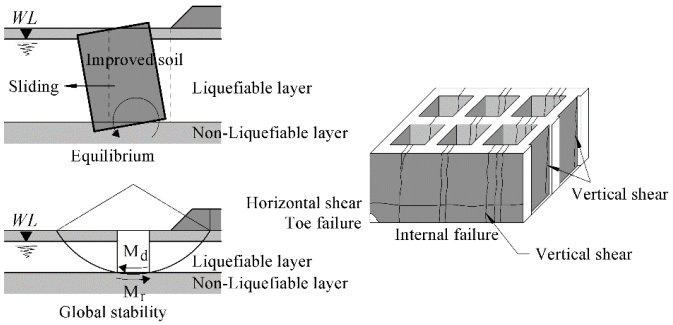


Figure 6. Design considerations for the reinforcement method

The presented project assumes the application of the soil mixing technique for stabilizing the soil, which involves blending cement or similar stabilizing agents into sandy soil to solidify it. Various equipment types have been developed for this purpose. For large-scale stabilization, a rotating drum cutter on an excavator can mix soil with the stabilizer, typically up to depths of around 6 meters. Deeper treatments, reaching up to 30 meters or more, employ rotating augers or blades on rods to mix soils into vertical columns, a process known as deep soil mixing (DSM) – Figure 7.



Figure 7. Single-shaft Deep Soil Mixing (DSM) – schematic representation (left) and its actual execution in Bulgaria (right)

Figure 8 shows the conceptual design which adopts DSM method below the foundations of the silos' bases for the presented project. In order to solve the issue with liquefaction-induced damage, a grid of 6 by 6 m DSM containment cells (selected diameter of overlapping DSM columns is 900 mm) have been considered. Due to economic reasons the suggested improvement depth does not reach a non-liquefiable soil layer but is still expected to ensure acceptable performance.

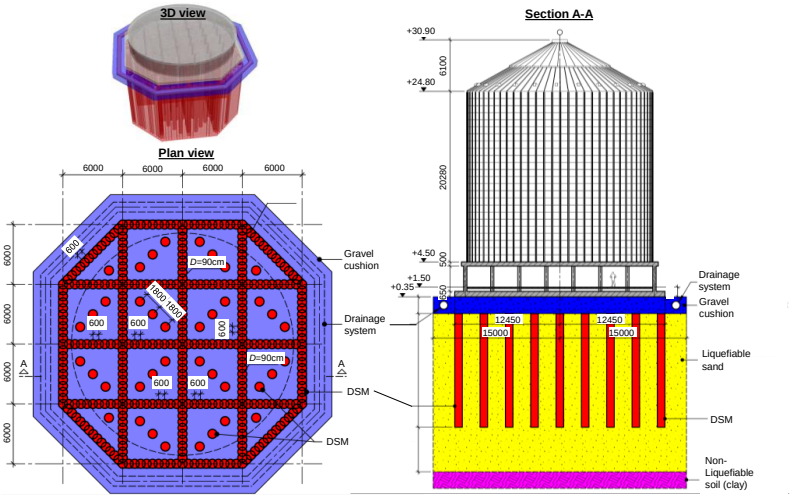


Figure 8. Conceptional design of a silo over a liquefiable layer – this study

8. CONCLUSIONS

The paper details a series of liquefaction engineering steps illustrated by a case study of silos at Varna's port in Bulgaria. Initially, the liquefaction potential was assessed, followed by the calculation of earthquake-induced settlement in susceptible soil zones. The resulting settlement surpassing allowable limits indicated inadequate facility performance. Consequently, the deep soil mixing (DSM) reinforcement method was chosen as a financially viable solution to this challenge.

REFERENCES

Andrews, D. C. A., and G. R. Martin. (2000). Criteria for liquefaction of silty soils. Paper 0312 in *Proceedings of the 12th World Conference on Earthquake Engineering*, 30 January–4 February 2000, Auckland, New Zealand. Upper Hutt, N.Z.: NZSEE.

Cetin K. O., Seed R.B., Der Kiureghian A., Tokimatsu K., Harder L.F. Jr, Kayen R.E., MossR.E.S. (2004). SPT-based probabilistic and deterministic assessment of seismic soil liquefaction potential, *Journal of Geotechnical and Geoenvironmental Eng.*, ASCE, 130(12), 1314-1340.

Idriss, I. M., and Boulanger, R. W. (2008). *Soil liquefaction during earthquakes*. Monograph MNO-12, Earthquake Engineering Research Institute, Oakland, CA, 261 pp.

Ishihara, K., and Yoshimine, M. (1992). Evaluation of settlements in sand deposits following liquefaction during earthquakes. *Soils and foundations*, 32(1), 173-188.

Moss, R. E. S., R. B. Seed, R. E. Kayen, J. P. Stewart, A. Der Kiureghian, and K. O. Cetin. (2006). CPT-based probabilistic and deterministic assessment of in situ seismic soil liquefaction potential. *Journal of Geotechnical and Geoenvironmental Engineering*, 132(8):1032–1051.

NCEER. (1997). Proceedings of the NCEER Workshop on Evaluation of Liquefaction Resistance of Soils, Edited by Youd, T. L., Idriss, I. M., *Technical Report No. NCEER-97-0022*.

Robertson, P. K., and C. E. Wride. (1998). Evaluating cyclic liquefaction potential using the cone penetration test. *Canadian Geotechnical Journal*, 35(3):442–459.

Seed, H. B., and Idriss, I. M. (1971). Simplified procedure for evaluating soil liquefaction potential. *Journal of the Soil Mechanics and Foundations division*, 97(9), 1249-1273.

Shamoto, Y., Zhang, J., and Tokimatsu, K. (1998). New charts for predicting large residual post-liquefaction ground deformation. *Soil Dynamics and Earthquake Engineering*, 17(7-8), 427-438.

Wu, J., Seed, R. B., and Pestana, J. M. (2003). Liquefaction triggering and post liquefaction deformations of Monterey 0/30 sand under unidirectional cyclic simple shear loading. *Geotechnical Engineering Research Rep. No. UCB/GE 2003/01*, University of California, Berkeley, California.

28th European Young Geotechnical Engineers Conference – EYGEC 2024
© 2024 Macedonian Association for Geotechnics, ISBN 978-608-4510-61-1

Analyses of pile driving impact using vibration monitoring method

Diyar Mukhanov[a], Askar Zhussupbekov[a], Abdulla Omarov[a], Abzal Khamzin[b], Gulnaz Zhairbaeva[a]

[a]*Department of Civil Engineering, L.N. Gumilyov Eurasian National University, Kazakhstan;*
[b]*LLP KGS-Astana, Kazakhstan*

ABSTRACT

The purpose of this paper is to determine the safety of existing facilities during the pile driving of pile foundations, and subsequently their operation. The method used for vibration monitoring involves vibration sensors. In this case, the main method of geotechnical monitoring of the existing building and construction is the equipment "Vibra Profound+". The vibration was produced at different distances from the excitation source created by a Banut 555 pile driver with a hydraulic hammer weighing 6.075 tons and a drop height of up to 1.0 m. Alarm level: 5.00 mm/s (0 to 10 Hz). Alarm type: Intelligent speed. Settings were done according to DIN 4150-3. Vibration detection standard: ISO 4866:2010. The highest value of vibration velocity was recorded in the z-direction - vertical axes. The influence of pile driving on the compressor foundation is relatively small: z=0,91; y=0,30; x=0,31 - for slab foundation and z=1,19; y=0,29; x=0,26 - for single-pile STU-1. The highest values of vibration velocity during driving were measured in the middle of pile driving (about 5-6 m of pile length). According to DIN 4150-3 standards, the vibration level during pile driving is within the permissible limits.

KEYWORDS

Vibration, Monitoring, Pile driving, Sensors.

1. INTRODUCTION

The tests were conducted over three days from June 24, 2021, to June 26, 2021, in Western Kazakhstan in five test pile driving sites. Eight piles were driven, and the sequence and norms of pile driving are shown. DIN 4150-3:2010 standard "Permissible values of vibration in construction" was used to determine the vibration. At the test site, the vibration source was created by a Banut 555 pile driver with a hydraulic hammer weighing 6.075 tons and a drop height of up to 1.0m. There are also several sources of vibration including a jacking crane and various types of trucks used to transport the piles to the installation site. The vibration measurement interval was 5 s. The maximum allowable vibration level is (acceleration index) 5.00 mm/s (from 0-10 Hz).

2. TESTING PROCESS

The sensors were placed in five different positions to detect vibration. Six vibration monitoring tests were carried out with the Vibra Profound+ equipment. The sensors were located between 40m and 114m from the source of pile driving vibration excitation. Vibration monitoring tests at two sensor locations (1-2 positions) were initiated before pile driving to determine the vibration, amplitude, and vibration before the test and to compare with the sensors installed and tested during pile driving.

2.1. Sensor positions

Position 1 (62-G-211): 72 meters from the drilling rig and during pile driving 1.

The geophone is attached to the turbocharger foundation. Monitoring was conducted 12 hours before pile driving (to monitor vibration of the turbocharger itself) and to monitor vibration during pile driving.
Position 2 (Pile 1): 58 meters from the piling rig during the driving of Pile 2 and 65 meters from the piling rig during the driving of Pile 7.
A geophone was previously attached to the pile head (to monitor vibration from the plant itself) and during pile driving.
Position 3 (Pile 2): 82 meters from the piling rig during the driving of Pile 4 and 114 meters from the piling rig during the driving of Pile 8.
A geophone was previously attached to the pile head (to monitor vibration from the plant itself) and during pile driving.
Position 4 (Pile 4): 40 meters from the piling rig while driving Pile 5.
The geophone was previously attached to the pile head (to control vibration from the plant itself) and during pile driving.
Position 5 (Pile 5): 40 meters from the piling plant while driving Piles 3 and 6.
The geophone was previously attached to the pile head (to monitor vibration from the plant itself) and during pile driving.

Table 1 describes the vibration monitoring tests performed on a particular pile driving.

Table 1. Sensor positions

Test	1	2	3	4	5	6	7	8	9
Geophone position	Pos.1	Pos.1	Pos.2	Pos.2	Pos.3	Pos.3	Pos.4	Pos.5	Pos.5
Pile position	No driving	1 Pile driving	2 Pile driving	7 Pile driving	4 Pile driving	8 Pile driving	5 Pile driving	3 Pile driving	6 Pile driving

3. TESTS AND RESULTS OF VIBRATION MONITORING DURING PILE DRIVING

Testing at position 1, before pile driving:

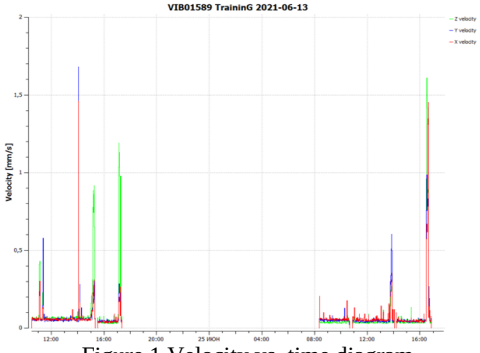


Figure 1 Velocity vs. time diagram.

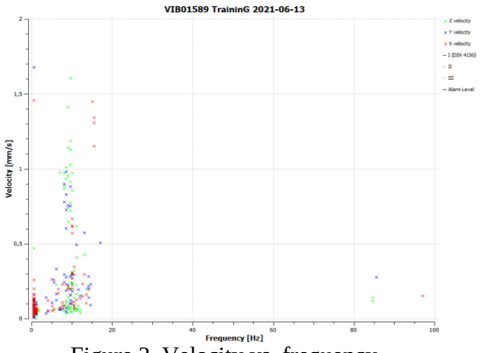


Figure 2. Velocity vs. frequency

Measurement 1
Location 1
No driving

Testing at position 1, during LTP-1 pile driving:

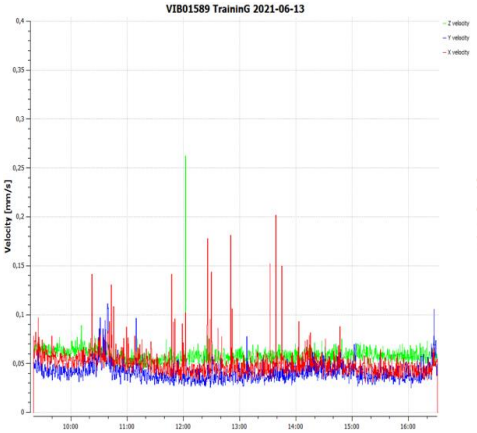


Figure 3. Velocity vs. time diagram.

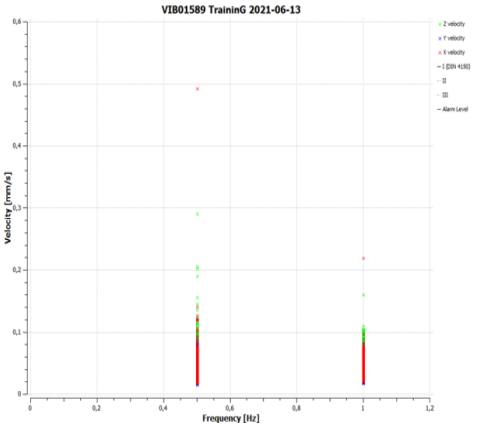


Figure 4. Velocity vs. frequency

Max velocity: X=0.2 Y=0.11 Z=0.26

Measurement 2
Location 1
Driving Pile LTP-1

Testing at position 2, during CTP-1 pile driving:

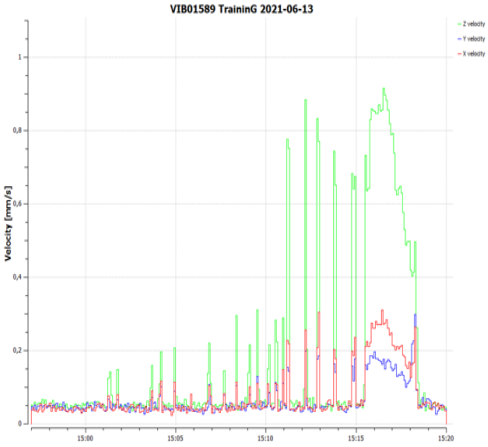


Figure 5. Velocity vs. time diagram.

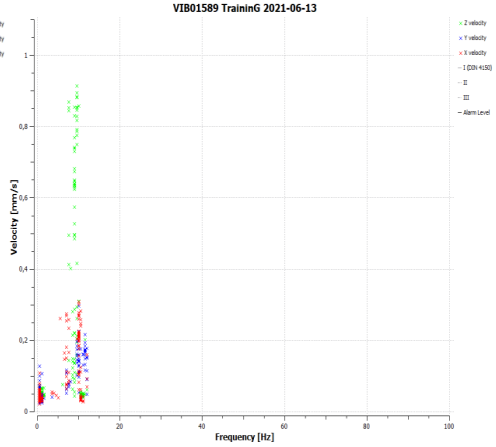


Figure 6. Velocity vs. frequency

Max velocity (before driving): X=0.06 Y=0.08 Z=0.07
Max velocity (during the driving): X=0.31 Y=0.30 Z=0.91

Measurement 3
Location 2
Driving Pile CTP-1

Testing at position 3, during TTP-1 pile driving:

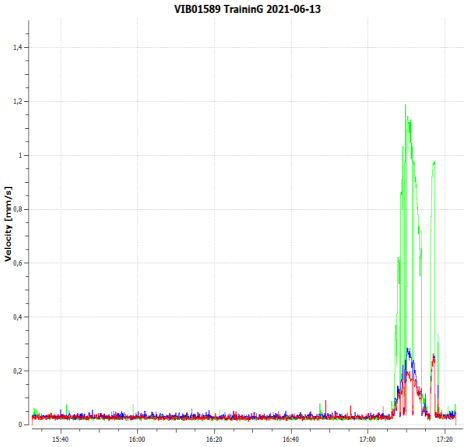


Figure 7. Velocity vs. time diagram.

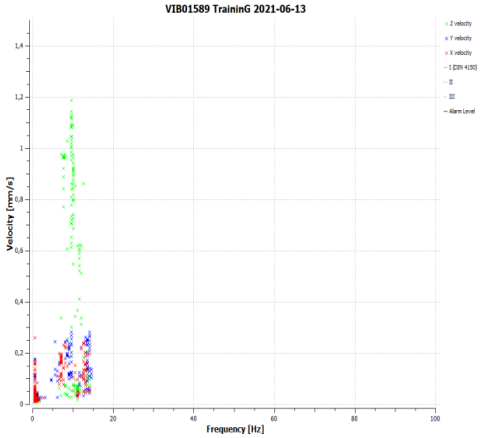


Figure 8. Velocity vs. frequency

Max velocity (before driving): X=0.08 Y=0.06 Z=0.07
Max velocity (during the driving): X=0.26 Y=0.29 Z=1.19

Measurement 4
Location 3
Driving Pile TTP-1

Testing at position 4, during TTP-1 pile driving:

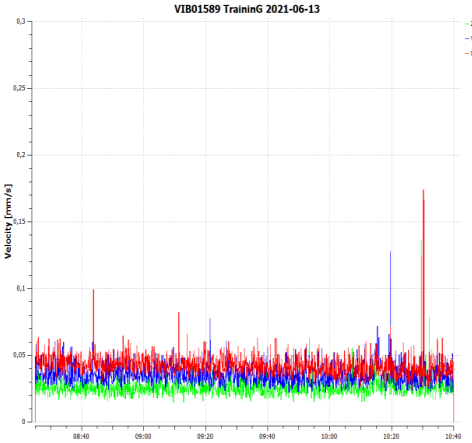


Figure 9. Velocity vs. time diagram.

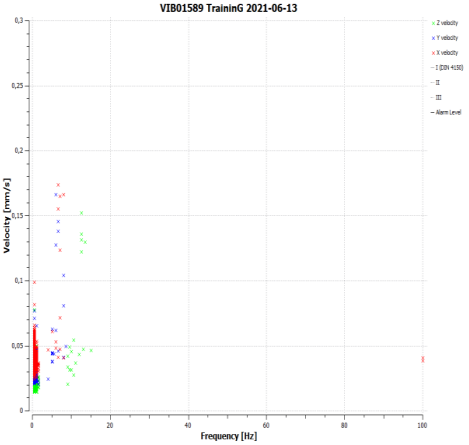


Figure 10. Velocity vs. frequency

Max velocity (before driving): X=0.10 Y=0.07 Z=0.06
Max velocity (during the driving): X=0.17 Y=0.16 Z=0.15

Measurement 5
Location 4
Driving Pile TTP-1

Testing at position 5, during TTP-1 pile driving:

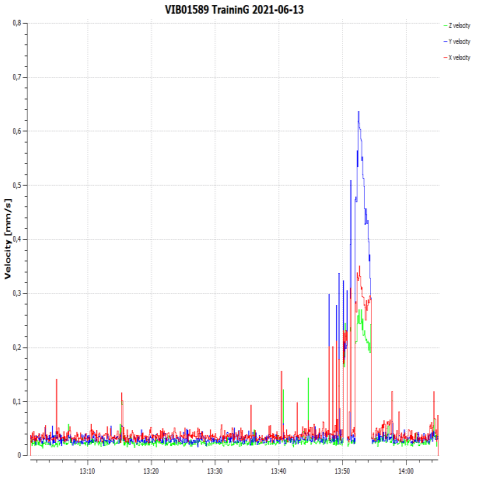


Figure 11. Velocity vs. time diagram.

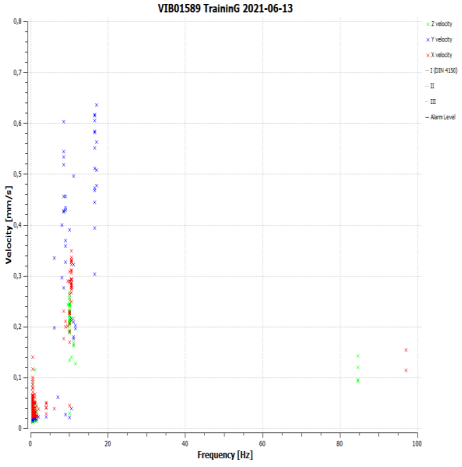


Figure 12. Velocity vs. frequency

Max velocity (before driving): X=0.15 Y=0.05 Z=0.14
Max velocity (during the driving): X=0.35 Y=0.64 Z=0.27

Measurement 6
Location 5
Driving Pile TTP-1

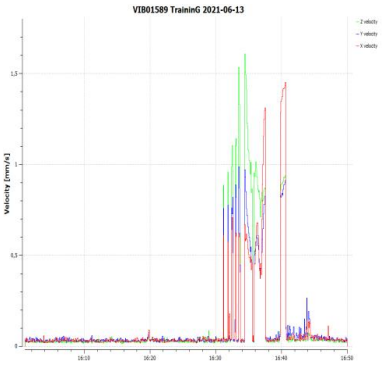


Figure 13. Velocity vs. time diagram.

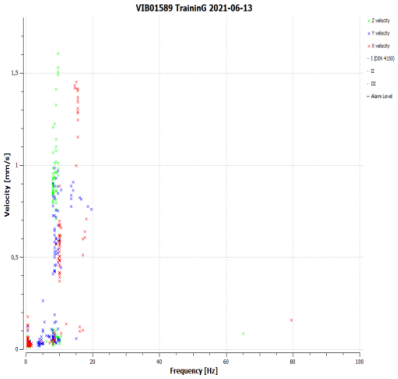


Figure 14. Velocity vs. frequency

Max velocity (before driving): X=0.09 Y=0.05 Z=0.09
Max velocity (during the driving): X=1,45 Y=0,98 Z=1,61

4. CONCLUSIONS

After the vibration monitoring test with the equipment "Vibra Profound+", the determined velocity, without movement (before pile driving): Z=0,26; Y=0,11; X=0,20. At the same time, the highest value of vibration was recorded in the direction of a certain value of z - z-vertical axes (Fig. 1).
The average value of the maximum velocity before pile driving: X=0.10 Y=0.06 Z=0.09, and the average value of maximum velocity after pile driving: X=0.51 Y=0.47 Z=0.63, after comparison we conclude that the level of vibration jump during pile driving is within the permissible limits of DIN 4150-3 standard.
The influence of pile driving on the compressor foundation is relatively small: Z=0.91; Y=0.30; X=0.31 - for slab foundation (87 m from the drilling rig) and Z=1.19; Y=0.29; X=0.26 - for single-pile STU-1 (at a distance of 63 m from the drilling rig). This is explained by the massive foundation partially damping the vibration impact.
The highest value of vibration, in the difference between before and after pile driving in the X-axis, was measured in test #3, in the Y-axis in test #6, which amounted to 0.59, and in the Z-axis in test #4.
After the collected data from all the tests, the results showed that the signal tolerance level of 5 mm/s (0 to 10 Hz) was not exceeded.
The highest values of vibration velocity during driving were measured in the middle of pile driving (about 5-6 m of pile length).

5. ACKNOWLEDGEMENTS

The author(s) would like to thank KGA LLP, for the opportunity to conduct the test, and for the equipment provided

REFERENCES

Zhussupbekov A.Zh., Omarov A.R., Lukpanov R.E., Zhukenova G.A., Tanyrbergenova G.K. Analysis of effect of pile driving on the existing foundation (vibration monitoring). *PNRPU Bulletin Construction and architecture*. 2016. Vol. 7, No. 1. Pp. 131-138. DOI: 10.15593/2224-9826/2016.1.08

Чубко, Ю. М., & Сало, Н. Ю. (2021). Анализ вибромониторинга, как следствие повышения эффективности ремонтной деятельности. *Международный научный журнал Вестник науки*, 5(5-1 (38)), 141-147.

Grizi, A., Athanasopoulos-Zekkos, A., & Woods, R. D. (2016). Ground vibration measurements near impact pile driving. *Journal of Geotechnical and Geoenvironmental Engineering*, 142(8), 04016035.

DIN 4150-3-2016-3, Vibration in construction. Part 3. Effect on building structures.

Issakulov, A., Omarov, A., Zhussupbekov, A., Mussakhanova, S., & Issakulov, B. (2023). Investigation of the interaction of the bored micro pile by DDS (FDP) technology with the soil ground. *GEOMATE Journal*, 24(105), 11-17.

Zhussupbekov, A., Dhanya, J. S., Issakulov, A., Omarov, A., Iskakov, S., & Mukhanov, D. (2023). Model and field tests of drilled displacement system piles. *In E3S Web of Conferences* (Vol. 410, p. 03024). EDP Sciences.

Nikitina, N. S., & Mukhanov, D. M. (2023). Load-bearing capacity of a single barette (case study for the Hanoi soil condition). *In Smart Geotechnics for Smart Societies* (pp. 1480-1486). CRC Press.

28th European Young Geotechnical Engineers Conference – EYGEC 2024
© 2024 Macedonian Association for Geotechnics, ISBN 978-608-4510-61-1

Geotechnical Perspective on Sustainable Construction in Sweden

David Nguyen[a]

[a]*Skanska Sverige AB, Gothenburg, Sweden*

ABSTRACT

With the signing of the Paris Agreement in 2015, the world committed to taking measures to limit the increase in the global average temperature to well below 2°C, with the aim of capping it at 1.5°C. To achieve this goal, greenhouse gas emissions must be halved by 2030 and reduced to near zero by 2050.

The Construction and Real Estate sector's greenhouse gas emissions account for about 22% of Sweden's total emissions. Additionally, the sector significantly contributes to emissions abroad through imported goods.

A recent study indicated that emissions from ground works accounted for approximately 33-36% of the total emissions of a 36-floor building in Gothenburg. This is significant, especially considering that only emissions slab foundations are included when submitting a climate declaration for a new building.

As a geotechnical engineer, tools for reducing the climate impact can be used. For instance, in the early stages, select construction sites that necessitate minimal geotechnical works or implement measures to reduce soil settlements. During the construction stage, conduct comprehensive field and laboratory investigations to optimize your temporary geotechnical works, accounting for materials while meeting safety requirements.

The gap in knowledge is still substantial concerning climate impact in relation to geotechnical works, but more focus is being invested in research, the subject is in demand and steps are being taken forward.

The construction and real estate sector are on the right path on helping Sweden fulfil the commitments of the Paris Agreement, but the clients and stakeholders need to shift their focus from cost-driven to climate-driven in future project for the climate impact to seriously reduce. Hopefully the shift is immense and of highest priority, if not for our sake, then for future generations.

KEYWORDS

Paris Agreement; Greenhouse Gas Emissions; Climate Impact; Geotechnical Works

1. INTRODUCTION

The climate has naturally been changing throughout the years. Although today's changes, primarily driven by human activities such as the emission of carbon dioxide and other greenhouse gases, are significant and rapid. The global average temperature is now approximately 1°C warmer than before the industrial era, see Figure 40 (Hansen, et al., 2017). A higher average temperature leads to severe consequences för both human and nature, including an increase in the frequency and intensity of natural disasters.

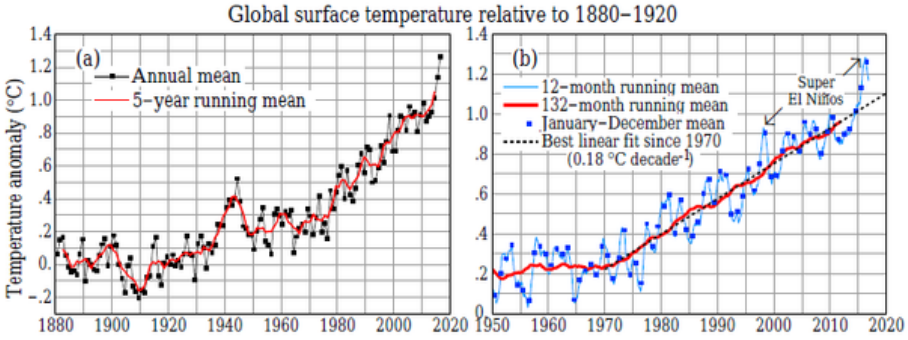


Figure 1. Global surface temperature relative to 1880-1920. (a) Annual and 5-year means since 1880. (b) 12- and 132-month running means since 1970 (Hansen, et al., 2017).

The world's countries came together in 2015 to reach a historic agreement in the fight against global warming. The signing of the Paris agreement signifies a commitment to limit the global warming to well below 2°C, striving to cap it at 1,5°C. To achieve this goal, global emissions must be halved by 2030 and reduced to near zero by 2050 (UNFCCC, 2024).

With the Paris agreement in mind, Sweden has set climate goals, aiming to achieve net-zero greenhouse gas emissions by no later than 2045. Furthermore, the ambition extends to achieving negative emissions, a goal that surpasses the requirements of the Paris Agreement (Fossil-free Sweden, 2024).

2. THE CONSTRUCTION AND REAL ESTATE SECTOR IN SWEDEN

The Construction and Real Estate sector accounts for approximately 22% of Sweden's greenhouse gas emissions (The Swedish National Board of Housing, Building and Planning, 2024). The impact primarily arises from the production of materials and products, as well as emissions related to energy use during the operational phase. Additionally, the sector significantly contributes to emissions abroad through imported goods. However, the analysis above did not include the emissions from geotechnical works.

As of 2022, submitting a climate declaration is mandatory for new buildings requiring building permits, with the purpose of reducing the climate impact from the construction stage. The construction stage comprises the extraction of raw materials, manufacture of construction products, work at the construction site and transports (The Swedish National Board of Housing, Building and Planning, 2024). At present, it’s not required to include emissions from geotechnical works except for slab foundations, in the submitted climate declaration. Conversely, for major infrastructure projects, the Swedish Transport Administration imposes climate requirements that apply during planning, design, construction, and operation and maintenance.

Considering the above, a research project was conducted to deepen the understanding of the climate and environmental impact of geotechnical works (Smart Built Environment, 2023). Within the research project geotechnical engineers and life cycle assessment analysts collaborated to produce quality-assured Swedish generic environmental data for 21 different types of geotechnical works. The generic environmental data encompass the life cycle modules A1-A5, see Figure 41.

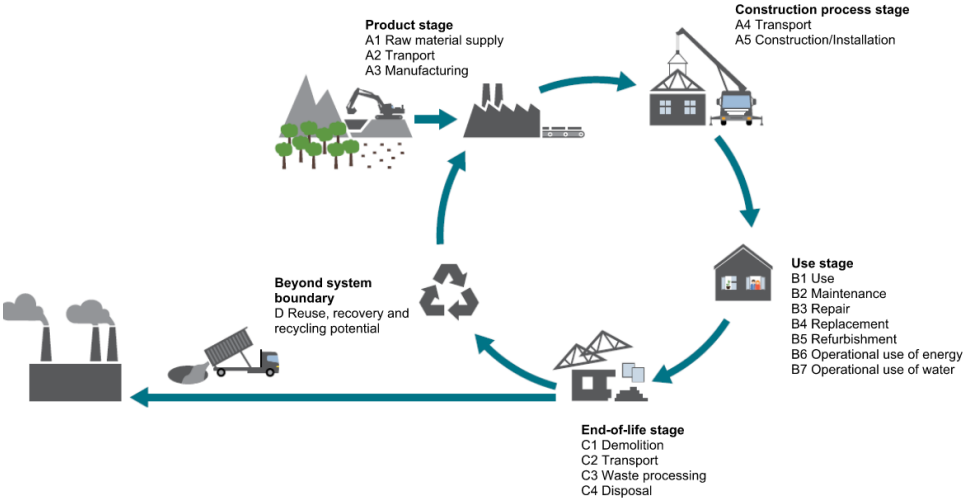


Figure 2. Stages and modules in a typical life cycle of a building (European Insulation Manufacturers Association, 2017).

Two case studies were conducted in the research project, and the results indicate that geotechnical works can account for a significant portion of a building's climate impact. In one case study, calculated for a 5-story building, the climate impact of geotechnical works represented 4% of the building's total climate impact. In the other case study, conducted for a 36-story building, the climate impact of geotechnical works amounted to approximately 33-36% (depending on how the calculation was made) of the building's overall climate impact during the construction stage. In general, several factors could contribute to the differences between the case studies, such as the geotechnical conditions of the site influencing the choice of geotechnical works and the amount of excavation mass transported for landfill disposal.

3. THE GEOTECHNICAL SECTOR AND IT'S TOOLS FOR CLIMATE-NEUTRAL CONSTRUCTIONS

As indicated in the research project, geotechnical works can contribute significantly to a building's overall climate impact. Questioning why geotechnical works are not currently included in the existing climate declaration is reasonable; however, it should be emphasized that an expansion of the legal requirements is currently under consideration. The results of the case studies imply that geotechnical engineers could play an important role in the transition to climate-neutral constructions, not only in Sweden but also worldwide.

Geotechnical engineers have access to several existing techniques and methods that can contribute to reducing the climate impact of a construction, for example, landscape planning, geotechnical field and laboratory investigations, foundation methods, climate-smart material choices, in-situ recycling but also research. Which method that is more applicable than another depends on the stage in the building process, see Figure 3.

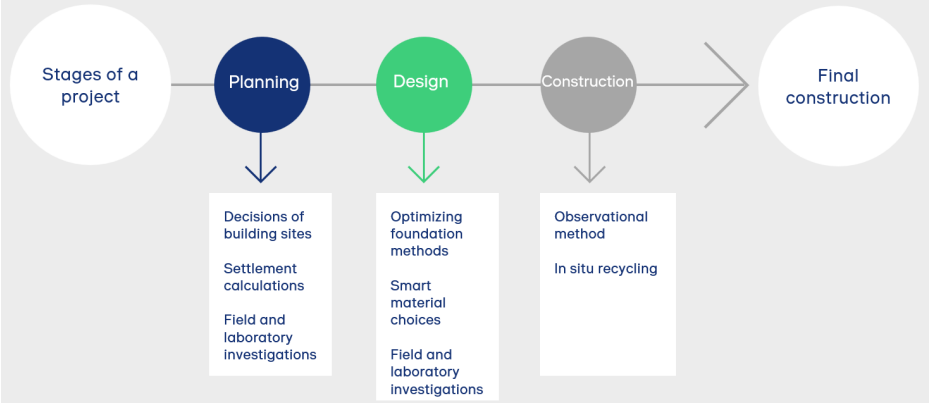


Figure 3. Example of tools a geotechnical engineer can utilize in different stages of a project for reducing the climate impact.

By integrating these existing techniques and methods in a systematic way, geotechnical engineers can contribute to reducing emissions and support the transition to climate-neutral constructions. However, achieving nete-zero requires ongoing innovation and the development of new technologies.

3.1. Landscape planning

In the early planning stages, geotechnical engineers can be involved in assessing prospective sites or participate in the landscape planning process, aiming to minimize the climate impact from the outset. If the land has already been acquired and the construction site determined, and time is on our side, geotechnical engineers can implement soil preloading to mitigate potential settlements. This, in turn, reduces the need for future compensation fills or a shift to an alternative foundation with another geotechnical work.

3.2. Geotechnical field and laboratory investigations

A geotechnical investigation can be conducted for various purposes and with different geotechnical inquiries. In the early planning stages, the geotechnical investigation can assess potential risks associated with land use. The level of detail in the investigation depends on how the land is intended to be used. The primary objective of a geotechnical investigation is to determine soil, rock, and groundwater conditions. This means that a geotechnical investigation conducted in the early planning stages may not necessarily capture the properties required to design your technical solution if the intended land use has changed during the process of the project.

Performing additional field and laboratory investigations as a supplement to the already conducted geotechnical investigation can be a tool to ultimately reduce the climate impact of a certain project. The better the geotechnical investigation, the more we know about soil properties, allowing us to utilize parameters more efficiently by reducing safety factors and optimizing technical solutions without compromising safety. Figure 43 illustrates a person heading towards a cliff with a fog clouding the view. The better the visibility, the closer the person can approach the edge without the risk of falling. Depending on the supplementary investigation, the more we disperse the fog. Incorporating supplementary field and laboratory investigations alongside with the observational method during the construction stage will further disperse the fog.

A supplementary geotechnical investigation with advanced lab tests will surely incur a cost, but an optimized technical solution will result in reduced climate impact and hopefully a lower total cost compared to the initial option without additional investigation. For construction projects, the primary focus is still on balancing the budget rather than being climate-smart, which sometimes hinders us from

lifting our gaze and thinking long-term. It is important to realize that the budget and climate impact can be intertwined, where the budget can affect the climate, but also where the climate can affect the budget.

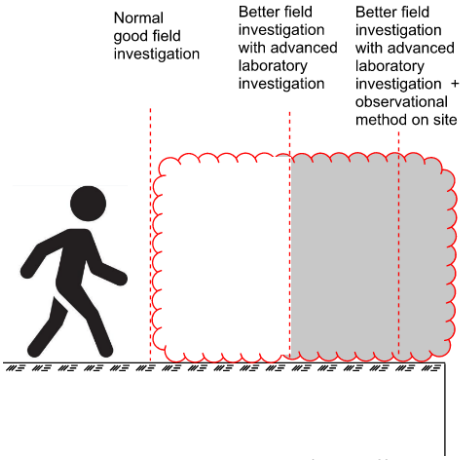


Figure 4. Illustration of how close a person can be to the edge of the cliff depending on the level of geotechnical investigations made.

3.3. Foundation methods and climate-smart material choices

By optimizing the foundation methods, the geotechnical works, and materials during the design stage, the climate impact could be reduced. For example, changing to steel piles from concrete piles or use foam glass or expanded lightweight aggregate instead of cellular plastic.

3.4. In-situ recycling

By assisting the project in identifying and locating suitable masses for in-situ recycling, the need for excavation, purchase of materials, transportation, and landfill disposal will decrease, resulting in a reduced climate impact. A research project conducted in 2020 aimed to explore the possibility of in-situ recycling of dry crust, a material typically sent to a landfill after excavation for disposal (Nguyen, 2020). The study revealed that dry crust could be a suitable backfill material under certain conditions, such as optimal natural water content, W_N, and purpose. With a natural water content between 15% to 30%, the choice of compaction method had minimal impact on achieving the required bearing capacity on the terrace. The project site reduced its climate impact by 17% through the reuse of dry crust. The potential in savings amount to 9,0 kg CO_2 equivalent (CO_2eq) per cubic meter (m^3) of clay dry crust and approximately between 190-290*SEK* per cubic meter (19-28€/m^3) from an environmental and cost perspective.

3.5. Research

There is currently a knowledge gap in the geotechnical sector in Sweden concerning questions related to climate impact. This is partly due to the relatively young nature of the research and the limited number of case studies conducted in Swedish conditions. However, in recent years, more funding has been allocated to research addressing these issues. For instance, two ongoing projects are of interests, one explores the possibilities and challenges within the municipal spatial planning process to reduce climate impact from geotechnical works (Song, et al., 2023). The other project aims to calculate generic values for the climate impact of geotechnical works and ground improvements through conducting case studies (Lindeberg, 2024).

4. CONCLUSIONS

The Construction and Real Estate sector have set a high goal in its efforts to help Sweden reduce its climate impact and fulfil its commitment to the Paris Agreement. A goal that geotechnical engineers and the geotechnical sector can significantly contribute to achieving within the Construction and Real Estate sector. The tools are available, climate work is becoming more prioritized, and our knowledge is increasing. Research can be an equally powerful tool in reducing future climate impact as mentioned above. By gaining a deeper understanding of what influences what and how we within the geotechnical industry can help make the planet habitable for future generations.

However, there are still obstacles. As long as constructing at the lowest cost is rewarded in procurements, climate work will be overshadowed by final costs. When clients and stakeholders begin to demand and prioritize the best technical solution in terms of climate impact, that is when reduced climate impact will truly start to become visible. We are on the right path, but the shift is not here yet. Hopefully, this scenario is imminent and of the highest priority, if not for our sake, then for future generations.

5. ACKNOWLEDGEMENT

I would like to express my sincere gratitude to my colleagues at Skanska, especially David Ekstrand and Anders Kullingsjö, for their support and being sounding boards in the process of this article. I would also like to thank my boss, Petter Karlsson, giving me the opportunity to take part in this conference. Further I would like to thank Xingqiang Song at the Swedish Geotechnical Institute, SGI, for reviewing and enhancing the quality of this article. Lastly, I would like to thank the Swedish Geotechnical Association, SGF, for sponsoring me and covering the travel and conference costs.

REFERENCES

European Insulation Manufacturers Association. (2017, September). Life Cycle Assessment of Buildings - A future proofed Solution in the digitalised World of Tomorrow.

Fossil-free Sweden. (2024, February 20). *Fossilfritt Sverige*. Retrieved from Road map, Bygg- och anläggningssektorn: https://fossilfrittsverige.se/roadmap/bygg-och-anlaggningssektorn/

Hansen, J., Sato, M., Kharecha, P., Von Schuckmann, K., J. Beerling, D., Cao, J., . . . Reudy, R. (2017). *Young people's burden: requirement of negative CO2 emissions.* Copernicus Publications on behalf of the European Geosciences Union.

Lindeberg, K. (2024, February 21). *SBUF*. Retrieved from SBUF: https://www.sbuf.se/projektresultat/projekt?id=4f415028-c0a5-4dc0-b42d-da8645939b53

Nguyen, D. (2020). *Användning av torrskorpelera som fyllnadsmassor.* Göteborg: Svenska Byggbranchens Utvecklingsfond, SBUF.

Smart Built Environment. (2023). *Klimatdata för geokonstruktioner.* Malmö: Smart Built Environment.

Song, X., Carlsson, C., Hedfors, J., Malmqvist, T., Trygg, K., van Well, L., & With, C. (2023, March 30). Bringing ground conditions upfront - Strategic planning för climate-smart geotechnical works (PlanGeoSmart). Sweden.

The Swedish National Board of Housing, Building and Planning. (2024, February 20). *Questions and answers about climate declarations*. Retrieved from Boverket: https://www.boverket.se/en/start/building-in-sweden/developer/rfq-documentation/climate-declaration/questions/

The Swedish National Board of Housing, Building and Planning. (2024, February 19). *Utsläpp av växthusgaser från Bygg- och fastighetssektorn*. Retrieved from Boverket: https://www.boverket.se/sv/byggande/hallbart-byggande-och-forvaltning/miljoindikatorer---aktuell-status/vaxthusgaser/

UNFCCC. (2024, February 19). *United Nations Climate Change*. Retrieved from United Nations Climate Change: https://unfccc.int/process-and-meetings/the-paris-agreement

28th European Young Geotechnical Engineers Conference – EYGEC 2024
© 2024 Macedonian Association for Geotechnics, ISBN 978-608-4510-61-1

Investigations of testing micropiles for static loading

M.Nurgozhina[a], A.Zhussupbekov[b], A. Omarov[c], A. Issakulov[d], D. Mukhanov[e]

[a,b, c,d,e] Department of Civil Engineering, L.N. Gumilyov Eurasian National University, Astana, Kazakhstan

ABSTRACT

This paper presents the results of model tests of reinforced concrete micro-piles. The methodology of determining the load-bearing capacity of micro-piles on the basis of the obtained load-settlement graph using a volumetric bench. Using the volumetric bench, static load was applied to the micro-piles and the corresponding settlements are measured at each stage of loading. The bench was prepared in five layers and each layer was compacted by tamping to relative density. This material is convenient for model testing. The bearing capacity of 3 micro-piles with different sizes corresponding to 1:20 scale was investigated. As a result of the test the settlement of the three micro-piles was within 10-12 mm. A comparative analysis of the laboratory results of the bearing capacity of micro-piles with the static method (SLT) was carried out. Practical recommendations were developed for the application of the micro-pile model in the volumetric bench to study the performance of micro-piles in difficult ground conditions. An important object of research is the comparison of bearing capacity of micro-piles with different lengths with static method. The results obtained in this work can be used in the use of micro-piles in difficult ground conditions.

KEYWORDS

Static loads, dynamic loads, volumetric stand, micropiles.

1. INTRODUCTION

In recent years, loads on the foundation have increased significantly, areas with complex engineering and geological conditions are used, and construction takes place in dense urban areas. This necessitated the development and use of new types of foundations and technologies for their construction. An effective design for constructing new and strengthening existing foundations are reinforced concrete micropiles, which are manufactured by the bored method in the form of a round rod with a diameter of up to 250 mm from cast concrete with a reinforcement cage.

The main purpose of the pile tests is to determine the load-bearing capacity of different types of structures under different conditions. For example, when building foundations in water, it is extremely important that the supports remain buried and firmly hold the structure even in strong currents. On freezing heaving soils, the ability to resist compressive loads is more important. In order to calculate the bearing capacity of this type of foundation, entire system methods for testing piles have been invented. Blade weld quality tests are also used. Ultrasonic testing (sounding of piles) is recommended at the product production stage.

According to GOST, piles must be subjected to two types of tests:

- static loads (pulling or pressing);
- dynamic loads.

Conducting field tests of soils with static loads on piles. Static tests are carried out in accordance with the requirements of GOST 5686-94 Soils. Methods for field testing of piles. The pile being tested is loaded in steps. The transition to the next loading stage is carried out after complete stabilization of the settlement at the previous stage. To measure the settlement of the pile being tested, four dial indicators with a division value of 0.01 mm are installed.

The reactive forces that arise when the pile under test is loaded are transmitted through the beam system to the anchor piles. To register possible pulling out of anchor piles, 2 dial indicators with a division value of 0.01 mm are installed on each pile. Taking into account the possible elongation of the upper part of the reinforcement frame, the pull-out of anchor piles during testing should not exceed 2 mm.

2. PAPER LAYOUT

Before loading the piles, zero reports are taken from all instruments. Next, reports are taken at each stage of pile loading using all instruments.

The criterion for conditional stabilization of bedformation is taken to be the rate of pile settlement at a given loading stage, not exceeding 0.1 mm over the last 30 minutes of observation.

The partial value of the ultimate resistance of the tested pile is taken to be the load at which loading of the pile stops.

The installation for testing soils with static load includes the following equipment:

-device for loading piles (jack)

- support structure or platform for receiving reaction forces (load platform);
- a device for measuring pile displacement during testing (reference system with measuring instruments);

The device for loading piles must ensure coaxial and central transfer of loads to the pile, the ability to transfer loads to the legs, and constant pressure at each stage of loading. The distance from the axis of the full-scale pile test for securing the pile should not be 3 diameters of the pile, but not less than one and a half meters. Instruments for measuring pile deformations (deflectometer) must provide a measurement accuracy of 0.1 mm. The number of devices installed symmetrically at the same (no more than two meters) distance from the tested pile must be at least 2 units. The deflectometer uses steel wire with a diameter of 0.3 mm. Before testing, the wire must first be stretched for two days with a load of at least four kilograms. During the test, the load on the wire should not exceed one and a half kilograms.

Table 1. Physical and mechanical characteristics of natural soil and equivalent material

Name of soils of full-scale and model material	Specific gravity, y, кN/м^3	Clutch, C, kPa	Angle of internal friction, φ, deg.	Modulus of deformation, E, MPa	Poisson's ratio, μ
Loam	20,5	40,0	29	-	-
model material	17,0	0,9	37	0,24	0,25

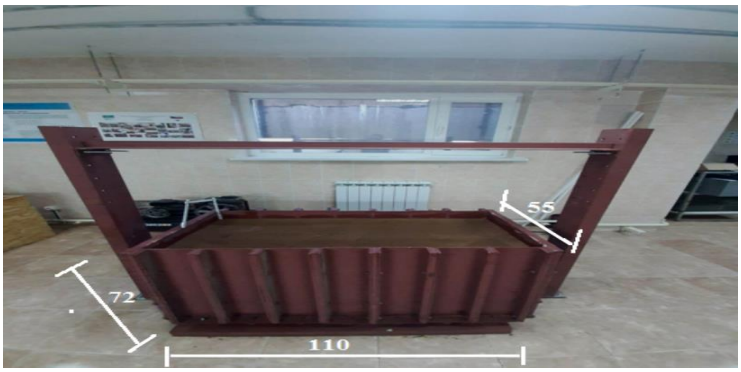


Figure 1. Volumetric stand.

On a volumetric stand under laboratory conditions, a static test was carried out on three model piles of circular cross-section, with corresponding lengths of 600mm, 500mm, 400mm.

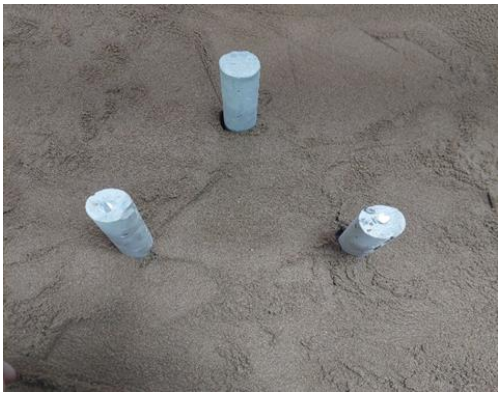


Figure 2. Testing of micropiles.

Static testing of model piles was performed using metal weights that were loaded on the piles. The weight of one weight was 4 kg. The load on the model piles was applied in steps of 39 N up to the ultimate load of 391 N.

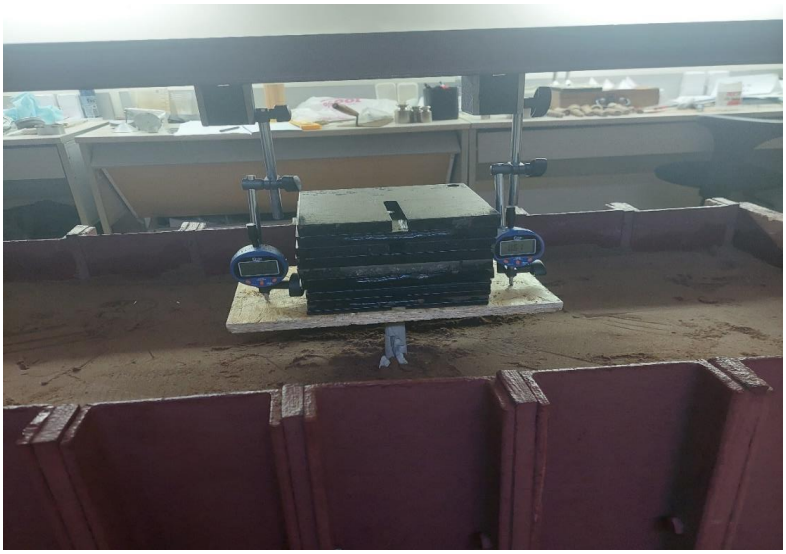


Figure 3. Micropile states under static load.



Figure 4. Micropiles after static load testing

3. CONCLUSIONS

Static tests of pile models (lengths 600mm, 500mm, 400mm) are carried out on a volumetric stand. After static tests, “design load” graphs were obtained. The settlement of a pile 600 mm long is 16.03 mm, the settlement of a pile 500 mm is 15.92 mm, the settlement of a pile 400 mm is 14.5 3 mm.

The test results show that the load-bearing capacity of 400mm length is higher than that of 500mm and 600mm lengths. It is observed that the length of the model model influences the test results.

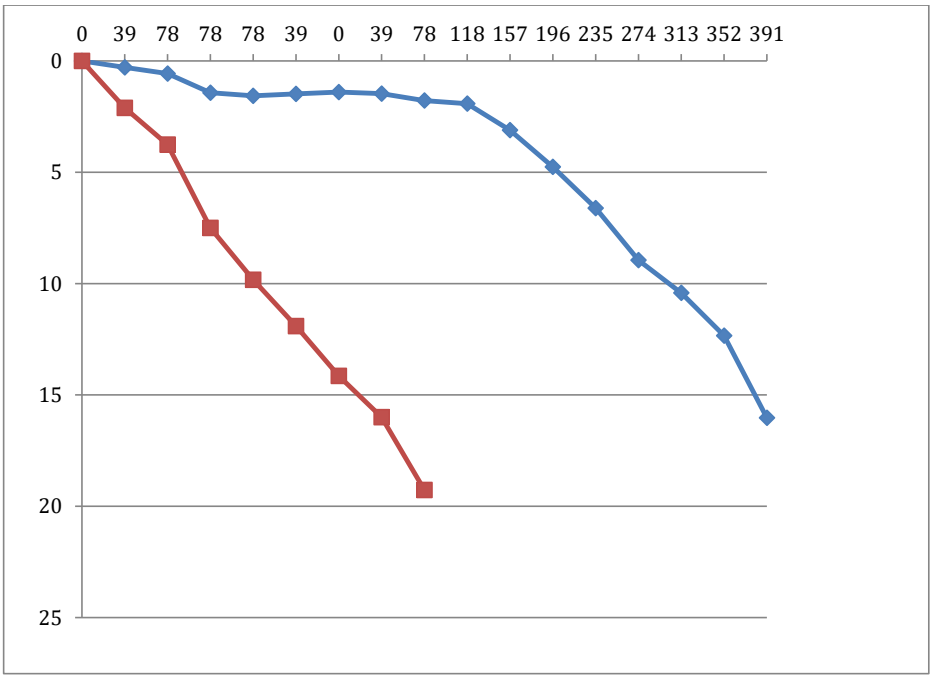


Figure 5. Load – settlement response of the micropile

4. ACKNOWLEDGEMENTS

The study was carried out with the support of the geotechnical laboratory of the Geotechnical Institute named after L.N. Gumilev of the Eurasian National University, Kazakhstan.

REFERENCES

Rad S.H., Ghareh S., Eslami A. *Experimental and feld studies on the behavior of drilled displacement piles* // Innovative Infrastructure Solutions 6, №188 – Springer Nature Switzerland, 2021. P. 1-11.doi.org/10.1007/s41062-021-00557-2.

Basu P., Prezzi M., Basu D. Drilled Displacement Piles – *Current Practice and Design* // DFI Journal The Journal of the Deep Foundations Institute . Hawthorne, USA, 2010. – P. 3-20.

Issakulov, A., Omarov, A., Zhussupbekov, A., Mussakhanova, S., Issakulov, B. *Investigation of the interaction of the bored micro pile by DDS (FDP) technology with the soil ground.* International Journal of GEOMATE, Vol. 24, Issue 105, 2023, pp. 11–17.

Yergen ASHKEY, *Interaction of CFA bored piles with soil condition in Astana* // A dissertation submitted in partial fulfillment of the requirements for the degree of DOCTOR OF PHILOSOPHY (Ph.D.)– Astana.: L.N. Gymileva ENU. -2008. – 52p.

Zhussupbekov A., Omarov A., Shakirova N., and Razueva D., *Complex analysis of bored piles on LRT construction site in Astana. Lecture Notes in Civil Engineering*, Vol. 49, 2020, pp.461–471.

A. Zh. Zhusupbekov and Y. Ashkey, T.Zh. Seidmarova, R.K. Bazilov, D.O. Bazarbayev, A.A. Zhusupbekov. *"Geotechnical and Geodisaster problems in Kazakhstan". Proceedings 4th International Conference on Disaster Prevention and Rehabilitation*, 2007, (Indonesia, Semarang), 28-40 pp.

Zhusupbekov A. Zh., Ashkey Y., *Geotekhnicheskij monitoring i razrabotka peredovyh tekhnologij ustrojstva svajnyh osnovanij zdanij i sooruzhenij v slozhnyh gruntovyh usloviyah Kazahstana s uchetom trebovanij inzhenerno-geologicheskih izyskanij.* Zaklyuchitel'nyj otchet o nauchno-issledovatel'skoj rabote. NC NTI RK.- Astana, 2007.-62 s.- Inv. №0208RK0039.

Decourt, L. *Behaviour of a CFA Pile in a Lateric Clay*.Proceedings of the 4th International Geotechnical Seminar on Deep Foundations on Bored and Auger Piles // BAP IV. Ghent, Belgium, 1993.- pp. 301-308.

A. B. Isakulov, A. Zh. Zhusupbekov, B. R. Isakulov, S. B. Iskakov. *Topyrak massivinin DDS tekhnologiyasy bojynsha ornatylgan byrgylanyp toltyrylgan қadalarymen ozara arekettesuin zertteu*. Vestnik evrazijskogo nacional'nogo universiteta imeni L.N.Gumileva. Seriya tekhnicheskie nauki i tekhnologii, Vol. №4, Issue 141, 2022, pp.19-29

28th European Young Geotechnical Engineers Conference – EYGEC 2024
© 2024 Macedonian Association for Geotechnics, ISBN 978-608-4510-61-1

Adaptability of flood embankments to climate change

Milena Raković[a], Veljko Pujević[b], Sanja Jocković[c], Nikola Obradović[d]

[a, b, c, d] *University of Belgrade, Faculty of Civil Engineering, Department of Geotechnical Engineering, Belgrade, Serbia*

ABSTRACT

In the context of growing concerns about climate change affecting precipitation patterns, there is a need to incorporate these changes into the design of flood defenses, particularly earthfill embankments. Although numerous geotechnical modeling techniques have improved understanding of soil embankment behavior, uncertainty regarding the impact of climate change to embankment performance still remains. Research in this field aims to identify instabilities that potentially could occur throughout an embankment's lifecycle, and development of corresponding solutions. Geotechnical modeling techniques and site-specific precipitation pattern projections, establish a comprehensive analysis framework, which allows assessing long-term behavior and resilience to a changing climate of existing and new embakments. The paper provides an overview of the climate-driven processes that are of greatest concern for hydro-mechanical behavior of earthfill flood embankments. Then, key aspects that need to be considered for predictive computational modeling, which combines geotechnical and climate modeling, are presented. Finaly, various strategies for embankment adaptation in order to improve their resilience to climate change are given.

KEYWORDS

Flood Embankments; Climate Change; Numerical Modelling; Adaptation Measures

1. INTRODUCTION

In recent years, few topics have captured global attention and concern as much as climate change. This phenomenon has emerged as one of the most pressing challenges facing humanity in the 21st century. From rising temperatures to extreme weather events, the impacts of climate change are being felt across the globe, transcending boundaries of geography, economy and culture. Climate change is occurring at a rate at least ten times faster than ever before in the history of our planet. Estimates suggest that Serbia is warming more rapidly than the global average. While the observed increase in the global average temperature is 1.1°C, Serbia has already experienced a rise of 1.8°C, reaching 2.6°C during the summer.

Additionally, since 2000, Serbia has faced several significant extreme climatic and weather events, resulting in substantial material and financial losses, as well as the loss of human lives (LCCRS, 2023). The lower bound estimates of total material damage caused by these events between 2000 and 2020 amounted to 6.8 billion euros, with over 70% attributed to droughts and high temperatures induced by climate change and extreme weather conditions. Floods have also been a major contributor to significant losses. According to *Desinventar* database (DesInventar) which contains 2196 records of damages and losses from floods in Serbia, the highest flood damage in Serbia during the period 1980-2022 was suffered by residential buildings and agricultural crops. Only in 2014, the flood damage amounted to around 1.6 billion euros. The observed consequences of floods, mostly caused by flash floods due to extreme precipitation events, include landslides, dam breaches, destruction of houses, etc. According to

the index developed by the American University of Notre Dame (ND-GAIN), Serbia ranks 86th in the world in terms of vulnerability to climate change and is the most vulnerable country in Europe. This index encompasses a range of indicators, from the concentration of urban population and preparedness for natural disasters to water availability and agricultural capacity. In addition, there is weak interaction between the networks of researchers, policy makers and stakeholders involved in addressing climate change issues in Serbia.

The frequency and intensity of climate hazards caused by climate change are expected to increase in the future, following a clear trend of change until the middle of the 21st century. Subsequently, the extent of these changes will depend on the successful implementation of climate change mitigation measures outlined in the Paris Agreement (LCCRS, 2023). This agreement represents a historic commitment by nearly every country in the world to limit global warming to well below 2°C above pre-industrial levels.

Geotechnical infrastructure, such as embankments and levees, is vital for flood defense and supporting transportation. Among the various manifestations of climate change, the increased intensity and frequency of extreme weather events pose significant challenges to flood embankments. Their integrity is increasingly threatened by the changing climate. This paper explores the impacts of climate change on flood embankments, highlighting the need for proactive adaptation strategies to mitigate risks and ensure the resilience of infrastructure in the face of a changing climate.

2. BACKGROUND

The increased frequency and intensity of extreme weather events strain the structural integrity of embankments, leading to erosion, breaches, and failure. Warmer temperatures intensify the hydrological cycle, leading to more intense rainfall events and prolonged periods of drought followed by heavy precipitation, both of which stress flood embankments. Another critical aspect is the alteration of vegetation patterns and soil moisture content due to climate change. Changes in vegetation cover and land use affect soil stability and infiltration rates, influencing the resilience of flood embankments against erosion and settlements. The engineering properties of soil, especially its response to moisture fluctuations, play a significant role in determining soil stability. Matric suction, which affects soil moisture content, is a critical factor in evaluating slope stability and must be carefully considered in infrastructure design and maintenance (Ghosh et al., 2024). Desiccation cracks, resulting from soil shrinkage during period of drought, further weaken the integrity of embankments and slopes. During rainfall, water infiltrates into these cracks, increasing the pore water pressure, which consequently reduces the shear strength of the soil and contributes to slope failure (Baninajarian et al., 2019). Climate change intensifies these problems by altering rainfall patterns and intensities, leading to more frequent and severe infrastructure failures.

The water exchange between soil and the atmosphere occurs through various processes, including precipitation infiltration, evaporation and transpiration through vegetation. These interactions lead to changes in soil moisture and pore water pressures, which are critical factors affecting the long-term stability of geotechnical structures like embankments. The interaction between the soil and the atmosphere is a dynamic process that regulates the continuous change of soil hydrological conditions (Pujević, 2021). The seasonal cycles of drying and wetting caused by these processes contribute to irreversible soil deformations and pose challenges for earthen structures. Prolonged droughts followed by extreme precipitations caused by climate change intensify this problem.

Furthermore, the shifting hydrological patterns associated with climate change pose challenges for the design and management of flood embankments. Traditional approaches to embankment design may become obsolete as historical flood data no longer provide accurate projections of future flood risks. As such, there is a critical need to incorporate climate change projections and uncertainty into the planning and design of flood infrastructure to ensure its effectiveness and resilience over the long term. Investments in resilient infrastructure and innovative engineering technologies are also essential for improving the capacity of flood embankments to handle the impacts of climate change.

The interaction between climatic conditions and soil properties is complex and requires thorough understanding and analysis. Climate prediction models can help anticipate future challenges and inform adaptive measures to enhance the resilience of critical infrastructure. Additionally, the relationship between soil moisture content and matric suction, as well as the influence of boundary conditions such as rainfall and evapotranspiration, must be carefully studied to develop effective mitigation strategies. Addressing these challenges requires interdisciplinary collaboration and a holistic approach that considers the mutual connection of natural and built environments.

The vulnerability of critical infrastructure to climate change underscores the urgent need for comprehensive research and proactive measures. By understanding the complex interactions between climatic factors, soil properties, and infrastructure design, we can enhance resilience and minimize the impacts of future disasters on communities and economies.

3. INTEGRATING CLIMATE CHANGE DATA INTO GEOTECHNICAL ENGINEERING PRACTICES

Integrating climate change data into geotechnical engineering practices has emerged as a crucial aspect in ensuring the stability and resilience of infrastructure vulnerable to the altering climatic conditions. Assessing the impact of climate change on geotechnical structures require a careful analysis of several complex processes (Ghosh et al., 2024). Firstly, it necessitates a comprehensive examination of future climate data. Climate projections provide crucial insights into the anticipated changes in temperature, precipitation patterns and extreme weather events. These projections serve as the foundational data for understanding the climate hazard that geotechnical infrastructures may face in the future. Secondly, calculating pore water pressures in slopes becomes imperative due to changes in variables induced by climate conditions. Pore water pressures play a pivotal role in slope stability, as they influence the shear strength of soil and can trigger slope failures under certain conditions. Lastly, estimating the stability of embankments based on the calculated pore water pressures emerges as a critical step in assessing their vulnerability to climate change.

By integrating climate-induced changes in pore water pressures into embankment stability analyses, engineers can ascertain whether embankments are at risk of failure under future climatic scenarios. This proactive approach enables the implementation of appropriate mitigation measures to enhance the resilience of geotechnical infrastructures in the face of a climate change.

3.1. Climate data

Projections of future climate change are derived from simulations with general circulation models (GCMs) and regional climate models (RCMs) using different scenarios for greenhouse gases emissions and socioeconomic scenarios. “Climate models are the most advanced tools available for modelling the state of the climate system and simulating its response to changes in atmospheric concentrations of greenhouse gases and aerosols. Models differ in their complexity, in the number of spatial dimensions and in the complexity of describing physical, chemical or biological processes” (IPCC, 2016).

Climate modeling plays an important role in understanding the complex dynamics of Earth's climate system and predicting future climate scenarios. While GCMs provide a global perspective, RCMs offer detailed insights into local climate conditions, variability and changes. RCMs utilize GCM outputs as boundary conditions and refine them using finer-scale atmospheric and land surface data. As expalned by the Intergovernmental Panel on Climate Change (IPCC), climate models operate on the basis of known properties of the climate system, encompassing a spectrum of complexities. Furthermore, climate scenarios such as Representative Concentration Pathways (RCPs) and Shared Socioeconomic Pathways (SSPs) provide a framework for assessing future climate conditions under different emission and socioeconomic scenarios (IPCC, 2016).

3.2. Predictive computational modelling

Human-induced climate change, beside causing alterations in long-term weather patterns, is expected to bring about more frequent occurrences of severe weather events like storms and droughts. Considering that flood embankments are directly exposed to natural environment, climate change induced increase in environmental stresses could potentially compromise their safety and adversely affect their long-term performance. Therefore, for the comprehensive estimation of flood embankment behaviour in light of ever-changing climate, two types of analyses - lifecycle assessment and resilience analysis - must be carried out. The objective of complete lifecycle analysis is to capture the general long-term behaviour, in particular the progression of deterioration processes and their impact on the duration of service life. On the other hand, resilience analysis place emphasis on the response of embankment to destructive short-term storms at different phases of its lifecycle.

As can be seen, the soil-atmosphere interaction governs both the long-term average as well as short-term performances of infrastructure embankments. At the center of soil-atmosphere interaction are the processes like rainfall infiltration, evapotranspiration and riverside water pressures that drive continuous change in water balance. To account for those dynamic variable processes and assess their impact on the stability, serviceability and resilience of earthfill flood embankments, advanced transient mass transfer analysis combined with unsaturated mechanical soil constitutive models and sophisticated climatic boundary conditions are necessary. Several different procedures have been suggested varying from simple pure hydraulic commonly combined with limit equilibrium method (Ghosh et al., 2024; Bračko et al., 2022; Pk et al., 2021), thermo-hydraulic (Archer, 2019) and hydro-mechanical (Guo, 2021; Pujević, 2021), to fully coupled thermo-hydro-mechanical analysis (Elia et al., 2017). Numerous studies (Briggs et al., 2016; Fredlund, 2000) have demonstrated the significance of hydraulic soil properties in dictating the flow-deformational behaviour of embankments under varying climatic conditions. Consequently, phenomena such as desiccation cracking and desaturation, that directly affects soil mass permeability, play a pivotal role in ensuring realistic and reliable predictions regarding the future performance of flood embankments.

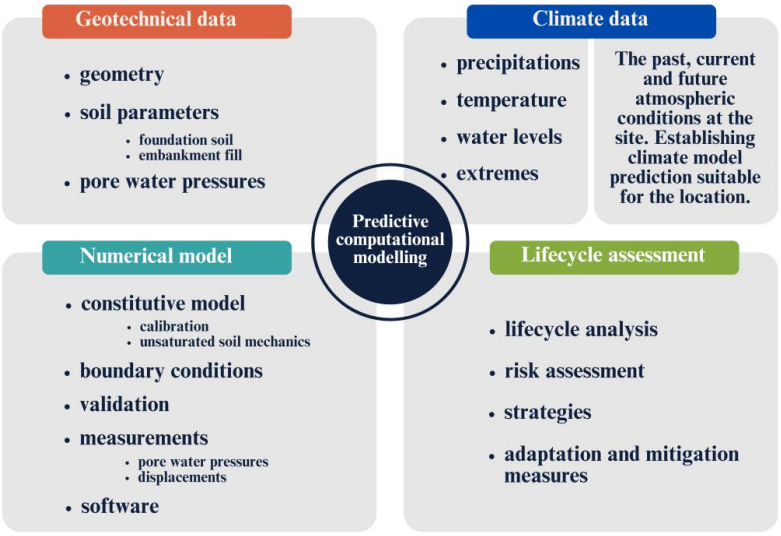


Figure 1. Methodology for predictive computational modeling

To account for climate changes, future climate data is necessary input. Methodology for projecting rainfall patterns in the long-term, consists of developing synthetic rainfall series that are continuous and characterised by summary statistics corresponding to measured rainfall data. Such artificial rainfall data series are then integrated with pertinent climate change factors to create predictive future rainfall models. The main difference between lifecycle and resilience analysis lies in the time resolution of

climatic variables, namely rainfall and hydraulic data. While the lifecycle analysis utilises monthly rainfall, much finer resolution (hourly) is needed to study the resilience of the embankment to storms. Resilience assessments serve as a secondary analysis aligned with critical stages throughout the embankment's lifecycle, conducted as part of the primary lifecycle analysis.

Developing a comprehensive methodology to address climate change impacts on flood embankments involves using advanced computational techniques and tools to simulate complex soil-atmosphere interactions. This implies the development of advanced numerical models. Through rigorous validation processes, these models need to be refined to accurately illustrate the response of flood embankments under various scenarios, ensuring their reliability in predicting performance and resilience. Then, by combining observed climate data with climate model projections, we provide robust boundary conditions for numerical analysis and assess future hazards for flood embankments, as shown in Figure 1. By incorporating future climate projections into geotechnical assessments, engineers can anticipate and mitigate the potential adverse effects of climate change on infrastructural integrity. This interdisciplinary approach underscores the imperative of integrating climate considerations into geotechnical engineering practices to build a more sustainable and resilient future.

4. ADAPTATION MEASURES FOR FLOOD EMBANKMENTS

Flood defence embankments are and will remain the major asset in a flood defence system and the process of protecting that system is essential for every community. Establishing a framework for designing and managing flood embankments based on risk assessment is a key aspect in that process. This framework must take into account the evolving hazards, vulnerabilities, and exposure levels in a changing climate (IPCC6, 2023). Together, those three elements form the basis for a detailed risk assessment in areas protected by flood embankments and are shown in the Figure 2. Climate hazard involves analysis of historical data, utilization of climate models, and prediction of future climate scenarios to understand the magnitude and frequency of extreme weather events and future floods. In context of this paper, vulnerability is considered as susceptibility of flood embankments to failure or damage under climate hazard. Exposure refers to the identification and characterization of assets, individuals or systems and critical infrastructures that are potentially at risk from a climate hazard. Exposure is a critical component of risk assessment because it helps determine the likelihood and severity of adverse consequences resulting from a climate hazard.

Through climate, hydrological and geotechnical modeling, using historical flood data analysis, and stakeholder consultations, the unique risks faced by embankments can be identified, providing a foundation for targeted adaptation efforts. Adaptation measures derived from risk assessment are crucial for effectively managing flood risk and enhancing the resilience of river flood embankments. Adaptation plans should prioritize measures that address the most critical vulnerabilities while considering factors such as effectiveness, feasibility, and cost-effectiveness.

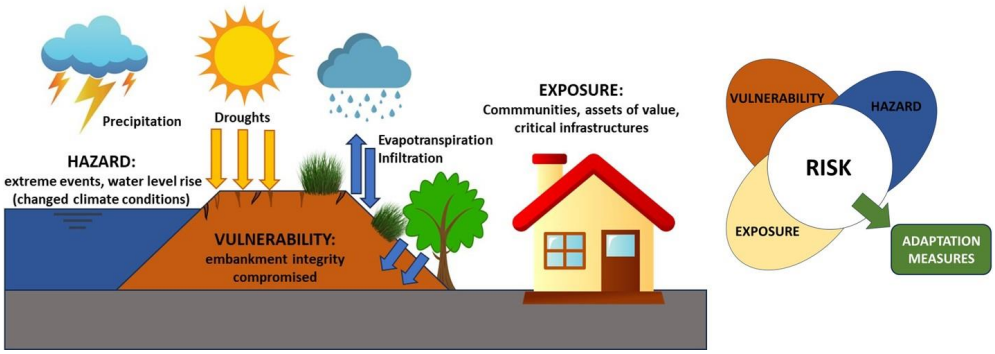


Figure 2. Three elements for risk assessment

In the latest Sixth Assessment Report (IPCC, 2022b, 2022a), justice and equity emerge as a key dimension of climate change adaptation, standing alongside effectiveness and feasibility. Two principal reasons support the inclusion of justice and equity in adaptation strategies are: firstly, they align with moral imperative, and secondly, scientific research show that considering justice can enhance the effectiveness of adaptation measures (Breil et al., 2021). Justice and equity in embankment adaptation strategies involves ensuring that vulnerable communities, often disproportionately affected by flooding, have equitable access to protective measures and resources. Adopting "*Leaving No One Behind*" principle and addressing disparities in exposure, vulnerability, and resilience, embankment adaptation strategies can contribute to fostering more equitable and sustainable outcomes for all communities.

Adaptation measures can be structural and non-structural, depending on their nature and function (EUFIWACC, 2016). Structural measures include embankment heightening and widening, embankment vegetation reinforcement, installation of flood walls, slope stabilization, barierrs and improved drainage systems. Non-structural measures for adaptation to climate change and flood risk are all about using proactive planning, community engagement, and policy interventions rather than relying on physical infrastructure and they include monitoring and early warning systems, planning and zoning, public awareness and community education.

Heightening and widening embankments are the most common adaptation measures and can provide additional capacity to contain floodwaters, reducing the risk of overtopping and flooding downstream areas. On the other hand, that measure suffers of the potential consequence of subsoil and embankment settlements, which could compromise the integrity of the embankments and increase the risk of flooding in the long term. Embankment reinforcement is a key adaptation measure aimed at enhancing structural integrity and resistance. Beneficial aspects of reinforcement with vegetation include erosion control, improved soil stability and enhanced biodiversity. While root systems can stabilize soil, the penetration of roots into embankment structures may compromise their integrity over time. Utilizing drainage system (surface and subsurface) as an adaptation measure for flood embankments involves implementing strategies to manage and control the flow of water, particularly during periods of heavy rainfall or flooding. Sustainable Drainage Systems (Petalas et al., 2022) are commonly used in urban environments. It is called the flood barrier and comprises two layers: an unsaturated compacted soil layer with water retention capabilities and a drainage layer made of coarse granular material. The granular layer serves as a capillary break and is installed above the native soil. The fundamental principle of this approach is to slow down and reduce quantity of surface water runoff.

In order to create a strategy for adapting river embankments in the light of climate change, an interdisciplinary approach is needed and it involves integrating knowledge and expertise from geotechnics, hydrology, climatology, ecology, and social sciences. By bringing together experts with diverse backgrounds, interdisciplinary teams can develop comprehensive solutions that consider the complex interactions between natural systems, human activities, and climate dynamics.

5. CONCLUSIONS

Climate change is identified as a critical challenge of the 21st century. Among the various manifestations of climate change, the increased intensity and frequency of extreme weather events strain the structural integrity of embankments the most, leading to erosion, breaches, and failure. Traditional approaches to embankment design may become obsolete as historical flood data no longer provide accurate projections of future flood risks. As such, there is a critical need to incorporate climate change projections and uncertainty into the planning and design of flood infrastructure to ensure its effectiveness and resilience over the long term. Assessing the impact of climate change on geotechnical earth structures requires a careful analysis of several complex processes: 1) a comprehensive examination of future climate data as the foundational data for understanding the climate hazard that geotechnical infrastructures may face in the future, 2) calculating pore water pressures in slopes because of changes in variables induced by climate conditions, 3) estimating the stability of embankments based on the calculated pore water pressures.

Further, for the comprehensive estimation of flood embankment behavior in the face of a changing climate, two types of analyses are required: lifecycle assessment and resilience analysis. While the objective of complete lifecycle analysis is to capture the general long-term behavior, particularly the progression of deterioration processes and their impact on the duration of service life, resilience analysis places emphasis on the response of the embankment to destructive short-term storms at different phases of its lifecycle.

Developing a comprehensive methodology to address climate change impacts on flood embankments is not easy. It involves using advanced computational techniques and tools to simulate complex soil-atmosphere interactions. By understanding the complex interactions between climatic factors, soil properties, and infrastructure design, we can enhance resilience and mitigate the potential adverse effects of climate change on infrastructural integrity.

Adaptation measures are means for mitigating risks associated with climate change effects. Depending on their nature and function they are categorized as either structural or non-structural. In order to create a strategy for adapting river embankments in the light of climate change, an interdisciplinary approach is needed and it involves integrating knowledge and expertise from geotechnics, hydrology, climatology, ecology, and social sciences. This interdisciplinary approach underscores the imperative of integrating climate considerations into geotechnical engineering practices to build a more sustainable and resilient future.

6. ACKNOWLEDGEMENTS

This paper is an output from the project Climate change resistant Danube river embankments (CHERUBIM) within the multilateral scientific and technological cooperation in the Danube region 2023-2025.

REFERENCES

Archer A. 2019. Climate change impact on unsaturated embankments considering temperature and humidity: centrifuge modelling. PhD Thesis, Hong Kong University of Science and Technology.

Baninajarian, L., Ghassemi, A., Sangiuliano, T., DeSira, A. and Bashir, R. 2019. Effect of climate change on soil embankment stability. *72nd Canadian Geotechnical Society Annual Conference*, St. John's, Newfoundland, Canada.

Bračko, T., Žlender, B. and Jelušič, P. 2022. Implementation of Climate Change Effects on Slope Stability Analysis. *Applied Sciences*, 12(16):8171. Available from: https://doi.org/10.3390/app12168171

Breil, M. et al., 2021, *"Leaving No One Behind"* in Climate Resilience Policy and Practice in Europe Overview of Knowledge and Practice for Just Resilience, ETC/CCA Technical Paper - 2021/2.

Briggs, K.M., Smethurst, J.A., Powrie, W. and Brien, A.S.O. 2016. The influence of tree root water uptake on the long term hydrology of a clay fill railway embankment. *Transportation Geotechnics*, 9, 31–48. Available from: https://doi:10.1016/j.trgeo.2016.06.001

Disaster Inventory System data base– DesInventar. https://www.desinventar.net/

EEA, 2016. Climate change, impacts and vulnerability in Europe 2016, *European Environmental Agency, Publications Office of the European Union*.

Elia, G., Cotecchia, F., Pedone, G., Vaunat, J., et al. 2017. Numerical modelling of slope–vegetation–atmosphere interaction: an overview. *Quarterly Journal of Engineering Geology and Hydrogeology*, 50 (3), 249–270.

EUFIWACC 2016, "Integrating Climate Change Information and Adaptation in Project Development", Available from: www.eib.org/attachments/press/integrating-climate-change-adaptation-in-project-development.pdf (accessed on 21 February 2018).

Fredlund, D.G. 2000. The 1999 R.M. Hardy Lecture: The implementation of unsaturated soil mechanics into geotechnical engineering. *Canadian Geotechnical Journal*, 37 (5), 963–986. Available from: https://doi:10.1139/t00-026

Ghosh, D., Banerjee, A., Puppala, A.J. and Kumar, P. 2024. Exploring the Influence of Climate Change on Earthen Embankments with Expansive Soil. *Geosciences*, 14(2):37.

Guo, B. 2021. Reuse and sustainability of flood defences. PhD Thesis, Imperial College London.

IPCC, 2022a, Climate Change 2022: Impacts, Adaptation and Vulnerability. Contribution of Working Group II to the Sixth Assessment Report of the Intergovernmental Panel on Climate Change, *Cambridge University Press*, Cambridge, UK and New York, NY, USA.

IPCC, 2022b, 'Summary for Policymakers', in: Pörtner, H.-O. et al. (eds), Climate Change 2022: Impacts, Adaptation, and Vulnerability. Contribution of Working Group II to the Sixth Assessment Report of the Intergovernmental Panel on Climate Change, *Cambridge University Press*. In Press., Cambridge, UK and New York, NY, USA, pp. 3-36.

IPCC, 2023. Climate Change 2023: Synthesis Report. Contribution of Working Groups I, II and III to the Sixth Assessment Report of the Intergovernmental Panel on Climate Change. *IPCC*, Geneva, Switzerland, pp. 35-115.

LCCRS Law on Climate Change of the Republic of Serbia (article 13, paragraph 2) 2023. "Adaptation program to changed climate conditions for the period from 2023 to 2030".

ND-GAIN Country Index. ND-GAIN Notre Dame Global Adaptation Initiative. https://gain.nd.edu/our-work/country-index/rankings/

Petalas, A. L., Tsiampousi, A., Zdravkovic, L. and Potts, D. M. 2022. Numerical investigation of the performance of engineered barriers in controlling stormwater runoff. *Geomechanics for Energy and the Environment*, 32, 100401.

Pk, S., Bashir, R. and Beddoe, R. 2021. Effect of climate change on earthen embankments in Southern Ontario, Canada. *Environmental Geotechnics*, 8, 148–169.

Pujević, V. 2021. Numerical modeling of the vegetation and atmosphere effect on the behaviour of civil infrastructure embankments. PhD Thesis, University of Belgrade.

28th European Young Geotechnical Engineers Conference – EYGEC 2024
© 2024 Macedonian Association for Geotechnics, ISBN 978-608-4510-61-1

Geotechnical characterization of the rockmass surrounding the Aljustrel mining compound

Tiago Rodrigues[a]

[a] *Instituto Superior Técnico, Lisbon, Portugal*

ABSTRACT

This document studies the ground surface geotechnical properties of the Aljustrel town. To achieve the objectives of this study, a database is considered compiling information relative to 2.175 vibration records measured at ten structures located in Aljustrel. These served as a basis to estimate, using multiple linear regression, 23 valid characteristic attenuation equations according to the mathematical expression presented by Johnson. Such equations consider categorical variables like the existence of a rock mass discontinuity created by an initial production blast; section of the town where the records were monitored; and geographical orientation between the blasting and the monitoring points. Additionally, a detailed study was performed considering four structures, where the respective building materials' waves propagation velocity and geometrical parameters are measured.

KEYWORDS

Ground vibration; Prediction models; Natural frequency; Aljustrel mining compound.

1. INTRODUCTION

In underground and open pit production scenarios where the rock mass characteristics hinder the usage of mechanical excavation methods due to economical, technical and/or environmental restrictions, drill and blast is preferred over the first alternative. However, despite its versatility and cost-benefit relationship, the usage of explosives is associated with undesirable side effects such as ground vibration, fly rock, air blast, dust and rock mass instability after overbreak. From these impacts, the first is the one that may be perceived at greater distances – most of the times, outside the mine perimeter – and originate complaints on behalf of neighbouring populations. Additionally, descriptors such as structures, equipment and ecosystems may also be affected by blast-induced ground vibration registering, in extreme cases, temporary or permanent damage. As such, considering the damage potential of this impact, most countries have created or adopted regulations and norms, suggesting limits concerning vibration amplitudes measured at nearby structures, to minimize subsequent impacts. Moreover, human exposure to this side effect is also regulated in some nations.

Explosive substances are defined as chemical compounds or a mixture of compounds which, when initiated by friction, impact or heat, decompose very rapidly, releasing substantial amounts of energy in the form of heat, gas and shock (Bernardo, 2004). However, only 5 to 15 % of the energy released upon detonation is effectively used in rock fragmentation, highlighting the relative amount of energy transmitted through the surrounding rock mass in the form of vibrations (Gama, 1998). Vibration may be defined as an oscillatory movement of any physical system (in the solid, liquid or gaseous state), which is displaced from its equilibrium condition. It is considered to be the ground elastic response to the stress (body and surface) waves that propagate through it until attenuation totally dissipates the initially transmitted energy. This phenomenon is usually described by the amplitude (expressed as a function of displacement, velocity or acceleration), period, wavelength, frequency and duration (Dowding, 1992).

Attenuation corresponds to a decrease in vibration amplitudes with time or distance (Dowding, 1992). The factors that contribute to it are the waves geometrical spreading; the progressive separation of surface, P and S waves components given the different propagation velocities associated with them; the presence of rock mass discontinuities and internal friction that causes frequency-dependent attenuation (Sarsby, 2013). Nevertheless, in stratified rock masses, waves may concentrate or overlap to reflected ones (constructive interference), measuring greater vibratory amplitudes at more distant points (Azevedo and Patrício, 2003).

When sensitive descriptors such as stakeholders or structures are located in the vicinity of mining operations that rely on drill and blast as the main excavation method and attenuation is not sufficient to guarantee satisfactory vibration velocities measured near such elements, additional measures have to be considered in such a way that the recommended limits suggested by standards in force are complied with, mitigating the impact of vibrations. Hence, measures such as the usage of electronic detonators, more accurate timewise (avoiding overlapping between different blastholes), multiple initiation and the reduction of the bench height are suggested (Lopez Jimeno et al., 1995; Heiniö, 1999; Bernardo, 2004; Dowding, 2011). Moreover, the optimization of the blasting pattern by taking into account its geometrical variables has equally the objective of reducing the operations unit costs and associated environmental impacts, and increasing the explosives energy efficiency – directly consumed in fragmentation.

Ground vibration amplitudes are directly proportional to the induced dynamic stress, σ_d, (Pa). The last, dependent upon the lithology on which structures are founded, can easily be correlated with the structures dynamic resistance (1) (Dowding, 1992).

$$\sigma_d = \rho \cdot c \cdot v \tag{1}$$

Where ρ and c represent the rock mass density (kg·m^{-3}) and typical wave propagation velocity (m·s^{-1}), respectively, and v the particles vibration velocity (mm·s^{-1}).

However, investigations show that frequency is also deemed as a structural damage criterion given the inverse relationship between this physical quantity and displacement – being the last an example of a structure response to vibration. Furthermore, once low-frequency waves are the most energetic ones, this response is a concern if resonance occurs, further incrementing eventual damage (Dowding, 2011). Some authors define resonance as an amplified structural vibratory response induced by the proximity of the dominant frequency of rock mass vibrations to one of the buildings natural frequency (Svinkin, 2008). According to previous studies (Bernardo, 2004), the structures natural frequency, f_n, (Hz) is influenced by its geometrical parameters and building material physical properties (2).

$$f_n = \frac{C_P}{2 \cdot \pi \cdot H_S} \cdot \sqrt{1 - n} \tag{2}$$

Where C_P is the respective building material's waves propagation velocity (m·s^{-1}), n the porosity, and H_S is equivalent to the building's height (m).

When considering the normative document in force in the respective country, that suggests the maximum vibration amplitude measured at structures, companies design blasting patterns based on those values, minimizing the likelihood of non-compliance and disturbance to humans. As such, the mathematical expression suggested by Johnson (1971) (3) is widely used in the construction and mining sectors as a ground vibration prediction model (Lopez Jimeno et al., 1995; Hustrulid, 1999).

$$v = a \cdot Q^b \cdot D^c \tag{3}$$

According to this equation, v is the resulting vibration velocity (mm·s^{-1}), depending on the maximum explosive charge per delay, Q, (kg) and distance between the detonation and monitoring points, D (m).

The dimensionless constants *a*, *b* and *c* are dependent upon the blast design and *in situ* parameters such as the explosives properties or burden and the rock/soil mass characteristics, respectively.

2. CASE STUDY MINES AND METHODOLOGY

The area of study corresponded to the town of Aljustrel (Alentejo province, Portugal). Here, two of Europe's biggest mines – Feitais and Moinho – are responsible for the production of copper, zinc, lead and silver concentrates from sulfide minerals namely pyrite. The area's surface is mainly composed by greywacke, wacke, schist and argillite, forming the Upper Sedimentary Unit (Schermerhorn and Stanton, 1969).

Given the proximity of the mines to the population, the license holder has been carrying out monitoring campaigns to assess the exploitation's impacts caused by blast-induced vibrations. These are performed by means of seismographs strategically placed between the mines perimeter (blasting source) and elements to protect such as constructions located within the Aljustrel exploitation concession. Motivated by the inexistence of ground vibration prediction models and the fact that disturbance and complaints on behalf of local populations are not uncommon, this work aims at modelling several expressions similar to (3), valid in the region of study, taking into account supplementary categorical variables. Additional structures were monitored between July 12th and August 8th, 2022, in a campaign parallel to the one continuously performed by the mining company. The considered structures location as well as both orebodies surface projection are illustrated in Figure .

In this figure, buildings represented in red (A and B), yellow (C, D, E and F) and green (G, H, I and J) correspond to sensitive, current and reinforced structures, respectively, according to the classification suggested by the Portuguese ground vibration standard: NP 2074. Three major sections within the Aljustrel mining compound can be identified: industrial area within the mine perimeter – IA Mine – (including H and J), industrial area outside this perimeter – IA Outside the Mine – (considering B, G and I), and urban area (remaining structures). The alternative vibration recording campaign was performed at structures C and E and registered three events over the trigger level (0,3 mm·s^{-1}).

The present work involved the creation of a database compiling information relative to production blasts which originated vibrations recorded by the seismographs: peak vector sum ($PVS - v$) and dominant frequency (f_d) – calculated using THOR^{TM} software. These parameters were previously determined and stored by the company. Variables such as the blast hole and seismograph coordinates, estimated considering georeferenced AutoCAD drilling patterns and using GNSS survey equipment, respectively (allowing the calculation of the distance between these points); maximum charge per delay (Q), type of blast (up-hole or downhole benching); and orientation between the blast and the receiver (N-S and E-W) were added into the compilation. In total, 2.175 valid vibration records collected between February 2018 and August 2022 were studied.



Figure 1. Surface projection of the Feitais and Moinho orebodies and location of the monitored points within the Aljustrel mining compound

It is noteworthy that, at the Feitais mine, the employed mining method is sublevel open stoping where stopes are blasted in two phases: an initial up-hole set of rings followed by the upper volume (downhole benching). On the other hand, at the Moinho mine, longitudinal bench and fill is used. Here, stopes are blasted in one phase and, as such, there is no discontinuity created by previous production blasts. At Feitais, given the influence created by the initial blasts, stress waves are deviated by the existing void, suffering successive reflections before reaching the surface. As such, one is going to test the influence of the presence of a discontinuity on the registered vibration amplitudes and three operational scenarios are going to be considered: vibration events registered after blasts from the Feitais mine without an existing discontinuity (FWOD) and with an existing discontinuity (FWD); and from the Moinho mine without a discontinuity (MWOD).

To estimate the Johnson's model constants a multiple linear regression tool available in SPSS software was used. It is important to consider, however, the data transformation in such a way that the formula present in (3) is adapted and the coefficients are easily calculated. This is performed by determining the logarithm of the variables v, Q and D such that the following expression is obtained (4):

$$v = a \cdot Q^b \cdot D^c \Leftrightarrow \log(v) = \log(a) + b \cdot \log(Q) + c \cdot \log(D) \equiv$$
$$y = b_0 + b_1 \cdot x_1 + b_2 \cdot x_2 \quad (4)$$

Thereby, after obtaining a linear relationship between the three variables, the rock mass constants can be determined by the following formulas: $a = 10^{b_0}$; $b = b_1$; and $c = b_2$. Given the fact that there is a direct relationship between v and Q, and an inverse proportionality between v and D, the obtained models are only valid if the coefficients a and b are positive, and c is negative.

To minimize the impact of anomalous values (outliers) on the estimated models, experimental data have to be analyzed and filtered out to identify and remove them, respectively. Usually, not more than 10 % of the samples should be removed (Bernardo and Torres, 2005). Thereby, given the considerable number of samples, a visual inspection of the data on the planes considering the dependent variable (v) versus the independent ones (Q and D) does not allow a clear identification of the outliers. Hence, samples were divided according to the three operational scenarios: FWOD, FWD and MWOD, and vibration amplitude prediction models were determined individually. For each situation, *PVS* was calculated according to the respective equation and the modulus of the residuals (difference between the real and estimated *PVS* values) corresponding to each sample was estimated.

To complement the study on ground vibrations in the Aljustrel mining area, one considers relevant the estimation of the monitored structures natural frequency by means of (2), allowing the identification of eventual resonance phenomena and consequent performance of changes in the blasting pattern to protect the considered buildings. Given their importance in terms of vibrations control – humans may be within these elements during the blasting period – the analyzed structures are A, C, D and E. Thus, to apply the mentioned mathematical expression, it is necessary to calculate the buildings height, respective porosity (dependent upon its geometrical parameters) and C_P. To determine the first two elements, a tape measure was used, whereas the last physical property was estimated by means of an ultrasound device equipped with two piezoelectric transducers. It should be noted that porosity is calculated by the division between the volume of voids of the structure and the total structure volume, where the numerator includes volumes in the structure which do not correspond to resistant elements such as pillars or slabs. The estimation of the building materials' waves propagation velocity was performed by placing the two transducers at a wall on a surface that contains structural elements such as pillars and at different known distances. Several distances from 5 to 30 cm and according to an interval of 5 cm were considered. The ultrasound equipment measures the travel time of the transmitted signal and the division between the distance and this physical quantity yields C_P.

3. RESULTS AND DISCUSSION

The initial manipulation of the data corresponded to the removal of outliers, according to the previously described methodology. For MWOD, FWOD and FWD 10 % of the samples with the greatest residuals were removed, which was equivalent to 4, 112 and 101 elements, respectively. As such, the filtered dataset contained 1.958 vibration records, in total.

To assess the heterogeneity of the rock mass at different sections of the Aljustrel town in terms of vibrations propagation, an initial set of models considering the three identified sections (IA Mine, IA Outside the Mine and Urban area) was analyzed. The obtained models are shown by Table 12.

The projection of the isokinetic curves on the Q vs. D plane is shown below (Figure 2). Once the mean f_d for the three groups lies between 10 to 40 Hz, according to NP 2074, a conservative vibration velocity equal to 3 mm·s^{-1}, corresponding to the limit for sensitive structures, is considered. Additionally, the propagation equation estimated by Remísio for schists and greywackes (predominant surface lithology) is going to be equally projected (Bernardo and Torres, 2005). The respective expression corresponds to $v = 1598 \cdot Q^{0,88} \cdot D^{-2,06}$. It is noteworthy that some models are not projected (MWOD and FWD Urban area) given their coefficients which contradict the previously mentioned conditions.

According to this figure, if D is less than 300 m, the rock mass attenuates stress waves originated from blasts carried out at the Moinho mine at a lower rate; and FWD IA Mine and IA Outside the Mine are less conservative than FWOD (for the same sections), suggesting the influence of the previously blasted volume within the proximity of the blast, which may attenuate part of the released energy. For events belonging to FWD IA Mine and IA Outside the Mine, and D over 300 m, these models show an evident convergence and are the most conservative ones. The least restrictive law is FWOD Urban area. For increasing distance values, equations developed for Feitais (excluding FWOD Urban area) converge to the theoretical model. However, the disparity between the inferred and the theoretical laws highlight the importance of the formulation of different models that have a better adjustment to the samples measured at an area characterized by a complex geology.

The second variable to be tested as an influencing factor of ground vibration is the orientation between the blasting and the monitoring points. Thereby, for each operational scenario, samples were divided according to a binary classification system (N-S and E-W) – and the calculated models were as follows (Table 13):

According to this table, the coefficient of determination (R^2) is greater in E-W models in all operational scenarios. This may indicate the lower impact rock mass discontinuities have on stress waves propagation in terms of constructive or destructive interference according to this direction, influencing the measured *PVS*. The six equations are valid and for v equal to 3 mm·s^{-1} the respective projection on the Q vs. D plane is depicted in Figure 3.

Table 12. Johnson's model constants for the three operational scenarios and sections within the Aljustrel

Operational scenario	Section	Number of samples	a	b	c	R²
MWOD	IA Mine	30	24.003	0,21	-1,73	0,43
	Urban area	6	0,2	-0,09	0,22	0,50
FWOD	IA Mine	296	9.300	0,55	-1,83	0,76
	IA Outside the Mine	657	7.695	0,49	-1,75	0,53
	Urban area	59	10	0,07	-0,45	0,20
FWD	IA Mine	276	4.673	0,64	-1,78	0,68
	IA Outside the Mine	586	3.597	0,57	-1,66	0,51
	Urban area	48	32	-0,26	-0,39	0,33

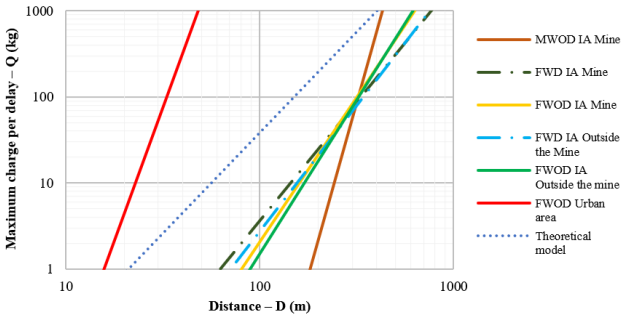


Figure 2. Isokinetic curves corresponding to the theoretical and inferred models for each operational scenario and section of the town considering v = 3 mm·s^{-1}

Table 13. Johnson's model constants for the three operational scenarios and according to the orientation

Operational scenario	Orientation	Number of samples	a	b	c	R^2
MWOD	N-S	27	220	0,07	-0,90	0,22
	E-W	9	1.973	0,03	-1,22	0,42
FWOD	N-S	724	7.893	0,52	-1,78	0,59
	E-W	288	687	0,46	-1,31	0,78
FWD	N-S	685	3.482	0,59	-1,68	0,54
	E-W	225	484	0,57	-1,32	0,80

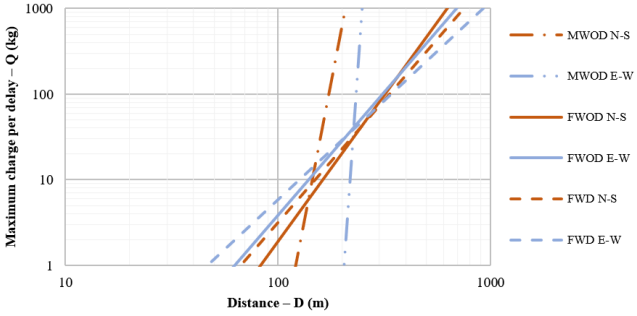


Figure 3. Isokinetic curves corresponding to the inferred models for each operational scenario and orientation considering v = 3 mm·s^{-1}

The results suggest that for the Moinho mine, in the E-W direction, the rock mass is more competent, offering less resistance to ground vibration propagation, involving thus more restrictive limits in terms of Q at a given distance. For D below 275 m, the N-S direction implies more conservative models at Feitais. Over this threshold, a consistent pattern is not observed, although FWD models are the most restrictive ones, when compared to those with the same orientation.

The second and last phase of this study consisted in the assessment on the existence of resonance phenomena at structures A, C, D and E as mentioned before. After following the methodology described in the previous section, the physical quantities relevant to estimate f_n according to (2) are summarized in Table 3. It should be mentioned that for each structure six measurements were performed. However, for structure A no accurate readings were obtained for distances of 25 and 30 cm.

Similar studies developed for buildings with characteristics similar to structure A have determined that C_P for masonry ranges between 1.050 and 3.050 m·s^{-1} (Zielińska and Rucka, 2018). This is greater than the waves propagation velocity for reinforced concrete, which according to the bibliography is about 2.140 m·s^{-1} (Feng and Yi, 2017). Lastly, Fabisiak et at. have concluded that the C_P of pine wood varies between 4.000 and 5.800 m·s^{-1} (Fabisiak et al., 2007). This diverges from the values measured in the field, suggesting that the possible aging and treatment the wood has suffered may contribute to a decrease in this physical quantity values. Consequently, the application of (2) yields the results compiled in Table 4, which also presents some statistical elements of f_d concerning events monitored at the addressed structures.

According to the results, the estimated structures f_n diverges from the events mean f_d. The ratio between the first and the second variables – lower than 39 % (for structures C, D and E) and equal to 288 % (for structure A) – indicates that no significant resonance is expected to occur. Therefore, the impact blast-induced vibrations have on the considered structures and humans located inside them is reduced and considerable damage is unlikely to occur.

Table 3. Results of the building materials' waves propagation velocity, structures height and porosity estimation

Structure	Sample material	Mean C_P (m·s^{-1})	Height (m)	Porosity (-)
A	Masonry	3.152,2	8,7	0,64
C	Reinforced concrete	2.189,7	8,1	0,91
D	Reinforced concrete	2.030,9	10,5	0,87
E	Wood	2.383,0	2,7	0,99

Table 4. Estimated natural frequency and statistical description of the variable dominant frequency for the considered structures, in Hz

Structure	Number of samples	Estimated f_n	Dominant frequency, f_d	
			Mean	Median
A	61	34,9	12,1	13,0
C	1	13,2	50,0	50,0
D	33	11,2	28,6	26,8
E	11	14,5	54,2	53,3

4. CONCLUSIONS

The present study had two main objectives: to model ground vibration amplitude prediction equations and to estimate the natural frequency by means of a theoretical formula, assessing then the existence of resonance at the considered structures.

The objectives proposed for this work were accomplished. In total, using a multiple linear regression tool in SPSS software, 20 models were estimated considering relevant variables v, Q and D as suggested by Johnson (1971). From these, three were deemed invalid ones. These equations were deducted based on a database that included information relative to 2.175 real ground vibration records originated after production blasts at the Aljustrel mines (Alentejo province, Portugal). The records were registered at ten different structures between February 2018 and August 2022. Other variables such as the existence of a rock mass discontinuity imposed by an initial production blast, section of the town where the events were monitored and orientation between the blasting and monitoring points were tested. Such models allow the estimation of ground vibration amplitudes and may be considered when performing blasting pattern designs.

Additional conclusions provided by the analysis of the valid models suggest that, for distance values below 300 m, models developed for the Feitais mine without an existing discontinuity are more conservative, highlighting the influence of the previously excavated stope volume on vibrations attenuation. At Feitais, within a 275 m perimeter around the blasting point, the north-south direction is less resistant to vibration propagation. At the four considered structures, given the dissimilarity between the mean dominant frequency that characterizes the events monitored at these locations and the estimated natural frequency, no resonance is expected to be verified and thus the impact ground vibration has on structures is not significant.

To diversify the monitoring locations and consider lower distances from the blast, vibration monitoring within underground infrastructure such as drifts adjacent to the blasts should be performed. This would allow the integration of the collected data to the existing database and consequent creation of a new model, and an eventual quantification of the influence underground infrastructure and stopes have on ground vibration amplitudes. Additionally, the inclusion of energy weighting factors to attenuation equations, rather than the maximum charge per delay that does not consider different thermodynamical properties of the explosives, is of relevance. Such properties may be the detonation energy and pressure.

References

Azevedo, F., and Patrício, J., 2003, "Critérios de Danos e de Incomodidade no Domínio das Vibrações Ambientes," *Ingenium, Ordem dos Engenheiros Magazine,* January, pp. 85–88.

Bernardo, P., 2004, "Impactes Ambientais do Uso de Explosivos na Escavação de Rochas, com Ênfase nas Vibrações". PhD Thesis, Lisbon, Portugal.

Bernardo, P., and Torres, V., eds., 2005, *Metodologia para a Prevenção de Danos e Controle Ambiental de Vibrações Causadas por Detonações em Maciços Rochosos,* Ordem dos Engenheiros.

Dowding, C.H., 1992, "Production Operations: Monitoring and Control of Blast," *SME Mining Engineering Handbook. Vol.1*, H. Hartman, ed., Colorado, United States of America, pp. 746–760.

Dowding, C.H., 2011, "Impacts and Control of Blasting," *SME Mining Engineering Handbook,* P. Darling, ed., pp. 1689–1704.

Fabisiak, E., Moliński, W., and Roszyk, E., 2007, "The propagation velocity of ultrasound waves along the grain in the juvenile and mature, normal and reaction wood of pine (Pinus sylvestris L.)," *Forestry and Wood Technology*, pp. 200–206.

Feng, H., and Yi, W., 2017, "Propagation characteristics of acoustic emission wave in reinforced concrete," *Results in Physics*, Vol. 7, pp. 3815–3819.

Gama, C.D., ed., 1998, *Ruídos e Vibrações Ligados à Utilização dos Explosivos e Equipamentos*.

Heiniö, M., 1999, "Rock Excavation Handbook".

Hustrulid, W., 1999, *Blasting Principles for Open Pit Mining*, Rotterdam, Netherlands, Balkema.

Lopez Jimeno, C., Lopez Jimeno, E., and Carcedo, F.J.A., 1995, *Drilling and blasting of rocks*, Rotterdam, Netherlands, A.A. Balkema.

Sarsby, R.W., 2013, *Environmental geotechnics*, London, United Kingdom, ICE Publishing.

Schermerhorn, L., and Stanton, W., 1969, "Folded overthrusts at Aljustrel (South Portugal)," *Geological Magazine*, 106(2), pp. 130–141.

Svinkin, M.R., ed., 2008, *Soil and Structure Vibrations from Construction and Industrial Sources*, Missouri, United States of America, Missouri University of Science and Technology, 15 pp.

Zielińska, M., and Rucka, M., 2018, "Non-Destructive Assessment of Masonry Pillars using Ultrasonic Tomography," *Materials (Basel, Switzerland)*, Vol. 11, No. 12.

28th European Young Geotechnical Engineers Conference – EYGEC 2024
© 2024 Macedonian Association for Geotechnics, ISBN 978-608-4510-61-1

Physical and mechanical properties of cohesive soil geopolymerized with the fly ash

Luiza I. Rzepczyńska[a]

[a] *SGGW Warsaw University of Life Sciences, Warsaw, Poland*

ABSTRACT

Expansive soils cause geotechnical problems due to volume changes caused by changes in their moisture content. To keep the volume changes in check, designers are forced to use a variety of solutions – from soil replacement to stabilisation with various additives. This research paper focuses on the potential improvement of cohesive soils by geopolymerization with the use of fly ash. Geopolymers are three-dimensional polymer chains composed of Si-O-Al-O bonds, which are formed by dissolving aluminium and silicon minerals in an alkaline solution. The paper presents the results of experimental tests demonstrating the effectiveness of geopolymerization in increasing the strength and stiffness of soil with additives subjected to this process, as well as reducing the shrinkage-swelling phenomenon depending on the moisture content, demonstrates the benefits of using Industrial Solid Wastes (ISW) products in earth construction and offers an expanded opportunity to improve and utilise cohesive soils. The following tests were performed: the granulometric composition of the samples with the addition of fly ash, Atterberg limits (liquidity and plasticity), uniaxial compressive strength of the soil before and after geopolymerization, and free swelling (before and after geopolymerization of the samples). The workability of the soils increased after the addition of fly ash, after geopolymerization of the soils the uniaxial compression strength increased more than 6 times, while the swelling phenomenon was reduced by 95 to 99%.

KEYWORDS

Geopolymerization; Industrial Solid Wase; Uniaxial compression strength; Free swell

1. INTRODUCTION

The raising of increasingly more massive engineering structures, the shortage of areas with suitable ground conditions for its foundations, and the development of communication infrastructure, which is characterised by the need to build in highly varying ground conditions, all contribute to the increasing development of ground stabilization methods and their application on an ever-increasing scale (Szajna, 2021). The expansive soils cause numerous geotechnical problems due to volume changes, that may damage the foundation subjected to extensive deformations. To sustain the volume changes, the designers are forced to apply expensive solutions from soil replacement to soil stabilization with various additions (Fazal, Xu, Babak i Memon, 2020; Puppala, Congress and Banerjee, 2019; Cheng et al., 2018). Chemical stabilisation of problematic soils, in addition to reducing volume changes, improves their engineering properties. Cement and lime stabilisation is effective and gives fast results, so this solution is widely used in geotechnics. Unfortunately, both cement and lime are additives that negatively affect the environment due to the high carbon dioxide emissions during production (Siemieniuk and Szatyłowicz, 2018; Uliasz-Bocheńczyk and Mokrzycki, 2003), which is why alternative approaches to stabilize expansive soils are still being developed. Of particular interest is the use of waste materials for these processes (Seco, Ramírez, Miqueleiz and García, 2011). One such material is fly ash (FA). An Industrial Solid Waste like FA is an alumino-silicate-based material used mostly in concrete. Nevertheless, the FA in the presence of sodium hydroxide can break the Si-O and Al-O ions which leads

to the creation of an inorganic binder named geopolymer. Geopolymerization is a reaction of aluminosilicates and oxides in an alkaline environment (Murmu, Jain and Patel, 2019; Behnood, 2018; Davidovits, 1989) and geopolymers are 3D polymeric chains comprised of Si-O-Al-O bonds created due to the dissolution of Al and Si minerals in an alkaline solution, then the polycondensation takes place forming a 3D geopolymer structure (Phummiphan, Horpibulsuk, Phoo-ngernkham, Arulrajah and Shen, 2017.; Davidovits, 1999).

2. MATERIALS AND METHODS

2.1. Materials

To create the mixtures subjected to testing, the following materials were used:

- Bentonite from the Technical and Trade Enterprise *Certech* "CERTIX G PLUS", containing 39.2% clay fraction and 60.8% silt fraction. Chemical composition analysis revealed that the material mainly consists of silicon dioxide SiO_2 (70.8%) and aluminum oxide Al_2O_3 (17.5%). The mineral composition includes smectite (47.0%), opal (20.0%), clinoptilolite (15.0%) and feldspar (12.0%) (Górniak et al., 2017).
- Kaolin from the "Surmin – Kaolin S. A." mine, containing 8% clay fraction, 34% silt fraction, and 58% sand fraction. Chemical composition analysis showed that the material mainly consists of silicon dioxide SiO_2 (52.1%) and aluminum oxide Al_2O_3 (34.1%). The mineral composition is primarily kaolinite/halloysite (82.0%) and quartz (12.0%) (Zsirka, Horváth, Makó, Kurdi and Kristóf, 2015).
- Siliceous fly ash from the *Puławy* Chemical Plants S.A., containing 8% clay fraction, 36% silt fraction, and 56% sand fraction. This material was obtained from the combustion of lignite coal mined at the *Bogdanka* mine in *Łęczna*. Chemical composition analysis revealed that the material mainly consists of silicon dioxide SiO_2 (55.3%), aluminum oxide Al_2O_3 (26.7%) and contains calcium oxide CaO in the amount of 2.4% (Gil and Golewski, 2018).
- Sodium hydroxide NaOH distributed by the trading company *Solgal*, appearing in granular form with a purity of at least 99%. The CAS number of the substance used is 1310-73-2.

From the above materials, 4 mixtures were created, with their proportions presented in the Table 1.

Table 1. Mix proportions for samples

Mixture	Material content [%]		
	Fly ash	Kaolin	Bentonite
MI0	0	80	20
MII8	8	76	16
MIII16	16	72	12
MIV24	24	68	8

All components were carefully mixed by hand in the designated proportions in a dry air condition. To form samples for testing, distilled water was added. In the next step, to prepare samples subjected to the geopolymerization process, a sodium hydroxide dissolved in distilled water was added to each mixture in an amount of 6% by dry weight of the mixed sample. The samples were cured for periods of 7 and 14 days.

2.2. Research methodology

The following geotechnical property tests were performed as part of the research:

- Determination of the granulometric composition of the dry, non-geopolymerized mixtures according to the guidelines of the Casagrande areometric method in Prószyński's modification.
- Determination of the liquidity limits of non-geopolymerized mixtures using the cone penetrometer method according to the Polish standard PN-88/B-04481.

- Determination of the plasticity limits according to the Polish standard PN-88/B-04481 on non-geopolymerized mixtures.
- Determination of free swelling in the Vasiliev Apparatus, in accordance with ASTM D 4546–03 standard in modification of method A, consisting in ending the test after 48 hours, due to a focus on primary swelling without loading the sample after this period (geopolymerized and not geopolymerized samples).
- Testing of uniaxial compressive strength in the INSTRON 596 apparatus of manually compacted samples in a cylinder using a Proctor hammer, using a standard compaction energy equal to 0.59 J/cm³ (geopolymerized and not geopolymerized samples).

3. RESULTS AND DISCUSSION

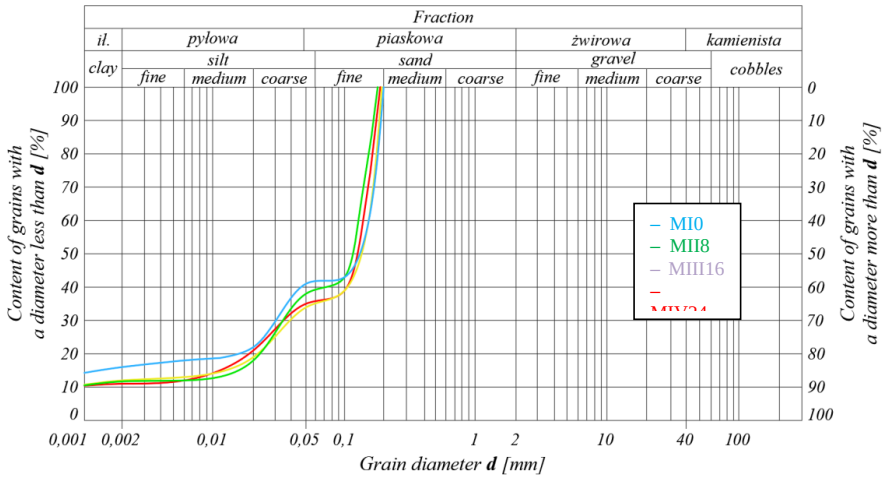


Figure 1. The granulometric curves of the soil mixtures tested.

The granulometric composition analysis for each sample yielded very similar results. The most significant difference was observed in MI0, which lacked the addition of fly ash. It can be characterized according to the PN-EN ISO 14688-1:2018 standard as silty clay, with 16% clay fraction, 27% silt fraction, and 57% sand fraction. MII8, with 12% clay fraction, 31% silt fraction, and 57% sand fraction, can also be classified as silty clay. The remaining two mixtures (MIII16 and MIV24), with the highest amounts of fly ash, are classified as clayey silt.

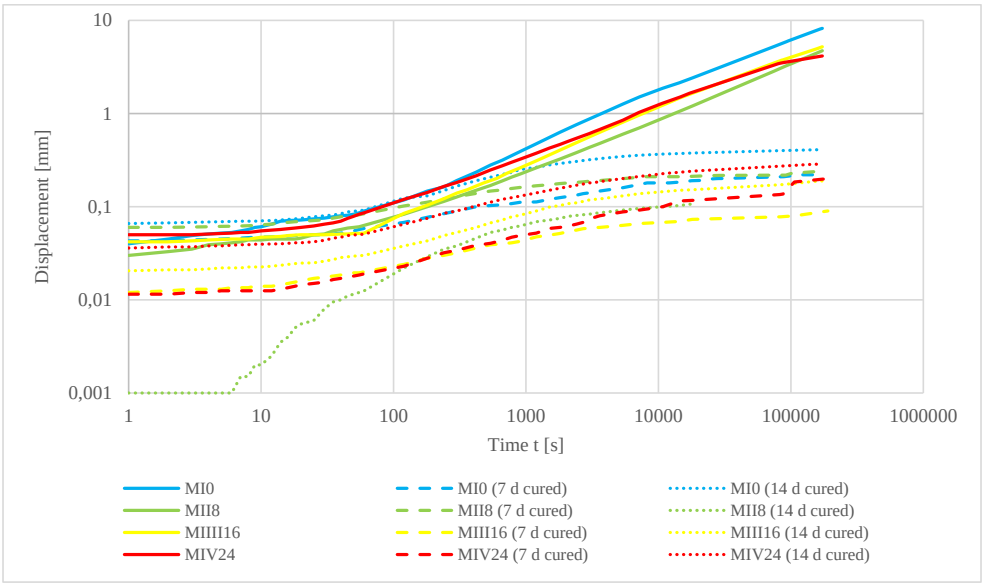


Figure 2. Free swelling diagrams for soil mixtures.

The free swelling test (Fig. 2) showed a significant inhibition of swelling in soils subjected to geopolymerization. It is difficult to pinpoint a specific amount of fly ash that would have the strongest impact on inhibiting this phenomenon. Non-geopolymerized samples, stabilized only with fly ash, did not yield as impressive results as all samples subjected to the geopolymerization process. However, they still inhibited soil swelling compared to the mix without additives by up to 3 mm (a nearly 40% decrease in swelling properties). After the geopolymerization process, the swelling effect of the soil decreased from 95% to 99%, depending on the curing time of the geopolymerized soil. None of the geopolymerized samples swelled by even 0.5 mm over two days, which, compared to the initial height of the samples at 20 mm, means swelling of less than 2.5%. For comparison, a sample of natural soil swelled by more than 8 mm (over 40%) in two days.

The plasticity limit decreases with the addition of fly ash. An exception is the MII8 sample, containing 8% fly ash. Due to the specificity of the plasticity limit test using the rolling method and the subjective evaluation of the moment when the soil transitions from a hard-plastic to a semi-solid state, this measurement can be considered less precise. However, overall, it seems reasonable to state that the plasticity limit decreases with the addition of fly ash to the base mixture.

Table 2. Atterberg limits of soil mixtures.

Mixture	Moisture content of the plasticity limit [%]	Moisture content of the liquid limit [%]
MI0	26.8	141.7
MII8	27.6	120.4
MIII16	24.5	101.5
MIV24	24.0	81.5

The liquidity limit test of the individual mixtures demonstrated how the liquidity limit decreases (on average by 20%) with an increase in the amount of fly ash (by 8 pp.) in the mixture (Fig. 3).

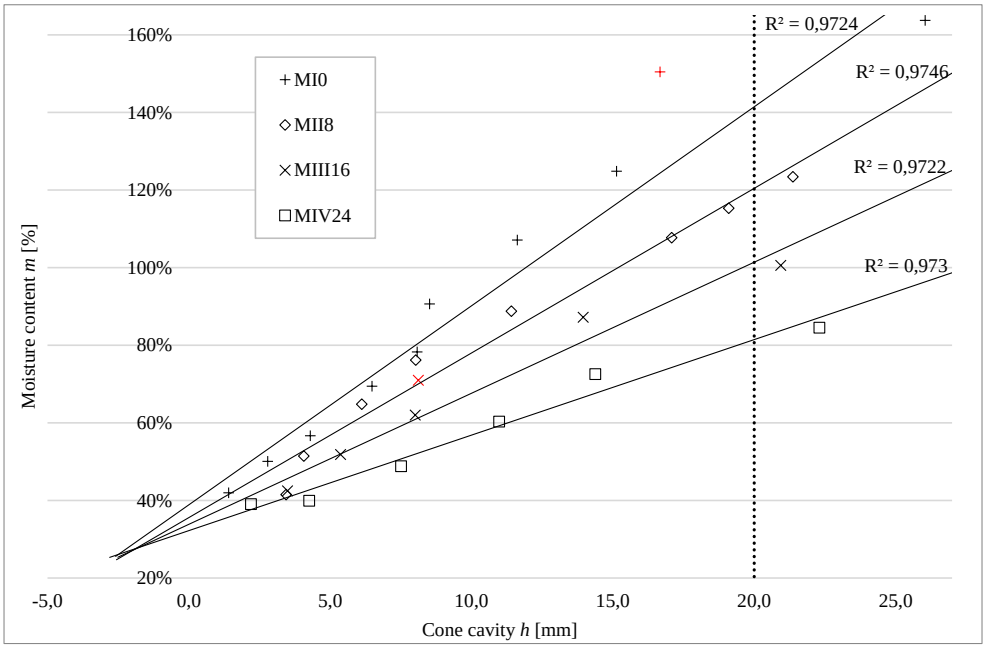


Figure 3. Moisture characteristics of the soil mixtures.

Considering the decrease in both the liquidity and plasticity limits, the plasticity index also decreases, resulting in a change in the soil classification position on the Casagrande plasticity chart. Reduced soil plasticity improves workability.

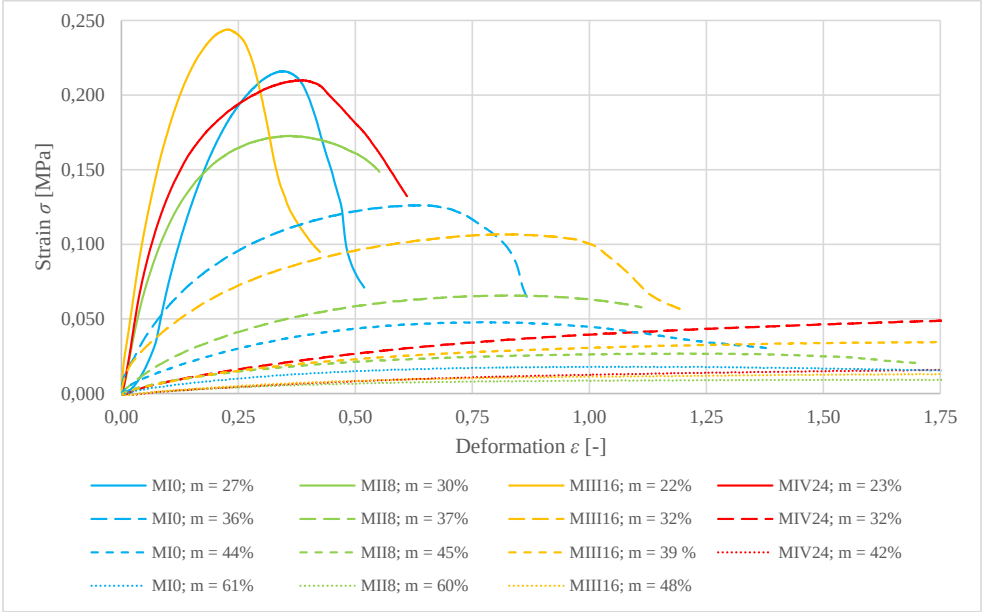


Figure 4. Compressed strength (deformation-strain) plots for non-geopolymerized soil mixtures.

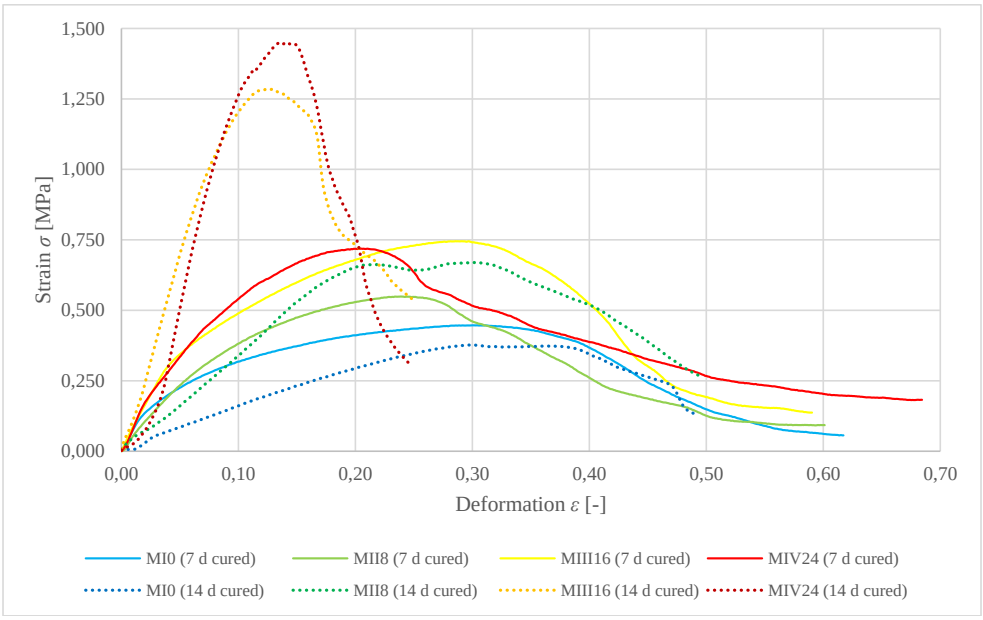


Figure 5. Compressed strength (deformation-strain) plots for geopolymerized soil mixtures.

The uniaxial compression tests precisely showed how geopolymerization of soil with an adequate amount of fly ash increases its strength. In the case of the created mixtures, the soil only needs to be sufficiently moist to be considered hard-plastic. Adding water in subsequent steps only weakened its strength parameters. Geopolymerized samples exhibited a significant increase in strength compared to non-geopolymerized samples after just 7 days of curing,

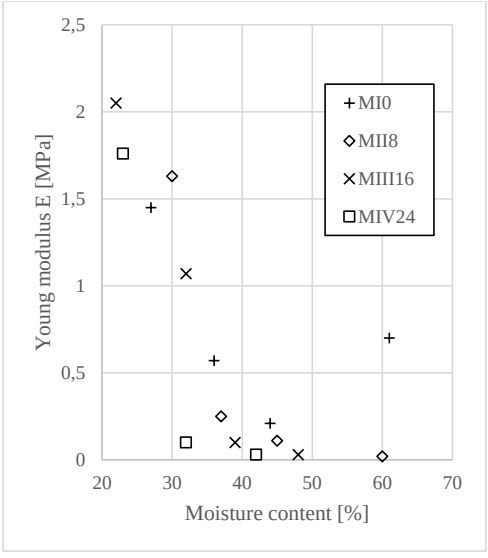


Figure 6. Young modulus of non-geopolymerized mixtures.

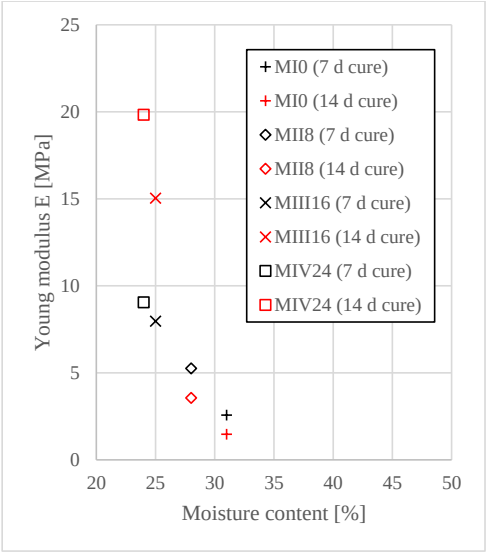


Figure 7. Young modulus of geopolymerized mixtures.

The best strength and stiffness results were shown by geopolymerized mixtures (having the largest amount of reactive aluminosilicate substances capable of reacting with the alkaline solution), compacted at moisture levels closest to their plasticity limit. Such a significant difference in strength results among the geopolymerized samples is a result of both the quantity of fly ash, responsible for the reaction with the sodium hydroxide solution, and the moisture content of the samples. Mixtures MIII16 and MIV24 were compacted using the least amount of water and, after a two-week curing period, showed compressive strength ranging from 1.27 to 1.44 MPa, which corresponds to the strength class $C_{1.2/1.5}$ for cement-stabilized soils according to the PN-EN 14227-10:2006 standard. It is also important to note that the samples tested in this study were cured for 14, not 28 days as the standard assumes. The curing time, which has a different characteristic in the case of geopolymerization compared to cement stabilization, may significantly affect the mechanical and physical properties even 360 days after stabilization, unlike cement stabilization, which reaches its final physical and mechanical property values after 28 days. Part 13 of the PN-EN 14227:2006 standard introduces the possibility of using hydraulic road binder for soil stabilization, while part 15 defines the layers that can be made from soils stabilized with hydraulic binders and the required stabilization classes. The tested geopolymerized mixtures, according to these standards, could theoretically be applied to improved substrates for roads *KR1 – KR7*.

An interesting characteristic of strength was exhibited by MI0 mixture – without fly ash content. The research showed that after 14 days of curing, the compressive strength of the sample slightly decreased in comparison to MI0 mixture cured for 7 days. This could be due to the difference in sample compaction, but it was the only one whose strength decreased or did not increase. Compared to non-geopolymerized soil, compacted at more optimal moisture, the strength only doubled, and the stiffness of the MI0 (m_c = 27%), compared to the sample MI0 (m_c = 31%) after 14 days of curing, almost did not change. This observation highlights the significant impact that the quality of sample preparation can have on the final properties of the soil. This task is especially challenging in the case of geopolymers, where water, the basic additive improving workability, is an undesired agent during the polymerization process. The next step in the development of this method is to find an alternative to water, thus improving workability and enhancing the effect of geopolymerization.

4. CONCLUSIONS

The increasing built-up area along with a growing population forces engineers to construct buildings on lands previously considered economically unfeasible or technologically challenging to tame. An example of such terrain includes locations where the subsoil contains expansive soils. It's sensitivity to the presence of water manifests as a change in their volume depending on the water saturation state. For this reason, when these soils are located directly under the foundations of a building, they cause damage by inducing cracks in parts of the structure. In order to prevent such adverse effects, soil replacement or reinforcement methods are used. Soil improvement is most commonly understood as soil stabilisation using cement or lime. A promising direction for stabilisation is also stabilisation with fly ash, which also serves as a recycling method. On the basis of the laboratory tests carried out, it was determined that soil swelling decreased by 95 - 99% in the case of geopolymerised soil after 14 days of treatment, which, from a practical point of view, can be defined as a complete reduction of the swelling phenomenon in soil under geopolymerisation; the mechanical properties in the form of uniaxial compressive strength increased from 0.22 MPa (for the natural soil non-geopolymerized, compacted at near-optimal soil moisture) to 1.45 MPa (for the soil stabilised by geopolymerization with the addition of fly ash, cured for 14 days, compacted at near-optimal soil moisture) – by 659 % – which is the equivalent of concrete class $C_{1.2/1.5}$. Geopolymerization is a viable alternative to classic chemical stabilisation methods and will therefore increase the land available for construction and reduce the risk of damage to buildings.

REFERENCES

Elia, G., Cotecchia, F., Pedone, G., Vaunat, J., Vardon, P.J., Pereira, C., Springman, S.M., Rouainia, M., Van Esch, J., Koda, E., Josifovski, J., Nocilla, A., Askarinejad, A., Stirling, R., Helm, P., Lollino, P. and Osinski, P. 2017. Numerical modelling of slope–vegetation–atmosphere interaction: an overview. *Quarterly Journal of Engineering Geology and Hydrogeology*, 50(3), 249-270.

Morgan, R.P.C. and Rickson, R.J. 2003. *Slope stabilization and erosion control: a bioengineering approach*. Taylor and Francis.

Vanapalli, S.K. and Lane, J. 2002. A simple technique for determining the shear strength of unsaturated soils using the conventional direct shear apparatus. *Second Canadian Specialty Conference on Computer Applications in Geotechnique*, Winnipeg, Canada. pp.245-253.

ASTM D4546-03. 2003. Standard Test Methods for One-Dimensional Swell or Settlement Potential of Cohesive Soils. ASTM International, West Conshohocken.

Behnood, A. 2018. Soil and clay stabilization with calcium-and non-calcium-based additives: A state-of-the-art review of challenges, approaches and techniques. *Transportation Geotechnics, 17*, 14-32.

Cheng, Y., Wang, S., Li, J., Huang, X., Li, C. and Wu, J. 2018. Engineering and mineralogical properties of stabilized expansive soil compositing lime and natural pozzolans. *Construction and Building Materials, 187*, 1031 – 1038. DOI: 10.1016/j.conbuildmat.2018.08.061

Davidovits, J. 1989. Geopolymers and geopolymeric materials. *Journal of thermal analysis*, 35(2), 429-441.

Davidovits, J. 1999. Chemistry of geopolymeric systems, terminology. *In Geopolymer* (Vol. 99, No. 292, pp. 9-39).

Gil, D. M. and Golewski, G. L. 2018. Potential of siliceous fly ash and silica fume as a substitute for binder in cementitious concretes. *EDP Sciences: E3S Web of Conferences, 49(Article Number: 00003)* DOI: 10.1051/e3sconf/20184900030

Górniak, K., Szydłak, T., Gaweł, A., Klimek, A., Tomczyk, A., Motyka, J. and Bahranowski, K. 2017. Smectite-, silica- and zeolites-bearing raw materials (Hliník nad Hronom bentonite, Slovakia) – A new approach using integrated petrographic and mineralogical studies. *Applied Clay Science, 141*, 180 – 191. DOI: 10.1016/j.clay.2017.02.032

Jalal, F. E., Xu, Y., Jamhiri, B. and Memon, S. A. 2020. On the recent trends in expansive soil stabilization using calcium-based stabilizer materials (CSMs): a comprehensive review. *Advances in Materials Science and Engineering, Article ID 1510969.* DOI: 10.1155/2020/1510969

Murmu, A. L., Jain, A. and Patel, A. 2019. Mechanical properties of alkali activated fly ash geopolymer stabilized expansive clay. *KSCE Journal of Civil Engineering, 23(9)*, 3875-3888.

Uliasz–Bocheńczyk, A. and Mokrzycki, E. 2003. Emisja dwutlenku węgla w przemyśle cementowym. Polityka Energetyczna, tom 6. Zeszyt specjalny 2003, 367 – 375.

Phummiphan, I., Horpibulsuk, S., Phoo-ngernkham, T., Arulrajah, A., and Shen, S. L. 2017. Marginal lateritic soil stabilized with calcium carbide residue and fly ash geopolymers as a sustainable pavement base material. *Journal of Materials in Civil Engineering, 29(2)*, 04016195.

Puppala, A. J., Congress, S. S., and Banerjee, A. 2019. Research advancements in expansive soil characterization, stabilization, and geoinfrastructure monitoring. In *Frontiers in geotechnical engineering* (pp. 15-29). Springer, Singapore.

Seco, A., Ramírez, F., Miqueleiz, L. and García, B. 2011. Stabilization of expansive soils for use in construction. Applied Clay Science, 51(3), 348 – 352. DOI: 10.1016/j.clay.2010.12.027

Siemieniuk, J. and Szatyłowicz, E. 2018. Zmniejszenie emisji CO2 w procesie produkcji cementu. Budownictwo i Inżynieria Środowiska, 9(2).

Szajna, W. 2021. Stabilizacja chemiczna gruntów problematycznych. *Przegląd Budowlany, 92(nr 11 – 12)*, 38 – 43.

Zsirka, B., Horváth, E., Makó, É., Kurdi, R. and Kristóf, J. 2015. Preparation and characterization of kaolinite nanostructures: reaction pathways, morphology and structural order. *Clay Minerals, 50(3)*, 329 – 340. DOI: 10.1180/claymin.2015.050.3.06

28th European Young Geotechnical Engineers Conference – EYGEC 2024
© 2024 Macedonian Association for Geotechnics, ISBN 978-608-4510-61-1

Numerical Analysis of Under-Reamed Pile in layered clay Subjected to Pullout Force

Husam M. Saleh [a*], Maher Murad Jebur [b*], Adnan Qahtan Mohammed [c] Mahdi. O. Karkush

[a] *National Center for Engineering Consultations, Baghdad, Iraq.*
[b,c] *Department of Reconstruction and Projects, University of Baghdad, Baghdad, Iraq*
[a*] husam88mahdi@gmail.com, [b*] maher.murad@coeng.uobaghdad.edu.iq
[c] adnan.k@uobaghdad.edu.iq , mahdi_karkush@coeng.uobaghdad.edu.iq>

ABSTRACT

Under-Reamed Piles (URP) are concrete bored piles with bulbs in the stem. However, the reaction of these piles is poorly understood especially in the pullout conditions. In this article, numerical analyses have been carried out using three-dimensional Finite Element Method (FEM) to investigates the behaviour of (URP) in clayey soils under pullout force. The analysies were carried out using soil properties obtained from field tests. Different reamed position was modelled along the pile stem length L (L, 0.75 L, 0.5 L, 0.25L) to examine the influence of bulb location on the uplift capacity of the (URP) in homogeneous clay. The obtained results were then compared with the uplift capacity of a conventional pile (i.e., without under-reamed). The result proved that the reamed with pile can decrease the vertical displacement for all positions. Furthermore, it was found that (URP) and surrounding soil worked together when the bulb position was 0.75 L, and the tensile bearing capacity (Q_b) increased about 95%, 125% and 83% compared to the straight shaft pile. Overall, the study demonstrated the beneficial impact of the double under reamed pile in enhancing pile foundation capacity in the pull out conditions.

KEYWORDS

Under-reamed pile; finite element method; clayey soil; pullout conditions

1. INTRODUCTION

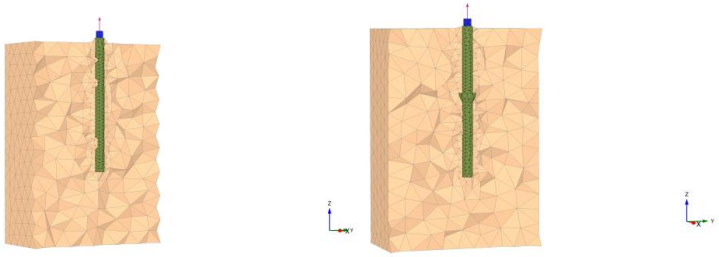
Under-reamed piles were first introduced for expansion of soil in Texas, U. S. A. to considerable ground movement due to soil moisture change. These reams increase the bearing and friction surface of the capacity of the pile in compressive loading (Jebur and Ahmed, 2020). They also improve the pile's bearing uplift (Q_b) by resisting uplift forces similar to an anchor. These piles' higher tensile bearing capacity makes them suitable for use as the foundation for tanks, suspension bridges, and overhead buildings.(Sharma et al., 1978, Jebur et al., 2020). (Shrivastava and Bhatia, 2008) determine the ultimate (Q_b) of single-bulb under-reamed piles in several soils using the (FEM). The result of this study was an equation for the (Q_b) of (URP) in soft clay, loose sand, and silt. (Farokhi et al., in 2014) examined the impact of full-bulb, half-bulb, and uniform cross-section piles with equal volumes on the bearing capacity of these piles under tensile loading. According to this study, uniform cross-section piles of the same length and volume and full-bulb under-reamed bulbs had lower tensile (Q_b) than half-bulb (URP) piles. (Ibrahim and Karkush, 2024) study the behaviour of multi-belled piles that was compared with uniform pile (without bell) in multilayers soil. Single and piles group with single and double bells constructed in two layers of soil were analysed by (FEM) using PLAXIS 3D software. The load-settlement curves of belled piles showed a significant decrease in the settlement compared with a uniform pile range from (0.024 m to 0.0114 m), but no significant difference between single and double belled piles.(Ziyara and Albusoda, 2021) examined how inclined loads affect the behavior of under-reamed piles. The findings demonstrated that while the under-reamed pile experiences less lateral

displacement with increasing vertical load, the normal pile experiences limited effects from compound loads. When compared to a lateral load, the effect of an inclined load on the moments resulting from the combined loads could reach 10%. Additionally, the presence of a bulb in a pile close to ground level seemed to lessen the moments generated for the same load. (Mahdi and Jihad, 2021) shown the experimental model of undreamed piles under static load, which was created by simulating a steel plate on the pile cap. Next, the load-settlement curve, bearing force, and friction force were developed based on the examination of various reamed patterns. When using triple under-reamed piles, it was discovered that several bulbs had a significant reduction in settlement reach of 93%. This is the greatest result when compared to other patterns and the reference pile of the uniform cross-section in the wet state.In this paper, the under-reamed pile performance in clayey soils was studied. Reamed position and its diameter were variables, while the pull-out force required the creation of a vertical displacement equal to 20 mm.

2. MATERIALS AND METHODOLOGY

2.1. Numerical Analysis Methodology

Position and diameter of reamed are more effective in the (Q_b) of (URP), The diameter of the bulb (Du) is two times that of the pile stem (d) in this study, which is equal to 500mm. The pile tip applies the force transmission; in pull-out loads, the (Q_b) of under-reamed pile in cohesion soil is contributed by the adhesion force of the bulb surface and pile surrounding surface(Shrivastava and Bhatia, 2008). Plaxis 3D software in three-dimensional space is used to model the (URP). Additionally, pullout forces are used, with the load that results in a 20 mm vertical displacement serving as a reference point and the maximum bearing capacity of a single under-reamed pile under a tensile load being taken into account. In order to comprehend the (URP) failure mechanism, the maximum bearing capacity of various modelled piles (different bulb positions) has been measured and compared. The hardening soil model has been used to model the soil. The description of the materials used in this study is shown in Table 1.and the soil layer is considered homogeneous. The linear elastic model has been used to simulate the pile with modules of elasticity $3*10^7$ KN/m^2 and unit weight 24 KN/m^3. Optional interface elements are positioned at the edges of under-reamed piles in the software. Interfaces are modelled in conjunction with the pile, and 0.8 was determined to be the reduction factor Rinter. Figure 1 illustrates the 15-noded wedges that are the modelling elements. Along with the modelled piles, Figure 1 also displays the three-dimensional geometry of the numerical model meshing. Figure 1 depicted the vertical displacement of the embedded (URP) in the soil.



(a) (b)

Figure 1. The kind of elements used and the 3D meshing in the Plaxis 3D Foundation (a) uniform pile (b) under-reamed pile.

Table1. Description of the soil material properties used(Phien-Wej et al., 2012).

Soil layer	Su (KPa)	E_{50}^{ref}(MPa)	E_{ur}^{ref} (MPa)	E_{oed}^{ref} (MPa)
Soft clay	17	4.2	33.6	4.2
Medium clay	35	9.2	73.6	9.2
Stiff clay	75	10.2	102	10.2

A series of finite element models were used to study the behaviour of bulbs position in single and double under-reamed pile in three types of cohesion soil, (soft, medium and stiff clayey soil). For each case, four different bulb positions were considered to show the impact of bulbs on the uplift bearing capacity; the dimensions chosen for all the full-scale piles were fixed to be 0.5 m in diameter, 10 m in length, and the bulb diameter Du 1.0 m as depicted in Figure 2.

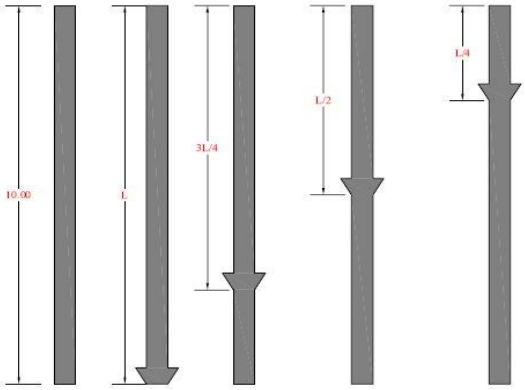


Figure 2. Geometric location of the under-reamed pile and bulb position

3. NUMERICAL MODEL VALIDATION

The accuracy and performance of the proposed PLAXIS 3D software are assessed by comparing the deformation calculated by the programme with those calculated by(Kurian and Srilakshmi, 2010) who studied the behaviour of a (URP) with a bulb diameter of 75 cm using the (FEM) and ANSYS software. Table 2 lists the model's dimensions and the characteristics of the soil that were used to validate the PLAXIS 3D programme. Figure 3 displays the distribution of the under-reamed pile's vertical displacement as determined by (Kurian and Srilakshmi, 2010) and PLAXIS 3D software, where a good agreement is noted, proving the applicability of PLAXIS 3D software for the (URP) analysis.

Table 2. Material properties used in the 3D plaxis model (Kurian and Srilakshmi, 2010)

Material	Dimensions (m)	E (kPa)	γ ($kN/m^{3)}$	υ	C (kPa)	ϕ Degree	ψ Degree	R interface
Pile	4.5 (L) × 0.3 (dia.)	25×10^3	25	0.15	-	-	-	-
Soil	10×10×8	8×10^3	17	0.30	50	10	10	0.12

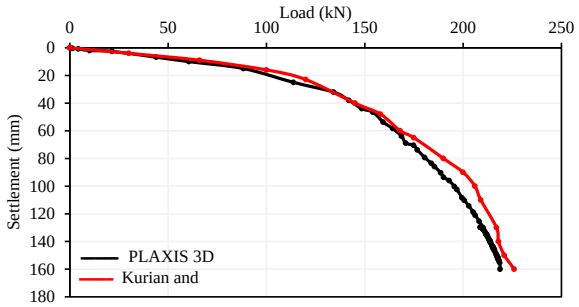


Figure 3. Comparison of the model test result by(Kurian and Srilakshmi, 2010) and the numerical analysis by Plaxis 3D.

4. RESULTS AND DISCUSSION

4.1. Effect of Single Bulb

In this study, a bulb of diameter 1.0 m is provided on the 10m of pile stem, where the bulb position is made to vary. The numerical analysis was carried out to predict the effect of bulbs position and different soil cohesions on the pullout capacity of the (URP). Figure (4-a) presents the deformation shading of the uniform pile (in soft clay) for vertical displacement equal to 20 mm, which is used as a reference point compared with (URP) for different bulbs position. The bulging failure of the soil uplift bearing capacity can be observed.

Figures (4-b-c-d-e) show the deformation shading variations in pullout capacity as the bulbs position change. Here, the optimum bulb position displays in 3L/4 due to shearing soil resistance surrounding the bulbs. This reveals the soil-under-reamed pile interaction mechanism under pull out loading in which the ultimate capacity is highest than other bulbs position and uniform pile.

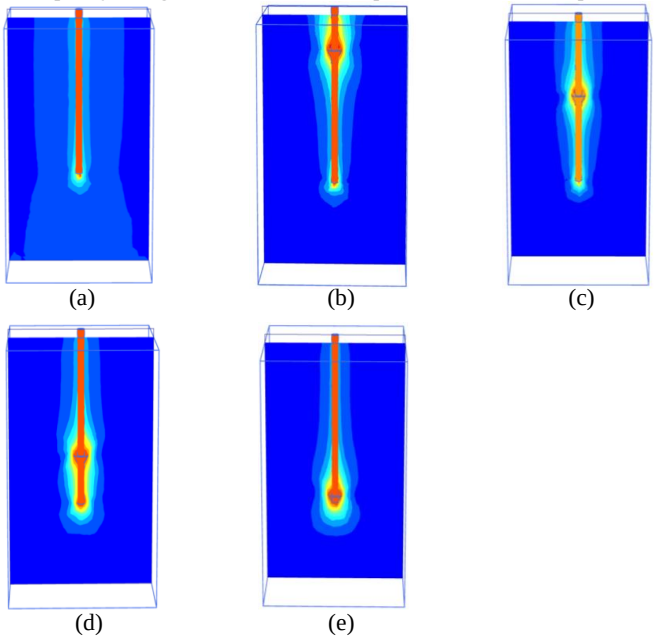


Figure 4. The Deformation Shading of The Single Under-Reamed Pile with Different Bulb Position in Soft Clay Soil (a) Straight Pile (b) 0.25 L (C) 0.5 L (d) 0.75L (e) Bottom

Figure (5-a) shows the relationship between the uplift force and the vertical displacement of pile in soft clay soil, where it is noted that the ultimate load is about (292.78 kN) in the case of a straight pile, and the pile resistance to the uplift force increases when the bulb is placed at different distances relative to the length of the pile. In the case of the position of the bulb (0.25 L) from top, it is observed that the value of the resistance to the uplift force is about (503.84), and when the position of the bulb is at (0.5L) and (0.75L), the uplift force is about (535.15) (571.92) kN respectively, as the maximum value of resistance is reached when the position of the bulb is at (0.75L). The resistance value also decreases to approximately (523 kN) when the bulb position is at the bottom.

In the case of medium clay soil as shown in Figure (5-b), it is observed that the value of resistance to uplift forces increases as a result of the increase in the cohesion value of the soil. It is observed that the most suitable location for the bulb is at (0.75L), where the resistance value reaches a higher value (1204 KN) than it was in the case of the straight pile (535 kN). While the resistance values of the uplift forces are (860-1075 kN) when the bulb location is at (0.25 L-0.5L) respectively. Also, when the bulb is it bottom, the value of resistance to the uplift forces decreases to (967 kN).

Finally, when the soil is stiff as shown in Figure (5-c), the resistance to uplift forces increases clearly, as it is observed that the resistance value of the pile in a straight line is about (1029 kN) and when there is a bulb at the locations (0.25 L-0.5L-0.75L-L) the resistance force is about (1710-1774-1870-1739 kN) respectively.

The importance of the under-reamed is due to providing greater expanded area, it leads to the distribution of applied load over a larger contact area. This reduces the stresses transmitted to the soil and increases the resistance to uplift load.

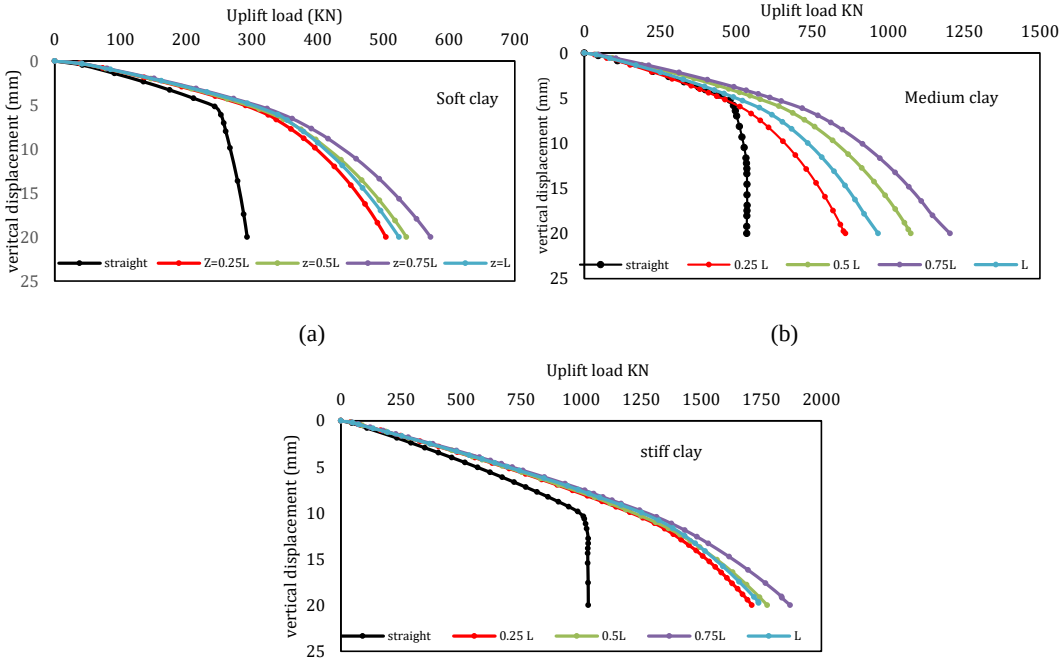


Figure 5. The load-settlement relationship for various locations of bulbs
(a) soft clay (b) medium clay (c) stiff clay

Figure 6 shows that the consistency of the soil has a role in increasing the improvement of the soil resistance to uplift loads, as increasing the consistency of the soil leads to an increase of the skin friction of the pile. The adhesion and cohesion of the soil-bulb system increases if the soil strength increases, which means that the interaction between the soil and the bulb increase to resist uplift load.

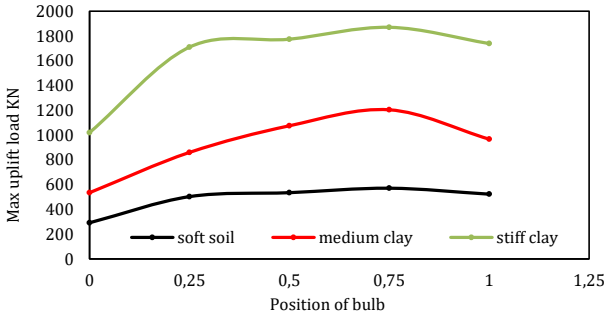


Figure 6. Maximum uplift load under reamed pile for different soil cohesion

4.2. Effect of Double Bulb

In this part, the impact of the double bulb on the pile resistance to uplift force was investigated. First, the most appropriate location for the double bulb in the middle was studied relative to the location of the first bulb that was fixed at a distance (0.75 L) along the length of the pile. The results obtained are shown in the table 3, where it is noted that the resistance to the uplift forces increases when the second bulb located at (D-2D-3D) and at a distance (4D) the increase is somewhat smaller than it was at the location of (3D). It is concluded that the best location for the bulb in the middle when it is on (3D). After that, a comparison was made between the location of the double bulb at a distance (3D) and a distance (0.25 L) from the top of the pile as well as at the location of bulb at bottom of the pile.

Figures 7 shows the relationship between the uplift force and the vertical displacement for soft, medium and stiff soils. It is noted that the location of the double bulb in the middle at (3D) position from the original bulb gives the highest resistance to the uplift force compared to the location of double bulb at the bottom of the pile and the upper part. For the soft soil, the results show that the maximum value of the uplift load of pile is (659 kN) when the bulb is located at the bottom, and it increases to reach (725 kN) when the second bulb is located in the middle and at a distance of (3 D) from the first bulb. In the case of medium and stiff soil, the results show that the maximum value of resistance the pile to uplift force is (1320-2055 kN) respectively. when the location of the bulb is at the bottom, and it increases to reach (1460-2250 kN) when the location of the second bulb is in the middle at (3D) position from the original bulb.

As for the location of the second bulb at the top and at a distance (0.25 L), the results show that the soil failure occurs on the upper side surrounding the bulb as shown in Figure 8. It means that the upper bulb loses the importance in increasing resistance to the uplift load as a result of working separately from the original bulb. This leads to the formation of soil deformation, which reduces the resistance value to the uplift loads. The results are obtained in agreement with results of (Nasr et al., 2022).

Table 3. Maximum Uplift load (KN)

Soil	D	2D	3D	4D
Soft clay	671	692	725	728
Medium clay	1348	1385	1460	1470
Stiff clay	2111	2171	2250	2261

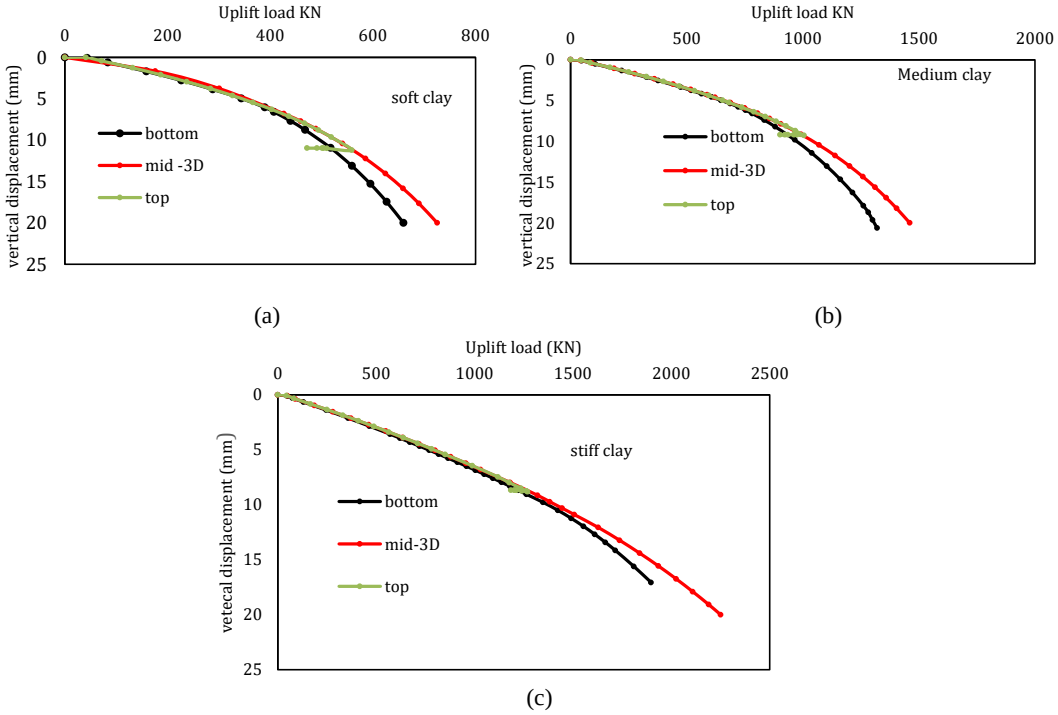


Figure 7. Load-vertical displacement relationship for different double bulb location (a) soft clay (b) medium clay (c) stiff clay

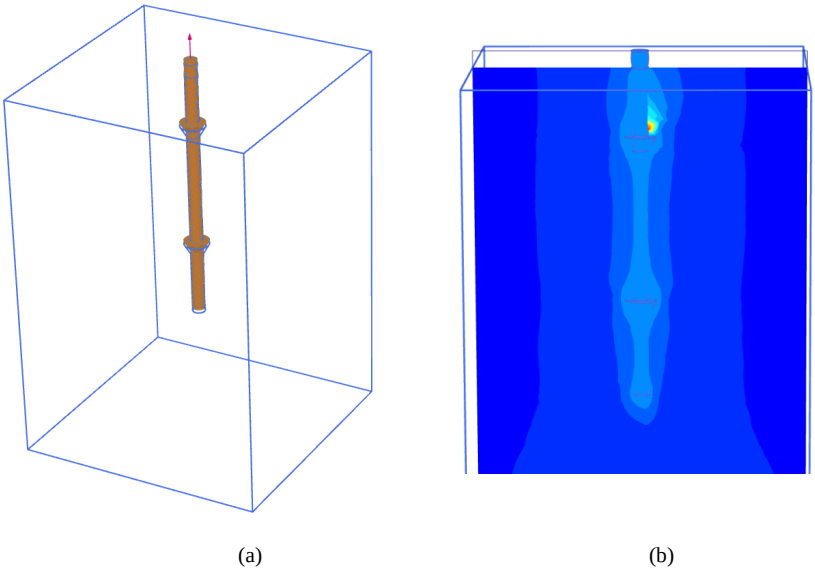


Figure 8. Under reamed pile (a) Section of Double Bulb Under Ream Pile (b) Deformation Shading of the Double Bulb

5. CONCLUSION

- The under reamed pile with bulb is important to enhance resistance to uplift loads compared to the straight pile.
- In the case of a single-bulb pile, the ideal location is where it is (0.75 L), as it gives the maximum resistance to uplift loads compared to other locations.
- In the case of a pile with multi-bulb, the most suitable location for the second bulb is in the middle and at a distance (3D) from the original bulb.
- Increased soil cohesion improves pile resistance to uplift loads

REFERENCES

FAROKHI, A. S., ALIELAHI, H. & MARDANI, Z. 2014. Optimizing the performance of under-reamed piles in clay using numerical method. *Electronic Journal of Geotechnical Engineering,* 19**,** 1507-1520.

IBRAHIM, A. A. & KARKUSH, M. Numerical modeling of multi-belled piles in multi-layers soils under static axial loading. AIP Conference Proceedings, 2024. AIP Publishing.

JEBUR, M., AHMED, M. & KARKUSH, M. Numerical analysis of under-reamed pile subjected to dynamic loading in sandy soil. IOP conference series: materials science and engineering, 2020. IOP Publishing, 012084.

JEBUR, M. M. & AHMED, M. D. Experimental investigation of under reamed pile subjected to dynamic loading in Sandy soil. IOP conference series: materials science and engineering, 2020. IOP Publishing, 012003.

KURIAN, N. P. & SRILAKSHMI, G. 2010. Studies on the geometrical features of under-reamed piles by the finite element method. *Journal of Karunya University,* 2**,** 1-14.

MAHDI, H. A. & JIHAD, A. G. Performance of Under-Reamed Piles in Collapsible Soil. E3S Web of Conferences, 2021. EDP Sciences, 01015.

NASR, A. M., AZZAM, W. & HARRAN, I. 2022. The Behavior of Single Under-Reamed Piles under Compression Load in Clay-Numerical Study. *Journal of Engineering Research,* 6**,** 1-7.

PHIEN-WEJ, N., HUMZA, M. & AYE, Z. Z. 2012. Numerical modeling of diaphragm wall behavior in Bangkok soil using hardening soil model. *Geotechnical Aspects of Underground Construction in Soft Ground***,** 715-722.

SHARMA, D., JAIN, M. & PRAKASH, C. 1978. *Handbook on underreamed and bored compaction pile foundations*, Jain.

SHRIVASTAVA, N. & BHATIA, N. Ultimate bearing capacity of under-reamed pile-finite element approach. The 12th International Conference of International Association for Computer Methods and Advances in Geomechanics (IACMAG), 2008. 1-6.

ZIYARA, H. M. & ALBUSODA, B. S. Impact of Inclined Load on the Performance of Under-Reamed Piles in Clay Soil. IOP Conference Series: Earth and Environmental Science, 2021. IOP Publishing, 012052.

28th European Young Geotechnical Engineers Conference – EYGEC 2024
© 2024 Macedonian Association for Geotechnics, ISBN 978-608-4510-61-1

Determination of the heterogeneity of a dense sand specimen and its evolution in triaxial compression

Selma Schmidt[a], Ivo Herle[a]

[a] *Technische Universität Dresden, Institut für Geotechnik, Dresden, Germany*

ABSTRACT

Standard laboratory tests, such as the triaxial test, are commonly considered to be element tests. With the help of x-ray CT, numerous studies have analysed the grain kinematics and the evolution of the soil fabric inside specimens in triaxial compression. It has been found that the specimen is highly heterogeneous from the beginning of the test and therefore cannot be treated as one single representative elementary volume (REV). Instead, the specimen consists of multiple smaller homogeneous regions. With the help of the REV, the specimen heterogeneity and its evolution can be characterised so that it can be considered in the constitutive modelling of the soil. In this study, the size of the REV is determined for a Hostun sand specimen in triaxial compression regarding not only the void ratio but also two contact fabric descriptors – the coordination number and the scalar anisotropy factor. The REVs are then used to study the heterogeneity of the soil specimen in different loading states. All of the variables localise during the triaxial test but only the contact fabric shows early signs of localisation. Furthermore, the influence of the grid size on the distribution of the variables is analysed as well as the evolution of specific specimen regions. While there is much smaller change below the shear band, the soil above and inside the shear band, respectively, behaves oppositely.

KEYWORDS

Heterogeneity; X-ray CT; REV; Sand

1. INTRODUCTION

The development and calibration of constitutive models, aiming to mathematically describe the soil behaviour, is mostly based on the results of standard laboratory tests, such as the triaxial test. In those tests, the soil specimen is considered to be one single homogeneous element and therefore, the macroscopic response of the specimen is assumed to represent the element behaviour of the soil. But, especially in triaxial tests, one can oftentimes observe the formation of a shear band throughout the test which is opposed to the assumption of homogeneity. Even if no shear band can be observed from the outside, a complex pattern of shear bands can form inside the specimen resulting in a highly heterogeneous specimen. This was already discovered some decades ago by Desrues et al. (1996) for different sand specimens as an early application of x-ray computed tomography (CT) in the field of soil mechanics.

Since then, x-ray CT, and especially micro-focus CT (μCT), has been extensively used to study the soil on the grain scale and major advancements have been made regarding equipment and image analysis tools. With the help of such advanced tools, Desrues et al. (2018) revisited their original experiments and not only confirmed their original results but also discovered localised zones long before reaching the stress peak in the triaxial tests. The formation of shear bands inside the sand specimen seems to be inevitable and starts at such an early stage of the test that their neglect cannot be justified. As Muir Wood (2012) already stated: “the heterogeneous state is the natural state of soils”. Hence, this heterogeneity should also be considered in the development and calibration of the constitutive models.

In order to determine the specimen heterogeneity and its evolution throughout the test with respect to different soil variables, the minimum size of a representative elementary volume (REV) is determined for each variable. The specimen is not assumed to be one single homogeneous element but to consist of multiple smaller homogeneous regions which behave very differently. This was already observed over 50 years ago by Oda (1972) but is usually not considered in the interpretation of triaxial tests. With the help of the REV, the evolution of the soil variables is extracted from specific specimen regions. Furthermore, the distribution of the variables inside the specimen is determined by placing the REV in a regular grid as shown by Hasan and Alshibli (2010). The influence of the grid size on the distribution as well as its evolution are also analysed.

2. IMAGE ANALYSIS

The analysed triaxial test of a dense Hostun sand sample was performed by Wiebicke et al. (2021). The test was performed at 100 kPa cell pressure and 13 µCT images were acquired during the test. Hostun sand has a narrow grain size distribution and a mean grain diameter d_{50} = 338 µm. The image analysis procedure developed by Wiebicke et al. (2019) was applied here in order to reliably detect the grain contacts and calculate the contact orientations. The open-source software spam (Stamati et al., 2020) was used for the entire image analysis. The greyscale images were first binarised using a global threshold and then segmented with a watershed segmentation algorithm. To enhance the contact detection, a local threshold was applied and the contact orientations were calculated based on a random walker segmentation of the contacting grain pair. This allows the contact area to be determined on a sub-pixel level and therefore increases the accuracy of the contact orientation.

Three variables are analysed in this work: the void ratio, the coordination number and the scalar anisotropy factor of the contact orientations. The evolution of those variables for the complete specimen is displayed in Figure 1 together with the macroscopic stress-strain curve. The anisotropy increases with increasing vertical stress as the contacts align with the stress direction but a little delayed because such alignment requires sufficient grain displacements. The void ratio increases as well, which is expected for a dense specimen, and the coordination number decreases as contacts are lost when the grains move apart. The coordination number decreases faster than the void ratio increases as it is more sensitive to changes inside the specimen. This is because very small grain displacements can lead to contacts being lost or gained while larger displacements are needed to change the void ratio noticeably.

In this study, the variables are calculated for cubic elements. The void ratio e is determined by counting all void and solid voxels inside the cube. For the calculation of the fabric variables, a set of grains needs to be defined for the element. All grains with their center of mass inside the cube are assigned to the element here. The coordination number Z, which is the average number of contacts per grain, is then calculated by:

$$Z = \frac{1}{N_p} \sum_{i=1}^{N_p} N_{c,i} \tag{1}$$

where N_p is the number of particles inside the cube, i runs over all grains and $N_{c,i}$ is the number of contacts for each grain. The scalar anisotropy factor a is calculated by:

$$a = \sqrt{\frac{3}{2} \boldsymbol{D} : \boldsymbol{D}} \tag{2}$$

where $\boldsymbol{D}$ denotes the deviatoric fabric tensor calculated from the fabric tensor $\boldsymbol{N}$ composed of the orientations $\boldsymbol{o}$ of all contacts where at least one grain is assigned to the element:

$$\boldsymbol{N} = \frac{1}{N_c} \sum_{\alpha=1}^{N_c} \boldsymbol{o}^{\alpha} \otimes \boldsymbol{o}^{\alpha} \tag{3}$$

with N_c being the number of all considered contacts.

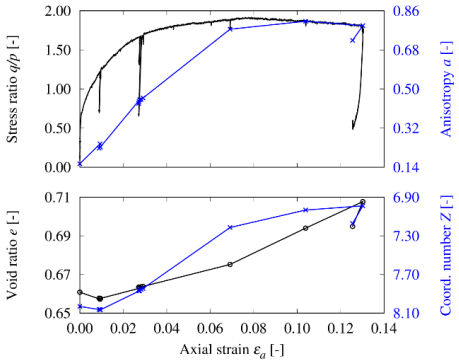


Figure 1. Macroscopic response of the Hostun sand sample to triaxial compression (Schmidt et al., 2022)

3. REV SIZE

The size of the REV was determined as described by Schmidt et al. (2022). For each µCT image, i.e. loading state, cubic elements with increasing size were extracted from four positions along the vertical center line of the specimen. For each size and position, the three variables were calculated and their evolution with increasing element size was determined for each position. The mean and the variance of each variable were calculated from the four positions and their evolution with increasing size was analysed. Following the work of Gitman et al. (2007), a χ^2 test was conducted with a critical value corresponding to an accuracy of 95 % before the formation of the shear band and 90 % after its development. Combining those criteria, a REV size was determined for each variable and loading state and, finally, the maximum size of all loading states was chosen to be the size of the REV for a specific variable.

The REV size for the void ratio is 3.55 d_{50} while it is 5.33 d_{50} for both contact fabric variables. The identified size is the lower limit of the REV size. The upper limit was not determined in this work but most likely relates to the size of the localisation. The smallest possible REV size is used in this study in order to extract the soil variables and their evolution from the individual regions without smearing them too much.

4. SPECIMEN HETEROGENEITY

4.1. Evolution of the heterogeneity

In order to study the heterogeneity of the Hostun sand specimen at each loading state, the REV is placed in a regular grid throughout the sample. The distance between element centers was chosen to be 2.22 d_{50} in order to extract information on a fine grid. The grid was fixed throughout the complete analysis. Elements on the boundary of the specimen, which do not contain a sufficient number of grains to be representative regarding the contact fabric or a sufficient total volume of soil, consisting of grains and voids between them, to be representative regarding the void ratio, are excluded and displayed as black voxels in Figures 2-4.

The evolution of the void ratio distribution throughout the triaxial test is displayed in Figure 2 for a slice through the 3-dimensional specimen. The slice was chosen so that it would contain the shear band. The images correspond to different loading states along the main loading path of the test (cf. Figure 1). Although the same scale is used for all images, a significant variation of the void ratio at the initial state is obvious. The localisation of the void ratio becomes visible at around 7 % of global axial strain and continues to develop until the end of the test. Inside the localised zone, the void ratio strongly increases whereas it does not change much or even decreases outside the localisation.

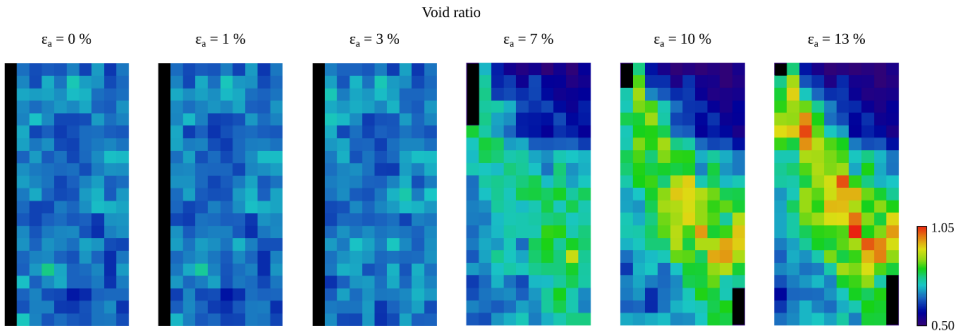


Figure 2. Evolution of the void ratio distribution throughout the triaxial test for a chosen slice through the 3D specimen. Black pixels represent excluded elements with an insufficient total volume of soil inside them

As described above, the coordination number is more sensitive to changes inside the specimen than the void ratio. Therefore, early signs of the localisation of the coordination number are already visible at around 3 % of global axial strain, as can be seen in Figure 3. The coordination number also varies significantly at the initial state and strongly decreases inside the localised zone. The width of the localisation at the end of the test is larger than for the void ratio which implies that the shear band influences the coordination number in a wider zone than the void ratio. This also relates to the higher sensitivity of the coordination number.

The anisotropy shows a similar pattern as the coordination number but with a much more pronounced variation at the initial state and a highly visible localisation already at around 3 % of global axial strain, as can be seen in Figure 4. It can be clearly observed that the localisation originates in the top left and bottom right corner and then develops into a localisation band. The localisation is even broader than for the coordination number which indicates an even higher sensitivity of the anisotropy and hence a wider zone of influence of the shear band.

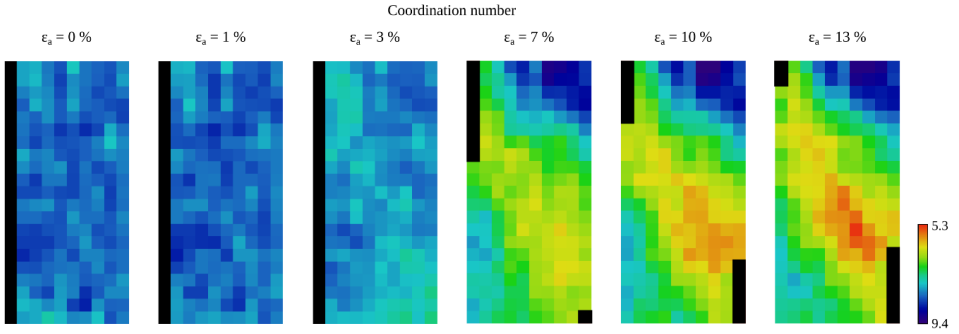


Figure 3. Evolution of the coordination number distribution throughout the triaxial test for a chosen slice through the 3D specimen. Black pixels represent excluded elements with an insufficient number of particles inside them

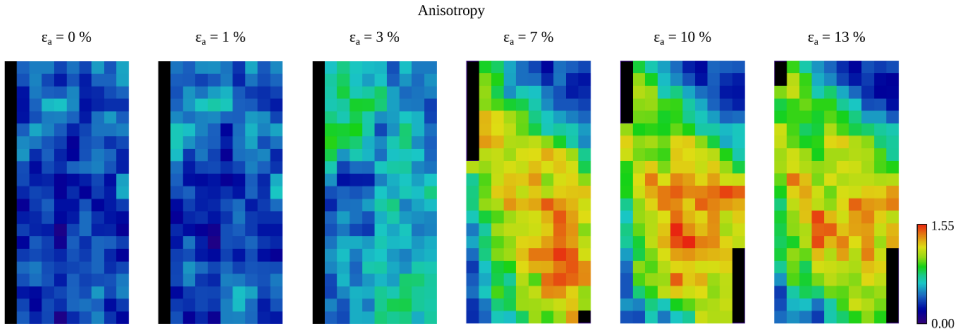


Figure 4. Evolution of the anisotropy distribution throughout the triaxial test for a chosen slice through the 3D specimen. Black pixels represent excluded elements with an insufficient number of particles inside them

4.2. Influence of the grid size

In addition to the visual analysis of the evolution of the specimen heterogeneity, the mean value and the standard deviation of the three variables is calculated for each loading state. To ensure that the chosen grid size does not influence the mean and the standard deviation too much, the calculation is done for three grid sizes and the results are plotted in Figure 5. The distance between the element centers is 2.22 d_{50} for the fine grid, which is the same as above, 4.44 d_{50} for the medium grid size and 8.88 d_{50} for the coarse grid.

For each grid size, the evolution of the mean value and the standard deviation of the variables is displayed as well as the evolution of the min/max range. Although the min/max range changes significantly with an increasing distance between the elements, the mean and the standard deviation do not vary much as can be seen in Table 1 for the void ratio. The minimum and maximum values that can be found inside the elements are very much dependent on the element positions and therefore on the chosen grid. To determine the mean and the standard deviation of the distribution, a smaller sample of elements distributed equally over the specimen can be used.

The results presented in Table 1 highlight ones more the heterogeneity of the specimen and the significant variation already present at the initial state. The standard deviation of the void ratio at the initial state is approx. 4 % with respect to the mean value. At the end of the test, the standard deviation has increased to approx. 17 % in terms of mean value, which is due to the localisation of the void ratio. The coordination number has an initial standard deviation of approx. 2 % and a standard deviation of 12 % with respect to the mean value at the end of the test. The standard deviation of the anisotropy is approx. 30 % in terms of mean value and is the same at the beginning and the end of the test.

Table 1. Mean value and standard deviation of the void ratio for different grid sizes

Axial strain ε_a [%]	Mean value [-]			Standard deviation in terms of mean value [%]		
	Fine grid	Medium grid	Coarse grid	Fine grid	Medium grid	Coarse grid
0	0.661	0.662	0.659	4.22	4.15	3.87
7	0.699	0.698	0.685	10.69	10.85	11.04
13	0.762	0.755	0.746	16.99	17.03	17.63

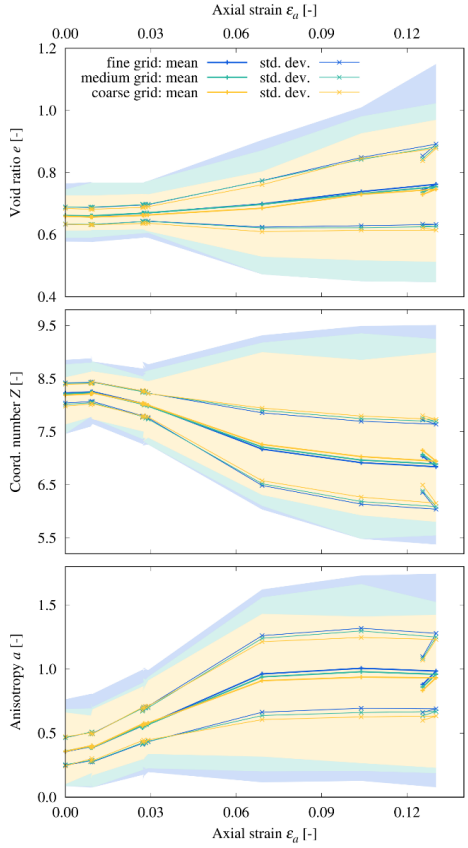


Figure 5. Influence of the grid size on evolution of the fabric distribution inside the specimen. The colored areas display the min/max range of the respective variables

5. FABRIC EVOLUTION INSIDE AND OUTSIDE THE SHEAR BAND

To further analyse the evolution of the three variables in different regions of the specimen, three REVs along the vertical center line of the specimen are chosen and their evolution regarding the void ratio and the contact fabric variables is displayed in Figure 6. Inside the shear band, a strong increase of the void ratio and the anisotropy as well as a strong decrease of the coordination number can be observed, which is also visible in Figures 2-4. Above the shear band, the variables evolve oppositely and below the shear band they show much less evolution. This might be due to the different boundary conditions at the top and bottom of the specimen. The specimen is loaded from the bottom and while the bottom plate is able to rotate, the top plate is completely fixed. It seems that after the formation of the shear band, the soil mass below the shear band acts as a rigid body whereas considerable grain displacements are present above the shear band.

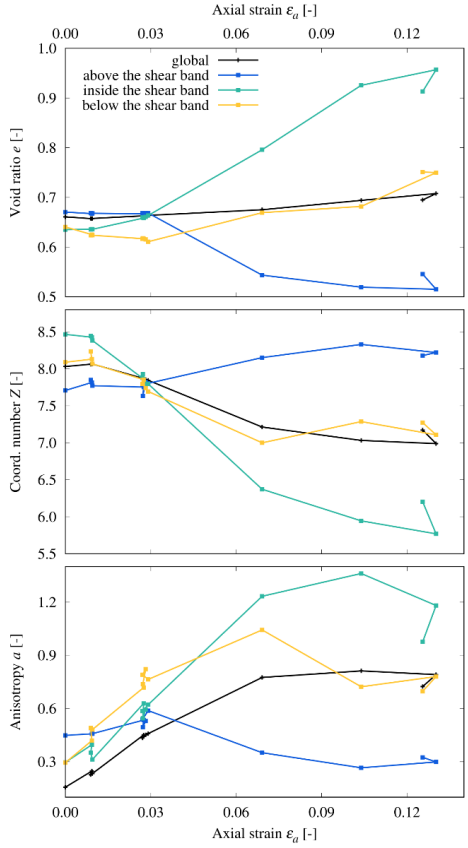


Figure 6. Fabric evolution in REVs above, inside and below the shear band in comparison to the evolution for the complete specimen

6. CONCLUSIONS

In this work, the heterogeneity of a dense Hostun sand sample regarding the void ratio, the coordination number and the contact fabric anisotropy and its evolution throughout a triaxial test is analysed. For this purpose, the size of the REV was determined for each variable and the REV was then placed in a regular grid throughout the specimen. For both contact fabric variables, a REV size of 5.33 d_{50} was identified while the REV size was 3.55 d_{50} for the void ratio. All variables show a significant initial variation and localise throughout the test. The contact fabric, and especially the anisotropy, shows early signs of localisation whereas the void ratio localises later during the test. The distribution of the variables was characterised through the mean value and the standard deviation and the influence of the grid size on those values was studied. The mean and the standard deviation remained approximately the same for the three analysed grid sizes.

In addition, the evolution of the variables inside, above and below the shear band was compared in this work. The regions behave completely differently, which underlines the necessity to consider the heterogeneity of the specimen rather than assuming it to be homogeneous. The initial distribution of the variables and its evolution could serve as a basis for an enhanced calibration of the constitutive models.

It has become clear that the common interpretation of triaxial tests is not in agreement with what is actually observed in those tests for dense sand specimens and that we need to incorporate the soil heterogeneity instead of neglecting it.

7. ACKNOWLEDGEMENTS

We express our thanks to Max Wiebicke, Edward Andò and Gioacchino Viggiani for the allocation of the x-ray CT images analysed in this work. We thank the Center for Information Services and High Performance Computing (ZIH) at TU Dresden for generous allocations of computing resources. The research leading to these results has been funded by the Deutsche Forschungsgemeinschaft (DFG, German Research Foundation) – No. 508562211.

REFERENCES

Desrues, J., Chambon, R., Mokni, M. and Mazerolle, F. 1996. Void ratio evolution inside shear bands in triaxial sand specimens studied by computed tomography. *Géotechnique*, 46(3), 529–546. https://doi.org/10.1680/geot.1996.46.3.529

Desrues, J., Andò, E., Mevoli, F. A., Debove, L. and Viggiani, G. 2018. How does strain localise in standard triaxial tests on sand: Revisiting the mechanism 20 years on. *Mechanics Research Communications*, 92, 142–146. https://doi.org/10.1016/j.mechrescom.2018.08.007

Gitman, I. M., Askes, H. and Sluys, L. J. 2007. Representative volume: Existence and size determination. *Engineering Fracture Mechanics*, 74(16), 2518–2534. https://doi.org/10.1016/j.engfracmech.2006.12.021

Hasan, A. and Alshibli, K. A. 2010. Experimental assessment of 3D particle-to-particle interaction within sheared sand using synchrotron microtomography. *Géotechnique*, 60(5), 369–379. https://doi.org/10.1680/geot.2010.60.5.369

Muir Wood, D. 2012. Heterogeneity and soil element testing. *Géotechnique Letters*, 2(3), 101–106. https://doi.org/10.1680/geolett.12.00019

Oda, M. 1972. Deformation Mechanism of Sand in Triaxial Compression Tests. *Soils and Foundations*, 12(4), 45–63. https://doi.org/10.3208/sandf1972.12.4_45

Schmidt, S., Wiebicke, M. and Herle, I. 2022. On the determination and evolution of fabric in representative elementary volumes for a sand specimen in triaxial compression. *Granular Matter*, 24(4), 97. https://doi.org/10.1007/s10035-022-01262-2

Stamati, O., Andò, E., Roubin, E., Cailletaud, R., Wiebicke, M., Pinzon, G., Couture, C., Hurley, R., Caulk, R., Caillerie, D., Matsushima, T., Bésuelle, P., Bertoni, F., Arnaud, T., Laborin, A., Rorato, R., Sun, Y., Tengattini, A., Okubadejo, O., Colliat, J.-B., Saadatfar, M., Garcia, F., Papazoglou, C., Vego, I., Brisard, S., Dijkstra, J. and Birmpilis, G. 2020. spam: Software for Practical Analysis of Materials. *Journal of Open Source Software*, 5(51), 2286. https://doi.org/10.21105/joss.02286

Wiebicke, M., Andò, E., Šmilauer, V., Herle, I. and Viggiani, G. 2019. A benchmark strategy for the experimental measurement of contact fabric. *Granular Matter*, 21(3), 54. https://doi.org/10.1007/s10035-019-0902-x

Wiebicke, M., Herle, I., Andò, E. and Viggiani, G. 2021. Measuring the fabric evolution of sand – application and challenges. *Geotechnik*, 44(2), 114–122. https://doi.org/10.1002/gete.202000019

28th European Young Geotechnical Engineers Conference – EYGEC 2024
© 2024 Macedonian Association for Geotechnics, ISBN 978-608-4510-61-1

Investigating the Impact of Inhomogeneous Soil Parameters on Shear Strength in Biaxial Tests

Mona Siahkouhi[a], Gertraud Medicus[a], Franz Tschuchnigg[b], Barbara Schneider-Muntau[a]

[a] *Universität Innsbruck, Computational and Experimental Soil Mechanics, Unit of Geotechnical Engineering, 6020, Innsbruck, Austria*
[b] *Computational Geotechnics Group, Institute for Soil Mechanics and Foundation Engineering, Graz University of Technology, Austria*

ABSTRACT

The creation of shear bands in soils is a complex and important geotechnical mechanism that is controlled by different factors, such as soil parameters, loading conditions and loading history. Understanding the development of shear bands is important in order to reliably predict the behaviour of soil in diverse engineering and geotechnical contexts, including slope stability, foundation design and earthworks. Therefore, this study simulates the effect of soil inhomogeneity on the peak shear strength in fine-meshed finite element biaxial tests by using the Hypoplasticity and Mohr-Coulomb constitutive model. For this purpose, hypoplastic calculations were carried out by distributing the initial void ratio with a normal distribution across all elements in a certain range. Similarly for Mohr-Coulomb models, equivalent cohesion, friction angle and elastic modulus were distributed among the elements. The results indicate that the presence of inhomogeneity leads to reaching the peaks strength at lower strain levels. Furthermore, increasing the inhomogeneity leads to a reduction in shear strength for both hypoplasticity and the Mohr-Coulomb model.

KEYWORDS

Inhomogeneous Soil; Shear Strength; Numerical Simulation; Constitutive models

1. INTRODUCTION

Obtaining a comprehensive understanding of the mechanical properties of soil under different loading conditions is essential in the field of geotechnical engineering. In the scientific field of soil behaviour, the presence of inhomogeneity within the soil mass arises as a crucial component that has a substantial impact on its shear strength and deformation patterns (Schneider-Muntau et al., 2021). The presence of inhomogeneity in soil, which is defined by variations in characteristics like density, moisture content, particle distribution, and void ratio, can result in complex stress-strain relationships, the occurrence of strain localization phenomena, and early shear band formation (e.g. Medicus & Schneider-Muntau, 2018; Desrues et al., 2017; 2018). These factors present difficulties for conventional geotechnical analysis and design principles.

Since producing identical samples with the same inhomogeneity patterns is not possible in standard laboratory tests, experimental methods cannot be used to accurately investigate the impact of heterogeneity on peak strength and shear band formation. Consequently, in this study numerical methods are used for the systematic investigations.

2. LITERATURE REVIEW

The impact of soil heterogeneity on shear parameters and the influence on results of finite element simulations has been widely studied in several fields, but mostly focusing und variation of undrained shear strength. Hicks and Samy (2002) employed finite element analysis to determine the effect of heterogeneity on the stability of a clay slope with a spatially varied undrained shear strength c_u. The findings suggested that, for a given factor of safety, reliability in the simulation results is optimum when c_u is constant with depth. As c_u increases linearly with depth, reliability reduces due to the wider variety of probable rupture surfaces. In this study, horizontal anisotropy (of heterogeneity) produces minor variations in reliability. Nevertheless, situations have been observed in which anisotropy is expected to have a substantial impact. Hicks and Spencer (2010) studied the effect of heterogeneity in undrained shear strength on the performance of a long slope cut in clay. Random field theory is used to model heterogeneity. It has been demonstrated that, while the selected slope geometry, loading conditions and mean strength profile are all two-dimensional, the presence of 3D material heterogeneity indicates that the slope is not genuinely 2D. Ching and Phoon's (2013) research primarily focused on studying simple and uniform stress situations. Undrained compression and shear were applied to a 12.8 m wide by 48 m high plane strain soil specimen using finite element analysis (FEA). The mobilized strength statistics are found to be closely related to the statistics generated by the minimum of line averages along possible slip curves. The orientations of critical slip curves are mostly influenced by mechanics rather than spatial variation. However, the vertical positions are somewhat random and depend on the realizations of random fields. The crucial slip curve's line average is the lowest value among the line averages for the potential slip curves. Li et al. (2014) studied the infinite slope reliability with spatially varying shear strength parameters that rise linearly with depth. The spatial variability of undrained shear strength and friction angle is described using random field theory. The influence of geographical heterogeneity on critical slip line depth and failure probability is examined using infinite slope instances. The results show that the clay slope stability is affected by the mean trend of shear strength parameters. Ignoring a linearly rising shear strength trend will overestimate failure probability. Critical slip lines at the slope bottom are less likely when the mean trend of undrained shear strength is included. The distribution of sandy slope critical failure depths is affected by the friction angle's linearly rising mean trend. Anoyatis et al. (2023) represented soil inhomogeneity by using a power law relationship to describe the variation of shear modulus with depth. Their study emphasized the impact of inhomogeneity on the interaction between soil and piles during vertical vibrations and provided a new analytical solution for piles that are subjected to axial loads in heterogeneous soils. Chidichimo et al. (2014) performed an investigation by using 1-g shaking table test results on the effect of soil inhomogeneity and nonlinear simulation on kinematic soil-pile interaction and its bending by passage of vertically propagating seismic shear waves. The inhomogeneity was applied by using two vertical layers of soil that have different strength parameters. The findings demonstrate that these parameters have a significant impact on both site response and kinematic pile bending. Therefore, nonlinear analysis is essential for accurately predicting the dynamic response of pile foundations. Schneider-Muntau et al. (2021) investigated the scattering in strength by comparing results of compression drained triaxial tests at different stress levels and with repeated test on samples with the same mean density. The impact of the number of stress levels on determination of the shear strength parameters, was assessed quantitively. Results demonstrated that repeatability of laboratory experiments are not given, even when same sample preparation procedure, same mean density and same stress level are investigated. This leads to a statistically wide range of potential shear parameters that can be obtained due to inhomogeneities in sample preparation.

Most of mentioned investigations tried to study the effect of inhomogeneity on the strength parameters, by applying inhomogeneity in different ways e.g. variation of water content on density, shear modulus inside the studied samples. Since producing a sample with controlled inhomogeneity is experimentally very difficult, this study aims in performing numerical simulations of fine meshed biaxial tests with two different constitutive models to investigate the influences observed by soil heterogeneity. In this study inhomogeneity was implemented by variation of void ratio which is a state variable in hypoplasticity.

3. METHODOLOGY

3.1. Numerical Simulation Framework

This work utilizes the finite element software ABAQUS 2019 for numerical modelling to investigate the effect of inhomogeneity on the soil behaviour. Due to the influence of element size and shape function on the precision of numerical models, especially in investigations related to strain localization, mesh dependency analysis was performed. This procedure entailed doing initial simulations to assess the impact of various element sizes on the outcomes. We have observed the expected influence of mesh dependency also in our results. However, to obtain comparable results, in this study all analyses were performed based on the same finite element mesh.

2D consolidated and drained biaxial tests with 5000 plane strain elements with a bilinear shape function were simulated. Boundary conditions and the geometry are shown in Figure 1. The sample is fixed at the middle node of the bottom plate and horizontal displacement of the bottom elements is allowed, while they are constrained in vertical direction. The side boundaries are free to move in vertical and horizontal direction. The displacement-controlled shearing is applied by a prescribed displacement δ of the top nodes. This indicates that the soil sample has the ability to undergo vertical and horizontal expansion or contraction. Samples were subjected to three different confining pressure levels. (σ'_3 = 50, 120, and 200 kPa)

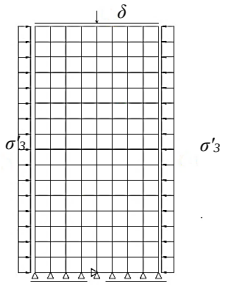


Figure 1. Schematic boundary and loading conditions

In our investigations, three different mean values for the void ratio distribution (e_{mean}) were considered: 0.51, 0.57, and 0.64. To achieve modelling inhomogeneous samples, standard deviation values (*SDV*) of 0.01, 0.05, and 0.08 from the mean values were taken into account, and the void ratio was normally distributed across the elements of soil sample.

3.2. Material

This study uses Weald clay as material (Weifner and Kolymbas, 2008; Mašín, 2013). The determination of the range of possible e_{mean} was done based on critical state relationships, considering the loading range between 50 – 300 kPa. The hypoplastic parameters φ_c = 24º, N = 0.8, λ^* = 0.059 and κ^* = 0.018 were chosen according to Mašín (2013). Modulus. For the Mohr-Coulomb model dilatancy angle ψ and Poisson's ratio ν assumed to be respectively 0 and 0.3.

3.3. Constitutive Models

For the first series of simulations hypoplasticity was chosen to simulate the soil behaviour. This model employs void ratio as one of the state variables ($\dot{\boldsymbol{\sigma}} = \mathbf{h}(\boldsymbol{\sigma}, \boldsymbol{D}, e)$) and enables us to apply variations in the void ratio to represent the inhomogeneity. This represents well what is expected to be relevant in real soil samples.

In the second step a series of modelling was performed using the Mohr-Coulomb constitutive model. To establish comparability between the two sets of simulations, equivalent values for cohesion c, friction

angle φ, and elastic modulus E were chosen based on the corresponding void ratio value e in the hypoplastic model. As the void ratio scatters in the fine meshed sample, a wide range of void ratios had to be considered: e = 0.400-0.799.

In order to calculate the equivalent parameters a series of hypoplastic single element triaxial compression tests (CD) with three different confining pressures (50, 120 and 200 kPa) were simulated. Cohesion, friction angle and elastic modulus were derived from the triaxial stress-strain relationships (Equation (1), (2)) obtained from the simulation with hypoplasticity for each of the relevant void ratios by using the following formulations where ε_{ii}, γ_{ij}, σ_{ii}, τ_{ij} represent normal strains, shear strains, normal stresses and shear stresses, M is the slope of trend line drawn between peak deviatoric stresses (q_{peak}), p' shows the effective mean stress, q_{50} = 0.5. q_{peak}, ε_{q50} would be the value of deviatoric strain corresponding to q_{50} and E_{50} is considered as elastic modulus for the Mohr-Coulomb model.

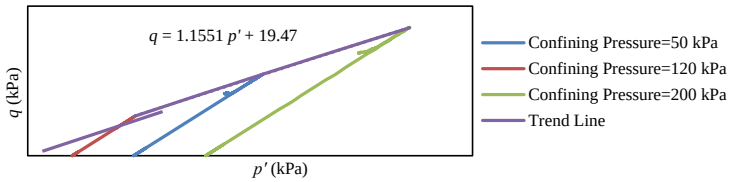


Figure 2. A sample of p'-q diagram for determining equivalent Mohr-Coulomb parameters for e =0.450

$$\varepsilon_q = \sqrt{\frac{2}{9}[(\varepsilon_{22}-\varepsilon_{33})^2+(\varepsilon_{33}-\varepsilon_{11})^2+(\varepsilon_{22}-\varepsilon_{11})^2]+\frac{1}{3}(\gamma_{23}{}^2+\gamma_{31}{}^2+\gamma_{13}{}^2)} \quad (1)$$

$$q = \sqrt{\frac{1}{2}[(\sigma'_{22}-\sigma'_{33})^2+(\sigma'_{33}-\sigma'_{11})^2+(\sigma'_{22}-\sigma'_{11})^2]+3(\tau_{23}^2+\tau_{31}^2+\tau_{12}^2)} \quad (2)$$

$$M = \frac{6\sin\varphi}{3-\sin\varphi} \quad (3)$$

$$q = Mp' + M\frac{c}{\tan\varphi} \quad (4)$$

$$E_{50} = \frac{q_{50}}{\varepsilon_{q50}} \quad (5)$$

With this procedure, we obtain a parameter set of cohesion, friction angle and young's modulus for each single void ratio. In the last step a series of fine meshed simulations were performed by using the linear elastic - perfectly plastic Mohr-Coulomb constitutive model and scattered parameters to observe the soil behaviour in case of heterogeneity presence in soil sample. In order to have comparable results, according to the void ratio e of each element in the hypoplastic fine meshed simulation, the equivalent cohesion c, friction angle φ, and elastic modulus E were assigned to the corresponding element. As it was expected the same inhomogeneity pattern was produced for all shear parameters as can be observed in the plots (Figure 3). Hence, we would have samples with identical inhomogeneity distribution to investigate the soil behaviour with two different constitutive models.

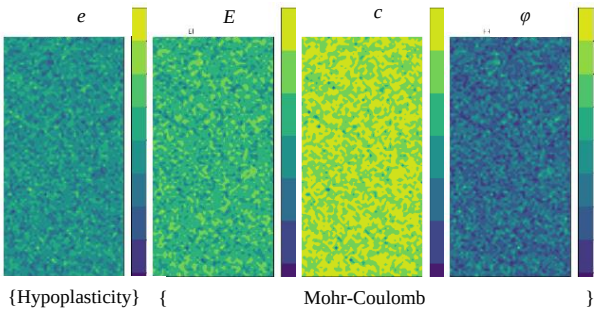


Figure 3. Contour plot of soil sample with scattered void ratio (hypoplasticity), elastic modulus, cohesion and friction angle respectively from left to right (Mohr-Coulomb)

4. RESULTS

The results in Figure 4 show the relationship between the average value of deviatoric stress q and the deviatoric strain ε_q for all elements of soil samples modelled with the hypoplasticity constitutive model (HP) for confining pressure σ'_3 = 120 kPa. Each curve represents a soil sample with a certain mean void ratio (e_{mean}) which is normally distributed in a range represented by the standard deviation value *SDV*. As mentioned before 0.51, 0.57, and 0.64 were considered as e_{mean} values and 0.01, 0.05, and 0.08 as *SDV* in the simulations. It should be noted that in the following text the term void ratio e refers to the mean value of this parameter in a soil sample.

The highest influence on peak strength is given by e_{mean}, that shows reduction of shear strength due to decrease in e_{mean}. This can be explained with the peak strength for denser samples. The charts further illustrate that by increasing the *SDV* from the mean void ratio e_{mean}, there is a tendency for the peak deviatoric stress q_{peak} of the soil to decrease. These findings show that a higher scattering in the soil sample leads to a drop in shear strength. The influence of *SDV* on both shear strength and stress-strain behaviour is visible in all values of e_{mean}. Nevertheless, the impact is more prominent when e_{mean} is smaller. Within a given sample, it is observed that the deviatoric strain ε_q corresponding to q_{peak} tends to decrease as the *SDV* increases. This suggests that soil samples with more heterogeneity have decreased brittleness. After the peak state, the curves exhibit a tendency to reduce the q value, particularly in samples with higher e_{mean} values. This suggests that samples with e_{mean}, indicating a denser soil, show a more noticeable q reduction behaviour. The q reduction rate and extent seem to be affected by the variability in void ratio, since more homogeneous samples (with lower *SDV*) exhibit a sharper decrease after reaching the peak, suggesting a more brittle failure.

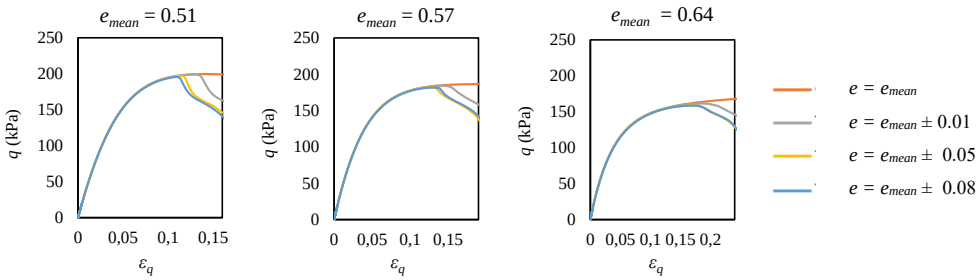


Figure 4. q (kPa) - ε_q results for Simulation of CD biaxial test using HP (σ'_3 = 120 kPa)

Although the Mohr-Coulomb model may not reflect soil's non-linear behaviour, it can still offer valuable observations into the general trends of the inhomogeneity effect on the shear strength of soil.

The graphs in Figure 5 global behaviour shows a continuous reduction in peak deviatoric stress as *SDV* increases. The observed pattern is consistent with the hypoplasticity studies, indicating that greater inhomogeneity reduces soil shear strength. When comparing with the results from simulations with hypoplasticity, it is clear that the strain at peak stress shows smaller values and remains rather similar across varied *SDV*. However, there is a clear trend in which samples with smaller strength and stiffness parameters (which correlate to higher void ratios) exhibit peak stress at higher strains.
Given the findings on hypoplasticity, the curves generated using the Mohr-Coulomb model (MC) show a drop after the peak stress, indicating a global q reduction reaction. This behaviour indicates that the soil experiences a decrease in shear strength, which is due to the localization of the deformation in shear bands.

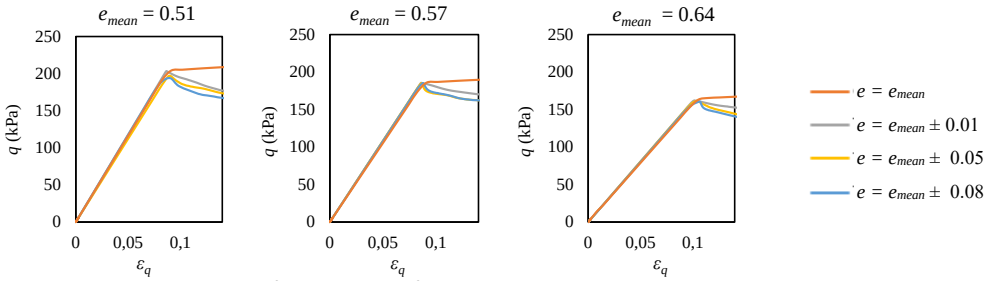


Figure 5. q (kPa) - ε_q results for Simulation of CD biaxial test using MC constitutive model (σ'_3 = 120 kPa)

In Figure 6 results of samples respectively simulated by using hypoplasticity and Mohr-Coulomb as constitutive model, demonstrate the effect of mean void ratio e_{mean} and confining pressure on the shear strength of soil samples. q_{peak}, representing the maximum deviatoric stress of a soil sample with scattered parameters is normalized by $q_{constant}$, which is the maximum deviatoric stress for a sample with constant void ratio e_{mean}. This value is displayed in dependency of the *SDV* of the void ratio. The ratio of q_{peak} /$q_{constant}$ is always ≤ 1, when the *SDV* ≥ 0. This means scattering the void ratio leads to a reduction in shear strength.

By comparing Figure 6 (a and b) it can be noted that the effect of *SDV* on shear strength becomes less considerable in higher e_{mean}. In general, it can be observed that Mohr-Coulomb gives lower q_{peak} /$q_{constant}$ in samples that are heterogeneous and therefore is even more sensitive to inhomogeneity in comparison to hypoplasticity. It can be concluded that weak elements within the soil sample play the role in failure mechanism.

Figure 6 (c and d) illustrate the effect of confining pressure on the shear strength of soil. For both cases increasing the confining pressure reduces the effect of inhomogeneity. This influence is more obvious in looser samples with lower e_{mean}.

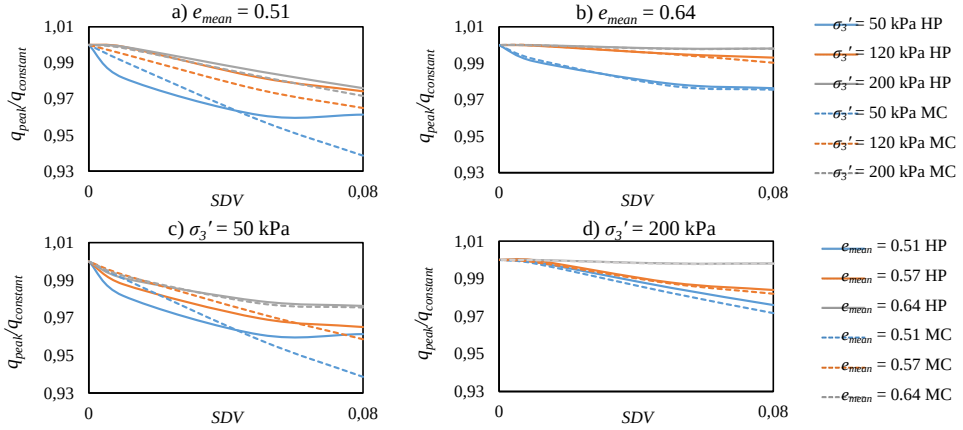


Figure 6. Effect of mean void ratio (a, b) and confining pressure on shear strength variation (c, d)

To summarize the results, it can be concluded that inhomogeneity causes reduction in shear strength and as the inhomogeneity level increases this effect would be more obvious and significant. This effect can be controlled by the confining pressure where in higher pressures inhomogeneity would have less effects on shear strength.

5. DISCUSSION

It is predicted by both hypoplastic and Mohr-Coulomb models that soil heterogeneity, as demonstrated by the use of non-uniform void ratio in hypoplasticity and non-uniform c, φ, and E in Mohr-Coulomb model, significantly impacts shear strength of biaxial tests in numerical simulations. Under the same circumstances, the Mohr-Coulomb model showed a more substantial reduction in shear strength than the hypoplasticity model, with increase in void ratio variability. As hypoplasticity incorporates a stress dependent stiffness, simulations with hypoplasticity show in general higher deviatoric strain at peak. For a given void ratio, both models show that deviatoric strain ε_q in q_{peak} decreases as *SDV* grows, the sample behaves less stiff.

One major difference between the two constitutive models chosen for this simulation, lies in the fact that for hypoplasticity, the void ratio is a state variable. This means the void ratio changes within the elements during the simulation procedure and with this localization effects can be better reproduced. In the Mohr-Coulomb model, the assigned strength and stiffness parameters are not updated during the simulation. This means, the original pattern of parameters remains constant during the simulation.

Given how inhomogeneity affects soil shear strength and strain, this behaviour of the soil promotes the significance of considering it in geotechnical design. Since all constitutive models have their advantages and shortcomings, it is important to select a constitutive model that fits the needs of a given geotechnical study. The results show how important it is to characterize soil properly and choose constitutive models in numerical models suitably. When it comes to numerical analysis and design, the apparent impact of soil inhomogeneity on shear strength is crucial. The findings are applicable in constructions where soil shear strength plays the main role in the failure process and soil inhomogeneity is a determining factor.

6. CONCLUSION

The study conducted numerical simulations to obtain a qualitative insight on how soil inhomogeneity affects shear strength and strain localization in biaxial tests. In this study hypoplasticity and Mohr-Coulomb constitutive models were used. The investigation yields the following conclusions:

- The results showed that the variability in shear parameters of soil within a sample has a substantial impact on determining the soil's shear strength. Both constitutive models indicated a reduction in shear strength as the variability range of the parameters increased, highlighting the importance of soil inhomogeneity assessment in analysis.
- It was observed that the effect of variability in shear parameters is more obvious in lower ranges of confining pressure and for looser soil samples. This observation shows the remarkable influence of loading condition on soil behaviour. Increasing the confining pressure leads to a higher shear strength, independent of the *SDV* and e_{mean} value.
- The strain corresponding to the peak strength showed higher values in the hypoplastic model than in the Mohr-Coulomb model. The scattering influences the stiffness of the sample, the higher the inhomogeneity, the less stiff the sample behaves.

As a conclusion, the study demonstrated the significance of selecting an appropriate constitutive model and accurate shear parameters on the outcomes of the simulation. The approach of having the void ratio as a state variable in the constitutive models is advantageous when simulating soils with inhomogeneous density in laboratory experiments.

REFERENCES

ABAQUS Analysis user's manual 6.14-EF (2014). Dassault Systems Simulia Corp. Providence, RI, USA.

Anoyatis, G., François, S., Orakci, O., & Tsikas, A. (2023). Soil–pile interaction in vertical vibration in inhomogeneous soils. Earthquake Engineering & Structural Dynamics, 52(14), 4582-4601.

Chidichimo, A., Cairo, R., Dente, G., Taylor, C., & Mylonakis, G. (2014). 1-g experimental investigation of bi-layer soil response and kinematic pile bending. Soil Dynamics and Earthquake Engineering, 67, 219-232. https://doi.org/10.1016/j.soildyn.2014.07.008

Ching, J., & Phoon, K. K. (2013). Mobilized shear strength of spatially variable soils under simple stress states. Structural Safety, 41, 20-28.

Desrues, J., Andò, E., Bésuelle, P., Viggiani, G., Debove, L., Charrier, P., & Toni, J. B. (2017). Localisation precursors in geomaterials?. In Bifurcation and Degradation of Geomaterials with Engineering Applications: Proceedings of the 11th International Workshop on Bifurcation and Degradation in Geomaterials dedicated to Hans Muhlhaus, Limassol, Cyprus, 21-25 May 2017 11 (pp. 3-10). Springer International Publishing.

Desrues, J., Andò, E., Mevoli, F. A., Debove, L., & Viggiani, G. (2018). How does strain localise in standard triaxial tests on sand: Revisiting the mechanism 20 years on. Mechanics Research Communications, 92, 142-146.

Hicks, M. A., & Samy, K. (2002). Influence of heterogeneity on undrained clay slope stability. Quarterly Journal of Engineering Geology and Hydrogeology, 35(1), 41-49.

Hicks, M. A., & Spencer, W. A. (2010). Influence of heterogeneity on the reliability and failure of a long 3D slope. Computers and Geotechnics, 37(7-8), 948-955.

Li, D. Q., Qi, X. H., Phoon, K. K., Zhang, L. M., & Zhou, C. B. (2014). Effect of spatially variable shear strength parameters with linearly increasing mean trend on reliability of infinite slopes. Structural safety, 49, 45-55.

Mašín, D. (2013). Clay hypoplasticity with explicitly defined asymptotic states. Acta Geotechnica, 8, 481-496.

Medicus, G., & Schneider-Muntau, B. (2018). Simulations of fine-meshed biaxial tests with barodesy. Geosciences, 9(1), 20.

Schneider-Muntau, B., Medicus, G., Desrues, J., Andò, E., & Viggiani, G. (2021). Investigation of Uncertainty in Strength Parameter Identification. In Challenges and Innovations in Geomechanics: Proceedings of the 16th International Conference of IACMAG-Volume 1 16 (pp. 277-284). Springer International Publishing.

Wang, S., Gao, X., Ma, W., Li, G., Shi, C., & Zhang, P. (2021). Empirical formulas of shear modulus and damping ratio for geopolymer-stabilized coarse-grained soils. Frontiers in Physics, 9.

Weifner, T., & Kolymbas, D. (2008). Review of two hypoplastic equations for clay considering axisymmetric element deformations. Computers and Geotechnics, 35(5), 760-774.

28th European Young Geotechnical Engineers Conference – EYGEC 2024
© 2024 Macedonian Association for Geotechnics, ISBN 978-608-4510-61-1

Dynamic simulation and optimisation of plate compactors for subballast compaction during rail track rehabilitation

Julian Sigmund[a], Johannes Pistrol[a], Dietmar Adam[a]

[a] *Institute of Geotechnics, TU Wien, Vienna, Austria*

ABSTRACT

The sufficient compaction of the formation protective layer (FPL) during track rehabilitation is a crucial process to improve the longevity of railways. Plate compactors are used to ensure sufficient compaction during track-bound rehabilitation works. The most common plate compactor in Austria (Wimmer WBB 530) comprises a frame and a dynamically decoupled, vibrating base plate which includes a rotating mass type of exciter. As the FPL has a thickness of 40 cm (after compaction) ensuring a sufficient compaction presents a challenge to the comparatively light plate compactor. During prior investigations, a mechanical model was developed to determine the motion behaviour of the plate compactor and the interaction between plate compactor and soil during compaction. Additionally, the motion behaviour of the given plate compactor was monitored and analysed during field tests. This paper juxtaposes the simulated motion behaviour and the interaction between plate compactor and soil with data collected during experimental field tests. The investigation shows that the mechanical model can sufficiently replicate the different modes of operation which occur during compaction and can be used for an optimization of the compactor. The measured data corresponds to the simulations. However, the measurements also show that the plate compactor and its periodic loading of the soil highly depends on a careful selection of process parameters.

KEYWORDS

Dynamic Compaction; Plate Compactor; Motion Analysis; Data Processing.

1. INTRODUCTION

Ensuring the correct positioning of railway tracks is crucial for a functioning railway system. The quality of the substructure, which comprises the quality of the ballast as well as the subballast and the subgrade is critical in minimizing track geometry deterioration. Throughout the life cycle of a track formation the quality of the substructure changes and degrades but can be prevented by a formation rehabilitation. Although ballast rehabilitation by tamping (and subsequently ballast compaction) can be achieved more easily, the ballast has less influence on severe track geometry errors compared to the subballast or the subgrade. Tough the rehabilitation of the subballast is much more complex as it requires removing the ballast and the formation protective layer and laying them out again. Depending on the rehabilitation method the track grid may need to be removed as well (Li et al., 2015).

In Austria the AHM 800-R (AHM) is a commonly used track bound formation rehabilitation machine from Plasser & Theurer – Export von Bahnbaumaschinen Gesellschaft m.b.H. (P&T). It enables a rehabilitation without removing the track grid and thus increases the efficiency compared to traditional formation rehabilitation methods (Auer et al., 2008). The AHM is equipped with two excavation chains that operate beneath the lifted track grid. The first excavation chain removes the approximately 30 cm thick layer of ballast. The old ballast is then crushed and mixed with new FPL material. The subgrade excavation chain then removes the existing subgrade and the lower area of the ballast layer and transports the material to the rear of the machine for subsequent disposal.

After excavation, the formation level of excavation is smoothed with a vibrating screed and a geotextile can be installed to minimize mixing of the subgrade with the new FPL layer. The FPL material, which is a mix of quality-assured FPL material and up to 50% of reprocessed ballast material, is then placed on the geotextile with a layer thickness of approximately 50 cm (uncompacted). The FPL material is then compacted resulting in a layer thickness of approximately 40 cm. The compaction is performed using six Wimmer WBB 530 plate compactors in parallel (see Figure 1).

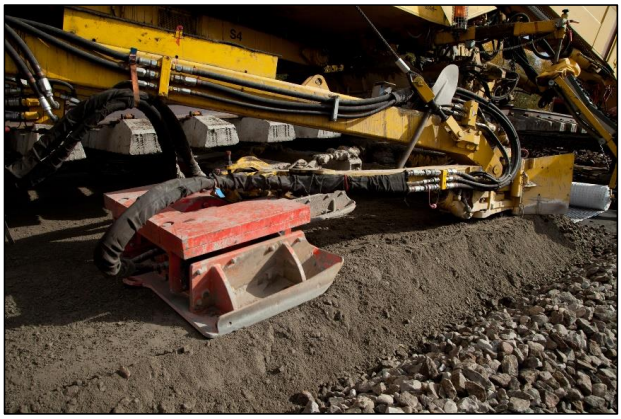


Figure 1. Plate compactor WBB 530 of the AHM 800-R during compaction of the FPL. Source: P&T

Due to the limited workspace beneath the tracks, the plate compactor is restricted in size and weight. The compaction of a 40 cm thick layer of soil presents a challenge for a comparably light plate machine and may cause irregular motion behaviour of the plate compactor and/or an insufficient compaction of the FPL, which could significantly reduce the expected life cycle of the track formation.

Field tests were carried out to analyse the motion behaviour of the plate compactor during FPL compaction to improve the efficiency of the plate compactors and the quality of the compaction. Additionally, the theoretical motion behaviour of the plate compactor under different soil properties and machine parameters was investigated using a mechanical model (Pistrol et al., 2022). This paper juxtaposes the simulated motion behaviour and the interaction between plate compactor and soil with data collected during experimental field tests.

2. THEORETICAL SIMULATION

Pistrol et al. (2022) presented a simplified mechanical model to describe the interaction between the plate compactor and the soil. While various simplifications are made and boundary conditions need to be defined, the model accurately depicts the contact conditions between the two mechanical subsystems (plate compactor and soil). One of the most important simplifications with regard to the equation of motion is the consideration of only vertical motion quantities as the load applied on the soil by the plate compactor is directed in a mostly vertical direction (Pistrol et al., 2022). This simplification has been used in similar investigations for vibratory rollers and showed sufficient accuracy (Adam, 1996; Kopf, 1999). The model can reliably describe three different operation phases: loading, unloading, and loss of contact. Figure 2 shows the simplified mechanical model and its subsystems: soil and plate compactor. The interaction between these two subsystems is described by contact conditions. The plate compactor can be further divided into an upper part (frame) and a lower part (base plate). These parts are connected by rubber buffers which allow for a separate description of those parts (Stefan, 2020).

Equation (1) gives the motion equation of the frame. The force in the rubber buffers as a result of their stiffness and damping properties is summarised in Equation (2) (Pistrol et al., 2022).

$$\left(m_f + m_a\right) \ddot{z}_2 - F_r = \left(m_f + m_a\right) g \tag{1}$$

$$F_r = c_r \left(\dot{z}_1 - \dot{z}_2\right) + k_r \left(z_1 - z_2\right) \tag{2}$$

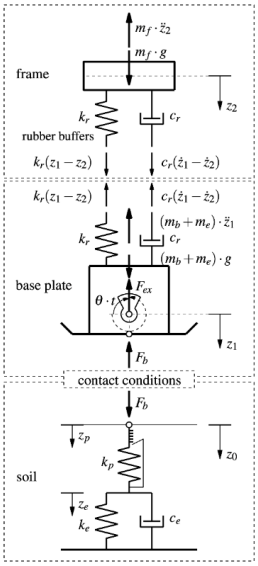


Figure 2. Mechanical model with plate compactor and soil subsystem. The plate compactor is split up in its components frame and base plate (Pistrol et al., 2022).

Equation (3) gives the equation of motion for the base plate. Equation (4) shows the equation to determine the exciter force F_{ex}. Equation (3) can be transformed to determine the soil contact force F_b (see Equation (5)), which defines the interaction between plate compactor and soil as it includes the motion equations of the frame as well as the base plate (Pistrol et al., 2022).

$$\left(m_b + m_e\right) \ddot{z}_1 + F_r + F_{ex} + F_b = \left(m_b + m_e\right) g \tag{3}$$

$$F_{ex} = m_e e \theta^2 \sin(\theta t + \varphi_0) \tag{4}$$

$$F_b = \left(m_b + m_e\right) g - F_r - F_{ex} - \left(m_b + m_e\right) \ddot{z}_1 \tag{5}$$

The soil subsystem is modeled with an elastic-plastic material behavior. The vertical displacement z_0 comprises elastic and plastic components as shown in Equation (6). The elastic behaviour is modeled with a Kelvin-Voigt element, the plastic behaviour with an elastic spring, which is only active during loading (Stefan, 2020). The spring stiffness is based on the cone model by Wolf (1994).

$$z_0 = z_e + z_p \tag{6}$$

The input parameters and variables for the given equations are defined in Table 1. Additionally, Table 1 shows the values of the input parameters used for the simulation for the three chosen time frames in the analysis and comparison.

Table 1. Parameters and variables of the mechanical model and values for the time frames 1 to 3

Variable	Description	Unit	Frame 1	Frame 2	Frame 3
c_e	Soil dashpot coefficient (Kelvin-Voigt)	N/ms	2.3e5	3.1e5	2.1e5
c_r	Rubber buffer dashpot coefficient	Ns/m	15000	15000	15000
e	Eccentricity of eccentric mass	m	0.032	0.032	0.032
f	Excitation frequency	Hz	51	54	35
g	Gravitational acceleration	m/s^2	9.81	9.81	9.81
k_e	Soil spring stiffness (Kelvin-Voigt)	N/m	5.7e7	1.0e8	4.9e7
k_p	Soil spring stiffness for plastic deformation	N/m	3.2e8	5.8e8	2.8e8
k_r	Rubber buffer spring stiffness	N/m	2e6	2e6	2e6
m_b	Mass of base plate	kg	295	295	295
m_e	Eccentric mass	kg	20	20	20
m_f	Mass of frame	kg	385	385	385
F_b	Soil contact force	N			
F_{ex}	Excitation force	N			
F_r	Force in the rubber buffers	N			
t	Time	s			
z_0	Vertical displacement of soil	m			
z_1	Vertical displacement of base plate	m			
$\dot{z}_1$	Vertical velocity of base plate	m/s			
$\ddot{z}_1$	Vertical acceleration of base plate	m/s^2			
z_2	Vertical displacement of frame	m			
$\dot{z}_2$	Vertical velocity of frame	m/s			
$\ddot{z}_2$	Vertical acceleration of frame	m/s^2			
z_e	Elastic deformation of soil	m			
z_p	Plastic deformation of soil	m			
θ	Circular frequency of excitation	rad/s			
φ_0	Phase shift	rad			

3. FIELD TESTS

The field tests were conducted in a gravel pit located in Fischamend, Austria. A plate compactor was attached to an excavator by a special mount (see Figure 3 (a)) which allowed to apply vertical loads onto the plate compactor. The excavator was pulled along the test lanes (see Figure 3 (b)) to ensure a slow and constant speed equivalent to the travel speed of the AHM during formation rehabilitation (approximately 70 m/h). The test lanes consisted of regular FPL material with a layer thickness of about 40 cm. The series of field tests consisted of four reference measurements, in which the plate compactor was lifted and oscillated freely in the air and eight test runs with various machine configurations (Sigmund et al., 2023).



Figure 3. (a) Mounted plate compactor. (b) Excavator equipped with plate compactor is pulled along the test lanes during field test. (Sigmund et al., 2023)

The plate compactor was equipped with five MEMS 3D accelerometers; four were mounted on the base plate around the exciter unit to record the movement of the plate and one was attached to the frame to determine the influence of the plate's movement on the frame. Additionally, the exciter unit was equipped with four inductive proximity sensors to track the position of the unbalance during the field tests. In addition to the accelerometers and position sensors, a loading cell was used to monitor the force applied by the hydraulic cylinder.

4. ANALYSIS AND COMPARISON

The movement of the unbalance and the exciter frequency were determined from the data collected by the exciter units' proximity sensors. The results show that the hydraulic pressure of the excavator's engine was not sufficient to support both, a high exciter frequency and a high vertical load on the plate compactor. Therefore, high vertical loads could only be applied during phases of lower frequencies and vice versa.

The data analysis from the field tests indicates that the plate compactor's mode of operation changes with varying conditions. The applied vertical load and the exciter frequency are the main influencing factors on the plate compactor's behaviour. The data indicates that the soil contact force of the plate compactor was very low during phases of low vertical loads. This can be attributed to a suboptimal mount construction that lifted the plate compactor off the ground without sufficient vertical loads. However, after applying a certain vertical load, the data shows a significant increase of the soil contact force. However, low vertical loads cause the plate compactor's motion behaviour to be indistinctive. As the load increases, the motion behaviour becomes more periodic and distinctive (Sigmund, 2021).

For the comparison between field tests and simulation, three time frames are selected from the field test data that show a periodic and distinctive motion behaviour. The parameter sets of the time frames differ in exciter frequency and vertical load. The exciter frequency from the field data was then used for simulating the motion behaviour of the given time frame. Figures 4 to 6 show the comparison between the field test data and the simulation. Figure 4 to 6 (a) (left) compares the exciter force and the soil contact force of the given time frame. The lower graph compares the exciter force F_{ex} of simulation and field data and shows the difference (delta) to verify the frequency input of the model. The upper graph shows the soil contact force F_b of simulation and field data. Figure 4 to 6 (b) (right) show the orbital (vertical over horizontal) displacement of the plate compactor for the respective time frame. The red and green lines indicate the movement of the front and rear sensor. The movement of the centre is determined by weighting the displacements of the front and rear sensors according to the distance from the sensors to the centre. The grey lines connect time-equivalent points at the front and rear. As the distance between the sensors is not shown true to scale, the rotation of the base plate at any given time is significantly inflated.

During time frame 1 the plate compactor shows a distinctive, periodic motion behaviour (see Figure 4 (b)). Due to the unbalanced design of the plate compactor, the base plate starts to tilt during compaction. Depending on the rotation direction of the unbalance, the front end shows significantly larger amplitudes compared to the rear end.

The lower graph of Figure 4 (a) shows that the alignment of the exciter forces F_{ex} of model and field tests works sufficiently as the delta is negligible. The upper graph shows that the model as well as the field test data registered a 'spike' in the soil contact force F_b every other exciter period. Thus, after a high intensity impact the base plate loses contact and lifts off the ground for one full period before hitting the soil surface again. This mode of operation is referred to as 'double jump' in dynamic roller compaction (Adam, 1996). The difference in time at which the impact occurs can be explained by the slight rotation of the base plate during the field tests, resulting in an earlier contact initialisation between plate compactor and soil or with the load application point of the soil contact force deviating from the centre of the plate compactor, which can also cause a time discrepancy.

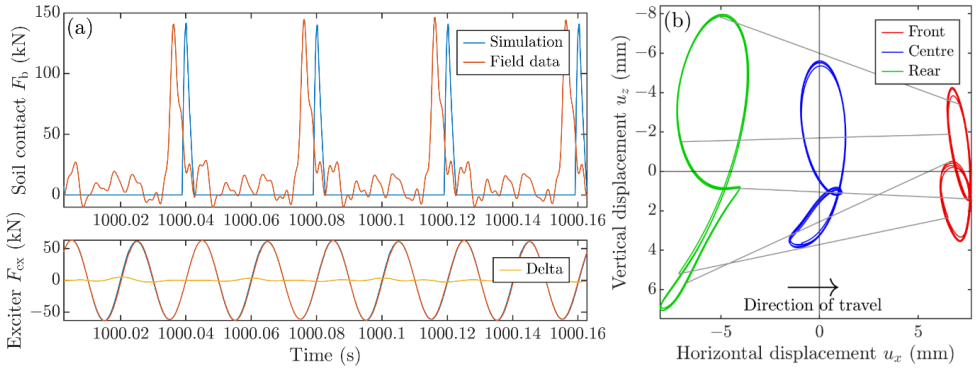


Figure 4. Time frame 1: (a) Comparison of soil contact force F_b and exciter force F_{ex} from simulation and field tests. (b) Orbital movement of the plate compactor from field tests (inflated rotation).

Figure 5 shows time frame 2. The delta of the exciter forces remains negligible. Similar to time frame 1 (Figure 4), the plate compactor shows a periodic motion behaviour (see Figure 5 (b)) but the higher frequency leads to a lower vertical load in this section which results in a slightly different movement of the front end for each exciter period. This time frame was selected from a second compaction run on a test lane. Therefore, an increased soil stiffness is expected compared to the first test run. The increased soil stiffness leads to an increased soil contact force, which is replicated in the mechanical model by an adjustment of the soil parameters, as shown in Figure 5 (a).

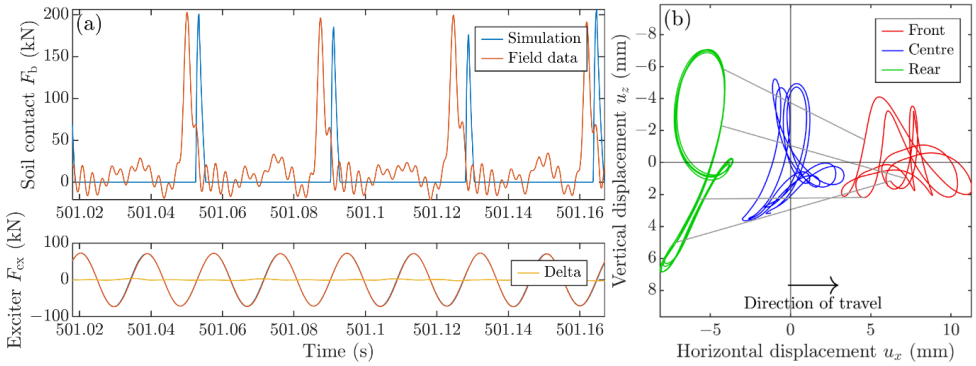


Figure 5. Time frame 2: (a) Comparison of soil contact force F_b and exciter force F_{ex} from simulation and field tests. (b) Orbital movement of the plate compactor from field tests (inflated rotation).

Time frame 3 shows a contrasting image to time frames 1 and 2. The unbalance's rotational direction changed, causing the front end to show larger displacement amplitudes compared to the rear end. The plate compactor's motion behaviour remains distinct and periodic over two exciter periods (as shown in Figure 6 (b)). However, in this case the mode of operation is not classified as 'double jump' but rather as a transition from 'loss of contact' to 'double jump' (Adam, 1996). Figure 6 (a) shows alternating impacts of low and high intensity. Additionally, the rotation of the plate compactor is more pronounced, resulting in a double impact on the soil. The two peaks of the field data's soil contact force also indicate this behaviour. With the given process parameters, the mechanical model cannot reproduce this mode of operation. The exciter frequency and thus the amplitude of the exciter force are relatively low. Therefore, the mechanical model does not transition from 'loss of contact' to 'double jump' regardless of the soil stiffness. Increasing the frequency changes the mode of operation to match the field data's mode of operation. This indicates that the transition areas between the modes of operation differ slightly between field tests and simulation. Additionally, due to its simplification, the mechanical model is unable to account for the rotation and double impact of the base plate.

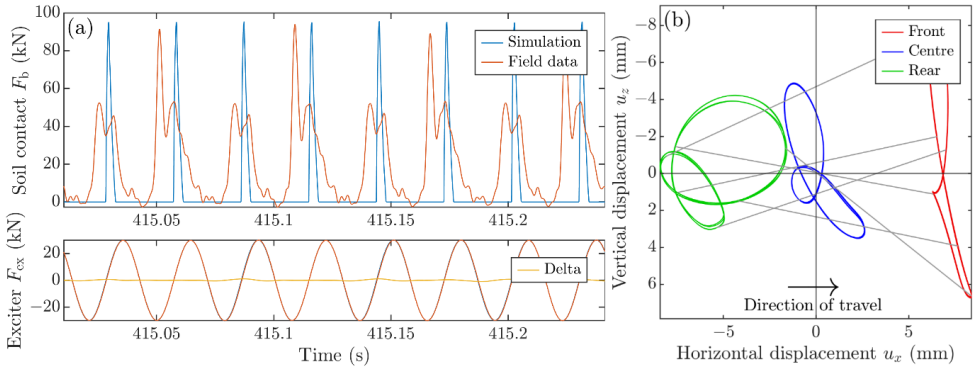


Figure 6. Time frame 3: (a) Comparison of soil contact force F_b and exciter force F_{ex} from simulation and field tests. (b) Orbital movement of the plate compactor from field tests (inflated rotation).

5. CONCLUSION

In this paper, the motion behaviour of a plate compactor of type WBB 530 was investigated during the compaction of a formation protective layer. The interaction between the plate compactor and the soil is compared to the results of a simplified mechanical model. The experimental data was collected during field tests.

The study shows that, under certain conditions, the mechanical model can reliably reproduce the motion behaviour of the plate compactor. The model can also replicate the higher soil contact forces that occur during a second compaction pass over an already compacted test lane by increasing the soil stiffness. However, the transition areas between the different modes of operation, which depend on various process parameters, differ slightly between the mechanical model and the field tests. Moreover, the mechanical model is not suitable for reproducing the indistinctive motion behaviour observed during the field tests. The field data also shows that the test setup, including the plate compactor mount, should be improved to collect reliable data for a wider range of process parameters. Additional validation of the mechanical model with more distinctive measurement data could provide more information about the motion behaviour of the plate compactor that potentially enables an optimization of the compaction equipment.

REFERENCES

Adam, D. 1996. *Continuous compaction control (CCC) with vibrating rollers* (German). Doctoral Thesis. TU Wien, Austria.

Auer, F., Zuzic, M., Schilder, R. and Breymann, H. 2008. 13 years of experience with rail-mounted formation rehabilitation on the Austrian network. *RTR* 29–36.

Kopf, F. 1999. *Continuous Compaction Control (CCC) for the compaction of soils by dynamic rollers with different types of excitation* (German). Doctoral Thesis, TU Wien, Austria.

Li, D., Hyslip, J., Sussmann, T. and Chrismer, S. 2015. *Railway Geotechnics*. CRC Press, London.

Pistrol, J., Adam, D., Hofbauer, T., Kopf, F., Anthony, B. and Auer, F. 2022. Subballast compaction in track rehabilitation by means of plate compactors. *ICSMGE - 20th International Conference on Soil Mechanics and Geotechnical Engineering*, Sydney, Australia, pp. 1005–1010.

Sigmund, J. 2021. *Measurement and analysis of the motion behaviour of plate compactors in railway construction* (German). Master's Thesis, TU Wien, Austria.

Sigmund, J.A., Pistrol, J. and Adam, D. 2023. Motion analysis of plate compactors in railway construction. *17th Danube – European Conference on Geotechnical Engineering*, Bucharest, Romania, pp. 89–93.

Stefan, T. 2020. *Subballast Compaction with Plate Compactors and Assessment of their Motion Behavior* (German). Master's Thesis, TU Wien, Austria.

28th European Young Geotechnical Engineers Conference – EYGEC 2024
© 2024 Macedonian Association for Geotechnics, *ISBN 978-608-4510-61-1*

Transpennine Route Upgrade: Geotechnical engineering solutions to replace failed structures caused by peat and dissolution hazards

Jordan Sinnott CEng MICE FGS; Senior Engineer (Geotechnical); (jsinnott@systra.com)

SYSTRA Ltd., Birmingham, United Kingdom

ABSTRACT

For the Transpennine Route Upgrade East (TRUe), SYSTRA and the TRUe Alliance delivered three new flood balancing structures as a replacement to a failed culvert on the Normanton and Colton Junction Line. Geotechnical research into the cause of the culvert failure and geological investigations into this region of North Yorkshire, identified that dissolution of gypsiferous material and the presence of peat deposits had been causing the rail embankment (through which the culvert was constructed) to displace.

Geological evidence indicates that a near-vertical brecciated pipe has formed to the sub-surface, allowing groundwater to rise and saturate peat and alluvial material above. This has resulted in the softening of superficial soils, causing settlement under the embankment weight. This culmination of geological phenomena resulted in the existing culvert to break. New structures had to be installed whilst keeping the line operational, meaning that launch and reception pits were excavated on either side of a Victorian-era embankment to allow for micro-boring. These works were undertaken away from the key geological hazards in order to reduce short and long-term risks to the railway, workers and public. The geotechnical solution of infilling the existing culvert and replacing with three new structures was completed during possession to minimise disruption, resulting in a successful engineering feat that pulled together multiple teams and organisations. This paper will present the scheme, the site's geological occurrences, the engineering proposals and the collaboration involved to safely construct whilst keeping the line operational.

1. NOTATION

ALL Alluvium: Silt and Clay overlying Gravel
AOD Above Ordnance Datum
BGS British Geological Survey
EA Environment Agency
EPS Expanded Polystyrene
DTM Digital terrain model
HEM Hemingbrough Glaciolacustrine Deposits (Vale of York Lake): Silt, Clay and Sand of Breighton Sands
MASW Multichannel Analysis of Surface Waves
NOC Normanton to Colton Junction Line
PPM Parts per million
TBM Tunnel Boring Machine
TRU Transpennine Route Upgrade
TSZ Track Support Zone

2. INTRODUCTION

The TRU project is the improvement of the railway between York and Manchester in the UK, via Leeds and Huddersfield. Between Leeds and York, this project is referred to as TRUe, and is delivered by the TRUe Alliance. Part of the railway improvement includes electrification of the route, more frequent trains and more reliable journey times. NOC/23 is the name given to a flood alleviation structure, present

crossing the NOC Line, South of Ulleskelf, North Yorkshire. This is a brick twin-arch underline structure, estimated to be 179 years in age. The structure services the embankment situated within a floodplain monitored by the Environment Agency, and is located along the local project chainage at 15,190m chains.

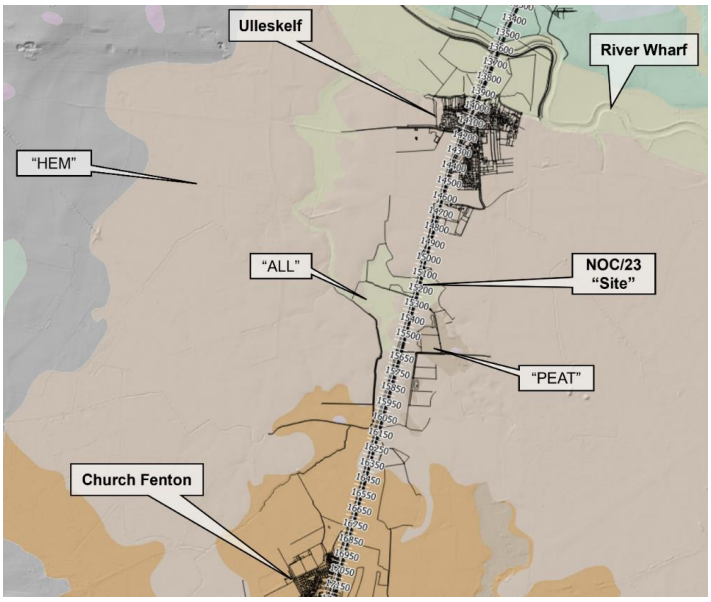


Figure 1: Site Location, with Superficial Geology (as mapped by the BGS 1:50,000 WMS Layer)

Structural examination identified that the base of the culvert barrel on the eastern inlet is at a level of 3.213mAOD, and that the western inlet level is at 4.90mAOD. There is approximately 1.1m of cover from the underside of the sleepers to the top of the culvert on the western (Leeds Lines) side, and 2.2m cover to the underside of the sleepers on the eastern (Normanton Lines) side. The structure no longer performs satisfactorily and is under constant remote monitoring. Significant fractures in the culvert barrel were surveyed and ballast top-up on the track above has been ongoing since the 1940s. This 1.7m difference in inlet level indicates that significant differential movement has occurred across the structure, resulting in its failure.

The scheme remit was to repair or replace the flood alleviation structure in a way to maintain the flood balancing status quo within the region. Several options were considered to repair and/or replace the failed structure, including:

- Option A - Installation of a singular culvert within the existing structure.
- Option B - Installation of two culverts within the existing structure.
- Option C - Installation of two culverts within the existing structure with an additional 1.5m diameter culvert outside of it.
- Option D - Infill the existing structure and install three 1.8m (internal) diameter culverts.

The selection of the most suitable option on the project was driven by the geological conditions present at the site, the requirement to provide minimum disruption to rail activity, and to provide cost efficiencies. The geotechnical input to this scheme was critical to establishing the most suitable option.

3. GROUND CONDITIONS

The existing NOC/23 flood alleviation structure is located within a region of North Yorkshire referred to as Ulleskelf Mires. These mires are an area of elevated flooding risk, with natural grassland and woodland flooding seasonally. The Mires can be identified from aerial imagery and are visible on Figure 1 aligning with the BGS mapped extent of Alluvium and Peat.

Alluvium is mapped underlying NOC/23, suggesting its presence immediately below the railway embankment. Alluvium, comprising clays, silts, sands and gravels, is an unconsolidated detrital material deposited by bodies of water (i.e., by rivers or on their floodplains). The Alluvium is reported to potentially contain layers of peats, tends to be soft and is prone to compressibility. Underlying Alluvium,

and present from ground level in the area surrounding Ulleskelf Mires, is the Hemingbrough Glaciolacustrine Deposits. Of Devensian age, these are Vale of York soils deposited from part of the "Glacial Lake Humber" (Ford et al. 2008), appearing as a mainly grey and brown laminated clay with partings of silt and sand. Ground investigation undertaken in the wider North Yorkshire region estimates that this formation is up to 25m in thickness. A public report by the BGS for the Environment Agency (Burke et al. 2017) determines that the zone from Ulleskelf to Church Fenton has the lowest rockhead elevation levels within the region.

Underlying the superficial deposits, the BGS maps the Roxby Formation. The Roxby represents the top of the Zechstein sequence in North Yorkshire, deposited in the Upper Permian. The Zechstein sequence dip gently eastwards, with the Roxby Formation weathered across its top. The formation comprises a calcareous and gypsiferous mudstone, with two significant sequences of gypsum. Within the middle of the formation's sequence is the Sherburn Anhydrite/Gypsum (up to 8m in thickness) and at the base of the sequence is the Billingham Anhydrite/Gypsum (up to 4m in thickness). Based upon this preliminary review, two key geotechnical hazards were identified as potentially present and causing distress in NOC/23. These were the Peats within the Alluvium superficial soils, which have the potential to change volume considerably over time; and dissolution of gypsum within the deeper Roxby Formation resulting in vertical displacement within the subsurface.

3.1. Previous Research – North Yorkshire Gypsum

Gypsum (hydrated calcium sulphate) has the potential to dissolve resulting in the loss of volume in rock and in situ weathering of materials that it was originally held within. The dissolution of gypsum is dependent on the presence of groundwater and groundwater flow, with dissolved chemicals within the water having a bearing on the rate of dissolution.

Cooper (2019) reports that the Sherburn Gypsum varies in thickness based upon public and commercial borehole records, with the variation in thickness being attributed to dissolution. It is suspected that cavities in the ground as a result of the dissolution is caused by jointing in rock, resulting in water supplied from underlying aquifers accessing the deposits. Caves are reported to have formed in relatively thin gypsum bands in the North of England, such as at the Vale of Eden (Ryder and Cooper, 1993). The Billingham Gypsum is not as well covered by boreholes, with evidence available to identify variation in thickness of gypsum being more sparse.

As the key cause of underground dissolution is the passage of groundwater through deeper aquifers, an upward flow of water would be expected. This may be exhibited at the surface and observed as springs and boggy ground (i.e., Ullekself Mires). Historic BGS boreholes within the region demonstrate evidence of subartesian and artesian conditions, indicating a mechanism for the development of dissolution features.

A further line of evidence that indicated the likelihood of dissolution occurring at depth within the region of NOC/23 was the presence of an elevated sulphate content within groundwater in historical boreholes. It is considered likely that any sulphate saturation would have resulted from the dissolution of Gypsum and rising upwards with groundwater flow. Research into this, by Cooper (2019) reviewed available borehole records surrounding NOC/23, identifying the following:

- BGS borehole SE53NW3 (at Church Fenton) reports historical records from Prof Kendall's notebook, page 107, that encounters artesian water that is "… safe perhaps, but evidentally charged with sulphates".
- BGS borehole SE53NW2 (at Church Fenton) noted spring water within the vicinity. Analysis of the spring water identified an elevation in calcium sulphate (1570ppm).
- BGS borehole SE53NW7 (1km southwest of NOC/23) yielded artesian water.
- BGS borehole SE53NW82 in Ulleskelf drilled to 320ft (approximately 97.5m) identified gypsum and poor-quality water. The borehole notes that due to the quantity of chlorides, nitrates and total solids, that this water was unfit for domestic use.
- BGS borehole SE53NW1B yielded water within 3700ppm solids, of which 1845ppm were sulphate and calcium carbonate. This borehole also penetrated gypsum and anhydrite.

- BGS borehole SE53W92 (1km to the west of the Site) yielded artesian water, containing 1500mg/l of sulphate and 592mg/l of calcium.

Based upon the above, dissolution of the Sherburn Gypsum is considered to be widespread, however is likely concealed (Cooper 1986) as a result of infilling of cavities and pipes with superficial soils. It was therefore considered a critical risk to the NOC/23 site and a potential cause of the failure of the structure. Given that the existing structure is located within Ulleskelf Mires, a particularly boggy region, the upward rising of groundwater was considered likely to be occurring at the Site.

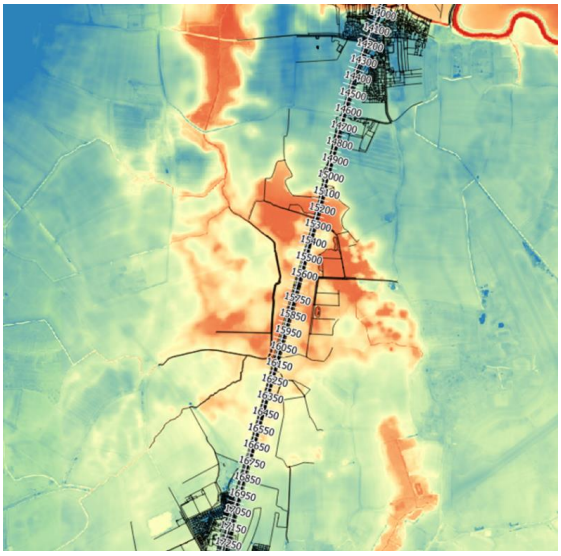


Figure 2: 1m LiDAR DTM dataset of Ulleskelf Mires, North Yorkshire (reproduced from the EA dataset, UK GOV)

The revised 1:10,000 Scale BGS map SE53NW, compiled by Cooper (2000) shows large areas of Alluvium and Peats (see Figure 1) that are likely gypsum subsidence features. The Department of the Environment gypsum subsidence study (Thompson et al. 1996) maps subsidence features from air photographs, illustrating sinkholes in the area north of Church Fenton. Based upon the Environment Agency Open-Source LiDAR datasets, mapping provided at Figure 2 shows the region of NOC/23 to be generally flat, however shows a depression, likely attributed to subsidence (orange), at NOC/23 and Ulleskelf Mires. Cooper (1986) identifies a similar pattern of hollows in subsidence surface patterns as a result of confirmed dissolution locations at Ripon. They are interpreted as amalgamated hollows, whereby subsidence occurs as a result of the first hollow collapsing the underlying cave, resulting in water flow to adjacent gypsum veins, allowing the subsidence area to grow.

3.2. Ground Investigation

A combination of multiple methods of ground investigation were undertaken within the vicinity of the Site, and along the majority of the Transpennine railway route as part of wider TRUe delivery works. Specific to NOC/23, ground investigation was undertaken on and off track by both intrusive and non-intrusive methods.

Seismic surveys were undertaken by P Wave and Shear Wave, and individually plotted (see Figures 3 and 4). The P Wave tomographic model indicates that from approximately chainage 15,160m, a gradually deepening zone of lower P Wave velocity, compared with the subsurface profile to the north (down chainage). A similar, but clearer trend is shown in Figure 4, whereby S Wave velocity is considerably lower in a conical shape around the location of NOC/23 (labelled as an underbridge on Figures 3 and 4).

The conical shape of the structure identified within both P Wave and S Wave plots align with the shape of an expected brecciated pipe that would occur as a result of dissolution of Gypsum within the Roxby Formation. These surveys supplemented research to provide evidence that the site is the location of a dissolution hazard. Based upon the above, gypsum is thought to have dissolved at depth, below -10mAOD, and has been infilled by overlying superficial stratum. This superficial stratum is thought likely to be softened further by subartesian water flow, responsible for the lower velocity of seismic waves. It would appear, based upon the seismic profiles that the northern boundary of the brecciated pipe is between 15,140m and 15,180m, with the southern boundary not established by the survey.

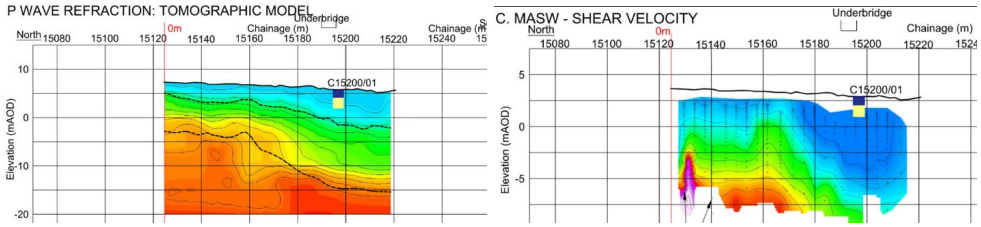


Figure 3: P Wave Refraction Tomographic Model (Left) and S Wave Velocity Model (Right), reproduced from integrated results of geophysical survey for TRU East of Leeds

Intrusive surveys identified an increase in embankment thickness around NOC/23. Holes drilled through the embankment around NOC/23 identified Made Ground at up to 8m thick in several places. This is considered to likely be due to embankment subsidence, resulting in ballast level top ups and embankment renewals to maintain rail level over its life. Boreholes undertaken in the vicinity of the extent of the brecciated pipe (as mapped on Figure 3 S Wave Velocity Model) identified organic clays and peats. In-situ SPT testing determined this material to be very soft, with majority of values ranging between 0 and 3. Looking spatially, to develop a 3D understanding of the extent of the peat deposits and potential shape of the brecciated pipe across track, peat levels significantly deepen towards the east side of the railway. This thickening of peats on the east side of NOC/23 provides a mechanism for the differential failure of the structure, as this side has the lower inlet level of 3.213mAOD, compared to 4.90mAOD on the west.

Off the brecciated pipe, and at depth, especially at Ch. 15,100m, the Vale of York deposits were recovered principally as the Hemingbrough Glaciolacustrine Clay. These laminated clays often included sand lenses and showed a clear trend of increasing strength with depth upon review of in-situ testing. Several boreholes encountered groundwater during drilling. Shallow water strikes did not rise and appear to be perched within sand lenses earlier identified. Two exploratory holes, C15180/05 and C15200/01, undertaken in the centre of the brecciated pipe, struck water between 13 and 14mAOD. Water rose in these holes after 20 minutes by approximately 12m, indicating deeper water tables exhibiting subartesian conditions.

4. CONSTRUCTION CONSIDERATIONS

4.1. Optioneering and Constraints

The research and geotechnical investigation undertaken provided strong evidence for the cause of the serious distress occurring within NOC/23. It is thought that the presence of a brecciated pipe, formed as a result of dissolution of gypsum within the Sherburn Gypsum of the Roxby Formation, has resulted in an upward propagation of groundwater flow and subsidence of overlying superficial soils into the pipe. It is likely that this process is ongoing, and as a result, vertical displacement of the entire rail embankment network is occurring. This is exacerbated by the presence of peats, generated by the brecciated pipe, which vary in thickness, and are likely the cause of differential displacement of the existing structure.

Reconstruction of NOC/23 was ruled out by the TRUe Alliance based upon the geotechnical hazards identified at the site. It was considered that due to the widespread nature of the brecciated pipe, that reconstruction would likely result in similar failures occurring, and that ground improvement would be extensive and expensive. Moreover, this hazard is impacting the wider rail infrastructure, not just NOC/23, and any effort to stabilise a reconstructed flood alleviation structure (by piling to mitigate some of the vertical displacement) would still result in differential movement of the track. This may cause an effective “hard-spot” whereby track deflections would require continual monitoring to avoid potential derailments.

Geotechnical effort in the research of the hazards and cause of the structure failure was fundamental in driving a preferred option of constructing off of Ulleskelf Mires. Construction of the new flood balancing structures (replacement culverts) needed to consider impacts to the rail infrastructure. The first option considered was top-down approach, whereby the embankment would be stripped back, culvert sections installed, and the embankment and railway reinstated. This would require closing the rail route by blockade. Possession of the railway would only potentially be available during the public holidays of Christmas and Easter, however, would likely require further possession times. Possession outside of these time periods were estimated to cost an additional £1 million, with added disruption to passengers, freight and the local economy.

The three culverts were proposed to be constructed as precast concrete pipes, installed by trenchless methods.

4.2. Proposed Structure Solution

The three new culverts of 1.8m diameter internal width had a proposed invert level of 4.9mAOD. New structures were assigned the names NOC/22C, NOC/22D and NOC/22E, and were located at local project chainages 15,111m, 15,121m and 15,131m respectively. This would site them off of the identified brecciated pipe, and off of recovered peat soils. Cover to new pipes varied across the embankment width, with the lowest amount of cover at NOC/22E below the Up Normanton Line (eastern most lone) of 1.634m. Each culvert would be 23.45m in length, a distance selected to ensure minimum tunnelling distance and time, whilst ensuring track support zones were stabilised both before and after jacking.

To facilitate pipe jacking, the launch pit was proposed on the east (Normanton) side of the embankment, with a 7.0m wide pit proposed. The reception pit on the opposite side to the track would be 4.0m in width. Each pit would be constructed by sheet piles in the temporary cases, with the concrete channel cast against this for the permanent case to allow for conversion to a drainage ditch to allow for flow of water to the south where ground level lowers.

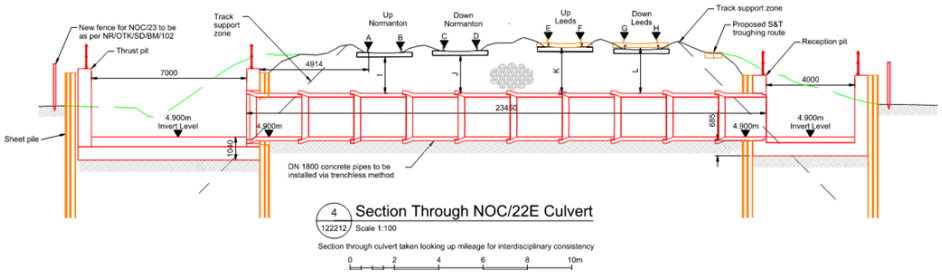


Figure 4: Extract of cross section, showing one of the proposed culverts (NOC/22E), against natural ground levels and existing embankment setting

With a proposed invert level of 4.9mAOD, proposed drainage channels/pits on either side of the embankment would require excavation from natural ground levels by approximately 3.5m. As the embankment was wider than the proposed culvert length of 23.45m, excavation of channels and pits would result in dig out of the toe of the embankments on both sides. It was noted that, when accounting for overdig in the worst-case, this would mean that sheet piles in the temporary case would need to retain 5m of railway embankment and underlying natural ground. In the temporary case, propping was required to support excavations during tunnel installation and channel formation.

As the existing rail embankments are of Victorian Era age and are life expired, global stability checks in the permanent and temporary cases were required to determine that change in use would not have a detrimental impact. Findings of the stability assessment advised that not only was propping necessary in both the permanent and temporary cases to keep pits and channels open, but also that sheet piles

would need to be of necessary length to prevent failure planes generating as a result of unloading of slope toes whilst excavating channels.

4.3. Existing Structure Solution

With the proposed replacement structures to the north, NOC/23 can be abandoned. However, there is a risk that abandoning without remediation may eventually result in catastrophic and ultimate failure of the structure, which poses a serious risk to track stability. Any intervention may inadvertently result in accelerated vertical displacement by settlement however, which again would also result in in track deflections. The proposal made by the geotechnical team was to infill the structure with a lightweight fill (i.e., a polystyrene). Design checks were required to inform differential settlements between the structure and the surrounding embankment, as well as an assessment of the long-term structural integrity of the culvert.

EPS blocks selected for use have a lower density than alternative infill materials, such as foamed concrete, making it the preferable option to reduce magnitudes of settlement. The settlement calculation undertaken was to provide guidance of likely displacement as a result of infilling to advise Network Rail in their monitoring efforts of the line. With the addition of an EPS, consolidation was estimated to be 10mm on both sides of the existing structure, compared to surrounding embankment movement.

5. CONSTRUCTION, MONITORING AND CHALLENGES

The construction of the new structures took place during the summer months of 2023. Construction commenced with both the launch and reception pits. 10.0m long sheet piles were installed to a toe level of -0.90mAOD comprising L605 grade (PU22-1/GU21N) sheets. Two frames were specified for the opening of pits, MP150 struts were installed in both pits.



Figure 5: Launch Pit, during operation of railway

Once culvert openings were cut through sheet piles and headwalls cast, the three mini TBMs, Nicola, Kathryn and Emma, were lowered into the launch pit. During Week 21, the three culverts were jacked simultaneously beneath the railway, the first time that this feat had been achieved in the United Kingdom. Tunnel designers considered there to be a significant risk of works inducing settlement to the overlying track. There was less than 1.7m cover below the railway tracks, and the risk was deemed very high. Extensive remedial works were required to maintain track geometry, which was monitored and rectified during the possessions. Contingencies were put in place within construction possession to action remediation and reinstatement based on hazards identified.

Pre-possession, the first two culvert sections were installed at each location (NOC/22C, NOC/22D and NOC/22E) from the launch pit side. These segments were installed up to the TSZ for the Up Normanton Line, which remained open until 01:00am on Saturday 19th August 2023. For the next 23 and ½ hours, the two Normanton Lines were blocked to all rail traffic (with all traffic sent down the Leeds Lines), allowing for the progression of the TBMs through the Normanton TSZ to install the next three culvert segments at each location. On Sunday 20th August 2023, both the Leeds Lines and the Normanton Lines were blocked from 00:30am and the TBMs were progressed through the overlapping TSZ's of both lines. There was a 7 hour and 15-minute window to install two culvert segments within this section. From 07:45am, the Normanton Lines were re-opened to all rail traffic. With TBMs outside of the Normanton TSZ, there was a 21 hour and 15-minute blockade on the Leeds Lines to install remaining

culvert sections. By Monday 21st August, at 05:00am, the Leeds Lines were repaired of any misalignments and all lines were fully re-opened to traffic.

The construction of the three tunnels was only possible due to the extensive contingency plans put in place. The two northern most culverts were progressed solely by TBM cutting faces, however the southern encountered clayey sandy soil, within the variable embankment make-up. This material was not conducive to being removed by the cutter head, and handheld breakers facilitated the removal of material which the cutter face could not dig. The contingency was acted upon and completed within the possession timeframes.

6. CONCLUSIONS

The distress and failure of the NOC/23 flood alleviation structure highlighted the impact of geological hazards present in North Yorkshire on the existing rail network. Preliminary geological assessments identified that the hazards of dissolution and peats are mechanisms for the vertical displacement of assets within the region.

Historical research in the wider region reported on the known presence of gypsum within the bedrock geology of the Roxby Formation. Evidence collated identified:

- Vertical displacement evidence in LiDAR imagery and topographical surveys, resulting in mappable sunken features at the surface,
- Historical borehole records encountering the Sherburn Gypsum, especially within the region of between Church Fenton and Ulleskelf,
- The elevation of sulphate particles within groundwater recovered from boreholes and wells within the wider site vicinity, and
- The mechanism of subartesian and artesian groundwater conditions rising up through dissolution features to saturate overlying superficial soils, often resulting in bogging and peat formation within near-surface soils.

Ground investigation tailored to identify these hazards dovetailed research findings, providing strong evidence to confirm the presence of a brecciated pipe below NOC/23 resulting in embankment displacement, along with the presence of thick layers of highly compressible peat.

Effective collaboration between multiple disciplines, and design and construction teams allowed for the proposal of an effective remedy, with geotechnical input critical in optioneering replacement structures off of the dissolution feature. Multidisciplinary interface developed a solution that saw the first simultaneous triple pipe jack beneath the railway in the UK. The solution allowed for construction without full closure of the line, minimising disruption to the public, freight traffic and the economy. This approach reduced carbon output and waste when compared to a potential cut/fill approach. The project also had a net biodiversity gain, with a 10% increase in trees planted as a result of site planning. All works undertaken were delivered within agreed possession arrangements, lines were fully reopened without delays and all core works were completed within agreed budgets.

REFERENCES

Burke, H., Ford, J.R., Hughes, L., Thorpe, S. & Lee, J.R., 2017. A 3D geological model of the superficial deposits in the Selby area, Commissioned Report CR/17/112. British Geological Survey.

Cooper, A.H., 1986, Subsidence and foundering of strata caused by the dissolution of Permian gypsum in the Ripon and Bedale areas, North Yorkshire, The English Zechtein and Related Topics, Geological Society Special Publication No. 22, pp. 127-139.

Cooper, A.H., 2019. Review of gypsum subsidence features and the geology of the Transpennine rail route from Church Fenton to Ulleskelf for TSP Proiects – Final Version,

Ford, J.R., Cooper, A.H., Price, S.J., Gibson, A.D., Pharaoh, T.C. & Kessler, H. 2008. Geology of the Selby district: a brief explanation of the geological map Sheet 71 Selby. British Geological Survey, Nottingham, UK.

Kemper, W.D., Olsen, J. & De Mooy, C.J., 1975. Dissolution rate of gypsum in flowing water. Proc. Soil Sci. Soc. Am. 39, 458-63.

Ryder, P.F. & Cooper, A.H., 1993. A cave system in Permian gypsum at Houtsay Quarry, Newbiggin, Cumbria, England. Cave Science, 20, 23 – 28.

Thompson, A., Hine, P.D., Greig, J.R., & Peach, D.W., 1996. Assessment of subsidence arising from gypsum dissolution with particular reference to Ripon. Symonds Travers Morgan, East Grinstead.

28th European Young Geotechnical Engineers Conference – EYGEC 2024
© 2024 Macedonian Association for Geotechnics, ISBN 978-608-4510-61-1

Reliability verification of the semi-probabilistic design of crane mats for the geotechnical stability of foundation machines at the construction site

Eleni Smyrniou[a], Mark van der Krogt[a]

[a] *Deltares, Delft, Netherlands*

ABSTRACT

The Dutch publication CUR689 describes a method for the geotechnical stability of foundation machines. The method is based on foundation calculations in accordance with Eurocode 7. This paper presents the reliability analyses that have been carried out to determine whether a sufficiently safe designs will be realised with this method and the partial load and material factors from Eurocode 7. We conclude that sufficiently safe designs can be realized with the current rules, but we also note that the current factors do not optimally match the uncertainties that are dominant for the bearing capacity of the foundation machines. We recommend using the results of this study to adapt the Eurocode 7 NEN-EN 1997 and the Dutch standard for existing geotechnical structures NEN8707 in the future.

KEYWORDS

Foundation Machines; Reliability Analysis; Code calibration; Eurocode

1. INTRODUCTION

As engineers, we are tasked with the responsibility of designing safe structures. In addition, we should pay attention to the safety during construction. As pile foundations are typically installed in situations where the soil has limited bearing capacity, additional measures are often needed for the soil to bear the weight of the pile driving machinery. This is particularly the case for the weak soils of the western Netherlands, where nearly each building has a pile foundation. In practice, timber crane mats are often used to distribute the weight of the machine to have sufficient bearing capacity of the subsoil.

In practice, the design of the timber crane mats is based on shallow foundation calculations from Eurocode 7 in combination with a load model demonstrated in the Dutch guideline CUR689 (CROW, 2017) to account for the effect of various eccentric horizontal and vertical loads that can act on a pile driver. The cumulative load effect on the crane mats is a vertical gravity load and an overturning moment. This load is typically schematized by a vertical load with a shifted center of gravity (CoG), compared to the centerline of the machine. The shifted CoG reduces the effective width over which the crane mats can transfer the load to the subsoil, reducing the effective bearing capacity. Because this loading situation is rather unique, it remains unclear whether crane mats have enough bearing capacity.

This paper evaluates the reliability of the semi-probabilistic design of foundations for foundation machinery with the partial factors for new structures in Eurocode 7 (CEN, 2007). However, as these foundations are typically temporary of nature, designers might consider choosing a lower level of reliability than for new structures. Note that such choice always requires consultation with the competent authority. The Dutch code NEN8707 (NEN, 2023) specifies target reliabilities for disapproval and renovation of existing structures. The lower limit is the ‘disapproval level’ offering a minimum human safety (an acceptable individual risk), and a little higher reliability for ‘renovation’ situations, where the additional costs for a safer design are efficient and proportional. To explore the applicability of the partial factors of rebuild and disapproval (NEN8700), we also considered these sets.

This paper first outlines the general approach and the methods used for probabilistic calculation, the load model, and the foundation calculation in the second section. Then, the third section goes into the case studies of which the results are discussed in the fourth section. The paper concludes with the general findings and recommendations from this study.

2. METHOD

2.1. General approach

The analyses aim to assess whether the current set of load factors, in conjunction with the calculation method outlined in CUR689, provides adequate safety or results in undesirable over-designing. We compare the achieved reliability using three different sets of partial factors: new construction (NEN-EN1997-1), renovation, and disapproval (both NEN8700/7). Note that these classes only exist in the Dutch code (NEN-EN1997-1) and are not part of the Eurocode. The reliability of a design with these load factors is expected to, on average, meet the target failure probability (reliability index) for the specific situation. These target reliability indices are specified as requirements in Eurocode 0 (CEN, 2002) and are presented in Table 2.

The core of the approach is to design the size of the foundation using the semi-probabilistic partial factors, and then verify the reliability of this design in a probabilistic analysis. To that end, we vary the length of the timber crane mats such that the semi probabilistic unity check reaches the value of 1.0. Then a probabilistic calculation is made, for that length, to obtain the reliability index of the design, which is then compared with the intended reliability target. To cover different variations in conditions, 9 cases were selected as typical combinations of a type of foundation machine (light, medium, heavy), and soil conditions (clay, weak clay, and sand). This approach is shown in Figure .

Therefore, the goal of the above analysis is not to derive the optimal set of partial factors as that would require more variations and optimization. Nonetheless, the analyses provide insight into which set of partial factors and/or calculation values are more efficient, and thus which adjustments are useful.

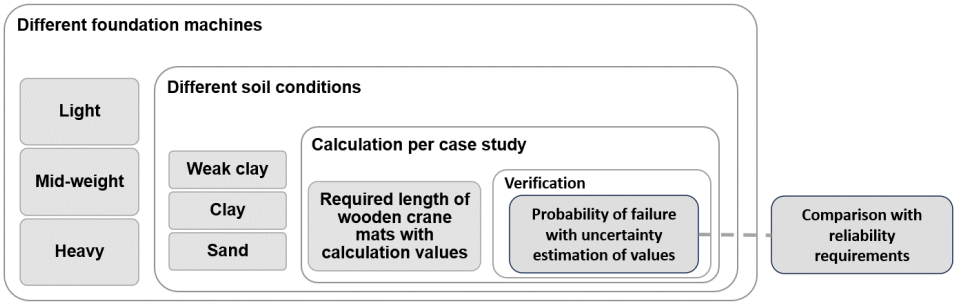


Figure 1. Set of analysis for every set of partial factors (new, renovation, disapproval)

2.2. Load model of the weights and forces of the machine

As already introduced in the first section of this paper, the CUR689 methodology is utilized to determine the vertical and horizontal resultant loads and their eccentricities. Loads such as the machine's own weight, external loads, and wind forces are individually calculated. The total overturning moment is converted to an eccentrically placed resultant of the vertical load (red arrow in Figure 2). The calculation considers the eccentricity of the machine and wind direction. A local coordinate system (x, y, z) is used for calculating forces above the slew bearing, while a global coordinate system (X, Y, Z) is used for the total resultant on the crane mats for the convenience of the calculation.

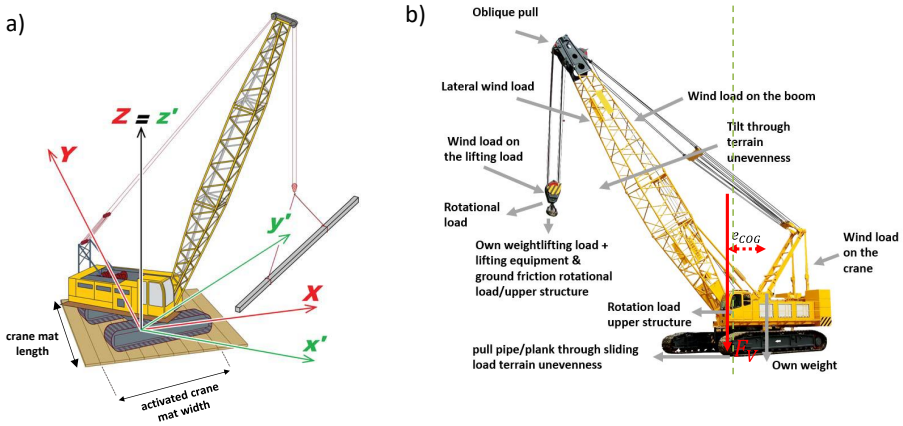


Figure 2. a) Local and global coordinate system; b) overview of the different load components (grey arrows) of the foundation machine and the resulting eccentric vertical force (red arrow)

2.3. Bearing capacity of the foundation (timber crane mats)

The bearing capacity of the soil beneath the timber crane mat is calculated using Eurocode 7 for shallow foundations. The bearing capacity of the foundation or R_d is calculated using formula (1).

$$R_{v,d} = \sigma'_{max;d} \times A', \tag{1}$$

where $R_{v,d}$ is the design value of the component of the bearing capacity perpendicular to the foundation surface; $\sigma'_{max;d}$ is the design value of the maximum foundation pressure on the effective foundation surface, in kPa and A' is the effective foundation surface, in m². The effective foundation surface is dependent on the eccentricity of the vertical resulting force (both in the length and the width).

2.4. Limit state

The unity check (u.c.), (2) for the (semi-probabilistic) design consists of comparing the calculated value of the vertical load ($E_{v,d}$, Effect) with the calculated value of the maximum vertical load ($R_{v,d}$, Resistance). In general, a design should have a unity check smaller than 1.0. To achieve this condition, the length of the timber crane mats is modified until u.c.= 1.0 is reached.

$$u.c. = \frac{E_{v,d}}{R_{v,d}} \leq 1.0. \tag{2}$$

In a failure probability calculation, the loads and strengths are modelled as stochastic variables $\boldsymbol{X}$ (using probability distributions for each load and strength). For any combination of parameters, failure occurs when the load exceeds the strength. To account for the possibility that the bearing capacity calculated by the simplified model deviates from the actual capacity in practice, the outcome is multiplied by a model uncertainty factor m. The above is modelled using a limit state function Z (equation (3)), where a value lower than 0 indicates failure.

$$Z(\boldsymbol{X}) = R_{v,d} \cdot m - E_{v,d} \tag{3}$$

where $R_{v,d}$ is the load-bearing capacity and $E_{v,d}$ the load effect. Both depend on the stochastic parameters in $\boldsymbol{X}$. The failure probability P_f is then equal to the probability that Z becomes smaller than 0, which is defined by equation (4) where $f_{\boldsymbol{X}}(\boldsymbol{x})$ is the probability density function of $\boldsymbol{X}$.

$$P_f = \int_{Z(\boldsymbol{X})<0} f_{\boldsymbol{X}}(\boldsymbol{x}) d\boldsymbol{x}. \quad (4)$$

The failure probability in this study is estimated using the First Order Reliability Method (FORM). The reliability index and failure probability can be converted into each other using the inverse of the cumulative standard normal distribution (Φ^{-1}).

$$\beta = \Phi^{-1}(1 - P_f) \quad (5)$$
$$P_f = \Phi(-\beta) \quad (6)$$

3. CASE STUDIES

3.1. Introduction

The information provided in this study is based on available data and a limited number of cases. It is essential to recognize that determining the loads and centre of gravity positions of the foundation machines can be a challenging task. The accuracy of the results depends on various factors, including the quality of input data, assumptions made during modelling, and uncertainties inherent in the process. Therefore, users should exercise caution and consider the limitations when interpreting and applying the findings presented in this paper.

3.2. Case description

Three foundation machines used for different purposes were considered (37, 100, and 275 tons), along with three simplified soil profiles (weak clay, clay, and sand; see Table). These nine combinations cover various practical scenarios. In the failure probability calculation, uncertainties in loads and strength were considered. Firstly, the uncertainty of the soil properties and groundwater level. Secondly, the uncertainty of the annual maximum wind load. Thirdly, expectation values and uncertainties of weights and center of gravity eccentricities for various machine components were determined in consultation with an experienced foundation machine designer.

Some uncertainties are modelled as correlated stochastic variables, such as the center of gravity positions of the mast, mast head, hammer, cap, and pile. Furthermore, we chose fixed values for the eccentricity of the machine on the crane mats (0.75 m), and a rotation of the upper carriage of 15°. As the hoist load can also be inclined, e.g. when hoisting a foundation pile, we assumed an angle of 35° relative to the vertical, and the probability of an angle > 45° being less than 5%.

Table 1. Applied subsurface schematizations.

Subsoil profile 1: clay, weak		Subsoil profile 2, clay		Subsoil profile 3, sand	
< 0.0 m- mv.*	Sand, loosely packed	< 0.0 m- mv.*	Sand, loosely packed	< 0.0 m-mv.*	Sand, loosely packed
	$\gamma_{sat;d}$ = 15.5/17.3 kN/m^3		$\gamma_{sat;d}$ = 15.5/17.3 kN/m^3		$\gamma_{sat;d}$ = 15.5/17.3 kN/m^3
	f'_d = 26.7°		f'_d = 26.7°		f'_d = 26.7°
< 1.0 m- mv.*	Clay, weak	< 1.0 m- mv.*	Clay	< 2.0 m- mv.*	Sand, medium packed
	$\gamma_{sat;d}$ = 12.7 kN/m^3		$\gamma_{sat;d}$ = 12.7 kN/m^3		$\gamma_{sat;d}$ = 18.2 kN/m^3
	$s_{u;d}$ = 7.2 kPa		$s_{u;d}$ = 12.0 kPa		f'_d = 29.0°
< 15.0 m- mv.*	Sand, medium packed	< 15.0 m-mv.*	Sand, medium packed	< 15.0 m- mv.*	Sand, medium packed
	$\gamma_{sat;d}$ = 18.2 kN/m^3		$\gamma_{sat;d}$ = 18.2 kN/m^3		$\gamma_{at;d}$ = 18.2 kN/m^3
	f'_d = 29.0°		f'_d = 29.0°		f'_d = 29.0°
Groundwater level	0.8 m- mv.	Groundwater level	0.8 m- mv.	Groundwater level	0.8 m- mv.

*) mv. refers to the Dutch word 'maaiveld' representing the surface level. The values presented are thus relative depths below the ground level.

3.3. Target reliability and partial factors in EC7

The target reliabilities and the prevailing partial factors used for the calculation are shown in *Table* . As it is not prescribed which loads on the crane are to be considered permanent and variable, we assumed the weights of the crane to be permanent loads, and the other loads acting externally to be variable loads (and wind as wind load).

Table 2. Target reliability and partial factors in from EC7 and NEN8707

Reliability class	Consequence class	Reliability index β_T (wind not dominant)	Partial factor for load		
			Permanent load	Wind load	Other variable load
Design of new structures (t_{ref} = 50 years)	CC1	3.3	1.20	1.35	1.35
	CC2	3.8	1.35	1.50	1.50
	CC3	4.3	1.50	1.65	1.65
Renovation of existing structures (t_{ref} = 15 years)	CC1	2.8	1.15	1.20	1.10
	CC2	3.3	1.25	1.40	1.30
	CC3	3.8	1.30	1.60	1.50
Disapproval existing structures (t_{ref} = 15 years)	CC1	1.8	1.00	1.10	1.05
	CC2	2.5	1.10	1.30	1.15
	CC3	3.3	1.25	1.50	1.30

4. RESULTS

4.1. Results of the crane mat design

In Figure 3, the calculated lengths of the crane mat lengths are shown. From the results a large variability appears in the designed length, depending on the loads and eccentricities, ground profile, consequence class and reliability level.

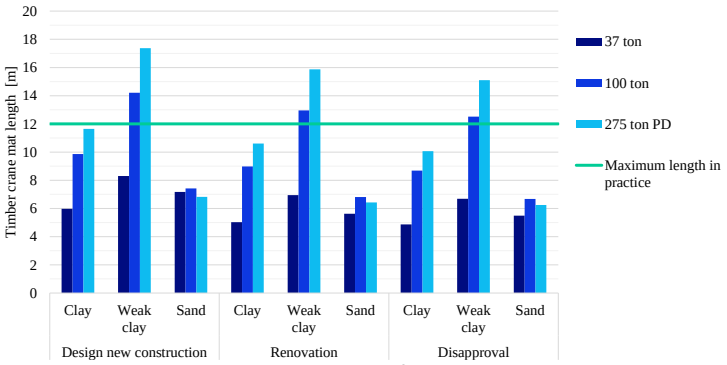


Figure 3. Required lengths of timber crane mats

The main observations from the results are:

- The longest timber crane mats are calculated with the design rules for new structures.
- Machines that are situated on sand show small differences in calculated crane mat length.
- The differences between the crane mat lengths of different reliability classes are small because the factors differ not so much between the reliability classes, whereas the load bearing capacity is independent of the reliability class.
- Differences in crane mat lengths are primarily caused by differences in the eccentricity of the resulting load. For example, the 275-ton machine is relatively stable with a relatively small

eccentricity compared to the 100-ton machine which has a larger overturning moment and eccentricity due to the relatively large horizontal component of the hoist load.

- Higher machine weight positively affects centre of gravity eccentricity and effective foundation surface. This results on average in shorter required lengths of the crane mats.

4.2. Results of the reliability analysis

The required lengths of the crane mats (Figure 4) are used as fixed value within the probabilistic analysis, and Figure 6 displays the realized reliability indices. The green lines represent target reliability (β_T, *Table*), indicating successful achievement in nearly all calculations for both new construction and renovation levels. Notably, average failure probabilities per consequence class meet requirements.

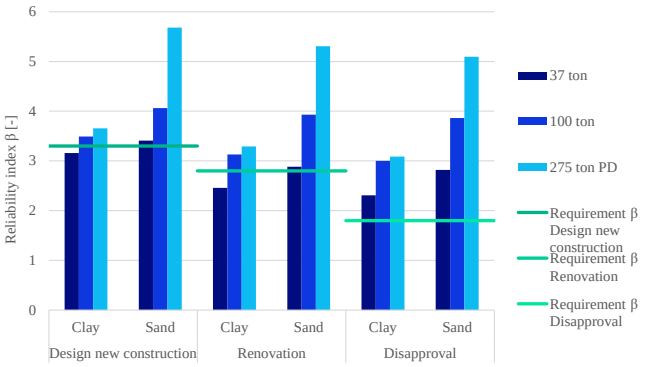


Figure 4. Reliability index of all investigated case studies

The calculations furthermore reveal the impact of uncertainties of the various parameters on the failure probability. The uncertainty of ground bearing capacity is consistently dominant, increasing with machine weight (35-70% on clay, 10-40% on sand). Combined effects of overturning moments (loads and eccentricities) inversely correlate with machine weights, indicating a positive influence on geotechnical stability. Model uncertainty significantly varies (2-17%) and is not negligible. Note that wind pressure uncertainty minimally affects the failure probability (due to truncated probability distribution), however its contribution to the eccentricity is in some cases substantial.

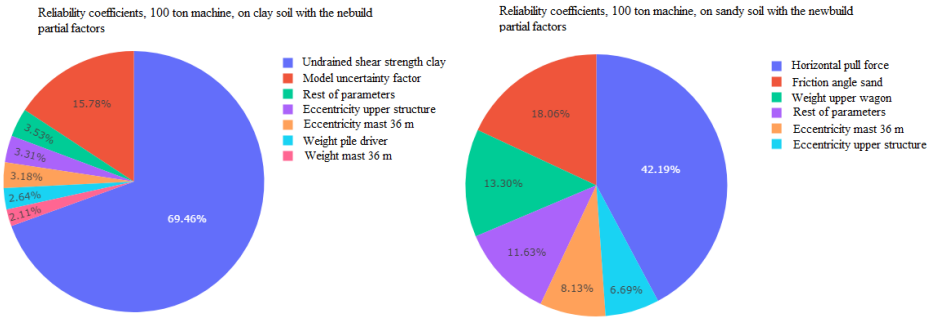


Figure 5. Contributions of influence factors

4.3. Case-specific partial factors

Some of the cases exceed the required reliability level (for example the disapproval level for all cases considered). This implies that the current set of load and material factors are not optimal. Ideally these

factors would be adjusted to achieve the target reliability for each design calculation. In this part of the study, case-specific (optimal) partial factors were calculated based on the influence factors of all parameters, and the target reliability for the different classes. The required material factors (partial factor on resistance, i.e. soil properties) have been calculated as follows:

$$\gamma_R = \frac{R_k}{R_d} = \frac{\mu_i \cdot (1 - Z_i \cdot VC_i)}{\mu_i \cdot (1 - \alpha_{R,i}{}^* \cdot \beta_T \cdot VC_i)} \tag{7}$$

A similar formulation applies for the calculation of the partial factors for loads:

$$\gamma_S = \frac{R_d}{R_k} = \frac{\mu_i \cdot (1 - \alpha_{s,i}{}^* \cdot \beta_T \cdot VC_i)}{\mu_i \cdot (1 - Z_i \cdot VC_i)}. \tag{8}$$

The calculated case-specific factors for the most important parameters are shown in Figure 6. The first observation is that the partial factor for the weight of the upper and lower wagon is smaller than 1. It appears that a heavier carriage is favorable for the safety, since the effect of an increase of the effective foundation area is larger than the effect of an increase of the load. The factor lower than 1,0 is in line with EC7 where favorable loads should be factorized by 0,9 rather than 1,2. However, in the CUR689 regulations this distinction is not made.

Generally, the optimal partial load factors are lower than what is prescribed in the Eurocode, however, a reduction might only be possible when compensatory adjustments are made in material factors for soil properties and in how we address model uncertainty. The optimal partial factors for model uncertainty were found between 1,0 and 1,2, whereas it is currently not specifically addressed by the Eurocode.

Another observation is that the case-specific partial factors for the friction angle is lower than currently in the Eurocode; in other words, the Eurocode is conservative in this regard. For the undrained shear strength, this is not the case. Because this uncertainty is dominant in our calculations, then case-specific necessary partial factor is quite high (for the design and renovation class). A strong dependency of material factors on the reliability level is found here.

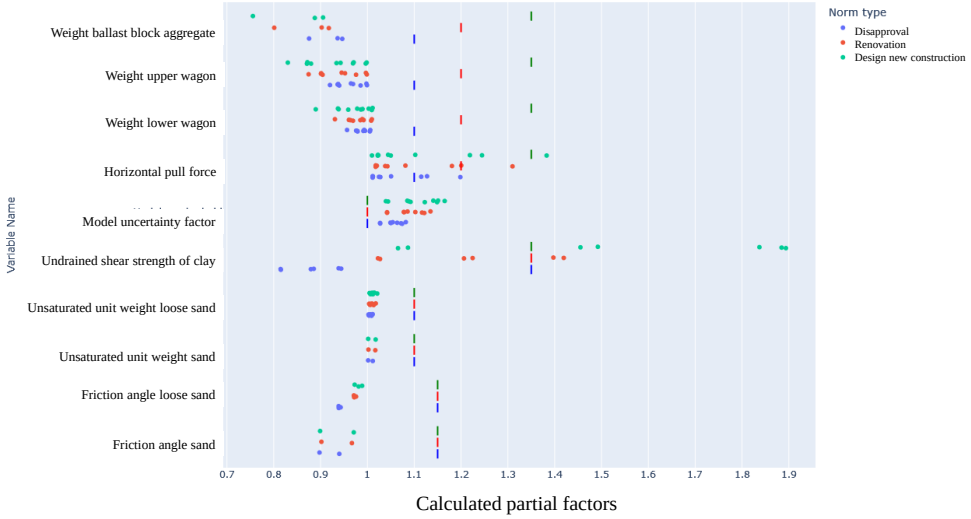


Figure 6. Case-specific partial factors for loads and materials. The prevailing factors from NEN-EN1997 are indicated by horizontal stripes

5. CONCLUSION

The analyses show that sufficiently safe designs can be realized with the current rules, i.e. the partial factors in EC7, for the considered cases. To generalize these conclusions, more different cases are needed. The results also show that the partial factors for the disapproval level might meet the lower limit for human safety in terms of structural safety (disapproval level in the Dutch NEN8700). Although the Dutch law prescribes the EC7 rules for new structures, such a higher reliability level would only be justified if the associated additional costs are proportional. With short-term foundation work, this is not always the case. If a designer wants to base on the disapproval level, one should discuss this with the competent authority.

Furthermore, the results show that the current load and material factors do not optimally match the uncertainties dominant for the bearing capacity of the crane mats under the eccentric loads of the foundation machinery. The results imply that there is room for lowering the partial factors for the loads, while simultaneously increasing the material factor for undrained shear strength. On balance, this would lead to more uniform reliability and on average shorter crane mats to be required.

Also, the results show that:

- a project-specific failure probability analysis can provide a tailored solution in case the current factors do not result in a practically realizable design;
- the target reliability is substantially exceeded in a number of cases; this implies that the current sets of load and material factors are not optimal;
- the model uncertainty has a relevant influence on the reliability, while this is not considered in the standards; we recommend that this aspect be considered in future modifications of NEN9997-1 and NEN8707.

Finally, to ensure safety, it is important that temporary foundations are reliably designed, and executed as such. Insufficient attention to design can lead to potentially dangerous situations. Design calculations with the correct assumptions and load factors, as well as supervision on the construction site, are crucial here. Furthermore, all above aspects are also relevant to ensure safety in other temporary structures and structures.

6. ACKNOWLEDGEMENTS

This project was executed together with the Dutch Ministry of Infrastructure or Rijkswaterstaat.

REFERENCES

CEN. 2002. Eurocode 0: Basis of Structural Design, EN1990. Technical report, European Committee for Standardisation.

CEN. 2007. Eurocode 7: Geotechnical Design. Part 1: General Rules, EN1997-1. Technical report, European Committee for Standardisation.

CROW. 2017. CRW 689.16. Begaanbaarheid van bouwterreinen. (in Dutch)

Deltares. 2023. Geotechnische stabiliteit van funderingsmachines. Technical report 11209211-003-GEO-0001. (in Dutch). Authors: Van der Krogt, M.G. and Smyrniou, E.

NEN. 2023. Assessment of an existing structure in case of reconstruction and disapproval – Geotechnical structures. NEN8707. Nederlands Normalisatie-instituut (NEN).

Rackwitz, R., and Fiessler, B. 1979. Structural reliability under combined random load sequences. Computers and Structures 9(5): 489-494.

28th European Young Geotechnical Engineers Conference – EYGEC 2024
© 2024 Macedonian Association for Geotechnics, ISBN 978-608-4510-61-1

Predictive modeling of sandy subgrade soil's resilient modulus using cyclic and static triaxial test variables and results

Tadas Tamošiūnas[a], Šarūnas Skuodis[b]

[a, b] *Department of Reinforced Concrete Structures and Geotechnics, Vilnius TECH, Vilnius, Lithuania*

ABSTRACT

To design a pavement the mechanical properties of it need to be determined, one of them is the resilient modulus (E_r), which is a measure of the ability of a material to resist deformation under repeated loading. The prediction of resilient modulus using different types of parameters is a well-known and commonly used practice. Three static and one cyclic triaxial tests were conducted with variously graded sand (SP) and the same type and number of tests were conducted with the well-graded sand (SG). Two dependencies were observed during the analysis of the tests results: 1) the power dependency between the resilient modulus and a ratio of maximum and minimum values of deviatoric stress, and 2) natural logarithmic dependency between the ratio of resilient modulus to maximum and minimum values of deviatoric stress, and a ratio of secant modulus from the static triaxial tests to a maximum and minimum value of deviatoric stress. Developed prediction dependencies showed a good agreement compared to the resilient modulus values received from the direct test results.

KEYWORDS

Resilient modulus; cyclic triaxial test; static triaxial test; predictive models; sand.

1. INTRODUCTION

To design a pavement the mechanical properties of it need to be determined, one of them is the resilient modulus (E_r), which is a measure of the ability of a material to resist deformation under repeated loading (Transportaions officials, 1993; Transportaions officials, 2008; EN 13286-7, 2004). It provides a measure of the stiffness of the pavement material and its ability to resist rutting and fatigue (Behiry, 2012; Sas et al., 2016), so it is commonly used in the design of flexible pavements. There are several factors affecting the resilient modulus such as the type and amount of loading, the temperature, and the moisture content of the material (Jin et al., 1994; Filotenkovas and Vaitkus, 2022). The cyclic triaxial pressure tests are performed in the laboratory to determine the resilient modulus. These tests are difficult to perform due to several reasons, such as the duration of the tests, expensive equipment, and a need for highly qualified specialists which makes these tests relatively expensive (Tamošiūnas and Skuodis, 2023; Tilti et al., 2006). To solve this issue a predictive modeling of resilient modulus has been introduced (Tamošiūnas et al., 2022; Fathi et al., 2021; Pahno et al., 2021). The purpose of this research work is to find the dependencies between soil parameters that were used and received during the static and cyclic triaxial test campaign and the resilient modules that were received after the performance of the cyclic triaxial tests.

2. TEST PROCEDURE

To determine the secant modulus (E_{50}) the static isotropic consolidated drained (CD) triaxial compression tests were conducted for every type of soil according to the procedure described in LST EN ISO 17892-9. Three different values of confining stress σ_3 were applied during the consolidation and loading phases: 20 kPa, 50 kPa, and 70 kPa. To determine the resilient modulus the isotropic unconsolidated drained cyclic triaxial tests were performed according to the low-stress test program provided in EN 13286-7 (method B), which was adjusted using three different values of confining stress,

20 kPa, 50 kPa, and 70 kPa, the same values as for static isotropic consolidated drained triaxial compression tests. The minimum value of the deviator σ_d was fixed at the limit of 10 kPa due to the limitations of the test apparatus. The number of cycles and the maximum deviator stress for a particular state of specimen loading are described in Table 1. The loadings of the specimen were performed at a frequency of 1 Hz with data recording intervals ranging from 100 to 150 times per second. Conditioning of specimens was performed with 20'000 periodic cyclic loadings at the same frequency of 1 Hz with variable stress deviator ranging from 10 to 200 kPa as described in EN 13286-7 (lowest 10 kPa stress deviator was applied due to limitations of the equipment). The dimensions of the samples for static and cyclic triaxial tests were the same, 100 mm in diameter and 200 mm in height. Both types of tests were performed using Wille Geotechnik cyclic triaxial apparatus.

Table 1. Test program for cyclic triaxial test after the conditioning phase

Confining stress σ_3, kPa	Deviator stress σ_d, kPa	
constant	min	max
20	10	20
20	10	35
20	10	50
20	10	70
50	10	50
50	10	70
50	10	90
50	10	120
50	10	160
70	10	70
70	10	90
70	10	120
70	10	160
70	10	200

3. MATERIALS

Static and cyclic triaxial tests were performed with two types of soils which were classified according to the LST 1331 standard. The first one is variously graded sand (SP), and the second one is well-graded sand (SG). Additionally, the classification according to the Unified Soil Classification System (USCS)(Daryati et al., 2019) was performed on the soils mentioned above, and the resulting types can be seen in Table 2, as well as coefficients of curvature (C_c), and uniformity coefficients (C_u).

Table 2. Classification of soils

Type of specimen	C_u	C_c	Soil Classification	
			LST 1331	USCS
SP	4.74	0.75	Variously graded sand (SP)	Poorly graded sand (SP)
SG	6.23	1.07	Well-graded sand (SG)	Well-graded sand (SW)

4. PREDICTIVE MODELS

The prediction of resilient modulus using different types of parameters is well-known and commonly used in practice. There are many predictive models that help to predict the values of residual modulus using the mechanical and physical properties of the soil (Zhang et al., 2021a; 2021b; Hanandeh et al., 2020). Another group of predictive models that are commonly used are models based on the stress state of the soil. The universal Witczak model (Yoder and Witczak, 1975; Al-Dulaimi et al., 2022), the Uzan model (Uzan, 1985; Hopkins et al., 2020), the K-θ model (Hicks, 1970; Adomako et al., 2022; Chowdhury, 2021), and the Rahim and George model (Rahim and George, 2005; Fedakar et al., 2022) can be taken as an example of such type of models. A new Octahedral Shear Stress (OSS) predictive model based on the stress state of the soil was developed (Tamošiūnas and Skuodis, 2023) by the current article authors:

$$E_r = K_1 \tau_{oct} - K_2, \quad (2)$$

where (τ_{oct}) is the octahedral shear stress equal to ($\sqrt{2}/3$)(σ_1- σ_3), and $K_{1\text{-}2}$ are regression coefficients. This new model predicts resilient modulus with a regression coefficient K_1 ranging from 15.58 to 16.24 depending on the soil type, regression coefficient K_2 ranging from 19.46 to 77.73, also depending on the soil type, and a coefficient of determination (R^2) ranging from 0.85 to 0.99.

5. RESULTS AND DISCUSSION

Three static and one cyclic triaxial tests were conducted with variously graded sand (SP) and the same type and number of tests were conducted with the well-graded sand (SG). The results for variously graded sand (SP) are presented in Tables 3-4.

Table 3. Cyclic triaxial test results for variously graded sand (SP)

Cyclic triaxial						
Number of cycles	$\sigma_{3,max}$	$\sigma_{d,min}$	$\sigma_{d,max}$	E_r	$\sigma_{d,max}$ /$\sigma_{d,min}$	E_r / ($\sigma_{d,max}$ / $\sigma_{d,min}$)
20'000 - 20'100	20.7	10.5	21.0	125.8	2.0	63.2
20'100 - 20'200	20.6	11.5	35.9	211.4	3.1	67.4
20'200 - 20'300	20.5	12.4	51.2	315.8	4.1	76.3
20'300 - 20'400	23.6	12.7	67.5	437.5	5.3	82.7
20'900 - 21'000	50.8	10.7	51.9	355.7	4.9	73.2
21'000 - 21'100	50.8	11.3	73.2	507.0	6.5	78.1
21'100 - 21'200	50.9	11.8	92.8	653.5	7.8	83.4
21'200 - 21'300	51.0	12.3	123.2	881.1	10.0	87.7
21'300 - 21'400	52.5	13.2	150.2	1066.5	11.3	94.0
21'400 - 21'500	71.0	10.5	71.8	516.6	6.8	75.5
21'500 - 21'600	71.0	10.7	92.8	674.3	8.7	77.6
21'600 - 21'700	70.7	11.1	123.8	886.9	11.1	79.6
21'700 - 21'800	70.9	11.6	163.5	1186.4	14.1	84.3
21'800 - 21'900	71.1	12.6	199.0	1440.5	15.7	91.5

Table 4. Static triaxial test results for variously graded sand (SP)

Static triaxial		
σ_3	E_{50}	E_{50} ($\sigma_{d,max}$ / $\sigma_{d,min}$)
20.0	14.0	27.9
20.0	14.0	43.9
20.0	14.0	57.9
20.0	14.0	74.1
50.0	34.9	169.6
50.0	34.9	226.5
50.0	34.9	273.4
50.0	34.9	350.4
50.0	34.9	395.8
70.0	42.2	288.8
70.0	42.2	366.6
70.0	42.2	470.4
70.0	42.2	593.7
70.0	42.2	664.2

The results for variously well-graded sand (SG) are presented in Tables 5-6. The picture of well-graded sand (SG) after the static and cyclic triaxial tests is presented in Figures 1-2.

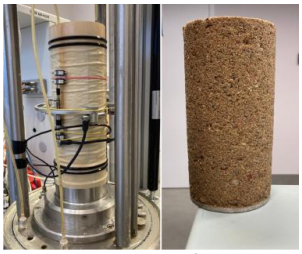


Figure 1. Well-graded sand (SG) after the cyclic triaxial test

Table 5. Cyclic triaxial test results for variously well-graded sand (SG)

Cyclic triaxial						
Number of cycles	$\sigma_{3,max}$	$\sigma_{d,min}$	$\sigma_{d,max}$	E_r	$\sigma_{d,max}$ /$\sigma_{d,min}$	E_r / ($\sigma_{d,max}$ / $\sigma_{d,min}$)
20'000 - 20'100	20.1	9.0	22.5	75.3	2.5	30.2
20'100 - 20'200	20.2	10.4	36.5	150.2	3.5	42.7
20'200 - 20'300	19.9	11.2	51.7	255.7	4.6	55.3
20'300 - 20'400	23.0	12.0	68.1	411.0	5.7	72.5
20'900 - 21'000	49.8	11.1	52.6	281.6	4.7	59.5
21'000 - 21'100	50.9	11.0	73.6	489.0	6.7	73.3
21'100 - 21'200	50.5	11.5	92.8	601.6	8.1	74.5
21'200 - 21'300	50.3	12.5	123.8	816.2	9.9	82.3
21'300 - 21'400	52.9	13.3	150.8	1016.5	11.3	89.9
21'400 - 21'500	70.7	10.3	72.3	386.5	7.0	55.3
21'500 - 21'600	71.0	11.0	93.0	606.0	8.4	71.9
21'600 - 21'700	71.0	11.9	124.1	906.9	10.4	87.0
21'700 - 21'800	71.2	12.9	163.6	1223.3	12.7	96.3
21'800 - 21'900	71.1	13.5	200.0	1403.8	14.8	94.8

Table 6. Static triaxial test results for variously well-graded sand (SG)

Static triaxial		
σ_3	E_{50}	E_{50} ($\sigma_{d,max}$ / $\sigma_{d,min}$)
20.0	11.8	29.4
20.0	11.8	41.5
20.0	11.8	54.6
20.0	11.8	66.9
50.0	24.4	115.6
50.0	24.4	162.8
50.0	24.4	197.0
50.0	24.4	242.1
50.0	24.4	275.9
70.0	38.9	272.0
70.0	38.9	327.9
70.0	38.9	405.7
70.0	38.9	494.1
70.0	38.9	576.1



Figure 2. Well-graded sand (SG) after the static triaxial test

After receiving the results of cyclic triaxial tests, a power dependence was observed between resilient modulus and a ratio of maximum and minimum values of deviatoric stress. The dependency can be seen in Figure 3.

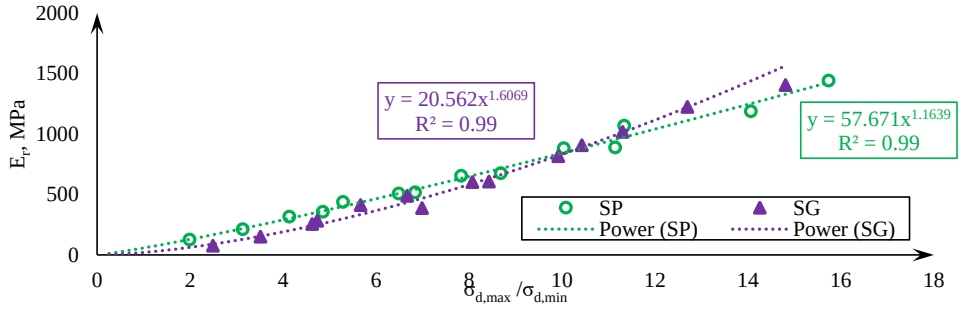


Figure 3. A power dependency between resilient modulus and a ratio of maximum and minimum values of deviatoric stress

As can be seen from Figure 3 the power dependence between resilient modulus and a ratio of maximum and minimum values of deviatoric stress has a coefficient of determination of 0.99. Based on these results, the authors of the paper propose the following dependency equations (3) and (4):

$$E_{r,p}^{SP} = 57.671 \left(\frac{\sigma_{d,max}}{\sigma_{d,min}}\right)^{1.1639}, \quad (3)$$

$$E_{r,p}^{SG} = 20.562 \left(\frac{\sigma_{d,max}}{\sigma_{d,min}}\right)^{1.6069}, \quad (4)$$

where $E_{R,p}^{SP}$ is a predictive value of resilient modulus for variously graded sand (SP), and $E_{r,p}^{SG}$ is a predictive value of resilient modulus for well-graded sand (SG). After receiving the results of cyclic and static triaxial tests, a natural logarithmic dependence was observed between the ratio of resilient modulus to maximum and minimum values of deviatoric stress and a ratio of secant modulus from the static triaxial tests to a maximum and minimum values of deviatoric stress. The dependency can be seen in Figure 4.

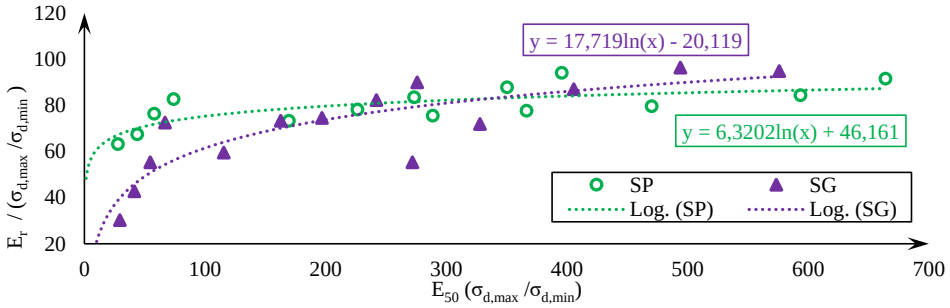


Figure 4. A natural logarithmic dependency between the ratio of resilient modulus to maximum and minimum values of deviatoric stress and a ratio of secant modulus from the static triaxial tests to a maximum and minimum values of deviatoric stress

Based on a natural logarithmic dependence between the ratio of resilient modulus to maximum and minimum values of deviatoric stress and a ratio of secant modulus from the static triaxial tests to a maximum and minimum values of deviatoric stress, the authors of the paper propose the following dependency equations (5) and (6):

$$E_{r,p}^{SP} = \left[6.3202 \ln\left(E_{50}\frac{\sigma_{d,max}}{\sigma_{d,min}}\right) + 46.161\right]\left(\frac{\sigma_{d,max}}{\sigma_{d,min}}\right), \quad (5)$$

$$E_{r,p}^{SG} = \left[17.719 \ln\left(E_{50}\frac{\sigma_{d,max}}{\sigma_{d,min}}\right) - 20.119\right]\left(\frac{\sigma_{d,max}}{\sigma_{d,min}}\right). \quad (6)$$

All four proposed equations (3), (4), (5), and (6) for predicting the resilient modulus were used and the results can be seen in Tables 7-8.

Table 7. Prediction results using power dependence equations (3) and (4)

Number of cycles	SP				SG			
	$\sigma_{dmax}/\sigma_{dmin}$	$E_{r,p}$	E_r	1 - ($E_{r,p}$ / E_r)	$\sigma_{dmax}/\sigma_{dmin}$	$E_{r,p}$	E_r	1 - ($E_{r,p}$ / E_r)
20'000 - 20'100	2.0	128.7	125.8	-2.2%	2.5	89.3	75.3	-18.6%
20'100 - 20'200	3.1	218.1	211.4	-3.2%	3.5	154.9	150.2	-3.1%
20'200 - 20'300	4.1	301.3	315.8	4.6%	4.6	241.1	255.7	5.7%
20'300 - 20'400	5.3	401.1	437.5	8.3%	5.7	334.1	411.0	18.7%
20'900 - 21'000	4.9	363.1	355.7	-2.1%	4.7	250.3	281.6	11.1%
21'000 - 21'100	6.5	508.5	507.0	-0.3%	6.7	434.1	489.0	11.2%
21'100 - 21'200	7.8	633.2	653.5	3.1%	8.1	589.5	601.6	2.0%
21'200 - 21'300	10.0	845.1	881.1	4.1%	9.9	821.2	816.2	-0.6%
21'300 - 21'400	11.3	973.9	1066.5	8.7%	11.3	1013.0	1016.5	0.3%
21'400 - 21'500	6.8	541.0	516.6	-4.7%	7.0	468.0	386.5	-21.1%
21'500 - 21'600	8.7	714.0	674.3	-5.9%	8.4	632.1	606.0	-4.3%
21'600 - 21'700	11.1	954.4	886.9	-7.6%	10.4	889.7	906.9	1.9%
21'700 - 21'800	14.1	1251.4	1186.4	-5.5%	12.7	1221.2	1223.3	0.2%
21'800 - 21'900	15.7	1426.1	1440.5	1.0%	14.8	1562.9	1403.8	-11.3%

After the predictive modeling of resilient modulus using power dependence equations (3) and (4), it can be seen in Table 7 that the predicted resilient modulus had a good agreement compared to the resilient modulus value received from test direct test results, error margin ranging from -7.6% to 8.7% for variously graded sand (SP), and error margin ranging from -18.6% to 18.7% for well-graded sand (SG).

Table 8. Prediction results using natural logarithmic dependence equations (5) and (6)

Number of cycles	SP					SG				
	σ_{dmax} /σ_{dmin}	E_{50}	$E_{r,p}$	E_r	1 - ($E_{r,p}$ / E_r)	σ_{dmax} /σ_{dmin}	E_{50}	$E_{r,p}$	E_r	1 - ($E_{r,p}$ / E_r)
20'000 - 20'100	2.0	14.0	133.9	125.8	-6.4%	2.5	11.8	99.3	75.3	-31.8%*
20'100 - 20'200	3.1	14.0	219.7	211.4	-4.0%	3.5	11.8	161.2	150.2	-7.3%
20'200 - 20'300	4.1	14.0	297.3	315.8	5.9%	4.6	11.8	234.9	255.7	8.1%
20'300 - 20'400	5.3	14.0	388.3	437.5	11.2%	5.7	11.8	308.2	411.0	25.0%*
20'900 - 21'000	4.9	34.9	381.9	355.7	-7.4%	4.7	24.4	303.3	281.6	-7.7%
21'000 - 21'100	6.5	34.9	522.0	507.0	-3.0%	6.7	24.4	467.8	489.0	4.3%
21'100 - 21'200	7.8	34.9	639.5	653.5	2.1%	8.1	24.4	593.3	601.6	1.4%
21'200 - 21'300	10.0	34.9	835.3	881.1	5.2%	9.9	24.4	765.4	816.2	6.2%
21'300 - 21'400	11.3	34.9	952.3	1066.5	10.7%	11.3	24.4	898.4	1016.5	11.6%
21'400 - 21'500	6.8	42.2	561.0	516.6	-8.6%	7.0	38.9	553.8	386.5	-43.3%*
21'500 - 21'600	8.7	42.2	725.2	674.3	-7.5%	8.4	38.9	695.7	606.0	-14.8%
21'600 - 21'700	11.1	42.2	948.1	886.9	-6.9%	10.4	38.9	899.9	906.9	0.8%
21'700 - 21'800	14.1	42.2	1217.2	1186.4	-2.6%	12.7	38.9	1140.3	1223.3	6.8%
21'800 - 21'900	15.7	42.2	1373.0	1440.5	4.7%	14.8	38.9	1369.9	1403.8	2.4%

After the predictive modeling of resilient modulus using natural logarithmic dependence equations (5) and (6), it can be seen in Table 8 that the predicted resilient modulus had a good agreement compared to the resilient modulus value received from test direct test results, error margin ranging from -8.6% to 11.2% for variously graded sand (SP), and error margin ranging from -14.8% to 11.6% for well-graded sand (SG). In Table 8 values marked with the symbol (*) can be held as outliers due to human and machine error while performing the tests.

6. CONCLUSIONS

After the determination and investigation of the static and cyclic triaxial tests results of variously graded sand (SP) and well-graded sand (SG), the following conclusions can be drawn:

- The power dependence equations (3) and (4), proposed by the authors of the paper, for predictive modeling of resilient modulus, showed a good agreement compared to the resilient modulus values received from direct test results. The error margin ranges from -7.6% to 8.7% for variously graded sand (SP), and from -18.6% to 18.7% for well-graded sand (SG).
- The natural logarithmic dependence equations (5) and (6), proposed by the authors of the paper, for predictive modeling of resilient modulus, showed a good agreement compared to the resilient modulus values received from test direct test results. The error margin ranges from -8.6% to 11.2% for variously graded sand (SP), and from -14.8% to 11.6% for well-graded sand (SG).
- The developed equations can serve as a two-step method predicting the values for resilient modulus for variously graded sand (SP) and well-graded sand (SG).

7. ACKNOWLEDGEMENTS

The equipment and infrastructure of the Civil Engineering Scientific Research Center of Vilnius Gediminas Technical University were employed for investigations. This research was supported by the Center of Excellence project “Civil Engineering Research Centre” (Grant No. S-A-UEI-23-5).

REFERENCES

Adomako, S.; Engelsen, C.J.; Thorstensen, R. T.; Barbieri, D.M. Repeated load triaxial testing of recycled excavation materials blended with recycled phyllite materials. *Materials*, 2022, 15.2, pp. 621.

Behiry, A.E.A.E.M. Fatigue and rutting lives in flexible pavement. *Ain Shams Engineering Journal*, 2012, 3.4, pp. 367-374.

Chowdhury, S.R.M. Evaluation of resilient modulus constitutive equations for unbound coarse materials. *Construction and Building Materials*, 2021, 296, 123688.

Daryati, D.; Widiasanti, I.; Septiandini, E.; Ramadhan, M.A.; Sambowo, K.A.; Purnomo, A. Soil characteristics analysis based on the unified soil classification system. *Journal of Physics: Conference Series. IOP Publishing*, 2019, 022028.

EN 13286-7. Unbound and Hydraulically Bound Mixtures–Cyclic Load Triaxial Test for Unbound Mixtures. CEN, 2004.

F Al-Dulaimi, Y.; M Awed, A.; Gabr, A.R.; El-Badawy, S.M. Predicting Resilient Modulus of Unbound Granular Base/Subbase Material.(Dept. C). MEJ. *Mansoura Engineering Journal*, 2022, 47.1, pp. 1-10.

Fathi, A.; Tirado, C.; Rocha, S.; Mazari, M.; Nazarian, S. A Machine-Learning Approach for Extracting Modulus of Compacted Unbound Aggregate Base and Subgrade Materials Using Intelligent Compaction Technology. *Infrastructures*, 2021, 6.10, pp. 142.

Fedakar, H.I. Developing New Empirical Formulae for the Resilient Modulus of Fine-Grained Subgrade Soils Using a Large Long-Term Pavement Performance Dataset and Artificial Neural Network Approach. *Transportation Research Record*, 2022, 2676.4, pp. 58-75.

Filotenkovas, V.; Vaitkus, A. Influence of the aggregate shape and resistance to fragmentation on unbound base layer resilient modulus. *The Baltic Journal of Road and Bridge Engineering*, 2022, 17.3, pp. 104-119.

Hanandeh, S.; Ardah, A.; Abu-Farsakh, M. Using artificial neural network and genetics algorithm to estimate the resilient modulus for stabilized subgrade and propose new empirical formula. *Transportation Geotechnics*, 2020, 24, 100358.

Hicks, R.G. *Factors influencing the resilient properties of granular materials*. University of California, Berkeley, 1970.

Jin, M.S.; Lee, K.W.; Kovacs, W.D. Seasonal variation of resilient modulus of subgrade soils. *Journal of Transportation Engineering*, 1994, 120.4, pp. 603-616.

LST 1331. Automobilių kelių gruntai. Klasifikacija [Soil for roads. Classification]. LSD, 2022.

LST EN ISO 17892-9:2018. Geotechnical Investigation and Testing—Laboratory Testing of Soil—Part 9: Consolidated Triaxial Compression Tests on Water Saturated Soils. Lithuanian Standards Board: Vilnius, Lithuania, 2018.

Ni, B.; Hopkins, T.C.; Sun, L.; Beckham, T.L. *Modeling the resilient modulus of soils. In: Bearing Capacity of Roads, Railways and Airfields*. CRC Press, 2020. p. 1131-1142.

Pahno, S.; Yang, J.J.; Kim, S.S. Use of machine learning algorithms to predict subgrade resilient modulus. *Infrastructures*, 2021, 6.6, pp. 78.

Rahim, A. M.; George, K. P. Models to estimate subgrade resilient modulus for pavement design. *International Journal of Pavement Engineering*, 2005, 6.2, pp. 89-96.

Sas, W.; Głuchowski, A.; Soból, E.; Bąkowski, J.; Szymański, A. Analysis of the multistage cyclic loading test on resilient modulus value. *Ann. Wars. Univ. Life Sci.–SGGW-Land Reclam*, 2016, 48, pp. 53-65.

Tamošiūnas, T.; Skuodis, Š. Predictive Stress Modeling of Resilient Modulus in Sandy Subgrade Soils. *Infrastructures* 8.2 (2023): 29.

Tamošiūnas, T.; Žaržojus, G.; Skuodis, Š. Indirect determination of soil Young's modulus in Lithuania using cone penetration test data. *The Baltic journal of road and brodge engineering*, 2022, 17.2, pp. 1-24.

Titi, H.H.; Elias, M.B.; Helwany, S. Determination of typical resilient modulus values for selected soils in Wisconsin. 2006

Transportation officials. AASHTO Guide for Design of Pavement Structures, 1993. AASHTO, 1993.

Transportation officials. Mechanistic-empirical pavement design guide: a manual of practice. AASHTO, 2008

Uzan, J. Characterization of granular material. *Transportation research record*, 1985, 1022.1, pp. 52-59.

Yoder, E. J.; Witczak, M. W. Chapter 2: Stresses in flexible pavements. *Principles of Pavement Design*. New York: John Wiley and Sons INC, 1975, pp. 24-76.

Zhang, J.; Peng, J.; Liu, W.; Lu, W. Predicting resilient modulus of fine-grained subgrade soils considering relative compaction and matric suction. *Road Materials and Pavement Design*, 2021, 22.3, pp. 703-715.

Zhang, J.; Peng, J.; Zeng, L.; Li, J.; Li, F. Rapid estimation of resilient modulus of subgrade soils using performance-related soil properties. *International Journal of Pavement Engineering*, 2021, 22.6, pp. 732-739.

28th European Young Geotechnical Engineers Conference – EYGEC 2024
© 2024 Macedonian Association for Geotechnics, ISBN 978-608-4510-61-1

Modeling and response of retaining wall subjected to strong ground motions

Maria K. Topalska[a]

[a]*Eng., University of Architecture Civil Engineering and Geodesy, Sofia, Bulgaria*

ABSTRACT

This research explores the seismic response of a flexible retaining wall, designed on a construction site in the city of Sofia, Bulgaria. Time-history analyses were carried out using the finite element modeling. The FEM models were created with Plaxis 2D software. The dynamic behaviour of structure and soil is investigated for a set of real accelerograms. A package of amplitude and integral parameters of the earthquakes is analyzed for each accelerogram. Several strong ground motions whose characteristics are compatible with the geological conditions and frequency parameters of the soils on the construction site were selected. For the purpose of soil-structure interaction analysis the retaining structure is modeled as a linear elastic element. The specific non-linear behaviour of soils is modeled by using the complex constitutive laws HSsmall. According to the results from the performed solutions a comparative analysis is developed. The influence upon the seismic response of structure and soil of varying strong ground motion parameters is considered.

KEYWORDS

Embedded retaining wall; Seismic impact; Accelerogram; Time-history analysis

1. INTRODUCTION

The embedded retaining walls are a widespread method for an excavation support. Their relevance is mainly determined by the need of construction in densely build-up areas and the implementation of underground levels as part of residential and public buildings.

In most cases the decisive load combination for ultimate and serviceability limit state verification is the seismic one. In order to model the soil-retaining structure interaction for seismic impact, the classical approaches of pseudostatic methos are often applied. The pseudostatic methods suggest that the seismic earth pressure depends entirely on the peak ground acceleration *PGA* and remains constant through the time of loading. These methodologies do not explain the soil and structure`s real response during an earthquake event. For more accurate representation a nonlinear time-history analysis should be carried out. It gives the opportunity for more comprehensive description of the strong ground motion, material behaviour under cyclic loads and geometry of structure.

This study is aimed at investigation of the influence on the retaining structure`s stressed and deformed state of several peak and integral parameters of the strong ground motion. For the purpose of this a finite element modeling is conducted by the Plaxis 2D software. The seismic loading is presented by accelerograms. Six accelerograms are used with different ground motion characteristics. Before applying the impact in a FE model to a soil foundation with an adjacent retaining wall, the earthquake records are subjected to a deconvolution procedure. It consists of a process of evaluation of seismic motion at varying depths of a soil profile. The deconvolution is carried out by the ProShake 2.0 software. The retaining wall is modeled as linear elastic structure. To model the soil the HSsmall constitutive model is used. It successfully describes the nonlinear hysteretic behaviour of soil due to cyclic dynamic loading (such as the seismic one).

Studies on the values of the soil parameters according to the HSsmall model have been carried out in the sources (Kerenchev, 2015), (Kerenchev and Milev, 2019).

2. DESCRIPTION OF THE DESIGN STRUCTURE

For the purpose of the study an embedded retaining wall of the Soldier Pile Wall type is examined. The structure is designed to strengthen a deep excavation for the construction of a residential building in the city of Sofia. The geometry of the wall is shown on Figure 1. The vertical load-bearing elements are steel 2T profiles with an axial distance between them of 1,0m. The 2T profiles are 6,5m long. The embedded part is 1,5m long, so the exposed part is 5,0m long. The wall is single row supported by a brace at 45° related to the ground surface.

3. FINITE ELEMENT ANALYSES OF THE SOIL-RETAINING WALL INTERACTION

3.1. Two dimensional FE model

To investigate the soil-retaining wall interaction a plain strain numerical model is built using the Plaxis 2D software (Figure 2). The soil body is discretized by 15-node triangular elements with node displacements U_x and U_y in the xy plane. The wall is modeled by 5-node frame elements which work for bending moments, axial and shear forces. The soil-wall interaction is modeled by interface elements. Along the border of the assumed soil body a damper boundary condition is associated for the purpose of absorbing seismic energy and thus simulating an infinite soil space.
The mesh generation in Plaxis 2D is automatic but it can be controlled and changed. When it comes to dynamic analysis the size of the finite element has to be synchronized with the frequency content of the input motion and the shear wave velocity. According to (Kuhlmeyer and Lysmer, 1973) the average element size *AES* is expressed by Equation 1.

$$AES \leq \frac{V_{s,\min}}{8 f_{\max}}, \tag{1}$$

where: $V_{s,min}$ – the lowest shear wave velocity [m/s^2], f_{max} – the maximum frequency of the input wave [Hz].

Five stages of excavation works are simulated. Calculations and obtained results refer to 1,0 m of the structure.

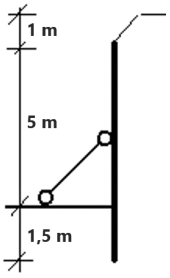


Figure 1. Structure`s cross section

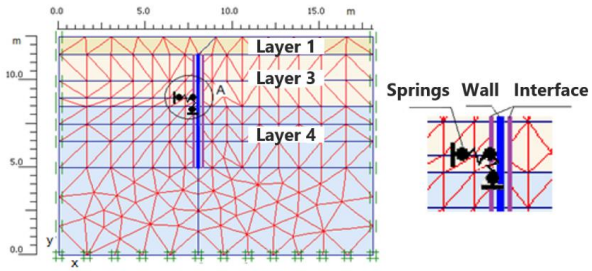


Figure 2. Finite element plane strain model

3.2. Geotechnical materials

The behaviour of dispersed soils under cyclic dynamic impact is described by the Hardening Soil Small (HSsmall) model. According to this model the soil is represented as nonlinear elastoplastic material. It

takes into account for the stiffness degradation of the soil due to cyclic dynamic impact. The decreased stiffness is expressed by the shear modulus reduction G/G_{max}, depending on the shear strain γ. The adopted diagram for volumetric strains ε is shown in (Schanz et al., 1999). A typical diagram for the shear modulus reduction curve can be seen in (Kramer, 1996). The HSsmall model uses the Mohr-Column failure criteria and a set of parameters for the soil layers, which are shown in Table 1.

Table 1. Conventional soil characteristics and parameters of the HSsmall model

Parameter	Symbol	Measure	Layer 1	Layer 3	Layer 4
Bulk density	γ_n	kN/m^3	18,0	20,0	18,5
Cohesion	C	kPa	24,0	31,8	26,0
Angle of friction	φ	°	18,0	34,0	19,0
Reference stress for stiffness	p_{ref}	kPa	100	100	100
Tangent stiffness for primary oedometer loading	$E_{oed,ref}$	kPa	12 000	26 000	20 000
Secant stiffness in the standard drained triaxial test	$E_{50,ref}$	kPa	12 000	26 000	20 000
Unloading/Reloading stiffness	$E_{ur,ref}$	kPa	36 000	80000	60 000
Initial shear modulus	$G_{0,ref}$	kPa	80 000	150 000	120 000
Poisson's ratio	ν'	-	0,3	0,3	0,3
Poisson's ratio for unloading/reloading	ν_{ur}	-	0,2	0,2	0,2
Shear strain for the 0.722 of the reduction of the shear modulus	$\gamma_{0.7}$	%	0,06	0,015	0,05
Power factor for the stress-level dependency of stiffness	m	-	0,6	0,6	0,6
Failure ratio	R_f	-	0,9	0,9	0,9
Angle of dilatancy	ψ	°	0	2	0
Coefficient of lateral earth pressure	k_0	-	0,700	0,470	0,642

3.3. Derivation of design seismic excitation

For the purpose of FE modeling of dynamic response of soil and structure the seismic excitation needs to be applied at the base of the finite domain of soil body. The strong ground motion which corresponds with the depth of the soil body`s base can be obtained by a deconvolution procedure.
Lets look at a 1D column of a soil profile which is presented as a SDOF system. The main idea is to explore the shear wave propagation through the soil layers and to generate a motion at a given depth in the soil profile. The latter is achieved by implementing the concept of transfer function, which is expressed by Equation 2.

$$H_{ij}(\mathrm{w}) = \left|\ddot{u}_i(w)\right| \Big/ \left|\ddot{u}_j(w)\right|, \tag{2}$$

where: $\ddot{u}_i(w)$ – Fourier spectrum amplitude of the free surface motion, $\ddot{u}_j(w)$ – Fourier spectrum amplitude of the base motion.

Here in a conventional frequency-domain solution is used in order to deconvolve the surface ground motion to the base of the FE model (Poul and Zerva, 2018). The software ProShake 2.0 is used. The soil nonlinear behaviour is taken into account by applying the equivalent-linear constitutive model. To predict the corresponding shear modulus G and damping ratio ξ for each FE node i an iterative procedure is needed. The values of G_i and ξ_i, dependent on the maximum shear strain $\gamma_{max,i}$, are defined according to the reduction curves of (Vucetic & Dobri, 1991). As a result the design seismic excitations are obtained, which are applied to the base of the FE 2D model.
The retaining structure is examined for 6 earthquakes, selected to cover a large range of frequencies. The seismic impact is defined via accelerograms, scaled up to PGA = 1 m/s^2 – Figures 3, 5, 7, 9, 11 and 13.

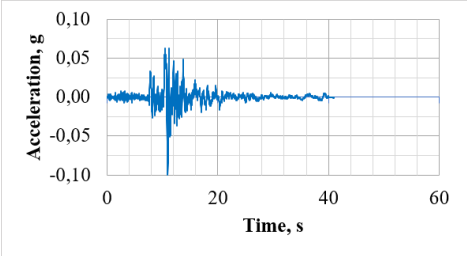


Figure 3. Accelerogram of the Loma Prieta EQ

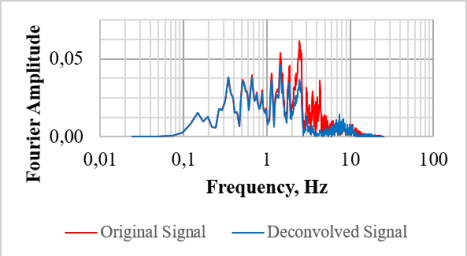


Figure 4. Fourier spectrum of the Loma Prieta EQ

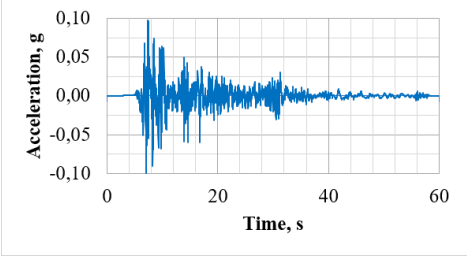


Figure 5. Accelerogram of the El Sentro EQ, 1940

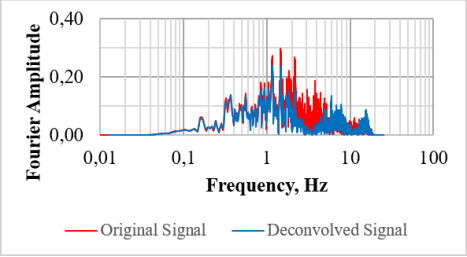


Figure 6. Fourier spectrum of the El Sentro EQ, 1940

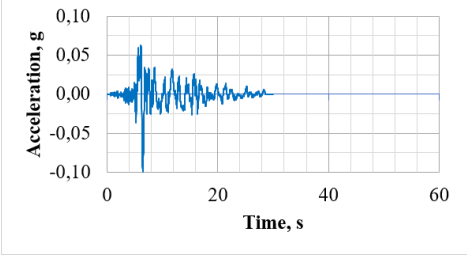


Figure 7. Accelerogram of the Cape EQ, 1992

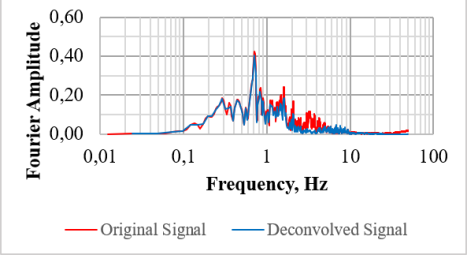


Figure 8. Fourier spectrum of the Cape EQ, 1992

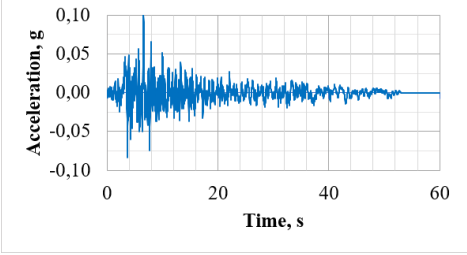


Figure 9. Accelerogram of the Taft EQ, 1952

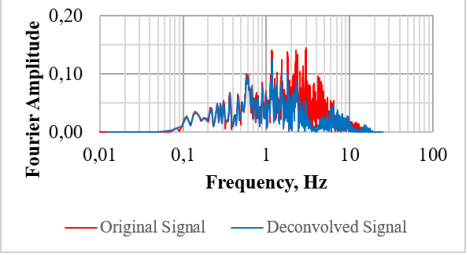


Figure 10. Fourier spectrum of the Taft EQ, 1952

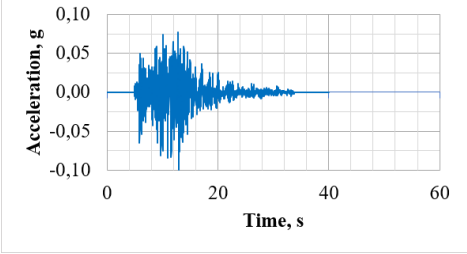


Figure 11. Accelerogram of the Northridge EQ, `94

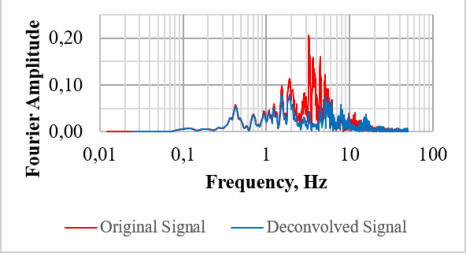


Figure 12. Fourier spectrum of the Northridge EQ,`94

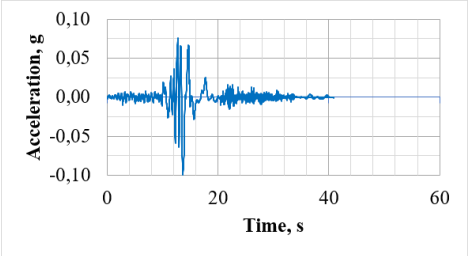


Figure 13. Accelerogram of the Loma Prieta EQ, record from Santa Cruz MTNS

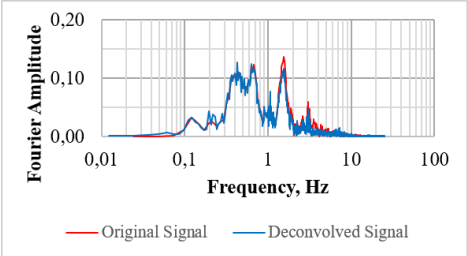


Figure 14. Fourier spectrum of the Loma Prieta EQ, record from Santa Cruz MTNS

In Figures 4, 6, 8, 10 and 12 a comparison between the original (surface) motions and the deconvolved ones is shown. It can be seen that the Fourier amplitude is increased when the seismic wave travels from the profile base to the terrain surface.
The design seismic impacts are rated by a set of peak and integral parameters. The characteristics are related to the deconvolved ground motions, which are used for the dynamic FE analysis. The ground motions` parameters are shown in Table 2.

Table 2. Parameters of the design seismic impacts

Eathquake	α_{max}	Predominant period, T_p	Mean period, T_m	Significant Duration, t_s	Arias Intensity, I_A
-	m/s^2	s	s	s	m/s
Loma Prieta EQ	1,0	0,40	0,86	24,02	0,054
El Sentro EQ	1,0	0,12	0,57	24,02	1,211
Cape Mendocino EQ	1,0	0,58	1,27	11,89	1,165
Taft, Kern County EQ	1,0	0,44	0,72	30,80	0,269
Northridge EQ	1,0	0,18	0,34	11,58	0,346
Loma Prieta EQ, Santa Cruz record	1,0	0,64	1,28	15,65	0,279

3.4. Frequency parameters of the foundation soil

The natural frequency of excitation is of essential importance for the effect of the ground motion on the retaining structure and the foundation soil. When the foundation soil`s natural period matches with the period of the earthquake, a state of resonance occurs. The resonance is associated with amplifying the dynamic load and its effects, which lead to failure of structure and soil.
The system soil-retaining wall, subjected to seismic load, is located in the city of Sofia, Bulgaria. The natural period is determined by Equation 3 (Kramer, 1996). The resulting value is T_s = 1,0 s.

$$T_S = \frac{4H}{V_S}, \tag{3}$$

where: H – thickness of the foundation soil [m]; V_s – shear wave velocity [m/s^2].

4. ANALYSIS OF THE RESULTS

Six dynamic analyses are performed with strong motions presented in Table 2. From the conducted solutions the diagrams of active and passive earth pressures are drawn. Here in Figure 16 are shown 3 typical diagrams of the examined seismic cases. The results for maximum earth pressures from analyses are listed in Table 3.
From the obtained results the envelope diagrams of bending moment M, shear force Q in the retaining wall and maximum horizontal displacement U_x, are reported. The values of the mentioned parameters,

related to proper point of the wall, are placed in Table 3. In Figure 16 the general mode of M and Q diagrams are shown. The force`s distribution along the structure is typical for the adopted scheme.

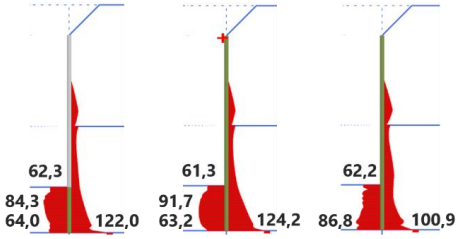


Figure 15. Typical modes of earth pressure diagrams Loma Prieta EQ, Northridge EQ and Loma Prieta EQ (SC)

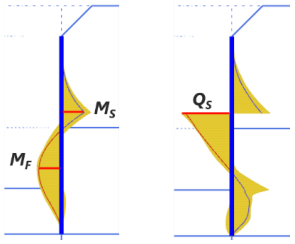


Figure 16. Typical modes of the envelope diagrams for bending moments and shear forces

Table 3. Results from the performed solutions

Earthquake	T_P	T_m	Bending moment, M_F	Bending moment, M_S	Shear force, Q_S	Lateral dis., U_x	Axial brace force, N	Earth pressure, p_a
-	s	s	kNm / m	kNm / m	kN / m	m	kN	kPa / m
Loma Prieta EQ	0,40	0,86	19,88	14,05	40,91	0,09	64,18	122,0
El Sentro EQ	0,12	0,57	20,24	13,99	42,48	0,05	68,29	120,7
Cape Mendocino EQ	0,58	1,27	26,26	16,41	49,94	0,12	79,15	125,0
Taft, Kern County EQ	0,44	0,72	20,70	13,81	41,18	0,08	64,39	122,2
Northridge EQ	0,18	0,34	18,46	13,14	38,55	0,03	61,05	124,2
Loma Prieta EQ, Santa Cruz record	0,64	1,28	28,63	17,78	50,81	0,13	83,00	100,9

Based on the strong ground motion parameters (Table 2) and the results presented in Table 3, several graphs are drawn. In Figure 17 to Figure 22 charts are shown, which illustrate the variation of bending moments (BM) M_F, shear forces (SF) Q_S and lateral displacement (LD) U_X versus predominant period T_P (graphic in red) and mean period T_m (graphic in blue).

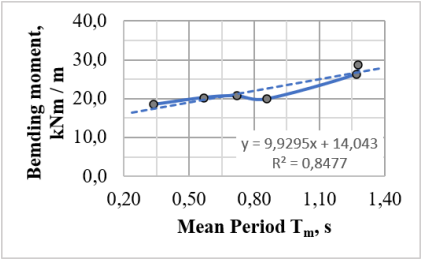


Figure 17. BM M_F versus mean period T_m

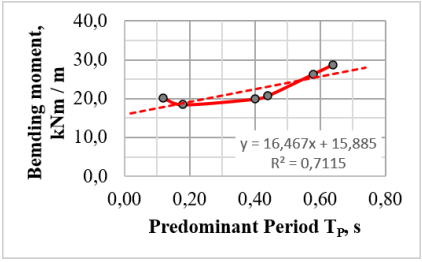


Figure 18. BM M_F versus predominant period T_P

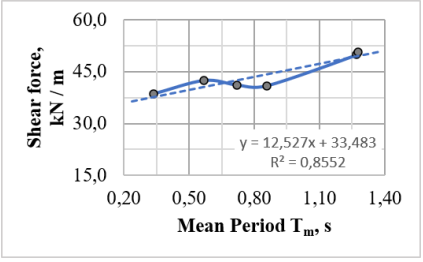


Figure 19. SF Q_F versus mean period T_m

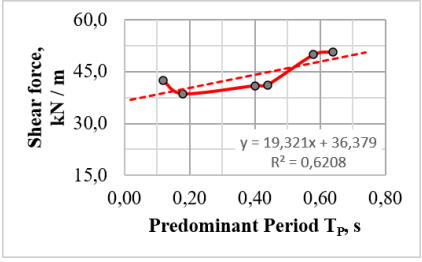


Figure 20. SF Q_F versus predominant period T_P

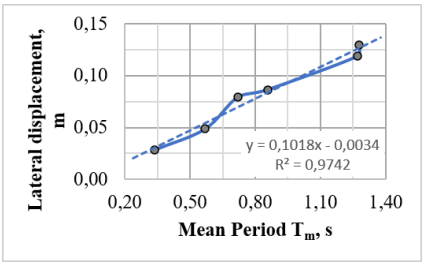


Figure 21. LD U_X versus mean period T_m

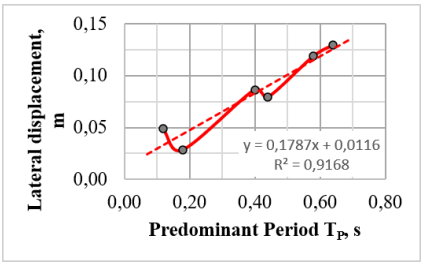


Figure 22. LD U_X versus predominant period T_P

A comparison is performed between the initial (target) seismic signal and the convolved one, obtained from the non-linear analysis in Plaxis 2D. The latter is reported from the free field of the soil body in the FE model. The comparison is made for one seismic motion – Taft EQ, but the results are valid for all the other motions. In Figure 23 and Figure 24 the time-histories and the Fourier spectrums are shown. Obvious distinctions are stated. The difference in the maximum acceleration amplitude is insignificant, but the frequency content is considerably different. The gap of mean period T_m for the pair of impacts amounts of almost 10%, but for the predominant period T_P it is more than 50%.

The quite different solution approaches and applied constitutive models for soils are pointed as the main reason for the observed discrepancies. Additional purposes are pointed as inconsistency of the boundary conditions between ProShake and Plaxis 2D, as well as inconformity of the modeled geometry (one-dimensional for ProShake and two-dimensioanl for Plaxis).

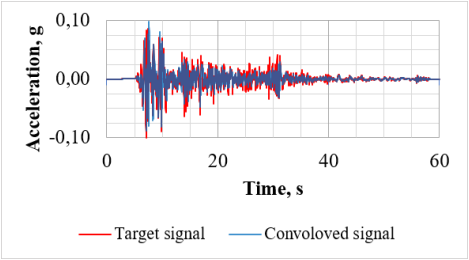


Figure 23. Comparison between target and convolved accelerograms of the Taft EQ, 1952

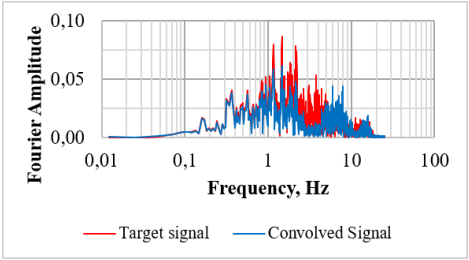


Figure 24. Comparison between target and convolved Fourier spectrums of the Taft EQ, 1952

Based on the comparative analysis the following conclusions can be drawn:

[1] The diagram of active earth pressure is lightly increasing as the bottom of the wall approaches – Figure 15. There is a leap in the diagram marked by the presence of a brace. The maximum value of active earth pressure is obtained for the Cape Mendocino EQ which is 20% higher than the minimum active earth pressure, accomplished by the Loma Prieta (Santa Cruz record) time history;

[2] The diagram of passive earth pressure receives various forms depending on the applied ground motion. For example – for the Loma Prieta EQ (Santa Cruz record) the passive pressure gradually increases as the bottom of the wall approaches. In contrary, for the case of Loma Prieta EQ the passive pressure decreases with depth. In similarity with the active pressure, the highest value of passive pressure is obtained from the Cape Mendocino EQ;

[3] According to the distributions on Figure 17 – Figure 22, a general trend of increasing in forces and displacements as the natural period of foundation soil T_S approaches, is formed;

[4] As the presented diagrams evidence (Figure 17 – Figure 22), the forces and displacements` distribution for the mean period T_m is more satisfactory than the one for the predominant period T_p. The difference in values of the coefficient of correlation amounts of 16% for the BM and 27% for the SF. This leads to the conclusion that the seismic response of structure depends mainly and more accurately on the mean period T_m;

[5] The Cape Mendochino EQ and the Loma Prieta EQ (Santa Cruz record) are the most unfavourable ground motions, that is proved by the highest values for inertial forces, lateral displacement and earth

pressure. This is because the seismic loadings have a mean period T_m = 1,2 – 1,3 s, which is the closest value to the natural period of soil T_P = 1s. In such a case the foundation soil falls into a state close to the resonance. Then an amplification of the impact and the subsequent reaction of the structure take place, which is the purpose for the most adverse response;

[6] For the Cape Mendochino EQ and the Loma Prieta EQ (Santa Cruz record) similar stress values are accomplished. Taking into account for the frequency parameters, the latter statement is fully understandable. The stresses for the Loma Prieta EQ are little higher. The difference in stresses is barely 10% for the BM and 15% for the SF. This is explained with the higher significant duration of the Loma Prieta EQ, which calls forth more reversal cycles and increased degradation of shear stiffness of soil;

5. CONCLUSIONS

In the present study a set of solutions are carried out in order to examine the seismic response of an embedded retaining wall. The soil-structure interaction is simulated by a FE plane strain model. The Plaxis 2D software is used. The hysteresis behaviour of soils due to cyclic dynamic loading is taken into account by applying the HSsmall constitutive model.

The seismic impact is determined by accelerograms. Six accelerograms of real earthquake events are used. The records are previously subjected to a deconvolution procedure in order to obtain the input signal to the base of the FE model. The deconvolution is performed by the ProShake software for 1D wave propagation analysis.

Based on the analysis and comparisons of the obtained results conclusions are drawn. It is shown that the seismic response of the wall depends mostly on the frequency characteristics of the foundation soil and the ground motion – in particular the natural period of soil T_s and the mean period of the earthquake impact T_m.

It is proved that the deconvolution procedure conducted by the ProShake software is not the most appropriate method when there is a non-linear analysis subsequently carried out. Some discrepancies between the convolved time-history signal from the non-linear analysis and the initial (target) time history will surely occur. They are presented mostly by differences in the amplitude and frequency content of the ground motion. That is why a deconvolution of seismic waves from time-domain non-linear analysis is recommended.

REFERENCES

Kerenchev, N. 2015. Analysis of seismic slope stability and deformations PhD Thesis. *University of Architecture Civil Engineering and Geodesy*, Sofia, Bulgaria

Kerenchev, N., Milev, N. 2019. Assessment of the dynamic soil properties for the FEM model of the Liuliakovitsa Tailings Dam. *Proc. of the 8th Conference Geotechnics in Civil Engineering*, Vrnjačka Banja, Serbia

Kramer, S. 1996. Geotechnical Earthquake Engineering. *Prentice Hall, Upper Saddle River, New Jersey 07458*

Kuhlmeyer, R.L., Lysmer, J. 1973. Finite element method accuracy for wave propagation problems. *Journal of the soil mechanics and foundation division*, Vol. 99, pp. 421-427

Poul, M. K., Zerva, A. 2018. Efficient time-domain deconvolution of seismic ground motions using the equivalent-linear method for soil-structure interaction analyses.

Schanz T., Vermeer P.A., Bonnier P.G. 1999. The hardening soil model: Formulation and verification. *Beyond 2000 in Computational Geotechnics - 10 Years of PLAXIS*, Balkema, Rotterdam

Vucetic, M., Dorby, R.. 1991. Effect of soil plasticity on cyclic responses. *Journal of geotechnical engineering*, ASCE 117(GT1), pp. 89–107

28th European Young Geotechnical Engineers Conference – EYGEC 2024
© 2024 Macedonian Association for Geotechnics, ISBN 978-608-4510-61-1

Assessment of geotechnical parameters for wind turbine foundation design based on CPT, DMT and laboratory tests

Vișan I. Alexandra, Rebegea E. Angela, Cireșoiu A. Maria

SAIDEL Engineering SA, Bucharest, Romania

ABSTRACT

In the international context of the climate crisis, renewable energy plays an important and growing role in the energy system of the European Union. Wind energy is one of the main sources of renewable energy, being harnessed through wind turbines both onshore and offshore. Geotechnical design of wind turbine foundations requires detailed knowledge of the mechanical behaviour of the soil. This paper presents the assessment of geotechnical parameters based on CPT, DMT and laboratory tests results at various wind farm locations. Correlations used worldwide are applied to Romanian soils in order to verify their reliability to determine the geotechnical parameters from the in-situ tests results. The aim of this study is to assess the reliability and feasibility of using in-situ tests to calculate the geotechnical parameters required for wind turbine foundation design.

KEYWORDS

CPT; DMT; Laboratory testing; Renewable energy.

1. INTRODUCTION

In Romanian practice, there is a predominant reliance on laboratory tests. However, with advancements in soil modelling, there is a growing necessity to complement these laboratory tests with in-situ investigations for all soil types.

As the internationally used correlations for granular soils have been validated for several projects, the available correlations for cohesive soils applied especially to collapsible loess soils (specific for South-Eastern part of Romania) resulted in values that did not accurately correlate with laboratory results.

In order to obtain statistically valid sets of data, results obtained for 48 wind turbines located in the South-Eastern part of Romania were analysed, compared and correlated.

The in-situ investigations program consisted in cone penetration tests (CPT), as well as geotechnical boreholes with undisturbed sampling on all 48 locations and Dilatometer Marchetti Tests (DMT) on 20 locations. All geotechnical investigations were used in order to statistically correlate the soil stratigraphy and the geotechnical strength and deformability parameters (linear deformation modulus, friction angle and cohesion in undrained conditions) for cohesive, as well as for granular soils.

This paper presents the results and correlations obtained out of the in-situ investigations, as DMT and CPT and in conjunction with usual laboratory tests (direct shear tests and oedometer tests) on collapsible loess soils (specific for South-Eastern part of Romania).

2. GENERAL DATA

For this paper were analysed geotechnical investigations performed on wind turbine locations within a wind farm in Constanta County. The investigated lithology is presented below.

Table 1. Synthetic stratification in the wind farm area

Layer	Name	Description
Layer 0	Topsoil	Topsoil
Layer I	Clayey-silty complex (Loess)	Composed of clayey silt and silty clays with limestone concretions, brownish to yellowish, sensitive to moistening (collapsible)
Layer II	Clay complex	Composed of clay and silty clay with weathered limestone, limestone concretions, Mn and Fe oxides, brown to reddish
Layer III	Clay complex with fragments of weathered limestone	Composed of reddish clays with fragments of weathered limestone
Layer IV	Weathered limestone	Composed of weathered shell limestone in a silty clay matrix and fragments of shell limestone. In some places, the limestone appears highly weathered, resembling whitish limestone sand, with varying degrees of cementation from very weakly cemented to medium cemented.

3. NEW CORRELATIONS PROPOSAL BETWEEN GEOTECHNICAL PARAMETERS OF COHESIVE LAYER IN WIND FARM AREA - LAYER I

According to the norm NP 125-2010 - Norm regarding the foundation of constructions on collapsible soils - Annex 2, one of the documents used to classify soils types in Romania, the site is located in an area characterized by the presence of group A collapsible soils.

Collapsible soils are the macroporous cohesive soils unsaturated, which in contact with water undergoes sudden and irreversible changes in internal structure, leading to additional settlement (collapse) and decrease in the mechanical parameters of the soil. Collapsible soils are: loess, and silty soils with high porosity.

Globally, loess has a low degree of spread (about 10% of the land area) and in Romania loess soils occupy about 17% of the country's territory. For these types of soils, the correlations in the literature are based on local studies and cannot be applied to the general level.

In this chapter new correlations in order to determine loess parameters specific to Romania loess will be proposed. The new correlation obtained have been validated by a parallel analysis with laboratory results.

In order to obtain plausible results, the most qualitative of the laboratory and in-situ investigations were selected. The following criteria selection was used:

1. It was selected a site with a uniform stratification. It is important to use layers without extensive changes (for example, fills or layers with hydrocarbons were excluded). These external factors may affect the geotechnical characteristics of the layers.

2. The shortest possible distance between the investigation points was an important criterion in their selection.

3. Outliers from both laboratory results and in situ investigations were excluded.

Determination of new correlations for collapsible, moisture-sensitive, loess layer

The following linear correlations were determined:

- Between cone resistance q_c and dilatometer modulus M_{DMT},
- Between cone resistance q_c and undrained shear resistance determined from Marchetti dilatometer test c_{uDMT},
- Between cone resistance q_c and internal friction angle from shear strength parameters *tan φ*
- Between cone resistance q_c and oedometer modulus $E_{100\text{-}200}$.

The correlations that have been gained are presented below. These were based on the geotechnical parameters obtained from laboratory tests and on those obtained directly from site or in situ tests and boreholes.

In order to analyze whether there is a linear correlation between the pair of geotechnical parameters presented above, the regression function of the form y=ax+b was used, where a and b are the parameters of the regression line y obtained using the least squares method.

The values of the correlation coefficients vary between 0 and 1. If r=0 and r^2=0 there are no correlation. If coefficient values are close to 1, there is a strictly linear correlation between the studied parameters. According to current geotechnical engineering a satisfactory value of correlation coefficient is considered r >0.7-0.8 and r^2>0.5-0.64.

Cone pressure q_c [MPa] and undrained shear strength c_u [kPa] determined using DMT were correlated using approximately 30 points. The figure below shows the obtained correlation.

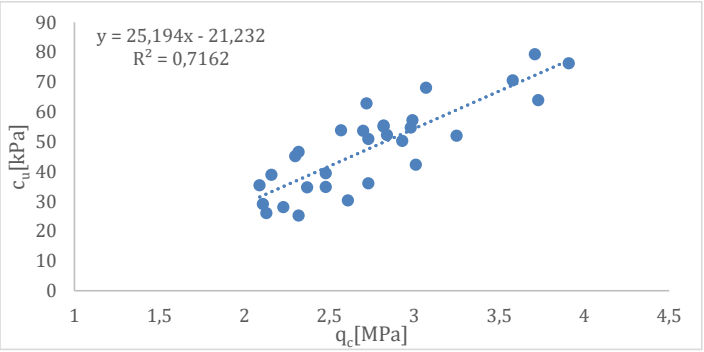


Figure 1. Correlations between cone resistance q_c and the cohesion c_u

According to Figure 1, the results of correlation coefficients show a good level of correlation.

Table 2. Results obtain based on linear correlations between q_c and c_u

Root-mean-square deviation		Correlation coefficients	
S_c	s	r	r^2
7.8	14.65	0.85	0.7

Cone pressure q_c [MPa] and dilatometer modulus M_{DMT} [MPa] were correlated using approximately 31 points. Figure below shows the correlation obtained.

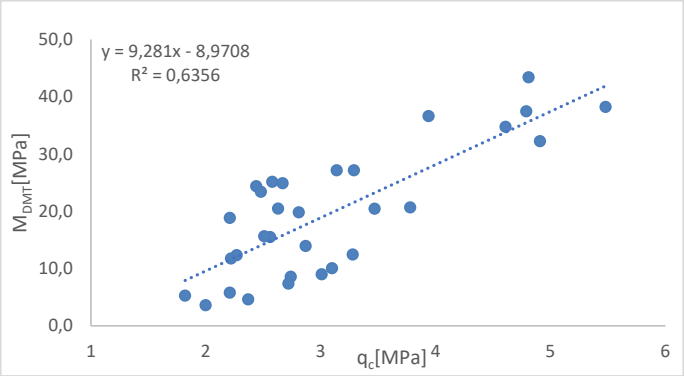


Figure 2. Correlations between cone resistance q_c and dilatometer modulus M_{DMT}

According to Figure 2, the results of correlation factors are presented below.

Table 3. Results obtain based on linear correlations between q_c and M_{DMT}

Root-mean-square deviation		Correlation coefficients	
S_c	s	r	r^2
6.6	10.9	0.8	0.6

Cone pressure q_c [MPa] and oedometer modulus $E_{100\text{-}200}$ [MPa] from laboratory were correlated using the most relevant undisturbed samples until 10 m depth, taken from the loess layer. Figure below shows the obtained correlation.

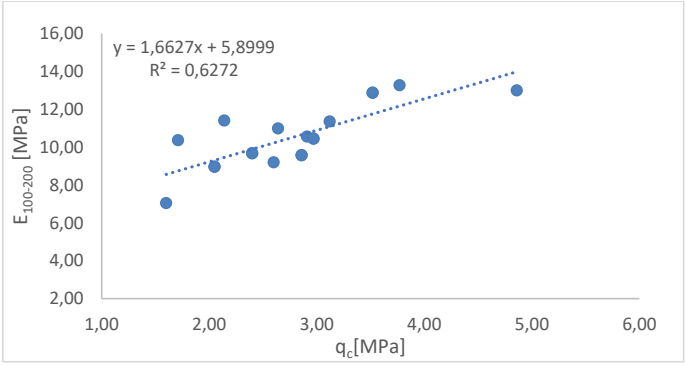


Figure 3. Correlations between cone resistance q_c and the cohesion $E_{100\text{-}200}$

According to Figure 3, the results of correlation factors are presented below.

Table 4. Results obtain based on linear correlations between q_c and $E_{100\text{-}200}$

Root-mean-square deviation		Correlation coefficients	
S_c	s	r	r^2
0.97	1.60	0.78	0.63

Figure 4 shows the correlation of cone pressure q_c [MPa] and the tangent of the internal friction angle φ [-], determined using 22 points.

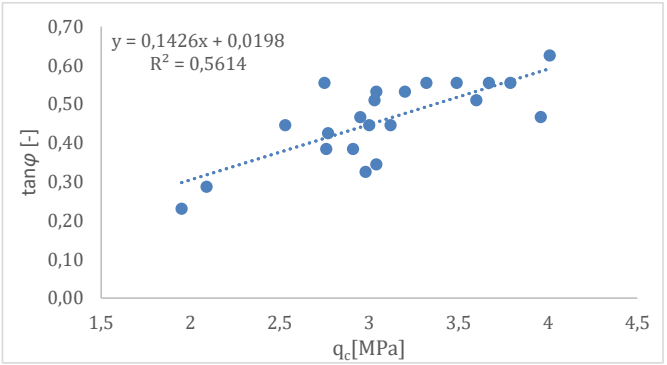


Figure 4. Correlations between cone resistance q_c and the cohesion *tan φ*

According to Figure 4, the results of correlation factors are presented below

Table 5. Results obtain based on linear correlations between q_c and tan φ

Root-mean-square deviation		Correlation coefficients	
S_c	s	r	r^2
0.07	0.10	1.00	0.6

The correlations presented in Figures 1 to 4, obtained using the data from the investigations performed for the loess layer are centralized in the table below. The safe correlation gives an assured value and involves translating the correlation slope by the value of the standard deviation.

Table 6. New proposed correlations obtained on Loess layer

Parameters	New correlation	Correlation coefficients	Standard deviations	Safe correlation
Cone resistance q_c and the cohesion c_u	25.19 q_c - 21.23 [kPa]	0.85	7.8 [kPa]	25.16 q_c – 29.03 [kPa]
Cone resistance q_c and dilatometer modulus M_{DMT}	9.28 q_c - 8.97 [MPa]	0.80	6.60 [MPa]	9.28 q_c – 15.57 [MPa]
Cone resistance q_c and oedometric modulus $E_{100\text{-}200}$ from laboratory	1.66 q_c + 5.90 [MPa]	0.78	0.97 [MPa]	1.66 q_c+ 4.93 [MPa]
Cone resistance q_c and the tangent of the internal friction angle φ	0.143 q_c + 0.02 [-]	1.00	0.07	0.143 q_c - 0.05

4. VALIDATION OF THE NEW CORRELATION

This chapter aims to validate the new correlations obtained in Chapter 3 and to demonstrate their applicability to the specific loess of Romania. The proposed correlations have been compared with those from literature, representing a calibration of the existing correlations.

Table 7. New and literature correlations for undrained shear strength specific to silty clay complex, sensitive to moistening – collapsible

Parameters	c_u		
	New correlation	Soil type	Observations
New correlation	0.025 q_c - 0.021 [kPa]	Cohesive soil	c_u obtained from DMT tests
New safe correlation	0.025 qc - 0.029 [kPa]	Cohesive soil	c_u obtained from DMT tests
(Trofimenkov &	0,0116 qc + 0,0125	Cohesive soil	-

Parameters	c_u		
	New correlation	Soil type	Observations
Vorobkov, 1974)			

In Figure 5 the proposed correlation and the safe correlation are graphically presented in comparison to the literature one (Trofimenkov & Vorobkov, 1974). The measured values of c_u are assigned to a value of q_c between 1.5 [MPa] and 4 [MPa]. The shaded area represents the range of values corresponding to a 95% confidence level of the undrained shear strength c_u determined for a collapsible soil.

By analysing the graph, one can notice that the new correlation tends to overestimate the values of c_u assigned to values of q_c over 2.5 [MPa]. The underestimated values of c_u assigned to a value of q_c lower than 2.5 [MPa] are insignificant. Using the correlation available in literature (Trofimenkov & Vorobkov, 1974), the values of c_u are more conservative due to the safety coefficient applied.

From the graph, it can be noticed that the values of c_u assigned to values of q_c lower than 3.5 [MPa] are underestimated according to the safe correlation. On the other hand, the values of c_u from the literature correlation assigned to the same values of q_c are overestimated.

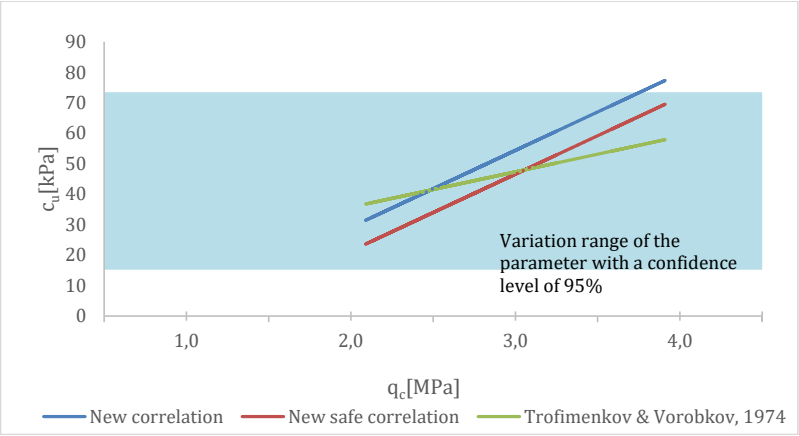


Figure 5. Silty clay complex (loess), comparison of results for new correlations and literature correlations for undrained shear strength c_u

Table 8 presents the new correlations obtained in Chapter 4 and the literature correlations used to indirect determination of deformation modulus E.

Table 8. New and literature correlations for deformation modulus E specific to silty clay complex, sensitive to moistening – collapsible

Parameters	$E_{100\text{-}200}$		
	New correlation	Soil type	Observations
New correlation	1.66 q_c + 5.9	Cohesive soil	Oedometer modulus between 100 and 200 kPa vertical stress
New safe correlation	1.66 q_c+ 4.93	Cohesive soil	Oedometer modulus between 100 and 200 kPa vertical stress
(Marcu, 1983)	4.8 q_c	Cohesive soil	In this case E can be approx. with $E_{100\text{-}200}$

In Figure 6 the propose correlation and safe correlation are graphically presented in comparison to the literature ones (Marcu, 1983). The values of E (deformation modulus) are assigned to a value of q_c between 1.5 [MPa] and 5 [MPa]. The shaded area represents the range of values corresponding to a 95% confidence level of the deformation modulus E determined for a collapsible soil.

A remarkable difference between the values obtained out of the new correlations and of the literature one was noticed by analyzing the graph below. It can be observed that the values of E (deformation modulus) assigned to values of q_c over 2 [MPa] are underestimated. The literature correlation is assigned a safety coefficient leading to differences between this and new correlations obtained in Chapter 3. The data set used to determine the correlations results out of tests carried out on loess specific to Romania.

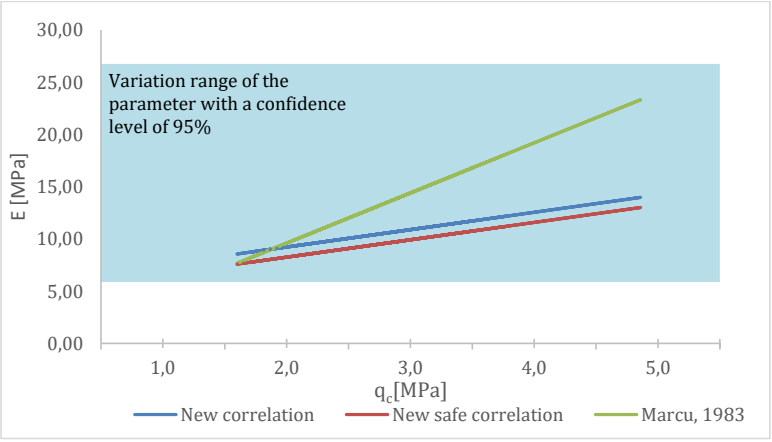


Figure 6. Silty clay complex (loess), comparison of results for new correlations and literature correlations for deformation modulus E

The table below presents the new correlations and the correlation from literature used for indirect determination of the tangent of the internal friction angle φ.

Table 9. New and literature correlations for the tangent of the internal friction angle φ specific to silty clay complex, sensitive to moistening – collapsible

Parameters	Friction angle φ (tan φ)		
	New correlation	Soil type	Observations
New correlation	0.143 q_c + 0.02	Cohesive soil	tanφ determined using direct shear test CUn
New safe correlation	0.143 q_c + 0.05	Cohesive soil	tanφ determined using direct shear test CUn
Trofimenkov & Vorobkov, 1974	0,045 q_c + 0,260	Cohesive soil	-

In Figure 7 the proposed correlation and the safe correlation are graphically presented in comparation to the literature one (Trofimenkov & Vorobkov, 1974). The values of *tang* φ are assigned to a value of q_c between 2 [MPa] and 4 [MPa]. The shaded area represents the range of values corresponding to a 95% confidence level of the tangent of the internal friction angle *tang* φ determined for a collapsible soil.

In the graph below, it can be noticed that the new correlation leads to overestimated values of *tang* φ assigned to a value of q_c bigger than 2.4 [MPa]. On the other hand, values of *tang* φ based on safe correlation and assigned to a value of q_c bigger than 3.10 [MPa] leads to underestimated values compared to the values based on literature correlation.

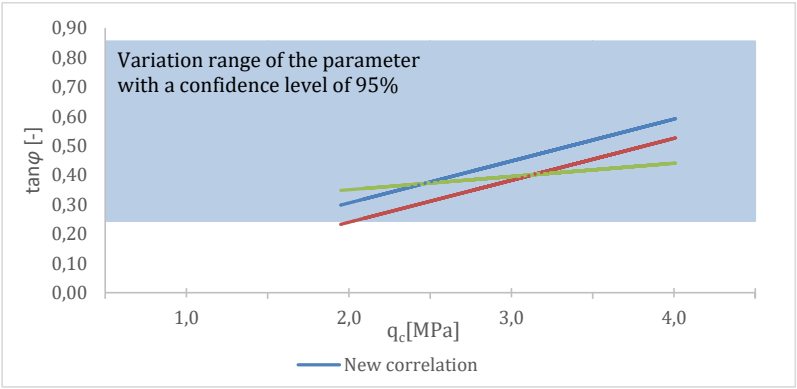


Figure 7. Silty clay complex (loess), comparison of results for new correlations and literature correlations for tangent of the internal friction angle φ

Taking an overview at the graphs presented in this Chapter it can be observed that in all cases analyzed there were differences between new correlations and literature correlations. These differences can be explained by the fact that the new correlations are gained particularly for the collapsible soils of the South-Eastern area of Romania, while existing correlations are valid for more extended areas and not for collapsible loess. The general expressions provided in the Romanian National Annex to Eurocode 7- 2 do not address geotechnical parameters specific to moisture-sensitive soils. NP 125:2010 (Normative on the foundation of buildings on sensitive soils) is the Romanian standard that refers to the variations in the values of geotechnical parameters specific to loess.

5. CONCLUSIONS

Using correlation methods tailored to local specifics, in-situ tests can provide reliable data for foundation design and for modelling of soil behaviour in a shorter time and for a lower budget. In order to achieve the aim, parameters from in situ and laboratory tests carried out for Constanta Wind farm were used. In order to check the accuracy of the new correlations, they were compared with correlations in the literature. By analysing the graphs presented in Chapter 4, it was observed that from the existing correlations a more conservative range of values results are obtained compared to the values from the new correlations.

In conclusion, the proposed correlations in this paper lead to a parameter set optimized for collapsible soil of the South-Eastern area of Romania compared to the parameters obtained from the existing ones.

The new correlations determined are based on data obtained from geotechnical investigations on Constanta Wind farm. By extending the database the proposed correlations can be possibly corrected or their accuracy can be increased. By integrating more sites, it is possible to detail the proposed new correlations according to the area.

REFERENCES

A. Marcu, Fundații speciale. *Cercetarea terenului de fundare și determinarea caracteristicilor geotehnice de calcul*. Institutul de Construcții București, 1983.

NP 122. (2010). *Normativ privind determinarea valorilor caracteristice și de calcul ale parametrilor geotehnici.*

Robertson, P.K. (1990). *Soil classification using the cone penetration test*. Canadian Geotechnical Journal, 151-8.

Trofimenkov, I., & Vorobkov, L. (1974). *Polevie metodi issledovania stritelnih svoistv gruntov*. Gosetroiizdat, Moskva.

28th European Young Geotechnical Engineers Conference – EYGEC 2024
© 2024 Macedonian Association for Geotechnics, ISBN 978-608-4510-61-1

Rock-scour protection settlement due to seismic liquefaction for offshore wind applications

Diarmid .M. Xu[a], Gopal S.P. Madabhushi[b], John M. Harris[c], Richard J.S. Whitehouse[d]

[a] *Ph.D Student, Department of Engineering, University of Cambridge, Cambridge, UK*
[b] *Professor, Department of Engineering, University of Cambridge, Cambridge, UK*
[c] *Research and Innovation Director, HR Wallingford, Wallingford, UK*
[d] *Technical Director, HR Wallingford, Wallingford, UK*

ABSTRACT

Offshore wind is a growing industry that forms a key part in reducing the carbon footprint of electricity generation. Current and future windfarms in North America and East Asia will be built on loose sand in seismically active areas, some of which are both prone to seismic liquefaction and to scour. The most common method to combat or remediate against scour is rock dump, however, there is very limited research into the behaviour of these rocks when subject to seismic liquefaction. From previous work, we know that significant rock loss will occur with a medium earthquake, so this is a valuable area of research. This paper presents the results of multiple saturated, dynamic centrifuge tests, studying the behaviour of scour protection rocks. Rock settlement data are presented and compared, with variations on rock size and rock weight. The results form part of a wider research project that aims to both understand the behaviour, and also to make recommendations to the future design of scour protection rock berms.

KEYWORDS

Offshore wind; Centrifuge testing; Scour protection; Seismic liquefaction.

1. INTRODUCTION

Offshore wind will form a key part in the electricity generation of the future if we are to reduce our carbon emissions whilst keeping up with the ever-growing electricity demand of society. These wind farms contain hundreds of turbines, each the height of a skyscraper, with so many structures, any added certainty or cost savings on a particular foundation, once multiplied across all the turbines on a farm, will mean enormous cost savings for the whole project.

The most common type of offshore wind foundation is the monopile, a large steel tube upwards of 8-10 metres in diameter, which are driven or hammered into the seafloor. Some areas where monopile are installed will be prone to scour, a phenomenon whereby the foundation disturbs the natural flow of currents of the ocean. The effect is the accelerating of the flow close to the structure and increasing the turbulence intensity due to the formation of vortices (Harris et al. 2019). The speed-up in flow may amplify the bed shear stress beyond the value for the threshold of motion for the seabed sediment with vortices helping to remove sediment from around the foundation, resulting in a reduction of embedment depth.

To counter or remediate against scour, rock dump is often used. Quarried rock is loaded onto ships, then dumped around offshore foundations, with the rocks being many thousand times the size and weight of sand, they resist the forces of the redirected current.

Rock berms are typically 30 m in diameter for an 8 m diameter monopile. A 1.5 m high layer of graded rocks will have a bottom filter layer typically consists of 0.1 to 0.2 m diameter rocks, poured to a height of approximately 0.5 to 1 m. This is then covered by an armour layer, for example made of 0.5 m rocks, over 1 m in height. Alternatively, a layer of widely graded rocks of ~ 1.5 m thickness can provide both functions (The Rock Manual, 2007).

While the phenomenon of scour has been recorded and studied in detail, such as the work by Harris and Whitehouse (2017), Harris et al. (2019) Whitehouse and Draper (2020), and Qu et al. (2024). However, the sinking of scour rock due to seismic liquefaction is a relatively new and complex area of research. There is very limited experimental or field data, in addition, the timescale uncertainties associated with scour hole formation mean current designs guidelines leave room for improvement. There are three options for designing a monopile prone to scour (DNV GL 2021):

- Apply scour protection during or right after installation.
- Design the monopile with a deep enough embedded depth that even post scour, the structure remains stable.
- Monitor the foundation and remediate when necessary.

Previous studies by Escribano and Brennan (2017) and Xu et al. (2022) both showed significant settlement of the scour protection rocks, of around 0.35m. Xu et al. (2023) further explored the effect of scour protection rock density. This paper presents the rock berm settlements of several dynamic, saturated centrifuge tests, with varying sand densities and rocks present. Observations and comparisons are made.

2. EXPERIMENTAL METHODOLOGY

2.1. Centrifuge testing

A geotechnical centrifuge is able to spin and accelerate a model to create an elevated gravitational field environment for experimental testing. This is useful because of the non-linear behavior of soils and clays. At the small scale, but at a high g level, the stress and strains of the model can be made to match that of the prototype, avoiding the need for scale testing, which is either impossible or impractical, or prohibitively expensive.

The Turner Beam Centrifuge at the Schofield Centre at the University of Cambridge is 10 m in diameter and has a 150 g-ton capacity, meaning it can take a 1000 kg payload to 150 times earth's gravity (Madabhushi, 2014). A set of scaling laws (Schofield, 1980) can be used to convert between model and prototype scales, when designing the experiment and when studying the test results.

2.2. Model design

The model box measures 730 mm x 250 mm x 400 mm. Figure 1 shows a cross section view of the general test schematic. The tests carried out use a combination of loose sand, dense sand, or a combination of both, with rocks too of different sizes and weights. Table 1 lists the different test ID's and their test parameters.

Figure 2 is a schematic of the rock berm; its size remained the same for all tests. For larger rocks, each rock was placed by hand, while the smaller rocks and coarse sand were gently poured into place. The overburden pressure acting on the sand by the berm also remained the same between tests when only the rock size was changed.

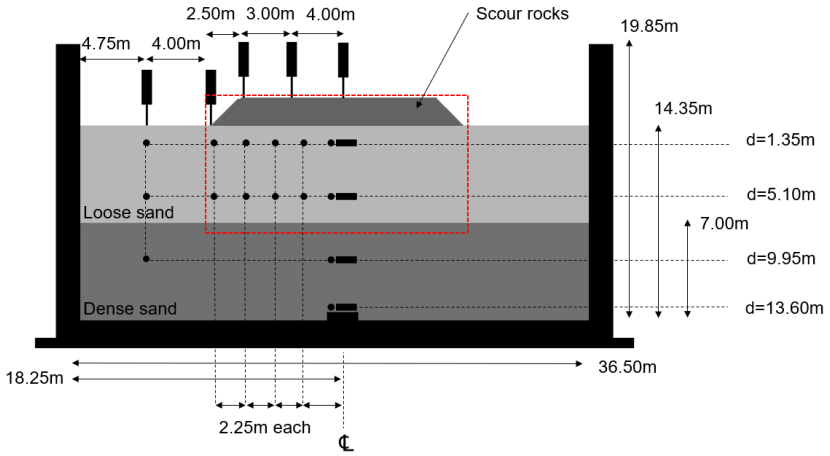


Figure 1. General cross section test schematic

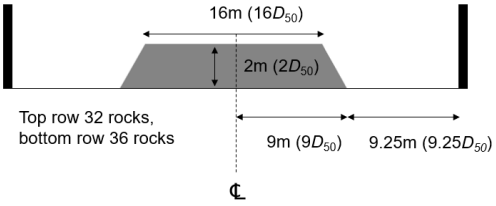


Figure 2. Rock berm schematic

Table 1. Test ID's and test parameters

Test ID	Rock	Prototype rock size (model)	Rock Gs	Sand
DMX01	Initial experiment to determine area of research			
DMX02	Limestone	1.0m (20mm)	2.62	Loose
DMX03	Granite	1.0m (20mm)	2.88	Loose
DMX04	Limestone	0.5m (10mm)	2.62	Loose
DMX05	Experiment with a model rigid plate as rock berm			Loose
DMX06	Gravel	0.4m (8mm)	2.53	Dense over loose
DMX07	Fraction A Sand	0.1m (1.75mm)	2.67	Dense over loose
DMX08	Limestone	0.3m (6mm)	2.59	Dense over loose

2.3. Model soil

Hostun HN31 sand was used for all tests. The sand is naturally white, though a proportion had been dyed black to create contrast for the purpose of particle image velocimetry (PIV), which is beyond the scope of this paper. As this sand is manufactured, its properties are well known and kept constant. Hostun is used as it is a fine grain sand, prototype sand grains cannot be scaled down to model size (as this will result in a clay, which behaves fundamentally different to sand), but as long as the sand grain to rock or structure ratio is greater than 15, then reasonable overall scaling is maintained (Madabhushi, 2014).

An automatic sand pourer (Madabhushi et al., 2006) was used to pour the sand models. By varying the nozzle diameter, nozzle travel speed and drop height, one can vary the volume of sand deposited per unit time, and therefore the resulting relative density (R_d). For these tests, loose sand had an average R_d of 45% and dense sand at 90%, both with a range of ±4%.

Lastly, the model was saturated with methylcellulose to model the sea water. Due to the scaling laws, the fluid at model scale needs to be 50 times as viscous compared to water for a test at 50 g. The "Cam Sat" system (Stringer and Madabhushi, 2009) was used to regulate a partial vacuum to slowly draw fluid into the model from the bottom. The flowrate was kept below 1.5 kg per hour to ensure the sand is not disturbed. Figure 3 shows an example of a completed model.

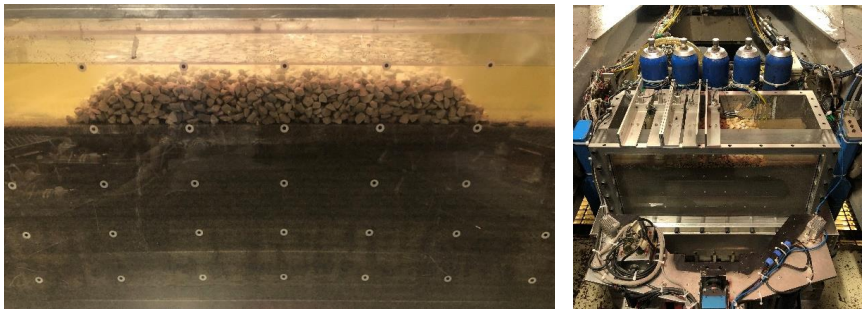


Figure 3. Completed model with rock berm from test DMX08 (left) and the model loaded onto the centrifuge from test DMX06 (right)

2.4. Load sequence

Table 2 shows the load sequence of each test flight. The first small Kobe earthquake is used to test the experiment systems and data acquisition. Next, two large earthquakes are fired to induce liquefaction. Finally, a small earthquake is fired at the end to show little to no settlement on the now densified sand model.

Table 2. Earthquake sequence for tests

ID	Earthquake	Peak bedrock acceleration (prototype g)
EQ1	Kobe, 0.15V	0.045
EQ2	Sine wave, 50Hz, 15 cycles, 2.50V	0.283
EQ3	Sine wave, 50Hz, 15 cycles, 3.00V	0.324
EQ4	Sine wave, 50Hz, 15 cycles, 0.75V	0.050

A servo hydraulic shaker (Madabhushi et al., 2012) was used to simulate earthquakes. Due to centrifuge scaling, the shaker needs to accelerate and move a 25,000 kg block, back and forth a few millimetres, up to 100 times a second (1 Hz earthquake at 100 g). This enormous amount of energy is supplied and stored in high pressure oil, with a fast acting value to control the shake action.

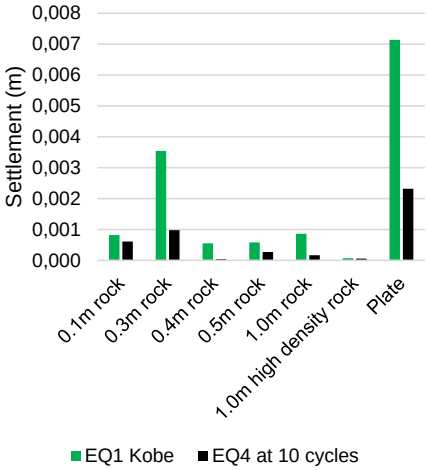
2.5. Instrumentation

The model is made gradually, layer by layer. At certain depths, sensors are placed within the sand model as per figure 1. There are both pore pressure transducers and piezo accelerometers within the sand, and LVDT's on top of the rocks to measure vertical surface displacements in terms of settlements and heave. During the test, sensor data is recorded via DASYLab v13.0 at 6000 Hz. These raw voltages are then filtered, calibrated and scaled to prototype parameters. During all tests high speed cameras record each earthquake so that PIV can be carried out, though this is outside the scope of this paper.

3. RESULTS

The results presented here are of the different mid berm settlements from different earthquakes. Example settlement, pore pressure and acceleration time histories can be found in Xu et al. (2022) and Xu et al. (2023). Figure 4 shows the settlements due to small earthquake input motions, and Figure 5 shows those

of large earthquakes. A mixture of 10 and 15 cycles earthquakes were used in the test series, so all the results presented have been taken at the 10 cycle mark for a fair comparison.



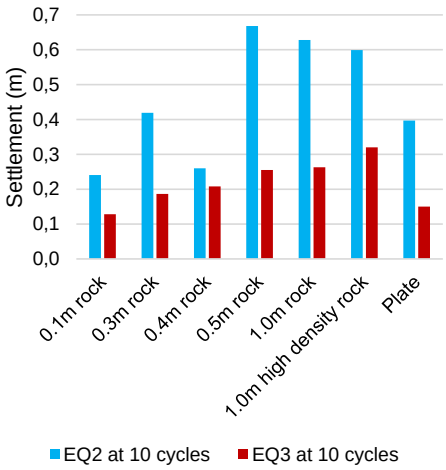


Figure 4. (left) Mid rock berm settlement due to small earthquakes and Figure 5. (right) Mid rock berm settlements due to large earthquakes

From Figure 4 it can be seen that small input motions will cause very small settlements, in the order of a few millimeters, here there is little concern for the stability of the offshore foundation. It is worth noting that an approximate settlement based on a shallow foundation will in fact give a safe over estimate of the actual rock settlement.

In Figure 5 it is shown that there is no linear correlation between rock size and the resulting rock settlement. The peak settlement occurs around 0.5 m, but suddenly drops down for 0.4 m, before increasing again at rocks of 0.3 m. The governing factor is the ingress of sand between the gap of the rock, if there is a lot of ingress, then a higher rock settlement is observed. Depending on the sand particle to rock size ratio, one will find both the maximum ingress (and thus rock settlement) and minimum ingress sizes. From the data presented here, a possible range of scour protection rock settlements are shown for a variety of rock sizes, this ranges from a few millimetres, up to over half a metre, this means losing over a whole layer of rock in some situations.

4. CONCLUSIONS

From the centrifuge tests presented, it can first be seen that there is no linear correlation between rock size and rock settlement. The phenomenon governing the amount of settlement is the ease of ingress of sand in between the rocks, and therefore there must be a combination of rock and sand particle size which either facilitates sand ingress (and thus causing maximum settlement), or a size combination where minimal ingress occurs, which results in minimal settlements.

While the small earthquakes produce very similar settlements, on the order of a few millimetres, one can take make assumptions based on a shallow plate foundation and know that this is a ‘safe’ overestimate of the maximum possible rock settlement.

Lastly, these experiments also give us the range of possible rock settlement resulting from a medium to large earthquake, as the range of rocks used match the sizes present out in the field. The 1 m diameter rocks are the benchmark case and also the worst case scenario (armour rocks without a filter layer). The settlement range is from a few millimetres up to loosing over half a metre of rock, which can be over a

whole rock diameter in some cases. It is important to highlight that it does not take full liquefaction to achieve significant loss of rock.

Future planned work including further investigating berm geometry, the inclusion of a model monopile, and testing global scour conditions. The work presented here form part of a larger Phd project with the aim to better understand the behavior of scour protection rocks under seismic liquefaction.

5. ACKNOWLEDGEMENTS

The authors acknowledge the generous funding from EPSRC and HR Wallingford that made this project possible, and the help and advice of the academics, technicians, and other students at the Schofield Centre.

REFERENCES

Escribano, D. and Brennan, A. 2017. Stability of scour protection due to earthquake-induced liquefaction: Centrifuge modelling. *Coastal Engineering*, 129, pp. 50–58.

Harris, J. M. and Whitehouse, R. 2017. Scour Development around Large-Diameter Monopiles in Cohesive Soils: Evidence from the Field. *Journal of Waterway, Port, Coastal, and Ocean Engineering*, 143(5), p. 4017022. doi: 10.1061/(ASCE)WW.1943-5460.0000414.

Harris, J. M., Whitehouse, R.J.S., Tavouktsoglou, N.S., and Godinho, P.M. 2019. Foundation Scour as a Geohazard. *Journal of Waterway, Port, Coastal, and Ocean Engineering*, 145(6), p. 4019022. doi: 10.1061/(ASCE)WW.1943-5460.0000523.

Madabhushi, S.P.G., Houghton, N.E., Haigh, S.K. 2006. A new automatic sand pourer for model preparation at University of Cambridge. *6th ICPMG'06 - Proceedings of the 6th International Conference on Physical Modelling in Geotechnics*. pp. 217–222.

Madabhushi, G.S.P. et al. 2012. Development of a servo-hydraulic earthquake actuator for the Cambridge Turner beam centrifuge. *International Journal of Physical Modelling in Geotechnics*, 12(2), pp. 77–88.

Madabhushi, G.S.P. 2014. Centrifuge Modelling for Civil Engineers. doi: 10.1201/9781315272863.

Qu, L., An, H., Draper, S., Watson, P., Zhao, M., Harris, J. M., Whitehouse, R.J.S., Zhang, D. 2024. A review of scour impacting monopiles for offshore wind. *Ocean Engineering*, 301, p. 117385. doi: https://doi.org/10.1016/j.oceaneng.2024.117385.

Standard DNVGL-RP-0585. 2021. Available at: https://www.dnv.com/energy/standards-guidelines/dnv-rp-0585-seismic-design-of-wind-power-plants.html.

Stringer, M.E. and Madabhushi, S.P.G. 2009. Novel Computer-Controlled Saturation of Dynamic Centrifuge Models Using High Viscosity Fluids. *Geotechnical Testing Journal - GEOTECH TESTING J*, 32.

The Rock Manual. 2nd Edition 2007. Ciria.

Schofield, A.N. 1980. Cambridge Geotechnical Centrifuge Operations. *Géotechnique*, 30(3), pp. 227–268.

Whitehouse, R. and Draper, S. 2020. Sediment transport and scour in the ocean environment - knowledge and future directions. *ISFOG 2020 – Proccedings of the 4th International Symposium on Frontieres in Offshore Geotechnics*. Available at: http://www.dfi.org/pubdetail.asp?id=3434.

Xu, D.M., Abadie, C.N., Madabhushi, G.S.P., Harris, J. M., and Whitehouse, R.J.S. 2022. Response of armour rock-scour protection to earthquake-induced liquefaction for offshore wind applications. *10th ICPMG 2022 - Proceedings of the 10th International Conference on Physical Modelling in Geotechnics*. pp. 500-503.

Xu, D.M., Madabhushi, G.S.P., Abadie, C.N., Harris, J. M., and Whitehouse, R.J.S. 2023. Effect of rock density on the response of scour protection to earthquake-induced liquefaction for offshore wind applications. *9th SUT OSIG 2023 - Proceedings of the 9th International SUT OSIG Conference*. pp. 1451-1456.

28th European Young Geotechnical Engineers Conference – EYGEC 2024
© 2024 Macedonian Association for Geotechnics, ISBN 978-608-4510-61-1

Geogrid Reinforced Soil Model Calibration Based on Laboratory Testing

Mindaugas Zakarka[a], Šarūnas Skuodis[a], Johannes Kuhlmann[b]

[a] *Department of Reinforced Concrete Structures and Geotechnics, Vilnius Gediminas Technical University, Vilnius, Lithuania*
[b] *Chair of Geotechnical Engineering, Department of Civil Engineering, University of Siegen, Siegen, Germany*

ABSTRACT

Geogrids are widely applied in infrastructure projects to enhance load-bearing capacity and mitigate soil settlement. Understanding the behaviour of soil reinforced with geogrids is crucial for optimizing design practices. This study investigates the mechanical properties of sand samples reinforced with geogrids through laboratory testing and numerical simulations. Triaxial compression tests were conducted for unreinforced and geogrid-reinforced sand samples with a variable confining pressures. The tests revealed an increase in cohesion (apparent cohesion) and minimal change in the angle of internal friction with geogrid reinforcement. Numerical simulations using the Hardening Soil model in PLAXIS 3D were performed to replicate laboratory tests, with adjustments made to improve alignment between numerical and experimental results. The numerical simulations demonstrated good agreement with laboratory-derived deviator peak values, with minor discrepancies observed at low cell pressures. Adjustments to the power index (m) and ultimate stiffness modulus (E_{ur}) were necessary to achieve better alignment, particularly regarding deformations at which the deviator peak occurred. The study concludes that the modelling approach is suitable for accurate triaxial compression tests simulations for soils reinforced with geogrids. The findings contribute to the advancement of geotechnical engineering practices, facilitating more accurate design and analysis of geogrid-reinforced structures.

KEYWORDS

Geogrid reinforcement; Hardening soil model; Triaxial compression test; Numerical simulation.

1. INTRODUCTION

Geogrids are widely utilized in various infrastructure projects to enhance load-bearing capacity and reduce soil settlement (Bhardwaj and Mittal, 2022). Their application aims to improve mechanical properties, which are crucial for ensuring the stability and durability of engineered structures (Zornberg, 2017). Understanding the behaviour of soil reinforced with geogrids is essential for optimizing design and construction practices, prompting extensive research efforts employing numerical simulations, analytical methods, laboratory experiments, and in situ investigations (Makkar, 2019; Zakarka and Skuodis, 2024).

Numerical analysis has become a prevalent tool in geotechnical engineering, offering insights into complex soil-structure interactions and aiding in the optimization of engineering projects (Ikeagwuani and Nwonu, 2019). Constitutive soil models play a pivotal role in numerical simulations, allowing for the representation and prediction of stress-strain behaviour under varying conditions. Among these models, the Hardening Soil model has demonstrated accuracy in simulating triaxial compression test behaviour (Pacheco et al., 2021).

However, the accuracy of numerical simulations heavily relies on the quality of input parameters derived from laboratory or field tests (Konyushkov et al., 2023; Lankaran et al., 2022). Model calibration is often necessary to ensure accurate representation of soil behaviour in numerical models (Calvello and

Finno, 2004). While Mohr-Coulomb strength parameters (c' and φ') are well-established for unreinforced soils (Wu and Tung, 2020), challenges persist in determining mechanical properties for geogrid-reinforced soils (Zakarka et al., 2023).

In particular, understanding compressibility is crucial for accurately simulating deformations in numerical models like PLAXIS 3D. The power index m is a key parameter influencing compressibility, with recommendations varying for different soil types: 0.5 for Norwegian sands and silts (Janbu, 1963), 1.0 for normally consolidated clay (Surarak et al., 2012), 0.45 for rockfill material (Honkanadavar and Sharma, 2016). However, specific recommendations for geogrid-reinforced soils remain scarce, highlighting the need for further investigation.

This study aims to address this gap by conducting consolidated drained (CD) triaxial compression tests on unreinforced sand and sand reinforced with geogrid across a wide range of confining pressures (20, 50, 70, 100, 200, 300 kPa). The obtained parameters will be utilized to simulate laboratory tests using the Hardening Soil model in PLAXIS 3D. By comparing the simulation results with laboratory findings, this research seeks to determine the suitability of existing recommendations for simulating triaxial compression tests for geogrid-reinforced soils.

2. MATERIAL AND METHOD

2.1. Soil Material

The material utilized for this investigation was sand (SaU), conforming to LST EN ISO 14688-2 (Lithuanian Standards Board, 2020). It exhibited a uniformity coefficient (C_U) of 2.25, curvature coefficient (C_C) of 1.08, and an average particle size (d_{50}) of 0.19 mm. The particle size distribution is presented in Figure 1. To ensure consistent testing conditions, soil samples were carefully prepared by recompaction to reach optimal density at the optimal water content, as determined by Proctor compaction testing (Lithuanian Standards Board, 2015). The optimal water content was found to be 14.3%, resulting in a bulk density of the prepared sample of 1.86 g/cm^3.

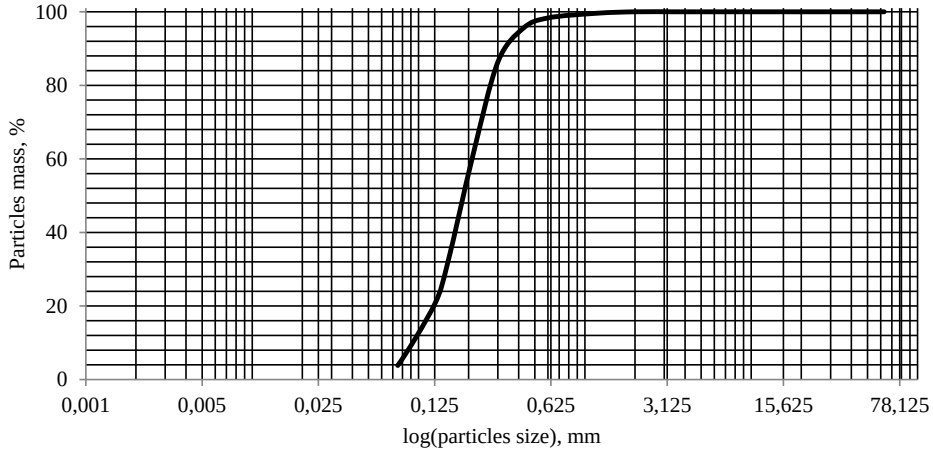


Figure 1. Particle size distribution curve

2.2. Geogrid Reinforcement

Flexible polyester (PET) geogrid with a mesh size of 25 × 25 mm and an ultimate tensile strength of 40 kN/m was employed to reinforce the soil samples. The geogrid was carefully cut into circles with

diameters 3-5 mm smaller than the soil sample's diameter (100 mm), as illustrated in Figure 2, to prevent potential membrane damage.

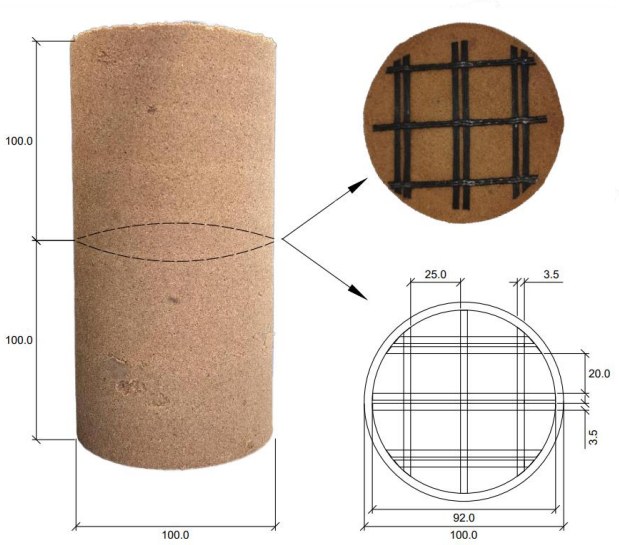


Figure 2. Preparation of the samples example used in the triaxial cell: (left) – prepared soil sample, (right) – geogrid top view in the middle of the sample

2.3. Specimen Preparation

Two types of cylinder specimens were prepared for triaxial compression testing: unreinforced soil and soil reinforced with a single layer of geogrid positioned at the center of the sample. Each specimen had a diameter of 100 mm, and a height of 200 mm. Remolding was achieved through 10 layers at the optimal water content to achieve optimal density.

2.4. Triaxial Compression Testing

Consolidated drained (CD) triaxial compression tests were conducted, initially on soils without geogrid reinforcement, followed by tests on geogrid-reinforced soils. Six different cell pressures (σ_3) were applied during consolidation and loading phases: 20, 50, 70, 100, 200, and 300 kPa. Test conditions were selected in accordance with LST EN ISO 17892-9:2018 (Lithuanian Standards Board, 2018). The consolidation period was set at 30 minutes, with the rate of vertical displacement of the load frame adjusted to 0.95%/min. The test concluded upon loading the specimen up to 15% of vertical deformation.

2.5. Numerical Simulation

Finite element method (FEM) and the SoilTest module of PLAXIS 3D software were employed to model the triaxial compression tests. The Hardening Soil Model (HS) was utilized to simulate the tests, based on plasticity theory, where the stress-strain relationship due to primary load is hyperbolic (Brinkgreve and PLAXIS BV, 1999). The ultimate deviatoric stress (q_f) was determined using the Mohr-Coulomb criterion:

$$q_f = \frac{2\sin\varphi'}{1-\sin\varphi'}(\sigma_3' + c' \cdot \cot\varphi') \quad (1)$$

where c' and φ' are the effective shear strength parameters and σ_3' is the confining stress in the cell.

The confining stress-dependent stiffness modulus (E_{50}) was calculated:

$$E_{50} = E_{50}^{ref} \left(\frac{\sigma_3' + c' \cdot \cot \varphi'}{p^{ref} + c' \cdot \cot \varphi'} \right)^m \quad (2)$$

where E_{50}^{ref} is the reference secant stiffness modulus to be determined from the drained triaxial test, p^{ref} is the reference isotropic stress where a default value equal to 100 kPa is recommended by the software.

The power index *m* is the exponent that defines the strain dependence value of the stress state. The *m* value was obtained by Figure 3.

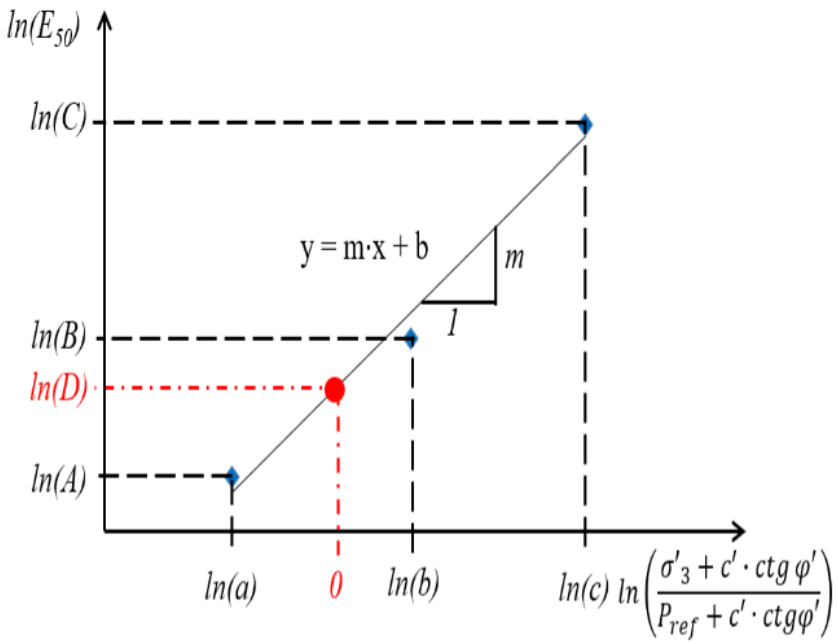


Figure 3. Determination of the Power Parameter *m* Graphically (Konyushkov et al., 2023)

where a trend line:

$$y = a \cdot x + b \quad (3)$$

where *y*:

$$y = \ln E_{50} \quad (4)$$

where *x*:

$$x = \ln \left(\frac{\sigma_3' + c' \cdot \cot \varphi'}{p^{ref} + c' \cdot \cot \varphi'} \right) \quad (5)$$

Other necessary parameters for simulations were determined based on PLAXIS recommendations: E_{oed} equal to E_{50}, E_{ur} equal to $3E_{50}$, ν equal to 0.3, K_0^{nc} equal to $1-\sin \varphi'$ for normally consolidated soils.

3. RESULTS

3.1. Laboratory Testing Results

Interpretation of the results was carried out using the Mohr-Coulomb criterion. For soil samples without geogrid reinforcement, the angle of internal friction (φ) was determined to be 40.67°, with a cohesion c of 0.66 kPa. In contrast, soil samples reinforced with geogrid exhibited an angle of internal friction of 40.93° and a cohesion of 12.62 kPa. The secant stiffness modulus E_{50} values ranged from 17.62 to 90.42 MPa for soil without geogrid reinforcement and from 16.04 to 86.37 MPa for soil with geogrid reinforcement (see Table 1). Additionally, power indexes m were determined as 0.5853 for soil without geogrid and 0.6194 for soil with geogrid (see Figure 4), facilitating the determination of corresponding E_{50}^{ref} values (see Table 1). The average E_{50}^{ref} values were 44.71 MPa for soil without geogrid reinforcement and 49.27 MPa for soil with geogrid reinforcement.

Table 1. Results of Secant Stiffness E_{50} and Power Indexes m

Cell pressure, kPa	Without geogrid			With geogrid		
	Secant stiffness, MPa		Power index	Secant stiffness, MPa		Power index
	E_{50}	E_{50}^{ref}	m	E_{50}	E_{50}^{ref}	m
20	17.62	45.33	0.5853	16.04	42.34	0.6194
50	34.01	51.07		38.24	58.35	
70	32.87	40.51		43.25	53.79	
100	38.03	38.03		44.97	44.97	
200	68.75	45.80		79.93	52.20	
300	90.42	47.51		86.37	43.93	
Average		44.71			49.27	

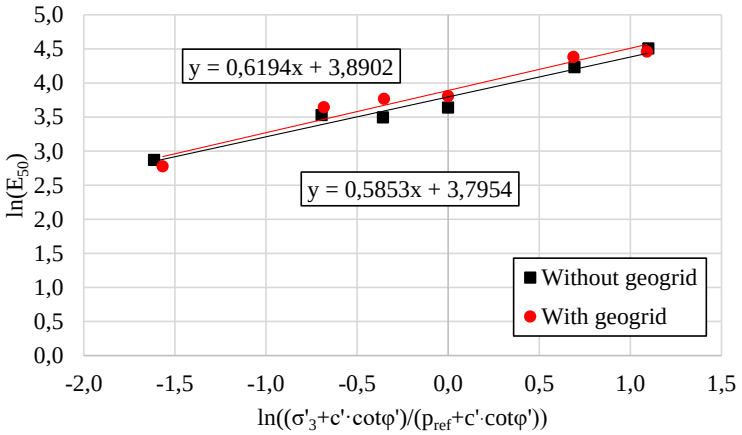


Figure 4. Determination of Power Indexes m for Soil Samples with and without Geogrid Reinforcement

3.2. Numerical Simulations Results

The deviator peak determined by the laboratory tests exceeded that obtained through modelling, particularly evident at a cell pressure of 20 kPa, where discrepancies reached 27.32% for soil without geogrid and 10.06% for soil with geogrid (see Table 2). Although better agreement was observed at higher cell pressures, differences still existed, ranging from -8.67% to 7.75% for soil without geogrid and from -11.85% to 3.53% for soil with geogrid. Significant disparities were also noted in the deformations at which the deviator peak occurred (see Table 2). While laboratory tests indicated

variations from 2.85% to 4.75% for soil without geogrid and from 3.33% to 4.80% for soil with geogrid, modelling yielded a wider range, from 2.10% to 6.00% and from 2.85% to 6.15%, respectively.

Table 2. Results of Deviator Peak (σ_1-σ_3) and Vertical Deformation $(\varepsilon_1)_{100}$ at which the Deviator Peak Occurred

Cell pressure, kPa	Without geogrid					
	Deviator peak σ_1-σ_3, kPa			Vertical def. $(\varepsilon_1)_{100}$, %		
	Experimental	Numerical	Difference	Experimental	Numerical	Difference
20	106.94	77.73	-27.32	2.85	2.10	-26.30
50	208.04	190.00	-8.67	3.38	2.70	-20.13
70	275.35	264.85	-3.81	3.32	3.90	17.40
100	356.29	377.13	5.85	4.11	4.65	13.02
200	697.33	751.37	7.75	4.13	5.10	23.36
300	1147.01	1125.63	-1.86	4.74	6.00	26.53
	With geogrid					
20	145.98	131.29	-10.06	3.33	2.85	-14.31
50	244.19	245.28	0.45	3.41	3.30	-3.13
70	364.48	321.28	-11.86	3.48	3.90	12.17
100	443.51	435.27	-1.86	4.30	4.20	-2.30
200	863.70	815.24	-5.61	4.43	5.40	21.81
300	1154.49	1195.21	3.53	4.80	6.15	28.18

3.3. Parameter Adjustments for Improved Fit

The initial simulations yielded discrepancies in the deformations at which the deviator peak occurred, prompting the need for calibration. To achieve better alignment between laboratory tests and simulation results, iterative adjustments were made to the power index m and ultimate stiffness modulus E_{ur}. Specifically, the values of the power index m and E_{ur} were iteratively adjusted until the simulated deformations closely matched those observed in the laboratory tests. Optimal values of m equal to 0.8 were determined for both soil with and without geogrid, while E_{ur} was set to 3.5 times E_{50} for soil without geogrid and 6 times E_{50} for soil with geogrid. These adjustments resulted in vertical deformations at which the deviator peak occurred varying from 2.85% to 4.65% for soil without geogrid and from 3.15% to 4.80% for soil with geogrid (see Table 3). The final fit between laboratory tests and simulation is illustrated in Figure 5.

Table 3. Results of Vertical Deformations at which the Deviator Peak Occurred $(\varepsilon_1)_{100}$

Cell pressure, kPa	Without geogrid			With geogrid		
	Vertical def. $(\varepsilon_1)_{100}$, %					
	Experimental	Numerical	Difference	Experimental	Numerical	Difference
20	2.85	2.85	0.03	3.33	3.15	-5.29
50	3.38	3.30	-2.38	3.41	3.45	1.27
70	3.32	3.60	8.37	3.48	3.60	3.54
100	4.11	3.90	-5.21	4.30	3.90	-9.27
200	4.13	4.35	5.22	4.43	4.35	-1.88
300	4.74	4.65	-1.94	4.80	4.80	0.04

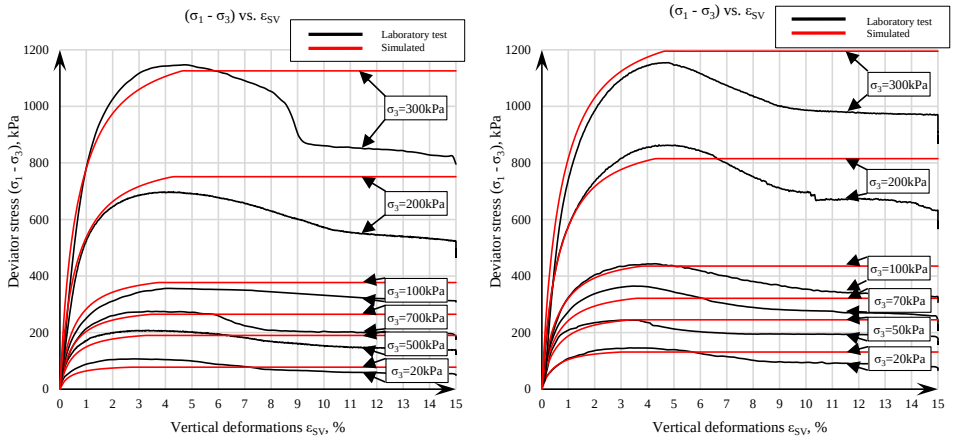


Figure 5. Deviator Stress and Vertical Deformations: (left) – for Soil Samples without Geogrid, (right) – for Soil Samples with Geogrid

The Hardening Soil model accurately simulates soil behaviour up to the deviator peak value, corresponding to vertical deformations ranging from 2.80% to 4.80%. However, it fails to model the post-peak behaviour due to limitations in capturing the residual shear strength, which is a crucial aspect for a comprehensive understanding of geogrid-reinforced soil behaviour.

4. CONCLUSIONS

Based on the findings derived from triaxial compression tests and modelling simulations, several key conclusions can be drawn:

1. Introduction of geogrid reinforcement into sand samples resulted in the creation of apparent cohesion (increasing from 0.66 kPa to 12.62 kPa), while the angle of internal friction exhibited minimal change (from 40.67° to 40.93°).

2. Modelling results demonstrated good agreement with laboratory-derived deviator peak values, with minor discrepancies observed primarily at low cell pressures (e.g., 20 kPa), where model-predicted values were slightly lower.

3. While initial modelling attempts using power index *m* values derived from triaxial compression tests provided satisfactory results for the deviator peak, adjustments to *m* and the ultimate stiffness modulus E_{ur} were necessary to achieve better alignment with laboratory test results, particularly regarding deformations at which the deviator peak occurred.

4. Notably, the modelling approach demonstrated no significant difference between soil samples with and without geogrid reinforcement, suggesting that the method is applicable for accurately modelling triaxial compression tests for soils reinforced with geogrids.

Overall, this study underscores the importance of both laboratory testing and modelling simulations in understanding the behaviour of geogrid-reinforced soils. The insights gained from this research contribute to the advancement of geotechnical engineering practices, facilitating more accurate design and analysis of geogrid-reinforced structures.

5. ACKNOWLEDGEMENT

This research was conducted during the ATHENA and Erasmus research programs, where the numerical simulations using PLAXIS 3D were performed. The conference participation was supported by the Center of Excellence project “Civil Engineering Research Centre” (Grant No. S-A-UEI-23-5).

REFERENCES

Bhardwaj, A., Mittal, S., 2022. Influence of Biaxial Geogrid at the Ballast Interface for Granular Earth Railway Embankment. Balt. J. Road Bridge Eng. 17, 1–20. https://doi.org/10.7250/bjrbe.2022-17.566

Brinkgreve, R.B.J., PLAXIS BV (Eds.), 1999. Beyond 2000 in computational geotechnics: ten years of PLAXIS International ; proceedings of the International Symposium Beyond 2000 in Computational Geotechnics, Amsterdam, the Netherlands, 18 - 20 March 1999. Presented at the International Symposium Beyond 2000 in Computational Geotechnics, Balkema, Rotterdam.

Calvello, M., Finno, R.J., 2004. Selecting parameters to optimize in model calibration by inverse analysis. Comput. Geotech. 31, 410–424. https://doi.org/10.1016/j.compgeo.2004.03.004

Honkanadavar, N.P., Sharma, K.G., 2016. Modeling the triaxial behavior of riverbed and blasted quarried rockfill materials using hardening soil model. J. Rock Mech. Geotech. Eng. 8, 350–365. https://doi.org/10.1016/j.jrmge.2015.09.007

Ikeagwuani, C.C., Nwonu, D.C., 2019. Emerging trends in expansive soil stabilisation: A review. J. Rock Mech. Geotech. Eng. 11, 423–440. https://doi.org/10.1016/j.jrmge.2018.08.013

Janbu, N., 1963. Soil compressibility as determined by oedometer and triaxial tests. Proc ECSMFE 1, 19–25.

Konyushkov, V., Penkov, D., Fedorenko, E., 2023. Initial data for Hardening Soil model. E3S Web Conf. 371, 02019. https://doi.org/10.1051/e3sconf/202337102019

Lankaran, Z.E., Nik Daud, N.N., Rostami, V., Yusoff, Z.Md., 2022. Consolidated Drained Triaxial Test on Treated Coastal Soil and Finite Element Analysis Using PLAXIS 2D. Adv. Mater. Sci. Eng. 2022, 1–15. https://doi.org/10.1155/2022/7263333

Lithuanian Standards Board, 2020. Geotechnical Investigation and Testing—Identification and Classification of Soil—Part 2: Principles for a Classification.

Lithuanian Standards Board, 2018. Geotechnical Investigation and Testing—Laboratory Testing of Soil—Part 9: Consolidated Triaxial Compression Tests on Water Saturated Soils.

Lithuanian Standards Board, 2015. Unbound and Hydraulically Bound Mixtures—Part 2: Test Methods for Laboratory Reference Density and Water Content—Proctor Compaction.

Makkar, F.M., 2019. A Review on the Behaviour of Soil against Different Geosynthetic Interfaces. Presented at the International Conference on Geotechnics for High Speed Corridors, India.

Pacheco, K.W., Matheus, B.C., Pacheco, L.M., Sampa, N.C., Dienstmann, G., 2021. Analysis Of Araquari Sand Behavior Thought Numerical Modeling Of Triaxial Tests, Proceedings of the joint XLII Ibero-Latin-American Congress on Computational Methods in Engineering and III Pan-American Congress on Computational Mechanics, ABMEC-IACM, Rio de Janeiro, Brazil, November 9-12.

Surarak, C., Likitlersuang, S., Wanatowski, D., Balasubramaniam, A., Oh, E., Guan, H., 2012. Stiffness and strength parameters for hardening soil model of soft and stiff Bangkok clays. Soils Found. 52, 682–697. https://doi.org/10.1016/j.sandf.2012.07.009

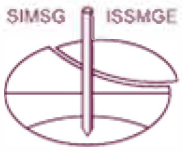
Wu, J.T.H., Tung, S.C.-Y., 2020. Determination of Model Parameters for the Hardening Soil Model. Transp. Infrastruct. Geotechnol. 7, 55–68. https://doi.org/10.1007/s40515-019-00085-8

Zakarka, M., Skuodis, Š., 2024. Analysis of Soil-Geogrid Interaction and Alternative Soil Layer Approach for Improved Road Embankment Stability, in: Barros, J.A.O., Kaklauskas, G., Zavadskas, E.K. (Eds.), Modern Building Materials, Structures and Techniques, Lecture Notes in Civil Engineering. Springer Nature Switzerland, Cham, pp. 643–649. https://doi.org/10.1007/978-3-031-44603-0_66

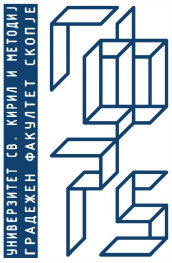
Zakarka, M., Skuodis, Š., Dirgėlienė, N., 2023. Triaxial Test of Coarse-Grained Soils Reinforced with One Layer of Geogrid. Appl. Sci. 13, 12480. https://doi.org/10.3390/app132212480

Zornberg, J.G., 2017. Functions and Applications of Geosynthetics In Roadways. Procedia Eng. 189, 298–306. https://doi.org/10.1016/j.proeng.2017.05.048













CHAMBER OF CERTIFIED ARCHITECTS
AND CERTIFIED ENGINEERS OF REPUBLIC OF MACEDONIA





CON
CEPT
STRUC
TURE

HUESKER
Ideas. Engineers. Innovations.

BRUGG
Geobrugg

ISCHEBECK
TITAN

HYPER FIBERS

Tensar
A Division of CMC





GEING
Excellence in Engineering

GeoMint

MACCAFERRI
BALKANS

БИТЕМ

ГЕОИНГ
+389 2 308 16 18
geoing@geoing.mk
www.geoing.mk
Бул. М.Теодосие Гологанов бр.147/III/лок.5
1000 Скопје, Македонија

IRD ENGINEERING

ИНВЕСТИНГ

Друштво за трговија, градежништво и услуги
ИНВЕСТИНГ ДООЕЛ Радовиш

CIVIL ENGINEERING INSTITUTE
MACEDONIA

ПЕЛАГОНИЈА
А.Д. ГОСТИВАР

Гео Дизајн Инженеринг
Друштво за градежништво, проектирање,
инженеринг, посредување и услуги

ТЕМПЕСТ
трговија на големо и мало

"ТЕМПЕСТ" дооел експорт-импорт
Т.Ц. "13-ти Ноември" спрат I - локал 2, 1000 Скопје,СЕВЕРНА МАКЕДОНИЈА тел. ++ 389 75 231 953
жиро-сметка 300000000220905 е.д.с 4030990238740 депонент на "Комерцијална банка" а.д. Скопје
www.matest.com

РУДНИК ЗА БАКАР
БОРОВ ДОЛ
BOROV DOL
COPPER MINE

GEO5

rocscience

CIP - Каталогизација во публикација Национална и универзитетска библиотека „Св. Климент Охридски“, Скопје

624.13(062)

EUROPEAN Young Geotechnical Engineers Conference – EYGEC (28 ; 2024 ; Demir Kapija)
Proceedings of the 28th European Young Geotechnical Engineers Conference – EYGEC 2024 / 25-29.6.2024, Demir Kapija, R. N. Macedonia. - Skopje : Macedonian Association for Geotechnics, 2024. - [**361**] стр. : илустр. ; 24 см

Библиографии: стр. **361**

ISBN 978-608-4510-61-1

а) Геотехника – Собири

COBISS.MK-ID 63907845

28TH

European Young Geotechnical Engineers Conference

